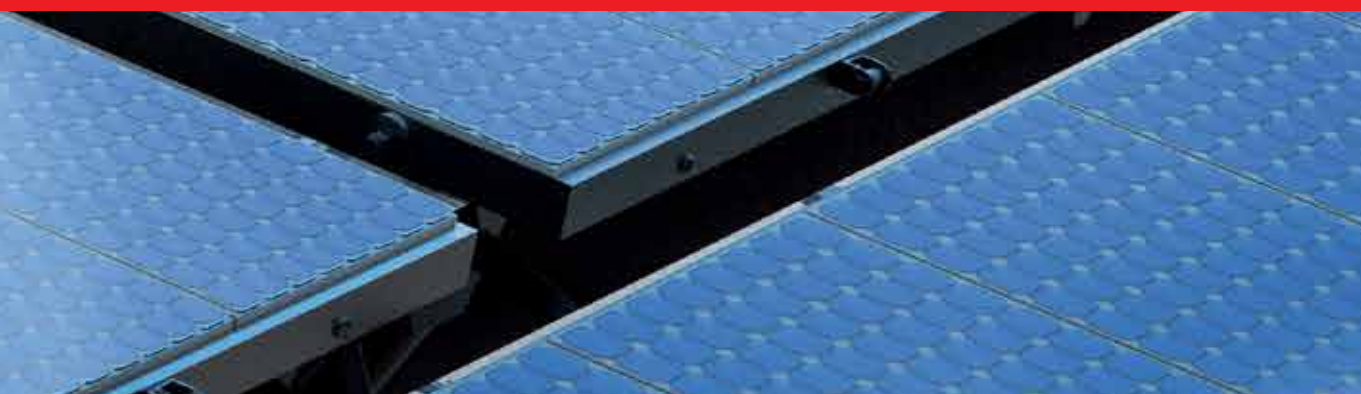# Solar Cells
Dye-Sensitized Devices

Edited by Leonid A. Kosyachenko

SOLAR CELLS – DYE-SENSITIZED DEVICES

Edited by **Leonid A. Kosyachenko**

Solar Cells - Dye-Sensitized Devices
http://dx.doi.org/10.5772/1757
Edited by Leonid A. Kosyachenko

Contributors

Periyayya Uthirakumar, Xiang-Dong Gao, Xiaomin Li, Cailu Wang, Yong Woo Kim, Deug Woo Lee, Khalil Ebrahim Jasim, Hyung-Shik Shin, Sadia Ameen, Seigo Ito, Qiquan Qiao, William Vallejo, Cesar Quiñones, Johan Alexander Hernandez, Ho-Gyeong Yun, Yongseok Jun, Byeong-Soo Bae, Man Gu Kang, Motonari Adachi, Katsuya Yoshida, Takehiro Kurata, Jun Adachi, Katsumi Tsuchiya, Yasushige Mori, Fumio Uchida, Sheng Meng, Yang Jiao, Fan Zhang, Yahia Chergui, N Nehaoua, Djamel Eddine Mekki, Ying-Hung Chen, Ju-Liang He, Keh-Chang Chen, Shu-Yuan Wu, Chen-Hon Chen, Chiung-Hsun Chen, Ming-Yi Hsu, Masaya Chigane, Mitsuru Watanabe, Tsutomu Shinagawa, Lorenzo Dominici, Daniele D'Ercole, Girolamo Mincuzzi, Daniele Colonna, Thomas M. Brown, Andrea Reale, Aldo Di Carlo, Francesco Michelotti, Riccardo Riccitelli, Jin-Kook Lee, Mi-Ra Kim, Eliane F. Chinaglia, Nair Stem, Sebastião G. Dos Santos Filho, Zhigang Chen, Minghua Tang, Qiwei Tian, Junqing Hu, Elias Stathatos, Matthew James Griffith, Attila Mozer, King-Chuen Lin, Chun-Li Chang

Notice

Statements and opinions expressed in the chapters are these of the individual contributors and not necessarily those of the editors or publisher. No responsibility is accepted for the accuracy of information contained in the published chapters. The publisher assumes no responsibility for any damage or injury to persons or property arising out of the use of any materials, instructions, methods or ideas contained in the book.

We are IntechOpen,
the world's leading publisher of Open Access books
Built by scientists, for scientists

4,100+
Open access books available

116,000+
International authors and editors

120M+
Downloads

151
Countries delivered to

Our authors are among the

Top 1%
most cited scientists

12.2%
Contributors from top 500 universities

Interested in publishing with us?
Contact book.department@intechopen.com

Numbers displayed above are based on latest data collected.
For more information visit www.intechopen.com

Meet the editor

Dr. Leonid A. Kosyachenko is professor of National University of Chernivtsi, Ukraine. After receiving his Doctor of Sciences Degree in Physics and Mathematics in 1983, he founded and became a head of Optoelectronics Department – the first department of this kind at Ukrainian universities. About twenty of his pupils have performed work to obtain the degrees of Candidate (Ph.D.) and Doctor of Sciences. His research interests have been in physics and technology of solar cells, semiconductor X-ray and γ-ray detectors, light-emitting and photosensitive devices. He is author (co-author) of several books and numerous scientific articles; presented reports at international scientific conferences and meetings in Germany, Italy, England, Japan, China, Greece, Spain, Belgium, Russia. He was the leader of several collaborative projects with the institutions of Russia, Belorussia and is one of the leaders of the long-term projects of the European Commission. Prof. L.A. Kosyachenko is a member of the Ukrainian Physical Society and the guest editor of journal "Solar Energy Materials and Solar Cells".

Contents

Preface

Most solar modules used in photovoltaics are currently produced from crystalline and polycrystalline silicon wafers, the representatives of so-called first generation of solar cells. This type of devices are among the most efficient but at the same time the most expensive since they require the highest purity silicon and involve a lot of stages of complicated processes in their manufacture. Wafer-based silicon photovoltaics is giving place to thin-film technology, which provides much higher performance and lower cost of products, but inferior to silicon solar modules in photoelectric efficiency. Intensive search for materials and solar cell structures for photovoltaics is continuing. They are mostly yet too immature to appear in the market but some of them are already reaching the level of industrial production.

The second book of the four-volume edition of "Solar cells" is devoted to dye-sensitized solar cells (DSSCs), which are considered to be extremely promising because they are made of low-cost materials with simple inexpensive manufacturing procedures and can be engineered into flexible sheets. DSSCs are emerged as a truly new class of energy conversion devices, which are representatives of the third generation solar technology. Mechanism of conversion of solar energy into electricity in these devices is quite peculiar. The achieved energy conversion efficiency in DSSCs is low, however, it has improved quickly in the last years. It is believed that DSSCs are still at the start of their development stage and will take a worthy place in the large-scale production for the future.

It appears that chapters presented in this volume will be of interest to many readers.

Professor, Doctor of Sciences, Leonid A. Kosyachenko
National University of Chernivtsi
Ukraine

Chasing High Efficiency DSSC by Nano-Structural Surface Engineering at Low Processing Temperature for Titanium Dioxide Electrodes

Ying-Hung Chen, Chen-Hon Chen, Shu-Yuan Wu, Chiung-Hsun Chen, Ming-Yi Hsu, Keh-Chang Chen and Ju-Liang He
Department of Materials Science and Engineering, Feng Chia University
Taichung, Taiwan,
R.O.C.

1. Introduction

The rapid shortage of petrochemical energy has led to the great demand in developing clean and renewable energy sources; such as solar cells in these years. The first commercially available photovoltaic cell (PV) by using solar energy is silicon-based solar cell however with high production cost and high energy payback time. This limited the usage and agitated vigorous studies on the next-generation solar cells in order to reduce cost and increase efficiency. It was until 1991, dye-sensitized solar cells (DSSCs) have attracted increasing interests by the pioneering work of O'Regan and Grätzel. They used a Ru-based dye to achieve higher conversion efficiency in a cell made of titania (TiO_2) as the active layer. Recent development of solar cells in dye-sensitized type devices is one great step forward in the field. The DSSCs take advantages in simple fabrication technique and low production costs in contrast to those conventional silicon-based solar cells.

The DSSC device (Fig. 1) is basically comprised of two facing electrodes: a transparent photoanode, consisting of a mesoporous large band gap semiconductor as an active layer, modified with a monolayer of dye molecules and a Pt counter electrode, both deposited on conductive glass substrates, for example: indium tin oxide (ITO) glass. An appropriate medium containing the redox couple (usually I^-/I_3^-) is placed between the two electrodes to transfer the charges. Among other semiconductors employed as the active layer of the DSSCs, titania known to have wide energy band gap, can absorb dye and is capable of generating electron-hole pairs via photovoltaic effect. DSSCs based on mesoporous titania, which exhibits very high specific surface area (and better dye-absorbing) has been drawn much attention over the past few years. A number of surface modification techniques have been reported to produce nanostructural TiO_2 layer. Moreover, researchers suggested that one dimensional nanostructural TiO_2 such as nano-rods, nano-wires or nano-tubes is an alternative approach for higher PV efficiency due to straightforward diffusion path of the free electron once being generated. For these reasons, we use several cost-effective manufacturing methods to develop the nanostructural TiO_2 electrode at near room

temperature to form several types of DSSC device configuration and to investigate their PV efficiency. The aim is to develop feasible routes for commercializing DSSCs with high PV efficiency.
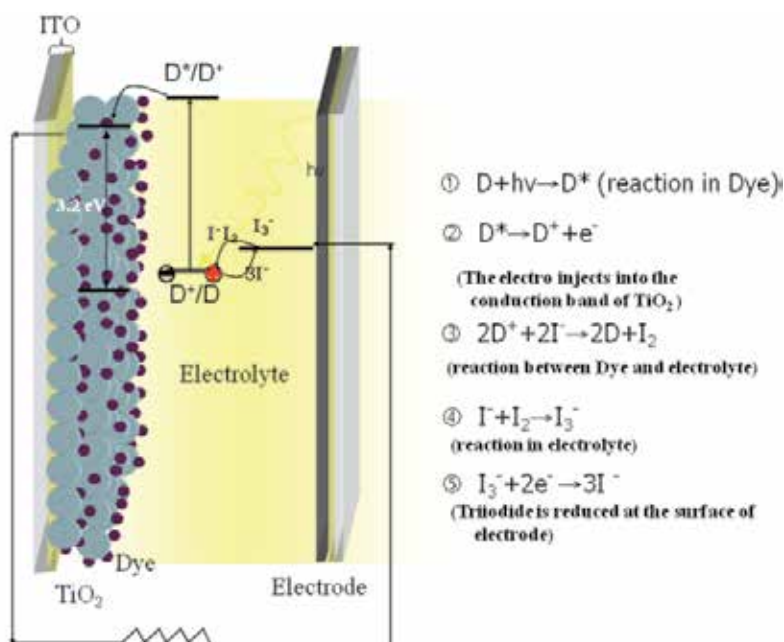
Fig. 1. Schematic of the principle for dye sensitized solar cell to indicate the electron energy level in different phases. (The electrode sensitizer, D; D*, electronically excited sensitizer; D+, oxidized sensitizer)

This chapter demonstrates four kinds of manufacturing methods to obtaion nanostructural photoanode for the purpose of achieving high efficiency DSSCs. These manufacturing methods were involved with each method chosen with good reason, but went out with different performance. These involves *liquid phase deposition (LPD) to grow TiO₂ nanoclusters layer*, *hydrothermal route (HR) to obtain TiO₂ nanowires*, *PVD titanium followed by anodic oxidation to grow TiO₂ nanotubes*, and *eventually microarc oxidation (MAO) /alkali etching to produce nanoflaky TiO₂*. The first three methods can directly grow TiO₂ layer on ITO glass and the specimens were assembled into ITO glass/[TiO₂(N3 dye)]/I₂+LiI/Pt/ITO glass device. The last method can only obtain TiO₂ layer on titanium and was assembled into Ti/[TiO₂(N3 dye)]/I₂+LiI/Pt/ITO glass inverted-type device. Microstructural characterization and observation work for the obtained nano featured TiO₂ were carried out using different material analyzing techniques such as field-emission scanning electron microscopy, high-resolution transmission electron microscopy and X-ray diffractometry. All the PV measurements were based on a large effective area of 1 cm x 1cm. The DSSC sample devices were then irradiated by using a xenon lamp with a light intensity of 6 mW/cm², which apparently is far lower than the standard solar simulator (100 mW/cm²). It would then be true for the photovoltaic data reported in this article for cross-reference within this article and not validated for inter-laboratory cross-reference. Photocurrent–voltage (*I–V*) characteristics were obtained using a potentiostat (EG&G 263A). Photovoltaic efficiency of

each cell was calculated from *I-V* curves. The results for each study are reported and discussed with respect to their microstructure as below.

2. Nanocluster-TiO$_2$ layer prepared by liquid phase deposition

The LPD process, which was developed in recent years, is a designed wet chemical film process firstly by Nagayama in 1988. Than Herbig et al. used LPD to prepare TiO$_2$ thin film and studied its photocatalytic activity. Most vacuum-based technologies such as sputtering and evaporation are basically limited to the line-of-sight deposition of materials and cannot easily be applied to rather complex geometries. By contract, the easy production, no vacuum requirement, self-assembled and compliance to complicated geometry substrate has led many LPD applications for functional thin films. In order to directly grow nanocluster-TiO$_2$ on ITO glass, the simplest method - LPD process was firstly considered by using H$_2$TiF$_6$ and H$_3$BO$_3$ as precursors. The reaction steps involved to obtain nanocluster-TiO$_2$ are illustrated as followed. The H$_3$BO$_3$ pushes eq. (1) to form eventually Ti(OH)$_6{}^{2-}$ which transforms into TiO$_2$ after thermal annealing.

$$(TiF_6)^{2-} + nH_2O \leftrightarrow TiF_{6-n}(OH)_n^{2-} + nHF \tag{1}$$

$$H_3BO_3 + 4HF \leftrightarrow BF^{4+} + H_3O + 2H_2O \tag{2}$$
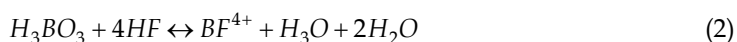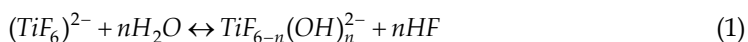
Here, the influence of deposition variables including deposition time and post-heat treatment on the microstructure of TiO$_2$ layer and the photovoltaic property was studied. The LPD system to deposit titania film is schematically shown in Fig. 2.
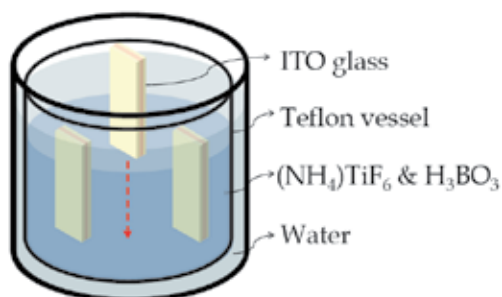
Fig. 2. Schematic diagram of LPD-TiO$_2$ deposition system.

Figure. 3 shows the *I-V* characteristics of the DSSCs assembled by using TiO$_2$ films deposited for different time, with their corresponding surface and cross sectional film morphology also shown. It was indeed capable of producing nanocluster featured TiO$_2$ films shown in the surface morphology, regardless of the deposition time. It can also be found that the *I-V* characteristics are sensitive to the TiO$_2$ film deposition time, but unfortunately non-linearly responded to the deposition time. By careful examination on the surface morphology of these TiO$_2$ films deposited at different deposition time, the film obtained at longer period of deposition time, say 60 h presents no longer nanocluster feature, but cracked-chips feature instead. This significantly reduces the open circuit voltage (V_{oc}) as well as the short circuit current density (J_{sc}). It shall be a consequence of the cracks that leads to the direct electrolyte contact to the front window layer (to reduce V_{oc}) and the

reduced specific surface area (to reduce J_{sc}). Further exam cross sectional morphology of the TiO_2 films as a function of deposition time, it was found that the film thickness does not linearly respond to the deposition time. This shall be the gradual loss of reactivity of the electrolyte liquid. Therefore, it is not practical to increase the film thickness by an extended deposition time. Still, we believed that by constant precursor supplement into the electrolyte liquid, it would refresh the liquid and certainly the increased film growth rate, of course with the price of process monitoring automation.
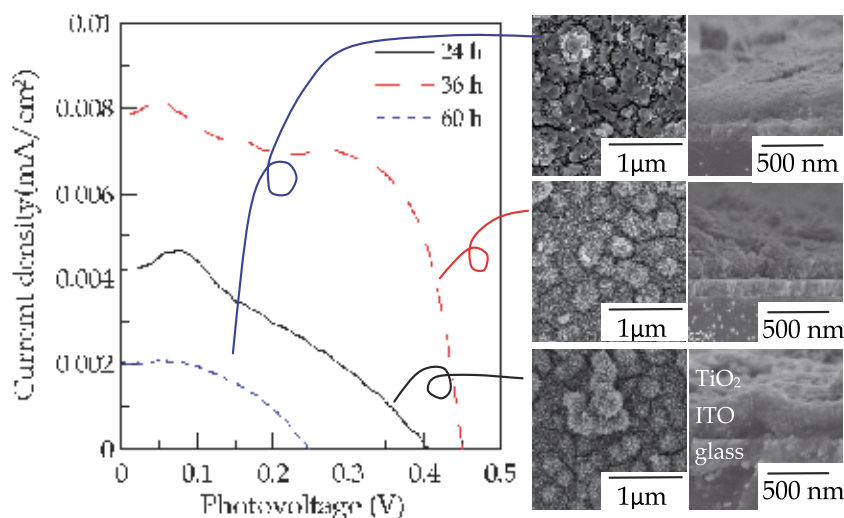
Fig. 3. *I-V* characteristic of the cell assembled by LPD-TiO_2 under different deposition time, with their corresponding surface and cross sectional film morphology.

Fig. 4 shows the XRD patterns of the TiO_2 film with different annealing temperature. The results indicate that the as-deposited film was amorphous due to the low LPD growth temperature. Annealing provides thermal energy as a driving force to overcome activation energy that required for crystal nucleation and growth. The exact TiO_2 phase to be effective for DSSC has been known to be anatase, which can found that the peak ascribed to anatase phase A(101) can only appear over 400 °C and become stronger over 600 °C, ie. better crystallinity of the film annealed at higher temperature. Over an annealing temperature of 600 °C leads to the ITO glass distortion.

The *I-V* characteristics of the DSSCs assembled by using TiO_2 films with different annealing temperatures, with their corresponding surface and cross sectional film morphology are shown in Fig. 5. The TiO_2 film surface forms numerous tiny nanocracks and needle-like structures with increasing annealing temperature. It can be found that the *I-V* characteristics are sensitive to the TiO_2 film annealing temperatures and the J_{sc} increases straight up to a maximum when annealed at 600 °C. Apparently, the increase of J_{sc} shall be associated with the reformation of the TiO_2 film morphology and the increased film crystallinity. By reforming numerous tiny nanocracks and needle-like structures, the TiO_2 film has more specific surface area after post-annealing and achieves higher efficiency dye adsorbing. However, the negative effect of annealing occurred to the significant increase of the ITO electrical resistance that causes the V_{oc} drop off as can be seen in Fig. 5. Anyhow, the overall increased photovoltaic efficiency as a function of annealing temperature is an encouraging

result of this study using PLD to obtain TiO_2 film and post-annealing for DSSC photoanode preparation.
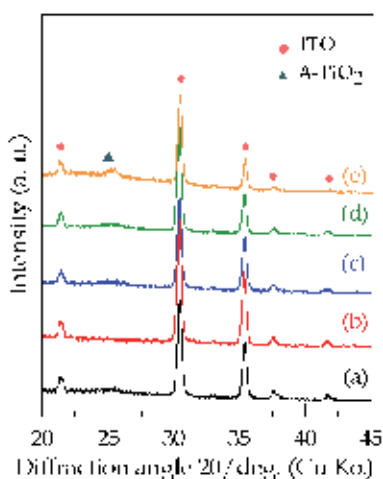
Fig. 4. XRD patterns of (a) ITO glass substrate, (b) TiO_2 as-deposited specimen, and the post annealed specimens obtained at (c) 200, (d) 400 and (e) 600 °C for 30 min.
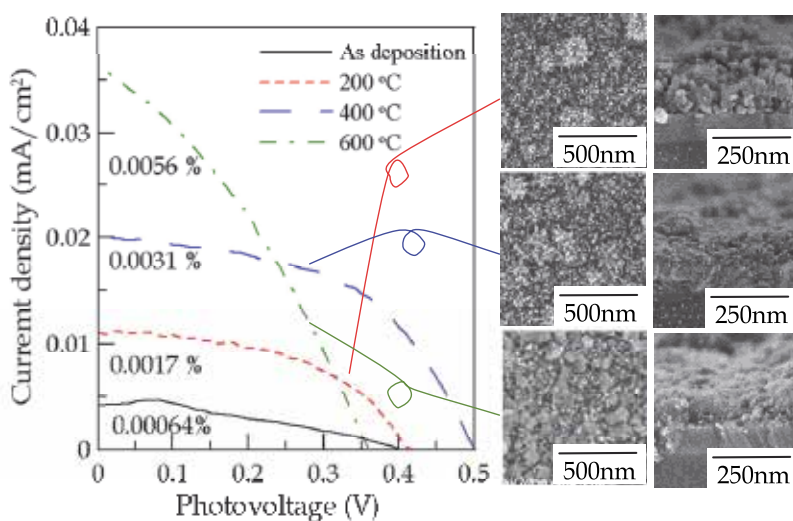
Fig. 5. *I-V* characteristic of the cell assembled by LPD-TiO_2 under different annealing temperature, with their corresponding surface and cross sectional film morphology.

2.1 Summary

In this paragraph, a LPD system is used to prepare the TiO_2 layer on ITO glass at the room temperature followed by post-annealing as the photoanode in DSSC. The result is closely connected to the variation of microstructure including both the specific surface area and crystal structure. This demonstration work confirms the truth that the LPD method is capable of obtaining nanocluster TiO_2 and with crystallinic anatase structure through

suitable annealing treatment. Unfortunately, the unacceptable LPD-TiO$_2$ film growth has led some other attempts to obtain nano-structural TiO$_2$ layer. These methods are sketched as below.

3. TiO$_2$ nanowires growth on TiO$_2$ template via hydrothermal route

As being well acknowledged that pressurized hydrothermal route is able to synthesize 1D nanomaterials without using catalysts. Due to 1D nanomaterials (such as nanowires) having a relatively higher interfacial charge transfer rate and specific surface area compared with the spherical TiO$_2$ particles and nanocluster TiO$_2$, the simple operation, fast formation and low cost process interested us using this method to produce TiO$_2$ nanowires. The idea was that via the hydrothermal (HR) growth of TiO$_2$ nanowires on an arc ion plated (AIP) TiO$_2$ layer (as a template during HR and a barrier layer during service that pre-deposited on ITO glass), the obtained film would be able to exhibit the desired photoanode properties. AIP is known to be capable of producing high growth rate, high density and strong adhesion films without additional substrate heating, the pre-deposited AIP-TiO$_2$ template might also be able to get rid of the autoclave while at least well-aligned or randomly-oriented TiO$_2$ nanowire can be grown. In this study, anatase Degussa TG-P25 powder was used as starting material. Eventually, the experimental result showed the randomly-orientated TiO$_2$ nanowires were formed on AIP-TiO$_2$ template. TiO$_2$ powder content in the HR bath (g/l) and post-annealing temperature were evaluated their microstructure and photovoltaic efficiency of the assembled DSSC devices. The HR system and preparation method to obtain TiO$_2$ nanowires is illustrated in Fig. 6.
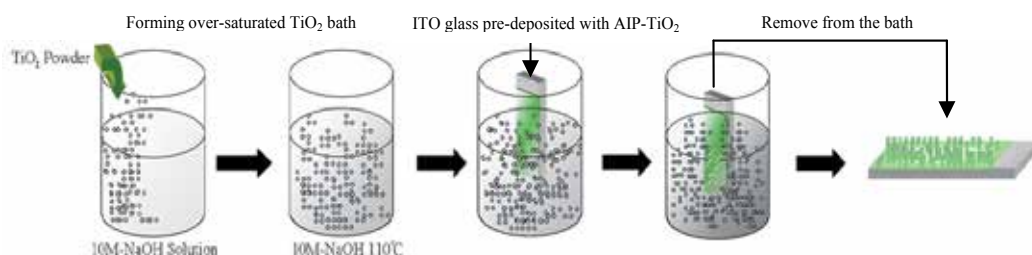
Fig. 6. The HR system and preparation method to obtain TiO$_2$ nanowires.

Figure. 7 shows the *I-V* characteristics of the DSSCs assembled by using HR-TiO$_2$ as the photoanode deposited at different TiO$_2$ powder content, with their corresponding surface and cross sectional film morphology also shown. The dense columnar AIP-TiO$_2$ bottom layer can partially be seen in cross sectional view for each specimen. The result of *I-V* curve for the DSSC assembled directly from Degussa TG-P25 as the photoanode is also shown. The HR was indeed capable of generating randomly-stacked TiO$_2$ nanowires on template, regardless of the TiO$_2$ content. It can also be found that the *I-V* characteristics are sensitive to the TiO$_2$ powder content, but unfortunately non-linearly responded. The HR-TiO$_2$ obtained at high TiO$_2$ content, say 75 g/l, presents no longer nanowires, but agglomerated powdery feature instead. This corresponds to a less specific surface area for dye adsorption and a decreased overall photovoltaic efficiency (mainly cause a reduction of the J_{sc}). From cross sectional image, the as-grown HR-TiO$_2$ thickness is insusceptible to the TiO$_2$ powder

content. Ultimately, the highest photovoltaic efficiency of 3.63 % is achieved for the HR-TiO$_2$ obtained at a 50 g/l TiO$_2$ powder content. Interestingly, some of the photovoltaic efficiency of DSSCs assembled from HR-TiO$_2$ nanowires surpassing that of the DSSC assembled from Degussa P-25 powder, proves that using the one-dimensional structure to enhance DSSC efficiency is conceptually correct.
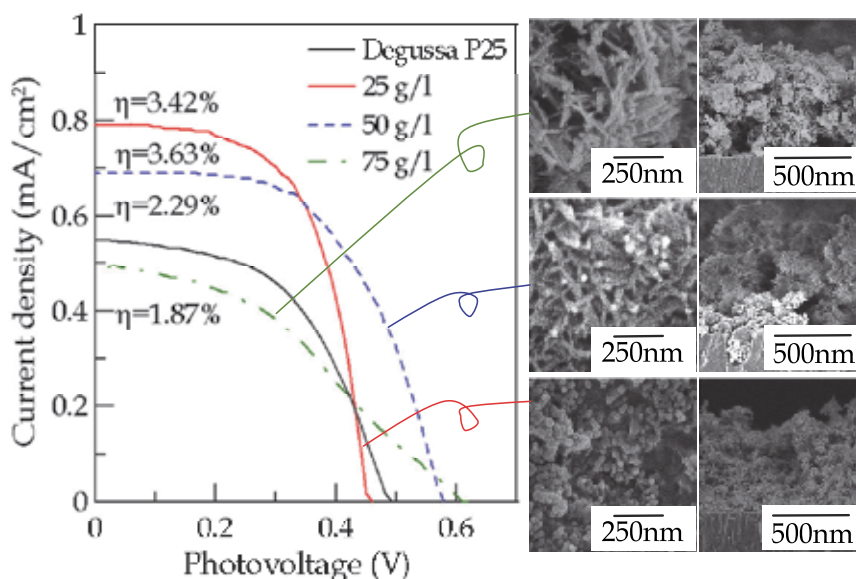
Fig. 7. *I-V* characteristic of the DSSCs assembled by HR-TiO$_2$ as photoanode prepared under different amount of TiO$_2$ powder, with their corresponding surface and cross sectional film morphology.

The *I-V* characteristics of the DSSCs assembled with HR-TiO$_2$ nanowires on template and annealed at different temperatures, with their corresponding XRD pattern and surface morphology are also shown in Fig. 8. Basically, the as-grown HR-TiO$_2$ nanowires are amorphous and account for the lowest J_{sc} of the assembled DSSCs. However, the high crystallinity of the AIP-TiO$_2$ bottom layer facilitates the diffraction peaks shown in the XRD patterns, even though amorphous HR-TiO$_2$ nanowires cover all over the top. By knowing this, the specimens with the HR-TiO$_2$ nanowires on template shown in XRD patterns give a gradual increase in peak intensity when annealing temperature is increased. Apparently, this shall be due to the improved crystallinity of the HR-TiO$_2$ nanowires by the annealing process. This helps for the increased J_{sc} of the assembled DSSCs as can be observed in Fig. 8. The annealing crystallized HR-TiO$_2$ nanowires provides more surface area for dye absorbing and thus the increased J_{sc} of the assembled DSSCs. The side effect accompanied with annealing to the TiO$_2$ nanowires is the decrease in V_{oc} of the assembled DSSCs as can be seen again in Fig. 8. This can be ascribed to the volume change of the re-grown HR-TiO$_2$ that pays for the open channel for the I$_2$+LiI liquid electrolyte to be in direct contact with the AIP-TiO$_2$ bottom layer. The ultimate PV efficiency of 3.63% can be achieved in this study. By using this method, annealing temperature shall however be carefully selected to trade-off the J_{sc} and V_{oc} of the assembled DSSCs.
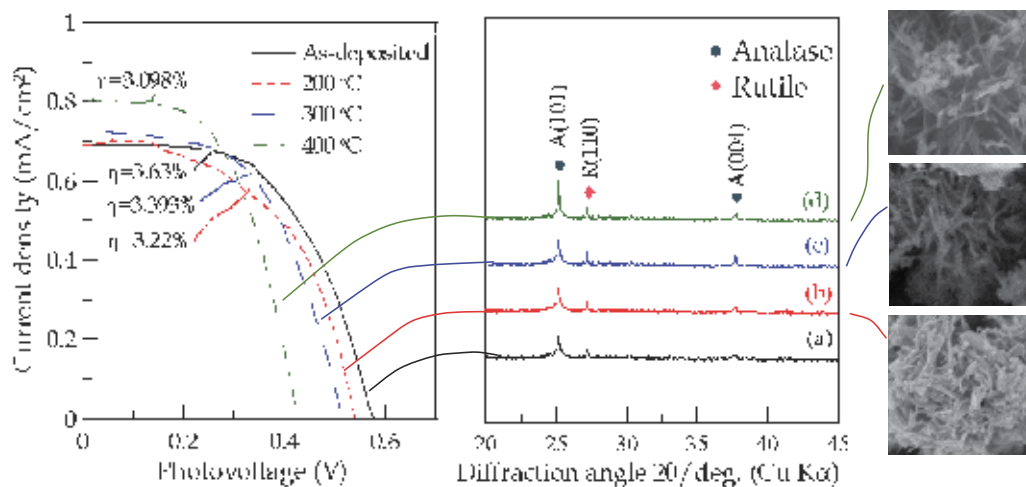
Fig. 8. (a) *I-V* characteristics of the DSSCs assembled with HR grown TiO$_2$ nanowires on template and annealed at (b) 200, (c) 300 and (d) 400 °C for 30 min, with their corresponding XRD pattern and surface morphology

3.1 Summary

In this study, hydrothermal method was demostrated to successfully prepare the randomly-orientated TiO$_2$ nanowires on AIP-TiO$_2$ template. A cell of ITO glass/AIP-TiO$_2$/[nanowire-TiO$_2$ (N3 dye)]/I$_2$+LiI electrolyte/Pt/ITO glass was constructed. Although TiO$_2$ nanowires randomly-orientated, it possesses remarkable PV efficiency. By optimizing hydrothermal process condition and annealing treatment, an ultimate PV efficiency of 3.63% can be achieved. The AIP-TiO$_2$ accidentally acts as a block layer for the I$_2$+LiI electrolyte in the assembled PV device. A hydrothermal treatment time so long as 24 hours shall be required for achieving this, which however has shorter treatment time than the LPD process and a fair PV efficiency without post-thermal annealing. This study also implicates a new possibility for 1-D nanomaterial, such as nanotubes, that can rapidly transfer of the charge carriers along the length of TiO$_2$ nanotubes. The method to grow the TiO$_2$ nanotubes is sketched as below.

4. PVD titanium followed by anodic oxidation to grow TiO$_2$ nanotubes

Anodization is one promising route to prepare long and highly ordered TiO$_2$ nanotubes array. This has been demonstrated by Shankar et al. who synthesized TiO$_2$ nanotube array on titanium foil with a tube length up to 220 µm. Very short anodic oxidation treatment time is required as compared to LPD and HR and might bring this technique a step further toward industrial practice. However, this tube-on-foil design may potentially only be applied as a back-side illuminated DSSCs which are predestined to deplete certain quantity of incident light while traveling through the I$_2$+LiI electrolyte. Direct growth of TiO$_2$ nanotubes array on transparent conducting oxide (TCO) glass substrate via anodizing a sputtering-deposited or evaporation-deposited titanium layer on TCO for constructing front-side illuminated DSSCs has been attempted, but suffering with a problem of easy detachment of the TiO$_2$ nanotubes array. By considering this, a two-step method involving

AIP metal titanium film on ITO glass followed by anodic oxidation was proposed. A tenaciously and dense AIP titanium layer was obtained and was bearable for subsequent anodic oxidation. In this approach, TiO_2 nanotubes array was successfully formed by anodizing the pre-deposited AIP metal Ti on ITO glass. A 5 µm-thick metal Ti layer can be used to convert into a 10 µm-thick amorphous TiO_2 nanotubes array by anodic oxidation for 2 h. NH_4F and H_2O addition in the ethylene glycol (EG) bath and post-heat treatment on the microstructure of TiO_2 nanotube array in responding to the photovoltaic property of the assembled DSSCs were investigated.

For better morphological control of TiO_2 nanotubes before further evaluation on the microstructure and photovoltaic property, the TiO_2 nanotubes growth mechanism was revealed during anodic oxidation, anodic current occurring to the specimen was recorded and the accompanied surface morphology was observed through the whole stages as shown in Fig. 9. It is seen that a rapid decrease of current density is caused when a thin passivated oxide layer was developed on the Ti surface in the beginning stage as can be seen in Fig. 9(a). Then, localized dissolution of the oxide layer begins to form pits over the entire oxide layer surface. This causes a small turbulent current density as presented in Fig. 9(b). At the bottom of each pit, the relatively thinner oxide layer (than that around the periphery) facilitates a localized electric field intensity across the oxide layer and drives the pit growth inward further. The continuing growth of the pit pushes oxide/metal interface inward while charge exchange occurs to the inner wall of the pit to form nanotube. At the same time, a steady-state current density is observed as can be seen in Fig. 9(c). An extended anodizing time can completely consumes the pre-deposited titanium metal layer and rapid decrease in current density is observed as shown in Fig. 9(d).
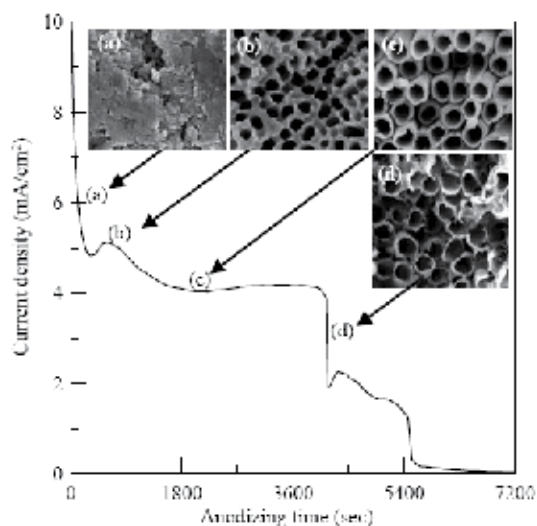
Fig. 9. Current density and surface morphology variation during anodic oxidation.

For exploring the effect of anodizing bath composition on the microstructural evolution of the grown TiO_2 nanotubes, five different types of bath composition were evaluated and their composition were listed in Table 1, where bath A, B and C are different in content of H_2O addition and bath B, D and E are different in content of NH_4F addition. Fig. 10 shows the SEM observation result of the TiO_2 nanotubes arrays anodized in the bath A, B, C, D and E.

It was indeed capable of producing nanotube featured TiO_2 films shown in the SEM morphology, regardless of the electrolyte composition. It can be noted that the entire grown TiO_2 nanotubes array (using whatever electrolyte bath) are strongly adhered on the ITO glass. Some TiO_2 nanotubes grow slower at specific electrolyte composition (bath D and E for example) and leave a remnant titanium layer (identified separately as α-titanium) beneath the nanotubes.

Electrolyte bath	Composition
A	1 L EG + 3 g NH_4F + 0.1 g H_2O
B	1 L EG + 3 g NH_4F + 20 g H_2O
C	1 L EG + 3 g NH_4F + 40 g H_2O
D	1 L EG + 1.5 g NH_4F + 20 g H_2O
E	1 L EG + 2 g NH_4F + 20 g H_2O

Table 1. Electrolyte composition used in this study for anodization to obtain TiO_2 nanotubes.

More quantitative comparison of the SEM observations, the tube length, inner diameter and outer diameter of the TiO_2 nanotubes anodized in electrolytes A, B, C, D and E are measured and drawn in Fig. 10. For electrolyte A, B and C (in sequence of increasing water content of the electrolyte), the tube length and tube diameter (inner and outer) are bar chart illustrated in Fig. 10 (upper right). The water content is found to not only influence the tube diameter but also the tube length. With increasing water content, the tube length decreases, but the tube diameters increase. One explanation for this is that the H_2O not only inhibits nanotubes growth but also dilutes the reactivity of NH_4F of the electrolyte. On the other hand for electrolyte D, B and E (in sequence of increasing NH_4F content of the electrolyte), the tube length and tube diameter (inner and outer) are also bar chart illustrated in Fig. 10 (bottom right). It can be found that increasing NH_4F content of the electrolyte prompts the tube growth rate to obtain longer tubes while at the same time with a decreased diameter. In this regard, NH_4F behaves as the active regent for the formation of nanotubes and restricts lateral growth of the nanotubes. As a whole of anodizing variables study here, it demonstrates a feasible way to convert AIP metal titanium layer into TiO_2 nanotubes array on the ITO glass by anodic oxidization procedure. The firmly adhered AIP metal titanium layer guarantees the successful growth of TiO_2 nanotubes. By knowing this and compromising tube length and diameters, the following *I-V* characteristics study for the DSSCs assembled by using TiO_2 nanowirs are based on the electrolyte B.

The *I-V* characteristics of the DSSCs assembled by using TiO_2 nanowirss with different annealing temperatures, with their corresponding XRD pattern was also shown in Fig. 11. As opposed to those Ti layer obtained by using sputter deposition, the AIP-deposited Ti layer exhibits mainly crystallinic α-Ti phase and account for the strong film adhesion. The as-anodized TiO_2-nanotube array presents an X-ray amorphous structure with trace amount of remnant α-Ti. The diffraction peaks corresponding to anatase phase TiO_2 can be found to appear in the specimens annealed over 250 °C indicating that the crystallization occurs to the amorphous TiO_2 nanotubes after post-annealing. The intensity increase of the diffraction peaks corresponding to the anatase phase TiO_2 shows that crystallinity of the nanotubes increases with the annealing temperature. However, the disappearing of the diffraction peak corresponding to remnant α-Ti can only be observed for the specimen annealed at 450 °C. This suggests that complete thermal oxidation of remnant α-Ti layer took place at a temperature over 450 °C. Furthermore, it can also be found that the *I-V* characteristics are

sensitive to the annealing temperature, the J_{sc} in particular (due to the enhanced crystallinity of nanotubes). The V_{oc} unfortunately on the contrary decreases with increasing post-annealing temperature because of the negative effect devastated by the increased sheet resistance of the ITO film (measured but not shown). An overview of the photovoltaic efficiency of the cell assembled from the as-anodized and post-annealed TiO$_2$-nanotube array, when an annealing temperature is over 350 °C, a maximum efficiency of 1.88% can be obtained and subsequent a decrease in J_{sc} occurs leading to a decreased efficiency of 0.53%. Apparently, this result from two opposite competitive factors, i.e. the sheet resistance of the ITO film and the profitable crystallinity of TiO$_2$ nanotubes, which can be affected by the post-annealing. When increasing post-annealing temperature, the improved crystallinity of the anatase TiO$_2$ nanotubes array facilitates a more ideal electron migration path from dye to ITO front electrode, therefore an increased J_{sc}, but the abrupt increase in sheet resistance of the ITO film (over 450 °C) seriously hinders electron current flowing through it.
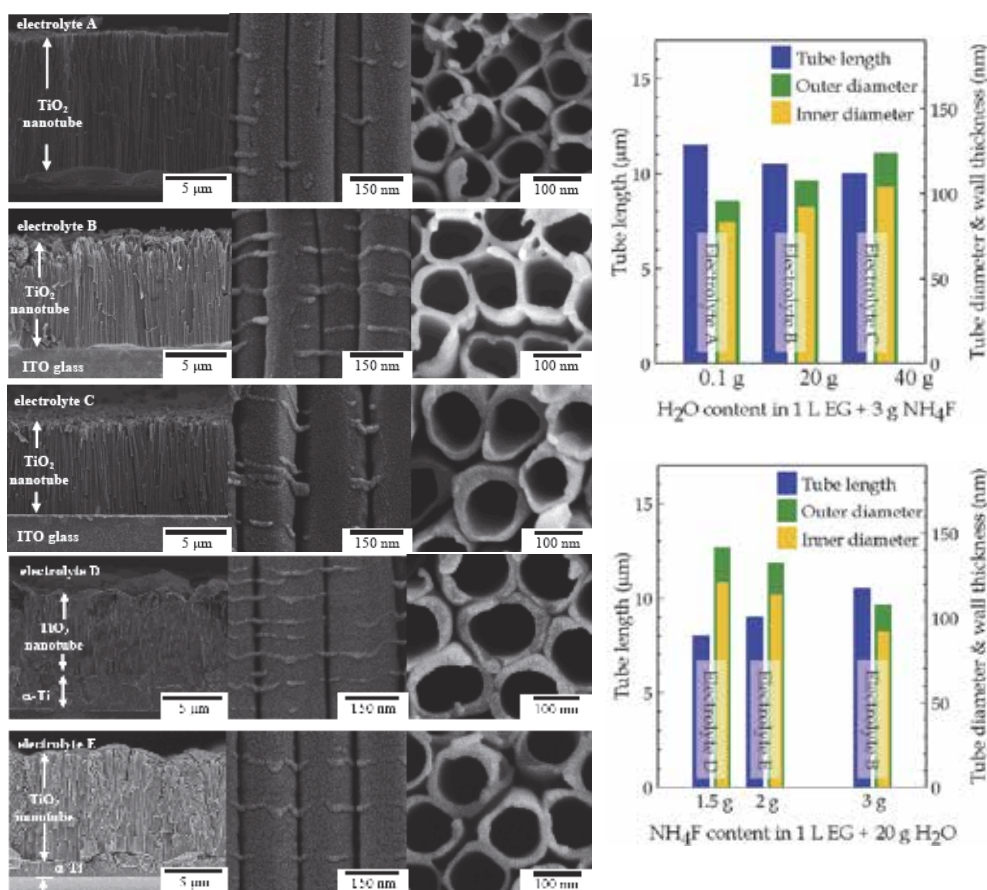
Fig. 10. SEM images of TiO$_2$ nanotubes anodized in electrolyte bath A, B, C, D and E. The left pictures are through-thickness cross sectional view of the TiO$_2$ nanotubes at low magnification, the middle pictures are magnified image of the tubes, the right pictures are top-view of the tubes. The tube length, inner diameter and outer diameter of the TiO$_2$ nanotubes anodized in electrolytes A, B, C, D and E are also measured and compared.
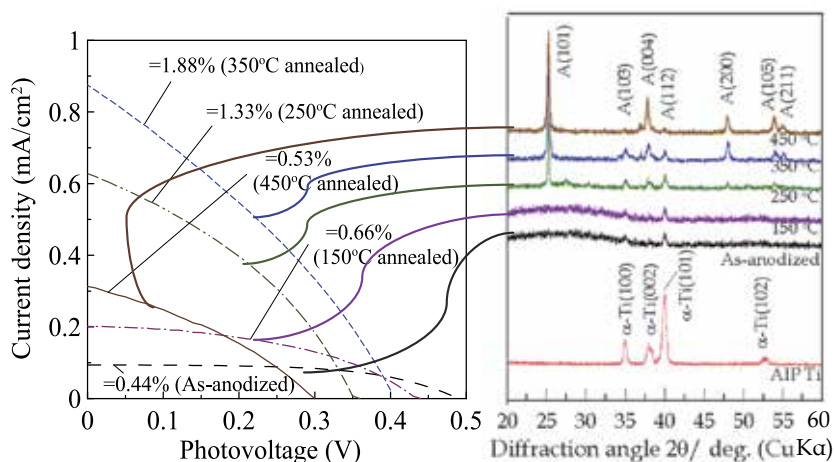
Fig. 11. *I-V* characteristic of the cell assembled from the as-anodized and post-annealed TiO$_2$-nanotube array which was produced by anodic oxidation with their corresponding XRD patterns of AIP-deposited Ti, as anodized TiO$_2$ nanotubes array and post-annealed TiO$_2$ nanotubes array.

4.1 Summary

Successful demonstration to prepare TiO$_2$ nanotubes array by arc ion plating pre-deposit metal Ti layer on ITO glass followed by anodic oxidation has been carried out in this study to reveal the influence of anodization electrolyte variables and post-heat treatment on the microstructure of TiO$_2$ nanotubes array and the photovoltaic behavior of the assembled DSSCs device. The key to successfully develop 10 micrometer long TiO$_2$ nanotubes array lies in the strongly adhered Ti-layer which tolorates the electrolyte attack during anodic oxidation. Ultimate photovoltaic efficiency of 1.88% appears on the DSSC assembled from TiO$_2$ nanotubes array which was annealed at 350 °C. However, the annealing temperature that requires to form anatase phase through post-annealing would be detrimetal to the ITO front electrode and limits further increase in photovoltaic efficiency.

5. Micro-arc oxidation and alkali etching to produce nanoflaky TiO$_2$

Micro-arc oxidation (MAO) technique is a relatively convenient and effective technique for producing micrometer scale porous crystalline anatase TiO$_2$ over a metal titanium surface. This technique involves the anodically charging of a metal (similar to conventional anodic oxidation but with a higher level of discharge voltage) in a specific electrolyte to reach a critical value at which dielectric breakdown takes place, and initiates micro-arc discharge over the entire metal surface. The micro-arc discharge enables the rapid oxidation of the metal due to the effect of impact or tunneling ionization over the metal surface. The schematic MAO system to obtain TiO$_2$ films is shown in Fig. 12. First attempt using MAO technique to grow microporous TiO$_2$ over a Ti surface for applying as DSSC electrode has also demonstrated, with however limited photovoltaic efficiency due to unsatisfactory specific surface area. In responding to the demanding in high efficiency PV device, we have developed another two-step method for the Ti foil to grow nanoflaky TiO$_2$. An idea is proposed in this study simply by using alkali etching to develop nanoflaky morphology

over the pre-micro-arc oxidized Ti (i.e. MAO-TiO$_2$) as the ideal electron emitter (or TiO$_2$ electrode). Such a nano featured TiO$_2$ layer shall be able to exhibit very large specific surface area and capable of efficient dye absorbing and eventually high photovoltaic efficiency. The alkali etching began with the immersion the MAO treated titanium foil into a NaOH solution and soaking for 12 h to develop nano-featured TiO$_2$. Later on, an alkali etching treatment followed by MAO was proposed to develop 3D-network nanostructural anatase TiO$_2$ without annealing, with the accompanied photovoltaic efficiency substantially improved. In this work, a further detailed observation on the microstructural development of the nanostructural anatase TiO$_2$ is carried out as a function of alkali bath concentration and post-heat treatment effect to the associated photovoltaic efficiency is correlated.
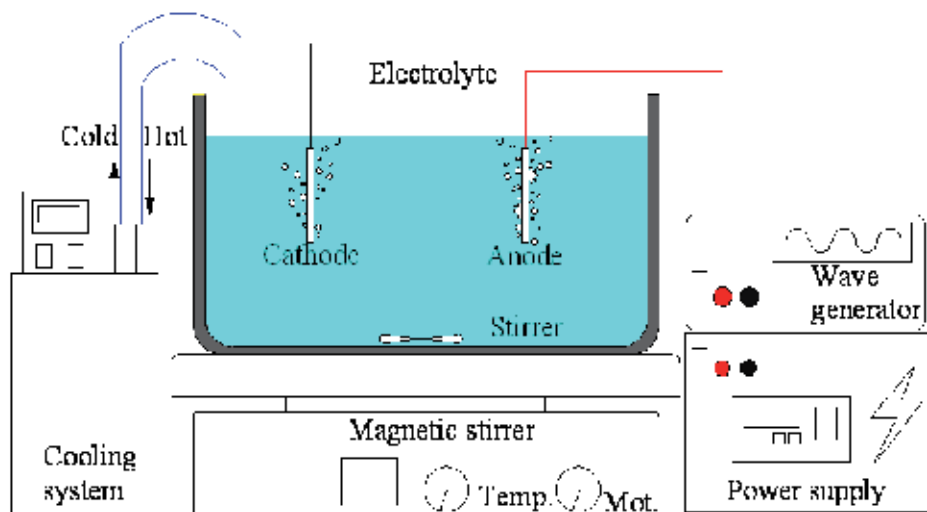
Fig. 12. Schematic diagram of micro-arc oxidation system to obtain MAO-TiO$_2$.

Figure. 13 shows the surface and cross sectional morphology of the MAO formed titania layer as well as the alkali etched TiO$_2$ layers obtained at different bath concentration. After MAO treatment, the titanium forms porous crystallinic anatase TiO$_2$ layer (as identified and described elsewhere) with numerous micrometer scale holes as observed in Fig. 13(a). These holes are discharge channels induced by the electrical breakdown of the oxide layer during the MAO treatment. It is worth noting that the surface is roughened, which is based on the fact that an intensive microdischarge occurs at a high voltage; as a result (Fig. 13(a)), the coating itself appears to be a microscopically splashed surface under the strong discharge effect. The morphology of the specimens alkali etched at different NaOH concentration shown in Fig. 13(b)~(d) reveal that nanoflaky TiO$_2$ can be developed through the alkali etching. The nano featured layer was developed over the MAO-TiO$_2$ scaffold surface with free interspace and nanoflakes of about 50~100 nm in size. As can be seen from the figure, these nanoflakes uniformly distribute over the entire surface of the treated specimen. The results revealed that alkali solution concentration appear to be an important variable in nanostructural control. Moreover, the higher NaOH concentration leads to much bigger free interspace and deeper nanoflaky TiO$_2$ layer as well as bigger nanoflake size. It is therefore out of question that the TiO$_2$ layer reformed by the alkali etching can have higher specific surface area than the MAO-TiO$_2$. Through the evaluation of a series of alkali-etched specimen at different NaOH concentrations, the size of the developed nanoflakes is found to

be determined by the NaOH concentration. The morphological development of the nanoflakes is thought to be associated with the complicated dissolution and re-precipitation mechanism that involves the attack by hydroxyl groups and negatively charged $HTiO_3^-$ ions formed on the surface. The $HTiO_3^-$ ions are thought to be consequently attracted and dissolved by the positively charged ions in the NaOH solution. In our case, it is hypothetically proposed that the low-concentration NaOH solution gives rise to the diffusion control mode enabling charged ion exchange between the MAO specimen surface and the alkali solution, where a limited ion flux yields a low reaction rate that favors fine structure formation. Contrarily, the high NaOH bath concentration enables fast exchange of the charged ion species and fast structure formation (accompanied by the flakes grown in larger dimension and larger interspace). In addition, cracks occur to the nanoflaky TiO_2 layer when NaOH bath concentration is increased. The results reflected in Fig. 13(c) and (d) indicate that the cracks began to form on the MAO specimen surface and grow with the increasing NaOH concentration.
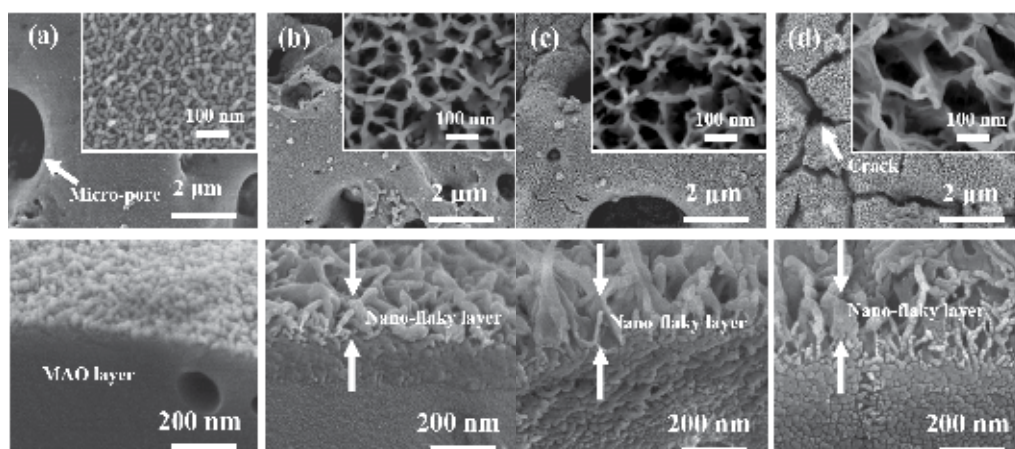
Fig. 13. Surface morphology (upper, with different magnification) and cross sectional morphology (lower) of the (a) MAO treated specimen, and alkali etched specimen in NaOH bath concentration of (b) 0.50 M (c) 1.25M and (d) 2.50 M, respectively.

Further exam of the detailed microstructure of nanoflakes by using transmission electron microscope (TEM) in high magnification bright field images taken from specimen with alkali etching at 40 °C for 12 h are shown in Fig. 14. It can be seen that the hair-like structure (corresponds to the nanoflaky structure as been observed in Fig. 13) exists over the TiO_2 surface as shown in Fig. 14(a). Here, it clearly presents a 3D network fine structure. In addition, the hair-like structure grown from the inner wall of the pore as also observed in the Fig. 14(b) is again seen as a 3D network feature. These 3D nanoflakes led to a significant increase in specific surface area and presumably photovoltaic efficiency. It should also be noted that these pores and voids are opened to the alkali etched and their surfaces are also involved with the reforming process via dissolution and re-deposition. This means that the nanoflakes grow not only on the TiO_2 surface but also grow deep into the inner surfaces, thereby significantly increase specific surface area, even though these nanoflakes unfortunately appear to be amorphous as identified by TEM selected area diffraction technique and described elsewhere.
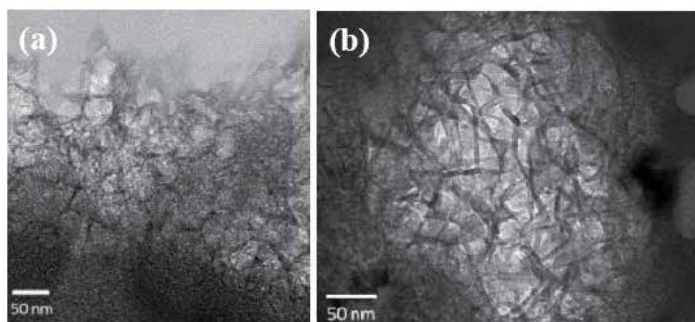
Fig. 14. Bright field image of nanoflaky TiO_2 grown from (a) the MAO-TiO_2 surface and (b) the inner pore of the MAO-TiO_2.

The *I-V* curves of DSSCs assembled with the MAO-TiO_2 and alkali etched TiO_2 obtained at different concentrations are shown in Fig. 15.
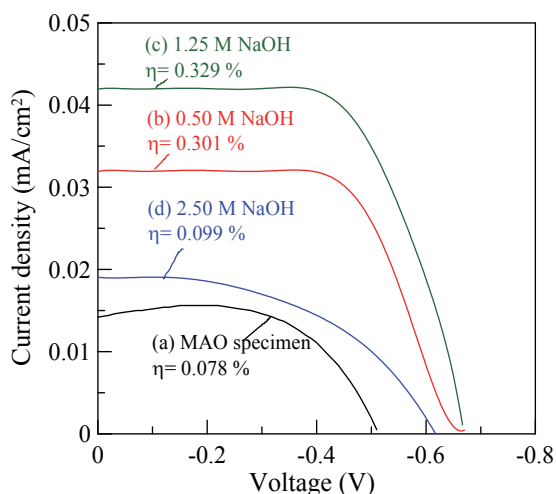
Fig. 15. *I-V* characteristic of the DSSC device assembled using (a) MAO treated specimen and alkali etched specimens at different NaOH bath concentration.

Photovoltaic efficiency of the assembled DSSC is substantially increased by alkali etching. Apparently, the remarkable increase in the J_{sc} and V_{oc} of the cell assembled from alkali etched specimens appear to be contributed to by the nanoflaky surface structure, which possesses a markedly higher specific surface area than the MAO layer. Note that the J_{sc} is significantly dropped for the DSSC using alkali etched TiO_2 specimen prepared at 2.5 M NaOH. This is due to the cracks formed and distributed over the entire oxide layer leaving the I_2+LiI electrolyte to directly contact with fresh metallic titanium plate. A close look at Fig. 13(b), (c) and (d), the DSSC assembled by the alkali etched specimen at 1.25 M NaOH solution performs the highest J_{sc} and V_{oc} among the three alkali etched specimens. Good explanation is that this is a compromising of the effect of the enlarged specific surface area and the effect of crack formation caused by the alkali etching, i.e. the increased NaOH bath concentration not only results in the increased specific surface area but also the increased free interspace and even worse the crack formation. As revealed in Fig. 13(d), the cracks

causing the discontinuity of path for charge carrier shall be the main reason for the significant decrease in photovoltaic efficiency of the assembled DSSC which employs specimen alkali etched at 0.50 M NaOH. By comparison, the DSSC assembled by using MAO scaffold presents a photovoltaic efficiency of 0.078%, while it present a highest photovoltaic efficiency of 0.329% (over four times increment) for the DSSC assembled by the alkali etched specimen. Through this simple and low cost alkali etching route, it is able to produce nano structural TiO_2 electrode for photovoltaic DSSC.

The *I-V* characteristics of the DSSCs assembled by using specimens with MAO-TiO_2 and nanoflaky TiO_2 (as-etched and annealed at 400 °C), with their corresponding XRD patterns are shown in Fig. 16. The annealing work significantly improves the crystallinity of the nanoflakes and consequently photovoltaic efficiency can be dramatically increased for the device assembled with the specimen with nanoflaky TiO_2. It was 0.329% for the specimen with the as-etched nanoflaky TiO_2 and 2.194% for the specimen with annealed nanoflaky TiO_2. Both are however greater than that of the MAO-TiO_2 specimen only with 0.061%. By contrast, the J_{sc} and V_{oc} of the solar cell assembled by alkali etched specimen are substantially higher. Apparently, the dramatic increase in J_{sc} and V_{oc} of the cell assembled by alkali treated specimens is contributed by the nanoflaky surface structure, which possesses far higher specific surface area than MAO layer does. With this simple and low cost post-alkali etching demonstration, the photovoltaic efficiency of the DSSC using the MAO treated Ti foil as the back electrode can be significantly increased. The increased crystallinity provides higher dye-absorption for generating more electron-hole pairs and suppresses the electron loss due to the recombination of electron-hole pairs. Therefore, the DSSC assembled with Ti electrode which synthesized by MAO, treated by alkali etching and annealing, presents highest photovoltaic efficiency.
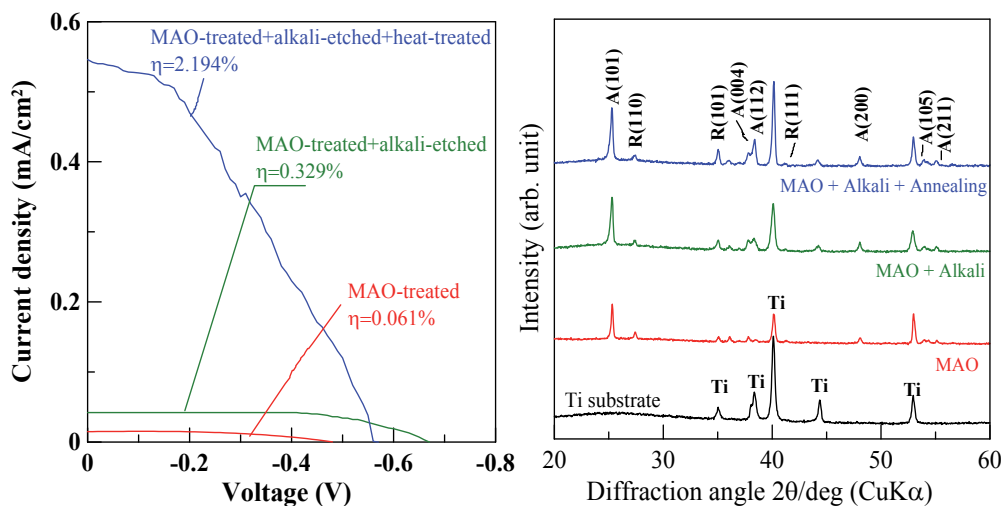
Fig. 16. The *I-V* characteristics of the DSSCs assembled by using specimens with MAO-TiO_2 and nanoflaky TiO_2 (as-etched and annealed at 400 °C), with their corresponding XRD patterns.

5.1 Summary

Here at last, a method to combine with micro-arc oxidation and post-alkali etching has succeeded in forming an 3D network nanoflaky anatase TiO_2 layer on the surface of a Ti substrate. The nanoflaky TiO_2 completely cover the upmost surface of the MAO TiO_2 layer as well as the inner pores and voids, therefore provides very large surface area for dye absorption to increase the efficiency of the assembled DSSCs. Without post-annealing, maximum photovoltaic efficiency of 0.329% for the DSSC is achieved with the amorphous nanoflaky TiO_2 layer alkali etched at 1.25 M NaOH. Post-annealing at 400 °C significantly enhances crystallinity of the nanoflaky TiO_2 layer and ultimately photovoltaic efficiency 2.194% for the DSSC is achieved. The above results have shown that the method to combine with micro-arc oxidation and post-alkali etching was a potential and low-cost process for developing the nano featured TiO_2 photoanode for obtaining high efficiency DSSC. However, post-annealing shall not be abandoned for additional windfall of the photovoltaic efficiency.

6. Conclusion

Here, we begin our conclusion by reviewing the results in previously described. We started developing nano featured TiO_2 layer by using LPD method and found that it is capable of obtaining nanocluster TiO_2 with unacceptable growth rate. Crystallinic anatase TiO_2 layer can be obtained through suitable annealing treatment to achieve only 0.0056% photovoltaic efficiency. In the work of TiO_2 nanowires growth on AIP-TiO_2 template via hydrothermal route, an ultimate PV efficiency of 3.63% can be achieved by optimizing hydrothermal process condition and annealing treatment. A hydrothermal treatment time so long as 24 hours shall be required for achieving this, which however has shorter treatment time than the LPD process and a fair PV efficiency. In the work of preparing TiO_2 nanotubes array by arc ion plating pre-deposit metal Ti layer on ITO glass followed by anodic oxidation, the key to successfully develop 10 micrometer long TiO_2 nanotubes array lies in the strongly adhered Ti-layer which tolorates the electrolyte attack during anodic oxidation. Ultimate photovoltaic efficiency of 1.88% appears on the DSSC assembled from TiO_2 nanotubes array which was annealed at 350 °C. Although the tube length and diameter is controllable, it is expected to exhibit higher photovoltaic efficiency by further reducing tube diameter for more specific surface area of the photoanode. At last, a DSSC assembled from the nanoflaky TiO_2 prepared by using micro-arc oxidation and alkali etching was demonstrated. Ultimate photovoltaic efficiency 2.194% for the DSSC is achieved.

Results in these studies are remarkably consistent with what we expected. Cost saving and easy operation processes for obtaining TiO_2 photoanode has been achieved. Despite the encouraging result of this study as the positive effect of nanostructural surface engineering, future research is required in a number of directions about chasing high efficiency DSSCs. However, a step further has been taken in the improved photovoltaic efficiency by nanostructural surface engineering and an opportunity for commercializing DSSC using low-cost process.

7. References

O'Regan, B. & Grätzel, M. (1991). *Letters to nature*, Vol.353, pp. 733-740

Nagayama, H., Honda, H. & Kawahara., H. (1988). *Journal of the Electrochemical Society*, Vol.135, pp. 2013-2014

Herbig, B. & Löbmann, P. (2004). *Journal of Photochemistry and Photobiology A: Chemistry*, Vol.163, pp. 359-365

He, J. L., Chen, C. H. & Hsu, M. Y. (2006). *The Chinese Journal of Process Engineering,* Vol.6, pp. 224-227

Rao, C. N. R., Satishkumar, B. C., Govindaraj, A., Vogl, E. M. & Basumallick, L. (1997). *Journal of Materials Research,* Vol.12, pp. 604-606

Kasuga, T., Hiramatsu, M., Hoson, A., Sekino, T. & Niihara, K. (1999). *Advanced Materials*, Vol.11, pp. 15-18

He, J. L., Hsu, M. Y., Li, H. F. & Chen, C. H. (2006). *The Chinese Journal of Process Engineering*, Vol.2, pp. 228-234

Shankar, K., Mor, G. K., Prakasam, H. E., Yoriya, S., Paulose, M., Varghese, O. K. & Grimes, C. A. (2007). *Nanotechnology*, Vol.18, pp.065707

Chen, C. H., Chen, K. C. & He, J. L. (2010). *Current Applied Physics*, Vol.10, pp. S176

Yerokhin, A. L., Nie, X., Leyland, A., Matthews, A. & Dowey, S.J. (1999). Surface and Coatings Technology, Vol.122, pp. 73-93

Song, W., Xiaohong, W., Wei, Q. & Zhaohua, J. (2007). *Electrochimica Acta*, Vol.53, pp.1883-1889

Wei, D., Zhou, Y., Jia, D. & Wang, Y. (2008). *Acta Biomaterialia*, Vol.254, pp.1775-1782

Wu, S. Y., Lo, W. C., Chen, K. C. & He, J. L. (2010). *Current Applied Physics*, Vol.10, pp.S180–S183.

Wu, S. Y., Chen, Y. H., Chen, K. C. & He, J. L. (2010). *Japanese Journal of Applied Physics*, Vol.10, pp.180–183.

Chu, P. J, Wu, S. Y., Yerokhin, A., Matthews, A. & He, J. L. (2009). *Program and Abstract Book of TACT 2009 International Thin Films Conference*, (December 2009.) pp.115-116

Investigation of Dyes for Dye-Sensitized Solar Cells: Ruthenium-Complex Dyes, Metal-Free Dyes, Metal-Complex Porphyrin Dyes and Natural Dyes

Seigo Ito

Department of Electrical Engineering and Computer Sciences,
Graduate School of Engineering, University of Hyogo, Hyogo,
Japan

1. Introduction

Following the first report on dye-sensitized solar cells (DSCs) by Prof. Grätzel in 1991, thousands of papers have been published with the aim of making DSCs commercially viable (Fig. 1). They are attractive because of their low-cost materials and convenient fabrication by a non-vacuum, high-speed printing process. One of the key materials in DSCs is the sensitizer dye. Ruthenium-complex dyes are used to make DSCs with conversion efficiencies of over 10%; recently, the Grätzel group reported a DSC using ruthenium dye (Z991) which achieved a conversion efficiency of 12.3%. Research into synthetic ruthenium-free dyes, including metal-free organic dyes and metal-complex porphyrin dyes, has intensified because of the high cost of ruthenium. Indoline dyes and oligothiophene dyes are used to make DSCs with conversion efficiencies greater than 9% and 10%, respectively. A zinc-porphyrin dye produced a conversion efficiency of 11.4%.
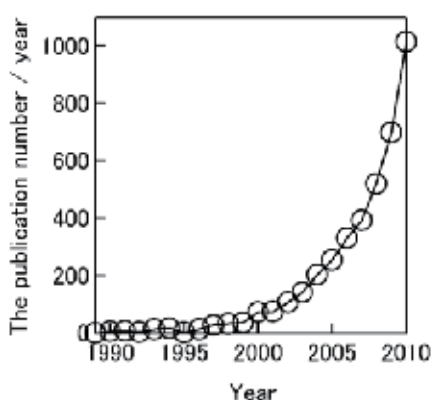
Fig. 1. Number of publications on DSCs in each year from 1989 to 2010. The data was obtained by searching online databases (Scopus, Elsevier). The keywords were "dye", "solar" and "cell", and the document type was limited to "article".

Natural dyes have also been studied for use in DSCs because they are cheaper than synthetic dyes, and exhibit moderate energy conversion efficiency. Natural chlorophyll dyes show energy conversion efficiencies of over 4% and Monascus yellow dye yielded a conversion efficiency of 2.3%. Despite the wide variety of natural dyes available, other natural dyes do not yield energy conversion efficiencies of over 2%, although some natural dyes derivatives are capable of higher energy conversion efficiencies. In this review, the principles and fabrication methods of DSCs are explained, and recent research on sensitizing dyes, including ruthenium-complex dyes, metal-free organic dyes, metal-complex porphyrin dyes, and natural dyes, is reviewed.

2. Ruthenium-complex dyes

Ruthenium dye DSCs were first reported in 1991 by O'Regan and Grätzel in Nature [1]. These first ruthenium dye DSCs achieved a 7.1% conversion efficiency (Fig. 2). However, the structure of the ruthenium dye was complicated and contained three ruthenium metal centers. In 1993, Nazeeruzzin *et al.* published DSCs with 10.3% conversion [2], using a ruthenium dye sensitizer (N3, Fig. 3: [*cis*-di(thiocyanato)bis(2,2-bipyridine-4,4-dicarboxylate)ruthenium]]), which contained one ruthenium center and was thus simpler than the ruthenium dye reported in 1991. At the end of the 1990s, Solaronix SA (Switzerland) began selling the materials for constructing DSCs: ruthenium dyes, electrodes, electrolytes, TiO$_2$ paste, fluorine-doped tin oxide (FTO)/glass plates, and sealing materials. This led to a blossoming of DSC research, using the N3 dye (Fig. 3) and nanocrystalline-TiO$_2$ electrodes made using doctor-blading methods, which resulted in the development of sandwich-type solar cells (Fig. 4).
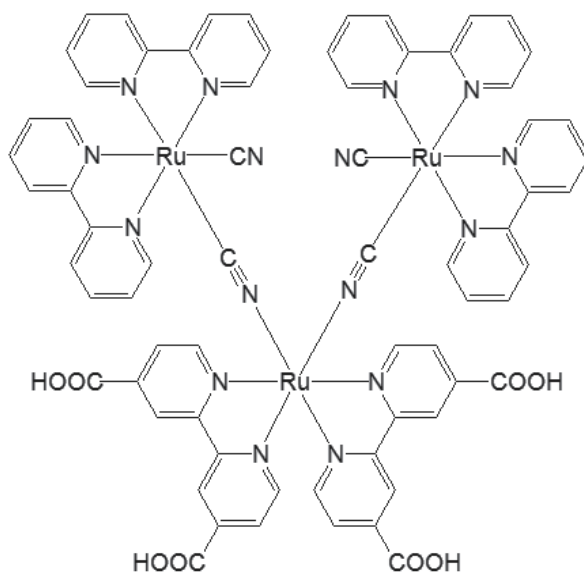
Fig. 2. A ruthenium dye reported in *Nature* (1991) by Dr. O'Regan and Prof. Grätzel [1].
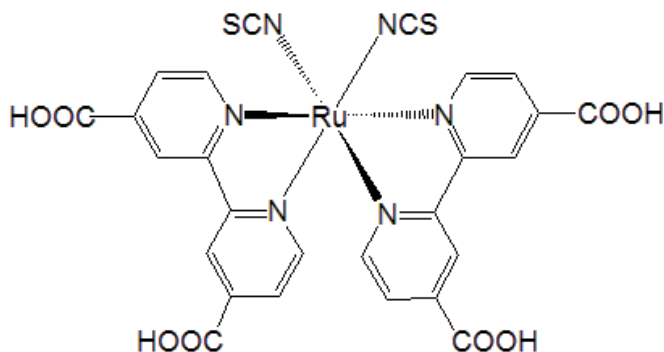
Fig. 3. The ruthenium dye N3, which achieved 10% conversion efficiencies in DSCs, reported by Dr. Nazeeruddin of the Grätzel group [2].
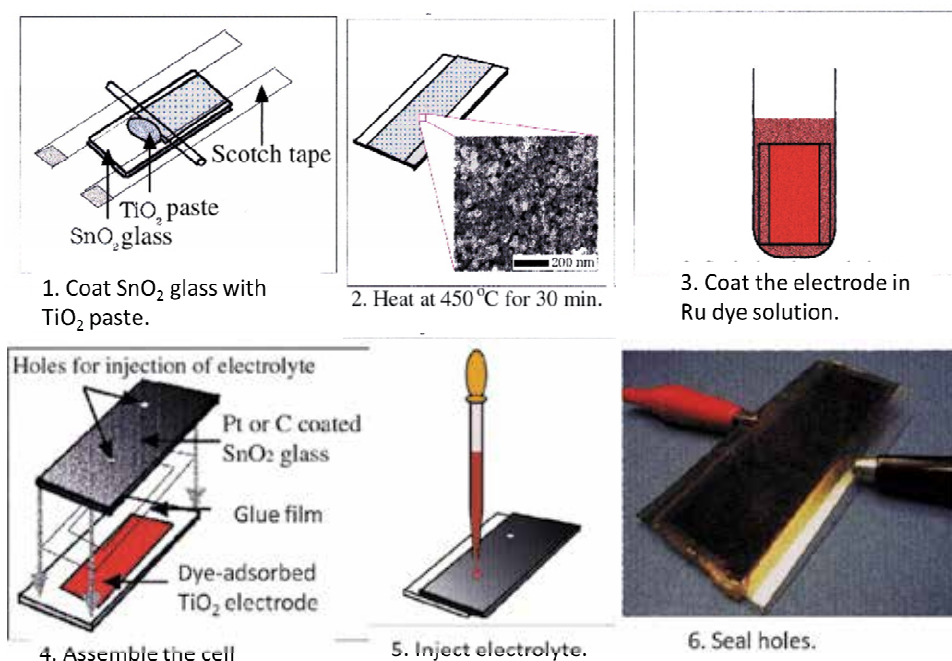
Fig. 4. DSC fabrication methods.

The high performance of the N3 sensitizer adsorbed on to nanocrystalline-TiO_2 films (Fig. 5) brought a significant advance in DSC technology. The sensitizer adsorbed on to the TiO_2 surface absorbs a photon to produce an excited state, which efficiently transfers one electron to the TiO_2 conduction band (Fig. 6). The oxidized dye is subsequently reduced by electron donation from an electrolyte containing the iodide/triiodide redox system. The injected electron flows through the semiconductor network to arrive at the back contact then through the external load to the counter electrode, which is made of platinum sputtered conducting glass. The circuit is completed by the reduction of triiodide at the counter electrode, which regenerates iodide.
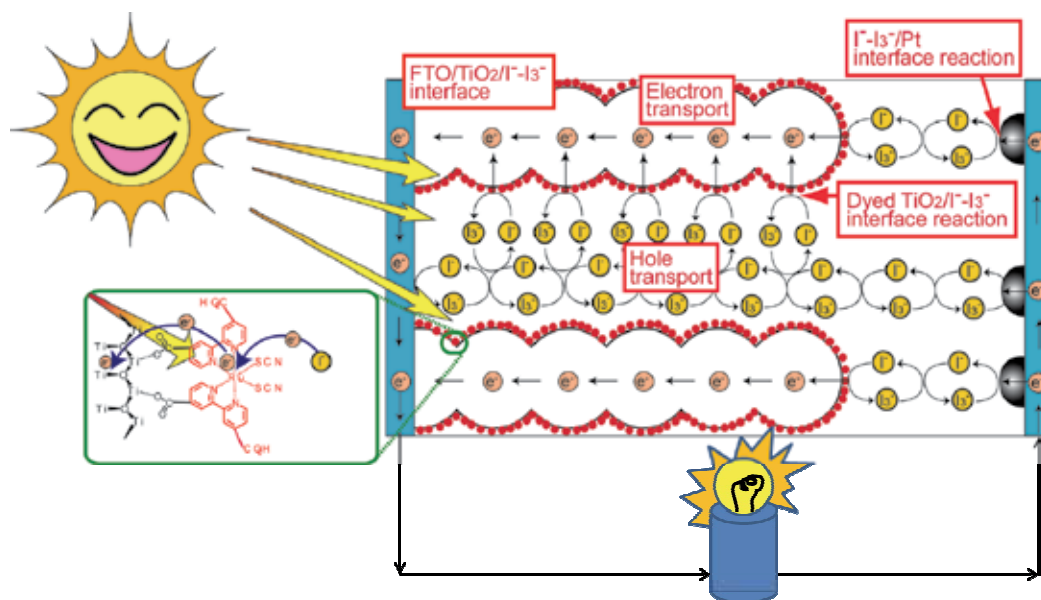
Fig. 5. Structure and electron movement in DSCs.
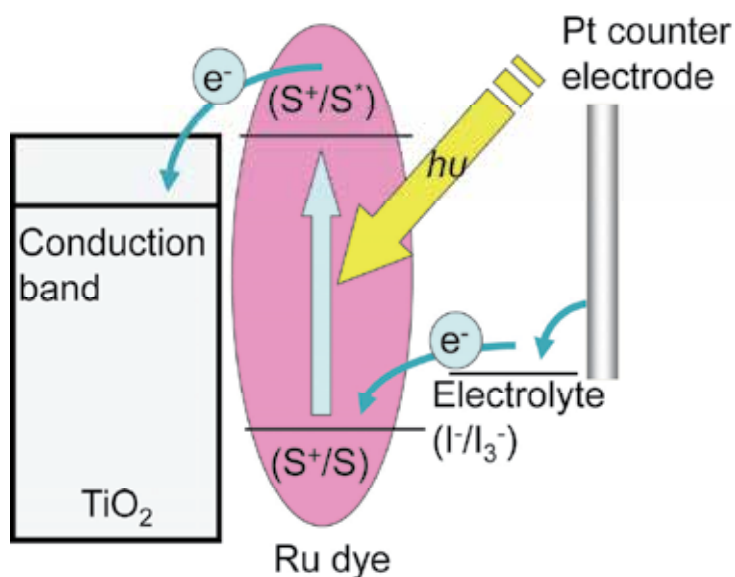
Fig. 6. Electron transfer in DSCs.

The high performance achieved by dye-sensitized TiO_2 solar cell devices depends on several factors, such as the broad range of visible light absorbed by the dye and the dye's relatively long-lived excited states with energies near those of the TiO_2 conduction band. Moreover, the presence of terminal carboxylic acid groups allows the sensitizer to be stably anchored to the semiconductor surface, ensuring high electronic coupling between the dye and the semiconductor, which is required for efficient charge injection.

However, it was difficult to reproduce the 10% efficiency observed in the first published DSCs. In 2001, Nazeeruzzin *et al.* reported DSCs with 10.4% efficiency using a ruthenium dye called 'black dye' in the *Journal of the American Chemical Society* (Fig. 7) [3]. Although black dye looks green in solvent, on a porous nanocrystalline-TiO$_2$ electrode the DSC looks black, because its wide absorption band covers the entire visible range of wavelengths. The conversion efficiency was confirmed by the National Renewable Energy Laboratory in the United States. Subsequently, using black dye, Wang *et al.* (AIST, Japan) reported a 10.5% efficiency [4], and Chiba *et al.* (Sharp Co. Ltd., Japan) reported an 11.1% efficiency, confirmed by AIST [5]. In 2006, Nazeeruzzin *et al.* reported a new dye, N179, which was similar to N3, but which achieved an 11.2% conversion efficiency in DSCs (Fig. 8) [6]. N3 has four H$^+$ counterions, whereas N719 has three TBA$^+$ and one H$^+$ counterions (Fig. 9). The change in the counterions alters the speed of adsorption onto the porous TiO$_2$ electrode; N3 is fast (3 h) whereas N719 is slow (24 h), thus N719 gives a higher conversion efficiency than N3.
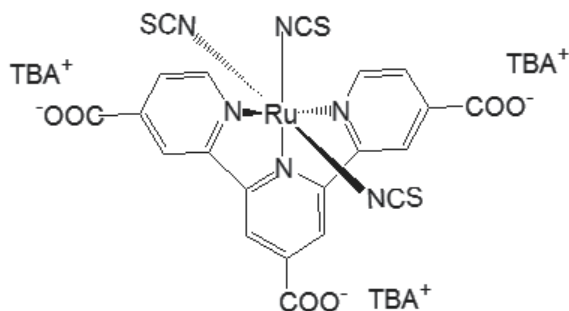
Fig. 7. Structure of black dye for DSCs [3]. TBA$^+$: tetrabutylammonium.
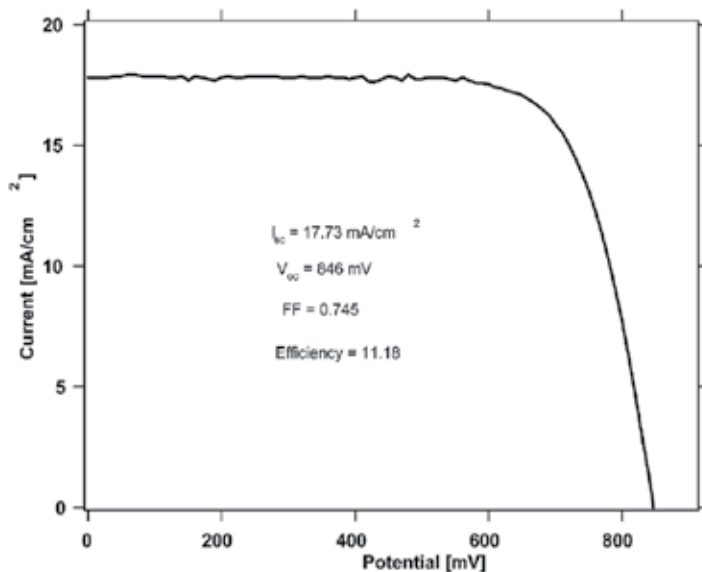
Fig. 8. Photo I-V curve for DSC with 11.1% conversion efficiency, using N719 [6].
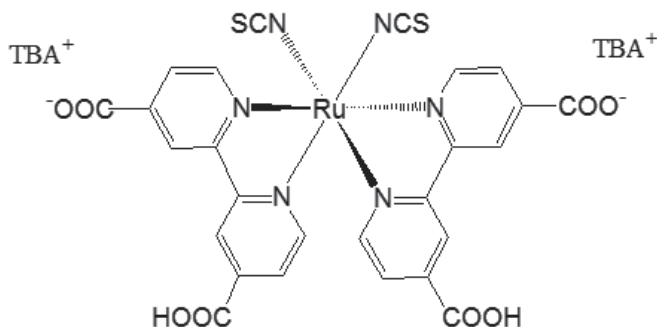
Fig. 9. A ruthenium dye (N719) for DSCs [6]. TBA$^+$: tetrabutylammonium.

In 2008, Ito *et al.* detailed DSC fabrication methods [7] that improved the reproducibility of the results for DSC conversion efficiencies (Fig. 10), and many papers have subsequently reported conversion efficiencies close to 10%. The components of high efficiency DSCs, such as the TiCl$_4$-treated photoelectrodes, the thickness of the transparent nanocrystalline-TiO$_2$-layer, the light-scattering layer (Fig. 11), and the anti-reflective film on transparent conducting oxide (TCO) substrates, have been optimized. These components have a significant effect on the conversion efficiency. TiCl$_4$ treatment is necessary for improving the mechanical strength of the TiO$_2$ layer. The thickness of the TiO$_2$ layer affects the photocurrent and the photovoltage of the devices. Furthermore, the photocurrent can also be increased by using an anti-reflective film. The combination of both transparent and light-scattering layers in a double layer system (Fig. 12) and an anti-reflective film creates a photon-trapping effect, which has been used to enhance the quantum efficiency, known as the incident photon-to-electricity conversion efficiency (IPCE).
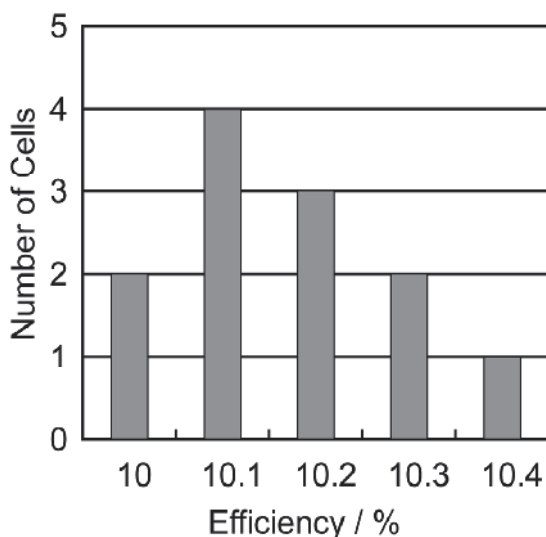
Fig. 10. Histogram showing the reproducibility of DSC conversion efficiencies. Reported values for 12 DSC devices produced over a 24 h period. [7].

In this section, the fabrication method and the influence of different procedures on the photovoltaic performance of high-efficiency DSCs is described [7]. Two types of TiO$_2$ paste containing nanocrystalline-TiO$_2$ (20 nm) and macrocrystalline-TiO$_2$ (400 nm) particles (Fig. 11) were prepared, which gave transparent and light-scattering layers, respectively (Fig. 12) [8]. The synthesis of *cis*-di(thiocyanato)-*N*,*N*'-bis(2,2'-bipyridyl-4-carboxylic acid-4'-tetrabutylammoniumcarboxylate)ruthenium(II) (N-719, Fig. 9) has previously been reported [6]. The purification of N-719 was carried out by repeating the following method three times. The N719 complex was dissolved in water containing 2 equiv of tetrabutylammonium hydroxide. The concentrated solution was filtered through a sintered glass crucible, applied to a water-equilibrated Sephadex LH-20 column, and then the adsorbed complex was eluted using water. The main band was collected and the pH of the solution was lowered to 4.3 using 0.02 M HNO$_3$. The titration was carried out slowly over a period of 3 h and then the solution was kept at –20 °C for 15 h. After allowing the flask to warm to 25 °C, the precipitated complex was collected on a glass frit and air-dried.
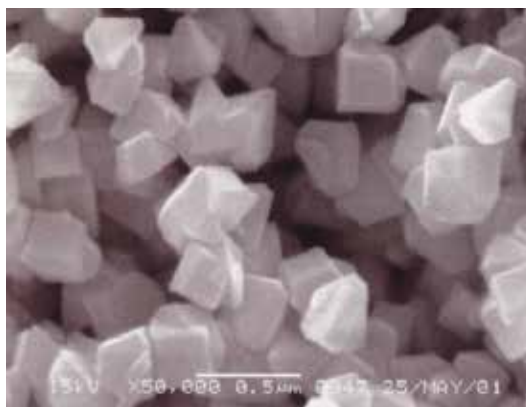
(a)
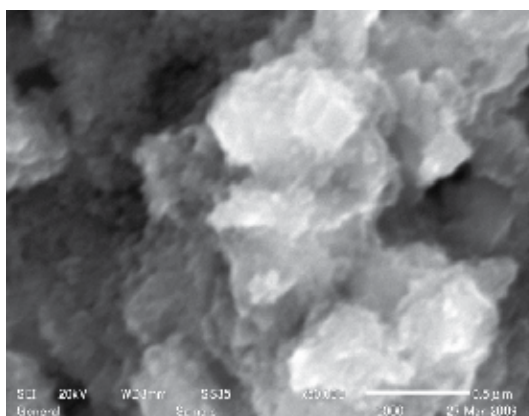
(b)

Fig. 11. SEM images of the surface of TiO$_2$ submicrometer particles (400C, JGC-CCIC) (upper) and a mixture of TiO$_2$ submicrometer particles and nanoparticles (PST-400C, JGC-CCIC) (lower). Images were acquired at 50,000× magnification [8].
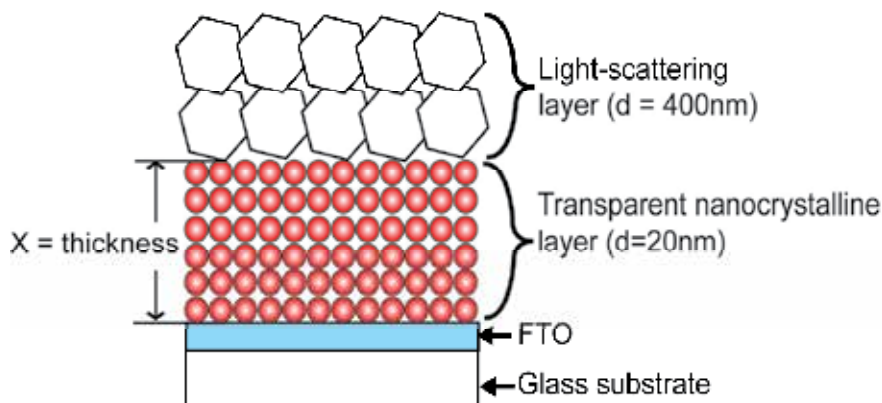
Fig. 12. Structure of DSC with a double layer of nanocrystalline-TiO$_2$ electrodes. X in Figure shows the thickness of the nanocrystalline-TiO$_2$ electrodes that was varied during the optimization of high-efficiency DSC [7, 8].

FTO glass was used as a current collector (4 mm thick, Solar, Nippon Sheet Glass). In order to prepare the DSC working electrodes, the FTO glass was first cleaned in a detergent solution using an ultrasonic bath for 15 min, and then rinsed with tap water, pure water, and ethanol. After treatment in a UV-O$_3$ system for 18 min, the FTO glass plates were immersed in a 40 mM aqueous TiCl$_4$ solution at 70 °C for 30 min, washed with pure water and ethanol and then dried. The FTO glass plate was coated with a layer of nanocrystalline-TiO$_2$ paste (anatase, d = 20 nm) by screen printing. The screen-printing procedure was repeated to get an appropriate thickness for the working electrode. After the nanocrystalline-TiO$_2$ paste was dried at 125 °C, two layers of macrocrystalline-TiO$_2$ paste (anatase, d = 400 nm) were deposited by screen printing to form a light-scattering TiO$_2$ film, 4-5 μm thick. The TiO$_2$-coated electrodes were gradually heated under an air flow at 325 °C for 5 min, at 375 °C for 5 min, at 450 °C for 15 min and at 500 °C for 15 min.

The sintered TiO$_2$ film was treated again with a 40 mM TiCl$_4$ solution as described above, rinsed with pure water and ethanol, and sintered again at 500 °C for 30 min. The TiO$_2$ electrode was allowed to cool to 80 °C, and was then immersed in a 0.5 mM acetonitrile/*tert*-butyl alcohol (1:1) solution of N-719 dye for 20-24 h at room temperature to ensure complete uptake of the sensitizer dye. The dye uptake time must be optimized for each dye, for example: indoline dyes, 4 h [9, 10]; porphyrin dyes, 1 h [11]; and natural dyes, 15 min [12].

To prepare the counter electrode, a hole was drilled in the FTO glass (2.2 mm thick, TEC 15 Nippon Sheet Glass) by sandblasting. The perforated sheet was washed with H$_2$O, and with a 0.1 M HCl solution in ethanol, and then cleaned by ultrasound in an acetone bath for 10 min. Residual organic contaminants were removed by heating in air for 15 min at 400 °C; then, the Pt catalyst was deposited on the FTO glass by coating the glass with a drop of H$_2$PtCl$_6$ solution (2 mg Pt in 1 mL ethanol) and repeating the heat treatment at 400 °C for 15 min.

The dye-covered TiO$_2$ electrode and Pt-counter electrode were assembled into a sandwich cell (Fig. 13) and sealed on a heating stage with a hot-melt gasket, made of an ionomer (25 μm thick, Surlyn 1702, DuPont). A drop of the electrolyte; a 0.60 M solution of butylmethylimidazolium iodide, 0.03 M I$_2$, 0.10 M guanidinium thiocyanate and 0.50 M 4-*tert*-butylpyridine in acetonitrile/valeronitrile (85:15 v/v) was introduced into the cell via vacuum backfilling. The cell was placed in a vacuum, and subsequent exposure to ambient

pressure pushed the electrolyte into the cell. Finally, the hole was covered by a hot-melt ionomer film (35 μm thick, Bynel 4164, Du-Pont) and a cover glass (0.1 mm thick), and sealed with a hot soldering iron.

The electrolyte must be optimized for each dye: black dye is used with 0.6 M dimethyl propyl imidazolium iodide, 0.1 M lithium iodide, 0.05 M iodine, and 0.5 M *tert*-butylpryidine in acetone [5]; D149, D205, and Monascus yellow (a natural dye) are used with 0.10 M lithium iodide, 0.60 M butylmethylimidazolium iodide, 0.05 M I2, and 0.05 M 4-*tert*-butylpyridine in acetonitrile/valeronitrile (85:15) [9, 10, 12]; YD-2 (a porphyrin dye) is used with 1.0 M 1,3-dimethylimidazolium iodide, 0.03 M iodine, 0.5 M *tert*-butylpyridine, 0.05 M LiI, 0.1 M guanidinium thiocyanate, in acetonitrile/valeronitrile (85:15 v/v) [13].

Photovoltaic measurements were taken using an AM 1.5 solar simulator (100 mW cm^{-2}). The power of the simulated light was calibrated using a reference Si photodiode equipped with an infrared (IR) cut-off filter in order to reduce the mismatch between the simulated light and the AM 1.5 spectrum in the 350-750 nm region to less than 2% [14]. The current-voltage (I-V) curves were obtained by applying an external bias to the cell and measuring the photocurrent with a digital source meter.
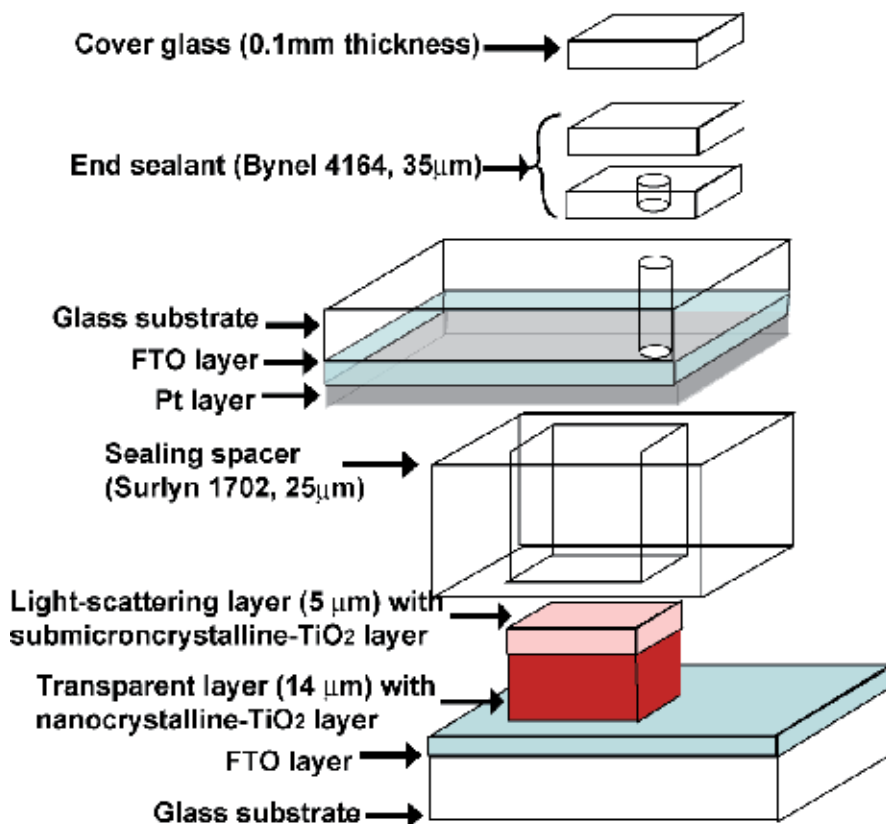
Fig. 13. Structure of DSCs.

In order to demonstrate the effect of the sensitizing dye on the photovoltaic performance, two types of TiO$_2$ working electrode were prepared on the FTO/glass substrate (Fig. 14)

[15]. The first type of working electrode, nano-TiO$_2$, is a double layer of mesoporous TiO$_2$ (TiO$_2$ nanoparticles d = 20 nm; nanocrystalline TiO$_2$ layer, 14 µm; microcrystalline TiO$_2$ layer, 4 µm) screen-printed onto the FTO. The second type of electrode, UL/nano-TiO$_2$, used a compact TiO$_2$ underlayer (UL) deposited by spray pyrolysis between the porous TiO$_2$ layer and the FTO. Figure 14 shows the dark I-V characteristics of the two types of mesoscopic-TiO$_2$ electrodes, with and without ruthenium dye. The onset of the dark current in the nano-TiO$_2$ electrode occurred at a low forward bias. The compact TiO$_2$ UL suppresses the dark current, shifting its onset by several hundred millivolts. This indicates that the triiodide reduction in the exposed part of the FTO layer is responsible for the high dark current observed in the nanocrystalline TiO$_2$ film alone. Adsorption of the N-719 dye onto the nano-TiO$_2$ electrode also suppresses the dark current (Fig. 15), indicating that the ruthenium sensitizer itself worked as an effective blocking layer on the FTO layer. In contrast, the dark-current curves of UL/nano-TiO$_2$ were shifted to slightly lower voltages by the adsorption of the N-719 dye (Fig. 15) indicating that the sensitizer increases the dark current on electrodes where the FTO surface is already blocked. This can be attributed to the TiO$_2$ band shifting to positive values by surface protonation; the protons can be supplied by the ruthenium dye. The photovoltaic results are shown in Figure 16 and confirm the trends observed in the dark currents. The dye loaded nanocrystalline TiO$_2$ film alone gave a lower conversion efficiency (Fig. 16, nano-TiO$_2$/Ru-dye). Introducing the compact TiO$_2$ UL in the nano-TiO$_2$/Ru-dye electrode increased the open-circuit photovoltage (V_{OC}) by 27 mV and the short-circuit photocurrent density (J_{SC}) by 1 mA cm^{-2}. The difference between the nano-TiO$_2$/Ru-dye and UL/nano-TiO$_2$/Ru-dye electrodes arose from the UL suppressing the charge recombination at the FTO layer. Mathematical modeling of charge-recombination carried out by Ferber *et al*. (Fig. 17) [16] shows good agreement with these I-V curves. Therefore, the observed improvement of the V_{OC} and J_{SC} from using a UL on the FTO layer agrees with the theoretical calculations. The suppression of dark current is enhanced by introducing a compact layer between the FTO and the TiO$_2$ nanocrystals, and leads to an increase in the V_{OC}. However, the performance of DSCs with spray-pyrolyzed TiO$_2$ ULs is less reproducible; to avoid this problem, TiCl$_4$ treatment between the FTO and nanocrystalline-TiO$_2$ layers is used instead (Fig. 10) [7].
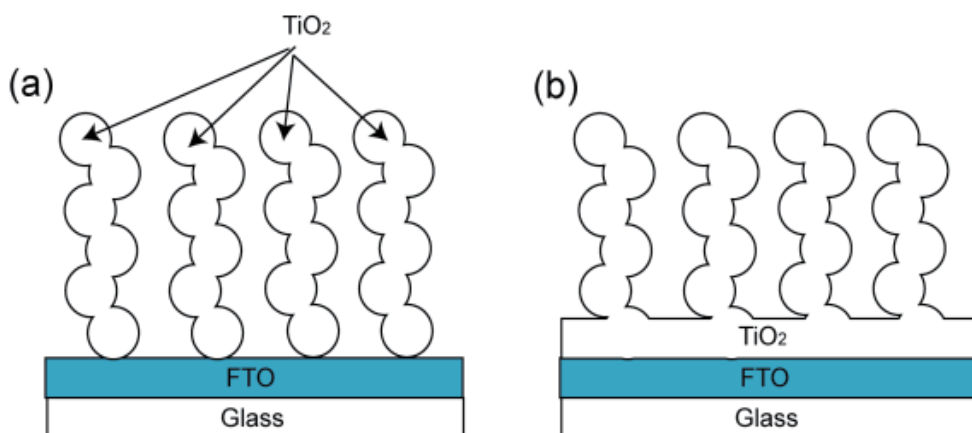
Fig. 14. Two types of TiO$_2$ working electrodes demonstrating the effect of the sensitizing dye on the photovoltaic results: (a) nano-TiO$_2$ and (b) UL/nano-TiO$_2$ [15].
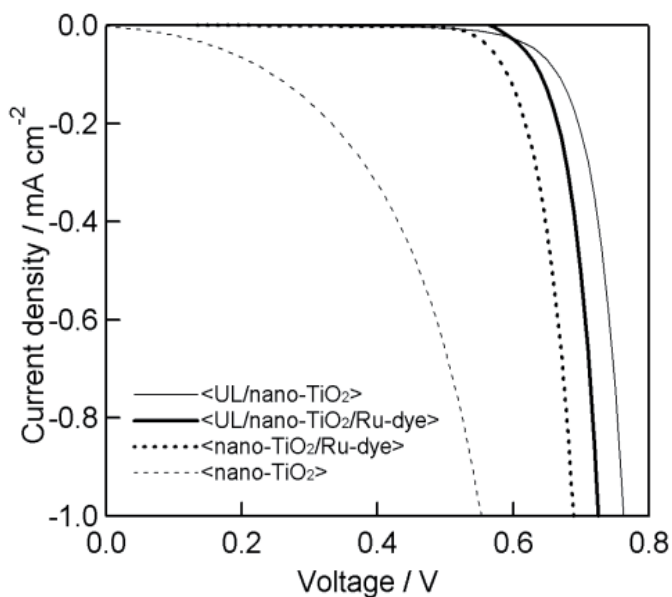
Fig. 15. Dark current-voltage characteristics of the mesoscopic TiO$_2$ electrodes shown in Fig. 14 in sandwich cells, with and without adsorbed ruthenium dye. The counter electrode was Pt-coated FTO [15].
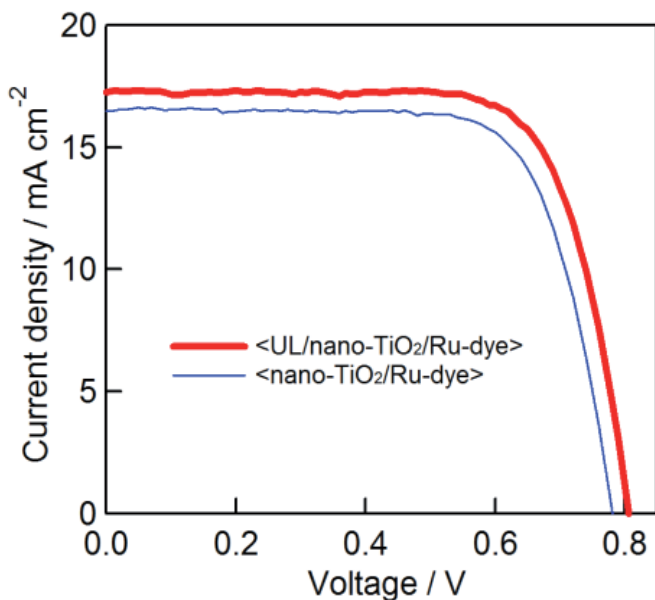
Fig. 16. Photovoltage-current curves for DSCs with two types of electrodes (shown in Fig. 14) under a solar simulator (AM 1.5, 100 mW cm^{-2}) [15].
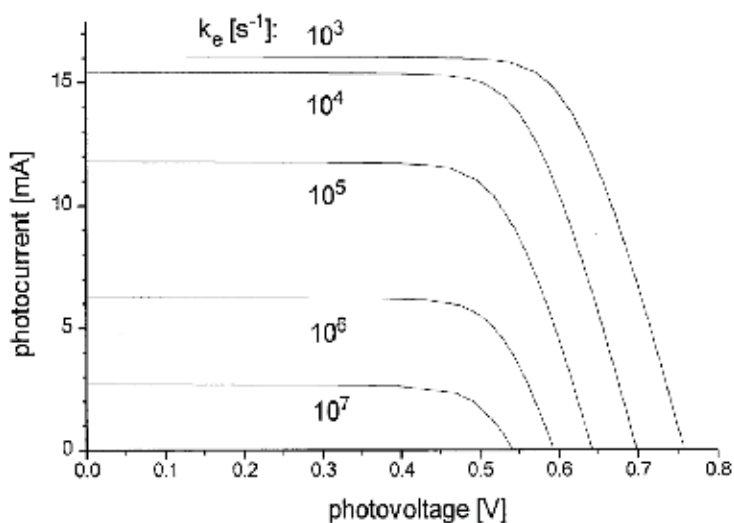
Fig. 17. The effect of the electron recapture rate constant k_e on the I-V curve of the modeled DSC. Base case parameters [16].

It was found that the V_{OC} was shifted by modifying the number of protons in the ruthenium dye (Fig. 18) [17]. When dyes that contain protonated carboxylic groups are adsorbed, the anchoring groups transfer most of their protons to the TiO_2 surface, and the positive charge of the surface shifts the Fermi level in a positive direction. The electric field, which is associated with the surface dipole generated by the positive charge, enhances the dye adsorption and assists electron injection from the sensitizer's excited state into the TiO_2 conduction band, thus increasing photocurrents. However, the positive shift in the Fermi level decreases the gap between the iodide/triiodide redox couple and the Fermi level, resulting in a lower open-circuit potential. In contrast, adsorption of a sensitizer that contains no protons shifts the Fermi level in a negative direction, leading to a higher value for the open-circuit potential, while the value of the short circuit current is low. Therefore, there is an optimum degree of protonation for the sensitizer, where the product of the short circuit photocurrent and the open circuit potential is high, thus maximizing the power conversion efficiency of the cell. Varying the degree of protonation of the sensitizer, however, also changes its electronic structure; therefore it is important to investigate how the energy and composition of the excited states change as a function of the protonation of the terminal carboxylic acid groups.

In order to enhance the photocurrent of DSCs, the mesoscopic surface area of the nanocrystalline-TiO_2 photoelectrode has been improved by chemical bath deposition of TiO_2 from $TiCl_4$ (Fig. 19) [7]. BET measurements confirmed that the surface area was increased by 20%. Moreover, a photon-trapping system has been applied to porous TiO_2 electrodes using double-layer system consisting of transparent and light-scattering layers (Fig. 12) [7, 8]. Figure 20 shows the photovoltaic characteristics of the DSC were improved by the $TiCl_4$ treatment and the double layer system (J_{SC} = 18.2 mA cm^{-2}, V_{OC} = 789 mV, FF = 0.704, and η = 10.1%). It has previously been reported that the light-scattering layer is important not only for the photon-trapping system, but also for photovoltaic generation. DSCs with the dye-sensitized light-scattering-TiO_2 layer, but without the transparent nanocrystalline-TiO_2 layer, gave a conversion efficiency of 5% [18].

(a)

(b)
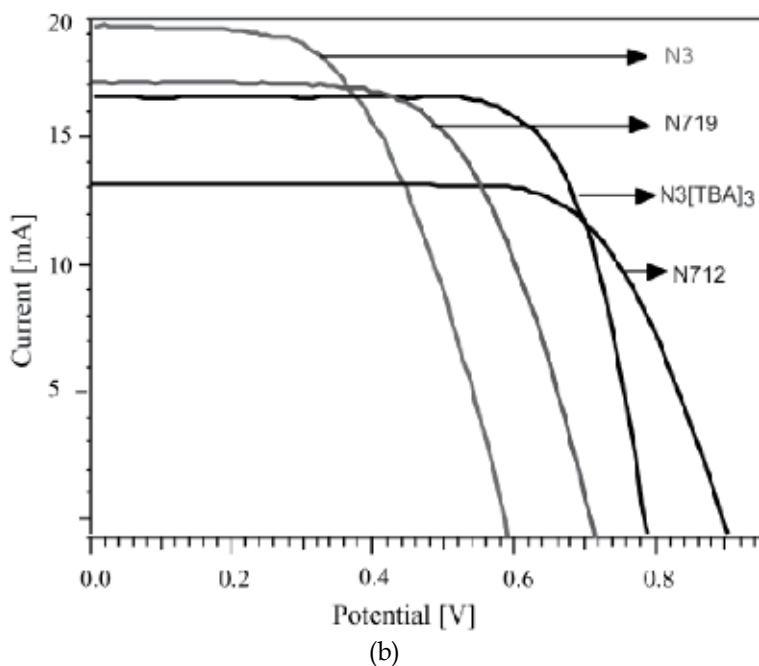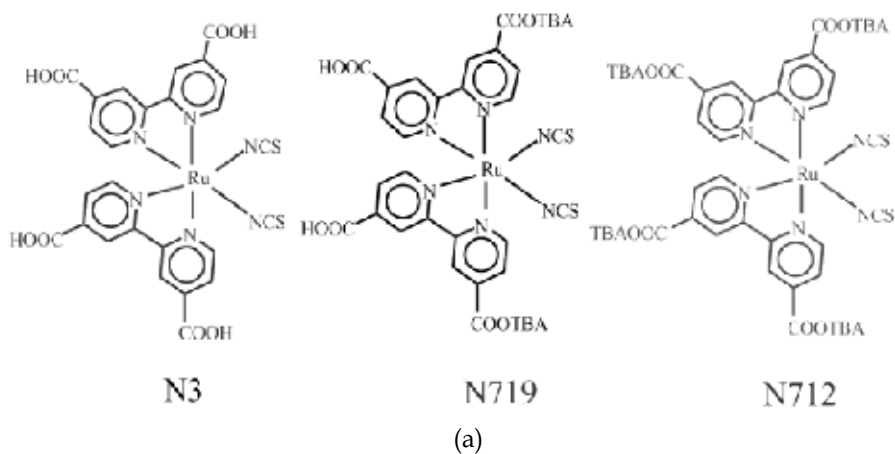
Fig. 18. (a) Structures of ruthenium dyes, and (b) the effect of dye protonation on photocurrent-voltage characteristics of nanocrystalline TiO_2 cell sensitized with N3 (4 protons), N719 (2 protons), N3[TBA]$_3$ (1 proton), and N712 (0 protons) dyes, measured under AM 1.5 sun using 1 cm^2 TiO_2 electrodes with an I$^-$/I$_3^-$ redox couple in methoxyacetonitrile [17].
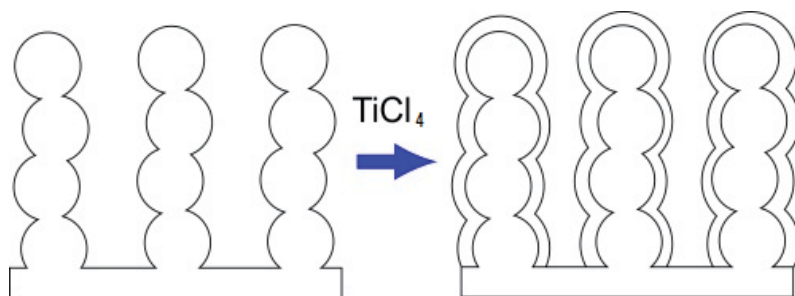
Fig. 19. Effect of the TiCl₄ treatment. An additional TiO₂ layer (1 nm thick) was coated on the surface of the nanocrystalline TiO₂ porous film [7].
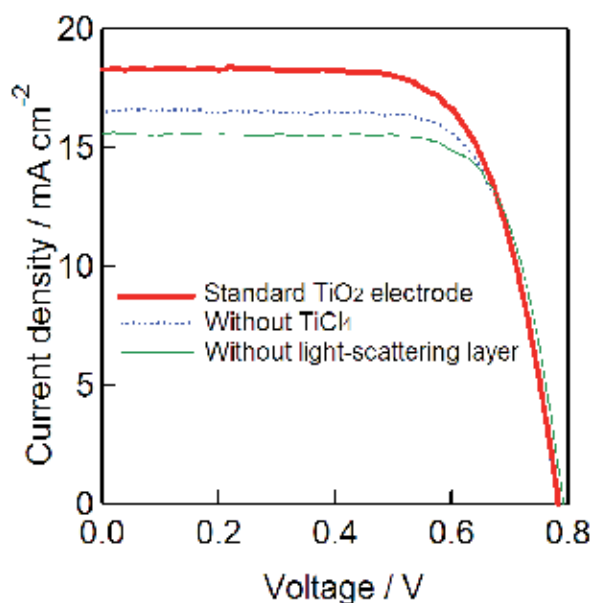
Fig. 20. Differences in the I-V curves from standard TiO_2 electrodes, electrodes with no $TiCl_4$ treatment and electrodes with no light-scattering layer. The transparent and light-scattering layers were 14 μm and 5 μm thick, respectively. Photovoltaic characteristics: standard TiO_2 electrode, J_{SC} = 18.2 mA cm⁻², V_{OC} = 789 mV, FF = 0.704 and η = 10.1%; without $TiCl_4$, J_{SC} = 16.6 mA cm⁻², V_{OC} = 778 mV, FF = 0.731 and η = 9.40%; without light-scattering layer, J_{SC} = 15.6 mA cm⁻², V_{OC} = 791 mV, FF = 0.740 and η = 9.12% [7].

Photoconversion happens on the surface of the dye-covered TiO₂ layer and the surface area can be calculated from the thickness of the porous layer. Therefore, in order to optimize the photovoltaic performance of DSCs, it is important to understand the relationship between the thickness of the nanocrystalline-TiO₂ layer and the conversion efficiency of the DSC (Fig. 21) [7, 11]. A thickness of around 14 μm was confirmed as the optimum for DSCs using N719 dye. Hence, the total optimum thickness of the TiO₂ layer, consisting of the transparent layer (14 μm) and the light-scattering layer (5 μm), was around 19 μm for N719.

However, a total thickness of 32 μm was necessary for DSCs using black dye, because it has a lower photo-absorbance coefficient than N719 [4].
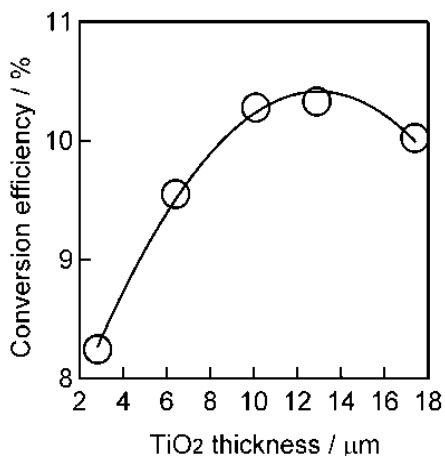
Fig. 21. Relationship between the thickness of the transparent nanocrystalline-TiO$_2$ layer (in Fig. 12) and the conversion efficiency of DSCs with anti-reflective films. Each point is the average of four cells [7].

Because glass substrates reflect 8-10% of the incident light, an anti-reflective film is necessary to enhance the photovoltaic performance of DSCs. The light-reflecting losses were eliminated by a self-adhesive fluorinated polymer film (Arktop, Asahi Glass) that also served as a 380 nm UV cut-off filter. Masks made of black plastic tape were attached to the Arktop filter to reduce scattered light. Figure 22 shows the IPCE of an electrode with anti-reflective film compared to the electrode without. The anti-reflective film enhances the IPCE from 87% to 94%, increasing the conversion efficiency by 5%.
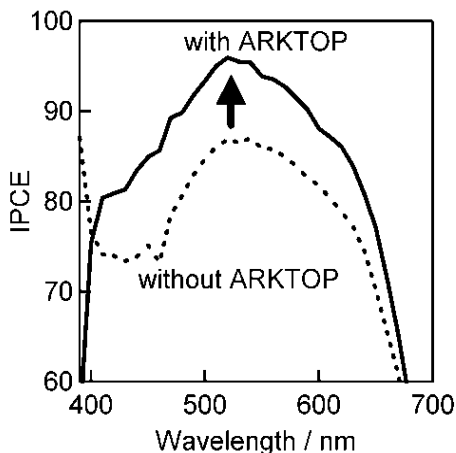
Fig. 22. Effect of anti-reflective film (Arktop) on the IPCE of DSC. A double-layer electrode (14 μm thick transparent and 5 μm light-scattering TiO$_2$ layers) was used.[7].

Optimizing the thickness of the nanocrystalline-TiO$_2$ layer, TiCl$_4$ treatments, and the anti-reflective film have allowed DSCs with conversion efficiencies of over 10% to be fabricated. Figure 10 shows the photoconversion efficiency of DSCs made at the same time; among the 12 devices, the reproducibility of DSCs with a conversion efficiency of over 10% was 100%. The error in the experimental results falls within the measurement error for a solar simulator, and therefore conversion efficiencies of 10.2 ± 0.2% is highly reproducible. Using the above technique, DSCs with efficiencies of 11.3% [19] and 12.3% [20] containing the dyes C101 (Fig. 23) and Z991 (Fig. 24), respectively, have recently been published by the Grätzel group, which are the highest conversion efficiencies published to date.
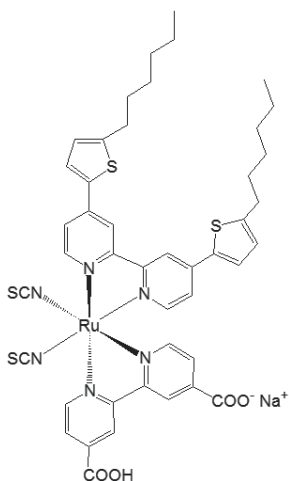
Fig. 23. The structure of the ruthenium dye C101, which achieved an 11.3% conversion efficiency in DSCs [19].
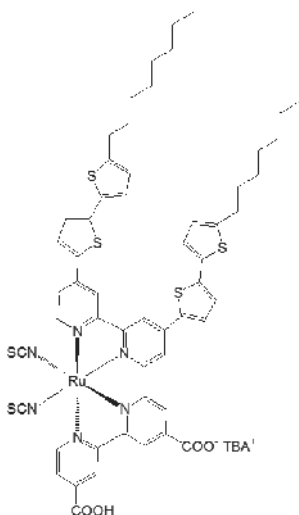
Fig. 24. The structure of the ruthenium dye Z991 which achieved a conversion efficiency of 12.3% in DSCs [20].

3. Metal-free dyes

Ruthenium complex dyes are capable of delivering DSCs with high photoenergy-conversion efficiencies. However, because ruthenium is a rare and expensive metal ruthenium dyes are not suitable for cost-effective, environmentally friendly photovoltaic systems. This limits the range of applications for these complexes, and makes the development of DSCs that use metal-free, organic dyes essential for their practical use. Recently, numerous organic dyes for high-efficiency DSCs have been reported. New organic dyes with efficiencies over 5% include hemicyanine dye (Fig. 25) (η = 5.1%) [21], polyene-diphenylaniline dye (Fig. 26) (η = 5.1%) [22], thienylfluorene dye (Fig. 27) (η = 5.23%) [23], phenothiazine dye (Fig. 28) (η = 5.5%) [24], thienothiophene-thiophene-derived dye (Fig. 29) (η = 6.23%) [25], phenyl-conjugated polyene dye (η = 6.6%) (Fig. 30) [26], *N,N*-dimethylaniline-cyanoacetic acid (Fig. 31) (η = 6.8%) [27, 28], oligothiophene dye (Fig. 32) (η = 7.7%) [29], coumarin dye (Fig. 33) (η = 8.2%) [30], indoline dye (Fig. 34) (η = 9.03%) [9, 31] and oligo-phenylenevinylene-unit dye (Fig. 35) (η = 9.1%) [32].
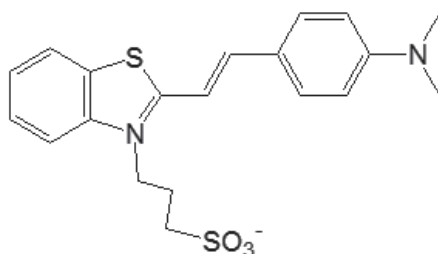
Fig. 25. Hemicyanine dye [21].
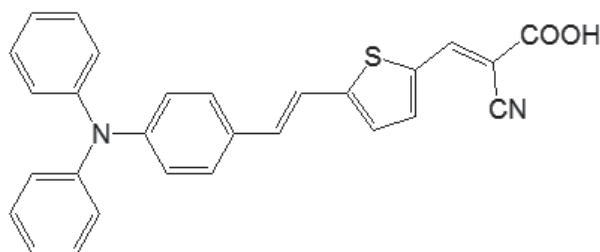
Fig. 26. Polyene-diphenylaniline dye [22].
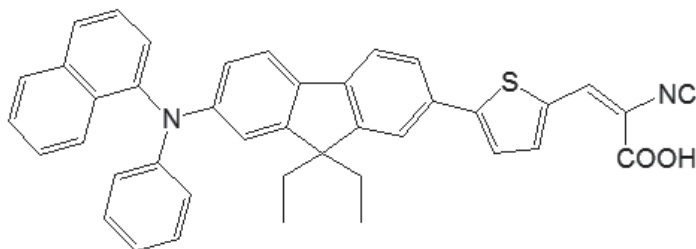
Fig. 27. Thienylfluorene dye [23].
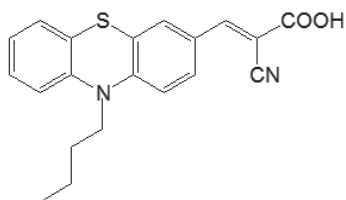
Fig. 28. Phenothiazine dye [24].
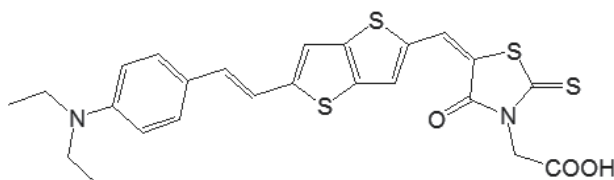
Fig. 29. Thienothiophene-thiophene-derived dye [25].
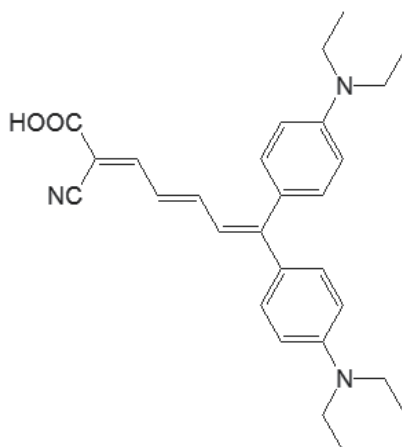
Fig. 30. Phenyl-conjugated polyene dye [26].
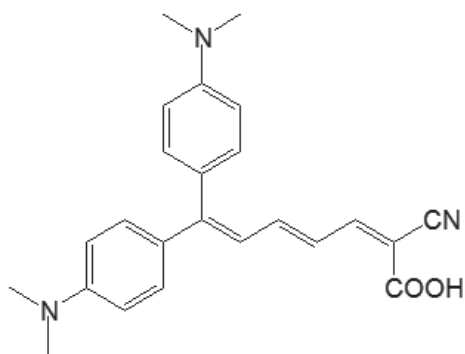
Fig. 31. *N*,*N*-dimethylaniline-cyanoacetic acid [27, 28].
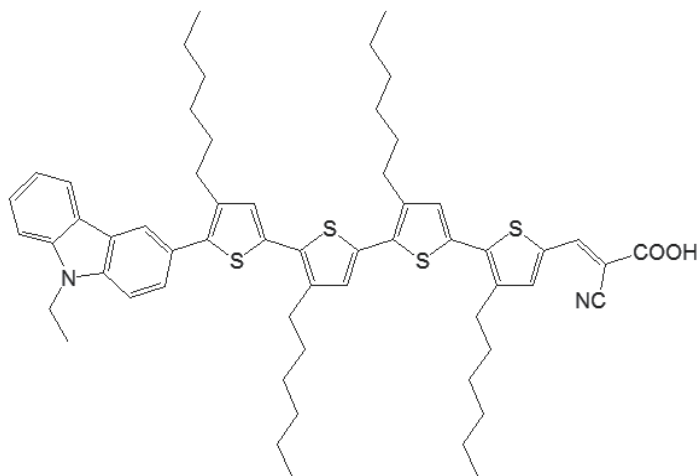
Fig. 32. Oligothiophene dye [29].
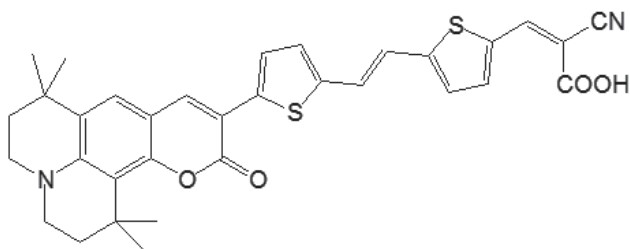
Fig. 33. Coumarin dye [30],
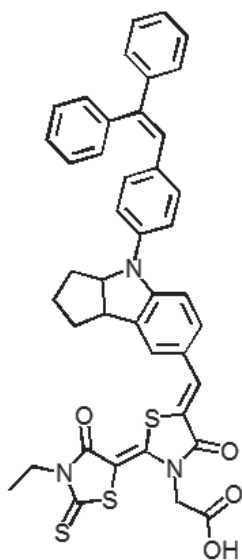
Fig. 34. Indoline dye (D149) [31].
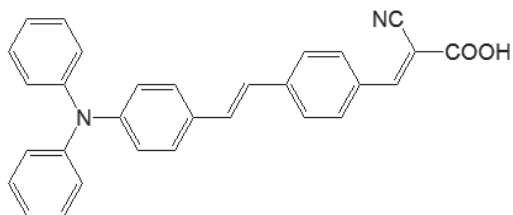
Fig. 35. Oligo-phenylenevinylene-unit dye [32].

In order to improve the conversion efficiency values, the structure of organic dye photosensitizers needed to be altered. For example, controlling the aggregation of dye molecules improves the photocurrent generation; π-stacked aggregation (D and H aggregation) on the nanocrystalline-TiO$_2$ electrodes should normally be avoided. Aggregation may lead to intermolecular quenching and the presence of molecules that are not functionally attached to the TiO$_2$ surface which act as filters. Some ruthenium complexes (black dye and N719) have shown their best results using chenodeoxycholic acid (CDCA), which functions as an anti-aggregation reagent and improves the photovoltaic effect. However, indoline dyes and coumarin dyes form photoactive aggregates on nanocrystalline-TiO$_2$ electrodes for DSCs, in a process known as J-aggregation.

In order to control the aggregation between dye molecules, an indoline dye with an n-octyl substituent on the rhodanine ring of D149 (Fig. 34) was synthesized, to give dye D205 (Fig. 36) [33]. Figure 37 shows the photovoltaic characteristics of DSCs using D149 and D205. Table 1 shows that n-octyl substitution increased the V_{OC} regardless of whether CDCA was present. CDCA increased the V_{OC} of D205 by approximately 0.054 V, but had little effect on D149, which only showed an increase of 0.006 V. The combination of CDCA and the n-octyl chain (D205) significantly improved the V_{OC} by up to 0.710 V, which is 0.066 V higher (by 10.2%) than that of D149 with CDCA. Kroeze et al. [34] showed that the alkyl substitution of dyes improved the V_{OC}, because of the blocking effect on the charge recombination between triiodide and electrons injected in the nanocrystalline-TiO$_2$ electrodes. Therefore, the V_{OC} variation observed in Figure 37 indicates that the charge recombination was impeded by the blocking effect, arising from the combination of the n-octyl chain and CDCA.
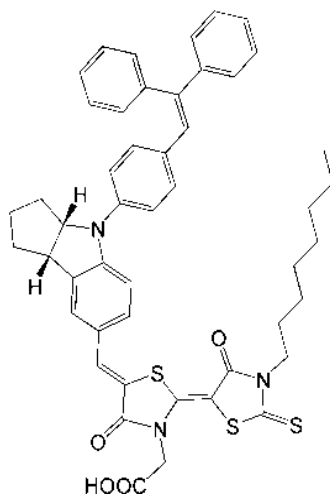
Fig. 36. Indoline dye (D205) [33].
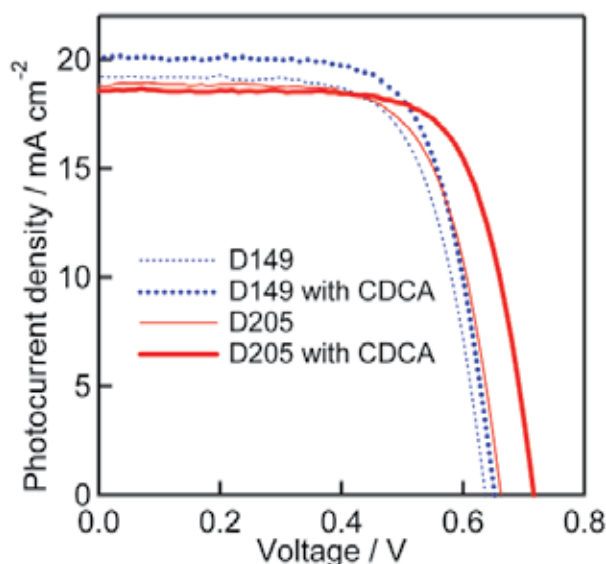
Fig. 37. Photovoltaic characteristics of DSCs using D149 and D205 with or without CDCA [33].

Photovoltaic parameter	Without CDCA		With CDCA	
	D149	D205	D149	D205
J_{sc} / mA cm^{-2}	19.08±0.26	18.99±0.19	19.86±0.10	18.68±0.08
V_{oc} / V	0.638±0.05	0.656±0.11	0.644±0.13	0.710±0.07
FF	0.682±0.06	0.678±0.09	0.694±0.06	0.707±0.09
η / %	8.26±0.09	8.43±0.16	8.85±0.18	9.40±0.12

Table 1. Photovoltaic characteristics of DSCs with indoline dyes shown in Figure 34 and 36. Each result was obtained from three DSCs [33].

Without CDCA, the variation in J_{SC} arising from n-octyl substitution on the rhodanine ring was small (0.5% of J_{SC}). However, in the presence of CDCA, the effect of the n-octyl chain was significant; the substitution of the n-octyl chain (from D149 to D205) with CDCA decreased J_{SC} by 5.9%. The effect of n-octyl substitution and CDCA on the FF was similarly small; without CDCA, the n-octyl substitution decreased the FF by 0.6%, and with CDCA, the n-octyl substitution increased the FF by 1.9%.

Without CDCA, the increase in conversion efficiency from D149 to D205 was only by 2.1%, and in the presence of CDCA, the increase was by 6.2%. The resulting average conversion efficiency for D205 with CDCA was an outstanding 9.40% (Table 2). The highest conversion efficiency value of 9.52% was achieved with a DSC based on D205 (J_{SC}: 18.56 mA cm^{-2}, V_{OC}: 0.717 V, and FF: 0.716). Reproducible efficiencies from 9.3% to 9.5% were obtained with the D205 solar cell.

Recently, the group of Prof. Peng Wang has reported the synthesis of organic dyes with conversion efficiencies in DSCs that rival those of ruthenium dyes; the highest value for a

ruthenium dye is 12.3%, under the same measurement conditions [20]. Dye C217 (Figure 38) produced DSCs with 9.8% conversion efficiency, [35] and dye C219 (Figure 39) achieved a 10.1% conversion efficiency [36]. These results strongly suggest that utilizing organic dye photosensitizers is a promising approach for producing high-performance, low cost, recyclable DSCs.
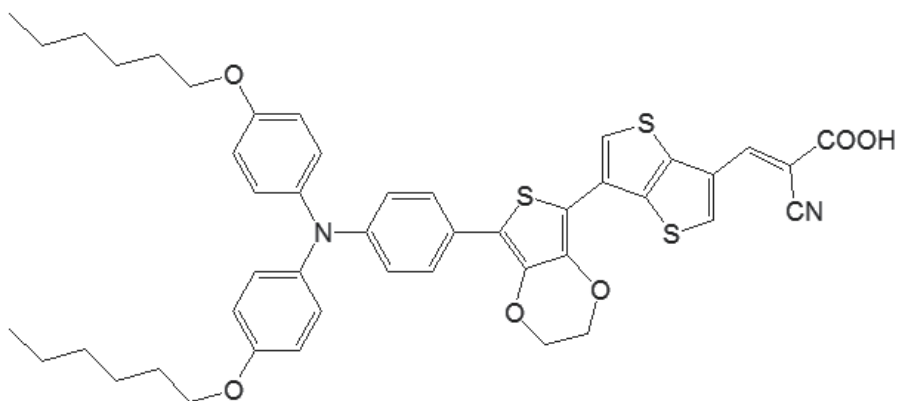
Fig. 38. C217 dye [35].
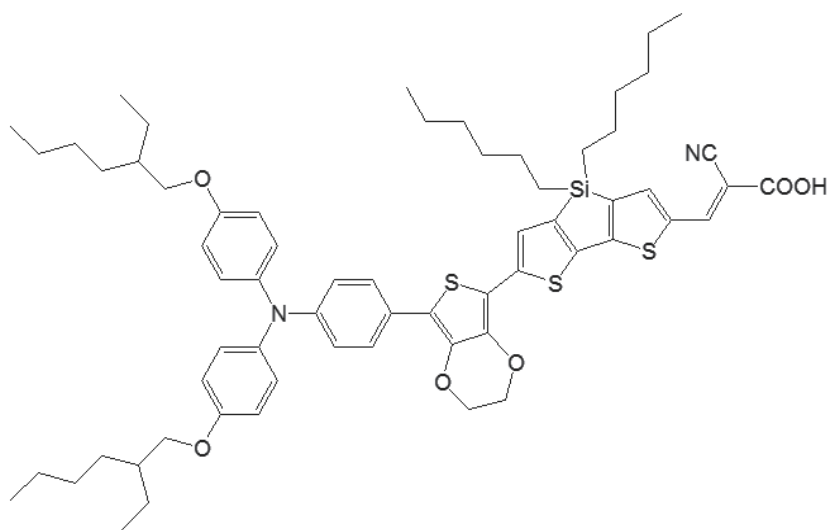
Fig. 39. C219 dye [36].

4. Metal-complex porphyrin dye

A further strategy for avoiding the use of expensive ruthenium in DSC dyes is to use complexes containing inexpensive metals. Large π-aromatic molecules, such as porphyrins and phthalocyanines, are attractive potential candidates for thin, low-cost, efficient DSCs, because of their photostability and high light-harvesting capability. Porphyrins show strong absorption and emission in the visible region, as well as tunable redox potentials. These

properties mean they have many potential applications, in areas such as optoelectronics, catalysis, and chemosensing. Self-assembled porphyrin molecular structures play a key role in solar energy research, because the photosynthetic systems of bacteria and plants contain chromophores based on porphyrins, which efficiently collect and convert solar energy into chemical energy. Various artificial photosynthetic model systems have been designed and synthesized in order to elucidate the factors that control the photoinduced electron-transfer reaction. Inspired by efficient energy transfer in naturally occurring photosynthetic reaction centers, numerous porphyrins and phthalocyanines have been synthesized and tested in DSCs.

Campbell *et al.* have reported zinc porphyrin dyes (Fig. 40) which have conversion efficiencies of 7.1% [37]. A recently reported series of zinc porphyrin dyes with donor–acceptor (D–A) substituents exhibit promising photovoltaic properties with a conversion efficiency of 6.8% (YD-2, Fig. 41) [38]. Bessho *et al.* optimized the fabrication method for YD-2-sensitized DSCs, resulting in the achievement of an 11% solar-to-electric power conversion efficiency under standard conditions (AM 1.5G, 100 mW cm^{-2} intensity) (Fig. 42) [13], which is the highest conversion efficiency for a DSC using a ruthenium-free dye so far.
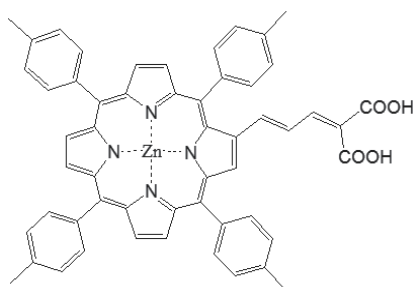
Fig. 40. Zinc porphyrin dyes by synthesized by Campbell *et al.* [37]
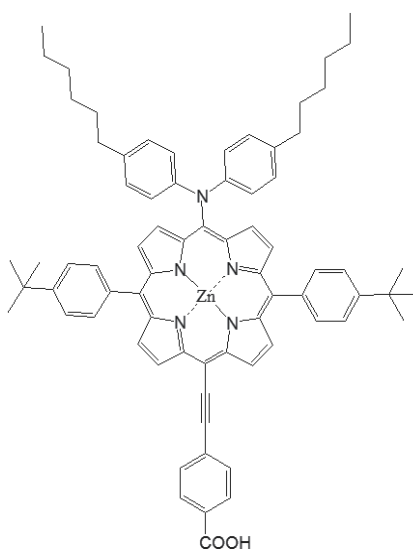
Fig. 41. Structure of porphyrin dye YD-2 [38].
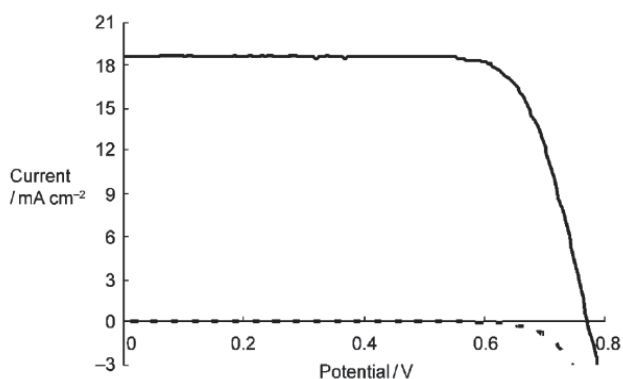
Fig. 42. Photocurrent density–voltage (J–V) characteristics of a device using YD-2 as sensitizer under AM 1.5G illumination (100 mWcm²). Values for dark current (solid line) and 100% sun (dotted line) are shown [13].

5. Natural dyes

Although high performance synthetic ruthenium-free dyes have been developed, their synthesis is time-consuming and laborious. Furthermore, they must be tested for toxicity before they can be used commercially. These problems could be solved if inexpensive, non-toxic, natural dyes, such as pigments used in food coloring, could be used in DSCs. Natural dyes are easily and safely extracted from plants, which means they are cheap and widely available, and do not require complex synthesis or toxicity testing. Therefore, the use of natural dyes is important for the development of cheap, commercially available DSCs. Natural dyes have shown moderate energy conversion efficiencies in DSCs [39-45]; natural chlorophyll dyes achieved energy conversion efficiencies of over 4% (Fig. 43) [39, 40]. However, despite the huge range of natural dyes, most of the other dyes tested yielded energy conversion efficiencies below 2%, although some derivatives synthesized from natural dyes have produced energy conversion efficiencies of over 2% [46, 47]).
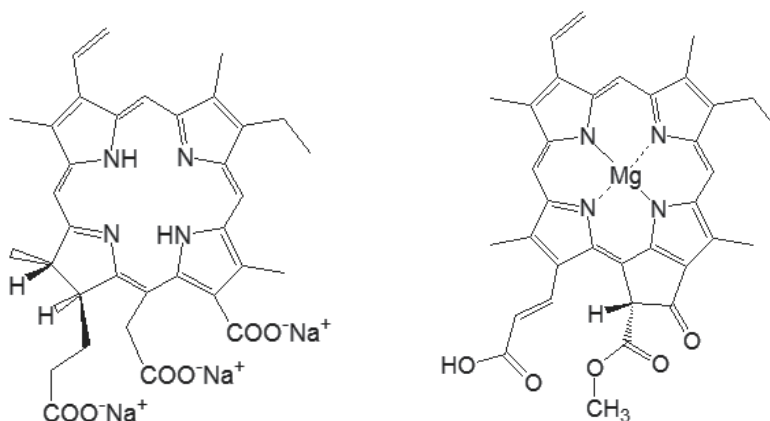
Fig. 43. Structures of chlorophylls for DSCs: Chlorin e6 (left) [39] and chlorophyll c (right) [40].

The natural dye Monascus yellow produces DSCs with over 2% conversion efficiency [12]. It is extracted from Monascus (red yeast rice), which is the product of *Monascus purpureus* fermentations. Monascus is a dietary staple in some Asian countries, and is traditionally made by inoculating rice soaked in water with *Monascus purpureus* spores. The mixture is incubated at room temperature for 3–6 days, and its core turns bright red and the outside turns reddish purple. Because of the low cost of cultivation, some producers have extracted the highly colored fermentation products to use as food pigment dyes. Monascus red, which is one of the red dyes in Monascus fermentations, has been used as a sensitizing dye for DSCs [41], which gave a 0.33% conversion efficiency. Monascus yellow, which is also extracted from Monascus fermentations (Fig. 44), was used as a novel sensitizer. The DSC with Monascus yellow achieved a photovoltaic performance where J_{SC} = 6.1 mA cm^{-2}, V_{OC} = 0.57 V, FF = 0.66, and η = 2.3% (Fig. 45).
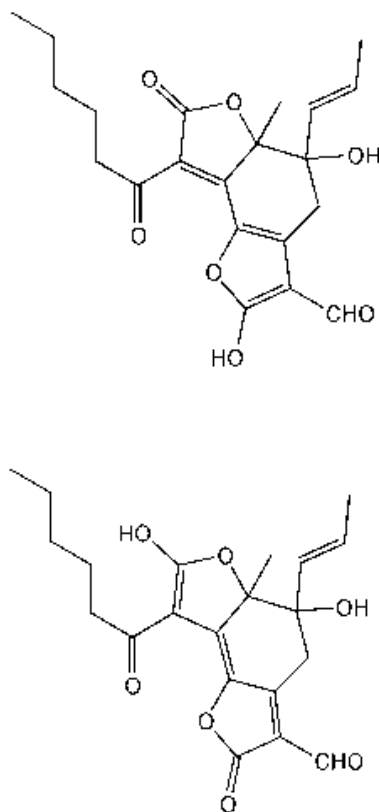
Fig. 44. Structures of dye molecules in Monascus yellow, supplied as a mixture of two isomers in an extract from Monascus fermentations [12].
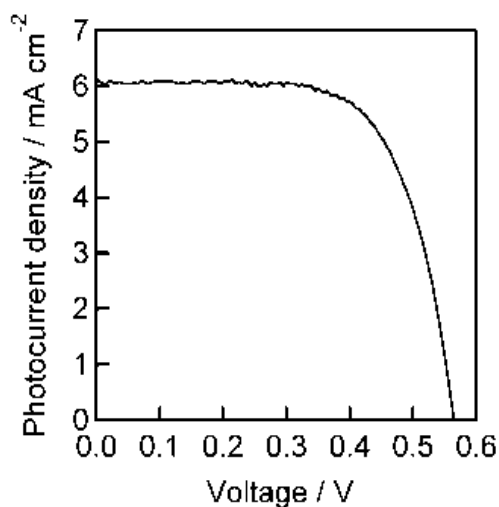
Fig. 45. I-V curve for DSC using Monascus yellow dye [12].

Figure 46 shows the UV–VIS absorption spectra and IPCE spectra of Monascus yellow on transparent nanocrystalline-TiO$_2$ electrodes (prepared using a TiO$_2$ paste, PST-18NR, CCIC, Japan) [12]. Without acetic acid treatment, the absorption peak at 426 nm was just 8% and the IPCE value was close to zero. After acetic acid treatment, the absorption peak increased to 69%, resulting in the IPCE value increasing to 47% at 450 nm. The action spectrum of the cell sensitized by Monascus yellow largely agrees with the absorption spectrum of the dye adsorbed to the TiO$_2$ film. The IPCE peak is red-shifted by 24 nm relative to the absorption peak. The strong absorption of blue light of the iodide/triiodide electrolyte is thought to decrease the IPCE value in the short wavelength region, resulting in the red shift of the peak in the action spectrum. The remarkable improvement in the IPCE value following treatment with acetic acid may be because the acetic acid promotes bonding between the Monascus yellow hydroxyl groups and the surface of the nanocrystalline-TiO$_2$ film. In addition, sensitizing dyes adsorbed onto TiO$_2$ surfaces are known to be desorbed by addition of bases such as NaOH and NH$_3$. Thus, the improvement of the photovoltaic performance upon addition of acetic acid can be attributed to a chemical bonding adsorption mode, in contrast to a physical (van der Waals) adsorption mode without acetic acid. When the dye is physically adsorbed onto the TiO$_2$ electrode, it cannot inject photoexcited electrons, resulting in a small absorption peak. In contrast, the dye adsorbed onto the TiO$_2$ surface with protons strengthening the chemical bonding, can efficiently inject photoexcited electrons from the dye into the electrode.

The effect of the nanocrystalline-TiO$_2$ layers, and the solvents used for rinsing them following dye uptake, were examined (Table 2) [12]. After rinsing with water, the conversion efficiency of the P25-based cell was higher than that of the PST-18NR-based cell. However, after rinsing with other solvents, the PST-18NR-based cell yielded higher conversion efficiencies than the P25-based cell, which arose from the difference in J_{SC}. This effect can be attributed to the surface area and pore size, which is related to the particle size. Generally, small TiO$_2$ particles fused together form a large surface area, which allows more dye to be loaded onto the surface. However, the small pore size prohibits the smooth transportation of redox species in the electrolyte solution, which fills the pore space. The

TiO$_2$ particle size in PST-18NR is smaller than that of P25, thus the amount of adsorbed molecules onto the PST-18NR surface should be higher than that on the P-25 surface. This rationalizes the higher photocurrent density from the PST-18NR-based cell compared with the P25-based cell. The TiO$_2$ particles of PST-18NR have a smaller pore size compared with P25. Therefore, more water molecules, which have a high boiling point, may remain inside the smaller pores of the PST-18NR-based electrode and inhibit the electrolyte diffusion into the pores. In contrast, the other volatile solvents evaporate easily after rinsing, leading to the high photocurrent density and thus high energy conversion efficiency. The values of the V_{OC} and FF did not show significant differences between the two electrodes.
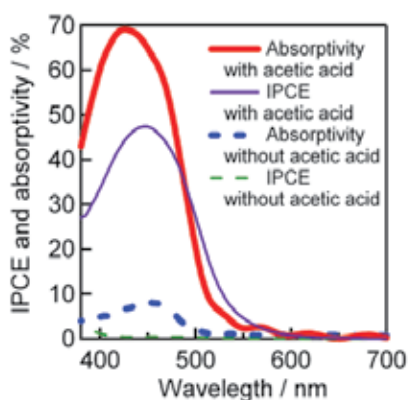
Fig. 46. UV-Vis absorption and IPCE spectra of Monascus yellow-sensitized TiO$_2$ electrodes showing the effect of acetic acid in the dye solution. The absorption spectra were measured using a transparent nanocrystalline-TiO$_2$ electrode. IPCE spectra were measured using a double-layered nanocrystalline-TiO$_2$ electrode. Each electrode was dipped in Monascus yellow solution with or without acetic acid, for 15 min. [12].

TiO$_2$ material	Rinsing solvent	J_{SC} / mA cm^{-2}	V_{OC} / V	FF	η / %
P25	water	3.50±0.30	0.537±0.021	0.697±0.018	1.29±0.04
	ethanol	3.40±0.00	0.504±0.009	0.653±0.011	1.14±0.01
	acetonitrile	3.12±0.04	0.535±0.019	0.714±0.009	1.19±0.01
	methanol	4.00±0.04	0.522±0.000	0.624±0.009	1.34±0.03
	acetone	3.72±0.04	0.504±0.009	0.692±0.009	1.39±0.02
PST-18NR	water	2.65±0.05	0.514±0.020	0.725±0.019	0.99±0.00
	ethanol	5.50±0.14	0.524±0.009	0.666±0.006	1.93±0.05
	acetonitrile	4.60±0.20	0.506±0.016	0.694±0.014	1.58±0.02
	methanol	5.54±0.22	0.547±0.002	0.633±0.002	1.92±0.00
	acetone	4.32±0.07	0.522±0.014	0.666±0.026	1.51±0.01

Table 2. Photovoltaic characteristics of DSCs using Monascus with different TiO$_2$ electrodes and rinsing solvents; short-circuit photocurrent density: J_{SC}, open-circuit photovoltage: V_{OC}, fill factor: FF, and energy conversion efficiency: η. Data were obtained using three independent measurements [12].

6. Conclusions and outlook

The main factors that affect the operation of DSCs have been discussed. The acidity of dye solution can be a critical factor for the uptake of the dye; for ruthenium dyes, the addition of TBA-OH was important for controlling the dye-uptake speed, whereas for natural dyes, the addition of acetic acid was necessary for adsorption onto nanocrystalline-TiO_2 electrodes. The resulting dye mono-layer on the nanocrystalline-TiO_2 electrodes can act as a blocking layer that maintains charge separation. Dye aggregation, which is a key factor in obtaining high-efficiency organic DSCs, can be controlled by combining substitution of the alkyl chain on the dye with the addition of CDCA. The thickness of the nanocrystalline-TiO_2 electrodes also needs to be optimized for each dye, because of the difference in the light-absorption coefficients. Screen printing methods are the most suitable for controlling the thickness of nanocrystalline-TiO_2 electrodes; the layers can be easily positioned and built up to the desired thickness. An anti-reflective film and a light-scattering TiO_2 layer on the transparent TiO_2 layer allows the incident light to be absorbed effectively, which enhances the photocurrent. The highest conversion efficiency achieved by DSCs was 12.3%, and used a ruthenium dye (Z991).

Replacing ruthenium complexes with fully organic sensitizers or complexes containing inexpensive metals is an attractive strategy for producing low cost, environmentally friendly DSCs. Ruthenium-free dyes are already producing excellent conversion efficiencies, which indicate that they are promising candidates for photosensitizers in DSCs. However, the mechanisms of dye aggregation in DSC photovoltaics are still not fully understood; in order to match the performance of ruthenium complexes, further research in this field is necessary.

Monascus yellow was found to be one of the best natural dye photosensitizers for DSCs, with a conversion efficiency of 2.3%. The chlorophyll dyes were the only natural dyes with a higher conversion efficiency of 4%. Natural food dyes are better for human health than synthetic dyes, thus Monascus yellow could be used in an educational kit for students studying DSCs.

In summary, DSCs offer a low cost, non-toxic option for the commercial production of high-performance solar cells.

7. References

[1] B. O'Regan and M. Grätzel, *Nature,* 1991, 353, 737.

[2] M. K. Nazzerruddin, A. Kay, I. Podicio, R. Humphy-Baker, E. Müller, P. Liska, N. Vlachopoulos and M. Grätzel, *J. Am. Chem. Soc.*, 1993, 115, 6382-6390.

[3] M. K. Nazeerudding, P. Péchy, T. Renouard, S. M. Zakeeruddin, R. Humphry-Baker, P. Comte, P. Liska, L.Cevey, E. Costa, V. Shklover, L. Spiccia, G. B. Deacon, C. A. Bignozzi and M. Grätzel, *J. Am. Chem. Soc.*, 123 (2001) 1613.

[4] Z.-S. Wang, T. Yamaguchi, H. Sugihara and H. Arakawa, *Langmuir,* 2005, 21, 4272-4276.

[5] Chiba, A. Islam, Y. Watanabe, R. Komiya, N. Koide and L. Han, *J. J. Appl. Phys.*, 2006, 45, L638.

[6] Md. K. Nazeeruddin, F. De Angelis, S. Fantacci, A. Selloni, G. Viscardi, P. Liska, S. Ito, B. Takeru and M. Grätzel, *J. Am. Chem. Soc.*, 2005, 127, 16835.

[7] S. Ito, T. N. Murakami, P. Comte, P. Liska, C. Grätzel, Md. K. Nazeeruddin and M. Grätzel, *Thin Soild Films*, 2008, 516, 4613.

[8] S. Ito, M. K. Nazeeruddin, S. M. Zakeeruddin, P. Péchy, P. Comte, M. Grätzel, T. Mizuno, A. Tanaka, T. Koyanagi, International Journal of Photoenergy 2009, Article ID 517609, doi:10.1155/2009/517609.

[9] S. Ito, S. M. Zakeeruddin, R. Humphry-Baker, P. Liska, R. Charvet, P. Comte, M. K. Nazeeruddin, P. Péchy, M. Takata, H. Miura, S. Uchida and M. Grätzel, *Adv. Mater*, 2006, 18, 1202-1205.

[10] S. Ito, H. Miura, S. Uchida, M. Takata, K. Sumioka, P. Liska, P. Comte, P. Péchy and M. Grätzel, *Chem. Commun.*, 2008, 5194-5196.

[11] H. Imahori, Y. Matsubara, H. Iijima, T. Umeyama, Y. Matano, S. Ito, M. Niemi, N. V. Tkachenko, H. Lemmetyinen, *J. Phys. Chem. C,* 20010, 114, 10656.

[12] S. Ito, T. Saitou, H. Imahori, H. Uehara, N. Hasegawa, *Energy Environ. Sci.*, 2010, 3, 905.

[13] T. Bessho, S. M. Zakeeruddin, C.-Y. Yeh, E. W.-G. Diau, M Grätzel, *Angew. Chem. Int. Ed.*, 2010, 49, 6646.

[14] S. Ito, H. Matsui, K. Okada, S. Kusano, T. Kitamura, Y. Wada, S. Yanagida, Sol. Energy Mater. Sol. Cells 82 (2004) 421.

[15] S. Ito, P. Liska, R. Charvet , P. Comte, P. Péchy, Md. K. Nazeeruddin, S. M. Zakeeruddin and M. Grätzel, *Chem. Commun.*, (2005) 4351.

[16] J. Ferber, R. Stangl, J. Luther, *Sol. Energy Mater. Sol. Cells,* 53 (1998) 29.

[17] M. K. Nazeeruddin, R. Humphry-Baker, P. Liska, M. Grätzel, *J. Phys. Chem. B* 2003, *107,* 8981.

[18] Z. Zhang, S. Ito, B. O'Regan, D. Kunag, S.M. Zakeeruddin, P. Liska, R. Charvet, P. Comte, Md. K. Nazeeruddin, P. Péchy, R. Humphry-Baker, T. Koyanagi, T. Mizuno, M. Grätzel, Z. Phys. Chem. 221 (2007) 319.

[19] F. Gao, Y. Wang, D. Shi, J. Zhang, M. Wang, X. Jing, R. Humphry-Baker, P. Wang[†], S. M. Zakeeruddin, M. Grätzel, *J. Am. Chem.* Soc., 2008, 130, 10720.

[20] M. Grätzel, *Acc. Chem. Res.*, 42 (2009) 1788; the 12.3% conversion efficiency was presented by Professor Grätzel in "International Symposium on Innovative Solar Cells 2009" (The University of Tokyo, Japan, 2nd-3rd, March, 2009).

[21] Z.-S. Wang, F.-Y. Li and C.-H. Huang, *J. Phys. Chem. B*, 2001, 105, 9210.

[22] D. P. Hagberg, T. Edvinsson, T. Marinado, G. Boschloo, A. Hagfeldt and L. Sun, *Chem. Commun.*, 2006, 2245.

[23] K. R. J. Thomas, J. T. Lin, Y.-C. Hsuc and K.-C. Ho, *Chem. Commun.*, 2005, 4098.

[24] H. Tian, X. Yang, R. Chen, Y. Pan, L. Li and A. Hagfeldt, L. Sun, *Chem. Commun.*, 2007, 3741.

[25] S.-L. Li, K.-J. Jiang, K.-F. Shao and L.-M. Yang, *Chem. Commun.*, 2006, 2792.

[26] T. Kitamura, M. Ikeda, K. Shigaki, T. Inoue, N. A. Anderson, X. Ai, T. Lian and S. Yanagida, *Chem. Mater.*, 2004, 16, 1806.

[27] K. Hara, M. Kurashige, S. Ito, A. Shinpo, S. Suga, K. Sayama and H. Arakawa, *Chem. Commun.*, *2003,* 252.

[28] K. Hara, T. Sato, R. Katoh, A. Furube, T. Yoshihara, M. Murai, M. Kurashige, S. Ito, A. Shinpo, S. Suga and H. Arakawa, *Adv. Funct. Mater.*, 2005, 15, 246.

[29] N. Koumura, Z.-S. Wang, S. Mori, M. Miyashita, E. Suzuki and K. Hara, *J. Am. Chem. Soc.*, 2006, 128, 14256.

[30] Z.-S. Wang, Y. Cui, Y. Dan-oh, C. Kasada, A. Shinpo and K. Hara, *J. Phys. Chem. C,* 2007, 111, 7224.

[31] T. Horiuchi, H. Miura, K. Sumioka and S Uchida, *J. Am. Chem. Soc.*, 2004, 126, 12218.

[32] S. Hwang, J. H. Lee, C. Park, H. Lee, C. Kim, C. Park, M.-H. Lee, W. Lee, J. Park, K. Kim, N.-G. Park and C. Kim, *Chem. Commun.*, 2007, 4887.

[33] S. Ito, H. Miura, S. Uchida, M. Takata, K. Sumioka, P. Liska, P. Comte, P. Péchy, M. Grätzel, *Chem. Commun.*, 2008, 5194.

[34] J. E. Kroeze, N. Hirata, S. Koops, Md. K. Nazeeruddin, L. Schmidt-Mende, M. Grätzel and J. R. Durrant, *J. Am. Chem. Soc.* 2006, 128, 16376.

[35] G. Zhang, H. Bala, Y. Cheng, D. Shi, X. Lv, Q. Yu, P. Wang, Chem. Commun., 2009, 2198.

[36] W. Zeng, Y. Cao, Y. Bai, Y. Wang, Y. Shi, M. Zhang, F. Wang, C. Pan, P. Wang, Chem. Mater. 2010, 22, 1915.

[37] W. M. Campbell, K. W. Jolley, P. Wagner, K. Wagner, P. J. Walsh, K. C. Gordon, L. Schmidt-Mende, Md. K. Nazeeruddin, Q. Wang, M. Grätzel and D. L. Officer, *J. Phys. Chem. C*, 2007, 11, 11760.

[38] H.-P. Lu, C.-Y. Tsai, W.-N. Yen, C.-P. Hsieh, C.-W. Lee, C.-Y. Yeh, E. W.-G. Diau, *J. Phys. Chem. C* 2009, *113*, 20990.

[39] M. Ikegami, M. Ozeki, Y. Kijitori and T. Miyasaka, *Electrochemistry,* 2008, 76, 140-143.

[40] X.-F. Wang, C.-H. Zhan, T. Maoka, Y. Wada and Y. Koyama, *Chem. Phys. Lett.,* 2007, 447, 79-85.

[41] D. Zhang, N. Yamamoto, T. Yoshida and H. Minoura, *Trans. Mater. Res. Soc. Jpn.*, 2002, 27, 811-814.

[42] K. Wongcharee, V. Meeyoo and S. Chavadej, *Solar Energy Mater. Solar Cells,* 2007, 91, 566-571.

[43] A. S. Polo and N. Y. M. Iha, *Solar Energy Mater. Solar Cells,* 2006, 90, 1936-1944.

[44] G. R. A. Kumara, S. Kaneko, M. Okuya, B. Onwona-Agyeman, A. Konno and K. Tennakone, *Solar Energy Mater. Solar Cells,* 2006, 90, 1220-1226.

[45] S. Hao, J. Wu, Y. Huang and J. Lin, *Solar Energy,* 2006, 80, 209–214.

[46] A. Kay and M. Grätzel, *J. Phys. Chem.*, 1993, 97, 6272-6277.

[47] X.-F. Wang, R. Fujii, S. Ito, Y. Koyama, Y. Yamano, M. Ito, T. Kitamura and S. Yanagida, *Chem. Phys. Lett.,* 2005, 416, 1-6.

Comparative Study of Dye-Sensitized Solar Cell Based on ZnO and TiO$_2$ Nanostructures

Y. Chergui, N. Nehaoua and D. E. Mekki

Physics Department, LESIMS Laboratory,
Badji Mokhtar University, Annaba,
Algeria

1. Introduction

The dye-sensitized solar cell (DSC) is a third generation photovoltaic device that holds significant promise for the inexpensive conversion of solar energy to electrical energy, because of the use of inexpensive materials and a relatively simple fabrication process. The DSC is based on a nano-structured, meso-porous metal oxide film, sensitized to the visible light by an adsorbed molecular dye. The dye molecules absorb visible light, and inject electrons from the excited state into the metal oxide conduction band. The injected electrons travel through the nanostructured film to the current collector, and the dye is regenerated by an electron donor in the electrolyte solution. The DSC is fully regenerative, and the electron donor is again obtained by electron transfer to the electron acceptor at the counter electrode (Ito et al, 2006). The current certified efficiency recordis11.1% for small cells, and several large-scale tests have been conducted that illustrate the promise for commercial application of the DSC concept. A schematic presentation of the operating principles of the DSC is given in Figure1. At the heart of the system is a mesoporous oxide layer composed of nanometer-sized particles which have been sintered together to allow for electronic conduction to take place. The material of choice has been TiO$_2$ (anatase) although alternative wide band gap oxides such as ZnO, and Nb$_2$O$_5$ have also been investigated. Attached to the surface of the nanocrystalline film is a monolayer of the charge transfer dye (Janne, 2002).

Nanocrystalline electronic junctions compose of a network of mesoscopic oxide or chalcogenide particles, such as TiO$_2$, ZnO, Fe$_2$O$_3$, Nb$_2$O$_5$, WO$_3$, Ta$_2$O$_5$ or Cds and CdSe, which are interconnected to allow for electronic conduction to take place. The oxide material of choice for many of these systems has been TiO$_2$. Its properties are intimately linked to the material content, chemical composition, structure and surface morphology. From the point of the material content and morphology, two crystalline forms of TiO$_2$ are important, anatase and rutile (the third form, brookite, is difficult to obtain). Anatase is the low temperature stable form and gives mesoscopic films that are transparent and colorless (Fang et al, 2010).

The application of ZnO in excitonic solar cells, XSCs, (organic, dye sensitized and hybrid) has been rising over the last few years due to its similarities with the most studied semiconductor oxide, TiO$_2$. ZnO presents comparable bandgap values and conduction band position as well as higher electron mobility than TiO$_2$. It can be synthesized in a wide variety of nanoforms applying straight forward and scalable synthesis methodologies.

Particularly, the application of vertically-aligned ZnO nanostructures it is thought to improve contact between the donor and acceptor material in organic solar cells (OSCs), or improve electron injection in dye sensitized solar cells (DSCs).[7] To date, DSC based on ZnO have achieved promising power conversion efficiency values of 6%.
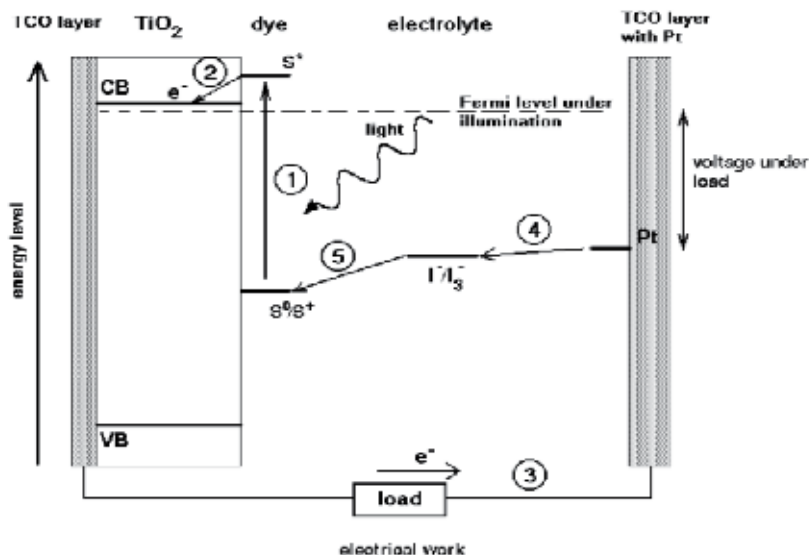
Fig. 1. Principle of operation and energy level scheme of the dye-sensitizednanocrystalline solar cell. Photo-excitation of the sensitizer (S) is followed by electron injection into the conduction band of the mesoporous oxidesemiconductor. The dye molecule is regenerated by the redox system, which itself is regenerated at the counter electrode by electrons passed through the load. Potentials are referred to the normal hydrogen electrode (NHE). The open-circuit voltage of the solar cell corresponds to the difference between the redox potential of the mediator and the Fermi level of the nanocrystallline film indicated with a dashed line (janne, 2002).

lthough most of the reported works on DSSC are based on TiO_2 porous thin films, various structures of ZnO are also being used for DSSC fabrication. The advantages of using ZnO over TiO_2 are its direct band gap (3.37 eV), higher exciton binding energy (60 meV) compared to TiO_2 (4 meV), and higher electron mobility (200 cm^2 V^{-1} s^{-1}) over TiO_2 (30 cm^{2}V^{-1} s^{-1}). However, the efficiency of the DSSC based on ZnO nanostructures is still very low (5%). Here we present a comparative study between ZnO and TiO_2 dye-sensitized solar cell (DSSC) by comparing its efficiency, fill factor, the current of short circuit I_{sc} and voltage of open circuit V_{oc} (Jingbin et al, 2010).

2. Materials

2.1 ZnO presentation

ZnO is an environment-friendly material (Myo et al, 2008), is a rogarded as one of the most promising substitution materials, and much interest has been paid to semiconductor nanostructures. Too, ZnO is one of the most important functional semi-conductor and is a very attractive material for application devices.

Zno is an environment-friendly material, is a promising candidate for exciton-related optoelctronic devices in the ultraviolet region, and it is also applicable to the devices based in reduced dimensional quantum effect because it can be grown in various crystalline form with submicron size such as whiskers, nanobelts, nanorods, nanowires, nanoplatelets, and so on. ZnO is a regarded as one of the most promising substitution materials for ITO (Introdium Thin Fims)today because of its good resistivity, high transmittance, nontoxicity, and low const. However pure ZnO thin films have a lower electric conductivity than ITO thin fims (You-Seung et al, 2008).

Recently, hollow micro/nanostructures have become of great interst because of their excellent characteristics such as density , high surface-to-volume ratio, and how coefficient sof thermal expansion and refractive index, which makes them attractive for applications ranging from catalystsupports, anti-reflection surface coatings, microwaves absorption (Lou et al, 2008; Zhong et al, 2000) , encapsulating sentive materials (Li et al, 2005; Dinsmore et al, 2002), drug delivery, and rechargeable batteries (Liang et al, 2004; Lee et al, 2003).

Rapid developments in the synthesis of hollow structures, such as CuO (Wang. et al, In press; Liu et al, 2009 Cu$_2$O (Teo et al, 2006; Chang et al , 2005), TiO$_2$ (Yu et al, 2007), SnO$_2$ (Cao et al, 2006; Wang et al, 2006), Fe$_2$O$_3$(Liu et al, 2009), Co$_3$O$_4$ (Park et al, 2009; Zhao et al, 2008), β-Ni(OH)$_2$ (Wang et al, 2005), α-MnO$_2$ (Li et al, 2006), CuS (Liu et al, 2007; Yu et 2000), Sb$_2$S$_3$ (Cao et al, 2006), ZnO (Zhou et al. 2007; Lin, et al, 2009), CdMoO$_4$(Wang et al, 2009; Wang et al, 2006), and ZnWO$_4$ (Huang et al, 2006), have greatly advanced our ability to tune their mechanical, optical, electrical, and chemical properties to satisfy the various needs of practical applications.

ZnO can be useful in many fields, such as in the rubber industry (Ibarra et al, 2002), photocatalysis(Hsu et al, 2005), sunthesis of ZnO (Hsu et al, 2005; Sun et al, 2007; Zhang et al, 2005). Cosmetic and pharmaceutical industries, and for therapeutic applications (Rosenthal et al, 2008), but little work have been done in these areas (Rosenthalet al, 2008; Chen et al, 2009; Pal et al, 2009). ZnO, as a wide gape semiconductor material, is becoming an increasing concern because of its biocompatibility, nontoxity, and good mechanical, optical, electrical properties. Thus, research about ZnO$_2$ and ZnO hollow spheres is of great importance and should be paid more attention (Ceng et al, 2009).

ZnO nanoparticules and quantium dots technologically important owing to their special properties and potential use in the fabrication of sensors, light emitters operating in the short-wavelegth range from blue to ultraviolet, transparent conducting oxides, and solar cells (özgör et al, 2005; Sakurai et al, 2002; Th et al, 2003).

Both high-quality p-and n-type ZnO thin films play an important role in the fabrication of optical devices. The production of ZnO with an n-type doping is simple without the need for intentional doping (Toshiya et al, 2008).

ZnO is expected to be one of the candidate host materials for impurity doping (Yamamoto et al, 2005; Ishizumi et al, 2005). However the optical properties of impurity-doped ZnO nanostructures are not well understood. very recently highly porous ZnO films have been successfully fabricated by electrodeposition using eosin Y(EY)dye molecules (T. Yoshida et al, 2003; T. Yoshida et al, 2004), and various lanthanoide ions were introduced into the films. (Pauporté et al, 2006). This fabrication method has been applied to high-efficiency dye-sensitized solar cells (Yoshida et al, 2004).

The application of ZnO inexcitonic solar cells, XSCs (organic, dye sensitized and hybrid) has been rising over the last few years due to its similarities with most studied semiconductor

oxide, TiO_2. ZnO presents comparable band gap value and conduction band position as well as higher electron mobility than TiO_2 (Quintana et al, 2007; Keis et al, 2002). It can be synthesized in a wide variety of nanoforms (Wang, et al, 2004) applying strainght forward and scalable synthesized methodologies (Fan et al, 2006; Greene et al, 2003). particularly, the application of vertically-alligned ZnO NANOSTRUCTURES it is thought to improve contact between the donor and acceptor material in organic solar cells (OSCs), or improve electron injection in dye sensitized solar cells (DSCs) (Gonzalez et al, 2009) To date, DSC based on ZnO have achieved promising power conversion efficiency values of ~6%.(Keis et al, 2002; Yoshida et al, 2009).

Yet ZnO is not an easy material. It is a semiconductor oxide, the properties of which are greatly influenced by external conditions like synthesis methods (Huang et al, 2001; Wu et al, 2002; Elias et al, 2008; Yoshida et al, 2009), temperature (Huang et al, 2007; Guo et al, 2005). Testing atmosphere air, vacuum(Cantu et al, 2006 , 2007 ; Ahn et al, 2007), or illumination (Kenanakis et al, 2008; Feng et al, 2004; Norman et al, 1978), for example ,minimal changes in the shape of the ZnO (nanoparticules, nanorods, nanotips, etc), can produce different properties which in turn , affects the interface with any organic semiconductor or dye molecule.

Moreover, the modification of properties likes hydrophilicity/ hydrophobicity, or the amount of chemisorbed species on the ZnO surface, have already been reported to be affected by UV irradiation. In DSC, a major drawback is associated with the interaction between dye molecules and ZnO itself. Dye loading on ZnO must be carefully controlled in order to obtain the optimal power conversion efficiency for every system.(Chou et al, 2007; Fujishima et al, 1976; Kakiuchi et al, 2006). An excess in loading time results in the formation of aggregates made by the dissociation of the ZnO and the formation of [Zn^{+2} –dye] complexes (Keis et al, 2002; 2000, Horiuchi et al, 2003).

In order to resolve these problems, research is currently focused on the study of new metal-free photosensitizers and the introduction of new anchoring groups (Guillén et al, 2008; Otsuka et al, 2008; Otsuka et al, 2008). Nevertheless, very recent reports indicate that the application of organic dyes could also be affected by factors like high concentration of Li^+ ions in the electrolyte or the photoinduced dye desorption (Quintana et al, 2009). As early as 178, V. J. Norman demonstrated that the absorption of organic dyes, like uranine and rhodamine B, on ZnO can be enhanced under light irradiation. A three- and two –fold increase on the amount of uranine and rhodamine B adsorbed on ZnO, respectively, was obseved after UV- light exposure (Norman et al, 1978). The latter presents important implications in ZnO-besed devices, like solar cells or diodes, since nanostructures layers of ZnO are increasingly being used on these devices, and some research groups have reported on the benefical effect of exposing ZnO-based devices to UV irradiation (Krebs et al, 2008; Verbakel et al, 2007,) .

2.2 TiO$_2$ presentation

Titanium dioxide is a fascinating material, with a very broad range of different possible properties, which leads to its use in application as different as toothpaste additive. TiO_2 thin films are synthesized for a broad range of different applications, which are summarized below (Estelle, 2002).

2.2.1 Optical coatings

Due to its high index of refraction, TiO$_2$ has been used for optical applications for more than 50 years (Hass et al, 1952). In particular, it is used as the high index of refraction material in multi-layer interference filtres, as anti reflection coating and as optical wave guides (Pierson, 1999). For many of these application, the mechanical and resistive of the layers are important in addition to the optical properties (Ottermann et al, 1997).

2.2.2 Microelectronics

In electric devices, the scaling down tendency leads to a decrease of the thickness of the gate oxide, which means that for fo the actually used SiO$_2$ layer, this thickness tends to atomic dimensions. Therefore, other materials are looked at with a higher dielectric constant such that a similar effective capacitance could be obtained with a thicker layer. TiO$_2$ is one of the promising materials (with Ta$_2$O$_5$ and the ternary titanate materials) for this application, due to its high dielectric constant (Pierson, 1999; Boyd et al, 2001).

2.2.3 Gas sensors

Titania fils are known to have sensing properties based on surface interactions of reducing or oxidizing species, which affect the conductivity of the film. Nano-crystalline material was in particular proven to exhibit a very high sensitivity.

Therefore, nano-grain TiO$_2$ under UV-irradiation is presently widely used as a photo catalyst different applications (water de-pollution (Rabani et al, 1998; Ding et al, 2000; Du et al, 2001), air de-odourization, NO$_x$ decomposition (Negishi et al, 2001), anti-bacteria treatment).

2.2.4 Solar cells

TiO$_2$ layers are used as photo-anodes in Grätzel's type solar cells,or in a solid state device (Bach et al, 1998). Additionaly, TiO$_2$ films used as passivation layers on silicon solar cells (Cardarelli, 2000).

2.2.5 Bio-compatible protective layers

Due to their relatively high corrosion resistance and good bio-compatibility, titanium and its alloys are commonly used for biomedical and dental implants. These beneficial properties are believed to be due to the formation of a native protective passive oxide layer. However, there is evidence that this natural layer does not prevent release from titanium in vivo, and therefore, studies have been devoted to deposition of denser, thicker and less oxygen deficient layers to improve the bio-compatibility (Pan et al, 1997). Additionally, TiO$_2$ was claimed to present good blood compatibility.

2.2.6 Protective and anti-corrosion coatings

Due to its hardness, TiO$_2$ is used as a protective layer on gold and precious metals (Battiston et al, 1999).

2.2.7 Membrans

TiO$_2$ coatings are used as membrane materials, with different porosities for different applications.

- Mesoporous membranes are used for ultra filtration or as supports for other Membranes.
- Micro-porous layers are prepared for nano filtration of liquids (Puhlfurss et al, 2000; Benfer et al, 2001).
- Ulra-microporous or dense layers are realized for gaz permselective membranes (Ha et al, 1996). Additionally, the photo catalytic properties of TiO₂ can be used in photo catalytic membrane reactors (Molinari et al, 2001).

2.2.8 As a component of ternary materials

Additionally,titanium dioxide is an important base for all the titanates materials. For instance, (Ba,Sr) TiO₂ which may become important for new geberation dynamic random access memories (Estelle, 2002).

TiO₂ is almost the only material suitable for industrial use at present and also probably in the future. This is because TiO₂ has the most efficient photo activity, the highest stability and the lowest cost (Kokoro et al, 2008). There are two types of photochemical reaction proceeding on a TiO₂ surface when irradiated with ultraviolet light. One includes the photo-induced redex reactions of adsorbed substances, and the other is the photo-induced hydrophilic conversion of TiO₂ itself. The former type has been known since the early part of the 20th centry, but the latter was found only at the end of the century. The combination of these two functions has opened up various novel applications of TiO₂, particularly in the field of building materials (Kokoro et al, 2008).

3. Experimental section

In the present section, we present an experimental comparaison between two dey-Sensitized solar cells based on ZnO nanotube and TiO₂ nanostructures.

First, an aligned ZnO nanotube arrays were fabricated by electrochemical deposition of ZnO anorods followed by chemical etching of the center part of the nanorods. The morphology of the nanotubes can be readily controlled by electrodeposition parameters. By employing the 5.1 μm length nanotubes as photoanodes for DSSC, an overall lightto- electricity conversion efficiency of 1.18% was achieved.

The current–voltage characteristic curves of DSSC fabricated using ZnO nanotubes with different lengths under simulated AM 1.5 light are shown in figure 2(A). The shortcircuit photocurrent densities (I$_{sc}$) obtained with nanotubes of 0.7, 1.5, 2.9 and 5.1 μm lengths were 0.68, 1.51, 2.50 and 3.24 mA cm−2, respectively. The highest photovoltaic performance of 1.18% (open-circuit voltage Voc = 0.68 V and fill factor FF = 0.58) was achieved for the sample of 5.1 μm length. This efficiency is attractive, taking into account that the film thickness is only 5.1 μm and no scattering layer is added. The Voc of the DSSC decreases upon increasing the length of the ZnO nanotubes, which is possibly related to the increase in the dark current which scales with the surface area of the ZnO film, in agreement with the previous reports on TiO2 nanotube-based DSSC.

The photon-current conversion efficiencies of DSSC using 0.7, 1.5, 2.9 and 5.1 μm length ZnO nanotubes were 0.32%, 0.62%, 0.83% and 1.18%, which were much higher than those of ZnO nanorod DSSCs (i.e. 0.11%, 0.20%, 0.39% and 0.59%). The photocurrent action spectra (figure 2(B)) display the wavelength distribution of the incident monochromatic photon-to-current conversion efficiency (IPCE). Themaximum of IPCE in the visible region is located at 520nm. This is approximately consistent with the expected maximum based on the

accompanying absorption spectrum for the N719 dye (with local maxima at 390 and 535 nm), both corresponding to a metal-to-ligand charge transfer transition.
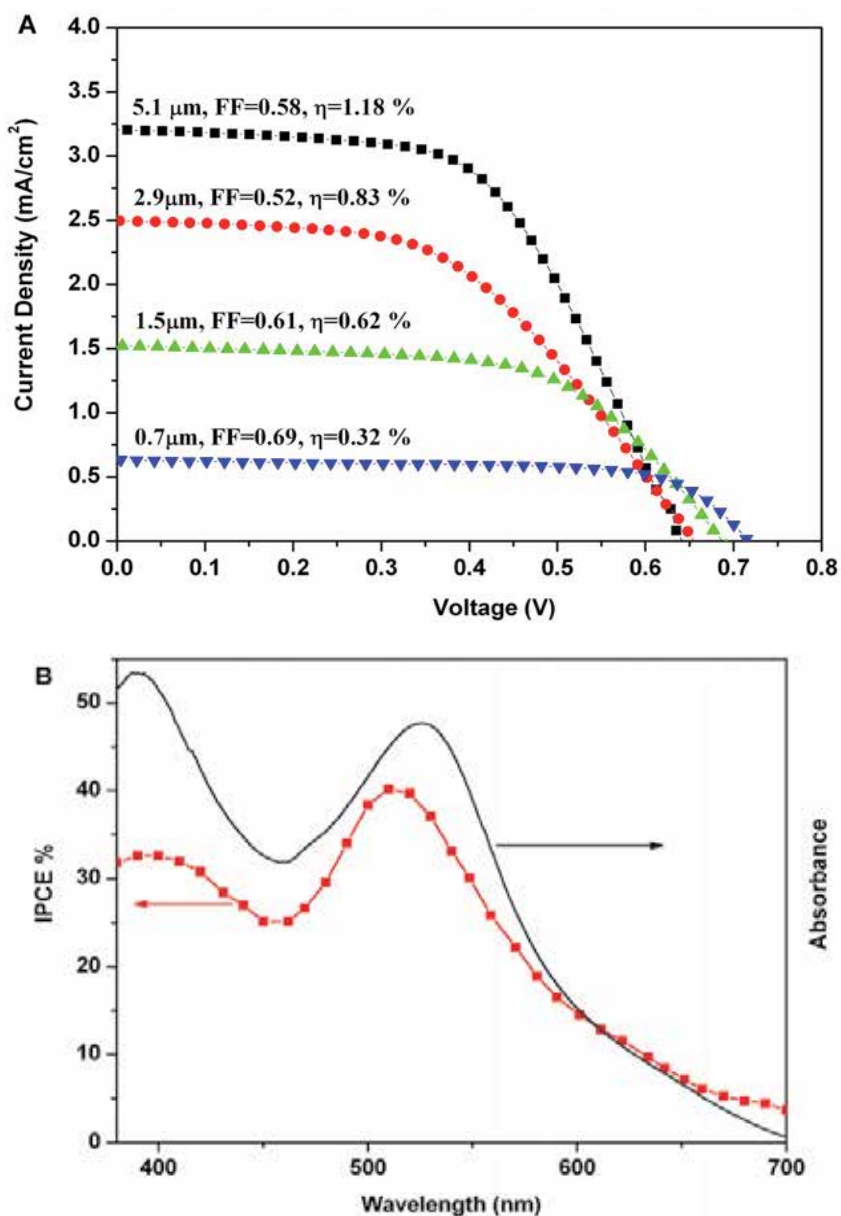
Fig. 2. Performance of the DSSC fabricated using ZnO nanotube array film under full-sun illumination: (A) current–voltage characteristic curves of DSSC with various lengths of ZnO nanotubes with Zn(OAc)2 treatment; (B) incident photon-to-current conversion efficiency (IPCE) of a ZnO nanotube-based device (square) and the absorption spectrum of the N719 dye in solution (solid line).

Second, The DSSCs based on TiO2 nanostructures grown in NaOH solution with different concentrations (0.5, 1, 3, and 10 M) are labeled as 0.5M-DSSC, 1M-DSSC, 3M-DSSC, and 10M-DSSC, respectively. To fabricate DSSCs, the substrates (FTO coated glasses) were first prepared by depositing a thin layer of nanocrystalline TiO2 paste onto FTOs using a screenprinting method. The as-prepared TiO2 membranes were then detached from the Ti plates and adhered onto the substrates as working electrodes. Besides, the DSSC comprised of commercial Degussa P25 TiO2 nanoparticles (labeled as P25-DSSC) was formed using doctor-blading method as a comparison. All of the TiO2 samples were dried under ambient conditions and annealed at 500 °C for 30 min. After cooling, they were chemically treated in a 0.2 M TiCl4 solution at 60 °C for 1 h and then annealed at 450 °C for 30 min to improve the photocurrent and photovoltaic performances. When the temperature decreased to 80 °C, the obtained samples were soaked in 0.3 mM dye solution (solvent mixture of acetonitrile and tert-butyl alcohol in volume ratio of 1:1) and kept for 24 h at room temperature. Here the cis-bis(isothiocyanato) bis (2,20-bipyridyl-4,40-dicarboxylato) ruthenium(II) bis- (tetrabutyl ammonium) (N719) was used as the sensitizer. These dye-coated electrodes were assembled into solar cells with Ptsputtered FTO counter electrodes and the electrolyte containing 0.5 M LiI, 0.05 M I2, and 0.5 M tert-butylpyridine in acetonitrile. photoinduced photocurrent density-voltage (I-V) curves of the constructed solar cells were measured on an electrochemical workstation (model CHI 660C, CH) under an AM 1.5 illumination (100 mW/cm2,model YSS-80A, Yamashita). Electrochemical impedance spectroscopic (EIS) curves of the DSSCs were also observed. The frequency range was from 0.1Hz to 100 kHz. The applied bias voltage was set to the open-circuit voltage (V_{OC}) of the DSSC, which had been determined earlier. The incident photo to current conversion efficiency (IPCE) was detected by the spectral response measuring equipment (CEP-1500, Bunkoh-Keiki. Japan). Figure 3 shows the current density voltage curves of the open cells based on different TiO2 photoelectrodes. The resultant photovoltaic parameters are summarized in Table 2.
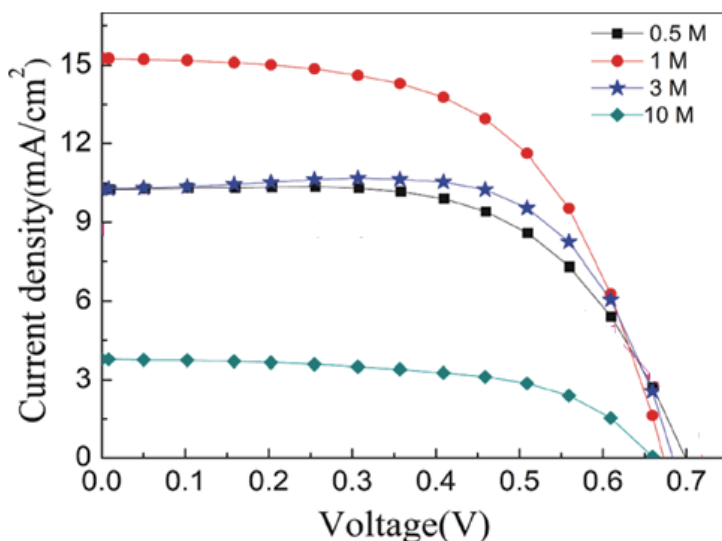
Fig. 3. I-V characteristics of dye-sensitized solar cells assembled with TiO2 films prepared with different concentrations of aqueous NaOH.

The resultant photovoltaic parameters are summarized in Table 1 for ZnO DSSC and in Table 2 for TiO2 DSSC.

Thickness(μm)	V_{oc} (V)	I_{sc} (mA cm^{-2})	FF (%)	η(%)
5.1	0.68	3.24	0.58	1.18
2.9	0.65	2.50	0.52	0.83
1.5	0.70	1.51	0.61	0.62
0.7	0.72	0.68	0.69	0.32

Table 1. Performance Characteristics of DSSCs Based onVarious ZnO nanotube.

DSSCs	V_{oc} (V)	I_{sc} (mA cm^{-2})	FF (%)	η(%)	Thickness(μm)
0.5M-DSSC	0.70	10.26	61.21	4.40	11.68
1M-DSSC	0.67	15.25	58.33	6.00	15.11
3M-DSSC	0.69	10.2	68.87	4.84	24.10
10M-DSSC	0.66	3.71	58.68	1.44	a

Table 2. Performance Characteristics of DSSCs Based on Various TiO2 Nanostructures.

From table 1 and 2, we observe the difference between the photovoltaic performance for these two type DSSC (TiO₂ Nanostructures and ZnO nanotobe), where a high photovoltaic performance is given by TiO₂ Nanostructured with different thickness and over the range of NaOH concentrations, conversion efficient increased from 4.40% at 0.5M to a maximum value of 6.00% at 1 M, which correspond to a high short-circuit photocurrent densities 15.25 mA cm⁻². Compared with ZnO nanotube DSSC, where the higher conversion efficient is 1.18% correspond to high short-circuit photocurrent densities 3.24 mA cm⁻². The cause of this difference is the based materials properties (ZnO and TiO₂), the method of fabrication and the different condition of measured I-V characteristics of temperature and illumination.

4. Simulation section

Now, to justify the experiment section, we use the computer simulation, which is an important tool for investigating the behaviour of semiconductor devices and for optimising their performance. Extraction and optimisation of semiconductor device parameters is an important area in device modelling and simulation (Chergaar. M et al, 2008; Bashahu M et al, 2007; Priyanka et al, 2007). The current–voltage characteristics of photocells, determined under illumination as well as in the dark, represent a very valuable tool for characterizing the electronic properties of solar cells. The evaluation of the physical parameters of solar cell: series resistance (R_s), ideality factor (n), saturation current (I_s), shunt resistance (R_{sh}) and photocurrent (I_{ph}) is of a vital importance for quality control and evaluation of the performance of solar cells when elaborated and during their normal use on site under different conditions. I-V characteristics of the solar cell can be presented by either a two diode or by a single diode model. Under illumination and normal operating conditions, the single diode model is however the most popular model for solar cells. In this case, the current voltage (I-V) relation of an illuminated solar cell is given by:

$$I = I_{ph} - I_d - I_p = I_{ph} - I_s \left[\exp\left(\frac{\beta}{n} \left(V + IR_s\right) \right) - 1 \right] - G_{sh}\left(V + IR_s\right) \tag{1}$$

I_{ph}, I_s, n, R_s and G_{sh} (=$1/R_{sh}$) being the photocurrent, the diode saturation current, the diode quality factor, the series resistance and the shunt conductance, respectively. I_p is the shunt current and $\beta = q/kT$ is the usual inverse thermal voltage. The circuit model of solar cell corresponding to equation (1) is presented in figure (4).
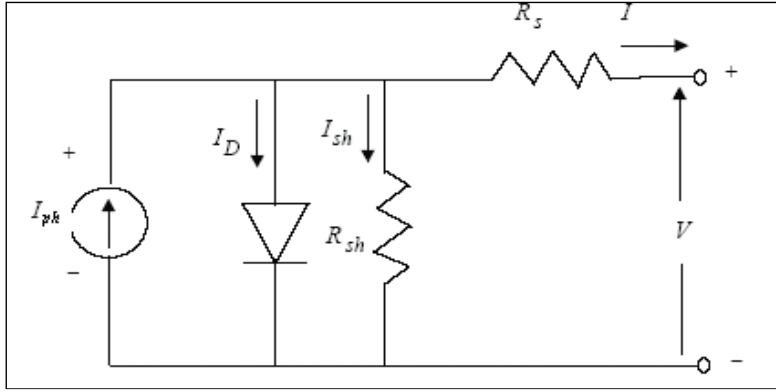
Fig. 4. Equivalent circuit model of the illuminated solar cell.

Determination of R_{sh}

The shunt resistance is considered Rsh = ($1 / G_{sh}$) >> R_s. the shunt conductance Gsh is evaluated from the reverse or direct bias characteristics by a simple linear fit (Nehaoua. N et al, 2010). The calculated value of G_{sh} gives the shunt current Ip = G_{sh}V.

Determination of n and R_s

Before extracting the ideality factor and the series resistance, our measured I-V characteristics are corrected considering the value of the shunt conductance as obtained from the linear fit and for V+R_sI>>kT, the current voltage relation becomes:

$$I = I_{ph} - I_s\left[\exp\left(\frac{\beta}{n}\left(V + IR_s\right)\right)\right] \tag{2}$$

The method concerns directly the usual measured I-V data by writing Eq. (2) in its logarithmic form:

$$\ln\left(I_{ph} - I\right) = \ln I_s + \frac{\beta}{n}\left(V + IR_s\right) \tag{3}$$

For a point defined by (V_0, I_0) we have:

$$\ln\left(I_{ph} - I_0\right) = \ln I_s + \frac{\beta}{n}\left(V_0 + I_0R_s\right) \tag{4}$$

By subtracting Eq. (3) and Eq. (4) and after a simplification we get a linear equation given by:

$$Y = \frac{\beta}{n}\left(R_s + X\right) \quad \text{For} \quad I>>I_s \tag{5}$$

where:

$$Y = \frac{1}{I - I_0} \ln \frac{(I_{ph} - I)}{(I_{ph} - I_0)} \tag{6}$$

and

$$X = \frac{(V - V_0)}{(I - I_0)} \tag{7}$$

(V_0, I_0) is a point of the I-V curve.

We consider a set of I_i-V_i data giving rise to a set of X-Y values, with i varying from 1 to N. Then, we calculate X and Y values for $I_0 = I_{i0}$ and $I=I_{i0+1}$ up to $I=I_N$. This gives (N-1) pairs of X-Y data. We start again with $I_0 = I_{i0+1}$ and $I = I_{i0+2}$ up to I_N and get (N-2) additional X-Y data, and so on, up to $I_0 = I_{N-1}$. Finally, we obtain N(N-1)/2 pairs of X-Y data that means more values for the linear regression. The linear regression of equation (5) gives n and R_s.

Determination of I_{ph}

For most practical illuminated solar cells we usually consider that $I_s \ll I_{ph}$, the photocurrent can be given by the approximation $I_{sc} \approx I_{ph}$, where I_{sc} is the short-circuit current. This approximation is highly acceptable and it introduces no significant errors in subsequent calculations (Nehaoua. N et al, 2010).

Determination of I_s

The saturation current I_s was evaluated using a standard method based on the I-V data by plotting $\ln(I_{ph} - I_{cr})$ versus V_{cr} equation (8). Note that I-V data were corrected taking into account the effect of the series resistance.

$$\ln\left(I_{ph} - I_{cr}\right) = \ln\left(I_s\right) + \frac{\beta}{n} V_{cr} \tag{8}$$

When we plot $\ln (I_c)$ where $(I_c = I_{ph} - I_{cr})$ versus V_{cr}, it gives a straight line that yields I_s from the intercept with the y-axis.

4.1 Application

The method is applied on the too type of Dey-sensitized solar cell, the first one is based on TiO₂ nanostructures and ZnO nanotube under different condition of fabrication, illumination and temperature. The current-voltage (I-V) characteristics of TiO₂ nanostructures DSSC is taken from the work of (Fang Sho et al, 2010) and The current-voltage (I-V) characteristics of ZnO nanotube is taken from the work of (Jingbin Han et al, 2010). The two characteristics correspond to the higher photovoltaice performance, where η=6.00%, FF=58.33%, I_{sc}=15.25mAcm⁻² and V_{oc}=0.67V for TiO₂ nanostructures, and for ZnO nanotube η=1.18%, FF=0.58%, I_{sc}=3.24mAcm⁻² and V_{oc}=0.68V.

4.2 Results and discussion

The shunt conductance $G_{sh} = 1 / R_{sh}$ was calculated using a simple linear fit of the reverse or direct bias characteristics. The series resistance and the ideality factor were obtained from the linear regression (5) using a least square method.

In order to test the quality of the fit to the experimental data, the percentage error is calculated as follows:

$$e_i = \left(I_i - I_{i,cal} \right) \left(100 / I_i \right) \qquad (9)$$

Where $I_{i,cal}$ is the current calculated for each V_i, by solving the implicit Eq.(1) with the determined set of parameters (I_{ph}, n, R_s, G_{sh}, I_s). (I_i, V_i) are respectively the measured current and voltage at the ith point among N considered measured data points avoiding the measurements close to the open-circuit condition where the current is not well-defined (Chegaar M et al, 2006).

Statistical analysis of the results has also been performed. The root mean square error (RMSE), the mean bias error (MBE) and the mean absolute error (MAE) are the fundamental measures of accuracy. Thus, RMSE, MBE and MAE are given by:

$$RMSE = \left(\sum |e|_i^2 / N \right)^{1/2}$$
$$MBE = \sum e_i / N \qquad (10)$$
$$MAE = \sum |e|_i / N$$

N is the number of measurements data taken into account.

The extracted parameters obtained using the method proposed here for the Dey-Sensitized solar cell based on TiO2 nanostructures and ZnO nanotube are given in Table 3. Satisfactory agreement is obtained for most of the extracted parameters. good agreement is reported. Statistical indicators of accuracy for the method of this work are shown in Table 3.

	DSSC-TiO$_2$ nanostructures	DSSC-ZnO nanotube
G_{sh} (Ω^{-1})	0.001269	0.000588
R_s (Ω)	0.025923	0.383441
n	1.629251	3.560949
I_s (μA)	0.33556	0.16553
I_{ph} (mA/cm^2)	15.99	3.25
RMSE	0.850353	1.875871
MBE	0.232276	0.727544
MAE	0.757886	1.053901

Table 3. Extracted parameters for Dey-Sensitized solar cell based on TiO$_2$ nanostructures and ZnO nanotube.

Figures 5 and 6 show the plot of I-V experimental characteristics and the fitted curves derived from equation (1) with the parameters shown in Table 3 for Dey-Sensitized solar cell based on TiO$_2$ nanostructures and ZnO nanotube. The interesting point with the procedure described herein is the fact that we do not have any limitation condition on the voltage and it is reliable, straightforward, easy to use and successful for different types of solar cells.

Extracting solar cells parameters is a vital importance for the quality control and evaluation of the performance of the solar cells, this parameters are: series resistance, shunt conductance, saturation current, the diode quality factor and the photocurrent. In this work, a simple method for extracting the solar cell parameters, based on the measured current-voltage data. The method has been successfully applied to dey-Sensitized solar cell based on TiO$_2$ nanostructures and ZnO nanotube under different temperatures.
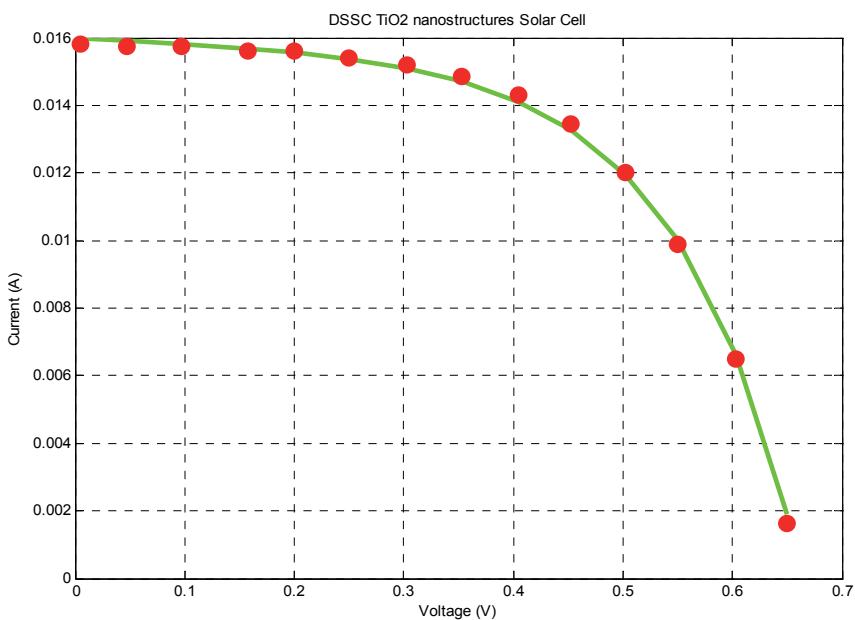
Fig. 5. Experimental (●) data and fitted curve of TiO₂ nanostructures DSSC.
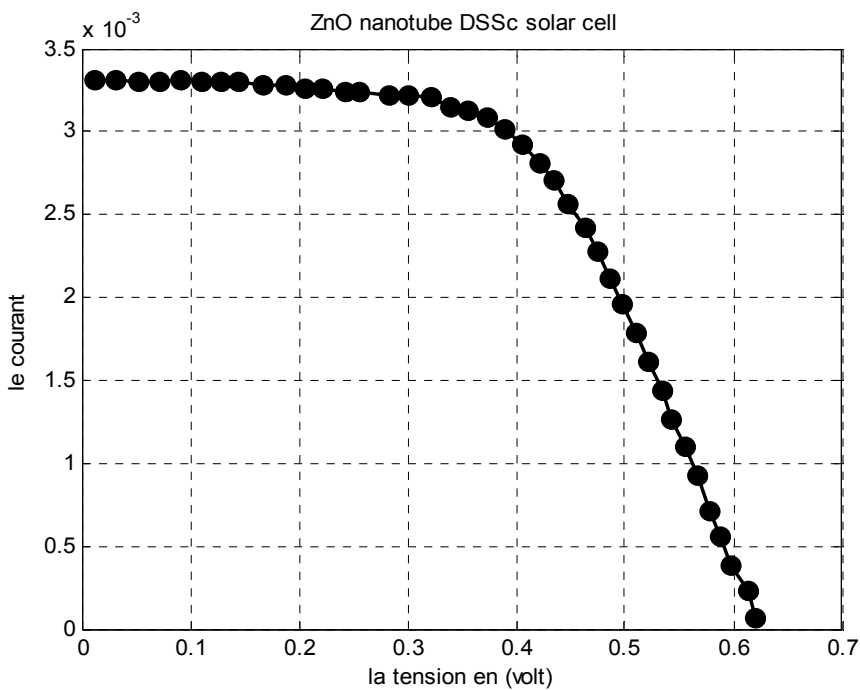
Fig. 6. Experimental (●) data and fitted curve of ZnO nanotube DSSC.

Figures 5 and 6 shows the plot of I–V experimental characteristics and the fitted curves derived from equation (1) with the parameters shown in Table 3 for the dey-Sensitized solar cell based on TiO_2 nanostructures and ZnO nanotube solar cell. Good agreement is observed for the different structure, especially for the TiO_2 nanostructures solar cells with statistical error less than 1%, and 2% for ZnO nanotube DSSC solar cells respectively, which attribute mainly to lower parasitic losses, where we can observe a low series resistance 0.025923Ω compared to 0.383441 Ω for TiO_2 nanostructures and ZnO nanotube solar cell respectively. The interesting point with the procedure described herein is the fact that we do not have any limitation condition on the voltage and it is reliable, straightforward, easy to use and successful for different types of solar cells.

5. Conclusion

In this contribution, a simple comparative study between experimental and simulation works to improve the dey-sensitized solar cell performance of two DSSCs based on TiO_2 nanostrucures and ZnO nanotube, under differents condition of temperature. We compare the different parameters which are: the conversion efficient, the fill factor, the short-circuit photocurrent and the open-circuit voltage, where we observe a high photovoltaic performance for TiO_2 nanostrucures with maximun conversion efficient 6% compared to 1.18% for ZnO nanotube. In second time, an evaluation of the physical parameters of solar cell: series resistance (R_s), ideality factor (n), saturation current (I_s), shunt resistance (R_{sh}) and photocurrent (I_{ph}) from measured current-voltage characteristics by using a numerical method proposed by th authors. Extracting solar cells parameters is a vital importance for the quality control and evaluation of the performance of solar cells when elaborated and during their normal use on site under different conditions. Good resuts are given by the differents DSSCs, and specialy for on dey-sensitized TiO_2 nanostrucures, which justify the experimental work.

6. References

Boyd, I. W. & Zhang, J. Y. (2001), *Solid-State Electronics*, 45, 1413

Benfer, S.; Popp, U.; Richter, H. et al.(2001) *Separation and Purification Technology*, 22-23. 231.

Bashahu M, Nkundabakura P. Solar energy 2007; 81:856-863.

Bach,U. ; Lupo, D. ;Comte, P. et al.(1998), *Nature*,395 ,583.

Battiston, G., A. ; Gerbasi, R. ; Porchia, M. et al. (1999), *Chemical Vapor Deposition*,5 ,73

Chang Y.; Teo, J. J. ; Zeng, H. C. (2005), *Langmuir*. 21(3), 1074-1079, 21(3), 1074-1079

Cao, Q. H. ; Gao, Y. Q. ; Chen, X. Y. ; Mu, L. ; Yu, W. C. & Qian, Y. T.(2006). *Chem. Lett.* 35(2), 178-179.

Cao, X. B. ; Gu, L. ; Zhuge, L. ; Gao, W. J.; Wang, W. C. & Wu, S. F.(2006) *Adv. Funct. Mater.* 16(7), 896-902.

Chegaar M, Nehaoua. N, Bouhemadou. A. Energy conversion and management 2008, 49:1376-1379.

Chegaar M, Azzouzi G, Mialhe P. Solid State Electronics 2006; 50:1234-1237.

Chen, W.; Lu, Y. H. ; Wang, M. ; Kroner, L. ; Paul, H. ; Fecht, H.J.; Bednarcik, J.; Stahl, K.; Zhang, Z. L.; Wiedwald, U.; Kaiser, U.; Ziemann.,P.; Kikegawa, T.; Wu, C. D. & Jiang, J. Z. J.(2009) *Phys. Chem. C* , 113(4),1320-1324.

Cardarelli, F.(2000), *in Materials Handbook A Concise Desktop Reference*(Springler-Verlag).

Dinsmore, A. D.; Hsu, M. F.; Nikolaides, M. G.; Marquez, M.;Bausch, A. R. & Weitz, D. A.(2002) *Science*, 298(5595),1006-1009.

Ding, Z. ; Hu, X. ; Lu, G. Q. ; et al.(2000), *Langmuir*, 16 ,6216.,

Du, G., H. ; Chen, Q. ; Che, R. C. et al. (2001), *Appl. Phys. Lett.*, 79 ,3702

Estelle Wagner (2002), thesis(selective light induced chemical vapour deposition of titanium dioxide thin films), EPFL, 2650.

Engeneering Chemical Research, (199), 3381

Elias, J.; Tena-Zaera, R. & Lévy-Clément, C.(2008*), J. Phys. Chem. C*, 112, 5736.

Fujishima,A.; Iwase, T. & Honda,K. J. Am, J.(1976). *Chem. Soc.*, 98(6), 1625.

Fan, H. j.; Werner, P. & Zacharias, M.(2006) Small. 2(6),700.

Fang shao, Jing sun, lian gao, Songwang, Jianqiang luo. Physical chemestry C. Dx.doiorg/10.1021/jp110743m.

E. Guillén et al. J. Phtochem. Photobiol., A, 2008,200,364.,

I. Gonzalez-Valls and M. Lira-Cantu.(2009), *Energy Environ*. Sci. 2,1

L. E. Greene,M. Law, J. Goldberger, F. Kim, J. C. Johnson,Y. Zhang, R. J. Saykally and P. D. Yang, Angew.(2003). Chem., Int. Ed., 42(26), 3031.

Guo, M.; Diao, P. and Cai, S. M. (2005), *J. Solid State Chem*. 178, 1864

Huang, M. H.; Mao,S. ;Feick, H.;Yan, H. Q.; Wu, Y. Y.; Kind, H.; Weber, E. Russo, & Yang, P. D.(2001), *Science*, 292, 1897.,

Hass, G. Vacuum, 11,(1952),331

Huang, J. H.; Gao, L.(2006), *J. Am. Ceram. Soc*. 89(12), 3877-3880.

Hsu, C. C.; Wu, N. L. (2005), *Photochem. Phtobiol. A* 172(3), 269-274.),

Horiuchi,H.; Katoh,R.; Hara, K. Yanagida, M.; Murata, S. Arakawa, H. & Tachiya, M.(2003), *J. Phys. Chem*. B, 107, 2570.

Ha, Y. H., Nam, S. W. ; S. W., ; Lim, T. H. L. et al.(1996), *Journal of Membrane Science*, 111, 81.

Ishizumi, A. & Kanemitsu, Y. (2005): *Appl. Phys. Lett*. 86(253106).

Ishizumi, A.; Y. Taguchi, Yamamoto, A. & Kanemitsu, Y.(2005): *Thin Solid Films* 486(50).

Ibarra. L. & Alzorriz, M. J.(2002), *Appl. Polym. Sci.* 84(3), 605-615.

Ibarra, L. ; Macros-Fernandez, A. & Alzorriz., M.(2002), *Polymer*, 43(5), 1649-1655.

Ibarra, L. & Alzorriz, M. (2002), *J. Appl. Polym. Sci.*,86(2), 335-340.

Ito, S., Zakeeruddin, S. M., Humphry-Baker, R., Liska, P., Charvet, R., Comte,P., Nazeeruddin, M., Péchy, P., Takata, M., Miura, H., Uchida, S. &Grätzel 2006, 'High-efficiency organicdye sensitized solar cells controlled by nanocrystalline-TiO2 electrodethickness,' *Adv. Mater*. 18, p. 1202.

Jain A, Kapoor A. Solar energy mater solar cells 2005; 86:197-205

Jingbin Han, Fengru Fan, chen xu, Shisheng Lin, Min wei, Xue duan, Zhong lin wang. Nanotechnology 2010, 21:405203(7p).

Janne Halme, thesis (2002), *Dye-sensitized nanostructured and organic photovoltaic cells: technical review and preliminary test*s, HELSINKI UNIVERSITY OF TECHNOLOGY.

Krebs, F. C. (2008*), Sol. Energy Mater. Sol. Cells*, 92,715.

Keis, K.; Bauer, C.; Boschloo, G.; Hagfeldt, A.; Westermark, K.; Rensmo, H. & Siegbahn, H.(2002), *J. Photochem. Photobiol., A*, 148.57 .

Keis, K.; Magnusson, E.; Lindström, H.; Lindquist, S. E. & Hagfeldt, A.(2002), *Sol. Energy Mater. Sol. Cells,* 73, 51.

Kakiuchi, K.; Hosono, E. & Fujihara, S.(2006). *J. Photochem. Photobiol. A* 179, 81.

Keis, K.; Lindgren, J.; S. E. Lindquist, S. E. & Hagfeldt, A.(2000), *Langmuir,* 16, 4688.

Kokoro et al. Appl. Phys. Express 1 (2008) 081202

Li, Z. Y.; Kobayashi, N.; Nishimura, A. & Hasatani.(2005), *M. Chem. Eng.Commun.* 12(7) ,18-932.

Liang, H. P.; Zhang, H. M.; Hu, J. S.; Guo, Y. G.; Wan, L. J.& Bai,C. L. Angew.(2004) *Chem., Int. Ed.* 43(12), 1540-1543.

Lee, K. T.; Jung, Y. S.; Oh, S. M.(2003), J. Am. Chem. Soc. 125(19), 5652-5653

Liu,X. M. ; Yin, W. D. ; Miao, S. B. & Ji, B. M.(2009). Mater. Chem. Phys. 113(2-3), 518-522

Li,B. X. ; Rong, G. X. ; Xie, Y. ; Huang, L. F. & Feng, C. Q.(2006), Inorg. Chem., 45(16), 6404-6410.

Liu, X. Y. ; Xi, G. C. ; Liu, Y. K. ; Xiong, S. L. ; Chai, L. L. & Qian, Y. T.(2007) *J. Nanosci. Nanotechnology.* 7(12), 4501-4507

Lou, X. W.; Archer, L. A. & Yang, Z. C.(2008), *Adv. Matter*. 20(21), 3987-4019.

Li, Z. Y.; Kobayashi, N.; Nishimura, A. & Hasatani, M.(2005), *Chem. Eng.Commun*. 12(7) ,18-932.

Lin, X. X. ; Zhu, Y. F. & Shen, W. Z.(2009), *J. Phys. Chem. C,* 113(5), 1812-1817 ,113(5), 1812-1817

Lira-Cantu, M. & Krebs, F. C.(2006), *Sol. Energy Mater. Sol. Cells*, 90,2076.

Lira-Cantu, M.; Norman, K.; Andreasen, J. W.; Casan-Pastor, N. & Krebs, F. C.(2007), *J. Electrichem. Soc.* 154(6), B508

Lira-Cantu, M.; Norrman, K.; Andreasen, J. W.& Krebs, F. C. (2006), Chem. Mater., 18, 5684.,

Molinari, R. ; Grande, C. ; Drioli, E. et al. (2001), *Catalysis Today*, 67,1.

Myo Than HTAY,; Minori ITOH,; Yoshio HASHIMOTO,& Kentaro ITO(2008),J. *Appl. Phys.* (47)541

Negishi, N. & Takeuchi, K.(2001), *Thin Sold Films*, 392, 249.

Norman, V. j.(1978), *Australian J. Chem.*, 25(6),1189.

Nehaoua N, Chergui Y , Mekki D E. Vacuum 2010 , 84 : 326–329.

Otsuka, A.; K. Funabiki, Sugiyama,N.; Mase, H.; T. Yoshida,T.; Minoura, H. & Matsui, M.(2008), *Chem. Lett*. 37(2), 176.

Ottermann, C. R. ; Ottermann, R. ;Kischnereit,R. ; Anderson, O. et al.(1997), *Mat. Res. Soc. Symp. Proc.*, 436 ,251

Otsuka et al. Dalton Trans., 2008,5439

Pan, J.; Leygraf, C.; Thierry, D. et al.(1997), *Journal of Biomedical Materials Research*, 35, ,309.

Pierson, H. O.(1999), *Handbook of chemical vapour deposition(CVD)*: *principles, technology and applications*, 2nd ed.(Park Ride, 1999).

Puhlfurss, P. ; Voigt, A. ; Weber, R. et al. (2000), *Journal of Membrane Science*, 174, 123.

Priyanka, Lal M , Singh S N. Solar energy material and solar cells 2007; 91:137-142.

Quintana,M.; Edvinsson,T.; Hagfeldt, A. & Boschloo, G.(2007), *J. Phys.Chem. C.* 111, 1035

Quintana, M.; Marinado, T.; Nonomura,K.; Boschloo, G. & Hagfeldt, A.(2009), J. *Photochem. Photobiol. A*, 202,159

Rabani, J.; Yamashita, K. ; Ushida K. et al. (1998). *J. Phys. Chem.,* 102, 1689.

K. Sakurai, T. Takagi, T. Kubo, D. Kajita, T. Tanabe, H. et al. J. Cryst. Growth 237-239(2002)514.

F. Verbakel, S. C. J. Meskers and R. A. J. Janssen.(2007), *J. Phys. C*, 111,10150

Verbakel,F.; Meskers, S. C. J. & Janssen, R. A. G..(2007), *J. Appl. Phys*. 102(8), 083701

Yamamoto, A. ; Atsuta S.; & Y. Kanemitsu, Y.(2005) ; *J. Lumin*, 112 (169).

Yamamoto,A., S. Atsuta, & Kanemitsue, Y.(2005): *Physica E* 26(96).

Wu, J. J. & Liu, S. C. (2002), *Adv. Mater*. 14(3), 215.

The Application of Inorganic Nanomaterials in Dye-Sensitized Solar Cells

Zhigang Chen, Qiwei Tian, Minghua Tang and Junqing Hu
State Key Laboratory for Modification of Chemical Fibers and Polymer Materials,
College of Materials Science and Engineering, Donghua University
China

1. Introduction

Energy crisis and environment pollution cause a great quest and need for environmentally sustainable energy technologies. Among all the renewable energy technologies, photovoltaic technology utilizing solar cell has been considered as the most promising one (Chen et al., 2007a; Gratzel, 2001). As early as in 1954, researchers demonstrated the first practical conversion from solar radiation to electricity by a *p-n* junction type solar cell with 6% efficiency (Chapin et al., 1954). Up to now, the common solar power conversion efficiencies of this type solar cell are beyond 15% (Tributsch, 2004). Unfortunately, the relatively high cost of manufacturing and the use of toxic chemicals have prevented their widespread use, which prompts the search for high efficient, low cost and environmentally friendly solar cells.

Semiconductor with a very large bandgap, such as TiO_2, ZnO and SnO_2, can be employed to construct solar cells. But these materials can only be excited by ultraviolet or near-ultraviolet radiation that occupies only about 4% of the solar light. Dye molecules as light absorbers for energy conversion have shaped evolution via the process of photosynthesis and photo-sensoric mechanisms (Tributsch, 2004). Dye sensitization of semiconductor with a wide band-gap has provided a successful solution to extending the absorption range of the cells to long wavelength region. This approach also presents advantages over the direct band-to-band excitation in conventional solar cells, since attached dyes, rather than the semiconductor itself, are the absorbing species (Garcia et al., 2000). Importantly, light absorption and charge carrier transport are separated, and the charge separation takes place at the interface between semiconductor and sensitizer, preventing electron–hole recombination. Since the discovery of the photocurrents resulting from dye sensitization of semiconductor electrodes in 1968, dyes have been widely used in electrochemical energy converting cells (Tributsch, 1972).

During the first years of the sensitized solar cell research, most studies were made with single crystal oxide samples, because by eliminating grain boundaries and high concentrations of surface states the interpretation of the results became more transparent (Tributsch, 2004). However, at that time, the power conversion efficiencies were very low (< 1%). Tsubomura *et al.* reported a breakthrough in the conversion efficiency in 1976 (Tsubomura et al., 1976). They used the powdered high porosity multi-crystalline ZnO instead of single crystal semiconductor, resulting in a significant increase of the surface area of the electrode. When the dye (Rose Bengal) was used as the sensitizer, an energy efficiency of 1.5% was obtained for light incident within the absorption spectrum of the sensitizer.

Later, in 1980, Tsubomura group increased the surface roughness of ZnO samples and demonstrated an energy efficiency of 2.5%, also for light incident within the absorption spectrum of the sensitizer (Matsumura et al., 1980).

A significant advance in the field of dye-sensitized solar cells (DSCs, also considered as Grätzel cell) was made through the efforts of Grätzel and coworkers in 1991 (Fig. 1) (Oregan & Gratzel, 1991). They greatly improved the power energy conversion efficiency from lower than 2.5 to 7%, and the main reasons for the improvement were as follows: (1) the preparation of nanostructured TiO_2 film (Desilvestro et al., 1985), (2) the use of ruthenium complex that was adequately bonded to TiO_2 nanoparticles and (3) the selected organic liquid electrolyte based on iodide/triiodide. The jump in solar energy conversion efficiency has attracted considerable attentions and motivated significant optimism with respect to the feasibility of DSCs as a cost-effective alternative to conventional solar cells.
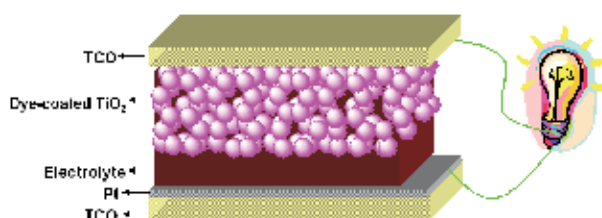
Fig. 1. Typical sandwich-type dye-sensitized TiO_2 nanocrystal solar cell.

The typical DSCs are composed of a transparent nanoporous semiconductor electrode on transparent conducting optically (TCO) glass, a very thin layer of light-absorbing material (dyes)—sensitizer on the entire surface of semiconductor (such as TiO_2) electrode, a counter electrode (such as Pt), and a transparent hole conductor (electrolyte) filling the pores, in contact with the light-absorbing layer at all points. The typical dye-sensitized TiO_2 nanocrystal solar cell is shown in Fig. 1. The operational principle of DSCs is described as follows. Photons enter DSCs and can be absorbed by dye molecules (D) at various depths in the film. The dye molecule after absorbing photon will then be promoted into its excited state (D^*) from where it is now energetically able to inject an electron into the conduction band of semiconductor, leaving an oxidized dye (D^+) on the semiconductor surface. The injected electrons percolate via the interconnected nanoparticles to the substrate and are fed into an electrical circuit, where it can deliver work. Subsequently, the electrons, which now carry less energy, enter the cell again via the counter electrode and transport to hole-conductor materials (commonly the organic electrolyte containing iodide/triiodide, this process can be described as: $I_3^- + 2e^- \rightarrow 3I^-$). The oxidized dye ($D^+$) is then reduced back to its original state by hole-conductor materials (such as, this process can be typically described as: $2D^+ + 3 I^- \rightarrow 2 D + I_3^-$). Then the cycle is completed.

The main issues for the development of DSCs are to improve their photoelectric conversion efficiency, thermostability and long-term stability, which are strongly dependent on the advances in nanotechnology and nanomaterials. It is well known that nanotechnology opens a door to tailing materials and creating various nanostructures for the use in dye-sensitized solar cells. A predominant feature of these nanostructures is that the size of their basic units is on nanometer scale (10^{-9} m), and inorganic nanomaterials therefore present an internal surface area significantly larger than that of bulk materials. Currently, inorganic nanomaterials have been widely used in all components in DSCs, including transparent

semiconductor electrode, counter electrode, electrolyte and light-absorbing material. In this chapter, the recent progress on the selection and utilization of inorganic nanomaterials in dye-sensitized solar cells are mainly introduced and discussed.

2. The application of semiconductor nanomaterials in photoanodes

Compared to bulk materials, semiconductor nanomaterials as photoanodes can offer a larger surface area for dye adsorption, contributing to optical absorption and leading to an improvement in the solar cell conversion efficiency. As photoelectrode materials in DSCs, the semiconductor nanostructures are usually classified into two types: (1) nanoparticles, which offer large surface area to photoanodes for dye-adsorption, however have recombination problem due to the existence of considerable grain boundaries in the film. To settle this issue, core-shell structure derived from the nanoparticles by forming a coating layer has been developed and applied to DSCs with a consideration of suppressing the interfacial charge recombination, while this kind of structure has been proved to be less effective and lack of consistency and reproducibility; (2) one-dimensional nanostructures such as nanowires and nanotubes, which are advantageous in providing direct pathways for electron transport much faster than in the nanoparticle film, however face drawback of insufficient internal surface area of the photoelectrode film, leading to relatively low conversion efficiency (Zhang & Cao, 2011). This section aims to demonstrate semiconductor nanomaterials as photoanodes, including nanoparticles, nanowires and nanotubes.

2.1 Semiconductor nanoparticles

Among different nanostructures, nanoparticles have been most widely studied for the use in DSCs to form photoelectrode film (Oregan & Gratzel, 1991). This is because, to a large extent, the photoelectrode films comprised of nanoparticles can give a high specific surface area, resulting in an efficient extinction of incident light within film which is a few microns thick. And the anodes of DSCs are typically constructed with the nanoparticles film (thickness: ~10 µm) of wide bandgap semiconductor including SnO_2, ZnO, and TiO_2.

Among these wide bandgap semiconductors, titania (TiO_2), an n-type semiconductor with a wide bandgap (3.2 eV for anatase), has been well known and widely used in the photoanode of DSCs. As early as 1985, Desilvestro et al (Desilvestro et al., 1985) have showed that if TiO_2 is used in a nanoparticle form, the power conversion efficiency of DSC can be drastically enhanced. The improvement of conversion efficiency lies in the superiority of nanoparticles to create large surface, which was demonstrated by a comparison between a flat film and a 10-µm-thick film that consisted of nanoparticles with an average size of 15 nm (Oregan & Gratzel, 1991). The latter, nanoparticle film, showed a porosity of 50-65% and gave rise to almost 2000-fold increase in the surface area. Fig. 2 shows typical cross-section morphology of TiO_2 nanoparticle film with thickness of about 4 µm.

For state-of-the-art DSCs, the employed architecture of the mesoporous TiO_2 electrode is as follows (Hagfeldt et al., 2010): (a) a TiO_2 blocking layer (thickness ~50 nm), coating TCO glass to prevent contact between the redox mediator in the electrolyte and TCO glass ; (b) a light absorption layer consisting of a ~10 µm thick film of mesoporous TiO_2 with ~20 nm particle size that provides a large surface area for sensitizer adsorption and good electron transport to the substrate; (c) a light scattering layer on the top of the mesoporous film, consisting of a ~3 µm porous layer containing ~400 nm sized TiO_2 particles; (d) an ultrathin overcoating of TiO_2 on the whole structure, deposited by means of chemical bath deposition(using aqueous $TiCl_4$ solution), followed by heat treatment.
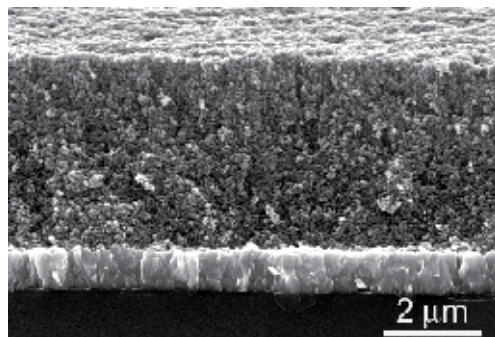
Fig. 2. Cross-section morphology of typical TiO$_2$ nanoparticle film.

Furthermore, it has mentioned that the performance of solar cell is intimately linked to the structure and morphology of the nanoporous oxide layer. For efficient dye distribution, the surface area of the membrane film must be large and porous. So the preparation procedure of TiO$_2$ nanoparticle film must be optimized so as to provide an optimal particle size and porosity features. Up to now, the main synthesis methods of TiO$_2$ nanoparticle film for DSCs include sol-gel/hydrothermal synthesis (Muniz et al., 2011), electrochemical deposition (Murakami et al., 2004), magnetron sputtering (Sung & Kim, 2007), chemical vapor deposition (Murakami et al., 2004) and so on.

The most common technique for the preparation of TiO$_2$ nanoparticles is sol-gel/hydrothermal synthesis, which involves the hydrolysis of a titanium precursor such as titanium (IV) alkoxide with excess water catalyzed by acid or base, followed by hydrothermal growth and crystallization. Acid or basic hydrolysis gives materials of different shapes and properties; while the rate of hydrolysis, temperature, and water content can be tuned to produce particles with different sizes. Transmission electron microscopy measurements revealed that for TiO$_2$ nanoparticles prepared under acidic conditions, crystalline anatase particles were formed exposing mainly the <101> surface (Zaban et al., 2000). Compared with nitric acid, employing acetic acid increases the proportion of the <101> face about 3-fold (Zaban et al., 2000). The differences can be explained by different growth rates: in acetic acid crystal growth is enhanced in the <001> direction compared with the growth in the presence of nitric acid (Neale & Frank, 2007). Hore et al. (Hore et al., 2005) found that base-catalyzed conditions led to mesoporous TiO$_2$ that gave slower recombination in DSCs and higher *Voc* but a reduced dye adsorption compared with the acid-catalyzed TiO$_2$. The produced TiO$_2$ nanoparticles are formulated in a paste with polymer additives and deposited onto TCO glass using screen printing techniques. Finally, the film is sintered at about 450 °C in air to remove organic components and to make electrical connection between the nanoparticles.

It has been found that pure TiO$_2$ nanoparticles are not perfect in terms of solar cell efficiency, since the charge recombination between the injected electrons in conductor band of TiO$_2$ and electron acceptors in the electrolyte is unavoidable to diminish both photovoltage and photocurrent, thus limiting the device efficiency (Gregg et al., 2001). To improve device efficiency, one effective approach is to grow a thin coating layer of another oxide on the surface of TiO$_2$ particles. Thus, coating TiO$_2$ nanoparticles with a different metal oxide to build core-shell structure has received much attention (Kay & Gratzel, 2002).

Now, two approaches have been developed to create such core-shell structure (Zhang & Cao, 2011). One involves a first synthesis of nanoparticles and then fabricating a shell layer

on the surface of nanoparticles. This leads to the formation of core-shell structured nanoparticles, with which the film photoanode is prepared then. Such an approach builds up a photoelectrode structure as shown in Fig. 3a, and an energy barrier is formed at the interfaces not only between nanoparticle/electrolyte but also between the individual core nanoparticles. In another approach, the nanoparticle film photoanode is prepared prior to the deposition of shell layer, receiving a structure as show in Fig. 3b. The latter approach is obviously advantageous in electron transport that happens within single material, but there is usually a challenge in the fabrication of shell layer regarding a complete penetration and ideal coating of the shell material. Metal oxides such as ZnO, $CaCO_3$, Nb_2O_3, $SrTiO_3$, MgO and Al_2O_3 have been usually used as the coating layer for TiO_2. Table 1 shows photoelectric conversion efficiencies of DSCs based on TiO_2 and metal oxides-coated TiO_2 electrodes, which demonstrates the improved efficiency of DSCs employing a core-shell structured TiO_2 electrode. This improvement should be attributed to the following two factors (Jung et al., 2005): First, the wide bandgap coating layer retards the back transfer of electrons to the electrolyte solution and minimizes electron-hole recombination. Second, the coating layer enhances the dye adsorption and increases the volume of the optically active component, leading to the improved cell performance. If pH of the coating oxides is more basic than that of TiO_2, the carboxyl groups in a dye molecule are more easily adsorbed to their surface.
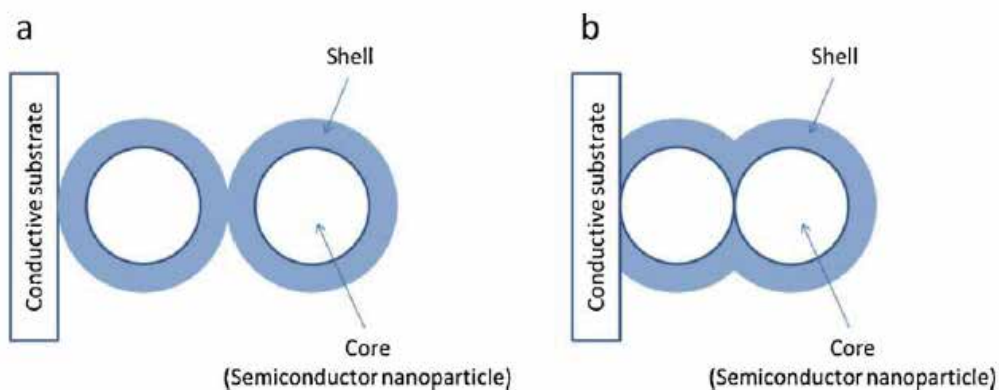
Fig. 3. Core-shell structures used in DSCs. (a) The shell layer is formed prior to the film deposition, (b) the shell layer is coated after the film deposition (Zhang & Cao, 2011).

metal oxides	ZnO	CaCO$_3$	Nb$_2$O$_3$	SrTiO$_3$	MgO	Al$_2$O$_3$
η^b(%)	7.7	6.9	3.6	3.81	3.1	3.93
η^c(%)	9.8	7.9	5.0	4.39	4.5	5.91
Ref.	(Wang et al., 2001)	(Wang et al., 2006)	(Chen et al., 2001)	(Diamant et al., 2003)	(Jung et al., 2005)	(Wu et al., 2008)

η^b : Conversion efficiency of DSC based on the bare TiO_2 film
η^c : Conversion efficiency of DSC based on the metal oxides-coated TiO_2 film

Table 1. Photoelectric conversion efficiency of DSCs based on TiO_2 and metal oxides-coated TiO_2 electrodes.

2.2 Semiconductor nanowires

Nanoparticle films have been regarded as a paradigm of porous photoanodes. However, the nanoparticle films are not thought to be ideal in structure with regard to electron transport. While one-dimensional nanostructures, such as nanowires, are advantageous in providing direct pathways for electron transport much faster and therefore giving electron diffusion length larger than in the nanoparticle films. Hence, semiconductor nanowires become a kind of promising candidate for making up the drawbacks of nanoparticle films.

2.2.1 TiO$_2$ nanowires

Oriented single-crystalline TiO$_2$ nanowires are an important one-dimensional nanostructure that has also attracted a lot of interests regarding an application in DSCs (Liu & Aydil, 2009). Hydrothermal growth has been reported to be a novel method for the synthesis of TiO$_2$ nanowire array on TCO glass substrate. In this method, tetrabutyl titanate and/or titanium tetrachloride are used as the precursor, to which an HCl solution is added to stabilize and control the pH of the reaction solution.

Liu et al. (Liu & Aydil, 2009) developed a facile hydrothermal method to grow oriented, single-crystalline rutile TiO$_2$ nanorod films on TCO glass substrate, as shown in Fig. 4a. The diameter, length, and density of the nanorods could be varied by changing the growth parameters, such as growth time, temperature, initial reactant concentration, acidity, and additives. The epitaxial relation between TCO galss and rutile TiO$_2$ with a small lattice mismatch played a key role in driving the nucleation and growth of the rutile TiO$_2$ nanorods. With TiCl$_4$-treatment, DSC based on 4 µm-long TiO$_2$ nanorod film exhibited a power conversion efficiency of 3%. Furthermore, Feng et al. (Feng et al., 2008) presented a straightforward hydrothermal method to prepare single crystal rutile TiO$_2$ nanowire arrays up to 5 µm long on TCO glass via a non-polar solvent/hydrophilic substrate interfacial reaction (Fig. 4b). The as-prepared densely packed nanowires grew vertically oriented from TCO glass along the (110) crystal plane with a preferred (001) orientation (Fig. 4c). The Cl⁻ ions were explained to play an important role in the growth of TiO$_2$ nanowires by attaching on the (110) plane of TiO$_2$ nanocrystal and thus suppressing the growth of this plane. DSCs based on 2-3 µm long nanowire array demonstrated a very encouraging power conversion efficiency of 5.02%.
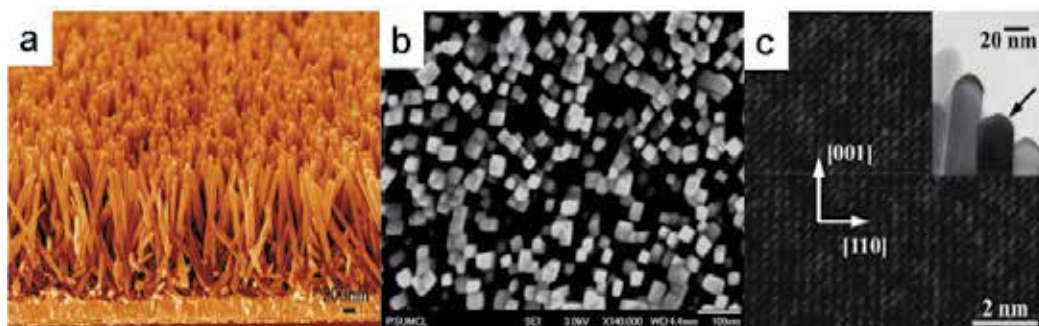
Fig. 4. DSCs with TiO$_2$ nanowires: (a) Cross sectional view of oriented rutile TiO$_2$ nanorod film grown on TCO substrate (Liu & Aydil, 2009); (b) top-view images of vertically oriented self-organized TiO$_2$ nanowire array grown on FTO coated glass (Feng et al., 2008); (c) TEM image illustrating the [001] orientation of TiO$_2$ nanowires (Feng et al., 2008).

In addition, Park et al. (Park et al., 2000) compared the performance between TiO_2 nanowires and nanoparticles which were both rutile phase. The efficiency achieved by TiO_2 nanowire film in 2-3 µm thick was higher than that obtained for the nanoparticle film in 5 µm thick. This is good evidence that the one-dimensional nanostructures may offer better charge transport than the nanoparticles. A further increase in the conversion efficiency most likely relies on the development of new fabrication techniques that can achieve longer TiO_2 nanowires.

2.2.2 ZnO nanowires

Zinc oxide (ZnO) has remarkable optical properties with a wide bandgap (3.2 eV) and a large exciton binding energy (60 meV). In 2005, Law et al. (Law et al., 2005) reported the preparation of ZnO nanowire array on TCO glass by seed mediated liquid phase synthesis method. The experiment was purposely designed to grow ZnO nanowires with a high aspect ratio so as to attain a nanowire film with high density and sufficient surface area (Fig. 5a and b). A ~25-µm-thick film consisting of ZnO nanowires in diameter of ~130 nm was mentioned to be able to achieve a surface area up to one-fifth as large as a nanoparticle film used in the conventional DSCs. The superiority of ZnO nanowires for DSC application was firstly demonstrated by their high electron diffusion coefficient, 0.05-0.5 cm^2 s^{-1}, which is several hundred times larger than that of nanoparticle films. Larger diffusion coefficient means longer diffusion length. In other words, the photoanode made of nanowires allows for thickness larger than that in the case of nanoparticles. This can compensate for the insufficiency of surface area of the nanowire-based photoanode. DSC based on ZnO nanowire gave a power conversion efficiency of 1.5%. In the same year, Prof. Aydil group also successfully prepared ZnO nanowire array on TCO glass and then fabricated a DSC with a conversion efficiency of 0.5% (Baxter & Aydil, 2005).
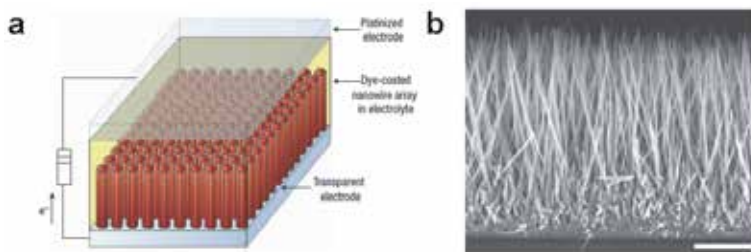
Fig. 5. Nanowire dye-sensitized cell based on ZnO wire array. (a) Schematic diagram of the cell; (b) Typical scanning electron microscopy cross-section of a cleaved nanowire array on TCO Scale bar=5 µm. (Law et al., 2005).

2.3 Semiconductor nanotubes

Nanotubes are a class of very important one-dimensional nanostructure since their hollow structure may usually give surface area larger than that of nanowires or nanorods. The nanotube arrays are ordered and strongly interconnected, which eliminates randomization of the grain network and increases contact points for good electrical connection.

2.3.1 TiO₂ nanotubes

TiO_2 nanotubes have been prepared by several methods including anodization, sol-gel, and hydrothermal synthesis and so on. Among these methods, anodization of titanium metal

has been an intensively employed method for the fabrication of the oriented TiO_2 nanotube array which could combine high surface area with well-defined pore geometry (Zhu et al., 2007). The vertical pore geometry of the nanotubes appears to be more suitable than the conventional random pore network for the fabrication of DSCs, especially DSCs with quasi-solid/solid-state electrolytes. It has been also reported that nanotube arrays give enhanced light scattering and improved collection efficiencies compared to conventional sol-gel-derived TiO_2 films with the same thickness (Zhu et al., 2007).
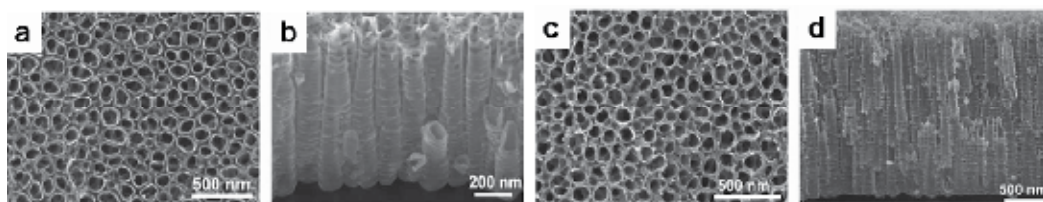
Fig. 6. SEM top-views (a, c) and cross-sections (b, d) for the ''short'' and ''long'' tubes (Macak et al., 2005).

By anodization of Ti metal in fluoride-based electrolytes, TiO_2 nanotubes can be prepared from Ti foil, but nanotube growth can also be obtained from Ti thin film deposited on TCO glass. The length of the nanotubes, wall thickness, pore diameter, and tube-to-tube spacing can be controlled by the preparation conditions, such as the anodization potential, time, and temperature, and the electrolyte composition (water content, cation size, conductivity, and viscosity) (Hagfeldt et al., 2010). In 2005, the first report on dye-sensitized TiO_2 nanotubes appeared (Macak et al., 2005) and the tubes were grown by Ti anodization in two different forms as ''long'' tubes (tube lengths ~2.5 μm) and ''short'' tubes (tube lengths ~500 nm), as shown in Fig. 6. Clearly sub-bandgap sensitization with Ru-dye (N3) was successful and led to considerable incident photon-to-current conversion efficiency (IPCE: up to 3.3%). They suggested that main factors that affect IPCE in the visible range were the structure of the tube (anatase better than amorphous), the dye concentration and the tube length. The increase in dye concentration and/or tube length leads to an increase in IPCE, which can be ascribed to a higher packing density of the dye on TiO_2 surface with a higher concentration and a higher light absorption length. So it turns out that for the longer tubes, a significantly lower dye concentration is needed to achieve maximum IPCE values.

TiO_2 nanotubes can also be obtained by anodization of aluminum films on TCO and subsequent immersion in a titanium precursor solution, followed by sintering in a furnace at 400 °C. The alumina template is then removed by immersing the samples in 6 M NaOH solution. Kang (Kang et al., 2009) fabricated highly ordered TiO_2 nanotubes using such nanoporous alumina template method. Such nanotubes with 15 μm lengths were heat treated at 500 °C for 30 min and soaked in N3 dye for 24 h. DSC based on the nanotubes showed a conversion efficiency of as high as 3.5% and a maximum IPCE of 20% at 520 nm.

In order to improve the overall solar cell efficiency, the amount of dye adsorbed by a unit solar cell volume needs to be higher enough. $TiCl_4$ treatment is an effective way to achieve a higher surface area for nanotube-based photoanodes. Roy et al. (Roy et al., 2009) investigated the effect of $TiCl_4$ treatments on the conversion efficiency of TiO_2 nanotube arrays. Typical morphology characterizations obtained for nanotube layers before and after this treatment are shown in Fig. 7. The results clearly show that by an appropriate

treatment, the inner as well as the outer wall of TiO_2 nanotubes are covered with a ~25 nm thick nanoparticle coating of TiO_2 nanoparticles with diameter of about 3 nm. This leads to a significant increase in surface area and therefore more dye can be adsorbed to the nanotube walls. Thus, the power conversion efficiency improves from 1.9% for untreated nanotutes to 3.8% for treated nanotubes.
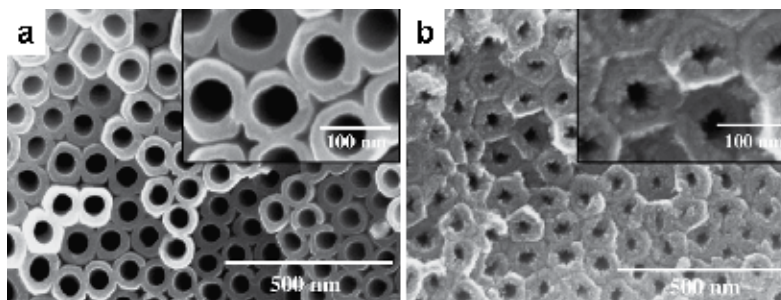
Fig. 7. Influence of $TiCl_4$ treatment: SEM images of TiO_2 nanotubes (a) before and (b) after $TiCl_4$ treatment (Roy et al., 2009).

2.3.2 ZnO nanotubes

ZnO nanotube arrays have been prepared by different methods for DSCs. There are chiefly three kinds of methods. Firstly, atomic layer deposition is an interesting technique to prepare well-defined and ordered ZnO nanotubes. For example, Martinson et al. (Martinson et al., 2007) reported ZnO nanotube photoanodes through atomic layer deposition in the pores of anodic aluminum oxide (AAO) membrane. However, the surface area of ZnO nanotubes is also very low due to a limit of the available size and pore density of the AAO membranes. Secondly, chemical etching is also effective for fabricating ZnO nanotubes, which involves two steps of process: a first growth of ZnO nanorods and a consequent treatment in alkaline solution; the latter is to convert the nanorods into nanotube structure through a chemical etching. Han et al (Han et al., 2010) fabricated high-density vertically aligned ZnO nanotube arrays on TCO substrates by such simple and facile chemical etching process from electrodeposited ZnO nanorods. The nanotube formation was rationalized in terms of selective dissolution of the (001) polar face. And the morphology of the nanotubes can be readily controlled by electrodeposition parameters for the nanorod precursor. DSC based on 5.1 μm-length ZnO nanotubes exhibited a power conversion efficiency of 1.18%. The conversion efficiency is generally low, which probably results from a fact that the length of ZnO nanotubes is limited by the fabrication method based on an etching mechanism. During the etching treatment, an accompanying dissolution of the ZnO occurs simultaneously and thus leads to a shortening of the nanorods (Zhang & Cao, 2011). At last, electrochemical deposition can also be used to directly prepare ZnO nanotube on TCO glass. Prof. Tang group reported for the first time the electrochemical deposition of large-scale single-crystalline ZnO nanotube arrays on TCO glass substrate from an aqueous solution (Fig. 8a) (Tang et al., 2007). The nanotubes had a preferential orientation along the [0001] direction and hexagon-shaped cross sections. The growth mechanism of ZnO nanotubes was investigated (Fig. 8b). They believed that the key growth step is the formation of oriented nanowires and their self-assembly to hexagonal circle shapes. The nanowires initiated subsequent growth of nanotubular structure. But not all the nanowire circle planes are

parallel to the horizontal plane because of the roughness of F–SnO$_2$ surface. Some nanotubes have certain angles with the substrate. This nanotube array has great potential for the application in DSCs.
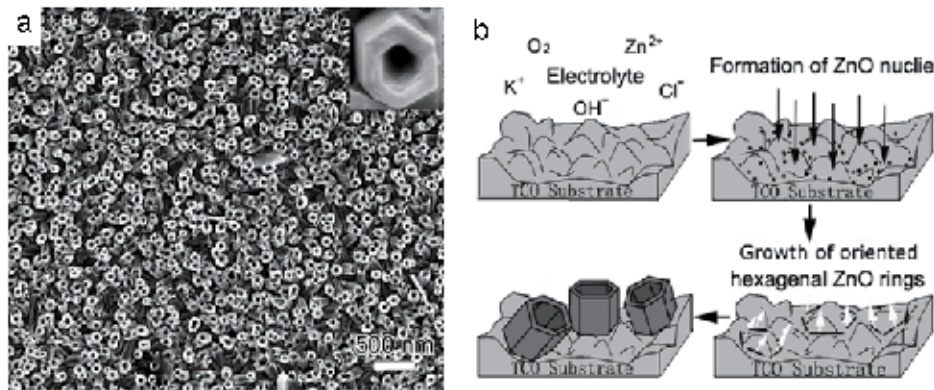
Fig. 8. Surface morphology of ZnO nanotube film (a) and illustration of the growth mechanism of ZnO nanotube array (b). (Tang et al., 2007)

3. The application of inorganic nanomaterials in photocathodes

The photocathode, namely counter electrode (CE) where the regeneration of the charge mediator (typical reaction: I$_3^-$ + 2e$^-$ (catalyst) → 3I$^-$) takes place, is one of the most important components in DSCs. The task of CE is twofold: firstly, it transfers electrons arriving from the external circuit back to the redox system (Fig. 9a), and secondly, it catalyzes the reduction of the redox species (Fig. 9b). In order to obtain an effective CE, main requirements for a material to be used as CE are good catalytic activity for the reaction (I$_3^-$/I$^-$), a low charge transfer resistance, chemical/electrochemical stability in the electrolyte system used in the cell, mechanical stability and robustness.
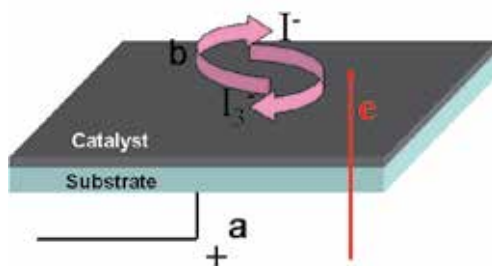
Fig. 9. Schematic representation of the counter electrode based on a I$^-$/I$_3^-$ redox couple.

At present, many kinds of CEs have been introduced, for example, metal material CEs, carbon material CEs, conducting polymer CEs, hybrid material CEs, and metallic compound nanomaterial CEs. Since each kind of CEs has their own unique advantages and disadvantages, the CE is chosen according to the particular application of DSCs. For example, the noble metal Pt CE is extremely expensive for large-scale production and may

be corroded by the iodide solution, but for 'champion cells' one must choose this highly catalytic CE with the lowest possible sheet resistance and a high rate of reduction of the redox electrolyte to speed up the reaction ($I_3^- + 2e^- \rightarrow 3I^-$). For power-producing windows or metal-foil-supported DSCs, one must employ a transparent counter electrode, e.g. a small amount of platinum deposited on TCO glass. On the other hand, large solar conversion systems producing electric power on the terawatt scale will prefer materials that are abundantly available. Carbonaceous material CE will be a good choice due to their advantages including good catalytic properties, electronic conductivity, corrosion resistance towards iodine, high reactivity, and abundance. In this section, we briefly introduce three kinds of inorganic nanomaterials as CEs with respect to their application in DSCs, including noble metal materials, carbon materials and metallic compounds nanomaterials.

3.1 Metal materials CEs

Up to now, noble metal-loaded substrates have already been widely used as the standard for the CE of DSCs, due to their unique properties, including (1) high electrochemical activity that can reduce the voltage loss due to charge-transfer overpotential of CE; (2) a low charge transfer resistance which can lead to minimum energy loss. A thin layer of noble metals, e.g. Pt, Au, is well established as the catalyst on CE substrate, such as TCO glass and metal foil. One of the important roles of noble metal in CE is to catalyze the reduction of triiodide (I_3^-) ions. This means that the available catalytic surface in the electrode plays a crucial role in determining the overall device current. So the rough/porous electrodes, which are characterized by a higher surface, are expected to assure a higher number density of catalytic sites. It is obvious that the use of metal nanoparticle film results in CE with high surface area. Therefore, the preparation methods of noble metal films will influence the final film structure/properties.

Generally all the synthetic methods of the noble metal film are roughly divided into two categories: the physical and chemical approaches. The difference between the two approaches arises from the starting point in the synthetic route to prepare the films. For the physical approaches, the film is prepared by the macroscopic precursors through subsequent subdivision in ever smaller particles by strong milling of solids or through lithographic processes including sputtering, laser ablation, vapor phase deposition, lithography, etc. While the chemical approaches start from their atomic and molecular precursors, through chemical reactions and modulating their self-assembling in order. The physical approaches (Terauchi et al., 1995) are generally quite expensive and resource-consuming, while chemical methods are generally cheaper and better fit for large scale applications. Moreover, since chemical methods allow in principle the control at a molecular level, they allow a fine size and polydispersity control and can be implemented to prepare 2D and/or 3D nanoparticle arrays to enhance the available catalytic site.

The catalytic activity is expressed in terms of the exchange current density (J_0), which is calculated from the charge-transfer resistance (R_{ct}) using the equation $R_{ct} = RT/nFJ_0$, in which R, T, n, and F are the gas constant, temperature, number of electrons transferred in the elementary electrode reaction (n = 2) and Faraday constant, respectively. Yoon et al (Yoon et al., 2008) used Nyquist plots to investigate R_{ct} on platinized TCO CEs prepared by either the electrochemical deposition (ED) method, the sputter-deposited (SD) method, or the thermal deposited (TD) method. The Nyquist plots suggest qualitatively that R_{ct} of a cell increases in the order of R_{ct} of ED-Pt film < R_{ct} of SD-Pt film < R_{ct} of TD-Pt film. The DSC fabricated with the ED-Pt CE rendered the highest power conversion efficiency of 7.6%, compared with

approximately 6.4% of the cells fabricated with the SD-Pt or most commonly-employed TD-Pt CEs. The improved performance of DSC with the ED-Pt CE is attributed to the improved catalytic activity of the reduction reaction (I_3^- +2e$^-\rightarrow$3I$^-$) and the decreased charge transfer resistance at CE/electrolyte interface. Hauch et al (Hauch & Georg, 2001) also used impedance spectra to investigate R_{ct} on platinized TCO CEs prepared by either the electron-beam evaporation (EB), SD or TD method. The 450 nm thick platinum electrode prepared by SD method gave the lowest R_{ct} of of 0.05 ohm/cm². The TD of a Pt film (<10 nm thick), using H_2PtCl_6 as a precursor on a TCO substrate, produced a low R_{ct} of 1.3 ohm/cm² comparable to the R_{ct} of the 40 nm thick sputtered Pt, confirming the superiority of the TD method.

3.2 Carbon material CEs

DSC is well known as potentially low-cost photovoltaic devices (Gratzel, 2004); from this perspective, the application of low-cost materials should be important. Low-cost carbon is the second most widely studied material for CEs after metal materials. Carbonaceous materials feature good catalytic properties, electronic conductivity, corrosion resistance towards iodine, high reactivity and abundance (Wroblowa & Saunders, 1973). Since the fact that Kay and Grätzel found good electrocatalytic activity of graphite/carbon black mixture in 1996 (Kay & Gratzel, 1996), various kinds of carbon are studied, such as hard carbon spherules (Huang et al., 2007), activated carbon (Imoto et al., 2003), mesoporous carbon (Wang et al., 2009a), nanocarbon (Ramasamy et al., 2007), single-walled carbon nanotubes (Suzuki et al., 2003), multiwalled carbon nanotubes (MWNTs) (Seo et al., 2010), carbon fiber (Joshi et al., 2010) and graphene nanoplates (Kavan et al., 2011). Nevertheless carbonaceous electrodes which would be superior to Pt were reported only rarely for certain kinds of activated carbon (Imoto et al., 2003). This result is mainly attributed to the poor catalytic activity for I_3^-/I$^-$ redox reaction. In addressing this issue, several optimizing methods have been developed, such as increasing the surface area, functionalizing the carbon materials to get more active sites for I_3^-/I$^-$ redox reaction.

To achieve a comparable activity to platinum, carbon-based CEs must have sufficiently high surface area. Although carbonaceous electrodes have poor catalytic activity for I_3^-/I$^-$ redox reaction, its exceptional surface area and conductivity, such as mesoporous carbon and graphene, have been shown to be quite effective and in some cases even exceeded the performance of platinum. Imoto et al (Imoto et al., 2003) compared several types of activated carbon with different surface areas ranging from 1000 m² g^{-1} to 2000 m² g^{-1} as the CE catalyst, assessing in addition the activity of several different types of activated carbon, glassy carbon, and graphite. The surface area of the glassy carbon and graphite was three orders of magnitude lower than those of the activated carbon catalysts. In the preparation of the latter electrodes, a certain amount of carbon black was included. In their results, the electrodes consisting of the lower sheet resistance materials, graphite and glassy carbon, gave lower J_{sc} values and fill factors, indicating the importance of the roughness of the carbon materials in achieving a better performance. They demonstrated an improvement in the J_{sc} and FF with increasing thickness (>30 µm) of the carbon material. Robert et al (Sayer et al., 2010) used the dense, vertical, undoped MWCNT arrays grown directly on the electrode substrate as CEs and got a greater short-circuit current density and higher efficiency than DSCs with Pt CE. The improved performance is attributed to increased surface area at the electrolyte/counter electrode interface that provides more pathways for charge transport. Prakash et al (Joshi et al., 2010) investigated the electrospun carbon nanofibers as CEs. The results of electrochemical impedance spectroscopy (EIS) and cyclic voltammetry measurements

indicated that the carbon nanofiber based CEs exhibited low charge-transfer resistance, large capacitance, and fast reaction rates for triiodide reduction. Joseph et al (Roy-Mayhew et al., 2010) found that functionalized grapheme sheets with oxygen-containing sites perform comparably to platinum. Using cyclic voltammetry, they demonstrated that tuning the grapheme sheets by increasing the amount of oxygen-containing functional groups can improve its apparent catalytic activity.

3.3 Metal compounds CEs

A possible approach is to utilize transition-metal compounds with similar properties to those of noble metals (Shi et al., 2004). Compared with metallic materials, transition-metal compounds have a great potential to be used as cost-effective CEs in DSCs due to their unique properties including a broad variety of low cost materials, a good plasticity, a simple fabrication, high catalytic activity, selectivity, and good thermal stability under rigorous conditions (Wu et al., 2011a). Recently, several kinds of transition-metal compounds CEs, e.g., nitrided Ni particle film, TiN nanotube arrays, MoC have been reported in DSCs which have a conversion efficiency superior to Pt.

Jiang et al (Jiang et al., 2009) used TiN nanotube arrays as CE in DSC for the first time, and the resulting DSC had photovoltaic performances comparable to those using the conventional TCO/Pt counter electrodes, which should be attributed to the obviously lower charge-transfer resistances at the CE/electrolyte interfaces and ohmic internal resistances. The exciting photovoltaic performances comparable to Pt CE inspire the researches on the transition-metal compounds used as the new kind of CEs. They also investigated the surface-nitrided nickel film as a low cost CE material, and the resulting DSCs presented an excellent photovoltaic performance competing with that with the conventional Pt CE (Jiang et al., 2010). Molybdenum and tungsten carbides embedded in ordered mesoporous carbon materials (MoC-OMC, WC-OMC) as well as Mo_2C and WC were prepared respectively by Wu et al (Wu et al., 2011a). They demonstrated that DSCs equipped with optimized MoC-OMC, WC-OMC, Mo_2C, and WC showed higher power conversion efficiency than those devices with a Pt CE. Very recently, they have developed another kind of CE, tungsten oxides, based on their excellent catalytic activity (Wu et al., 2011b). They found that WO_2 nanorods showed excellent catalytic activity for triiodide reduction, and the DSC based on a WO_2 CE reached a high energy conversion efficiency of 7.25%, close to that of the DSC using Pt CE (7.57%). Their results exhibit that tungsten oxides are promising alternative catalysts to replace the expensive Pt in DSCs system. Wang et al (Wang et al., 2009b) have demonstrated, for the first time, that CoS is very effective in catalyzing the reduction of triiodide to iodide in a DSC, superseding the performance of Pt as an electrocatalyst. They deposited the CoS layer on a flexible ITO/polyethylene naphthalate films. CoS based flexible and transparent CEs not only matched the performance of Pt as a triiodide reduction catalyst in DSCs, but also showed excellent stability in ionic liquids-based DSCs under prolonged light soaking at 60 °C. Clearly, the CoS has an advantage for large scale application as being a much more abundant, transparent and cheaper CE.

4. The application of inorganic nanomaterials in quasi-solid/solid-state electrolytes

The power conversion efficiency of DSCs with organic solvent-based electrolyte was reported to exceed 11% (Gratzel, 2004). However, the presence of organic liquid electrolytes

in cells causes problems, such as leakage, evaporation of solvent, high-temperature instability, and flammability, and therefore results in practical limitations to sealing and long-term operation. At present, many attempts have been made to substitute liquid electrolytes with solid state electrolytes (e.g. p-type semiconductors, organic hole-transport materials, solid polymer electrolytes, and plastic crystal electrolytes) or quasi-solid-state electrolytes (e.g. polymer gel, low-molecular-weight gel). Here, we focus our attention on the application of inorganic nanomaterials in quasi-solid/solid-state electrolytes, including *p*-type semiconductor nanoparticles as solid-state electrolytes and solidification of liquid electrolyte by inorganic nanoparticles.

4.1 p-type semiconductor nanoparticles as solid-state electrolytes

P-type semiconductors are the most common hole-transporting materials to fabricate solid-state DSCs. Several aspects are essential for any p-type semiconductor in a DSC: (a) It must be able to transfer holes from the oxidized dye; (b) It must be able to be deposited within the porous TiO_2 nanocrystal layer; (c) A method must be available for depositing the p-type semiconductors without dissolving or degrading the dye on TiO_2 nanocrystal; (d) It must be transparent in the visible spectrum, otherwise, it must be as efficient in electron injection as the dye. Copper-based materials, especially CuI and CuSCN (Tennakone et al., 1995), are found to meet all these requirements. CuI and CuSCN share good conductivity in excess of 10^{-2} Scm^{-1}, which facilitates their hole conducting ability (Smestad et al., 2003), hence, they have been widely used as complete hole-transporting layer for fabricating solid-state DSCs. Tennakone et al (Tennakone et al., 1995) first reported a nano-porous solid-state DSC based on CuI in 1995. DSCs were fabricated by sandwiching a monolayer of the pigment cyanidin adsorbed on nano-porous n-TiO_2 film within a transparent polycrystalline film of p-CuI, filling the intercrystallite pores of the porous n-TiO_2 film. The short-circuit current density reached about 1.5–2.0 mAcm^{-2} in sunlight (about 800 Wm^{-2}), however, they found that the polarization arising from mobile Cu$^+$ ions tends to decrease the open-circuit voltage of the cell. By replacing cyanidin with a Ru-bipyridyl complex dye, they (Tennakone et al., 1998) then fabricated a solid-state DSC with the structure of TiO_2/Ru(II)(dcbpy)$_2$(SCN)$_2$ /CuI in 1998. The efficiency and the stability of the solid-state DSC was less than those of the typical DSCs. They attributed it to the loosening of the contact between the *p*-type semiconductor and the dye monolayer, and to short-circuiting across the voids in the nanoporous TiO_2 film, which allows direct contact between CuI and the tin oxide surface. To solve this issue, they (Kumara et al., 2002) incorporated a small quantity (~10^{-3} M) of 1-methyl-3-ethylimidazolium thiocyanate (MEISCN) into the coating solution (i.e., CuI in acetonitrile) and the stability of the CuI-based DSC was greatly improved. In this case, MEISCN acted as a CuI crystal growth inhibitor, which enables filling of the pores of the porous matrix, resulting in the formation of more complete and secure contacts between the hole collector and the dyed surface. Meng et al (Meng et al., 2003) also utilized MEISCN to control the CuI crystal growth and act as a protective coating for CuI nanocrystals, improving the cells' efficiency to 3.8% with improved stability under continuous illumination for about 2 weeks. Another alternative for solid-state DSCs is CuSCN. O'Regan et al (Oregan & Schwartz, 1995) used CuSCN as a hole transport layer, and demonstrated that CuSCN is a promising candidate material as the hole-conducting layer. They found the UV illumination created an interfacial layer of (SCN)$_3^-$, and/or its polymerization product (SCN)$_x$, between the TiO_2 and the CuSCN, causing a dramatic improvement in the efficiency of DSCs (O'Regan & Schwartz, 1998). Later, they (O'Regan et al., 2000) substituted TiO_2 for ZnO, fabricating

ZnO/dye/CuSCN solar cell with a conversion efficiency of 1.5%. In 2005, they (O'Regan et al., 2005) made another solid-state DSC with the structure of TiO_2/dye/CuSCN with thin Al_2O_3 barriers between the TiO_2 and the dye. It is noteworthy that the Al_2O_3-treated cells showed improved voltages and fill factors but lower short-circuit currents. Nevertheless, the performance of DSCs with CuSCN is still lower than that of cells utilizing CuI, probably due to the relatively lower hole conductance.

In summary, compared to a liquid electrolyte DSC, the solid-state counterpart presents a relatively low conversion efficiency, which is probably due to three reasons (Kron et al., 2003): (a) the less favorable equilibrium Fermi-level position in the TiO_2; (b) poor conductivity of hole-transporting materials; (c) the much larger recombination probability of photogenerated electrons from the TiO_2 with holes as compared to recombination with the I^-/I_3^- redox couple. So it is necessary to make further efforts to design new and more efficient inorganic nanomaterial electrolytes for DSCs.

4.2 Solidification of liquid electrolyte by inorganic nanoparticles

Room-temperature ionic liquids (RTILs) such as imidazolium iodide have been widely used in DSCs as a solvent and a source of I^- or other ions, because of their favorable properties such as thermal stability, nonflammability, high ionic conductivity, negligible vapor pressure, and a possible wide electrochemical window. However, the fluidity of RTIL-based electrolytes, resulting in difficulty in seal, is still an obstacle for long-term operation. To reduce its fluidity, combination of RTILs with a framework material including small-molecular organogels, inorganic nanoparticles, and polymer, has been attempted by many groups.

Among these framework materials, inorganic nanoparticles have drawn more attention. In 2003, silica nanoparticles were used for the first time to solidify ionic liquids by Prof. Grätzel group (Wang et al., 2003a). The presence of silica nanoparticles has no adverse effect on the conversion efficiency, and the ionic liquid-based quasi-solid-state electrolytes are successfully employed for fabricating DSC with a conversion efficiency of 7%. This means that quasi-solid-state electrolytes offer specific benefits over the ionic liquids and will enable the fabrication of flexible, compact, laminated quasi-solid-state devices free of leakage and available in varied geometries. In addition, for their pore structures (2-50 nm) and large surface area, mesoporous materials may solidify liquid electrolytes and provide favourable channels for the triiodide/iodide diffusion. By using the mesoporous SiO_2 material (SBA-15) as the framework material, Yang et al (Yang et al., 2005) fabricated a quasi-solid-state electrolyte and then fabricated DSC with a energy conversion efficiency of 4.34%. ZnO nanoparticle also can be used to solidify the liquid electrolyte. For example, Huang group (Xia et al., 2007) used ZnO nanoparticles as a framework to form a quasi-solid-state electrolyte for DSC. The quasi-solid-state DSC with the quasi-solid-state electrolyte showed higher stability in comparison with that of the liquid device, and gave a comparable overall efficiency of 6.8% under AM 1.5 illumination.

Thermal stability is an urgent concern for quasi-solid DSCs based on RTIL gel electrolytes. Some room-temperature quasi-solid-state electrolytes usually become liquid at high temperature (40–80 °C), for example, 3-methoxypropionitrile (MPN)-based polymer gel electrolyte (viscosity: 4.34 MPa s at 80 °C) (Wang et al., 2003b) and plastic crystal electrolytes (m.p. 40–45 °C) (Wang et al., 2004). Since the working temperature of DSCs may reach 60 °C under full sunlight, it is necessary that at high temperature (60–80 °C), the electrolytes are still in the quasi-solid or solid state and that the DSCs maintain high overall energy-

conversion efficiency (>4%). We (Chen et al., 2007b) have developed a succinonitrile-based gel electrolyte by introducing a hydrogen bond (O–H…F) network upon addition of silica nanoparticles and BMI·BF$_4$ (1-Butyl-3-methylimidazolium tetrafluoroborate) to succinonitrile. When the content of fumed silica nanoparticles was over 5 wt%, the succinonitrile–BMI·BF$_4$–silica system became a gel, and the succinonitrile–BMI·BF$_4$–silica (7 wt%) system still remained in the gel state even at 80 °C, as shown in the inset of Fig. 10, which confirms that the addition of silica nanoparticles and BMI·BF$_4$ is critical for the gelation and thermostability of succinonitrile-based electrolytes. The appropriate addition of BMI·BF$_4$ and silica nanoparticles in this gel electrolyte can greatly improve the thermostability but has no adverse effects on the conductivity, ionic diffusion coefficients and the cell performance. Moreover, the relatively high succinonitrile content in the electrolyte is also very important because the electrolyte without succinonitrile has very low conductivity and results in poor cell performance. Herein, the obtained succinonitrile-based gel electrolyte satisfies the need for both thermostability and high conductivity in electrolytes. DSCs with this gel electrolyte showed power conversion efficiencies of 5.0–5.3% over a wide temperature range (20–80 °C). Furthermore, the aging test revealed that the cell still maintained 93% of its initial value for the conversion efficiency after being stored at 60 °C for 1000 h, indicating an excellent long-time durability.
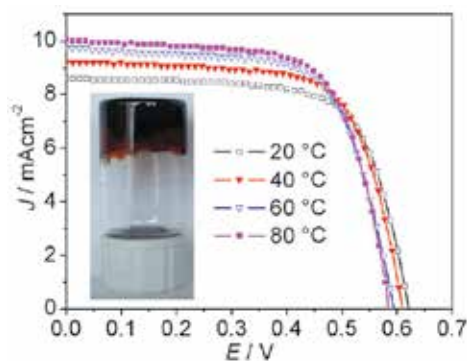
Fig. 10. Photos of succinontrile–BMI·BF$_4$–silica (silica: 7 wt% of succinontrile–BMI·BF$_4$) at 80 °C (Chen et al., 2007b).

5. Inorganic nanomaterials as light-absorbing materials

5.1 Semiconductor QDs

The emergence of semiconductor quantum dots (QDs) has opened up new ways to utilize them as a possible replacement for ruthenium complexe dyes (sensitizers) in DSCs. QDs have many advantages including good thermal stability under rigorous conditions, tunable bandgaps, sharp absorption onset, large absorption coefficients and low cost etc. Hence, the QD-sensitized solar cells (QD-SCs) have attracted more attention. In the past few years, a rapid increase of the conversion efficiency of QD-SCs has been reported, reaching values of around 4-5% at 1 sun (Chang et al., 2010). The efficiency of QD-SC still lags behind those of DSC; however, a further performance improvement for QD-SCs can be anticipated.

Recently, various QDs (CdSe (Levy-Clement et al., 2005), PbSe (Leschkies et al., 2009), CuInS$_2$ (Kaiser et al., 2001), etc.) as the sensitizer have been proposed, and various strategies have been developed for maximizing photoinduced charge separation and electron transfer

processes to improve the power conversion efficiency. This section aims to introduce the recent developments in the synthesis methods of high quality QDs and the performance optimization strategies of QD-SC.

5.1.1 Synthesis of QDs

QDs used as sensitizer in DSC have been fabricated by using two fundamentally different approaches. The first and most common route employs the *in situ* preparation of QDs onto the nanostructured semiconductor metal oxide film. The second approach is *ex situ* growth approach, which can take advantage of the tremendous developments in controlling the growth of monodisperse, highly crystalline and diverse QDs. This method is to synthesis the QDs independently, and subsequently to attach the pre-synthesized QDs to the photoanode by a bifunctional linker molecule or direct adsorption. Both of these preparation methods have their limitation respectively, hence it is still necessary to develop a new method in the future.

5.1.1.1 *In situ* preparation of QDs

The *in situ* preparation method, where the QDs are directly generated on the surface of metal oxide film electrode, mainly includes chemical bath deposition (CBD) (Diguna et al., 2007) and successive ionic layer adsorption and reaction (SILAR) (Lee et al., 2009a). There are many of advantages of the *in situ* deposition approaches. Firstly, the *in situ* deposition approaches are easy to process since it does not need any expensive equipment and multiple complicated steps. Secondly, the QDs are in direct electronic contact with metal oxide, which not only makes the QDs good anchoring to the electrodes but also shortens the electron diffusion length. Thirdly, they can easily produce metal oxide films with high surface coverage of the sensitizing QDs, which increases the absorption of light. However, this method still has several intrinsic limitations. For example, it is difficult to control chemical composition, crystallinity, size distribution and surface properties of QDs, which may hamper the effective exploitation of QDs advantages. .

For CBD method, QDs are deposited *in situ* by immersing the wide-bandgap nanostructured electrode (usually metal oxide) into a solution that contains the cationic and anionic precursors, which react slowly in one bath under different temperature. Most of the sulfides and selenides can be prepared by this method. Lee et al developed a method coupling self-assembled monolayer and CBD, as well as a modified CBD process performed in an alcohol system to assemble CdS into a TiO_2 film (Lin et al., 2007). These modified processes have been proved to be efficient for CdS QD-SC, and CdS QD-SCs exhibit a power conversion efficiencies of 1.84% and 1.15% respectively for iodide/triiodide and polysulfide electrolytes (Lin et al., 2007).

In the SILAR approach, the cationic and anionic precursor solution is placed in two vessels respectively. Firstly, the nanostructured electrode is immersed into the solution containing the metal cation, and then the nanostructured electrode absorbing the metal cation on the surface is taken out from the metal cation solution and dip into the second precursor solution containing the anion. After the second rinsing step, the deposition cycle completes. The average QD size can be controlled by the number of deposition cycles. This method has been used in particular to prepare metal sulfides, but recently it has been expanded to metal selenides and tellurides. For example, Grätzel et al deposited the CdSe and CdTe QDs *in situ* onto mesoporous TiO_2 films using SILAR approach (Lee et al., 2009b). After some

optimization of these QD-sensitized TiO$_2$ films in solar cells, over 4% overall efficiency was achieved at 100 W/m^2 with about 50% IPCE at its maximum (Lee et al., 2009b).

5.1.1.2 *Ex situ* growth approach

The *ex situ* growth approach is based on a two-step process, whereby QDs are first independently synthesized using established colloidal synthesis method and then QDs are subsequently linked on to the metal oxide film electrodes to achieve effective QD-electrode junctions that would promote charge separation while minimizing surface trapping and hence losses (Kamat, 2008). This approach can take advantage of the tremendous developments in controlling over the chemical, structural, and electronic properties of QDs compared to the in situ approaches. However, since QDs, unlike dyes, do not possess an anchoring functional group for coupling to the metal oxide film surface, this approach provides limited control over the metal oxide film sensitization process and degree of QD-metal oxide film electronic coupling. In addition, the as prepared QDs are typically passivated with a layer of organic ligands, such as tri-n-octylphosphine oxide (TOPO), aliphatic amines, or acids, which serve as an impediment to effective metal oxide film sensitization and as a barrier to efficient charge transfer across the QD/metal oxide film and QD/electrolyte interfaces.

The first step of the *ex situ* growth approach is the synthesis of the monodisperse QDs (Fig. 11a). The most common synthesis approach is to control the nucleation and growth process of particles in a solution of chemical precursors containing the metal and the anion sources (Overbeek, 1982). In a typical process, the solvent containing molecules (e.g. trioctylphosphine and trioctylphosphine oxide) is heated to 150-350 °C under the vigorously stirred with protective atmosphere, and then the organometallic precursor and related species are injected. Consequently, a large number of nucleation centers are initially formed, and the coordinating ligands in the hot solvent prevent or limit particle growth via Ostwald ripening. Typical reactions used for the synthesis of II-VI (CdSe, CdTe, CdS) (Peng & Peng, 2002), III-V (InP, InAs) (Talapin et al., 2002), and IV-VI (PbSe (Talapin & Murray, 2005)) QDs are outlined by reactions 1-3 (Fig. 11a).
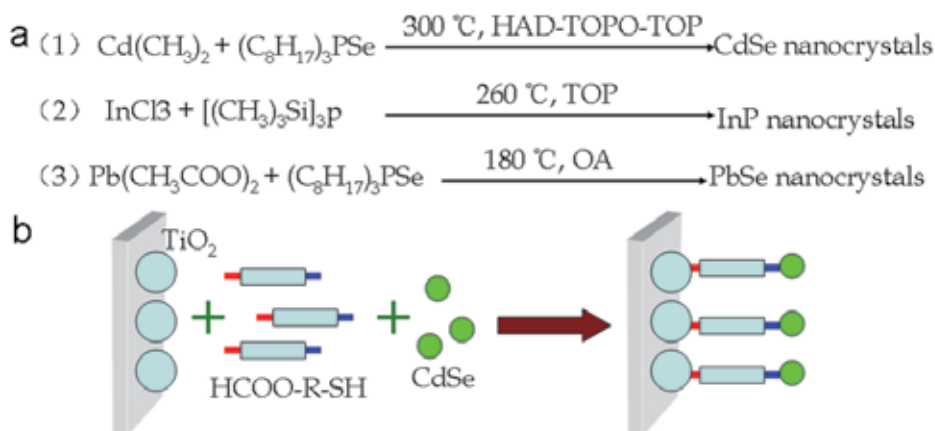
Fig. 11. (a) Typical reactions used for the synthesis of QDs. (b) Scheme of attaching the pre-synthesized QDs to the electrode material by a bifunctional linker molecule (Robel et al., 2006).

The second step of the *ex situ* growth approach is to attach the pre-synthesized QDs to the electrode material by a bifunctional linker molecule (usually HOOC-R-SH, where R is the organic core of the linker) or direct adsorption (Fig. 11b). The carboxyl group attaches to the nanostructured metal oxide film, while the thiol remains free for connecting QDs. Then the modified film is immersed in the QD solution (for several hours or days) for the adsorption of QDs, which typically involves fractional ligand exchange. For instance, Kamat et al (Robel et al., 2006) immersed the TiO$_2$ films into a solution of acetonitrile containing carboxy alkane thiols (Mercaptopropionic acid, thiolacetic acid and mercaptohexadecanoic acid) for ~4 h as shown in the Fig. 11b. Resulting TiO$_2$ films functionalized with these bifunctional surface modifiers, were then washed with both acetonitrile and toluene, and transferred to a glass vial containing a suspension of CdSe QDs in toluene. The electrodes were kept immersed in the CdSe solution for approximately 12 h. QDs self-assembly had also been used on dispersed TiO$_2$ crystals, where the photoelectrode was fabricated after QD sensitization by a pressing route (Ardalan et al., 2011). Direct adsorption was recently proposed for deposition of monodisperse QDs without molecular linkers to the surface of the metal oxide nanostructure. This procedure has already been employed to sensitize TiO$_2$ with QDs, such as CdSe QDs (Shen et al., 2009), although the obtained photocurrents at 1 sun intensity are low. One possible explanation is that directly adsorbed colloidal QDs provides a low surface coverage of about 14% (Gimenez et al., 2009). It is obvious that higher surface coverage of colloidal QDs on TiO$_2$ substrate will result in QD-SCs with higher conversion efficiency.

5.1.2 Performance optimization of QDs in the QD-SCs

Theoretically, there are many advantages of the QDs for sensitizing the nanoporous oxide film electrode, such as higher absorption of QD coating, greater stability of the semiconductor, and tailoring of optical absorption over a wider wavelength range (Hodes, 2008). Moreover, the demonstration of multiple exciton generation (MEG) by impact ionization in colloidal QDs could push the thermodynamic efficiency limit of these devices up to 44% (Klimov, 2006) instead of the current 31% of the Schockley-Queisser detailed balance limit. Although, up to now, the efficiencies of QD-SCs are far behind those of DSCs (DSC currently exceeds 11% at 1 sun illumination (Cao et al., 2009)), QD-sensitized nanostructured solar cells are attracting increasing attention among researchers and are progressing rapidly to values around 4-5% from quite low conversion efficiencies (Gonzalez-Pedro et al., 2010). Several methods have been developed to optimize the performance of the QD-SCs including (1) tuning of effective bandgaps from visible down to the IR range by changing their sizes and compositions, (2) utilizing the phenomena of MEG, Förster resonance energy transfer (FRET)-based charge collection, and direct charge transfer schemes, and (3) surface treatment.

5.1.2.1 Tuning of bandgaps of QDs

The most striking property of QDs is the massive changes in electronic structure as a function of size. As the size decreases, the electronic excitations shift to higher energy, and the oscillator strength is concentrated into just a few transitions (Murray et al., 1993). Therefore, controlling quantum size confinement in monodisperse QDs is the most obvious method not only to extend the range of the QDs absorbance from the visible to near infrared range but also to align the energy levels with respect to the wide-bandgap nanostructure. Herein, the CdSe QDs and TiO$_2$ system as a model is introduced for the direction of the optimization. The driving force for the electron separation and transfer is dictated by the

energy difference between the conduction band energies. The conduction band of TiO$_2$ is at -0.5 V vs NHE. If we assume the larger CdSe particles have band energy close to the reported value of -0.8 V vs NHE, we can use the increase in bandgap as the increase in driving force for the electron transfer. Since the shift in the conduction band energy is significantly greater than the shift in valence band energy for quantized particles (Norris & Bawendi, 1996), we can expect the conduction band of CdSe QDs to become more negative (on NHE scale) with decreasing particle size. As the particle size decreases from 7.5 to 2.4 nm, the first excitonic peak shifts from 645 nm to 509 nm and the conduction band shifts from -0.8 V vs NHE to -1.31 V, the electron transfer rate improve by nearly 3 orders of magnitude (Robel et al., 2007). PbS nanocrystals have similar properties with the light absorption range extending from visible to near infrared (Hyun et al., 2008).

Another method that can broaden the spectral absorption range is the use of nanocomposite absorbers (Lee & Lo, 2009). Semiconductor QDs are excellent building blocks for more sophisticated nanocomposite absorbers, which the QDs combined with each other with different size or type. The well-known example of the nanocomposite is the combination of CdS and CdSe QDs. The combination can be used as co-sensitizers to provide enhanced performance compared to the use of each individual semiconductor QDs. When CdSe QDs are assembled on a TiO$_2$/CdS electrode, the co-sensitized electrode (TiO$_2$/CdS/CdSe) has an absorption edge close to that of TiO$_2$/CdSe electrode but its absorbance is higher than those of TiO$_2$/CdS and TiO$_2$/CdSe electrodes both in the short wavelength region (<550 nm) where both CdS and CdSe are photoactive and long wavelength region (ca. 550–700 nm) which belong to the CdSe due to the complementary effect of the composite sensitizers. When CdS is located between CdSe and TiO$_2$, both the conduction and valence bands edges of the three materials increase in the order: TiO$_2$<CdS<CdSe, which is advantageous to the electron injection and hole recovery of CdS and CdSe. This clearly shows that nanocomposite absorbers can improve these systems through two different beneficial effects. On the one hand, the spectral absorption range can be broadened. On the other, the re-organization of energy levels between CdS and CdSe forms a stepwise structure of band-edge levels (Lee & Lo, 2009).

5.1.2.2 Utilizing the phenomena of MEG and energy/charge transfer

MEG can occur when absorption of a high-energy photon leads to production of an excited electron or a hole with an excess energy at least equal to or greater than the QD bandgap (Eg). These hot carriers can transfer the entire excess energy, or part of it, to one or more valence electrons, and excite them across the bandgap. In this way, absorption of a single photon leads to generation of two or more electron-hole pairs. The quantum yield for exciton generation is defined as the average number of electron-hole pairs produced by absorption of a single photon. The analogous phenomenon of multiple charge carrier generation per photon in bulk semiconductors is termed impact ionization and is considered an inverse of Auger recombination. MEG in QDs has mostly been described as a coherent process in which single and multi-exciton states are coupled via the Coulomb interaction (Beard et al., 2007). In 1982 it was recognized that it could be possible to increase solar cell efficiency for a single junction by utilizing MEG (Ross & Nozik, 1982). Under 1 sun AM1.5 spectrum the theoretical efficiency of a MEG-enhanced cell is over 44% (Klimov, 2006). Among the various QDs materials, PbS and PbSe are good candidates for solar cells, because they not only can be made to overlap the solar spectrum optimally, which the absorption wavelength of the first exciton peak can easily be extended into the infrared by controlling

their sizes (Vogel et al., 1994), but also show that two or more excitons can be generated with a single photon of energy greater than the bandgap (Ellingson et al., 2005). PbSe and PbS QDs have been shown to have quantum yields above 300% (Ellingson et al., 2005) and even above 700% (Schaller et al., 2006).

As a new approach, long range FRET, also known as electronic energy transfer, has been also utilized in the DSCs recently. The donor dye molecules, which are added to the redox solution, upon absorption of light, transfer the excitation energy to an acceptor dye adsorbed on the electrode followed by the standard charge separation process. However, the donor molecules are heavily quenched in the liquid electrolytes (Shankar et al., 2009). Similar geometries using other sensitizers, such as inorganic semiconductor nanocrystals, have been proposed (Chen et al., 2008). QDs have the advantage of a broad absorption spectrum, stretching from the band edge to higher energies, in contrast with the narrow absorption spectra typically exhibited by molecular dyes (Buhbut et al., 2010). The use of FRET has been contemplated as an alternative mechanism for charge separation and a way to improve exciton harvesting by placing the exciton close to the heterojunction interface (Liu et al., 2006). In inorganic QD-DSCs, the use of FRET to transfer the exciton generated in the QD to a high mobility conducting channel, such as a nanowire or a quantum well, has been proposed as a way to bypass the traditional limitations of charge separation and transport (Lu & Madhukar, 2007). Very recently, Sophia et al (Buhbut et al., 2010) presented a design which combines the benefits of QDs in terms of their broad absorption spectrum with the evolved charge transfer mechanism of DSC. They demonstrated that QDs serving as "antennas" could enhance light absorption, broaden the absorption spectrum, increase the number of photons harvested by solar cell effectively and funnel absorbed energy to nearby dye molecules via FRET successfully. Their design introduced new degrees of freedom in the utilization of QDs sensitizers for solar cells. In particular, it opens the way toward the utilization of new materials whose band offsets do not allow direct charge injection.

5.1.2.3 Surface treatment

Regarding the surface treatment, it is important to remark a significant difference between molecular dyes and semiconductors used as sensitizers. As suggested by Hodes (Hodes, 2008), the probable existence of surface states in the sensitizing semiconductor is a major difference between DSCs and QD-SCs. These surface states have been widely studied in colloidal QDs and can be detected by different techniques such as photoluminescence or scanning tunnelling microscopy. The observed behaviors strongly depended on the surface treatment or the type of capping ligand (Frederick & Weiss, 2010). Surface modification by dipoles provides a simple and efficient way to shift the QD energy level. For monodisperse QDs, fractional exchange of the capping ligands by molecular dipoles can be used to shift the electronic QD states with respect to their environment in a systematic fashion, as shown in the Fig. 12 (Ruhle et al., 2010).

5.2 Rare-earth up-converting nanophosphors

Light-absorbing materials developed for solar cells, such as silicon and dyes, can not efficiently absorb near infrared light. In contrast, some rare-earth phosphors, especially those co-doped with Yb^{3+} and Er^{3+}, can efficiently absorb near infrared light, such as 980-nm laser light, after which they exhibit up-converted luminescence in the visible range (Heer et al., 2004). Doping of rare-earth materials into solar cells has been demonstrated as a better
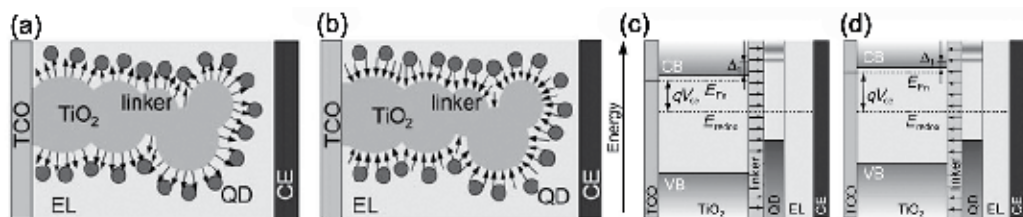
Fig. 12. (a) Schematic drawing of a mesoporous TiO_2 film, covered with linker molecules with a molecular dipole pointing towards the QD monolayer. (b) As in (a) but for linker molecules with a dipole pointing in the opposite direction. (c) Energy-band diagram showing a downward shift of the energy levels of the wide-bandgap nanostructure due to the dipole moment. (d) As in (c) but with linker molecules with a dipole moment pointing away from the QDs (Ruhle et al., 2010).

absorption of the long wavelength light in the solar spectrum, thus enhance the performance of solar cells (Shalav et al., 2005).

Recently, our group has developed 980-nm laser-driven photovoltaic cells (980LD-PVCs) firstly by introducing of a film of rare earth up-converting nanophosphors in conventional dye-sensitized solar cells. The novel photovoltaic cells were constructed by coating $Na(Y_{1.5}Na_{0.5})F_6$:Yb,Er nanorod films on N3 dye-sensitized TiO_2 films to create direct-current electricity under the irradiation of a 980-nm laser. Under the irradiation of a 980-nm laser with a power of 1 W, the visible up-converting luminescence of rare-earth nanophosphors could be efficiently absorbed by the dyes in 980LD-PVCs, and they exhibited a maximal output power of 0.47 mW. Because of the rather high transparency of biological tissue to 980-nm light, 980LD-PVCs efficiently provided electricity output even when covered by intestinal layers, which promises a new strategy to supply the electrical power for in-vivo nanorobots and other nanobiodevices (Chen et al., 2009).

6. Conclusion

DSCs have currently been attracting widespread scientific and technological interest as an alternative to conventional solar cells. The development and future of DSCs are seriously dependent on the optimal combination of high efficiency, good stability, and low cost, which lie on the design, preparation and modification of materials, especially inorganic materials with excellent properties. Nanotechnology opens a door to tailing inorganic materials and creating various nanostructures for the use in DSCs. Currently, inorganic nanomaterials have been widely used in all components. In this chapter, we describe four topics about the application of inorganic nanomaterials in DSCs. Firstly, the preparation and development of semiconductor nanomaterials, including nanoparticles, nanowires and nanotubes for film photoanodes have been demonstrated. Secondly, different nanomaterials, including metal materials, carbon materials and transition-metal compound, have been introduced for the use in photocathodes (counter electrode). Thirdly, the applications of inorganic nanomaterials in quasi-solid/solid-state electrolytes, including p-type semiconductor nanoparticles as solid-state electrolytes and solidification of liquid electrolyte by inorganic nanoparticles, have been discussed. At last, the development of semiconductor quantum dots and rare-earth up-converting nanophosphors as light-absorbing material has been presented.

However, these are initial results, and further research is still needed to improve the conversion efficiency and stability of DSCs. In order to further improve the efficiency and facilitate the practical application of DSCs, the following challenges should be addressed: (1) design and preparation transparent nanocrystalline film electrodes with higher surface area and faster electron transport property; (2) development of inorganic nanomaterials with low cost and high catalytic activity as counter electrode materials; (3) preparation of novel quasi-solid/solid-state electrolytes with high thermostability and excellent hole-transporting property; (4) design and construction of semiconductor quantum dots as effective light-absorbing material, especially quantum dots with excellent multiple exciton generation ability; (5) development of new techniques to better control the kinetic electron transfer processes at all interfaces.

7. Acknowledgment

8. References

Ardalan, P.; Brennan, T. P.; Lee, H. B. R.; Bakke, J. R.; Ding, I. K.; Mcgehee, M. D. & Bent, S. F. (2011). Effects of self-assembled monolayers on solid-state cds quantum dot sensitized solar cells. *ACS Nano*, VOL.5, NO.2, pp. 1495-1504.

Baxter, J. B. & Aydil, E. S. (2005). Nanowire-based dye-sensitized solar cells. *Appl. Phys. Lett.* , VOL.86, NO.5, pp. 053114.

Beard, M. C.; Knutsen, K. P.; Yu, P. R.; Luther, J. M.; Song, Q.; Metzger, W. K.; Ellingson, R. J. & Nozik, A. J. (2007). Multiple exciton generation in colloidal silicon nanocrystals. *Nano Lett.* , VOL.7, NO.8, pp. 2506-2512.

Buhbut, S.; Itzhakov, S.; Tauber, E.; Shalom, M.; Hod, I.; Geiger, T.; Garini, Y.; Oron, D. & Zaban, A. (2010). Built-in quantum dot antennas in dye-sensitized solar cells. *ACS Nano*, VOL.4, NO.3, pp. 1293-1298.

Cao, Y. M.; Bai, Y.; Yu, Q. J.; Cheng, Y. M.; Liu, S.; Shi, D.; Gao, F. F. & Wang, P. (2009). Dye-sensitized solar cells with a high absorptivity ruthenium sensitizer featuring a 2-(hexylthio)thiophene conjugated bipyridine. *J. Phys. Chem. C* VOL.113, NO.15, pp. 6290-6297.

Chang, J. A.; Rhee, J. H.; Im, S. H.; Lee, Y. H.; Kim, H. J.; Seok, S. I.; Nazeeruddin, M. K. & Gratzel, M. (2010). High-performance nanostructured inorganic-organic heterojunction solar cells. *Nano Lett.* , VOL.10, NO.7, pp. 2609-2612.

Chapin, D. M.; Fuller, C. S. & Pearson, G. L. (1954). A new silicon p-n junction photocell for converting solar radiation into electrical power. *J. Appl. Phys.* , VOL.25, NO.5, pp. 676-677.

Chen, S. G.; Chappel, S.; Diamant, Y. & Zaban, A. (2001). Preparation of Nb_2O_5 coated TiO_2 nanoporous electrodes and their application in dye-sensitized solar cells. *Chem. Mater.* , VOL.13, NO.12, pp. 4629-4634.

Chen, Z. G.; Chen, H. L.; Hu, H.; Yu, M. X.; Li, F. Y.; Zhang, Q.; Zhou, Z. G.; Yi, T. & Huang, C. H. (2008). Versatile synthesis strategy for carboxylic acid-functionalized upconverting nanophosphors as biological labels. *J. Am. Chem. Soc.* , VOL.130, NO.10, pp. 3023-3029.

Chen, Z. G.; Li, F. Y. & Huang, C. H. (2007a). Organic d-Π-a dyes for dye-sensitized solar cell. *Curr. Org. Chem.* , VOL.11, pp. 1241-1258.

Chen, Z. G.; Yang, H.; Li, X. H.; Li, F. Y.; Yi, T. & Huang, C. H. (2007b). Thermostable succinonitrile-based gel electrolyte for efficient, long-life dye-sensitized solar cells. *J. Mater. Chem.* , VOL.17, NO.16, pp. 1602-1607.

Chen, Z. G.; Zhang, L. S.; Sun, Y. G.; Hu, J. Q. & Wang, D. Y. (2009). 980-nm laser-driven photovoltaic cells based on rare-earth up-converting phosphors for biomedical applications. *Adv. Funct. Mater.* , VOL.19, NO.23, pp. 3815-3820.

Desilvestro, J.; Gratzel, M.; Kavan, L.; Moser, J. & Augustynski, J. (1985). Highly efficient sensitization of titanium-dioxide. *J. Am. Chem. Soc.* , VOL.107, NO.10, pp. 2988-2990.

Diamant, Y.; Chen, S. G.; Melamed, O. & Zaban, A. (2003). Core-shell nanoporous electrode for dye sensitized solar cells: the effect of the $SrTiO_3$ shell on the electronic properties of the TiO_2 core. *J. Phys. Chem. B* VOL.107, NO.9, pp. 1977-1981.

Diguna, L. J.; Shen, Q.; Kobayashi, J. & Toyoda, T. (2007). High efficiency of CdSe quantum-dot-sensitized TiO_2 inverse opal solar cells. *Appl. Phys. Lett.* , VOL.91, NO.2, pp.

Ellingson, R. J.; Beard, M. C.; Johnson, J. C.; Yu, P. R.; Micic, O. I.; Nozik, A. J.; Shabaev, A. & Efros, A. L. (2005). Highly efficient multiple exciton generation in colloidal PbSe and PbS quantum dots. *Nano Lett.* , VOL.5, NO.5, pp. 865-871.

Feng, X. J.; Shankar, K.; Varghese, O. K.; Paulose, M.; Latempa, T. J. & Grimes, C. A. (2008). Vertically aligned single crystal TiO_2 nanowire arrays grown directly on transparent conducting oxide coated glass: synthesis details and applications. *Nano Lett.* , VOL.8, NO.11, pp. 3781-3786.

Frederick, M. T. & Weiss, E. A. (2010). Relaxation of exciton confinement in CdSe quantum dots by modification with a conjugated dithiocarbamate ligand. *ACS Nano*, VOL.4, NO.6, pp. 3195-3200.

Garcia, C. G.; de Lima, J. F. & Iha, N. Y. M. (2000). Energy conversion: from the ligand field photochemistry to solar cells. *Coord. Chem. Rev.* , VOL.196, pp. 219-247.

Gimenez, S.; Mora-Sero, I.; Macor, L.; Guijarro, N.; Lana-Villarreal, T.; Gomez, R.; Diguna, L. J.; Shen, Q.; Toyoda, T. & Bisquert, J. (2009). Improving the performance of colloidal quantum-dot-sensitized solar cells. *Nanotechnology*, VOL.20, NO.29, pp. 295204.

Gonzalez-Pedro, V.; Xu, X. Q.; Mora-Sero, I. & Bisquert, J. (2010). Modeling high-efficiency quantum dot sensitized solar cells. *ACS Nano*, VOL.4, NO.10, pp. 5783-5790.

Gratzel, M. (2004). Conversion of sunlight to electric power by nanocrystalline dye-sensitized solar cells. *Journal of Photochemistry and Photobiology a-Chemistry*, VOL.164, NO.1-3, pp. 3-14.

Gratzel, M. (2001). Photoelectrochemical cells. *Nature*, VOL.414, NO.6861, pp. 338-344.

Gregg, B. A.; Pichot, F.; Ferrere, S. & Fields, C. L. (2001). Interfacial recombination processes in dye-sensitized solar cells and methods to passivate the interfaces. *J. Phys. Chem. B* VOL.105, NO.7, pp. 1422-1429.

Hagfeldt, A.; Boschloo, G.; Sun, L. C.; Kloo, L. & Pettersson, H. (2010). Dye-sensitized solar cells. *Chem. Rev.* , VOL.110, NO.11, pp. 6595-6663.

Han, J. B.; Fan, F. R.; Xu, C.; Lin, S. S.; Wei, M.; Duan, X. & Wang, Z. L. (2010). ZnO nanotube-based dye-sensitized solar cell and its application in self-powered devices. *Nanotechnology*, VOL.21, NO.40, pp. 405203.

Hauch, A. & Georg, A. (2001). Diffusion in the electrolyte and charge-transfer reaction at the platinum electrode in dye-sensitized solar cells. *Electrochim. Acta* VOL.46, NO.22, pp. 3457-3466.

Heer, S.; Kompe, K.; Gudel, H. U. & Haase, M. (2004). Highly efficient multicolour upconversion emission in transparent colloids of lanthanide-doped $NaYF_4$ nanocrystals. *Adv. Mater.* , VOL.16, NO.23-24, pp. 2102-2105.

Hodes, G. (2008). Comparison of dye- and semiconductor-sensitized porous nanocrystalline liquid junction solar cells. *J. Phys. Chem. C* VOL.112, NO.46, pp. 17778-17787.

Hore, S.; Palomares, E.; Smit, H.; Bakker, N. J.; Comte, P.; Liska, P.; Thampi, K. R.; Kroon, J. M.; Hinsch, A. & Durrant, J. R. (2005). Acid versus base peptization of mesoporous nanocrystalline TiO_2 films: functional studies in dye sensitized solar cellst. *J. Mater. Chem.* , VOL.15, NO.3, pp. 412-418.

Huang, Z.; Liu, X. H.; Li, K. X.; Li, D. M.; Luo, Y. H.; Li, H.; Song, W. B.; Chen, L. Q. & Meng, Q. B. (2007). Application of carbon materials as counter electrodes of dye-sensitized solar cells. *Electrochem. Commun.* , VOL.9, NO.4, pp. 596-598.

Hyun, B. R.; Zhong, Y. W.; Bartnik, A. C.; Sun, L. F.; Abruna, H. D.; Wise, F. W.; Goodreau, J. D.; Matthews, J. R.; Leslie, T. M. & Borrelli, N. F. (2008). Electron injection from colloidal PbS quantum dots into titanium dioxide nanoparticles. *ACS Nano*, VOL.2, NO.11, pp. 2206-2212.

Imoto, K.; Takahashi, K.; Yamaguchi, T.; Komura, T.; Nakamura, J. & Murata, K. (2003). High-performance carbon counter electrode for dye-sensitized solar cells. *Sol. Energy Mater. Sol. Cells* VOL.79, NO.4, pp. 459-469.

Jiang, Q. W.; Li, G. R. & Gao, X. P. (2009). Highly ordered TiN nanotube arrays as counter electrodes for dye-sensitized solar cells. *Chem. Commun.* , NO.44, pp. 6720-6722.

Jiang, Q. W.; Li, G. R.; Liu, S. & Gao, X. P. (2010). Surface-nitrided nickel with bifunctional structure as low-cost counter electrode for dye-sensitized solar cells. *J. Phys. Chem. C* VOL.114, NO.31, pp. 13397-13401.

Joshi, P.; Zhang, L. F.; Chen, Q. L.; Galipeau, D.; Fong, H. & Qiao, Q. Q. (2010). Electrospun carbon nanofibers as low-cost counter electrode for dye-sensitized solar cells. *ACS Appl. Mater. Interfaces* VOL.2, NO.12, pp. 3572-3577.

Jung, H. S.; Lee, J. K.; Nastasi, M.; Lee, S. W.; Kim, J. Y.; Park, J. S.; Hong, K. S. & Shin, H. (2005). Preparation of nanoporous MgO-Coated TiO_2 nanoparticles and their application to the electrode of dye-sensitized solar cells. *Langmuir*, VOL.21, NO.23, pp. 10332-10335.

Kaiser, I.; Ernst, K.; Fischer, C. H.; Konenkamp, R.; Rost, C.; Sieber, I. & Lux-Steiner, M. C. (2001). The eta-solar cell with $CuInS_2$: A photovoltaic cell concept using an extremely thin absorber (eta). *Sol. Energy Mater. Sol. Cells* VOL.67, NO.1-4, pp. 89-96.

Kamat, P. V. (2008). Quantum dot solar cells. Semiconductor nanocrystals as light harvesters. *J. Phys. Chem. C* VOL.112, NO.48, pp. 18737-18753.

Kang, T. S.; Smith, A. P.; Taylor, B. E. & Durstock, M. F. (2009). Fabrication of highly-ordered TiO_2 nanotube arrays and their use in dye-sensitized solar cells. *Nano Lett.* , VOL.9, NO.2, pp. 601-606.

Kavan, L.; Yum, J. H. & Gratzel, M. (2011). Optically transparent cathode for dye-sensitized solar cells based on graphene nanoplatelets. *ACS Nano*, VOL.5, NO.1, pp. 165-172.

Kay, A. & Gratzel, M. (1996). Low cost photovoltaic modules based on dye sensitized nanocrystalline titanium dioxide and carbon powder. *Sol. Energy Mater. Sol. Cells* VOL.44, NO.1, pp. 99-117.

Kay, A. & Gratzel, M. (2002). Dye-sensitized core-shell nanocrystals: Improved efficiency of mesoporous tin oxide electrodes coated with a thin layer of an insulating oxide. *Chem. Mater.* , VOL.14, NO.7, pp. 2930-2935.

Klimov, V. I. (2006). Mechanisms for photogeneration and recombination of multiexcitons in semiconductor nanocrystals: Implications for lasing and solar energy conversion. *J. Phys. Chem. B* VOL.110, NO.34, pp. 16827-16845.

Kron, G.; Egerter, T.; Werner, J. H. & Rau, U. (2003). Electronic transport in dye-sensitized nanoporous TiO_2 solar cells-comparison of electrolyte and solid-state devices. *J. Phys. Chem. B* VOL.107, NO.15, pp. 3556-3564.

Kumara, G. R. A.; Kaneko, S.; Okuya, M. & Tennakone, K. (2002). Fabrication of dye-sensitized solar cells using triethylamine hydrothiocyanate as a CuI crystal growth inhibitor. *Langmuir*, VOL.18, NO.26, pp. 10493-10495.

Law, M.; Greene, L. E.; Johnson, J. C.; Saykally, R. & Yang, P. D. (2005). Nanowire dye-sensitized solar cells. *Nat. Mater.* , VOL.4, NO.6, pp. 455-459.

Lee, H.; Leventis, H. C.; Moon, S. J.; Chen, P.; Ito, S.; Haque, S. A.; Torres, T.; Nuesch, F.; Geiger, T.; Zakeeruddin, S. M.; Gratzel, M. & Nazeeruddin, M. K. (2009a). PbS and US quantum dot-sensitized solid-state solar cells: "old concepts, new results". *Adv. Funct. Mater.* , VOL.19, NO.17, pp. 2735-2742.

Lee, H.; Wang, M. K.; Chen, P.; Gamelin, D. R.; Zakeeruddin, S. M.; Gratzel, M. & Nazeeruddin, M. K. (2009b). Efficient CdSe quantum dot-sensitized solar cells prepared by an improved successive ionic layer adsorption and reaction process. *Nano Lett.* , VOL.9, NO.12, pp. 4221-4227.

Lee, Y. L. & Lo, Y. S. (2009). Highly efficient quantum-dot-sensitized solar cell based on co-sensitization of CdS/CdSe. *Adv. Funct. Mater.* , VOL.19, NO.4, pp. 604-609.

Leschkies, K. S.; Jacobs, A. G.; Norris, D. J. & Aydil, E. S. (2009). Nanowire-quantum-dot solar cells and the influence of nanowire length on the charge collection efficiency. *Appl. Phys. Lett.* , VOL.95, NO.19, pp. 193103.

Levy-Clement, C.; Tena-Zaera, R.; Ryan, M. A.; Katty, A. & Hodes, G. (2005). CdSe-Sensitized p-CuSCN/nanowire n-ZnO heterojunctions. *Adv. Mater.* , VOL.17, NO.12, pp. 1512-1515.

Lin, S.-C.; Lee, Y.-L.; Chang, C.-H.; Shen, Y.-J. & Yang, Y.-M. (2007). Quantum-dot-sensitized solar cells: Assembly of CdS-quantum-dots coupling techniques of self-assembled monolayer and chemical bath deposition. *Appl. Phys. Lett.* , VOL.90, NO.14, pp. 143517.

Liu, B. & Aydil, E. S. (2009). Growth of oriented single-crystalline rutile TiO_2 nanorods on transparent conducting substrates for dye-sensitized solar cells. *J. Am. Chem. Soc.* , VOL.131, NO.11, pp. 3985-3990.

Liu, Y.-X.; Summers, M. A.; Scully, S. R. & McGehee, M. D. (2006). Resonance energy transfer from organic chromophores to fullerene molecules. *J. Appl. Phys.* , VOL.99, NO.9, pp. 093521.

Lu, S. & Madhukar, A. (2007). Nonradiative resonant excitation transfer from nanocrystal quantum dots to adjacent quantum channels. *Nano Lett.* , VOL.7, NO.11, pp. 3443-3451.

Macak, J. M.; Tsuchiya, H.; Ghicov, A. & Schmuki, P. (2005). Dye-sensitized anodic TiO_2 nanotubes. *Electrochem. Commun.* , VOL.7, NO.11, pp. 1133-1137.

Martinson, A. B. F.; Elam, J. W.; Hupp, J. T. & Pellin, M. J. (2007). ZnO nanotube based dye-sensitized solar cells. *Nano Lett.* , VOL.7, NO.8, pp. 2183-2187.

Matsumura, M.; Matsudaira, S.; Tsubomura, H.; Takata, M. & Yanagida, H. (1980). Dye sensitization and surface structures of semiconductor electrodes. *Ind. Eng. Chem. Prod. Res. Dev.* , VOL.19, NO.3, pp. 415-421.

Meng, Q. B.; Takahashi, K.; Zhang, X. T.; Sutanto, I.; Rao, T. N.; Sato, O.; Fujishima, A.; Watanabe, H.; Nakamori, T. & Uragami, M. (2003). Fabrication of an efficient solid-state dye-sensitized solar cell. *Langmuir*, VOL.19, NO.9, pp. 3572-3574.

Muniz, E. C.; Goes, M. S.; Silva, J. J.; Varela, J. A.; Joanni, E.; Parra, R. & Bueno, P. R. (2011). Synthesis and characterization of mesoporous TiO_2 nanostructured films prepared by a modified sol-gel method for application in dye solar cells. *Ceram. Int.* , VOL.37, NO.3, pp. 1017-1024.

Murakami, T. N.; Kijitori, Y.; Kawashima, N. & Miyasaka, T. (2004). Low temperature preparation of mesoporous TiO_2 films for efficient dye-sensitized photoelectrode by chemical vapor deposition combined with UV light irradiation. *Journal of Photochemistry and Photobiology a-Chemistry*, VOL.164, NO.1-3, pp. 187-191.

Murray, C. B.; Norris, D. J. & Bawendi, M. G. (1993). Synthesis and characterization of nearly monodisperse CdE (E = S, Se, Te) semiconductor nanocrystallites. *J. Am. Chem. Soc.* , VOL.115, NO.19, pp. 8706-8715.

Neale, N. R. & Frank, A. J. (2007). Size and shape control of nanocrystallites in mesoporous TiO_2 films. *J. Mater. Chem.* , VOL.17, NO.30, pp. 3216-3221.

Norris, D. J. & Bawendi, M. G. (1996). Measurement and assignment of the size-dependent optical spectrum in CdSe quantum dots. *Physical Review B*, VOL.53, NO.24, pp. 16338-16346.

O'Regan, B. & Schwartz, D. T. (1998). Large enhancement in photocurrent efficiency caused by UV illumination of the dye-sensitized heterojunction TiO_2/RuLL ' NCS/CuSCN: Initiation and potential mechanisms. *Chem. Mater.* , VOL.10, NO.6, pp. 1501-1509.

O'Regan, B.; Schwartz, D. T.; Zakeeruddin, S. M. & Gratzel, M. (2000). Electrodeposited nanocomposite n-p heterojunctions for solid-state dye-sensitized photovoltaics. *Adv. Mater.* , VOL.12, NO.17, pp. 1263-1267.

O'Regan, B.; Scully, S.; Mayer, A. C.; Palomares, E. & Durrant, J. (2005). The effect of Al_2O_3 barrier layers in TiO_2/Dye/CuSCN photovoltaic cells explored by recombination and DOS characterization using transient photovoltage measurements. *J. Phys. Chem. B* VOL.109, NO.10, pp. 4616-4623.

O'Regan, B. & Gratzel, M. (1991). A low-cost, high-efficiency solar-cell based on dye-sensitized colloidal TiO_2 films. *Nature*, VOL.353, NO.6346, pp. 737-740.

O'Regan, B. & Schwartz, D. T. (1995). Efficient photo-hole injection from adsorbed cyanine dyes into electrodeposited copper(I) thiocyanate thin-films. *Chem. Mater.* , VOL.7, NO.7, pp. 1349-1354.

Overbeek, J. T. G. (1982). Monodisperse colloidal systems, fascinating and useful. *Adv. Colloid Interface Sci.* , VOL.15, NO.3-4, pp. 251-277.

Park, N. G.; van de Lagemaat, J. & Frank, A. J. (2000). Comparison of dye-sensitized rutile-and anatase-based TiO_2 solar cells. *J. Phys. Chem. B* VOL.104, NO.38, pp. 8989-8994.

Peng, Z. A. & Peng, X. G. (2002). Nearly monodisperse and shape-controlled CdSe nanocrystals via alternative routes: Nucleation and growth. *J. Am. Chem. Soc.* , VOL.124, NO.13, pp. 3343-3353.

Ramasamy, E.; Lee, W. J.; Lee, D. Y. & Song, J. S. (2007). Nanocarbon counterelectrode for dye sensitized solar cells. *Appl. Phys. Lett.* , VOL.90, NO.17, pp.

Robel, I.; Kuno, M. & Kamat, P. V. (2007). Size-dependent electron injection from excited CdSe quantum dots into TiO_2 nanoparticles. *J. Am. Chem. Soc.* , VOL.129, NO.14, pp. 4136-4137.

Robel, I.; Subramanian, V.; Kuno, M. & Kamat, P. V. (2006). Quantum dot solar cells. Harvesting light energy with CdSe nanocrystals molecularly linked to mesoscopic TiO_2 films. *J. Am. Chem. Soc.* , VOL.128, NO.7, pp. 2385-2393.

Ross, R. T. & Nozik, A. J. (1982). Efficiency of hot-carrier solar energy converters. *J. Appl. Phys.* , VOL.53, NO.5, pp. 3813-3818.

Roy-Mayhew, J. D.; Bozym, D. J.; Punckt, C. & Aksay, I. A. (2010). Functionalized graphene as a catalytic counter electrode in dye-sensitized solar cells. *ACS Nano*, VOL.4, NO.10, pp. 6203-6211.

Roy, P.; Kim, D.; Paramasivam, I. & Schmuki, P. (2009). Improved efficiency of TiO_2 nanotubes in dye sensitized solar cells by decoration with TiO_2 nanoparticles. *Electrochem. Commun.* , VOL.11, NO.5, pp. 1001-1004.

Ruhle, S.; Shalom, M. & Zaban, A. (2010). Quantum-dot-sensitized solar cells. *ChemPhysChem* VOL.11, NO.11, pp. 2290-2304.

Sayer, R. A.; Hodson, S. L. & Fisher, T. S. (2010). Improved efficiency of dye-sensitized solar cells using a vertically aligned carbon nanotube counter electrode. *Journal of Solar Energy Engineering-Transactions of the Asme*, VOL.132, NO.2, pp. 021007.

Schaller, R. D.; Sykora, M.; Pietryga, J. M. & Klimov, V. I. (2006). Seven excitons at a cost of one: Redefining the limits for conversion efficiency of photons into charge carriers. *Nano Lett.* , VOL.6, pp. 424-429.

Seo, S. H.; Kim, S. Y.; Koo, B. K.; Cha, S. I. & Lee, D. Y. (2010). Influence of electrolyte composition on the photovoltaic performance and stability of dye-sensitized solar cells with multiwalled carbon nanotube catalysts. *Langmuir*, VOL.26, NO.12, pp. 10341-10346.

Shalav, A.; Richards, B. S.; Trupke, T.; Kramer, K. W. & Gudel, H. U. (2005). Application of $NaYF_4:Er^{3+}$ up-converting phosphors for enhanced near-infrared silicon solar cell response. *Appl. Phys. Lett.* , VOL.86, NO.1, pp. 013505.

Shankar, K.; Feng, X. & Grimes, C. A. (2009). Enhanced harvesting of red photons in nanowire solar cells: Evidence of resonance energy transfer. *ACS Nano*, VOL.3, NO.4, pp. 788-794.

Shen, Y.; Bao, J.; Dai, N.; Wu, J.; Gu, F.; Tao, J. C. & Zhang, J. C. (2009). Speedy photoelectric exchange of CdSe quantum dots/mesoporous titania composite system. *Appl. Surf. Sci.* , VOL.255, NO.6, pp. 3908-3911.

Shi, C.; Zhu, A. M.; Yang, X. F. & Au, C. T. (2004). On the catalytic nature of VN, Mo_2N, and W_2N nitrides for NO reduction with hydrogen. *Applied Catalysis a-General*, VOL.276, NO.1-2, pp. 223-230.

Smestad, G. P.; Spiekermann, S.; Kowalik, J.; Grant, C. D.; Schwartzberg, A. M.; Zhang, J.; Tolbert, L. M. & Moons, E. (2003). A technique to compare polythiophene solid-state dye sensitized TiO$_2$ solar cells to liquid junction devices. *Sol. Energy Mater. Sol. Cells* VOL.76, NO.1, pp. 85-105.

Sung, Y. M. & Kim, H. J. (2007). Sputter deposition and surface treatment of TiO$_2$ films for dye-sensitized solar cells using reactive RF plasma. *Thin Solid Films* VOL.515, NO.12, pp. 4996-4999.

Suzuki, K.; Yamaguchi, M.; Kumagai, M. & Yanagida, S. (2003). Application of carbon nanotubes to counter electrodes of dye-sensitized solar cells. *Chem. Lett.* , VOL.32, NO.1, pp. 28-29.

Talapin, D. V. & Murray, C. B. (2005). PbSe nanocrystal solids for n- and p-channel thin film field-effect transistors. *Science*, VOL.310, NO.5745, pp. 86-89.

Talapin, D. V.; Rogach, A. L.; Shevchenko, E. V.; Kornowski, A.; Haase, M. & Weller, H. (2002). Dynamic distribution of growth rates within the ensembles of colloidal II-VI and III-V semiconductor nanocrystals as a factor governing their photoluminescence efficiency. *J. Am. Chem. Soc.* , VOL.124, NO.20, pp. 5782-5790.

Tang, Y. W.; Luo, L. J.; Chen, Z. G.; Jiang, Y.; Li, B. H.; Jia, Z. Y. & Xu, L. (2007). Electrodeposition of ZnO nanotube arrays on TCO glass substrates. *Electrochem. Commun.* , VOL.9, NO.2, pp. 289-292.

Tennakone, K.; Kumara, G.; Kottegoda, I. R. M.; Wijayantha, K. G. U. & Perera, V. P. S. (1998). A solid-state photovoltaic cell sensitized with a ruthenium bipyridyl complex. *Journal of Physics D-Applied Physics*, VOL.31, NO.12, pp. 1492-1496.

Tennakone, K.; Kumara, G.; Kumarasinghe, A. R.; Wijayantha, K. G. U. & Sirimanne, P. M. (1995). A dye-sensitized nano-porous solid-state photovoltaic cell. *Semicond. Sci. Technol.* , VOL.10, NO.12, pp. 1689-1693.

Terauchi, S.; Koshizaki, N. & Umehara, H. (1995). Fabrication of Au nanoparticles by radio-frequency magnetron sputtering. *Nanostruct. Mater.* , VOL.5, NO.1, pp. 71-78.

Tributsch, H. (1972). Reaction of excited chlorophyll molecules at electrodes and in photosynthesis. *Photochem. Photobiol.* , VOL.16, NO.4, pp. 261-269.

Tributsch, H. (2004). Dye sensitization solar cells: a critical assessment of the learning curve. *Coord. Chem. Rev.* , VOL.248, NO.13-14, pp. 1511-1530.

Tsubomura, H.; Matsumura, M.; Nomura, Y. & Amamiya, T. (1976). Dye sensitised zinc oxide: aqueous electrolyte: platinum photocell. *Nature*, VOL.261, NO.5559, pp. 402-403.

Vogel, R.; Hoyer, P. & Weller, H. (1994). Quantum-sized PbS, CdS, Ag$_2$S, Sb$_2$S$_3$, and Bi$_2$S$_3$ particles as sensitizers for various nanoporous wide-bandgap semiconductors. *J. Phys. Chem.* , VOL.98, NO.12, pp. 3183-3188.

Wang, G. Q.; Xing, W. & Zhuo, S. P. (2009a). Application of mesoporous carbon to counter electrode for dye-sensitized solar cells. *J. Power Sources* VOL.194, NO.1, pp. 568-573.

Wang, M. K.; Anghel, A. M.; Marsan, B.; Ha, N. L. C.; Pootrakulchote, N.; Zakeeruddin, S. M. & Gratzel, M. (2009b). CoS supersedes Pt as efficient electrocatalyst for triiodide reduction in dye-sensitized solar cells. *J. Am. Chem. Soc.* , VOL.131, NO.44, pp. 15976-15977.

Wang, P.; Dai, Q.; Zakeeruddin, S. M.; Forsyth, M.; MacFarlane, D. R. & Gratzel, M. (2004). Ambient temperature plastic crystal electrolyte for efficient, all-solid-state dye-sensitized solar CeN. *J. Am. Chem. Soc.* , VOL.126, NO.42, pp. 13590-13591.

Wang, P.; Zakeeruddin, S. M.; Comte, P.; Exnar, I. & Gratzel, M. (2003a). Gelation of ionic liquid-based electrolytes with silica nanoparticles for quasi-solid-state dye-sensitized solar cells. *J. Am. Chem. Soc.* , VOL.125, NO.5, pp. 1166-1167.

Wang, P.; Zakeeruddin, S. M.; Moser, J. E.; Nazeeruddin, M. K.; Sekiguchi, T. & Gratzel, M. (2003b). A stable quasi-solid-state dye-sensitized solar cell with an amphiphilic ruthenium sensitizer and polymer gel electrolyte. *Nat. Mater.* , VOL.2, NO.6, pp. 402-407.

Wang, Z.-S.; Yanagida, M.; Sayama, K. & Sugihara, H. (2006). Electronic-insulating coating of $CaCO_3$ on TiO_2 electrode in dye-sensitized solar cells: Improvement of electron lifetime and efficiency. *Chem. Mater.* , VOL.18, NO.12, pp. 2912-2916.

Wang, Z. S.; Huang, C. H.; Huang, Y. Y.; Hou, Y. J.; Xie, P. H.; Zhang, B. W. & Cheng, H. M. (2001). A highly efficient solar cell made from a dye-modified ZnO-covered TiO_2 nanoporous electrode. *Chem. Mater.* , VOL.13, NO.2, pp. 678-682.

Wroblowa, H. S. & Saunders, A. (1973). Flow-through electrodes: II. The I_3^-/I^- redox couple. *J. Electroanal. Chem. Interfacial Electrochem.* , VOL.42, NO.3, pp. 329-346.

Wu, M.; Lin, X.; Hagfeldt, A. & Ma, T. (2011a). Low-cost molybdenum carbide and tungsten carbide counter electrodes for dye-sensitized solar cells. *Angew. Chem. Int. Ed.*, VOL.50, NO.15, pp. 3520-3524.

Wu, M. X.; Lin, X. A.; Hagfeldt, A. & Ma, T. L. (2011b). A novel catalyst of WO_2 nanorod for the counter electrode of dye-sensitized solar cells. *Chem. Commun.* , VOL.47, NO.15, pp. 4535-4537.

Wu, S. J.; Han, H. W.; Tai, Q. D.; Zhang, J.; Chen, B. L.; Xu, S.; Zhou, C. H.; Yang, Y.; Hu, H. & Zhao, X. Z. (2008). Improvement in dye-sensitized solar cells with a ZnO-coated TiO_2 electrode by rf magnetron sputtering. *Appl. Phys. Lett.* , VOL.92, NO.12, pp. 122106.

Xia, J. B.; Li, F. Y.; Yang, H.; Li, X. H. & Huang, C. H. (2007). A novel quasi-solid-state dye-sensitized solar cell based on monolayer capped nanoparticles framework materials. *Journal of Materials Science*, VOL.42, NO.15, pp. 6412-6416.

Yang, H.; Cheng, Y. F.; Li, F. Y.; Zhou, Z. G.; Yi, T.; Huang, C. H. & Jia, N. Q. (2005). Quasi-solid-state dye-sensitized solar cells based on mesoporous silica SBA-15 framework materials. *Chin. Phys. Lett.* , VOL.22, NO.8, pp. 2116-2118.

Yoon, C. H.; Vittal, R.; Lee, J.; Chae, W. S. & Kim, K. J. (2008). Enhanced performance of a dye-sensitized solar cell with an electrodeposited-platinum counter electrode. *Electrochim. Acta* VOL.53, NO.6, pp. 2890-2896.

Zaban, A.; Aruna, S. T.; Tirosh, S.; Gregg, B. A. & Mastai, Y. (2000). The effect of the preparation condition of TiO_2 colloids on their surface structures. *J. Phys. Chem. B* VOL.104, NO.17, pp. 4130-4133.

Zhang, Q. F. & Cao, G. Z. (2011). Nanostructured photoelectrodes for dye-sensitized solar cells. *Nano Today*, VOL.6, NO.1, pp. 91-109.

Zhu, K.; Neale, N. R.; Miedaner, A. & Frank, A. J. (2007). Enhanced charge-collection efficiencies and light scattering in dye-sensitized solar cells using oriented TiO_2 nanotubes arrays. *Nano Lett.* , VOL.7, NO.1, pp. 69-74.

Fabrication, Doping and Characterization of Polyaniline and Metal Oxides: Dye Sensitized Solar Cells

Sadia Ameen[1], M. Shaheer Akhtar[2],
Young Soon Kim[1] and Hyung-Shik Shin[1]
*[1]Energy Materials & Surface Science Laboratory, Solar Energy Research Center,
School of Chemical Engineering, Chonbuk National University, Jeonju,
[2]New & Renewable Energy Material Development Center (NewREC),
Chonbuk National University, Jeonbuk,
Republic of Korea*

1. Introduction

The photoelectrochemical devices like dye sensitized solar cell (DSSCs) are the promising photovoltaic device for the utilization of solar into electricity energy by converting solar radiation through the generation of photogenerated carriers. DSSCs possess the benign properties of low cost, high conversion efficiency and ease of fabrication (Gratzel, 2005, 2004 & Frank, et al., 2004). Several significant advantages are associated to DSSCs such as the semiconductor-electrolyte interface (SEI) is easy to manufacture and it is cost effective for production, non sensitive to the defects, the two functions of light harvesting and charge-carrier transport are remain separated and favours the direct energy transfer from photons to chemical energy. Although, DSSCs are the promising photovoltaic technology for achieving reasonably high conversion efficiency but the improvements are still demanded to develop a high potential technology.

A typical DSSC is comprised of a dye-coated mesoporous nanocrystalline metal oxide semiconductor, machinated between two the conductive transparent electrodes as shown in Fig. 1. A liquid iodide/tri-iodide redox couple as an electrolyte is introduced to fill the pores of the film and to improve the contact between the nanoparticles (Gratzel, 2000). Upon photo excitation of the dye, the electrons are injected into the conduction band of the nanocrystalline metal oxide semiconductor and the original state of the dye is restored by the electron donation from the hole conductor. The regeneration of the sensitizer by the hole conductor intercepts the recapture of the conduction band electron by the oxidized dye and the hole conductor is regenerated at the counter-electrode. The circuit is completed via electron migration through the external load.

Nanocrystalline metal oxide semiconductor like TiO_2, ZnO and SnO_2 etc have been accepted as the effective photoanode materials for DSSCs due to their good optical and electronic properties. Till date, DSSCs constructed from TiO_2 nanocrystalline metal oxide electrodes has presented the highest solar to electricity conversion efficiency of 11.4%. These nanocrystalline metal oxide semiconductors possess high surface to volume ratio required
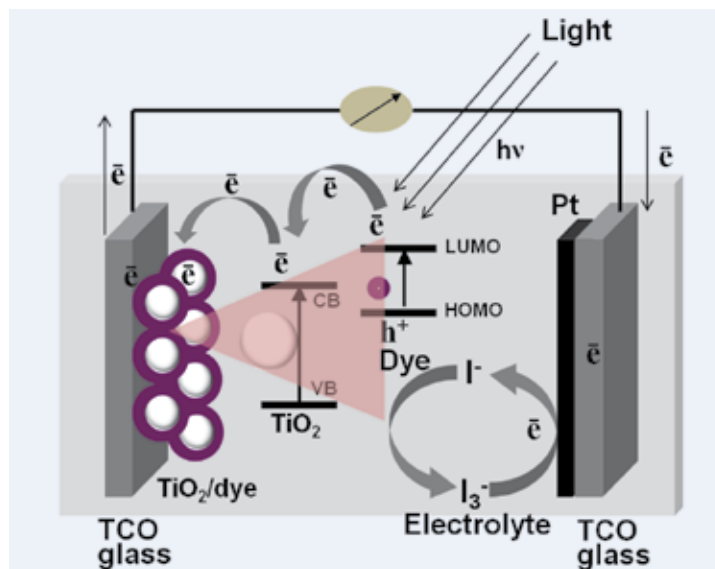
Fig. 1. Mechanistic diagram of dye sensitized solar cell under light illumination.

for the high absorption of dye molecules for the improved light harvesting efficiency but the challenges like enhancement in the electron transport rate, reduction of recombination rate and the improvement in the energy conversion efficiency are still associated with metal oxide semiconductor based DSSCs. It has been reported that the photoelectrodes made of metal oxides nanostructures like nanoparticles, nanorods, nanowires and nanotubes improve the photovoltaic properties of DSSCs such as J_{SC}, V_{OC}, FF and conversion efficiency by the effective electron transfer during the performance of DSSCs. The conducting polymers are the semiconducting polymers which exhibit good electrical properties similar to metals and possess unique properties like light weight, resistance to corrosion, flexibility and low cost. The nanostructures of conducting polymers are excessively exploited in the electronic devices due to the large surface area of the nanomaterials and their unique electronic properties (Huang et al., 2006, Zhnag et al., 2006, Wan, 2008, 2009 & Li et al., 2009). These perspectives have prompted the researchers for the rapid development of conducting polymers and the nanocrystalline metal oxide semiconductors for improving the processability, functionality and the conversion efficiency of DSSCs.

In this chapter, we have briefly surveyed the conducting polymers, its doping and the different morphologies of nanocrystalline metal oxide semiconductors for the effective processing, functionality and the fabrication of DSSCs. The chapter focuses the recent developments in the heterostructures diodes, Ohmic devices and DSSCs fabricated with polyaniline (PANI) and the nanostructured metal oxides. The morphology, structure and physiochemical properties of TiO_2 and ZnO nanostructure semiconductors have been reviewed as photoelectrode for the application of DSSCs. It has been reviewed that the performances of DSSCs are considerably affected by the preparation, morphology and the electrical properties of conducting polymers and metal oxide semiconductors. TiO_2 and ZnO nanostructures based photoelectrodes have shown comparable photovoltaic performance compared to the conventional TiO_2 nanoparticles based DSSCs. On the other hand, the conducting polymers as a hole transport materials are found as the potential candidates for

replacing the liquid electrolyte in DSSCs and the dopants have been discussed for enhancing the conducting properties of a particular polymer i.e. PANI.

2. Aspects of conducting polymers

The polymers are insulators due to the covalent bonded atoms in the polymer chain and thus, there is no scope for the delocalization of the valence electrons and consequently neither charge carriers nor the path for their movement are available (Stejskal et al., 2002). However, the important classes of polymers called as conducting polymers are semiconductors (Friend et al., 1999) and their band gaps could be tuned by alternating the chemical nature of either the polymer backbone or the side groups present in the polymeric chain. The overlapping of the molecular orbital for the formation of the delocalized molecular wave functions and secondly the partially filled molecular orbital for a free movement of electrons throughout the polymeric structure are the basic requirements for the polymers to become conducting in nature. These conducting polymers exhibit the unusual electronic properties such as electrical conductivity, low energy optical transitions, low ionization potential and high electron affinity (Park et al., 2010) due to the presence of extended π-conjugated systems along the polymeric chain (Gerard et al., 2002). The electrical properties of the conducting polymers could be easily tuned from insulating to metallic range by the reversible chemical, electrochemical and physical properties controlled by a doping/de-doping procedure. The electrical properties are changed by the partial oxidation or reduction of the polymer chain during the doping procedure. The conducting polymers possess the appended advantage of tailor-made property for accomplishing the requirements of the particular application through the modifications in the polymer structure. It is reported that the nanostructures of conducting polymer not only retain these unique characteristics, but also exhibit the properties like large surface area, size, and quantum effect etc which are important for designing and making the novel photovoltaic devices (Xia et al., 2010). Out of several conducting polymers, polyaniline (PANI) is the centre of scientific interest and has been considered as one of the most potential conducting polymers. The interest in PANI could possibly be linked to the numerous applications for various electrochemical, electro rheological and in the electronic fields such as batteries, sensors, controlling systems and organic displays (Smith, 1998, Wessling, 2001, Cho et al., 2002 & Choi et al. 2001) because of its facile synthetic process, good environmental stability, easy conductivity control and cheap production in large quantities. The high yield of PANI demands several essential conditions such as highly pured monomers, chemicals and solvents for obtaining the high quality polymer, the strict control on the polymerization conditions, inert and dry environment for the polymerization since the small variation in the polymerization conditions might alter the nature of the product, and as PANI might undergo isomerization reaction under light and heat therefore, the synthesized PANI products should be kept in a dark, cool and dry place (Ameen, et al., 2010)

3. General approaches for the synthesis of PANI

3.1 Interfacial polymerization

In a typical reaction (Huang, et al., 2003, Virji, et al., 2004, King, et al., 2005 & Huang et al., 2004) aniline monomer is dissolved into the organic solvents which have either low or high density than water like hexane, benzene, toluene, carbon tetrachloride, chloroform etc. A

separate aqueous solution of ammonium peroxydisulphate (APS) as an oxidant is prepared with the acids such as HCl, sulfuric acid, CSA, toluene sulfonic acid etc. The two solutions are then gently transferred to a glass vial for the generating the interface between the two layers. As the reaction proceeds, the green colored PANI is formed at the interface and gradually migrates into the aqueous phase and slowly the entire aqueous phase get filled homogeneously with dark-green PANI. The aqueous phase is collected through filtration after 24 h. The non-conducting PANI could be obtained by dialyzing the synthesized PANI with ammonia solution

3.2 Rapid mixing of reactants

This is the simplest method for synthesizing PANI and in place of conventionally slow addition of the aqueous APS solution, the aniline monomer is mixed rapidly with APS solution. Here, the initiator molecules are consumed rapidly after the initialization of the polymerization reaction due to the even distribution of aniline monomer and APS molecules in the solution.

3.3 Sonochemical synthesis

Jing et al (Jing, et al., 2006, 2007) has reported the synthesis of PANI similar to the synthesis procedure of conventional PANI. The acidic APS solution is added dropwise to an acidic aniline solution, and subjected to the ultrasonic irradiation which results to the high yield of PANI. It has been found that the excessive addition of aniline monomer or APS could contribute to the continuous formation of the primary PANI products or could lead the agglomeration of PANI. Unlike conventional procedure where irregular morphology of PANI is obtained, the sonochemical synthesis strictly prevents the further growth and agglomeration and thus, generates uniform morphology of PANI.

3.4 Electrophoretic synthesis

The first step of a reaction requires a preparation of conducting PANI through the chemical procedure using APS as oxidant. In the second step, a stock solution of PANI (1 mg/ml) is prepared in the formic acid and the colloidal suspension is prepared by adding 100 ml of the stock solution into acetonitrile for the preparation of an electrolyte. In the colloidal suspension, PANI dissociate into ions due to high dielectric medium which is offered by acetonitrile and thus, results to the formation of the positively charged PANI. The last step involves the electrophoretic film deposition where under the influence of applied voltage for a required time duration, positively charged colloid spheres of PANI in acidic colloidal suspension starts moving towards the negatively biased fluorinated tin oxide glass (FTO) electrode. This stepwise growth synthesis produces the uniform nanostructures of PANI on the surfaces of the FTO glass substrates.

3.5 Plasma polymerization

The plasma polymerization, as shown in Fig. 2 requires four parts (1) a reactor chamber quartz tube (2 cm), (2) Cu coil (4 in.), (3) plasma system (R.F. generator: 0-600 W, matching network frequency of 13.56 MHz) and (4) mechanical vacuum pump (speed 600 1/min). The glow discharges are introduced through RF amplifier with a resistive coupling mechanism at 13.5 MHz and power of 120 W. These discharges are set without carrier gas or any other additional chemical elements to prevent the contamination. The cleaned FTO glass

substrates are placed just below the RF coil, placed inside the quartz tube. Initially, the chamber is evacuated to a base pressure of 10^{-3} Torr through a rotator vacuum pump. After attaining the base pressure, aniline monomer is injected, using a hypodermic syringe and the reaction is promoted by the collisions of the aniline monomer molecules with the ions/particles present in the plasma.
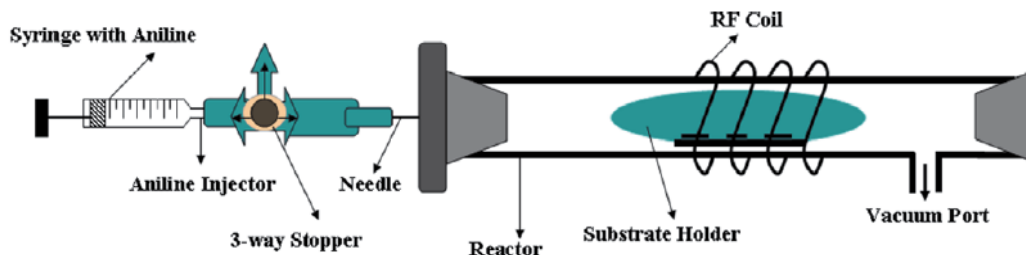
Fig. 2. Reactor setup for plasma synthesis of PANI. Reprinted with permission from [Ameen S. et al 2009], Superlatt. Microstruc. 46 (2009) 745. © 2009, Elsevier Ltd.

4. Concept of doping in PANI

Doping is the unique, central, underlying and unifying concept, which distinguishes PANI as conducting polymer from other insulating polymers. The controlled addition of known chemical species results in the dramatic changes in the electronic, electrical, magnetic, optical and structural properties of PANI. The doping procedures of inorganic semiconductors and for conducting polymers including PANI are fundamentally different from each other. In PANI, the dopant concentrations are exceptionally high compared to commonly doped inorganic semiconductors (typically in parts per million ranges) and the doping of PANI involves random dispersion or aggregation of dopants in molar concentrations in the disordered structure of entangled chains and fibrils. However, for inorganic semiconductors, the doping generates either holes in the valence band or electrons in the conduction band. The doping of PANI generates high conductivity primarily by increasing the carrier concentrations and leads to the conjugational defect like solitons, polarons, bipolarons in the polymer chain. Doping is a reversible produce which could be carried out chemically or electrochemically with the oxidation or reduction by accepting or donating the electrons respectively and thus, results to the positive or negative charges. Ameen et al have used various acids and binary mixtures as dopants to improve the electrical conductivity of PANI.

4.1 Doping with sulfamic acid

Sulfamic acid is one of the promising dopant which displays the properties of handling ease, solubility, and low corrosiveness. It is a dry, non-volatile stable solid acid, which is moderately soluble in water at room temperature. Wadia et al prepared the thin film of sulfamic acid doped PANI as electrochemical sensor for the determination of nitrite (Dhaoui, et al., 2007, 2008). Ameen et al reported the electrical conductivity of PANI nanostructures in the range of 1.1×10^{-4} – 4.50×10^{-3} ohm^{-1}cm^{-1}, doped with different wt% of sulfamic acid (Ameen, et al., 2007). Moreover, PANI nanofibers doped with sulfamic acid thin film was applied as counter electrodes for the fabrication of DSSCs and obtained the conductivity of 2.06×10^{-4} ohm^{-1}cm^{-1} by Ameen et al (Ameen, et al., 2010).

4.2 Doping with sodium thiosulphate

Sodium thiosulphate is an odorless translucent crystals or white crystalline powder which is soluble in water and exhibit the stability. It is incompatible with strong acid and is not hazardous. Ameen et al reported the electrical conductivity of PANI nanostructures in the range of 8.55×10^{-9} – 3.67×10^{-7} ohm^{-1}cm^{-1} after doping with sodium thiosulphate (Ameen, et al., 2009).

4.3 Doping with samarium (III) chloride

Samarium (III) chloride is a light yellow colored strong Lewis acid. This dopant is non hazardous and stable in nature and is reported to increase the conductivity of PANI nanostructure from 3.70×10^{-11} to1.30×10^{-9} ohm^{-1}cm^{-1} (Ameen, et al., 2009).

4.4 Doping with praseodymium (III) chloride

Praseodymium (III) Chloride is a green colored powder which does not show thermal decomposition and is stable in nature. It is an excellent water-soluble crystalline strong Lewis acid and after doping is reported to show the conductivity of PANI nanostructures in the range 1.87×10^{-11} – 2.22×10^{-10}ohm^{-1}cm^{-1} (Ameen, et al., 2008).

4.5 Doping with binary dopant: ZrO_2/AgI & ZrO_2/PbI$_2$

In this binary dopant mixture ZrO_2 is a luminescent material which usually makes no contribution in the conductivity of PANI. On the other hand, AgI is a non luminescent material which enhances the conductivity of PANI. The binary effects of these two materials have improved the optical and the electrical conductivity of PANI nanostructures in the range of 9.28×10^{-10} – 3.763×10^{-6} ohm^{-1}cm^{-1}(Ameen, et al., 2007). Shaoxu et al reported the synthesis, characterization and the thermal analysis of PANI-ZrO_2 nanocomposites (Wang, et al., 2006). The increased ZrO_2 concentration in the binary dopant mixture exhibits a high PL emission intensity which improves optoelectronic properties of PANI. Ameen et al reported the effect of ZrO_2/PbI$_2$ doping on the electrical properties of PANI and the conductivity improves from 2.70×10^{-13} to 8.81×10^{-4} ohm^{-1}cm^{-1}(Ameen, et al., 2009).

5. Applications of PANI in heterostructure devices

5.1 Electrophoretic deposition of PANI for heterostructure devices
5.1.1 Electrophoretically deposited PANI/ZnO heterostructure diodes

The fabrication of inorganic/organic heterostructure diodes is reported by the electrophoretic process for depositing organic materials (PANI, p-type) film on inorganic n-type ZnO NPs thin film substrate with top Pt thin layer contact by Ameen et al (Ameen, et al., 2009). The pristine ZnO film is composed of well crystalline ZnO nanoparticles of size ~50-70 nm, shown in Fig. 3 (a). The penetration of the PANI molecules into the crystalline ZnO NPs thin film upon electrophoretic deposition display the accumulation of ZnO NPs and thus, the size of ZnO nanoparticles get increased to ~90 nm (Fig. 3 (b)). This assemblage confirms the substantive interaction and incorporation of electrophoretic deposited PANI into the crystalline ZnO nanoparticles thin film substrates.

The FTIR studies (Fig. 4 (I)) shows the considerable shifting of the peaks might due to the bonding between the hydroxyl groups and the imine groups of the PANI molecules. Noticeably, the UV-visible spectra of PANI/ZnO thin film (Fig. 4 (II)) shows that the peak (a) retains its position, considerable large blue shift for peak (b) is noticed and small red shift
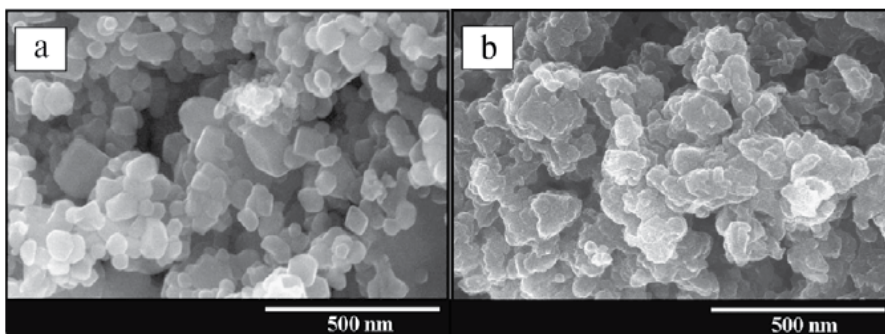
Fig. 3. Surface FE-SEM images of (a) synthesized ZnO nanoparticles (b) electrophoretically deposited PANI/ZnO thin film. Reprinted with permission from [Ameen S. et al, 2009], Superlatt. Microstruc. 46 (2009) 872. © 2009, Elsevier Ltd.
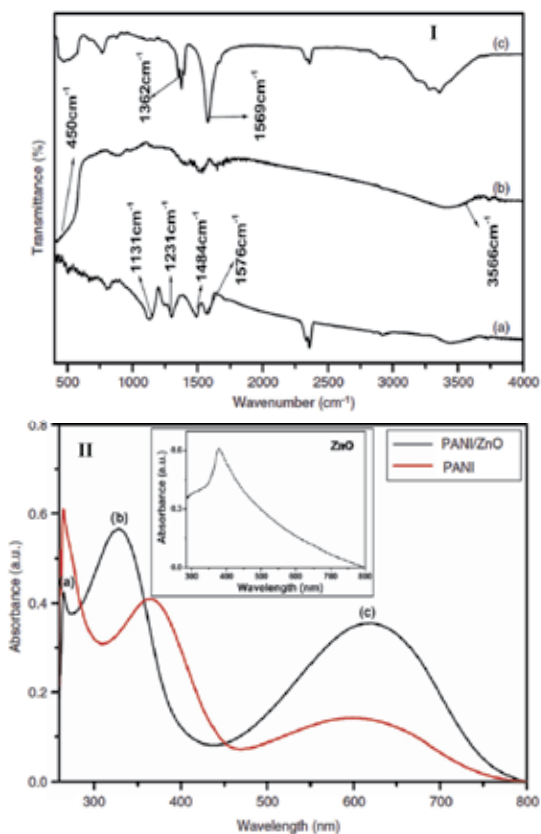
Fig. 4. (I): Typical FTIR spectrum of (a) pristine PANI (b) ZnO nanoparticles and (c) electrophoretically deposited PANI/ZnO thin film. (II): UV-Vis spectra of pristine PANI and electrophoretically deposited PANI/ZnO thin film. Inset shows the UV-Vis spectrum of ZnO nanoparticles. Reprinted with permission from [Ameen S., 2009], Superlatt. Microstruc. 46 (2009) 872. © 2009, Elsevier Ltd.

in peak (c) are noticed after the deposition of PANI and thus, ascribed to the selective interactions between ZnO and the quinoid ring of ES which facilitates the charge transfer from quinoid unit of ES to ZnO via highly reactive imine group. This interaction between ZnO and PANI contributes to the decrease in the degree of orbital overlap between the π electrons of the phenyl rings with the lone pair of the nitrogen atom in the PANI molecules and found to form a strong hydrogen bonding. Consequently, the extent of conjugation of PANI decreases, thus resulting in the increased intensity of the peak in PANI/ZnO thin film substrate and conclusively, the absorption of PANI/ZnO thin film increases over the whole range of visible light.

The I-V characteristics exhibit almost the symmetrical behavior both in the reverse and the forward bias and the current increases linearly with the increased applied voltage. The ohmic behavior is due to the formation of ohmic contacts at the interfaces of PANI and ZnO layers. Additionally, the presence of PANI minimizes the width of the depletion layer at the interface of ZnO nanoparticles and thus contributes to the typical ohmic system. The PANI/ZnO heterostructure reveals that the forward bias current increases by a factor two with an increase in the applied voltage. It is attributed that the formation of polarons and bipolarons in PANI increases rapidly and ultimately, contributes to the higher current in PANI at the high applied voltage.   A schematic diagram and I-V characteristics of PANI/ZnO p-n heterostructure diode is shown in Fig. 5 (a).
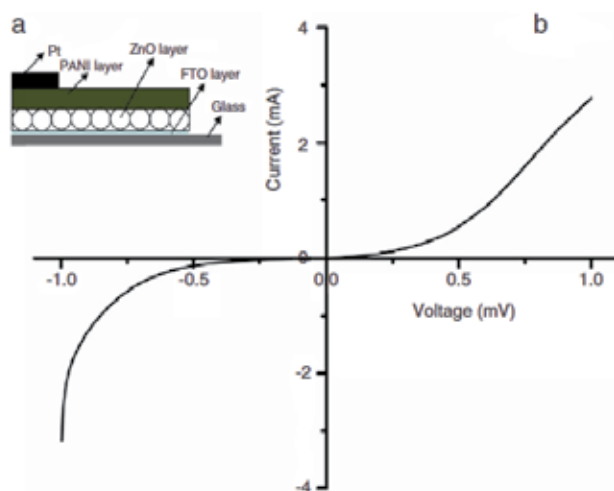
Fig. 5. (a) A schematic representation and (b) I-V characteristics of p-n heterostructure diode of Pt/PANI/ZnO. Reprinted with permission from [Ameen S., 2009], Superlatt. Microstruc. 46 (2009) 872. © 2009, Elsevier Ltd.

Current-voltage (I-V) measurements of PANI/ZnO heterostructure was carried out at 298 K with an applied voltage ranges from -1 V to +1 V. The obtained I-V characteristics exhibit weak rectifying with the non-linear nature of Pt/PANI/ZnO heterostructure diode where Pt thin layer might form a Schottky contact with PANI/ZnO layer as shown in Fig. 5 (b). The Pt layer on PANI/ZnO heterostructure might have originated a barrier between the interfaces of PANI/ZnO layer and Pt layer, and is responsible for the non-linear nature of I-V characteristics. The Pt/PANI/ZnO heterostructure diode displays the rectification ratio (I_f/I_r) of ~4.2 which is obtained from the forward (I_f) and reverse (I_r) current at 0.5 V. This

low I_f/I_r value indicates that the PANI/ZnO heterostructure exhibits a weak rectifying nature and attains low turn-on voltage of ~0.15 V and delivers reasonably high current of ~0.08 mA with broader breakdown voltage (~0.52 V) with very high leakage current of ~0.6 mA.

5.1.2 Electrophoretically deposited PANI/TiO₂ heterostructure diodes

PANI has been electrophoretically deposited (EPD) on the surface of TiO_2 nanoparticulate thin film for the fabrication of heterostructure devices by Ameen et al (Ameen, et al., 2011). The enhancements in the electron transport and current density have been explained in terms of the increased charge carriers mobility with improved optical absorption by the heterostucture diodes. Fig. 6 (a) shows the morphology of well crystalline TiO_2 nanoparticles thin film of size ~20–25 nm. However, upon EPD, the size of TiO_2 nanoparticles increased to ~70–80 nm (Fig. 6 (b)) might due to the penetration of PANI molecules into the pores of mesoporous TiO_2 nanoparticulate thin film. Additionally, the uniform deposition and the penetration of PANI on TiO_2 nanoparticulate thin film could be seen in the Fig. 6 (c).
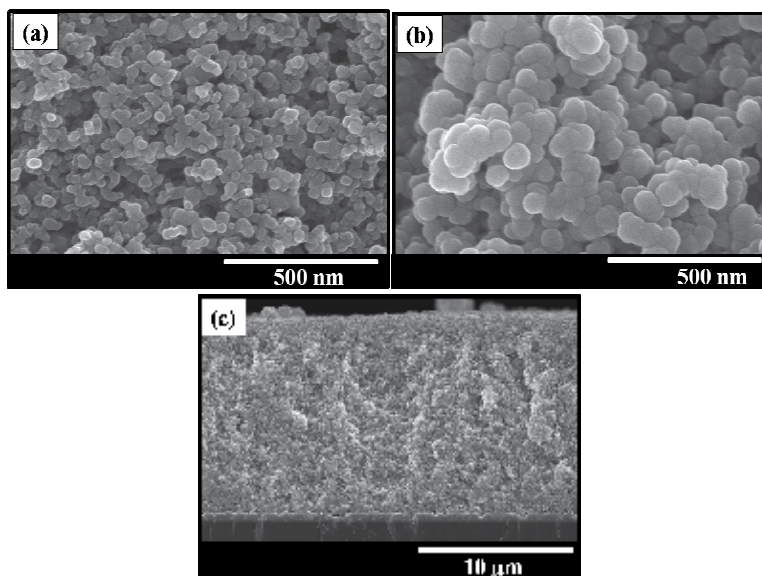
Fig. 6. Surface FESEM images of (a) TiO_2 nanoparticles (b) electrophoretically deposited PANI/TiO₂ nanoparticulate thin film and (c) cross-section image of electrophoretically deposited PANI/TiO₂ nanoparticulate thin film. Reprinted with permission from [Ameen S., 2011], J. Nanosci. Nanotech. 11 (2011) 1559. © 2011, American Scientific Publishers.

The shifting of FTIR peaks, as shown in Fig. 7 (a) indicates the existence of the hydrogen bonding between the surface hydroxyl groups of TiO_2 nanoparticles and the imine groups of PANI molecules (Somani, et al., 1999 & Nivetal, et al., 2003). The UV-Vis spectra of pristine PANI and PANI/TiO₂ nanoparticulate thin film is shown in (Fig. 7 (b)). The pristine PANI exhibits two characteristics bands at 331 and 625 nm which correspond to л–л* transitions of the phenyl rings of PANI and n-л* transitions respectively. In PANI/TiO₂ nanoparticulate thin film substrates, the peak at 269 nm retains its position, while the bands at 625 nm and

331 nm exhibit the blue shift to 599 nm and 321 nm respectively. These noticeable shifting and the intensity changes of the bands are ascribed to the bonding and the interaction between TiO$_2$ and the quinoid ring of PANI due to the hydrogen bonding in the form of NH$\cdots$O$-$Ti in PANI/TiO$_2$ nanoparticulate thin film. The extensive XPS studies, as shown in Fig. 8 have been examined to investigate the bonding between PANI and TiO$_2$ nanoparticles in PANI/TiO$_2$ nanoparticulate thin film. The four major peaks at $\sim$285.6 eV, 400.5 eV, 530.9 eV and 459.6/465.4 eV, are ascribed to carbon (C 1s), nitrogen (N 1s), oxygen (O 1s) and titanium (Ti 2p) respectively. The XPS studies favor the interaction of EPD PANI with TiO$_2$ nanoparticles by the existence of hydrogen bonding between the imine group of PANI and the surface hydroxyl of TiO$_2$ nanoparticles and thus, the electrophoretic deposition of PANI is a promising technique to construct the highly efficient PANI/TiO$_2$ nanoparticulate thin film.
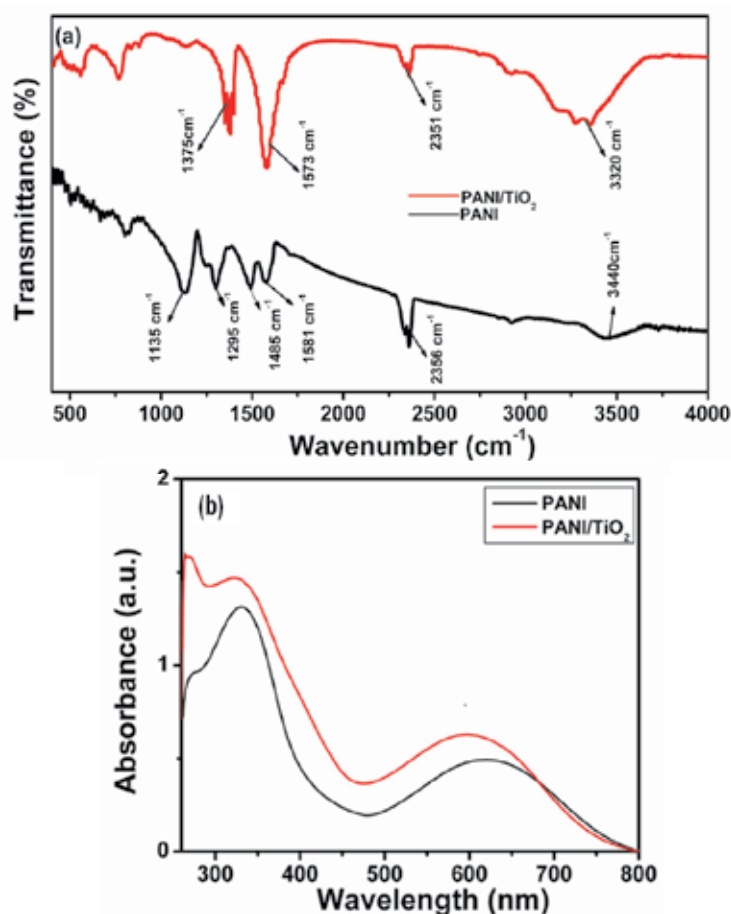
Fig. 7. (a) FT-IR spectra and (b) UV-Vis spectra of pristine PANI and electrophoretically deposited PANI/TiO$_2$ nanoparticulate thin film. Reprinted with permission from [Ameen S., 2011], J. Nanosci. Nanotech. 11 (2011) 1559. © 2011, American Scientific Publishers.
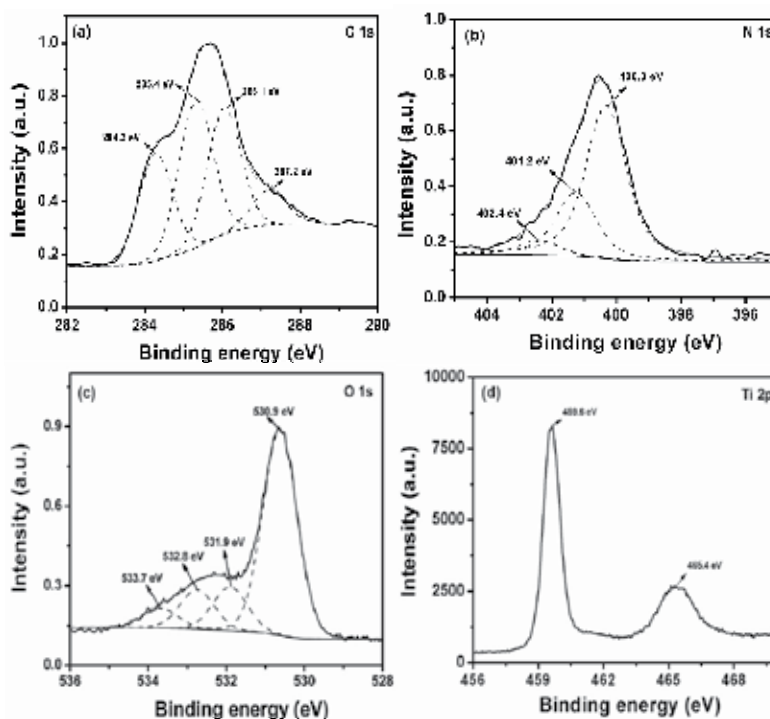
Fig. 8. (a) Resolved C1s, (b) N1s, (c) O1s and (d) Ti 2p XPS spectra of electrophoretically
deposited PANI/TiO₂ nanoparticulate thin film. Reprinted with permission from [Ameen S.,
2011], J. Nanosci. Nanotech. 11 (2011) 1559. © 2011, American Scientific Publishers.
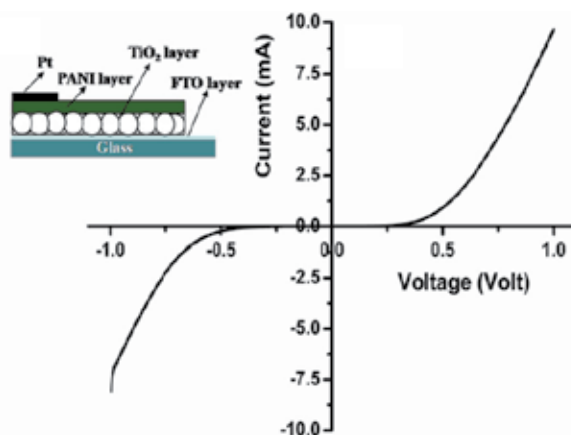
Fig. 9. Pt/PANI/TiO₂ nanoparticulate diode. Insets show the schematic representation of
the PANI/TiO₂ nanoparticulate heterostructure diode. Reprinted with permission from
[Ameen S., 2011], J. Nanosci. Nanotech. 11 (2011) 1559. © 2011, American Scientific
Publishers.

The current–voltage (I–V) characteristics of EPD PANI/TiO₂ nanoparticulate
heterostructure was carried out at different temperatures (25-150⁰C) with an applied voltage

ranges from −1V to +1V, as shown in Fig. 9. A schematic diagram of Pt/PANI/TiO$_2$ nanoparticulate heterostructure diode is shown in the inset of Fig. 9. The I–V characteristic of Pt/PANI/TiO$_2$ nanoparticulate heterostructure diode exhibits a rectifying and nonlinear behavior which might originate by the formation of schottky contact/barrier between Pt layer and EPD PANI/TiO$_2$ layer in Pt/PANI/TiO$_2$ nanoparticulate heterostructure diode. Moreover, the ratio of forward (I_f) and reverse current (I_r), called as rectification ratio (I_f/I_r) of the device is estimated as 7.0 at the bias voltage of 0.5 V. The I_f/I_r value indicates that the EPD PANI/TiO$_2$ nanoparticulate heterostructure shows a weak rectifying nature. The EPD PANI/TiO$_2$ heterostructure diode attains turn-on voltage of ~ 0.40 V and derives quite high current of ~0.25 mA at 298 K. A broader breakdown voltage (~0.51 V) and good leakage current of ~0.9 mA are achieved by Pt/PANI/TiO$_2$ nanoparticulate heterostructure diode. The low turn on voltage and high leakage current might result from the generation of high density of minority charge carriers from EPD PANI to *n*-type TiO$_2$. In a reverse bias, Pt/PANI/TiO$_2$ nanoparticulate heterostructure diode shows slightly high break down voltage (~0.55 V) which could be explained by the hopping effect originated from the conjugated bonding of PANI and the geometry/ morphology of TiO$_2$ nanoparticles. Therefore, the uniform and controlled thickness of PANI layer onto TiO2 nanoparticulates thin film substrate by the electrophoretic deposition provides the improved performance of the p–n heterostructure devices.

5.2 Plasma enhanced polymerization of PANI for heterostructure devices
5.2.1 Fabrication of PANI/TiO$_2$ heterostructure device

The formation of an inorganic/organic heterojunction structure by depositing the plasma polymerized PANI on n-type nanocrystalline titania (TiO$_2$) thin film substrate has been reported by Ameen et al (Ameen, et al., 2009). Fig. 10 (a) demonstrates a porous TiO$_2$ formed on the FTO substrates. The film is composed of the well crystalline TiO$_2$ nanoparticles of size ~25 nm, as shown in Fig. 10 (c). It is seen in Fig. 10 (b) that the PANI molecules are well penetrated into the porous TiO$_2$ thin film upon the plasma enhanced polymerization. The accumulation of TiO$_2$ nanoparticles occurs after the deposition of PANI on the surface of TiO$_2$ thin film, and could be seen in Fig. 10 (d). This assemblage confirms the internalization of plasma deposited PANI into porous TiO$_2$ nanoparticles thin film substrates. The I-V characteristics for PANI/TiO$_2$ heterojunction structure, as shown in our reported work (Ameen, et al., 2009,), indicates that no barrier is apparently present because the I-V characteristic curve is almost linear. The forward bias current increases with an increased applied voltage and have attained almost the linear curve. The proficient current in PANI/TiO$_2$ is attributed to well penetration of PANI molecules into the pores of TiO$_2$ nanoparticles layers which improves the degree of contact with TiO$_2$ and thus decreases the series resistance of the cell while increasing the current. The efficient charge movement at the junction of PANI and TiO$_2$ interfaces has made the heterojunction structure which behaves as a typical ohmic system. Moreover, in the reverse bias, the lower current is related to the decrease of the depletion layer because of the presence of the charge carriers at TiO$_2$ nanoparticles thin film.

5.2.2 Plasma deposited PANI on single and bilayer of TiO$_2$ thin film for the fabrication of PANI/TiO$_2$ heterostructure diodes

The organic/inorganic thin film is obtained by plasma enhanced p-type PANI deposited on the individual single and bilayer n-type TiO$_2$ thin film electrodes for the fabrication of p-n
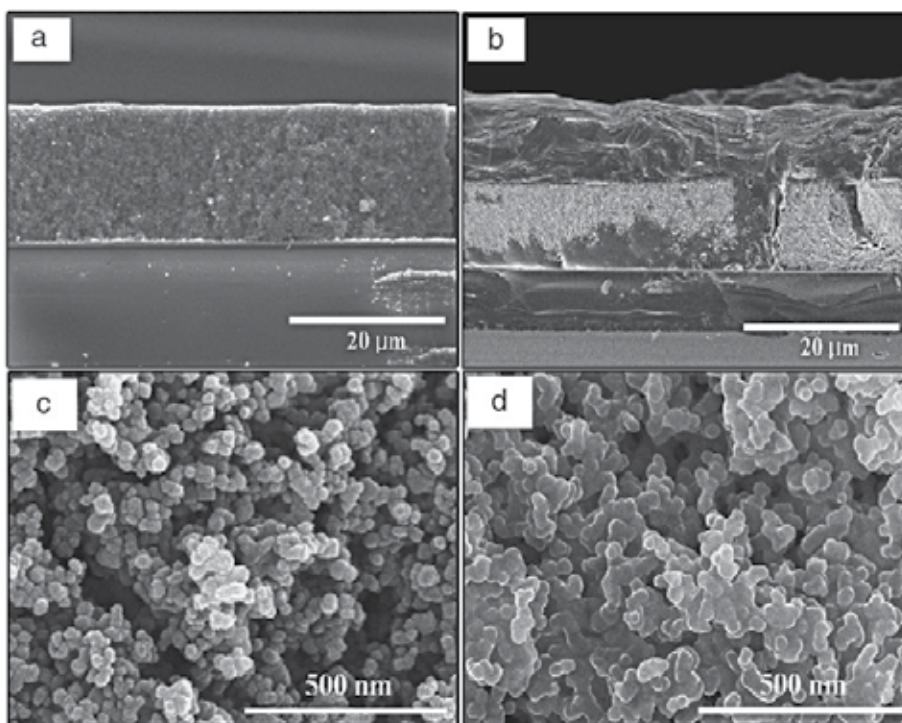
Fig. 10. Cross-sectioned FE-SEM images of (a) pristine TiO_2 (b) Plasma enhanced deposited PANI/TiO_2 thin film and surface FESEM images of (c) pristine TiO_2 (d) Plasma enhanced deposited PANI/TiO_2 thin film. Reprinted with permission from [Ameen S., 2009], Superlatt. Microstruc. 46 (2009) 745. © 2009, Elsevier Ltd.

heterostructure by Ameen et al (Ameen, et al., 2011). The single layer TiO_2 electrode exhibits non uniform and less penetration of PANI molecules by plasma enhanced polymerization into the pores of TiO_2 thin film. However, the extent of PANI deposition has drastically enhanced by the additional layer of TiO_2 on the single layered electrode due to the uniform and well penetration of PANI into the pores of TiO_2 nanoparticles.

The XPS characterizations suggest that the plasma polymerized PANI are interacted to TiO_2 by the formation of hydrogen bonding between imine group of PANI and surface hydroxyl of TiO_2. UV-Vis of PANI/TiO_2 thin film electrode exhibit the peaks at 324 nm corresponds to л–л* transitions centered on the benzenoid and quinoid units. This peak appears with high intensity in PANI/bilayer TiO_2 thin film electrode which indicates the enhanced deposition of PANI molecules on the surface of TiO_2. It could be attributed that highly porous surface of bilayer TiO_2 thin film absorbs large amount of PANI than the single layered TiO_2 thin film, as described in previous report (Ameen, et al., 2011).

The fabricated p-n heterostructure devices are comprised of plasma polymerized PANI (p-type) deposited on the single and bilayerTiO_2 thin film (n-type) coated on FTO glass substrates with a top Pt thin layer contact. The I-V curve of the fabricated PANI/single layer TiO_2 device attains low turn-on voltage of ~ 0.4 V and delivers reasonably high current of ~ 0.08 mA at 298 K, as described in previous report (Ameen, et al., 2011). However, a breakdown voltage (~0.57 V) with high leakage current of ~0.6 mA is obtained by Pt/PANI/single layer TiO_2

heterostructure device. On comparison, Pt/PANI/bilayer TiO_2 heterostructure device shows the lower turn on voltage and low breakdown voltage with high leakage current than single layer TiO_2 based heterostructure device. Here, the second layer of TiO_2 in PANI/bilayer TiO_2 provides a highly porous surface for the high loading of PANI molecules during the plasma enhanced polymerization and thus, produces high density of the minority charge carriers to n-type TiO_2 thin film layer and results to the high leakage current with small turn-on voltage and breakdown voltage. It is attributed that the additional TiO_2 thin film layer might increase the n-type character of the device. On the other hand, both the devices exhibit slight high reverse break down voltage (~0.58 V in single layer TiO_2 and ~0.5 V in bilayer TiO_2) which could be understood by considering the molecular geometry of PANI chains and geometry/morphology of TiO_2 nanoparticles deposited on the FTO substrates which likely generate the hopping effect. The current densities reported by Sadia et al in the forward bias are considerably better than the data reported elsewhere on PANI based or other conducting polymer based heterostructure device (Dhawale, et al., 2008, Nadarajah, et al., 2008 & Maeng, et al., 2008). Under light illumination, both the devices constitute the no current flowing condition i.e. called open circuit voltage condition (V_{OC}) and the maximum current condition called short circuit current (J_{SC}) at zero voltage condition. This phenomena is absent in I-V characteristics under dark condition, which means that the fabricated devices could absorb photons for the generation of current and having the photovoltaic behavior under light illumination and thus, Pt/PANI/bilayer TiO_2 heterostructure device is reported to achieve high J_{SC} (~0.32 mA) with low V_{OC} (~0.343 V) as compared with Pt/PANI/single layer TiO_2 heterostructure device (J_{SC} = ~0.20 mA and V_{OC} = ~0.462 V).

6. Applications of PANI in dye sensitized solar cells (DSSCs)

Organic solar cells have attracted considerable attention in recent years due to several advantages such as low cost, processing at low temperature, flexible and large area production etc (Thompson, et al., 2008, Gunes, et al., 2007 & Bundgoard, et al., 2007). Usually, the organic materials are not good in carrier transport and thus, the power conversion efficiency is limited by the low dissociation probability of excitons and the inefficient hopping carrier transport (Shaw, et al. 2008 & Sirringhaus, et al., 1999). Among various organic solar cells, polymer solar cells have demonstrated an impressive scale up on power conversion efficiency and improvement in lifetime. Right now a remarkable 8% power conversion efficiency has been reached at laboratory scale, 6–8% for normal and 3–4% for inverted configurations (Waldauf, et al., 2006, Steim, et al., 2010, 2008 & Ameri, et al., 2009). Still, much work must be done in order to overcome the main difficulties observed for the technology i.e. enhancement of efficiency and lifetime. Thus, the need for novel materials acting as acceptors and donors, and the understanding of the interplay between interfaces (electrodes, optical spaces) are currently under an intense investigation. Semiconductor oxides have been applied extensively like antireflection coatings and scattering layers (Lee, et al., 2008), as interfacial layers in organic solar cells (Steim, et al., 2010, 2008) and as part of the active constituents of the device acting as electron transport materials in and hybrid DSSCs (Cantu, et al., 2010, 2006, 2007, 2006,Valls, et al., 2010, 2009). The semiconductor nanostructures are therefore proposed to combine with the organic materials to provide not only a large interface area between organic and inorganic components for exciton dissociation but also a fast electron transport in semiconductors. Hybrid solar cells are a mixture of nanostructures of both organic and inorganic materials.

Therefore, they combine the unique properties of inorganic semiconductor nanoparticles with properties of organic/polymeric materials (Arici, et al., 2003). In addition to this, low cost synthesis, processability and versatile manufacturing of thin film devices make them attractive (Saraciftci, et al., 1992 & Yu, et al., 1995). Also, inorganic semiconductor nanoparticles might have high absorption coefficients and particle size induced tunability of the optical band-gap. Thus, the hybrid solar cell is becoming interesting and attractive in recent years.

6.1 PANI/TiO₂ thin film electrodes for the performance of DSSCs

The TiO_2/PANI and dye absorbed TiO_2/PANI electrodes are prepared by plasma enhanced polymerization using aniline monomer for the fabrication of DSSCs by Ameen et al (Ameen, et al., 2009). The TiO_2 thin film, prior to PANI deposition exhibits the particles of size ~20–25 nm, as shown in (Fig. 11 (b)). However, the proper attachment of plasma polymerized PANI on TiO_2 thin film substrates (Fig. 11 (d)) and increases the size of TiO_2 nanoparticles to ~50–60 nm indicate the effects of the penetration of PANI into TiO_2 nanoparticles. The current density–voltage (J–V) performance of solar cell FTO/TiO_2/Dye/PANI/Pt and FTO/TiO_2/PANI/Pt are shown in Fig.12 respectively. The electric contact of the hole conductor and the pore filling extent of the hole conductor into the dye-sensitized TiO_2 film are the two important factors which determine the photovoltaic behaviors of the devices. It has been found that the solar cell based on TiO_2/Dye/PANI electrode executes great improvement in the overall conversion efficiency with the incorporation of dye layer on TiO_2/PANI electrode and dramatically enhanced the photovoltaic properties such as open-circuit voltage (V_{OC}), short-circuit current (J_{SC}) and fill factor (FF) as compared to TiO_2/PANI electrode based DSSC. These improvements are resulted from the formation of TiO_2/PANI thin film, where the photon generated electrons could freely travel at the interface of the PANI and TiO_2 without decay, and dissociate into free charge carriers effectively.
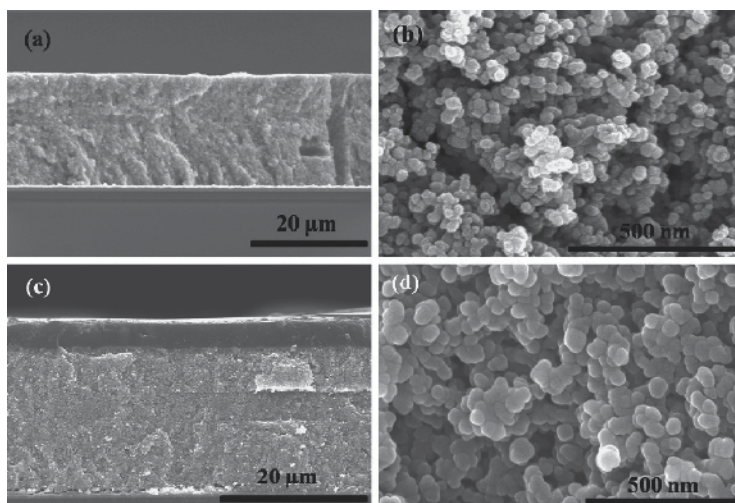
Fig. 11. (a) Cross-section and (b) surface view FESEM images of TiO_2 deposited on FTO substrate. (c) and (d) show the cross-section and surface view FESEM images of Plasma enhanced deposited PANI/TiO_2 film. Reprinted with permission from [Ameen S. et al, 2009], J. Alloys Compd.164 (2009) 382. © 2009, Elsevier Ltd.
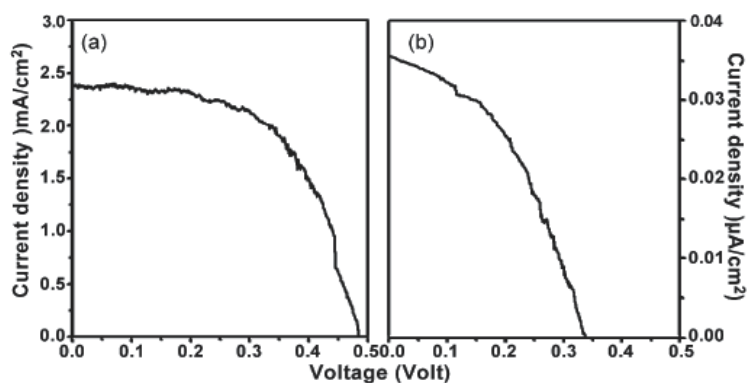
Fig. 12. J–V curve of fabricated solar cell (a) FTO/TiO$_2$/Dye/PANI/Pt (b) FTO/TiO$_2$//PANI/Pt. Reprinted with permission from [Ameen S. et al, 2009], J. Alloys Compd.164 (2009) 382. © 2009, Elsevier Ltd.

The DC conductivity vs 1000/T plots for the fabricated solar cells of FTO/TiO$_2$/Dye/PANI/Pt and FTO/TiO$_2$//PANI/Pt are shown in Fig.13. It is cleared that the conductivity of TiO$_2$/PANI is higher as compared to the pristine PANI. The room temperature conductivity of pristine PANI (28.36×10^{-3} ohm^{-1} cm^{-1}) is lower than the room temperature conductivity of PANI/TIO$_2$ thin film (75×10^{-3} ohm^{-1} cm^{-1}). The increase in conductivity might due to the increase of charged carrier concentration with improved mobility of the charged carriers. The rougher the surface, large-area defects and pinholes on PANI films exist and therefore, result to the high conduction of film. The effective electrical conductivity is thus, due to the retardation of both the transport of photoelectrons from counter electrode to hole conductor and the regeneration of the dye by the reduced-state hole conductors. Such improvements could suppress the recombination of photoelectrons, injected into the conduction band of TiO$_2$ from PANI and retards the internal resistance of the device.
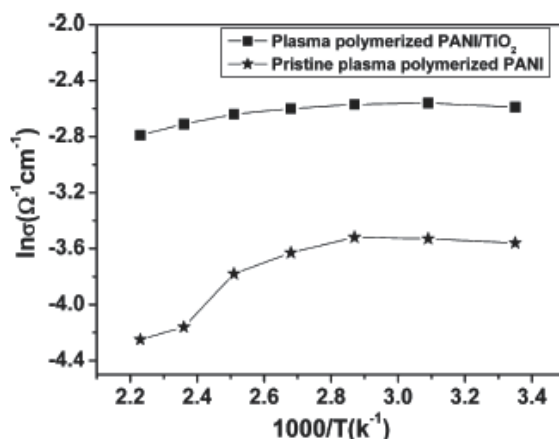
Fig. 13. Plots of DC conductivity vs 1000/T for pristine PANI and plasma enhanced deposited PANI/TiO$_2$ thin film. Reprinted with permission from [Ameen S. et al, 2009], J. Alloys Compd.164 (2009) 382. © 2009, Elsevier Ltd

AC impedance of FTO/TiO$_2$//PANI/Pt (Fig.14(a)) and TiO$_2$/Dye/PANI (Fig.14(b)) thin film electrode based DSSCs under the illumination of 100mW/cm^2 (AM1.5) by applying a 10mV AC signal at the frequency range from 10 Hz to 100 kHz are also measured by Sadia et al. A very high R$_{P/TCO}$ of 52.4Ω and R$_{CT}$ of 3700Ω was observed for TiO$_2$/PANI electrodes based cells. Comparatively, TiO$_2$/Dye/PANI based device showed the low R$_{P/TCO}$ (35.8Ω) and R$_{CT}$ (81.9Ω) due to the influence of dye layer which is placed between the TiO$_2$ and PANI layer of the electrode. It is found that the value of R$_{CT}$ in TiO$_2$/Dye/PANI based device is very low as compared to the R$_{CT}$ of TiO$_2$/PANI based device. Thus, it explains the high electron transfer at the junction of TiO$_2$ and PANI in TiO$_2$/Dye/PANI based device, resulting in the high photocurrent density and overall conversion efficiency.
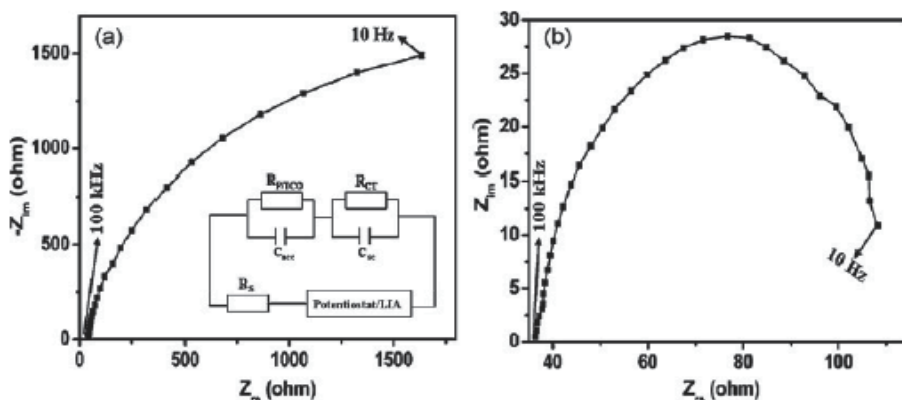
Fig. 14. AC impedance of (a) FTO/TiO$_2$//PANI/Pt and (b) TiO$_2$/Dye/PANI thin film electrode based DSSCs at the frequency range from 10 Hz to 100 kHz. Inset shows the equivalent circuit model of the device. Reprinted with permission from [Ameen S. et al, 2009], J. Alloys Compd.164 (2009) 382. © 2009, Elsevier Ltd.

6.2 PANI thin film electrode as counter electrode for DSSCs

Conducting polymers generally show p-type semiconducting behavior, good specific capacitance and catalytic activity for the reduction of I$_3^-$ ion. Owing to their specialty, the conducting polymers are used as counter electrode (CE) materials for DSSCs. In 2008, Saito et al reported the preparation of the counter electrode using p-toluenesulfonate (PEDOTTsO) or polystyrenesulfonate (PEDOT-PSS) doped poly (3, 4-ethylenedioxythiophene) (PEDOT) for DSSCs (Saito et al., 2004). They achieved a comparably high conversion efficiency of 4.6% with J$_{SC}$ =11.2 mA/cm^2, V$_{OC}$ = 670 mV and FF = 0.61 with the fabricated DSSCs. Consecutively, the composite films of graphene and PEDOT–PSS deposited on indium tin oxide (ITO) substrates by spin coating and applied as counter electrodes of DSSCs. The prepared CE exhibited high transmittance (>80%) at visible wavelengths and high electrocatalytic activity as compared to the above system with the similar conversion efficiency (4.5%). Q. Li et al group manufactured a microporous polyaniline (PANI) and applied as CE for the fabrication of DSSCs (Li, et al., 2008). The advanced microporous PANI CE with particle diameter of 100 nm possessed the lower charge-transfer resistance and higher electrocatalytic activity for the redox reaction. DSSC fabricated with microporous PANI CE exhibited reasonably high overall conversion

efficiency of 7.15% i.e. compared to DSSC with Pt CE. This report could open the utilization of the simple preparation technique with low cost and excellent photoelectric properties of PANI based counter electrode as appropriate alternative CE materials for DSSCs. Furthermore, J. Wu et al prepared polypyrrole (PPy) nanoparticle and deposited on a fluorine-doped tin oxide (FTO) glass for the construction of PPy counter electrode and applied to DSSC (Wu, et al., 2008). The fabricated DSSC achieved a very high conversion efficiency of 7.66% owing to its smaller charge transfer resistance and higher electrocatalytic activity for the I_2/I^- redox reaction. After this significant breakthrough, K. M. Lee et al developed poly (3, 4-alkylenedioxythiophene) based CE by electrochemical polymerization on FTO glass substrate for DSSC (Lee, et al., 2009). A high conversion efficiency of 7.88% was acquired by the fabricated DSSC which attributed to the increased effective surface area and good catalytic properties for I_3^- reduction. Progressively, the nanostructured polyaniline films were grown on FTO glass using cyclic voltammetry (CV) method at room temperature and applied as counter electrode for DSSCs. They found that the controlled thickness of nanostructured polyaniline (>70 nm) by the used method increased the reactive interfaces, which conducted the charge transfer at the interface and low resistance hinders electronic transport within the film. The fabricated DSSCs achieved a high overall conversion efficiency of 4.95% with very high J_{SC} of 12.5 mA/cm². Importantly, the nanostructured PANI electrode showed the 11.6% improvement in J_{SC} as compared to DSSC with an electrodeposited platinum counter electrode (Zhang, et al., 2010). Recently, Ameen et al synthesized the undoped and sulfamic acid (SFA) doped PANI nanofibers (NFs) via template free interfacial polymerization process and deposited on FTO substrates using spin coating to prepare counter electrode for DSSCs (Ameen, et al., 2010).

6.3 Sulfamic acid doped PANI Nanofibers counter electrode for DSSCs

Ameen et al developed a simple interfacial polymerization method for the synthesis of PANI nanofibers (NFs) and its doping with sulfamic acid (SFA) to increase the conductivity (Ameen, et al., 2010). These undoped and SFA doped PANI NFs were applied as new counter electrodes materials for the fabrication of the highly efficient DSSCs. The selection of SFA was based on its exclusively important properties such as high solubility, easy handling, nonvolatile stable solid acid, and low corrosiveness. The proposed doping mechanism for PANI with SFA is shown in Fig. 15. PANI NFs exhibit well-defined fibrous morphology with the diameter of 30 nm (Fig. 16 (b)) and the diameter of PANI NFs has considerably increased to ~40 nm after doping with SFA, as shown in Fig. 16 (a). The chemical doping of SFA causes some aggregation of PANI NFs, and therefore, the formation of voids into the fibrous network of PANI NFs are noticed. The TEM images of PANI NFs (Fig. 16 (c)) and SFA-doped PANI NFs (Fig. 16 (d)) justifies the doping effect on the morphology of PANI NFs. The entrapped SFA into the fibers of PANI results to the increase of average diameter by ~40 nm as compared to undoped PANI NFs.

The UV-Vis of SFA doped PANI-NFs, as shown in Fig. 17 (a), exhibits a slight blue shift of the peak at 296 nm from 298 nm and a considerably large red shift at 380 nm from 358 nm which indicates the interactions between SFA dopants and the quinoid ring of emeraldine salt (ES) and facilitate the charge transfer between the quinoid unit of ES and the dopant via highly reactive imine groups. The CV curves (Fig. 17 (b)) of SFA-doped PANI NFs electrode attains a reasonably high anodic peak current (I_a) of 0.24 mA/cm² and cathodic peak current (I_c) of -0.17 mA/cm² with a considerably high value of switching point (0.22 mA/cm²).

However, the undoped PANI NFs electrode exhibits a low I_a of 0.21 mA/cm² and I_c of -0.2 mA/ cm² with a low switching point (0.17 mA/cm²). These results suggest that the high peak current might increase the redox reaction rate at SFA-doped PANI NFs counter electrode, which may attribute to its high electrical conductivity and surface area.
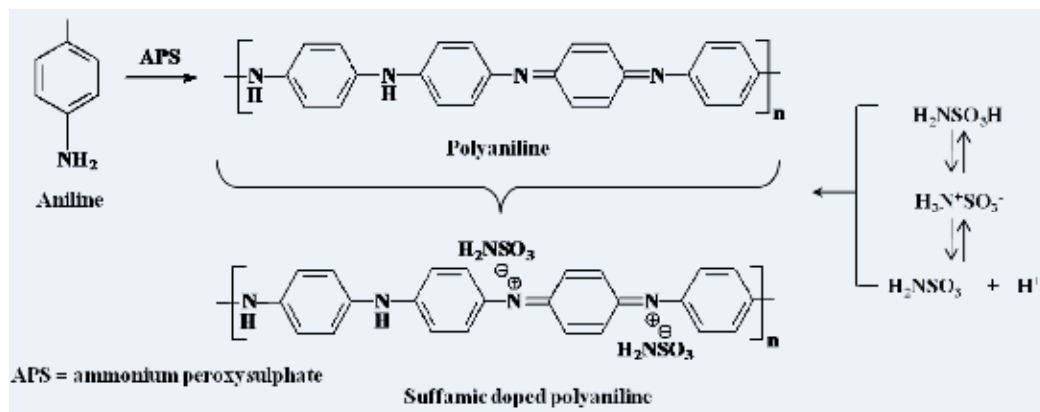
Fig. 15. Proposed mechanism of sulfamic doping into PANI NFs.
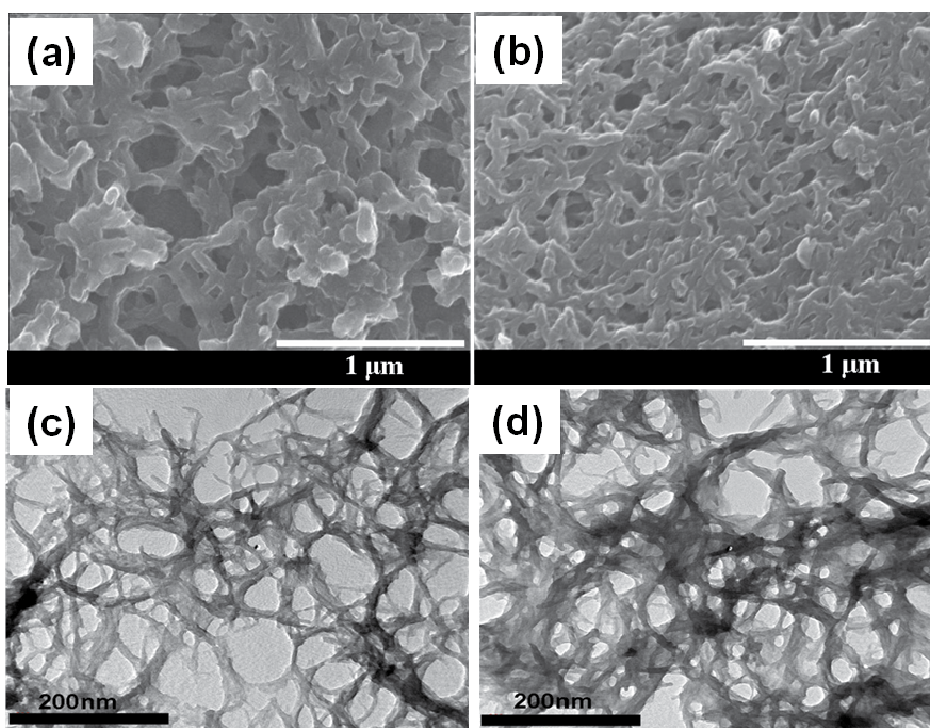
Fig. 16. FESEM images of (a) SFA doped PANI NFs and (b) PANI NFs. TEM images of (c) PANI and (d) SFA doped PANI NFs. Reprinted with permission from [Ameen S. et al, 2010], J. Phys. Chem. C 114 (2010) 4760. © 2010, ACS Publications Ltd.
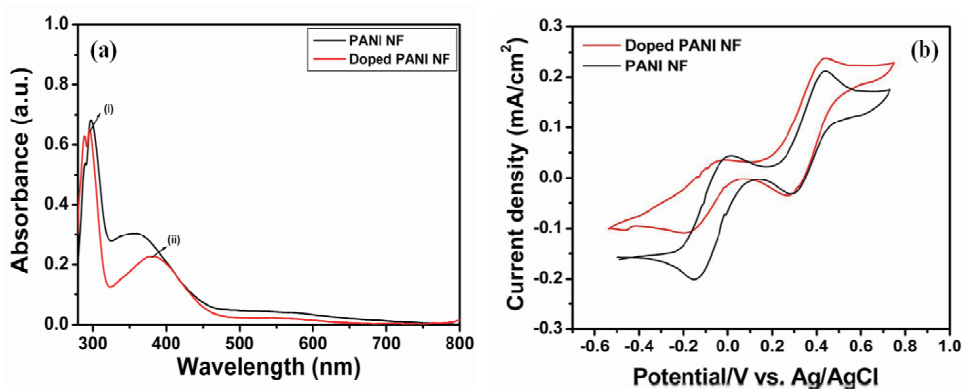
Fig. 17. (a) UV-vis spectra of PANI NFs and SFA-doped PANI NFs. (b) Cyclic voltammetry of iodide species on PANI NFs and SFA doped PANI NFs electrodes in acetonitrile solution with 10 mM LiI, 1 mM I_2, and 0.1M $LiClO_4$. Reprinted with permission from [Ameen S. et al, 2010], J. Phys. Chem. C 114 (2010) 4760. © 2010, ACS Publications Ltd.
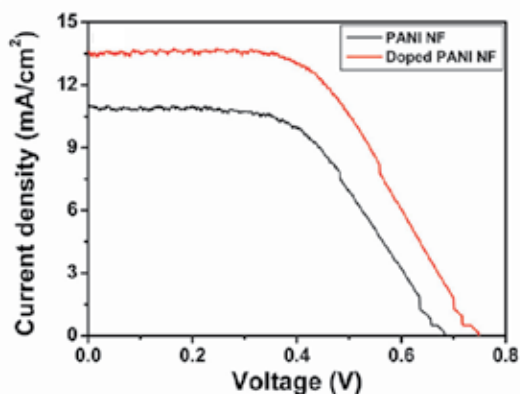
Fig. 18. J-V curve of fabricated solar cell of PANI NFs and SFA doped PANI NFs as counter electrodes under light illumination of 100 mW/cm². Reprinted with permission from [Ameen S. et al, 2010], J. Phys. Chem. C 114 (2010) 4760. © 2010, ACS Publications Ltd.

The Fig. 18 shows that the DSSCs fabricated with SFA-doped PANI NFs counter electrode achieve a high conversion efficiency (η) of 5.5% with a high short circuit current (J_{SC}) of 13.6 mA/cm² , open circuit voltage (V_{OC}) of 0.74 V, and fill factor (FF) of 0.53. The conversion efficiency increases by ~27% and thus, after SFA doping of PANI NFs the conversion efficiency reaches the value of 5.5% than that of DSSC fabricated with PANI NFs counter electrode (4.0%). Further, the SFA-doped PANI NFs counter electrode has significantly increased the J_{SC} and V_{OC} of ~20% and ~10%, respectively, as compared to the DSSC fabricated with PANI NFs counter electrode. It indicates that the SFA doping has increased the fast reaction of I^-/I_3^- species at counter electrode and therefore, the superior photovoltaic properties such as η, J_{SC}, and V_{OC} of the cell are attributed to the sufficiently high conductivity and electrocatalytic activity of doped PANI NFs, which alleviates the reduction of I_3^- at the thin SFA-doped PANI NFs layers. Importantly, the IPCE curves of DSSCs fabricated with PANI NFs counter electrode exhibit the low IPCE of ~54% in the absorption range of 400-650 nm.

The IPCE value has prominently increased by ~70% with the SFA doped PANI NFs counter electrode-based DSSCs. It is noteworthy that the IPCE of the device is considerably enhanced by ~24% upon SFA doping on PANI NFs-based counter electrodes. The enhanced IPCE in DSSCs with SFA-doped PANI NFs electrode results in the high J_{SC} and photovoltaic performance, which are related to its high electrical conductivity and the higher reduction of I_3^- to I^- in the electrolyte at the interface of PANI NFs layer and electrolyte.

7. Fabrication of DSSCs with metal oxide nanomaterials photoanodes

In DSSCs, the choice of semiconductor is governed by the conduction band energy and density of states which facilitate the charge separation and minimizing the recombination. Secondly, the high surface area and morphology of semiconductor are important to maximize the light absorption by the dye molecules while maintaining the good electrical connectivity with the substrate (Baxtera, et al., 2006).The semiconducting metal oxides such as TiO_2, ZnO and SnO_2 etc have shown good optical and electronic properties and are accepted as the effective photoelectrode materials for DSSCs. These metal oxide nanostructures present discrete morphologies of nanoparticles (Ito, et al., 2008) nanowires (Law, et al., 2005 & Feng, et al., 2008) and nanotubes (Macak, et al., 2005 & Mor et al., 2005) which are the key component in DSSCs for the effective dye adsorption and the efficient electron transfer during the working operation of DSSCs. To improve the light harvesting efficiency, the metal oxide nanostructures must possess high surface to volume ratio for high absorption of dye molecules. These metal oxide nanostructures are usually prepared by the methods like hydrothermal synthesis (Zhang, et al., 2003 & Wang et al., 2009) template method (Ren, et al., 2009 & Tan, et al., 2008) electrodeposition (Tsai, et al., 2009) and potentiostatic anodization (Chen, et al., 2009 & kang, et al., 2009) and are important for improving the photovoltaic properties of DSSCs such as J_{SC}, V_{OC}, FF and conversion efficiency. Out of these, TiO_2 has been intensively investigated for their applications in photocatalysis and photovoltaic (Regan, et al., 1991 & Duffie, et al., 1991). Particularly in DSSCs, the porous nature of nanocrystalline TiO_2 films provides the large surface for dye-molecule adsorption and therefore, the suitable energy levels at the semiconductor–dye interface (the position of the conduction-band of TiO_2 being lower than the excited-state energy level of the dye) allow for the effective injection of electrons from the dye molecules to the semiconductor. Compared with other photovoltaic materials, anatase phase TiO_2 is outstanding for its stability and wide band gap and thus, widely used in the devices (Gratzel, et al., 2001). On the other hand, ZnO nanomaterials are chosen as an alternative material to TiO_2 photoanode due to its wide-band-gap with higher electronic mobility which would be favorable for the efficient electron transport, with reduced recombination loss in DSSCs. Studies have already been reported on the use of ZnO material photoanode for the application in DSSCs. Although the conversion efficiencies of ZnO (0.4–5.8%) is comparably lower than TiO_2 (11%) but still ZnO is a distinguished alternative to TiO_2 due to its ease of crystallization and anisotropic growth. In this part of the chapter, the various nanostructures of TiO_2 and ZnO have been briefly summarized for the application for DSSCs.

7.1 Various TiO$_2$ nanostructures photoanodes for DSSCs
7.1.1 Photoanodes with TiO$_2$ nanotubes
TiO_2 nanotubes (NTs) arrays are generally synthesized by the methods like electrochemical approach (Zwilling, et al., 1999 & Gong, et al., 2001) layer-by-layer assembly (Guo, et al.,

2005) template synthesis, sol–gel method (Martin, et al., 1994, Limmer, et al., 2002 & Lakshmi, et al., 1997) etc and are the effective photoanode for the fabrication of DSSCs. The reported methods for the synthesis of TiO_2 NTs provide low yield and demand advanced technologies with the high cost of templates (anodic aluminum oxide, track-etched polycarbonate or the amphiphilic surfactants). A. J. Frank obtained the bundle-free and crack-free NT films by using the supercritical CO_2 drying technique and found that the charge transport was considerably increased with the decreased of NTs bundles which created the additional pathways through the intertube contacts. However, J. H. Park et al. reported a simple and inexpensive methodology for preparing TiO_2 NTs arrays on FTO glass and applied as photoanodes for DSSCs which exhibited the significantly high overall conversion efficiency of 7.6% with high J_{SC} of 16.8 mA/cm², V_{OC} of 0.733 V and a fill factor (FF) of 0.63. The enhanced photovoltaic performance was attributed to the reduced charge recombination between photoinjected electrons in the substrate via tubular morphology of TiO_2 photoanode (Park, et al., 2008).

7.1.2 Photoanodes with TiO_2 nanorods

The Highly crystalline TiO_2 nanorods (NRs) with lengths of ~100-300 nm and diameters of ~20-30 nm were grown by J. Jui et al using the hydrothermal process with cetyltrimethylammonium bromide surfactant solution (Jiu, et al., 2006). In this synthesis, the length of nanorods was substantially controlled and maintained by the addition of a tri-block copolymer poly-(ethylene oxide) 100-poly (propylene oxide) 65-poly (ethylene oxide) 100 (F127) and polymer decomposed after sintering of TiO_2 nanorods at high temperatures. The fabricated DSSCs attained a high overall conversion efficiency of 7.29% with considerably high V_{OC} of 0.767 V and fill factor of 0.728. The enhancement in the photovoltaic properties was attributed to increase the ohmic loss and high electron transfer through TiO_2 NRs. As compared to P-25 based DSSCs, the less amount of dye was absorbed by the TiO_2 NRs photoanode might due to the larger size of the nanorods and therefore, result a slightly lower photocurrent density of 13.1 mA/cm². B. Liu group proposed a hydrothermal process to develop the oriented single-crystalline TiO_2 NRs or nanowires on a transparent conductive substrate (Liu, et al., 2009). The DSSCs fabricated with $TiCl_4$ generated 4 μm-long rutile TiO_2 NRs electrode and demonstrated relatively low light-to-electricity conversion efficiency of 3% with J_{SC} ~6.05 mA/cm², V_{OC} of ~0.71 V, and FF of 0.7. The device delivered the improved IPCE of ~50% at the peak of the dye absorption. The improved V_{OC} and FF revealed that the $TiCl_4$ treatment decreased the surface recombination. Conclusively, TiO_2 NRs improved the dye adsorption and the optical density through the surface of oriented NRs.

7.1.3 Photoanodes with TiO_2 nanowires

Single-crystal-like anatase TiO_2 nanowires (NWs) as compared to NRs and NTs morphology are extensively applied as photoanode for the fabrication of DSSCs. The perfectly aligned morphology of TiO_2 NWs and networks of NWs could be achieved by the solution, electrophoretic and hydrothermal process due to the "oriented attachment" mechanism. The aligned TiO_2 network with single-crystal anatase NWs conducted the high rate of electron transfer and achieved significantly high overall conversion efficiency of 9.3% with high J_{SC} of 19.2 mA/cm², V_{OC} of 0.72 V, and FF of 0.675. The improved photovoltaic performance was ascribed to the network structure of single-crystal-like anatase NWs which acquired a high surface to volume ratio and thus, presented the high IPCE of ~ 90%. Recently, J. K. Oh

et al reported the branched TiO_2 nanostructure photoelectrodes for DSSCs with TiO_2 NWs as a seed material (Oh, et al., 2010). The prepared TiO_2 electrode possessed a three-dimensional structure with rutile phase and showed high conversion efficiency of 4.3% with high J_{SC} of 12.18 mA/cm². Compared to DSSCs with TiO_2 NWs, the cell performance and J_{SC} was enhanced by 2 times, which was due to the increased specific surface area and the roughness factor. However, the lower FF was originated from the branches of TiO_2 electrodes, resulting in the reduction of grain boundaries.

7.2 Various ZnO nanostructures photoanodes for DSSCs
7.2.1 Photoanodes with ZnO nanoparticles
The techniques like vapor liquid solid, chemical vapor deposition, electron beam evaporation, hydro thermal deposition, electro chemical deposition and thermal evaporation etc are generally applied for the synthesis of ZnO nanostructures. Out of these, the chemical solution method is the simplest procedure for achieving uniform ZnO nanoparticles (NPs) thin films and delivers almost the same performance as that of nanocrystalline TiO_2 with similar charge transfer mechanism between the dye and semiconductor. The synthesis of ZnO NPs is reported by the preparation of ZnO sols with zinc acetate as precursor and lithium hydroxide to form homogeneous ethanolic solutions (Spanhel, et al., 1991 & Keis, et al., 2001). Several researchers have fabricated DSSCs using sol–gel-derived ZnO NPs films and reported the low conversion efficiencies with values generally around 0.4–2.22% (Redmond, et al., 1994, Rani, et al., 2008 & Zeng, et al., 2006). Highly active ZnO nanoparticulate thin film through a compression method was prepared for high dye absorption by Keis et al for the fabrication of DSSCs (Keis, et al., 2002, 2002). The morphology of ZnO NPs, synthesized by a sol–gel route exhibited an average size of 150 nm. The thin film photoelectrodes were prepared by compressing the ZnO NPs powder under a very high pressure and the DSSCs fabricated with the obtained film achieved a very high overall conversion efficiency of 5% under the light intensity of 10 mWcm².

7.2.2 Photoanodes with ZnO nanosheets and other nanostructures
ZnO nanosheets (NSs) are quasi-two-dimensional structures that could be fabricated by a re-hydrothermal growth process of hydrothermally grown ZnO NPs (Suliman, et al., 2007). M. S. Akhtar et al prepared sheet-spheres morphology of ZnO nanomaterials through citric acid assisted hydrothermal process with 5 M NaOH solution (Akhtar, et al., 2007). The high conversion efficiency and high photocurrent of ZnO NSs based DSSCs was attributed to the effective high light harvesting by the maximum dye absorption via ZnO NSs film surface which promoted a better pathway for the charge injection into the ZnO conduction layer. Sequentially, C. F. Lin et al fabricated a prepared ZnO nanobelt arrays on the FTO substrates by an electrodeposition method and applied as photoelectrode for the fabrication of DSSCs (Lin, et al., 2008). Y. F. Hsu et al had grown a 3-D structure ZnO tetrapod nanostrcutures, comprised of four arms which were extended from a common core (Hsu, et al., 2008 & Chen, et al., 2009). The length of the arms was adjusted within the range of 1–20 mm, while the diameter was tuned from 100 nm to 2 µm by changing the substrate temperature and the oxygen partial pressure during vapor deposition.

7.2.3 Photoanodes with ZnO nanowires
Law et al designed ZnO nanowire (NWs) arrays to increase the electron diffusion length and was applied as photoelectrode for the fabrication of DSSCs (Law, et al., 2005 & Greene, et al.,

2006). The grown ZnO nanowires arrays films exhibited the relatively good resistivity values between the range of 0.3 to 2.0 Ω cm for the individual nanowires with an electron concentration of 1 - 5 x 10^{18} cm³ and a mobility of 1–5 cm²V⁻¹s⁻¹. The overall conversion efficiencies of 1.2-1.5% were obtained by DSSCs fabricated with ZnO nanowires arrays with short-circuit current densities of 5.3–5.85 mA/cm², open-circuit voltages of 0.610–0.710 V, and fill factors of 0.36–0.38. Another group synthesized ZnO NWs by the use of ammonium hydroxide for changing the supersaturation degree of Zn precursors in solution process (Regan, et al., 1991). The length-to-diameter aspect ratio of the individual nanowires was easily controlled by changing the concentration of ammonium hydroxide. The fabricated DSSCs exhibited remarkably high conversion efficiency of 1.7% which was much higher than DSSC with ZnO nanorod arrays (Gao, et al., 2007). C. Y. Jiang et al reported the flexible DSSCs with a highly bendable ZnO NWs film on PET/ITO substrate which was prepared by a low-temperature hydrothermal growth at 85 °C (Jiang, et al., 2008). The fabricated composite films obtained by immersing the ZnO NPs powder in a methanolic solution of 2% titanium isopropoxide and 0.02 M acetic acid was treated with heat which favored the good attachment of NPs onto NWs surfaces (Jiang, et al., 2008). Here, the conversion efficiency of the fabricated DSSCs was achieved less as compared to DSSCs based on NPs.

7.2.4 Photoanodes with ZnO nanorods

A. J. Cheng et al synthesized aligned ZnO nanorods (NRs) on indium tin oxide (ITO) coated glass substrate via a thermal chemical vapor deposition (CVD) (Cheng, et al., 2008) at very high temperature which affected the crystalline properties of ZnO NRs. The rapid large-scale synthesis of well-crystalline and good surface area of hexagonal-shaped ZnO NRs was carried out by A. Umar et al at very low temperature (70°C) for the application of DSSCs (Umar, et al., 2009). A high overall light to electricity conversion efficiency of 1.86% with high fill factor (FF) of 74.4%, high open-circuit voltage (V_{OC}) of 0.73V and short-circuit current (J_{SC}) of 3.41mA/cm² was achieved by fabricated DSSCs. M. S. Akhtar et al reported the morphology of ZnO flowers through hydrothermal process using Zinc acetate, NaOH and ammonia as capping agent. The photoanode was prepared by spreading the ZnO paste on FTO substrate by doctor blade technique for the fabrication of DSSCs (Akhatr, et al., 2007). Unfortunately, the DSSC presented a very low conversion efficiency of 0.3% with high FF of 0.54. The low performance might attribute to the low dye absorption on the surface of ZnO due to the less uniformity of the thin film with low surface to volume ratio. Furthermore, a flower like structures comprised with nanorods/nanowires can be assumed to deliver a larger surface area and a direct pathway for electron transport with the channels arisen from the branched to nanrods/nanowire backbone. Recently, hydrothermally grown ZnO nanoflower films accomplished improved overall conversion efficiency of 1.9% with high J_{SC} of 5.5mA cm², and a fill factor of 0.53 (Jiang, et al., 2007) which is higher than nanorod arrays films based DSSC of the conversion efficiency 1.0%, J_{SC} 4.5 mA/cm², and FF 0.36.

7.2.5 Photoanodes with ZnO nanotubes

L. Vayssiers et al grown the ZnO microtubes arrays by thermal decomposition of a Zn^{2+} amino complex at 90°C in a regular laboratory oven (Vayssieres, et al., 2001). The synthesized ZnO microtubes arrays possessed a high porosity and large surface area as compared to ZnO NWs arrays. A. B. F. Martinson et al fabricated the ZnO nanotubes (NTs) arrays by coating anodic aluminum oxide (AAO) membranes via atomic layer deposition

(ALD) and constructed the DSSCs which showed a relatively low conversion efficiency of 1.6% due to the less roughness factor of commercial membranes (Martinson, et al., 2007). In continuity, Ameen et al reported the aligned ZnO NTs, grown at low temperature and applied as photoanode for the performances of DSSCs (Ameen, et al., 2011). The ZnO seeded FTO glass substrate supported the synthesis of highly densely aligned ZnO NTs whereas, non-seeded FTO substrates generated non-aligned ZnO NTs. The non-aligned ZnO NTs photoanode based fabricated DSSCs reported the low solar-to-electricity conversion efficiency of ~0.78%. However, DSSC fabricated with aligned ZnO NTs photoanode showed three times improved solar-to-electricity conversion efficiency than DSSC fabricated with non-aligned ZnO NTs. Fig. 19 shows the surface FESEM images of ZnO NTs deposited on non-seeded and ZnO seeded FTO substrates. Fig. 19 (a & b) exhibits the highly densely aligned ZnO NTs, substantially grown on ZnO seeded FTO substrates. Importantly, the ZnO NTs possess a hexagonal hollow structure with average inner and outer diameter of ~150nm and ~300 nm, respectively, as shown in Fig. 19 (c & d). However, non-seeded FTO substrates (Fig. 19 (e)) obtain the random and non-aligned morphology of NTs with the average diameter of 800 nm. The high resolution image clearly displays the typical hexagonal hollow and round end of the NTs (Fig. 19 (f)). Fig. 20(a) of TEM image reveals hollow NT morphology with the outer and inner diameter of ~250nm and ~100 nm, respectively. SAED patterns (Fig. 20 (c)) exhibits a single crystal with a wurtzite hexagonal phase which is preferentially grown in the [0001] direction. It is further confirmed from the HRTEM image of the grown ZnO NTs, presented in Fig. 20(b). HRTEM image shows well-resolved lattice fringes of crystalline ZnO NTs with the inter-planar spacing of ~0.52nm. Additionally, this value corresponds to the d-spacing of [0001] crystal planes of wurtzite ZnO. Thus, the synthesized ZnO NTs is a single crystal and preferentially grown along the c-axis [0001].

The XRD peaks (Fig 21 (a)) of grown aligned ZnO NTs on the seeded substrates appear at the same position but with high intensity might due to high crystalline properties of aligned morphology of ZnO NTs. The UV-Vis spectra as shown in Fig 21 (b)) exhibit a single peak which indicates that the grown ZnO NTs do not contain impurities. Moreover, the aligned morphology of ZnO NTs attains high absorption, indicating the higher crystalline properties than non-aligned ZnO NTs.

The Raman spectra of non- aligned and aligned ZnO NTs is shown in Fig 22 (a). The grown ZnO NTs exhibits a strong Raman peak at ~437cm^{-1} corresponds to E_2 mode of ZnO crystal and two small peaks at ~330cm^{-1} and ~578cm^{-1} are assigned to the second order Raman spectrum arising from zone-boundary phonons $3E_{2H}$–E_{2L} for wurtzite hexagonal ZnO single crystals and E_1 (LO) mode of ZnO associated with oxygen deficiency in ZnO nanomaterials respectively (Exarhas, et al., 1995). Compared to non-aligned ZnO NTs, the stronger E_2 mode and much lower E_1 (LO) mode indicates the presence of lower oxygen vacancy. The Raman active E_2 mode with high intensity and narrower spectral width is generally ascribed to the better optical and crystalline properties of the materials (Serrano, et al., 2003) and thus, the grown aligned ZnO NTs results high crystallinity of ZnO crystals with less oxygen vacancies. Fig 22 (b) depicts the PL spectra of grown non-aligned and aligned ZnO NTs. An intensive sharp UV emission at ~378nm and a broader green emission at ~581nm are attributed to the free exciton emission from the wide band gap of ZnO NTs and the recombination of electrons in single occupied oxygen vacancies in ZnO nanomaterials (Vanheusden, et al., 1996). The high intensity and less broaden green emission indicates that

the aligned ZnO NTs exhibits less oxygen vacancies and considerable stoichiometric phase structure formation. Thus, the PL spectra suggest that ZnO seeding on FTO substrates might improve surface-to-volume ratio and optical properties of ZnO NTs.
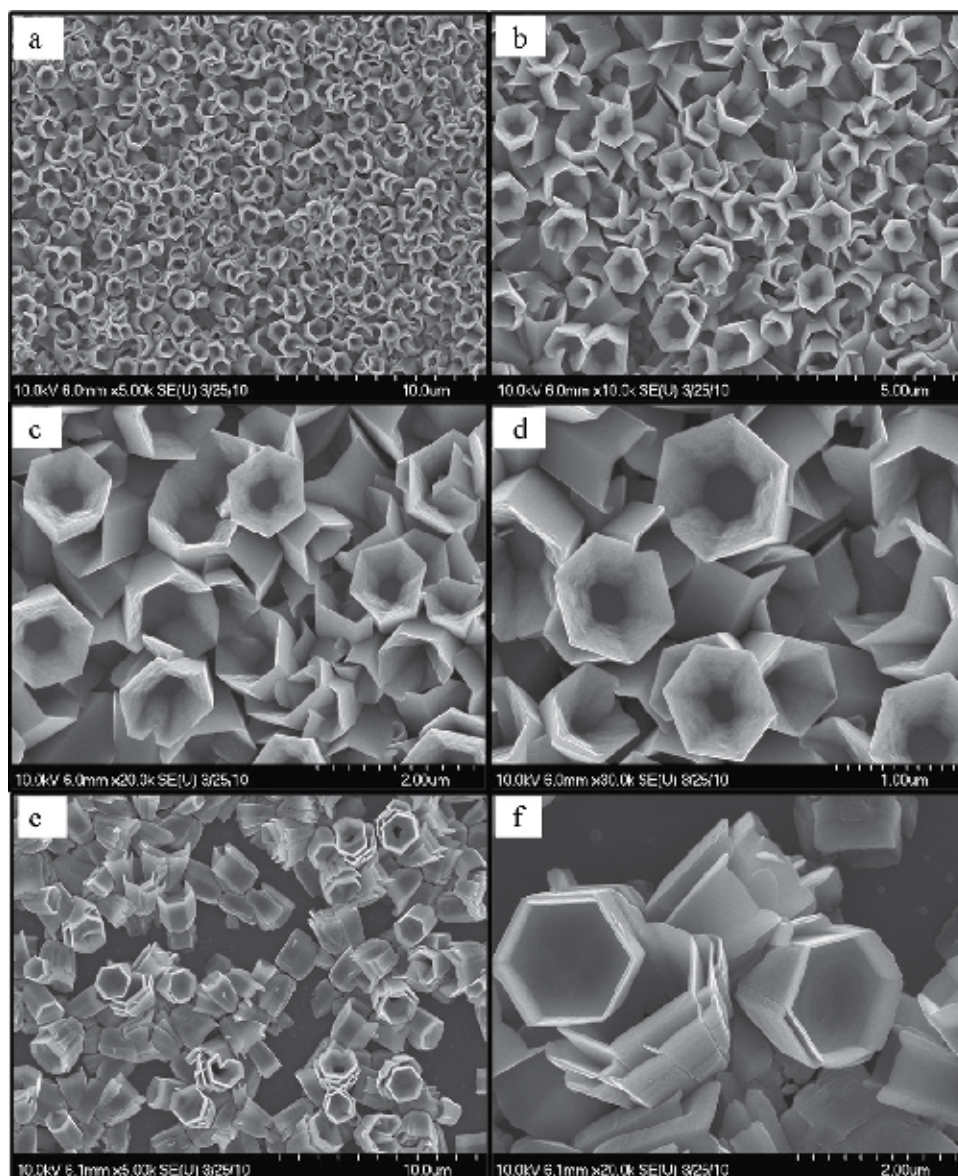
Fig. 19. FESEM images of aligned ZnO NTs (a) at low magnification and (b–d) at high magnification. (e) non-aligned ZnO NTs images at low magnification and (f) at high magnification. Reprinted with permission from [Ameen S. et al, 2011], Electrochim. Acta, 56 (2011) 1111. ©2011, Elsevier Ltd.
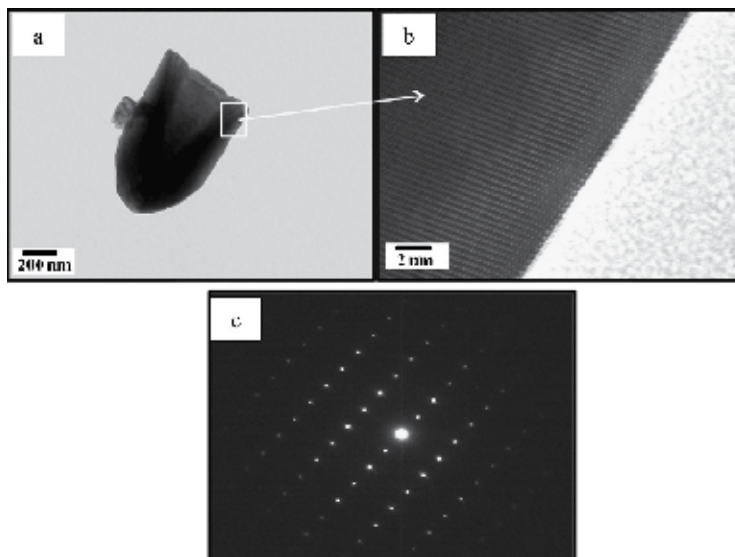
Fig. 20. (a) TEM, (b) HR-TEM and (c) corresponding SAED images of grown ZnO NTs.
Reprinted with permission from [Ameen S. et al, 2011], Electrochim. Acta, 56 (2011) 1111. ©
2011, Elsevier Ltd.
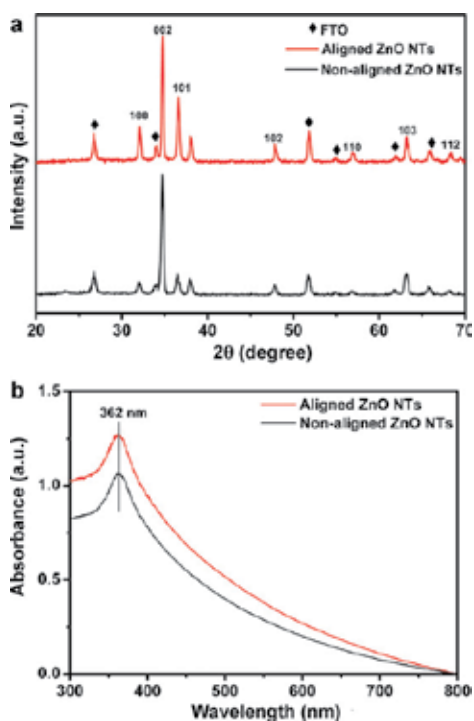
Fig. 21. (a) XRD pattern and (b) UV–Vis spectra of aligned and non-aligned ZnO NTs.
Reprinted with permission from [Ameen S. et al, 2011], Electrochim. Acta, 56 (2011) 1111. ©
2011, Elsevier Ltd.
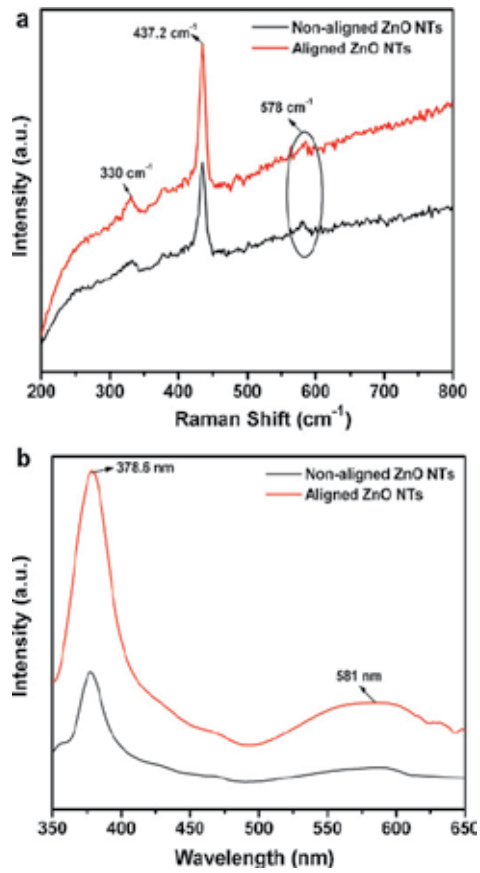
Fig. 22. (a) Raman spectra and (b) photoluminescence spectra of aligned and nonaligned
ZnO NTs. Reprinted with permission from [Ameen S. et al, 2011], Electrochim. Acta, 56
(2011) 1111. © 2011, Elsevier Ltd.
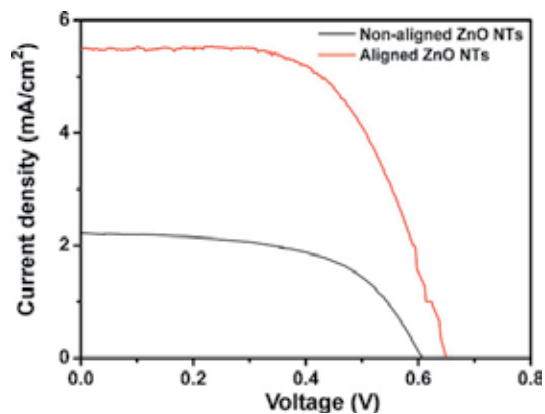
Fig. 23. J–V curve of the DSSCs fabricated with aligned and non-aligned ZnO NTs
photoanode. Reprinted with permission from [Ameen S. et al, 2011], Electrochim. Acta, 56
(2011) 1111. © 2011, Elsevier Ltd.
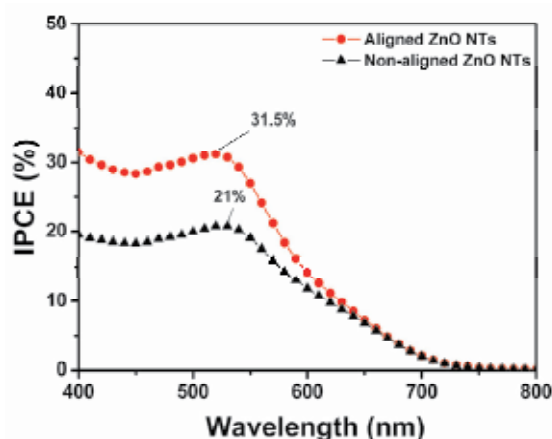
Fig. 24. IPCE curves of the DSSCs fabricated with aligned and non-aligned ZnO NTs photoanode. Reprinted with permission from [Ameen S. et al, 2011], Electrochim. Acta, 56 (2011) 1111. © 2011, Elsevier Ltd.

Fig 23 shows that DSSCs fabricated with aligned ZnO NTs photoanode achieve high solar-to-electricity conversion efficiency of 2.2% with a high short circuit current (J_{SC}) of 5.5 mA/cm^2, open circuit voltage (V_{OC}) of 0.65 V, and fill factor (FF) of 0.61. Compared with non-aligned ZnO NTs photoanode based DSSC, the aligned ZnO NTs photoanode has appreciably enhanced the conversion efficiency by three times with significantly improved J_{SC}, V_{OC} and FF. The DSSC fabricated with non-aligned ZnO NTs pho-to anode executes relatively low of 0.78 % with J_{SC} of 2.2mA/cm^2, V_{OC} (0.60 V) and FF of 0.57. The enhanced photovoltaic performances and the improved J_{SC} are mainly related to the highly dense morphology of aligned ZnO NTs and also, high dye absorption which leads to improved light harvesting efficiency. The aligned morphology might result from the sufficiently high surface area of ZnO NTs and thus, execute reasonably high charge collection and the transfer of electrons at the interface of ZnO NTs and electrolyte layer. While, low efficiency of non-aligned ZnO NTs might associate to low surface area of ZnO NTs and non-uniform surface which might result to low light harvesting efficiency and increases the recombination rate between the electrolyte and the FTO substrate. Ameen et al has reported that the performance of DSSCs with grown aligned ZnO NTs photoanode is significantly higher than the reported DSSCs with aligned ZnO nanorods, nanowires and nanotubes based photoanode (Pasquier, et al., 2006 & Singh, et al., 2010). Importantly, the aligned ZnO NTs based DSSC achieves a maximum IPCE value of ~31.5% at ~520nm as shown in Fig 24. The considerably low IPCE (~21%) is obtained with non-aligned ZnO NTs photoanode based DSSC and thus, the aligned ZnO NTs photoanode presents approximately two times improved IPCE compared to non-aligned ZnO NTs photoanode. The enhancement in IPCE imputes the influence of highly ordered aligned ZnO NTs morphology with high surface area which might improve the light scattering capacities and provides the better interaction between the photons and the dye molecules (Tachibana, et al., 2002).

8. Conclusions

The chapter summarizes the synthesis of PANI through simple and novel polymerization techniques, the concept of doping, types of dopants and the application of PANI in

heterostructure devices, diodes and DSSCs. Additionally, the recent surveys on various metal oxide nanomaterials nanomaterials have been thoroughly carried out in terms of their synthesis, morphology and applications in photovoltaic devices. The effective polymerization procedures for PANI particularly, electrophoretic and plasma enhanced deposition are the most promising techniques for optimizing the uniformity, penetration, thickness, electrical conductivity and form the uniform PANI thin films for the high performance and high quality of p-n heterostructure devices and diodes. The choices of dopants are crucial to define the conductive, electrical properties and performances of heterostructure devices such as diodes and DSSCs. The review analyzes various organic/inorganic acids as efficient dopants to enhance the conducting properties of PANI, which confirm that the electronic and optical properties of PANI could be easily controlled and tailored by the oxidizing/reducing agents and acid/base doping during the polymerization procedures. In the second part, the unique and the versatile properties of metal oxides nanostructures especially TiO_2 and ZnO show significant influences on the performances of electrical, electrochemical, and photovoltaic devices by delivering high surface to volume ratio for high absorption of dye molecules, which leads high light harvesting efficiency and increases the electron transfer as well as photocurrent density during the operation of DSSCs. Moreover, various sizes and shapes like nanorods, nanowires and nanotubes of metal oxides nanomaterials particularly TiO_2 and ZnO have been reviewed evidently in terms of morphology and the photovoltaic properties of DSSCs such as J_{SC}, V_{OC}, FF and conversion efficiency. Conclusively, the doping, and method of PANI deposition techniques improve the electrical conductivity and the electrocatalytic activity of the devices and exhibit the direct effect on the performances of DSSCs.

9. References

Grätzel, M., *Solar Energy Conversion by Dye-Sensitized Photovoltaic Cells*, Inorg. Chem., 44 (2005) 6841-6851.

Grätzel, M., *Conversion of sunlight to electric power by nanocrystalline dye-sensitized solar cells*, J. Photochem. Photobiol. A, 164 (2004) 1-14.

Frank, A. J., & Kopidakis, N., J. V. D. Lagemaat, *Electrons in nanostructured TiO₂ solar cells: transport, recombination and photovoltaic properties*, Coord., Chem. Rev., 248 (2004) 1165–1179.

Gratzel, M., *Perspectives for Dye-sensitized Nanocrystalline Solar Cells*, Prog. Photovolt. Res. Appl., 8 (2000) 171-185.

Huang, J., & Kaner, R. B., *The intrinsic nanofibrillar morphology of polyaniline*, Chem. Commun., (2006) 367-376.

Zhang, D., & Wang, Y., *Synthesis and applications of one-dimensionalnano-structured polyaniline: An overview*, Mater. Sci. Eng. B, 134 (2006) 9-19.

Wan, M., *A Template-Free Method Towards Conducting Polymer Nanostructures*, Adv. Mater., 20 (2008) 2926-2932.

Wan, M., *Some Issues Related to Polyaniline Micro-/Nanostructures*, Macromol. Rapid Commun., 30 (2009) 963-975.

Li, D., Huang, J., & Kaner, R.B., *Polyaniline Nanofibers: A Unique Polymer Nanostructure for Versatile Applications*, Acc. Chem. Res., 42 (2009)135-145.

Stejskal J. & Gilbert R. G., *Polyaniline. Preparation of a Conducting Polymer*, Pure Appl. Chem., 74 (2002) 857–867.

Friend, R. H., Gymer, R.W., & Holmes, A. B., *Electroluminescence in conjugated polymers*, Nature (London), 397 (1999) 121-128.

Park J. K. & Kwon O-P., *Enhanced electrical conductivity of polyaniline film by a low magnetic field*, Synth. Met. 160 (2010) 728-731.

Gerard, M., Chaubey, A., & Malhotra, B. D., *Application of conducting polymers to biosensors*, Biosensor Bioeleton., 17 (2002) 345-359.

Xia, L., Wei, Z., & Wan, M., *Conducting polymer nanostructures and their application in biosensors*, J. Coll. Interf. Sci., 341 (2010) 1-11.

Smith, J. D. S., *Intrinsically Electrically Conducting Polymers. Synthesis, Characterization and their Applications*, Prog. Polym. Sci., 23 (1998) 57-79.

Wessling, B., *From conductive polymers to organic metals*, Chem. Innov., 31 (2001) 34-40.

Cho, Y. H., Cho, M.S., Choi, H. J., & Jhon, M. S., *Electrorheological characterization of polyaniline-coated poly(methyl methacrylate)suspensions*, Colloid Polym. Sci., 280 (2002) 1062-1066.

Choi, H. J., Cho, M. S., Kim, J.W., Kim, C.A., & Jhon, M. S., *A yield stress scaling function for electrorheological fluids*, Appl. Phys. Lett., 78 (2001) 3806-3809.

Ameen, S., Akhtar, M. S., & Husain, M., *Polyaniline and Its Nanocomposites: Synthesis, Processing, Electrical Properties and Applications*, Sci. Adv. Mater., 2 (2010) 441-462.

Huang, J. X., Virji, S., Weiller, B. H., & Kaner, R.B., *Polyaniline Nanofibers: Facile Synthesis and Chemical Sensors*, J. Am. Chem. Soc., 125 (2003) 314-315.

Virji, S., Huang, J. X., Kaner, R. B., & Weiller, B. H., *Polyaniline Nanofiber Gas Sensors: Examination of Response Mechanisms*, Nano Lett., 4 (2004) 491-496.

King, R. C. Y., & Rousse, l. F., *Morphological and electrical characteristics of polyaniline nanifibers*, Synth. Met., 153 (2005) 337-340.

Huang, J. X., & Kaner, R. B., *A General Chemical Route to Polyaniline Nanofibers*, J. Am. Chem. Soc., 126 (2004) 851-855.

Jing, X. L., Wang, Y.Y., Wu, D., She, L., & Guo, Y., *Polyaniline Nanofibers Prepared with Ultrasonic Irradiation*, J. Polym. Sci., Part A: Polym. Chem., 44 (2006) 1014-1019.

Jing, X. L., Wang, Y. Y., Wu, D., & Qiang, J.P., *Sonochemical synthesis of polyaniline nanofibers*, Ultrason. Sonochem. 14 (2007) 75-80.

Dhaoui, W., Zarrouk, H., & Pron, A., *Spectroscopic properties of thin layers of sulfamic acid-doped polyaniline and their application to reagentless determination of nitrite*, Synth. Metals, 157 (2007) 564-569.

Dhaoui, W., Bouzitoun, M., Zarrouk, H., Ouada, H. B., & Pron, A., *Electrochemical sensor for nitrite determination based on thin films of sulfamic acid doped polyaniline deposited on Si/SiO_2 structures in electrolyte/insulator/semiconductor (E.I.S.) configuration*, Synth. Metals, 158 (2008) 722-726.

Ameen, S., Ali, V., Zulfequar, M., Haq, M. M., & Husain, M., *Electrical conductivity and dielectric properties of sulfamic acid doped polyaniline*, Curr. Appl. Phys., 7 (2007) 215-219.

Ameen, S., Akhtar, M. S., Kim, Y. S., Yang, O. B., & Shin, H. S., *Sulfamic Acid-Doped Polyaniline Nanofibers Thin Film-Based Counter Electrode: Application in Dye-Sensitized Solar Cells*, J. Phys. Chem. C, 114 (2010) 4760-4764.

Ameen, S., Ali, V., Zulfequar, M., Haq, M. M., & Husain, M., *Preparation and measurements of electrical and spectroscopic properties of sodium thiosulphate doped polyaniline*, Curr. Appl. Phys., 9 (2009) 478-483.

Ameen, S., Ali, V., Zulfequar, M., Haq, M. M., & Husain, M., *Photoluminescence, FTIR, and Electrical Characterization of Samarium (III) Chloride-Doped Polyaniline*, J. Appl. Polym. Sci., 112 (2009) 2315-2319.

Ameen, S., Ali, V., Zulfequar, M., Haq, M. M., & Husain, M., *Preparation and measurements of electrical and spectroscopic properties of praseodymium (III) chloride-doped polyaniline*, Physica E, 40 (2008) 2805-2809.

Ameen, S., Ali, V., Zulfequar, M. Haq, M. M., & Husain, M., *DC Conductivity and Spectroscopic Characterization of Binary Dopant (ZrO_2/AgI)-Doped Polyaniline*, J. Polym. Sci.: Part B: Polym. Phys., 45 (2007) 2682-2687.

Wang, S., Tan, Z., Li, Y., Sun, L., & Zhang, T., *Synthesis, characterization and thermal analysis of polyaniline/ZrO_2 composites*, Thermochim. Acta, 441 (2006) 191–194.

Ameen, S., Lakshmi, G. B. V. S., & Husain, M., *Synthesis and characterization of polyaniline prepared with the dopant mixture of (ZrO_2/PbI_2)*, J. Phys. D: Appl. Phys. 42 (2009) 105104-105109.

Ameen, S., Akhtar, M. S., Ansari, S. G., Yang, O. B., & Shin, H. S., *Electrophoretically deposited polyaniline/ZnO nanoparticles for p-n heterostructure diodes*, Superlatt. Microstr., 46 (2009) 872-880.

Ameen, S., Akhtar, M. S., Kim, Y.S., Yang, O. B., & Shin, H. S., *Diode Behavior of Electrophoretically Deposited Polyaniline on TiO2 Nanoparticulate Thin Film Electrode*, J. Nanosci. Nanotech., 11(2011) 1559-1564.

Somani, P. R., Marimuthu, R., Mulik, U. P., Sainkar, S. R., & Amalnerkar, D. P., *High piezoresistivity and its origin in conducting polyanilinerTiO2 Composites*, Synth. Met., 106 (1999) 45-52.

Niu, Z., Yang, Z., Hu, Z., Lu, Y., & Han, C. C., *Polyaniline-Silica Composite Conductive Capsules and Hollow Spheres*, Adv. Funct. Mater., 13 (2003) 949-954.

Ameen, S., Ansari, S. G., Song, M., Kim, Y. S., & Shin, H. S., *Fabrication of polyaniline/TiO_2 heterojunction structure using plasma enhanced polymerization technique*, Superlatt. Microstruc. 46 (2009) 745-751.

Ameen, S., Akhtar, M. S., Kim, Y. S., Yang, O. B., & Shin, H. S., *Electrical and Structural Characterization of Plasma Polymerized Polyaniline/TiO_2 Heterostructure Diode: A Comparative Study of Single and Bilayer TiO_2 Thin Film Electrode*, J. Nanosci. Nanotech. 11 (2011) 3306–3313.

Dhawale, D. S., Alunkhe, R. R. S., Patil, U. M., Gurav, K. V., More, A. M., & Lokhande, C. D., *Room temperature liquefied petroleum gas (LPG) sensor based on p-polyaniline/n-TiO_2 heterojunction*, Sens. Actua. B, 134 (2008) 988–992.

Nadarajah, A., Word, R. C., Meiss, J.,& Konenkamp, R., *Flexible Inorganic Nanowire Light-Emitting Diode*, Nano Lett., 8 (2008) 534-537.

Maeng, J., Jo, M., Kang, S. J., Kwon, M. K., Jo, G., Kim, T. W., Seo, J., Hwang, H., Kim D. Y.,& Park S. J., T. Lee. *Transient reverse current phenomenon in a p-n heterojunction comprised of poly (3,4-ethylene-dioxythiophene):poly(styrene-sulfonate) and ZnO nanowall*, Appl. Phys. Lett., 93 (2008) 123109-123111.

Thompson, B. C., & Frechet, J. M. J., *Polymer–Fullerene Composite Solar Cells*, Angew. Chem.-Int. Ed., 47(2008) 58-77.

Gunes, S., Neugebauer, H., & Sariciftci, N. S., *Conjugated Polymer-Based Organic Solar Cells*, Chem. Rev., 107(2007)1324-1338.

Bundgaard, E., & Krebs, F. C., *Low band gap polymers for organic photovoltaics,* Sol. Energy Mater. Sol. Cells, 91(2007) 954-985.

Shaw, P. E., Ruseckas, A., & Samuel, I. D. W., *Exciton Diffusion Measurements in Poly(3-hexylthiophene)*, Adv. Mater., 20 (2008) 3516-3520.

Sirringhaus, H., Brown, P. J., Friend, R. H., Nielsen, M. M., Bechgaard, K., Langeveld V. B. M. W., Spiering, A. J. H., Janssen, R. A. J., Meijer, E. W., Herwig, P., & Leeuw, D. M. D., *Two-dimensional charge transport in self-organized, high-mobility conjugated polymers*, Nature, 401(1999) 685-688.

Waldauf, C., Morana, M., Denk, P., Schilinsky, P., Coakley, K., Choulis, S. A., & Brabec, C. J., *Highly efficient inverted organic photovoltaics using solution based titanium oxide as electron selective contact*, Appl. Phys. Lett., 89 (2006) 233517-233519.

Steim, R., Kogler, F. R., & Brabec, C. J., *Interface materials for organic solar cells*, J. Mater. Chem., 20 (2010) 2499-2512.

Steim, R., Choulis, S. A., Schilinsky, P., & Brabec, C. J., *Interface modification for highly efficient organic photovoltaics*, Appl. Phys. Lett., 92 (2008) 093303-093305.

Ameri, T., Dennler, G., Lungenschmied, C., & Brabec, C. J., *Organic tandem solar cells: A review*, Ener. Environ. Sci., 2 (2009) 347-363.

Lee Y. J., Ruby, D. S., Peters, D.W., McKenzie, B. B., & Hsu, J. W. P., *ZnO Nanostructures as Efficient Antireflection Layers in Solar Cells*, Nano Lett., 8 (2008) 1501-1505.

Cantu, M. L., IddikiM, K. S, Rojas, D. M., Amade, R., & Pech, N. I. G., *Nb-TiO₂/polymer hybrid solar cells with photovoltaic response under inert atmosphere conditions*, Sol. Energy Mater. Sol. Cells, 94 (2010)1227-1234.

Cantu, M. L., Norrman, K., Andreasen, J.W., & Krebs, F.C., *Oxygen Release and Exchange in Niobium Oxide MEHPPV Hybrid Solar Cells*, Chem. Mater., 18 (2006) 5684-5690.

Cantu, M. L., Norrman, K., Andreasen, J.W., Pastor, N. C., & Krebs, F.C., *Detrimental Effect of Inert Atmospheres on Hybrid Solar Cells Based on Semiconductor Oxides*, J. Electrochem. Soc., 154 (2007) B508.

Cantu, M. L., & Krebs, F.C., *Hybrid solar cells based on MEH-PPV and thin film semiconductor oxides (TiO₂, Nb₂O₅, ZnO, CeO₂ and CeO₂–TiO₂): Performance improvement during long-time irradiation*, Sol. Energy Mater. Sol. Cells, 90 (2006) 2076-2086.

Valls, I. G., & Cantu, M. L., *Dye sensitized solar cells based on vertically-aligned ZnO nanorods: effect of UV light on power conversion efficiency and lifetime*, Ener. Environ. Sci., 3 (2010) 789-795.

Valls, I. G., & Cantu, M. L., *Vertically-aligned nanostructures of ZnO for excitonic solar cells: a review*, Ener. Environ. Sci., 2 (2009) 19-25.

Arici, E., Meissner, D., Schaffler, F., & Sariciftci, N.S., *Core/shell nanomaterials in photovoltaics*, Int. J. Photoenergy, 5 (2003) 199-208.

Sariciftci, N.S., Smilowitz, L., Heeger, A. J., & Wudl, F., *Photoinduced Electron Transfer from a Conducting Polymer to Buckminsterfullerene*, Science, 258 (1992) 1474-1476.

Yu, G., Gao, J., Hummelen, J.C., Wudl, F., & Heeger, A.J., *Polymer Photovoltaic Cells: Enhanced Efficiencies via a Network of Internal Donor-Acceptor Heterojunctions*, Science, 270 (1995) 1789-1791.

Ameen, S., Akhtar, M. S., Kim, G.S., Kim, Y. S., Yang, O. B., & Shin, H. S., *Plasma-enhanced polymerized aniline/TiO₂ dye-sensitized solar cells*, J. Alloys Compd., 487 (2009) 382-386.

Saito, Y., Kitamura, T., Wada, Y., & Yanagida, S., *Application of Poly (3,4-ethylenedioxythiophene) to Counter Electrode in Dye-Sensitized Solar Cells*, Chem. Lett. 31 (2002) 1060-1063., Y. Saito, W. Kubo, T. Kitamura, Y. Wada, S. Yanagida, *I⁻/I₃⁻ redox reaction behavior on poly(3,4-ethylenedioxythiophene) counter electrode in dye-sensitized solar cells*, J. Photochem. Photobiol. A. Chem. 164 (2004) 153-157.

Li, Q., Wu, J., Tang, Q., Lan, Z., Li, P., Lin, J., & Fan, L., *Application of microporous polyaniline counter electrode for dye-sensitized solar cells*, Electrochem. Commun. 10 (2008) 1299-1302.

Wu, J., Li, Q., Fan, L., Lan, Z., Li, P., Lin, J., & Hao, S., *High-performance polypyrrole nanoparticles counter electrode for dye-sensitized solar cells*, J. Power Sour. 181 (2008) 172-176.

Lee, K. M., Chen, P. Y., Hsu, C. Y., Huang, J. H., Ho, W. H., Chen, H. C., & Ho, K. C., *A high-performance counter electrode based on poly(3,4-alkylenedioxythiophene) for dye-sensitized solar cells*, J. Power Sour. 188 (2009) 313-318.

Zhang, J., Hreid, T., Li, X., Guo, W., Wang, L., Shi, X., Su, H., & Yuan, Z., *Nanostructured polyaniline counter electrode for dye-sensitised solar cells: Fabrication and investigation of its electrochemical formation mechanism*, Electrochim. Acta, 55 (2010) 3664–3668.

Baxtera, J. B., & Aydil, E. S., *Dye-sensitized solar cells based on semiconductor morphologies with ZnO nanowires*, Sol. Energy Mater. Sol. Cells, 90 (2006) 607-622.

Ito, S., Murakami, T. N., Comte, P., Liska, P., Grätzel, C., & Nazeeruddin, M. K., *Fabrication of thin film dye sensitized solar cells with solar to electric power conversion efficiency over 10%*, Thin Solid Films, 14 (2008) 4613-4619.

Law, M., Greene, L. E., Johnson, J.C., Saykally, R., & Yang, P.D., *Nanowire dye-sensitized solar cells*, Nat. Mater., 6 (2005) 455-459.

Feng, X. J, Shankar, K., Varghese, O. K., Paulose, M., Latempa, T. J., & Grimes, C. A., *Vertically Aligned Single Crystal TiO$_2$ Nanowire Arrays Grown Directly on Transparent Conducting Oxide Coated Glass: Synthesis Details and Applications*, Nano Lett., 11(2008)3781-3786.

Macak, J. M., Tsuchiya, H., & Schmuki, P., *High-Aspect-Ratio TiO$_2$ Nanotubes by Anodization of Titanium,* Angew. Chem. Int Ed, 14 (2005) 2100-2102.

Mor, G. K., Shankar, K., Paulose, M., Varghese, O. K., & Grimes, C. A., *Enhanced Photocleavage of Water Using Titania Nanotube Arrays*, Nano Lett., 1 (2005) 191-195.

Zhang, D. S., Yoshida, T., & Minoura, H., *Low-Temperature Fabrication of Efficient Porous Titania Photoelectrodes by Hydrothermal Crystallization at the Solid/Gas Interface*, Adv Mater., 10 (2003) 814-817.

Wang, H., Liu, Y., Li, M., Huang, H., Zhong, M.Y., & Shen, H., *Hydrothermal growth of large-scale macroporous TiO$_2$ nanowires and its application in 3D dye-sensitized solar cells*, Appl. Phys. A, 97 (2009) 25-29.

Ren, X., Gershon, T., Iza, D. C, Rojas, D. M., Musselman, K., & Driscoll, J. L. M., *The selective fabrication of large-area highly ordered TiO$_2$ nanorod and nanotube arrays on conductive transparent substrates via sol–gel electrophoresis*, Nanotechnology, 36 (2009) 365604-9.

Tan, L. K., Chong, M. A. S., & Gao, H., *Free-Standing Porous Anodic Alumina Templates for Atomic Layer Deposition of Highly Ordered TiO$_2$ Nanotube Arrays on Various Substrates*, J. Phys. Chem. C, 112 (2008) 69-73.

Tsai, T.Y., & Lu, S.Y., *A novel way of improving light harvesting in dye-sensitized solar cells – Electrodeposition of titania*, Electrochem. Commun., 11 (2009) 2180-2183.

Chen, Q.W., & Xu, D.S., *Large-Scale, Noncurling, and Free-Standing Crystallized TiO$_2$ Nanotube Arrays for Dye-Sensitized Solar Cells*, J. Phys. Chem. C, 113 (2009) 6310-6314.

Kang, T. S., Smith, A. P., Taylor, B. E., & Durstock, M. F., *Fabrication of highly-ordered TiO$_2$ nanotube arrays and their use in dye-sensitized solar cells*, Nano. Lett., 9 (2009) 601-606.

Regan, B. O., & Graetzel, M., *A low-cost, high-efficiency solar cell based on dye-sensitized colloidal TiO$_2$ films*, Nature, 353 (1991) 737-740.

Duffie, J., & Beckman, W., Solar Engineering of Thermal Processes. Wiley: U.S.A., 1991

Graetzel, M., *Photoelectrochemical cells*, Nature, 414 (2001) 338-344.

Zwilling, V., Aucouturier, M., & Ceretti, E. D., *Anodic oxidation of titanium and TA6V alloy in chromic media. An electrochemical approach*, Electrochem. Acta, 45 (1999) 921-929.

Gong, D., Grimes, C. A., Varghese, O. K., Hu, W., Singh, R. S., Chen, Z., & Dickey E.C., *Titanium oxide nanotube arrays prepared by anodic oxidation*, J. Mater. Res., 16 (2001) 3331-3334.

Guo, Y. G., Hu, J. S., Liang, H. P., Wan, L. J., & Bai, C.L., *TiO2-Based Composite Nanotube Arrays Prepared via Layer-by-Layer Assembly*, Adv. Funct. Mater., 15 (2005) 196.

Martin, C. R., *Nanomaterials: A Membrane-Based Synthetic Approach*, Science, 266 (1994) 1961-1966.

Limmer, S. J., Seraji, S., Wu, Y., Chou, T. P., Nguyen, C., & Cao, G. Z., *Template-Based Growth of Various Oxide Nanorods by Sol–Gel Electrophoresis*, Adv. Funct. Mater., 12 (2002) 59-64.

Lakshmi, B. B., Dorhout, P. K., & Martin, C. R., *Sol−Gel Template Synthesis of Semiconductor Nanostructures,* Chem. Mater., 9 (1997) 857-862.

Park, J. H., Lee, T.W., & Kang, M.G., *Growth, detachment and transfer of highly-ordered TiO2 nanotube arrays: use in dye-sensitized solar cells*, Chem. Commun., (2008) 2867-2869.

Jiu, J., Isoda, S., Wang, F., & Adachi, M., *Dye-Sensitized Solar Cells Based on a Single-Crystalline TiO2 Nanorod Film*, J. Phys. Chem. B, 110 (2006) 2087-2092.

Liu, B., & Aydil, E. S., *Growth of Oriented Single-Crystalline Rutile TiO2 Nanorods on Transparent Conducting Substrates for Dye-Sensitized Solar Cells*, J. Am. Chem. Soc., 131(2009) 3985-3990.

Oh, J. K., Lee, J. K., Kim, H.S., Han, S. B., & Park, K.W., *TiO2 Branched Nanostructure Electrodes Synthesized by Seeding Method for Dye-Sensitized Solar Cells*, Chem. Mater., 22 (2010) 1114-1118.

Spanhel, L., & Anderson, M. A., *Semiconductor clusters in the sol-gel process: quantized aggregation, gelation, and crystal growth in concentrated zinc oxide colloids,* J. Am. Chem. Soc., 113(1991) 2826-2833.

Keis, K., Vayssieres, L., Rensmo, H., Lindquist, S. E., & Hagfeldt, A., *Photoelectrochemical properties of nano-to microstructured ZnO electrodes*, J. Electrochem. Soc., 148 (2001) A149-153.

Redmond, G., Fitzmaurice, D., & Graetzel, M., *Visible Light Sensitization by cis-Bis(thiocyanato)bis(2,2'-bipyridyl-4,4'-dicarboxylato)ruthenium (II) of a Transparent Nanocrystalline ZnO Film Prepared by Sol-Gel Techniques*, Chem. Mater., 6(1994) 686-691.

Rani, S., Suri, P., Shishodia, P. K., & Mehra, R. M., *Synthesis of nanocrystalline ZnO powder via sol–gel route for dye-sensitized solar cells*, Sol. Energ. Mat. Sol. C, 92 (2008) 1639-1645.

Zeng, L. Y., Dai, S. Y., Xu, W. W., & Wang, K. J., *Dye-Sensitized Solar Cells Based on ZnO Films*, Plasma Sci. Tech., 8 (2006) 172-176.

Keis, K., Bauer, C., Boschloo, G., Hagfeldt, A., Westermark, K., Rensmo, H., & Siegbahn, H., *Nanostructured ZnO electrodes for dye-sensitized solar cell applications*, J. Photochem. Photobiol. A: Chem., 148(2002) 57-64.

Keis, K., Magnusson, E., Lindstrom, H., Lindquist, S. E., & Hagfeldt, A., *A 5% efficient photoelectrochemical solar cell based on nanostructured ZnO electrodes*, Sol. Energ. Mat. Sol. Cells, 73(2002) 51-58.

Suliman, A. E., Tang, Y. W., & Xu, L., *Preparation of ZnO nanoparticles and nanosheets and their application to dye-sensitized solar cells*, Sol. Energ. Mat. Sol. Cells, 91(2007) 1658-1662.

Akhtar, M. S., Khan, M. A., Jeon, M. S., & Yang, O. B., *Controlled synthesis of various ZnO nanostructured materials by capping agents-assisted hydrothermal method for dye-sensitized solar cells*, Electrochim. Acta, 53(2008) 7869-7874.

Lin, C. F., Lin, H., Li, J. B., & Li, X., *Electrodeposition preparation of ZnO nanobelt array films and application to dye-sensitized solar cells*, J. Alloys Compd., 462 (2008)175-180

Hsu, Y. F., Xi, Y. Y., Yip, C. T., Djurisic, A. B., & Chan, W. K., *Dye-sensitized solar cells using ZnO tetrapods*, J. Appl. Phys., 103(2008) 083114-083117.

Chen, W., Zhang, H. F., Hsing, I. M., & Yang, S. H., *A new photoanode architecture of dye sensitized solar cell based on ZnO nanotetrapods with no need for calcination*, Electrochem. Commun., 11(2009) 1057-1060.

Law, M., Greene, L. E., Johnson, J. C., Saykally, R., & Yang, P. D., *Nanowire dye-sensitized solar cells*, Nat. Mater., 4 (2005) 455-459.

Greene, L. E., Yuhas, B. D., Law, M., Zitoun, D., & Yang, P. D., *Solution-Grown Zinc Oxide Nanowires*, Inorg. Chem., 45(2006) 7535-7543.

Gao, Y. F., Nagai, M., Chang, T. C., & Shyue, J. J., *Solution-Derived ZnO Nanowire Array Film as Photoelectrode in Dye-Sensitized Solar Cells*, Cryst. Grow. Des. 7 (2007) 2467-2471.

Jiang, C. Y., Sun, X. W., Tan, K. W., Lo, G. Q., Kyaw, A. K. K., & Kwong, D. L., *High-bendability flexible dye-sensitized solar cell with a nanoparticle-modified ZnO-nanowire electrode*, Appl. Phy. Lett., 92(2008) 143101-143103.

Cheng, A. J., Tzeng, Y., Zhou, Y., Park, M., Wu, T.H., Shannon, C., Wang, D., & Lee, W., *Thermal chemical vapor deposition growth of zinc oxide nanostructures for dye-sensitized solar cell fabrication*, Appl. Phys. Lett., 92 (2008) 092113-092115

Umar, A., Al-Hajry, A., Hahn, Y.B., & Kim, D.H., *Rapid synthesis and dye-sensitized solar cell applications of hexagonal-shaped ZnO nanorods*, Electrochim. Acta, 54 (2009) 5358-5362.

Jiang, C. Y., Sun, X. W., Lo, G. Q., Kwong, D. L., & Wang, J. X., *Improved dye-sensitized solar cells with a ZnO-nanoflower photoanode*, Appl. Phy. Lett. 2007, 90, 263501-263503.

Vayssieres, L., Keis, K., Hagfeldt, A., & Lindquist, S. E., *Three-Dimensional Array of Highly Oriented Crystalline ZnO Microtubes*, Chem. Mater., 13(2001) 4395-4398.

Martinson, A. B. F., Elam, J. W., Hupp, J. T., & Pellin, M. J., *ZnO Nanotube Based Dye-Sensitized Solar Cells*, Nano Lett., 7(2007) 2183-2187.

Ameen, S., Akhtar, M. S., Kim, Y.S., Yang, O. B., & Shin, H. S., *Influence of seed layer treatment on low temperature grown ZnO nanotubes: Performances in dye sensitized solar cells*, Electrochim. Acta, 56 (2011) 1111-1116.

Exarhos, G. J., & Harma, S. K. S, *Influence of processing variables on the structure and properties of ZnO films*, Thin Solid Films, 270 (1995) 27-32.

Serrano, J., Manjon, F. J., Romero, A. H., Widulle, F., Lauck, R., & Cardona, M., *Dispersive Phonon Linewidths: The E_2 Phonons of ZnO*, Phys. Rev. Lett., 90 (2003) 055510-0555113.

Vanheusden, K., Warren, W. L., Seager, C. H., Tallant, D. R., Voigt, J. A., & Gnade, B.E., *Mechanisms behind green photoluminescence in ZnO phosphor powders*, J. Appl. Phys., 79 (1996) 7983-7990.

Pasquier, A. D., Chen, H., & Lu, Y., *Dye sensitized solar cells using well-aligned zinc oxide nanotip arrays*, Appl. Phys. Lett., 89 (2006) 253513-253515.

Singh, D. P., *Synthesis and Growth of ZnO Nanowires*, Sci. Adv. Mater., 2 (2010) 245-271.

Tachibana, Y., Hara, K., Sayama, K., & Arakawa, H., *Quantitative Analysis of Light-Harvesting Efficiency and Electron-Transfer Yield in Ruthenium-Dye-Sensitized Nanocrystalline TiO_2 Solar Cells*, Chem. Mater., 14 (2002) 2527-2535.

6

Dye Sensitized Solar Cells Principles and New Design

Yang Jiao, Fan Zhang and Sheng Meng
Beijing National Laboratory for Condensed Matter Physics and Institute of Physics, Chinese Academy of Sciences, Beijing China

1. Introduction

It is generally believed that fossil fuels, the current primary but limited energy resources, will be replaced by cleaner and cheaper renewable energy sources for compelling environmental and economic challenges in the 21st century. Solar energy with its unlimited quantity is expected to be one of the most promising alternative energy sources in the future. Devices with low manufacturing cost and high efficiency are therefore a necessity for sunlight capture and light-to-energy conversion.

The dye-sensitized solar cell (DSSC), invented by Professor M. Grätzel in 1991 (O'Regan & Grätzel, 1991), is a most promising inexpensive route toward sunlight harvesting. DSSC uses dye molecules adsorbed on the nanocrystalline oxide semiconductors such as TiO_2 to collect sunlight. Therefore the light absorption (by dyes) and charge collection processes (by semiconductors) are separated, mimicking the natural light harvest in photosynthesis. It enables us to use very cheap, wide band-gap oxide semiconductors in solar cells, instead of expensive Si or III-V group semiconductors. As a result, much cheaper solar energy at $1 or less per peak Watt ($1/pW) can be achieved. For comparison, the dominant crystalline or thin-film Si solar cells have a price of >$4-5/pW presently and are suffering from the world-wide Si shortage. The fabrication energy for a DSSC is also significantly lower, 40% of that for a Si cell.

In this book chapter, we will present the principles of DSSC and detail the materials employed in a DSSC device in section 2. In section 3, the fabrication processes are shown. Then we discuss the energy conversion mechanism at the microscopic level in section 4. After this we try to give new design of the dye molecule and adsorption anchoring configurations to give hints on improving the energy conversion efficiency and making more stable devices in section 5. At last we present our conclusion and perspectives.

2. Principles of dye sensitized solar cells

2.1 Components

The current DSSC design involves a set of different layers of components stacked in serial, including glass substrate, transparent conducting layer, TiO_2 nanoparticles, dyes, electrolyte, and counter electrode covered with sealing gasket. The typical configuration is shown in Fig. 1.
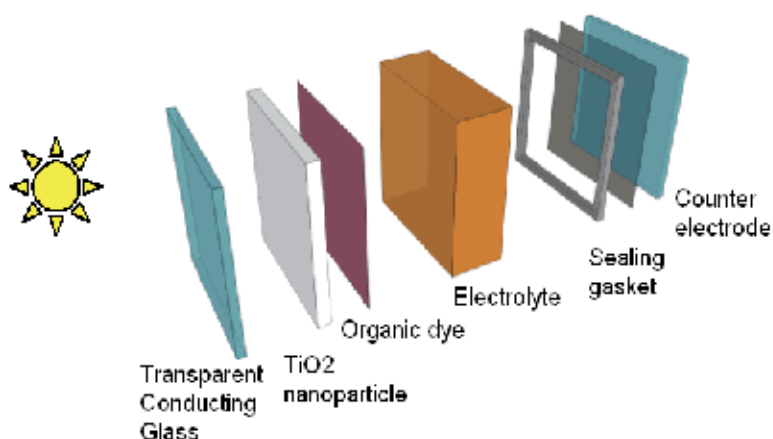
Fig. 1. Typical configuration of a DSSC.

2.1.1 Transparent conducting glass

In the front of the DSSC there is a layer of glass substrate, on top of which covers a thin layer of transparent conducting layer. This layer is crucial since it allows sunlight penetrating into the cell while conducting electron carriers to outer circuit. Transparent Conductive Oxide (TCO) substrates are adopted, including F-doped or In-doped tin oxide (FTO or ITO) and Aluminum-doped zinc oxide (AZO), which satisfy both requirements. ITO performs best among all TCO substrates. However, because ITO contains rare, toxic and expensive metal materials, some research groups replace ITO with FTO. AZO thin films are also widely studied because the materials are cheap, nontoxic and easy to obtain. The properties of typical types of ITO and FTO from some renowned manufacturers are shown in Table 1.

Conductive glass	Company	Light transmittance	Conductivity (Ohm/sq)	Thickness (mm)	Size (cm×cm)
ITO	Nanocs	>85%	5	1.1	1x3
ITO	PG&O	85%	4.5	1.1	2×3
FTO	NSG	>84%	<7	3	100×100

Table 1. Properties of a few types of commercial ITO and FTO materials.

2.1.2 TiO$_2$ nanoparticles

DSSC has a low efficiency less than 1% until Professor Grätzel employs porous TiO$_2$ as the anode material. Usually a layer of negatively doped TiO$_2$ (n-TiO$_2$) nanoparticles is used. The advantages of TiO$_2$ include high photosensitivity, high structure stability under solar irradiation and in solutions, and low cost. The typical particle size is 8-30 nm in diameter, and the TiO$_2$ films thickness is 2-20 μm, with the maximum efficiency located at a thickness of 12-14μm depending on dyes and electrolyte chosen (Ito et al., 2008). However, as a wide bandgap semiconductor (~3.2 eV), TiO$_2$ absorbs only UV light, which comprises only a small fraction (~5%) of solar spectrum. As a result, dye molecules are employed for visible light capture. Only nanocrystalline TiO$_2$ provides high light capture efficiency, with external

quantum efficiency (incident photon-to-charge efficiency) typically in the range of 60-90% using nanocrystal forms in comparison with <0.13% using the monocrystal form (Grätzel, 2005). The reason lies in the high surface-to-volume ratios for porous nanocrystal materials.
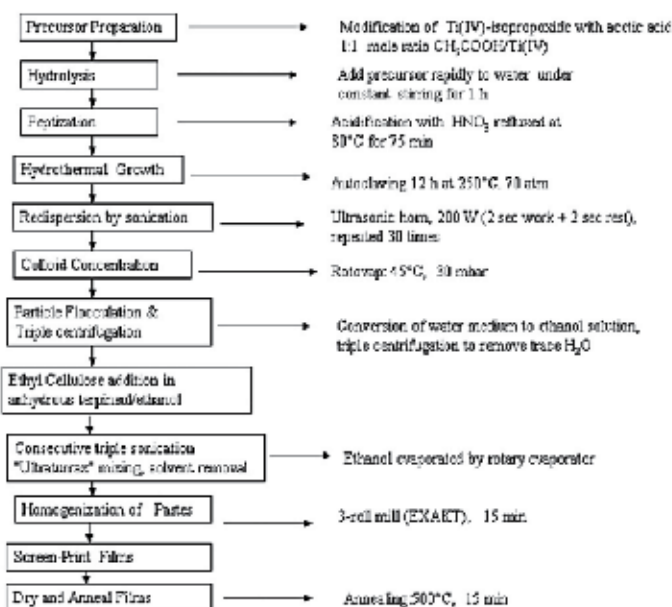
Scheme 1. Flow diagram depicting preparation of TiO$_2$ colloid and paste used in screen-printing technique for DSSC production. Adopted from (Ito et al., 2008). Copyright: 2007 Elsevier B. V.

2.1.3 Dyes

Dye molecules are the key component of a DSSC to have an increased efficiency through their abilities to absorb visible light photons. Early DSSC designs involved transition metal coordinated compounds (e.g., ruthenium polypyridyl complexes) as sensitizers because of their strong visible absorption, long excitation lifetime and efficient metal-to-ligand charge transfer (O'Regan & Grätzel, 1991; Grätzel, 2005; Ito et al., 2008). However, high cost of Ru dyes (>$1,000/g) is one important factor hindering the large-scale implementation of DSSC. Although highly effective, with current maximum efficiency of 11% (Grätzel, 2005), the costly synthesis and undesired environmental impact of those prototypes call for cheaper, simpler, and safer dyes as alternatives.

Organic dyes, including natural pigments and synthetic organic dyes, have a donor-acceptor structure called as push-pull architecture, thus improving short circuit current density by improving the absorption in red and infrared region. Natural pigments, like chlorophyll, carotene, and anthocyanin, are freely available in plant leaves, flowers, and fruits and fulfill these requirements. Experimentally, natural-dye sensitized TiO$_2$ solar cells have reached an efficiency of 7.1% and high stability (Campbell et al., 2007).

Even more promising is the synthetic organic dyes. Various types have recently been developed, including indolic dyes (D102, D149) (Konno et al., 2007), and cyanoacrylic acids (JK, C209). The same as some natural dyes, they are not associated with any metal ions,

being environmental benign and easily synthesized from abundant resources on a large scale. The efficiency has reached a high level of 10.0-10.3% (Zeng et al., 2010). They are relatively cheap, at the cost of one-tenth of corresponding Ru dyes. Light soaking experiments have confirmed they possess long-time stability: 80% efficiency has been maintained after 1,200 hours of light-soaking at 60 °C (~5 million turnovers). The commercialized production of these synthetic dyes has been established in China this year. A single dye usually has a limited adsorption spectrum, so some research groups use several kinds of dyes to relay energy transfer and compensate each other and have achieved good results (Hardin et al., 2010).

2.1.4 Electrolyte

Currently three different kinds of electrolytes have been used in real DSSCs with pros and cons of each kind: (i) the most common electrolyte is I^-/I_3^- in organic solvents, such as acetonitrile. Sometimes lithium ion is added to facilitate electron transport. This kind of electrolyte is good for ion diffusion and infiltrate well with TiO_2 film, keeping highest efficiency of all DSSCs. But limited long-term stability due to volatilization of liquid hinders its wide use. (ii) Inorganic ionic liquids made of salts or salt mixture. It looks like solid while it has properties of liquid and it performs well in conductivity. But after a long period of time, its efficiency declines. (iii) Solid electrolyte, such as spiro-MeOTAD or CuI (Konno et al., 2007). For CuI, its instability and crystallization makes it hard to fill in the porous TiO_2 films. The problem can be solved by adding ionic liquid into the electrolyte. Spiro-MeOTAD is a typical kind of organic hole conductor, which has been developed for years and the DSSC based on this kind of electrolyte has reached the efficiency of 5% (Yu et al., 2009).
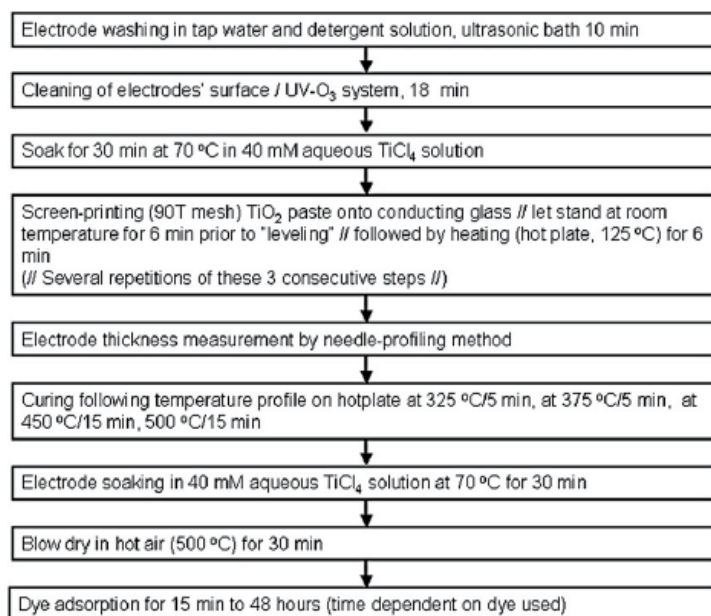
Scheme 2. Schematic representation for fabrication of dye-sensitized-TiO_2 electrodes. Adopted from (Ito et al., 2008). Copyright: 2007 Elsevier B. V.

2.1.5 Counter electrode

On the back of the DSSC there presents another glass substrate covered with a thin layer of Pt used as the catalyst to regenerate I- and as the cathode material. Pt is the best material to make efficient devices technically. But considering high expenses, carbon cathode has been an ideal substitute, such as carbon black, carbon nanotubes etc. In 2006, Grätzel's group employs carbon black as the material of counter electrode, and reaches an efficiency of 9.1%, which is 83% of that using Pt (Yu et al., 2009).

Conducting polymers can also be used. Polyaniline film on stainless steel by electrochemical polymerization bas been reported as a counter electrode of DSSC (Qin et al., 2010). It is cheap and non-fragile.

2.2 Fabrication

In this section, we introduce Grätzel's new fabrication technologies for DSSCs having a conversion efficiency of solar light to electricity power over 10% (Ito et al., 2008). It consists of pre-treatment of the working photoelectrode by TiCl$_4$, variations in layer thickness of the transparent nanocrystalline-TiO$_2$ and applying a topcoat light-scattering layer as well as the adhesion of an anti-reflecting film to the electrode's surface.

First, one prepares glass substrate with a transparent conducting layer. Then, the DSSC working electrodes are prepared as shown in Scheme 1 & 2. Scheme 1 depicts procedures to produce paste (A) containing 20 nm nanocrystalline TiO$_2$ particles. For the paste used in the light-scattering layers (paste B), 10nm TiO$_2$ particles which were obtained following the peptization step and in a procedure analogous to those of 20 nm TiO$_2$ outlined in Scheme 1, were mixed with 400 nm TiO$_2$ colloidal solution. Paste A and B are coated on FTO, forming the TiO$_2$ "double layer" film. It is treated with TiCl$_4$ before sintering. After cooling, the electrode is immersed in dye solutions.

Finishing fabrication of all parts, the dye-covered TiO$_2$ electrode and Pt-counter electrode are assembled into a sandwich type cell and sealed with a hot-melt gasket. For the counter electrode, a hole (1-mm diameter) is drilled in the FTO glass. The hole is made to let the electrolyte in via vacuum backfilling. After the injection of electrolyte, the hole is sealed using a hot-melt ionomer film and a cover glass as shown in Fig. 2.
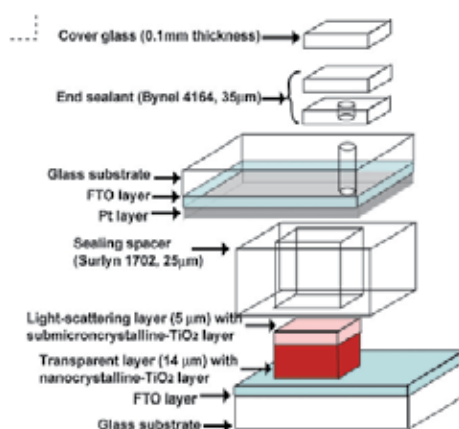
Fig. 2. Fabrication of the dye sensitized solar cells. Adopted from (Ito et al., 2008). Copyright: 2007 Elsevier B. V.

3. Processes

The way that DSSC works is quite simple, shown by the scheme in Fig. 3. The central idea is to separate the light absorption process from the charge collection process, mimicking natural light harvesting procedures in photosynthesis, by combining dye sensitizers with semiconductors. For most DSSC devices, the I^-/I_3^- couple is often used as a redox shuttle.

3.1 Sunlight absorption and electronic excitation

Photons of different energy in sunlight strike on the cell, penetrating into the dye layer since both the ITO layer with glass substrate and the TiO_2 nanocrystals are transparent to visible light. If photon energy is close to the energy gap of the dye molecule, namely, the energy difference between the highest occupied molecular orbital (HOMO) and lowest unoccupied molecular orbital (LUMO), it will be absorbed by the dye, promoting one electron from HOMO to LUMO. To be effective, usually it requires HOMO of the dye to reside in the bandgap of the semiconductor, and the LUMO to lie within the conduction band of the semiconductor. But this is not always true. Meng and collaborators have shown that electrons can be injected from cyanin dyes to the TiO_2 nanowire within 50 fs after excitation, although the dye LUMO is originally lower than the TiO_2 conduction band minimum (CBM) by 0.1-0.3 eV (Meng et al., 2008). This extends the current understanding of the mechanisms of DSSC operation and thus can enhance the ability to optimize their design and efficiency.
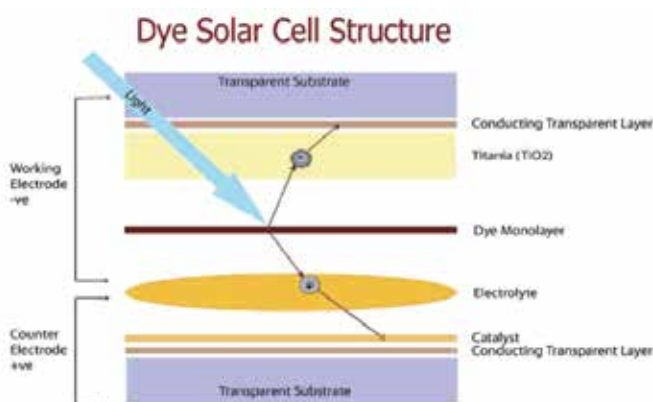
Fig. 3. Schematic illustration of the operation principle for molecular photovoltaic cell. Adopted from (Grätzel, 2009) Copyright: 1991 Nature Publishing Group.

3.2 Electron-hole separation, electron injection and collection

The excited electron will then inject into the conduction band of semiconductor through the interfacial bonds between the dye and the TiO_2, and then be transported and finally collected by the ITO electrode (the anode). On the other hand, the hole generated by photon excitation remains on the molecule during this process, since the HOMO of dye is separated from all other energy levels of the device.

3.3 Redox reaction at dye/electrolyte interface, and at counter electrode

There is no energy channels for the hole to diffuse into TiO_2 photoanode. As a result, the hole is eventually filled up by electrons from electrolyte ions, which conduct current

between the cathode and the dye molecule. At the same time, reduction of oxidized dye by iodide produces triiodide. The triiodide diffuses to counter electrode and accepts electrons from external load, regenerating the iodides. The overall process will provide electron flow from the ITO side (anode) to the outer circuit, with the potential difference equals to the incident photon energy if no voltage loss occurs during electron injection, diffusion and the neutral dye regeneration. In reality, however, these processes are always present. So the anode-cathode potential difference, namely, the open-circuit voltage Voc, is mainly determined by the difference between conduction band bottom and electrolyte anion energy level, typically around 0.6-0.9 V.

3.4 Recombination

In all solar cells, the light generated carriers have a probability to meet their conjugate carriers and recombine. Recombination reduces the output of electrical power in DSSC. The photo injected electrons in the TiO_2 have two possible recombination pathways: direct recombination with the oxidized dyes or with the I_3^- in the electrolyte (Haque et al., 2005), which are shown in Fig. 4. The latter process is dominant and has been thoroughly studied. It can be reduced by adding a thin TiO_2 under-layer between the FTO and the nanocrystalline porous TiO_2 layer, because the connection between the FTO and the electrolyte is an important recombination route (Liu et al., 2006).
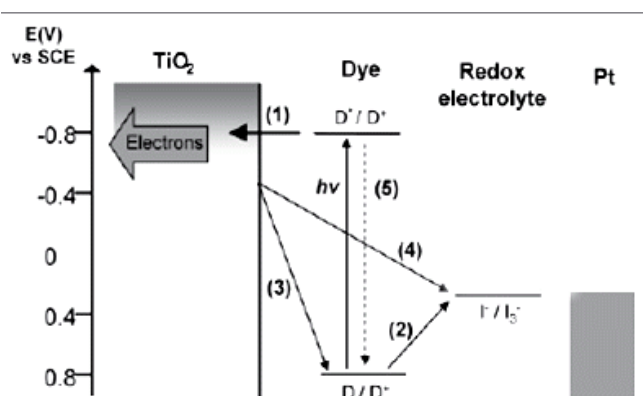
Fig. 4. Different electron transfer processes in the solar cell: (1) electron injection from dye excited state into the conduction band of TiO_2 semiconductor; (2) regeneration of the dye cation by electron transfer from the redox couple; (3) charge recombination to the cation of the dye; (4) recombination to the redox couple; and (5) excited state decay to the ground state. Adopted from (Haque et al., 2005), Copyright: 2005 American Chemical Society.

4. Electron dynamics in DSSC

A DSSC benefits from its imitation of natural photosynthesis in that it separates sunlight absorption--which requires a large space--from electron collection processes which need highly pure materials and being most efficient on a small lengthscale. The biggest challenge to develop DSSCs is to realize both functions in the same system and to improve efficiency on both sides. By combining dye sensitizers with oxide semiconductor nanoparticles, DSSCs resolve this conflict. Visible light absorption efficiency is improved by >1000 times on

nanoparticles compared to that of single-crystal surfaces, due to high surface/volume ratio of the former (Grätzel, 2005). Nevertheless, the mechanism and detailed dynamics of electron-hole separation at the dye/semiconductor interface, especially on a microscopic scale, remains elusive.

Experimentally it is observed that at various dye/TiO$_2$ interface, the timescale of excited electron injection ranges from the shortest 3 fs for biisonicontinic acid in vacuum to 100 ps for the triplet state injection of Ru-complex N719 in devices (see, for example, the summary in Meng & Kaxiras, 2010). The huge time span suggests rich physical factors may play a role. Understanding this process will help us tune charge transfer timescale and improve sunlight-to-electricity conversion efficiency. For instance, electron injection will be 3.3 times slower with the addition of a CH$_2$ group inserted between the dye molecule and the semiconductor, predicted from exponential decay of tunneling electron density when increasing separation distance in a non-adiabatic process. This is indeed observed in experiments using Re dyes (ReC1A-ReC3A) (Asbury et al., 2000). However, this pronounced time increase is not observed in experiments on Zn-porphyrins with one or four oligo(phenylethylny) bridges (Chang et al., 2009).

Meng et al. examined the influence of various factors on the electron injection efficiency using state-of-the-art first-principles calculations within the framework of time-dependent density functional theory (TDDFT). From TDDFT simulations, they found that among the three organic dyes they investigated longer molecules do involve a longer injection time, which is consistent with intuition (Meng & Kaxiras, 2010). Furthermore, the time elongation is only 1.2 times (by inserting a (CH)$_2$ group) or 1.3 times (inserting a thiophene group). This indicates that adiabatic processes play a major role in these cases, which also explains the Zn-porphyrin experiment. Figure 5 shows the structure of the three organic dyes and their absorption intensity in neutral and deprotonated states.
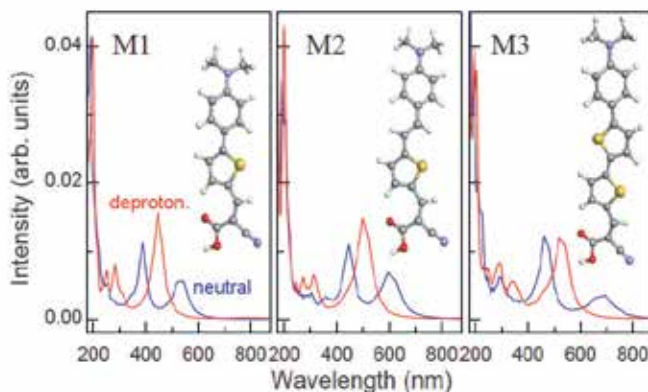
Fig. 5. Structure of the three organic dyes investigated and their absorption spectra. Blue lines: neutral dye; Red: deprotonated dyes. Adopted from (Meng & Kaxiras, 2010). Copyright: 2010 American Chemical Society.

On the basis of a previous work which illustrates an ultrafast electron-hole separation process at the anthocyanin/TiO$_2$ interface (Meng et al., 2008), they extended to demonstrate further that various factors including dye molecular size, binding geometry, and point defects on the TiO$_2$ surface will greatly influence electron collection efficiency. To analyze

quantitatively the charge transfer and electron-hole separation process, they use the integral of excited electron (hole) density projected onto the TiO_2 orbitals, χ , as a function of time after photon absorption, with χ defined as

$$\chi = \int dr\, |\psi(r)|^2 \qquad\qquad \psi(r) = \sum_{j \in TiO_2} c_j \varphi_j(r) \qquad\qquad (1)$$

where c_j are the coefficients of atomic basis states φ_j in the Kohn-Sham orbital $\psi_{KS}(r)$ of interest (either the excited electron or the hole)

$$\psi_{KS}(r) = \sum_j c_j \varphi_j(r) \qquad\qquad (2)$$

The curves in Fig. 6 show the injection probability, χ , of the excited electron and hole as a function of simulation time.
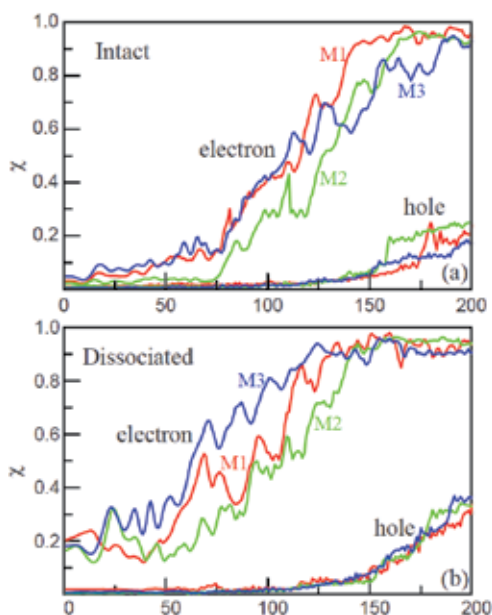
Fig. 6. Electron-hole dynamics from TDDFT simulations. Vertical axis demonstrates electrons injected into TiO_2, horizontal axis denotes time simulated. Adopted from (Meng & Kaxiras, 2010). Copyright: 2010 American Chemical Society

They also found that dye adsorption configurations significantly affect electron injection. By comparing to measured spectroscopy, intact and dissociative dye adsorptions are identified. The former is 30-50 fs slower than the latter. Different adsorption configurations of intact dyes result in injection time varies by three folds. The difference is mainly caused by the interface dipole moments. A positive dipole at the interface introduces an upshift of CBM, which will suppress excited electron transfer from the dye molecule to semiconductor conduction bands.

The semiconductor surface also imposes a fundamental influence on electron-hole dynamics. Dye adsorption on surface oxygen vacancies is very stable; it leads to a strong electronic coupling between the dye and the surface resulting in an electron injection time of ~50fs, 2-3 times faster than that on defect-free surfaces. But this improvement is at the cost of fast electron-hole recombination, which will reduce device efficiency. These simulations could explain well the two injection times at 40 fs and 200 fs observed in experiments, which would correspond to adsorption on defects and on clean surfaces, respectively.

They also studied electron back transfer after the excited electron has been completely injected into the TiO$_2$. All the research results indicate that electrons and holes are separated in space at a time ~200 fs, to assure DSSCs work well.

5. New design

Recent developments of effective all-organic dyes have introduced a novel Donor-π-Acceptor (D-π-A) structure, with the donor and acceptor connected via a molecular bridge conductor (π-group) and the acceptor directly bound to semiconductor surface. Upon excitation, electrons in the HOMOs, originally distributed around the donor group, are promoted to the LUMOs, which are centred around the acceptor. This excitation process effectively pushes extra electrons to the acceptor part of the dyes and leaves holes on the donor part. Importantly, the proximity between the acceptor and the semiconductor surface, mutually bound via covalent and/or hydrogen bonds, allows ultrafast transfer of excited electrons to the conduction bands of the semiconductor (Meng et al., 2008; Duncan & Prezhdo, 2007). Consequently, this leads to efficient electron-hole separation and ultimately electricity generation.

Laboratory development of D-π-A dyes often invokes a trial-and-error approach, which requires extensive chemical synthesis and expensive materials processing with a slow progress. In this regard, theoretical screening of potential organic dyes using state-of-the-art first principles computation shows a great promise, significantly reducing the cost to develop efficient dyes and expediting discovery of new ones.

5.1 Enhanced light absorption

Based on first principles calculations on the electronic structure and optical absorption of organic molecules, we design a set of Donor-π-Acceptor (D-π-A) type of dyes with inserting and changing intermediate spacer groups or electron acceptor groups, to be used in DSSCs for sunlight harvesting and energy conversion. We found that with these modifications, the electronic levels and corresponding optical absorption properties of organic dyes can be gradually tuned, with dyes having novel 1,4-cyclohexadiene groups as promising candidates for red light absorption and achieving high extinction coefficients. This study opens a way for material design of new dyes with target properties for further optimizing the performance of dye solar cells.

Our calculations are performed within the framework of DFT (Kohn & Sham, 1965) (for structure optimization) and TDDFT (Runge & Gross, 1984) (for excited states and optical absorption), using SIESTA (Soler et al., 2002) and Gaussian (Frisch et al., 2009) packages. It is well known that popular functionals (such as PBE and B3LYP) systematically underestimate charge-transfer excitation energies and result optical band splitting, leading to problematic predictions on optical excitations. Most recently, significant progresses have been made by including self-interaction correlations at the long range in hybrid fuctionals, to properly

account for the long-range charge transfer excitation while retain the reliable description of short-range correlation interactions. Our previous work shows that the long-range corrected (LC) functionals ωB97X (Chai & Head-Gordon, 2008) and CAM-B3LYP (Yanai et al., 2004)) yield better comparison with experiment. Since ωB97X has less parameters and shows better agreement with experimental results (after solvent effect correction of 0.1-0.3 eV (Pastore et al., 2010)), we use this functional in the following for predicting optical properties of new dyes.

For structure optimization, we use pseudopotentials of the Troullier-Martins type to model the atomic cores, the PBE form of the exchange-correlation functional, and a local basis set of double-ζ polarized orbitals. An auxiliary real space grid equivalent to a planewave cutoff of 680 eV is used for the calculation of the electrostatic (Hartree) term. A molecular structure is considered fully relaxed when the magnitude of forces on the atoms is smaller than 0.03eV/Å. Optical absorption are extracted from TDDFT simulations within the linear response regime at fixed dye geometry in gas phase. We use the 6-31G(d) basis set throughout this book chapter, which has been shown to yield negligible difference in electron density and energy accuracy compared with those including additional diffuse functions (Pastore et al., 2010). Within TDDFT, different functionals based on adiabatic approximation are used, including B3LYP and ωB97X. The latter one, belonging to LC functionals, are employed to correct excitation energies for charge-transfer excitations, which prevail in these dyes. The spectrum is obtained using the following formula based on calculated excitation energies and oscillator strengths,

$$\varepsilon(\omega) = 2.174 \times 10^8 \sum_I \frac{f_I}{\Delta} \exp\left[-2.773 \frac{(\omega - \omega_I)^2}{\Delta^2}\right], \qquad (3)$$

where ε is the molar extinction coefficient given in unit of M^{-1}cm^{-1}, energies and ω_I are in unit of cm^{-1} and f_I is the corresponding oscillator strength. Such a formula will satisfy the well-known relationship

$$4.32 \times 10^{-9} \int \varepsilon(\omega)d\omega = \sum_I f_I. \qquad (4)$$

We use a gaussian full-bandwidth of $\Delta = 3000\,\text{cm}^{-1}$ at half-height for optical band broadening to mimic thermodynamic oscillations in dye structures and excitations at room temperature in vacuum.

Organic dyes with the cyanoacrylic acid anchoring and electron with-drawing group have been very successful in real devices. We choose Y-1, Y-2 and Y-3 molecules (left column, Fig. 7) as the model dyes because they have a simple structure and have been successfully synthesized for DSSC applications (for example, as a1, b1, b2 dyes in reference Kitamura et al., 2004). Then the model dyes are modified by inserting a cyclohexadene in the C=C double bond on the backbone. The resulting dyes are named as dyes Y-1ben, Y-2ben, Y-3ben hereafter for convenience. Another model dye Y-1ben2 is constructed by inserting an additional cyclohexadene ring in the Y-1ben (right column, Fig. 7). All these dyes have a strong structural similarity with each other; we hope upon these variations in the dye structures, various aspects of the atomic structure, electronic structure, absorption character and therefore the structure-property relationship of organic dyes can be investigated.

The calculated optical absorption spectra are shown in Fig. 8. We found that the absorption spectra will be red shifted by prolonging the oligoene backbone (compare the green and red lines) and inserting cyclohexadiene moiety (compare the lines in the same colour). Attaching benzene rings to the amide nitrogen could enhance the absorption intensity a little but barely changes the position of maximum absorption (compare blue and green lines). On the other hand, inserting cyclohexadiene group could modify the spectra significantly, both in peak positions and intensity (compare the lines in Fig. 8 in the same colour). This would make dyes with cyclohexadiene group attractive candidates for future development of DSSC devices, especially for high extinction, long wavelength light absorption.

We analyse further the electronic energy level calculated using B3LYP/6-31G(d) and the first excitation energy from ωB97X/6-31G(d) (Table 1). It is known that the solvent effects will lower dye absorption energy by 0.1-0.3 eV (Pastore et al., 2010); therefore experimental values quoted in Table 2 which are measured in solution would have been corrected by 0.1-
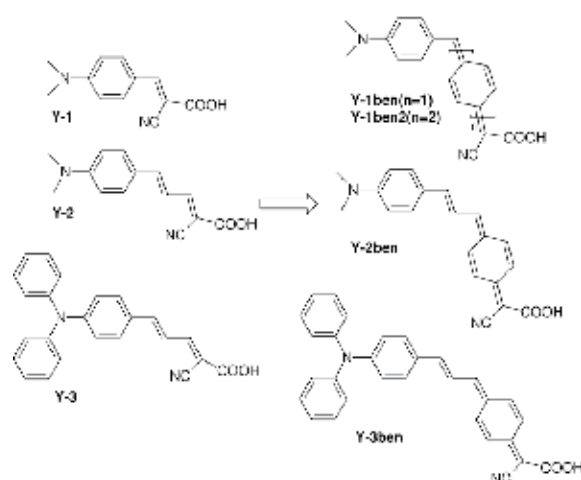
Fig. 7. Chemical structure of model dyes. The left column from up to bottom depicts Y-1, Y-2, Y-3, and the right column shows Y-1ben (Y-1ben2), Y-2ben, Y-3ben.
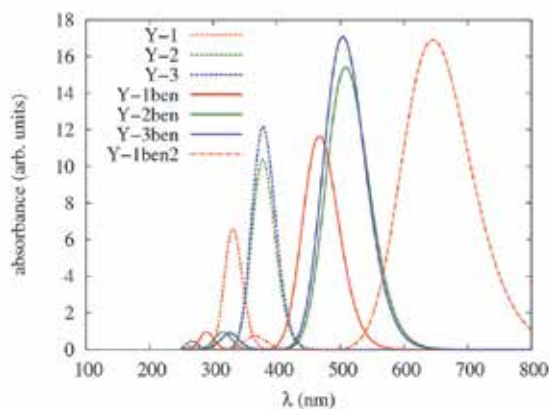
Fig. 8. Calculated optical absorption spectra of the model dyes.

0.3 eV, this leads to a better agreement with the results from LC-TDDFT for dyes in vacuum. For Y-1 dye the LC seems not necessary, maybe due to its short length.

Intuitively, the energy levels of the whole dye molecule are modified by the electric field introduced by the presence of chemical groups at the acceptor end. They would change according to the electronegativity of these chemical groups. The higher negativity, the lower the LUMO level, the smaller the energy gap would be. Our results proved this simple rule by showing that inserting electron withdrawing groups C=C or cyclohexadiene will down shift the LUMO level and producing a smaller energy gap (Table 1).

Following this way we obtain a small energy gap of 1.41 eV for Y-1ben2. In particular, we emphasize that the LUMO level is still higher by at least 0.7 eV than the conduction band edge (CBE) of anatase TiO_2, located at -4.0 eV (Kavan et al., 1996). This would provide enough driving force for ultrafast excited state electron injection. Another requisite in interface energy level alignment for DSSCs to work properly is that the dye HOMO has to be lower than the I^-/I_3^- redox potential at about -4.8 eV. The potential level is comparable to cyclohexadiene dye HOMOs in Table 2. However, we note here that by comparing calculated energy levels with experimental measured potentials, the HOMO and LUMO positions are generally overestimated by ~0.6 eV and ~0.3 eV, respectively. We expect the same trend would occur for dyes discussed in the present work; taking this correction into account, the designed new dyes would have a perfect energy alignment with respect to the CBE of TiO2 (more than 0.4 eV lower than LUMOs) and the I^-/I_3^- redox potential (~0.5-1 eV higher than HOMOs) favouring DSSC applications.

Dyes	Y-1	Y-2	Y-3	Y-1ben	Y-2ben	Y-3ben	Y-1ben2
LUMO	-2.22	-2.49	-2.63	-2.92	-3.05	-3.09	-3.30
HOMO	-5.64	-5.36	-5.38	-5.15	-5.02	-5.06	-4.71
gap	3.42	2.87	2.75	2.23	1.97	1.97	1.41
ωB97X	3.74	3.28	3.28	2.65	2.44	2.46	1.92
Exp.[a]	3.28	3.01	2.98				

Table 2. Electronic and optical properties of dyes predicted from first-principles calculations. The LOMO, HOMO and gap are results using B3LYP exchange-correlation potential. ωB97X indicates the first excitation energy using the ωB97X long correction.

[a] The data are from reference (Kitamura et al., 2004). The first absorption peak observed at 1.6×10^{-5} *mol • dm^{-3}* in ethanol. Energy levels are in unit of eV.

To further demonstrate the electronic properties for these promising dyes, we show the wavefunction plots for the molecular orbitals HOMO and LUMO of dye Y-1ben. The contour reveals that the HOMO and LUMO extend over the entire molecule. Other modified dyes have a similar characteristic.

We conclude that with the insertion of electron with-drawing groups C=C and cyclohexadiene in the backbone of oligoene dyes, we can tune the dye electronic levels relative to TiO_2 conduction bands and the corresponding optical absorption properties as shown in Fig. 8 and Table 2, for optical performance when used in real DSSC devices. In particular, we propose that the model dyes with cyclohexadiene group might be promising candidates for red to infrared light absorption, which may offer improved sunlight-to-electricity conversion efficiency when used alone or in combination with other dyes. The anchoring geometry will also influence the energy level alignment and energy conversion efficiency, which will be discussed in the next subsection.
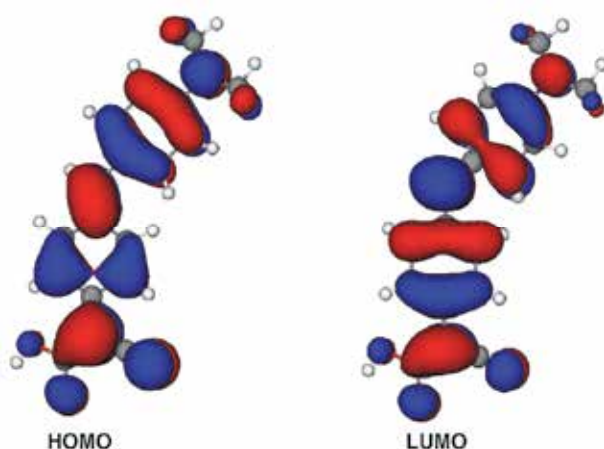
Fig. 9. Wavefunction plots for the representative dye Y-1ben. HOMO and LUMO orbitals are shown.

5.2 Stable anchoring

Following the similar principles, we have extended our study to the design of purely organic dyes with a novel acceptor, since the acceptor group connects the dye to the semiconductor and plays a critical role for dye anchoring and electron transfer processes. Our strategy is to test systematically the influence of chemical group substitution on the electronic and optical properties of the dyes.
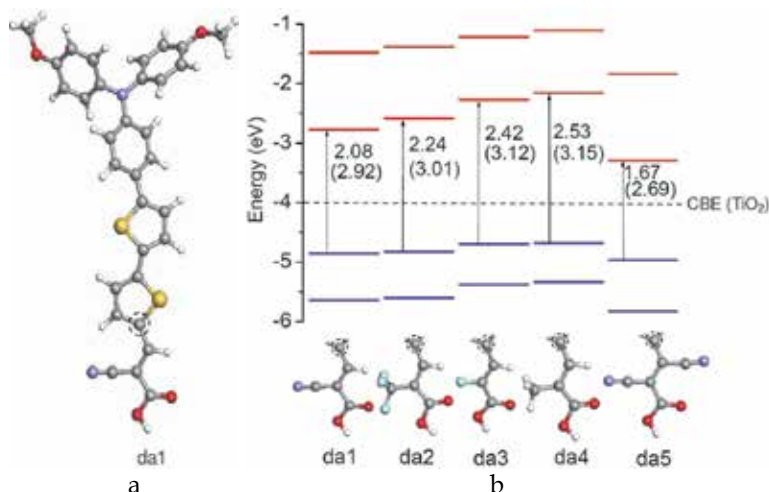
Fig. 10. (a) Optimized structure for the model dye da1. (b) The structure of acceptor groups by design and corresponding electronic level. The dashed circle marks the carbon atom connecting the acceptor part and the π bridge. Adapted from (Meng et al., 2011). Copyright: 2011 American Chemical Society.

Chemical groups of different electronegativity, size and shape and at different sites have been investigated. As an example, we consider here a specific modification on existing dye

structures: replacement of the -CN group of cyanoacrylic side with other elements or groups. This gives a group of new dyes which we label da-n (with n = 1-5, an index). Organic dyes with the carboxylate-cyanoacrylic anchoring group have been very successful in real devices. From the point of view of electronic structure and optical absorption, it is possible that the side cyano group (-CN) has a positive influence on light absorption and anchoring to the TiO_2 surface (Meng et al., 2010). Accordingly, we consider the possibility of replacing -CN by other chemical groups and examine the dependence of dye performance on these groups. In Fig. 10 we show the set of dye acceptor structures we have investigated. We have replaced the cyano -CN group in model dye da1 by $-CF_3$, -F, and $-CH_3$ groups, which are labelled da2, da3, and da4, respectively. Model dye da1, shown in Fig. 10, has a very similar structure to that of D21L6 dye synthesized experimentally (Yum et al., 2009), except that the hexyl tails at the donor end are replaced by methyl groups. The electronic energy levels of these modified dyes in the ground-state are also shown in Fig. 10, as calculated using B3LYP/6-31G(d). Compared to the relatively small gap of 2.08 eV for da1, the energy gap is increased by all these modifications. We have also tried many other groups, such as $-BH_2$, $-SiH_3$, etc., for substituting the -CN group. All these changes give a larger energy gap. This may explain the optimal performance in experiment of the cyano CN group as a part of the molecular anchor, which yields the lowest excitation energy favouring enhanced visible light absorption. The changes in electronic structure introduced by substitution of the -CN group by other groups are a result of cooperative effects of both electronegativity and the size and shape of the substituted chemical groups.

We did not find any single-group substitution for the -CN that produces a lower energy gap. Therefore we extended our investigation to consider other possibilities. We found that with the substitution of the -H on the next site of the backbone by another -CN group, the ground-state energy gap is reduced to 1.67 eV (see Fig. 10, dye da5). The LUMO level is higher than the conduction band edge of anatase TiO_2 (dashed line, Fig. 10) and HOMO level is lower than the redox potential of tri-iodide, providing enough driving force for fast and efficient electron-hole separation at the dye/TiO_2 interface. With the above systematic modifications of the dye acceptor group, the electronic levels can be gradually tuned and as a consequence dyes with desirable electronic and optical properties can be identified. Influence of these acceptor groups on excited state electron injection can be studied in the same way as that in Section 4.

We also strive to design dye acceptors that render a higher stability of the dye/TiO_2 interface when used in outdoors applications. It was previously found that some organic dyes do not bind to the TiO_2 photoanode strongly enough, and will come off during intensive light-soaking experiments, while other dyes show higher stability in such tests (Xu et al., 2009). Dye anchors with desirable binding abilities will contribute greatly to the stability of interface. A type of dye anchor under design is a cyano-benzoic acid group, whose binding configuration to the anatase TiO_2 (101) surface is shown in Fig. 11. A particular advantage of cyano-benzoic acid as a dye acceptor is that, it strongly enhances dye binding onto TiO_2 surfaces. We investigate the binding geometries of this organic dye on TiO_2 (101) using DFT. Among several stable binding configurations, the one with a bidentate bond and a hydrogen bond between -CN and surface hydroxyl (originating from dissociated carboxyl acid upon adsorption), is the most stable with a binding energy of 1.52 eV. The bond lengths are d_{Ti1-O1}=2.146 Å, d_{Ti2-O2}=2.162 Å, and $d_{CN...HO}$=1.80 Å. Since there are three bonds formed, the dye is strongly stabilized on TiO_2. Experimentally dyes with cyano-benzoic acid anchors have been successfully synthesized and the corresponding stability is under test (Katono et al., submitted).
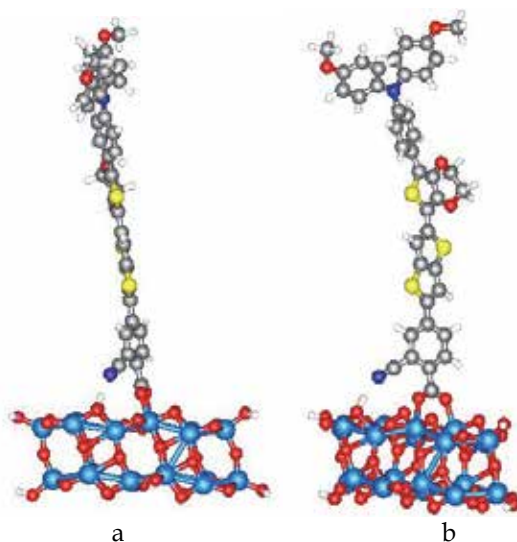
Fig. 11. (a) Side and (b) front views of adsorption of the dye with a cyano-benzoic acid anchor on a TiO₂ nanoparticle.

6. Conclusion

In summary, after a brief introduction of the principles of DSSCs, including their major components, the fabrication procedures and recent developments, we try to focus on the atomic mechanisms of dye adsorption and electron transport in DSSCs as obtained from accurate quantum mechanical simulations. We discovered that electron injection dynamics is strongly influenced by various factors, such as dye species, molecular size, binding group, and surface defects; more importantly, the time scale for injection can be tuned by changing these parameters. Based on the knowledge about the interface electronic structure and dynamics at the molecular level, we strive to design new dye molecules and anchoring configurations employing state-of-the-art first principles calculations. Our results show that upon systematic modifications on the existing dye structures, the optical absorption and energy levels could be gradually tuned. In particular, we propose that by inserting cyclohexadiene groups into spacing C=C double bonds, simple organic dyes could be promising candidates for enhanced red to infrared light absorption. This study opens a way for material design of new dyes with target properties to advance the performance of organic dye solar cells.

7. Acknowledgment

8. References

Asbury, J. B.; Hao, E.; Wang, Y. & Lian, T. (2000). Bridge Length-Dependent Ultrafast Electron Transfer from Re Polypyridyl Complexes to Nanocrystalline TiO2 Thin

Films Studied by Femtosecond Infrared Spectroscopy. *Journal of Physical Chemistry B* Vol 104, pp. 11957-11964, ISSN 1520-6106

Campbell, W. M.; Jolley, K. W.; Wagner, P.; Wagner, K.; Walsh, P. J.; Gordon, K. C.; Schmidt-Mende, L.; Nazeeruddin, M. K.; Wang, Q.; Grätzel, M. & Officer, D. L. (2007). Highly Efficient Porphyrin Sensitizers for Dye-Sensitized Solar Cells, *Journal of Physical Chemistry C,* Vol. 111, No.32, (August 2007), pp. 11760-11762, ISSN 1932-7447

Chai, J.-D.; Head-Gordon, M. (2008). Systematic Optimization of Long-Range Corrected Hybrid Density Functionals, *Journal of Chemical Physics*, Vol. 128, No.8, (February 2008) pp.084106, ISSN 0021-9606

Chang, C. W.; Luo, L.; Chou, C. K.; Lo, C. F.; Lin, C. Y.; Hung, C. S.; Lee, Y. P. & Diau, E. W. (2009). Femtosecond Transient Absorption of Zinc Porphyrins with Oligo(phenylethylnyl) Linkers in Solution and on TiO2 Films. *Journal of Physical Chemistry C* Vol 113, pp. 11524-11531, ISSN 1932-7447

Duncan, W. R.; Colleen, F. C.; Oleg, V. P. (2007). Time-Domain Ab Initio Study of Charge Relaxation and Recombination in Dye-Sensitized TiO_2, *Journal of the American Chemical Society*, Vol.129, No.27, (June 2007) pp.8528-8543, ISSN 0002-7863

Frisch, M. J. et al. (2009). Gaussian 09, Revision A.1, Gaussian Inc.: Wallingford, CT, 2009

Grätzel, M. (2005). Mesoscopic Solar Cells for Electricity and Hydrogen Production from Sunlight, *Chemistry Letters*, Vol.34, No.1, (January 2005), pp. 8-13, ISSN 0366-7022

Grätzel, M. (2009). Recent Advances in Sensitized Mesoscopic Solar Cells, *Accounts of Chemical Research,* Vol.42, No.11, (November 2009), pp. 1788-1798, ISSN 0001-4842

Haque, S. A.; Palomares, E.; Cho, B. M.; Green, A. N. M.; Hirata, N.; Klug, D. R. & Durrant, J. R. (2005). Charge Separation Versus Recombination in Dye-Sensitized Nanocrystalline Solar Cells: the Minimization of Kinetic Redundancy, *Journal of the American Chemical Society,* Vol.127, No.10, (March 2005), pp.3456-3462, ISSN 0002-7863

Hardin, B.E.; Yum, J.-H.; Hoke, E.T.; Jun, Y.C.; Pechy, P.; Torres, T.; Brongersma, M.L.; Nazeeruddin, M.K.; Graetzel, M.; & McGehee, M.D. (2010). High Excitation Transfer Efficiency from Energy Relay Dyes in Dye-Sensitized Solar Cells, *Nano Letters,* Vol. 10, pp. 3077-3083, ISSN 1530-6984

Ito, S.; Murakami, T. N.; Comte, P.; Liska, P.; Grätzel, C.; Nazeeruddin, M. K. & Grätzel, M. (2008). Fabrication of Thin Film Dye Sensitized Solar Cells With Solar to Electric Power Conversion Efficiency over 10%, *Thin Solid Films*, Vol.516, No.14, (May 2008), pp.4613-4619, ISSN 0040-6090

Katono, M.; Bessho, T.; Meng, S.; Zakeeruddin, S. M.; Kaxiras, E.; Grätzel, M. (2011). Submitted.

Kavan, L.; Grätzel, M.; Gilbert, S. E.; Klemenz, C.; Scheel, H. J. (1996). Electrochemical and Photoelectrochemical Investigation of Single-Crystal Anatase, *Journal of American Chemical Society.* Vol. 118, No.28 (July 1996) pp. 6716-6723, ISSN 0002-7863

Kitamura, T.; Ikeda, M.; Shigaki, K.; Inoue, T.; Anderson, N. A.; Ai, X.; Lian, T. & Yanagida, S. (2004). Phenyl-Conjugated Oligoene Sensitizers for TiO2 Solar Cells, *Chemcal Materials*, Vol.16, No.9, (February 2004) pp. 1806-1812, ISSN 0897-4756

Kohn, W.; Sham, L. J. (1965). Self-Consistent Equations Including Exchange and Correlation Effects. *Physical Review*, Vol.140, No.4A, (1965) pp. 1133-1138, ISSN 0031-899X

Konno, A.; Kumara, G. R. A.; Kaneko, S. (2007). Solid-state solar cells sensitized with indoline dye, *Chemistry Letters,* Vol.36, No.6, (June 2007), pp.716-717, ISSN 0366-7022

Liu, X.; Huang, Z.;Meng, Q. et al. (2006). Recombination Reduction in Dye-Sensitized Solar Cells by Screen-Printed TiO$_2$ Underlayers, *Chinese Physics letters*, Vol.23, No.9, (June 2006), pp.2606-2608, ISSN 0256-307X

Meng, S.; Ren, J. & Kaxiras, E. (2008). Natural Dyes Adsorbed on TiO2 Nanowire for Photovoltaic Applicaitons: Enhanced Light Absorption and Ultrafast Electron Injection, *Nano Letters*, Vol.8, No.10, (September 2008), pp.3266-3272, ISSN 1530-6984

Meng, S. & Kaxiras, E. (2010). Electron and Hole Dynamics in Dye-Sensitized Solar Cells : Influencing Factors and Systematic Trends, *Nano Letters*, Vol. 10, No.4 (April 2010), pp 1238-1247, ISSN 1530-6984

Meng, S.; Kaxiras, E; Nazeeruddin, Md. K. & Grätzel, M. (2011). Design of Dye Acceptors for Photovoltaics from First-principles Calculations, *Journal of Physical Chemistry C*, in press, ISSN 1932-7447

O'Regan, B. & Grätzel, M. (1991). A Low-Cost, High-Efficientcy Solar-Cell Based on Dye-Sensitized Colloidal TiO$_2$ Films, *Nature*, Vol.353, No.6346, (October 1991), pp. 737-740, ISSN 0028-0836

Pastore, M.; Mosconi, E,; De Angelis, F. & Grätzel, M. (2010). A Computational Investigation of Organic Dyes for Dye-Sensitized Solar Cells: Benchmark, Strategies, and Open Issues, *Journal of Physical Chemistry C*, Vol.114, No.15 (April 2010) pp. 7205-7212, ISSN 1932-7447

Qin, Q.; Tao, J. & Yang, Y. (2010). Preparation and Characterization of Polyaniline Film on Stainless Steel by Electrochemical Polymerization as a Counter Electrode of DSSC, *Synthetic Metals*, Vol.160, No.11-12, (June 2010) pp.1167-1172, ISSN 0379-6779

Runge, E.; Gross, E. K. U. (1984). Density-Functional Theory for Time-Dependent Systems. *Physical Review Letter*, Vol.52, No.12, (1984) pp.997-1000, ISSN 0031-9007

Soler, J. M.; Artacho, E.; Gale, J. D.; Garcia, A.; Junquera, J.; Ordejon, P. & Sanchez-Portal, D. (2002). The SIESTA Method for Ab Initio Order-N Materials Simulation, *Journal of Physics: Condensed Matter*, Vol.14, No.11, (March 2002) pp. 2745-2779, ISSN 0953-8984

Xu, M.; Wenger, S.; Bala, H.; Shi, D.; Li, R.; Zhou, Y.; Zakeeruddin, S. M.; Grätzel, M. & Wang, P. (2009). Tuning the Energy Level of Organic Sensitizers for High-Performance Dye-Sensitized Solar Cells, *Journal of Physical Chemistry C*, Vol. 113, No.7 (February 2009) pp.2966-2973, ISSN 1932-7447

Yanai, T.; Tew, D. P. & Handy, N. C. (2004). A New Hybrid Exchange-Correlation Functional Using the Coulomb-Attenuating Method (CAM-B3LYP), *Chemical Physics Letter*, Vol. 393, No.1-3 (July 2004) pp. 51-57, ISSN 0009-2614

Yum, J. H.; Hagberg, D. P.; Moon, S. J.; Karlsson, K. M.; Marinado, T.; Sun, L.; Hagfeldt, A.; Nazeeruddin, M. K & Grätzel, M. (2009). Panchromatic Response in Solid-State Dye-Sensitized Solar Cells Containing Phosphorescent Energy Relay Dyes, *Angewandte Chemie-International Edition*, Vol. 48, No.49 (2009) pp. 1576-1580, ISSN1433-7851

Yu, Z.; Li, D.; Qin, D.; Sun, H.; Zhang, Y.; Luo, Y. & Meng, Q. (2009). Research and Development of Dye-Sensitized Solar Cells, *Materials China*, Vol.28, No.7-8, (August 2009), pp. 7-15, ISSN 1674-3962

Zeng, W.; Cao, Y.; Bai, Y.; Wang, Y.; Shi, Y.; Zhang, M.; Wang, F.; Pan, C. & Wang, P. (2010). Efficient Dye-Sensitized Solar Cells with an Organic Photosensitizer Ferturing Orderly Conjugated Ethylenedioxythiophene and Dithienosilole Blocks. *Chemistry of Materials*, Vol.22, No.5, (March 2010) pp. 1915-1925, ISSN 0897-4756

Physical and Optical Properties of Microscale Meshes of Ti$_3$O$_5$ Nano- and Microfibers Prepared via Annealing of C-Doped TiO$_2$ Thin Films Aiming at Solar Cell and Photocatalysis Applications

N. Stem[1], E. F. Chinaglia[2] and S. G. dos Santos Filho[1]
[1]Universidade de São Paulo/ Escola Politécnica de Engenharia Elétrica (EPUSP)
[2]Centro Universitário da FEI/ Departamento de Física
Brazil

1. Introduction

Dye-sensitized nanocrystalline solar cells (DSSC) or photoeletrochemical solar cells were firstly described by Gratzel and O'Reagan in the early 1990s (Sauvage et. al., 2010) and they have reached the global photovoltaic market since 2007. Later on, the investments in nanotechnology enabled the rapid development of DSSC cells with nanostructured thin films. According to a review performed by Hong Lin et. al. (Lin et. al., 2009) the numbers of papers focusing on the development of the DSSC cells increased in last decade, being mainly originated in countries such as Japan, China, South Korea, Swiss and USA, where there is an enlarged integration of nanotechnology, electrochemical and polymers research and finantial supported projects like National Photovoltaic Program by Department of Energy (DOE) and NEDO's New Sunshine from USA and Japan, respectively. Some research groups of the institutions (Kim et. Al., 2010),which have recently obtained efficiencies around 10%, are EPFL (11.2% in 2005) and AIST (10% in 2006). They have used the N719 colorant in devices with area 0.16cm^2 and 0.25cm^2. On the other hand, Sharp, Tokyo University and Sumitomo Osaka Cell have used the black dye colorant in devices with areas of approximately 0.22cm^2, providing the efficiencies of about 11.1%, 10.2% and 10% in the years 2006, 2006 and 2007, respectively. In 2006, Tokyo University has also reached the efficiency of 10.5% in devices with 0.25cm^2 area, but using β-diketonide colorant.

Initially, the DSSC (Sauvage et. al., 2010) were based on a nanocrystalline semiconductor (pristine titanium dioxide) coated with a monolayer of charge-transfer dye, with a broad absorption band (generally, polypyridyl complexes of ruthenium and osmium), to sensitize the film. The principle of operation of these devices can be divided into: a) the photo-current generation that occurs when the incident photons absorbs in the dye, generates electron-hole pairs and injects electrons into the conduction band of the semiconductor (Ru^{2+} -> Ru^{3+} + e$^-$), and b) the carrier transport that occurs because of the migration of these electrons through the nanostructured semiconductor to the anode (Kim et. al., 2010). Thus, since this device requires an electrode with a conduction band with a lower level than the dye one, the

main desired properties for the electrode are optimized band structure and good electron injection efficiency and diffusion properties (Wenger, 2010).

Since Ru has become scarce and its purification and synthesis is too complex for production in large scale, new outlets for doping the titanium dioxide became necessary. Among the materials usually adopted for the electrode, TiO_2, ZnO, SnO_2, Nb_2O_5 and others have been employed (Kong et al., 2007), besides nanostructured materials. For instance, in a previous work, H. Hafez et. al. (Hafez et. al., 2010) made a comparison between the J-V curves of three different structures for the TiO_2 electrodes combined with N719 dye for dye-sensitized cells: a) pure nanorod with adsorbed dye of $2.1x\ 10^{-5}mol.cm^{-2}$; b) pure nanoparticle with adsorbed dye of $3.6x10^{-5}mol.cm^{-2}$ and c) a mix between nanorods and nanoparticles with adsorbed dye of $6.2x10^{-5}mol.cm^{-2}$. These cells presented the incident photon-to-current conversion efficiency, IPCE (at $\lambda=575nm$) of approximately 63.5%, 70.0% and 88.9%, and the efficiencies, 4.4%; 5.8% and 7.1%, respectively. A higher efficiency of 7.1% was found for a mixed structure of nanorods and nanoparticles and the efficiencies found for either pure nanoparticules or nanorods were around 5.8% and 4.4%, respectively.

Despite showing lower efficiency compared with the crystalline silicon solar cells, this thin film technology has been pointed as a potential solution to reduce costs of production. Also, they can be engineered into flexible sheets and are mechanically robust, requiring no special protection from environmental events like hail strikes. Other major points of DSSC technology is the fact that it is less sensitive to impurities compared with the conventional crystalline ones because the constituents used are low cost and abundant. Furthermore, differently from the Si-based modules, the performance of dye PV modules increases with temperature. For instance, comparing the Si-based modules with the dye PV modules, Pagliaro et. Al. (2009) showed for temperature varying from 25ºC to 60ºC that the percentage of power efficiency decreased approximately 40% for the silicon-based one and increased approximately 30% for the STI titania cells (Pagliaro et. al., 2009). Another important characteristic is associated with the color that can vary by changing the dye, being possible to be transparent, which is useful for application on windows surface. However, degradation under heat and UV light are the main disavantages and, in addition, the sealing can also be a problem because of the usage of solvents in the assembling, which makes necessary the development of some gelators combined with organic solvents. The stability of the devices is another important parameter to be optimized (Fieggemeier et. al., 2004), and the competitive light-to-energy conversion efficiencies must be tested. Recently, Wang et. al. (Wang et. al., 2003) have proved that it is possible to keep the device stable under outdoor conditions during 10 years in despite of the complexity of the system.

2. An overview of the techniques for producing titanium oxide nanofibers

The study of titania nanotubes (Ou & Lien, 2007) started in the nineties, with the development of the formation parameters of several processes (temperature, time interval of treatment, pressure, Ti precursors and alkali soluters, and acid washing). With the evolution of the characterization techniques, the thermal and post-thermal annealings were studied, and optimized for the several types of applications (photocatalysis, littium battery, and dye sensitized solar cells). The hydrothermal treatments have also been modified either physically or chemically depending on the desired application and on the desired stability after post-hydrothermal treatment and post-acid treatments.

Focusing on nanostructured materials developed for solar cells and photocatalysis, titanium dioxide (TiO_2) is one of the most promising due to its high efficiency, low cost and

photostability (Kim et. al. , 2007) (Varghese et. al., 2003). Some resources have been used for enlarging efficiency and for reducing costs. The enhanced porosity of the nanofibers, nanobelts or nanorods of these new structures, which can be used as photoanodes, were proved to have a better response than titanium-dioxide nanoparticles, because of their structure that facilitates the chemical adsorption for polymer electrolytes (Varghese et. al., 2003).   There is a wide variety of methods for producing nanofibers and nanotubes techniques, such as sol-gel techniques combined with low cost processes such as arc-plasma evaporation, electrospinning techniques, and hydrothermal methods (Chen and Mao, 2007), (Nuansing et. al., 2006) and (Park et. al., 2010) .

Another resource usually used for enhancing efficiency is the doping (Chennand and Mao, 2007) (Valentini et. al., 2005) , either with non-metallic elements (N, C, S or P) or halogens, in order to reduce bandgap and to shift the adsorption band edge to the visible-light range. And, for producing nanostructured materials, several precursor seeds have been successfully used including alkalines (Kukovecz et. al., 2005), carbon (Puma et. al., 2008) and (Varghese et. al., 2003) and water vapor (Yamamoto et. al., 2008), which also have the role as dopants. For instance, Khan et. al. (Khan et. al., 2009) showed that hydrothermally synthesized titanium dioxide doped with Ru, provided a significantly decrease in the energy bandgap and showed an increase (>80% higher after 140min) in their photocatalytic activity to degrade methylene blue (MB) under visible light compared with undoped tubes. Concomitantly, Zhang et. al. (Zhang et. al., 2010) report the doping of TiO$_2$ with transition metal ions, specially Fe(III) and Cr(III) as a good tool for improving photocatalytic properties.

According to previous works (Reyes-Garcia et. al., 2009) (Konstantinova et al., 2007), concerning with photocatalytic properties, carbon has been shown as one of the most proeminent dopant for titanium dioxide because it can provide a significant reduction of the optical band gap and the appearance of some C states in the mid-gap. For example, the energy of oxygen vacancies can be reduced from 4.2eV to 3.4eV (interstitional position in the titanium dioxide lattice) and to 1.9eV (substitutional one) for anatase phase and, from 4.4eV to 2.4eV for rutile phase for both positions, interstitial and substitutional. As a result, it has been showed that the photosensitization property is enhanced (Valentini et. al., 2005).

The hydrothermal route and calcination have been the most used techniques by varying time, atmosphere and temperature of annealing. In a previous work (Suzuki & Yoshikawa, 2004) , nanofibers of TiO$_2$ were synthesized by hydrothermal method (150 ^{o}C for 72 h) using natural rutile sand as the starting material and calcination at 700°C for 4 h. On the other hand, pure rutile phase TiO$_2$ nanorods (Chen et al., 2011) were also successfully synthesized under hydrothermal conditions, showing an increase of the photocatalytic activity for the times ranging from 1 to 15h because of the increase of the crystal domain. The best performance of DSSC measured under "1 sun condition" gave a current density <7.55 mA/cm^2, an open circuit voltage <0.70V, a fill factor <60%, and an energy conversion efficiency <3.16%. Meanwhile, Hafez et. al. (Hafez et. al., 2010) processed anatase TiO$_2$ nanorods by hydrothermal method and proved that the efficiency could increase from 5.8% to 7.1% if the DSSC electrodes were changed from nanoparticles to nanorods (Wang et. al., 2003). Wu et. al. (2009) proved that the use of ethanol as precursor for producing H-titanate nanotubes in inert N$_2$ atmosphere. Depending on the calcination temperature, the nanostructure could be altered, presenting either nanotubes, or nanowires or nanorods for calcination temperatures of 400°C, 500°C and 600°C, respectively. It is believed that during the calcination in N$_2$, the decomposed products of ethanol were not burnt out because there

was not observed oxygen in the environment. Thus, the residual carbon either remained in the TNTs or it doped the titanium dioxide by forming different nanostructures and, therefore, acting as seeds. Tryba (Tryba, 2008) has also demonstrated that the carbon-based coating of TiO_2, prepared by the calcination of TiO_2 with carbon precursor (polyvinylalcohol, poly (terephthalate ethylene), or hydroxyl propyl cellulose (HPC)) at high temperatures 700°C – 900°C retarded the phase transformation from anatase to rutile and increased the photoactivity, but the carbon coating reduced the UV radiation once it reached the surface of the TiO_2 particles and altered the absorbed light.

This work is focused on the development of new technique for producing carbon-doped TiO_2 thin films on silicon substrates together with Ti_3O_5 fiber meshes and on the investigations about the properties of this novel material. The innovation of the proposed technique relies on the fact that thermal evaporation is the most common method to fabricate single crystalline nanowires on silicon substrate by means of the Vapor-Liquid-Solid (VLS) mechanism (Dai et. al., 2002), (Yin et. al., 2002) and (Pan et. al., 2001). On the other hand, it is not an useful process for growing TiO_2 nanowires because Ti precursor can react with silicon to form Ti-Si alloys before nucleation and growth of TiO_2 nanowires (Wu et. al., 2005). Also, it is too difficult the production of titania nanowires by thermal treatment of Ti on Si substrate because $TiSi_2$ phases is favored before nucleation of titanium oxide nanowires in inert gas or high vaccum (Xiang et. al., 2005). On the other hand, a recent study has shown that single crystalline rutile TiO_2 nanowires could be obtained by annealing TiO_2 nanoparticles on silicon substrates at high temperature in air without catalysts (Wang et. al., 2009). Although it is possible to obtain titania nanowires on silicon by thermal annealing, there is a complete lack of information in literature about the effect of carbon as dopant on the physical and electrical properties of TiO_2 nanowires produced by thermal annealing of TiO_2 on silicon substrates. C-doped TiO_2 can evolve to lower oxides of titanium like Ti_4O_7, Ti_3O_5, and Ti_2O_3 after thermal annealing at 1000-1100°C in vacuum or argon. This process is known as carbothermal reduction of titanium dioxide in presence of carbon and can produce TiC powders of submicron size at a very high temperature of 1500°C (Sen et. al, 2011) and (Swift & Koc, 1999).

Thus , in the following, the formation mechanism of nano- and microfibers of Ti_3O_5 produced by annealing of carbon-doped TiO_2 thin films on silicon substrates at 900-1000°C for 120min in wet $N_2(0.8\%H_2O)$ is presented. The effects of concentration of carbon, concentration of water vapor and temperature on the formation of the nano and microfibers are addressed.

3. Nanofibers formation mechanism

Generally speaking, the formation of titania nanotubes has been explained by the sheet roll-up mechanism. In this process the nanosheet-like features produced after thermal treatment composed of highly distorted TiO_6 octahedra are believed to be formed by scrolling up, such that the driving force gets high enough because of the saturation of the undercoordinated sites or dangling bonds. In this structure, each Ti_{4+} ion is surrounded by an octahedron of six O_2- ions, and the distortion is generated with the aid of thermal treatment and precursor seeds (Chen & Mao, 2007) and (Kukovecz et. al., 2005). According to the previous work of Bavykin et. al. (Bavykin et. al., 2006) and (Bavykin et. al., 2009), the nanotubes are believed to be thermodynamically less stable than the nanofibers due to their increased surface area and the higher stress in the crystal lattice.

Figure 1 presents a simplified scheme of the possible formation mechanism of the nanofibers: a) starting from carbon-doped titanium dioxide crystals; b) after thermal annealings at temperatures lower than 900°C, it might occur delamination and the nanosheets are dettached; c) as the driving force is increased, the hollow nanofibers are formed, being composed by the distorted TiO$_6$ octahedra; d) after the hydrothermal annealing performed at 1000°C , the nanofibers probably are filled in because of the –OH bonds.
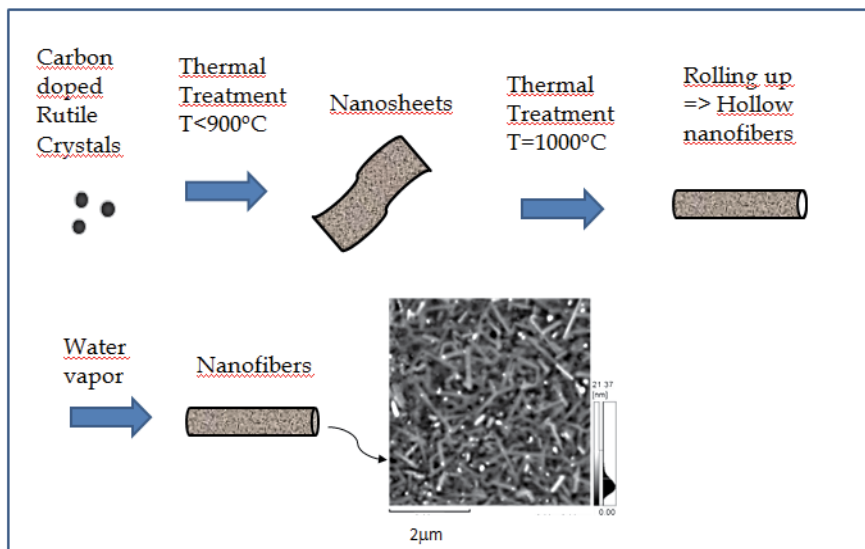
Fig. 1. The carbon doped crystals after thermal treatment are dettached in nanosheets. Increasing the temperature up to 1000°C, the sheet roll-up forming hollow nanofibers. Then, the nanofibers are filled in, probalby due to the presence of water vapor during annealing.

4. Details of sample preparation and cleaning monitoring

The initial wafer cleaning is a quite important to drop out: a) contaminant films, b) discrete particles, and c) adsorbed gases. While the RCA 1 is responsible for the organic compound dropping (such as condensed organic vapors from lubrificants, greases, photoresist, solvent residues or components from plastic storage containers), RCA 2 is responsible for the metallic (heavy metals, alkalis, and metal hydroxides) compound dropping.

Thus, a common cleaning for P-type Si (100) consists of the following sequence: a) RCA 1: 4 parts deionized (DI) water H$_2$O, 1 part 35% ammonium hydroxide (NH$_4$OH) , 1 part 30% hydrogen peroxideH$_2$O$_2$ (heated at 75°C during 15 min); b) RCA2: 4 parts DI water (H2O), 1 part 35% hydrogen chloride (HCl), 1 part 30% hydrogen peroxide (H$_2$O$_2$) (heated at 80°C during 15min) (Santos Filho et. al., 1995), (Kern, 1990) and (Reinhardt & Kern, 2008). According to S. G. Santos et. al. (Santos Filho et. al., 1995), the typical impurities found on the wafer surface analyzed by TRXFA after the conventional standard cleaning are up to 10^{10} atoms/cm^2, and the drying with the aid of isopropyl alchoholis was shown to be

efficient in removing a high percentage of particles of almost all measurable sizes (submicron and larger), as presented at table 1. Thus, after the deposition in order to perform the thermal annealings the samples were previously boiled in ultrapure isopropanol alcohol during 15 min, followed by rinsing in DI water during 5 min.

Elemental analysis were performed by using EDS technique, indicating the presence of the elements Ti, O, C or another contaminant before and after hydrothermal treatment. The EDS spectra presented show the obtained peaks for: a) as-deposited film, and b) for sample 1E (annealed at 1000°C) where the K_α line peaks of carbon, oxygen, silicon and titanium are indicated. The L line peak of the titanium (not shown) is superimposed to the K line of the oxygen.

Element	TXRFA Convencional 10^{10} atoms/cm²
S	<LD
K	<LD
Ca	70+30
Ti	40+20
Cr	20+10
Mn	<LD
Fe	45+8
Co	<LD
Ni	<LD
Cu	10+8
Zn	54+4

Table 1. TRXFA performed after the initial cleaning and drying at isopropyl alchoholis (Santos Filho et. al., 1995).

After the cleaning process, TiO₂ (rutile phase) and C were co-deposited on bare silicon by e-beam evaporation using the EB₃ Multihearth Electron Beam Source from Edwards and targets with 99.99% of purity from Sigma Aldrich. The carbon contents were fixed at two different concentrations: 1.5%wt or about 3.0%wt (Stem et al., 2010); (Stem et al., 2011). Then samples were boiled in a neutral ambient (isopropanol alcohol) aiming at the remotion of possible contaminants.

The deposition pressure was controlled in the range of $(2.3 \times 10^{-6} - 4.6 \times 10^{-6})$ Torr; the e-beam co-deposition current used was 150mA for a fixed time of 1min in order to produce a thickness close to 200nm.

After the co-deposition, hydrothermal annealing was performed in resistance-heated furnace with an open horizontal quartz tube; samples were introduced by a quartz boat. The temperature was adjusted in the range of 700°C to 1000°C for the following gases (2L/min): ultrapure N₂ or wet N₂ (0.8%H₂O), for 120min. As reported by Shannon et. al. (Shannon et. al., 1964), the presence of water can greatly promote the formation of oxygen vacancies, which increases the diffusivity of oxygen ions through TiO₂ layer and reduces diffusivity of titanium interstitials. In addition, wet inert gas plays a crucial role in triggering the much higher growth rate of titanium oxide nanowires (Liu et. al., 2010). A brief summary of the

sample preparation is presented at figure 2. In this figure, the AFM analysis of the samples just after the initial cleaning, the as-deposited film and after thermal annealing are shown. The EDS spectra of the as-deposited film and after annealing are also presented.
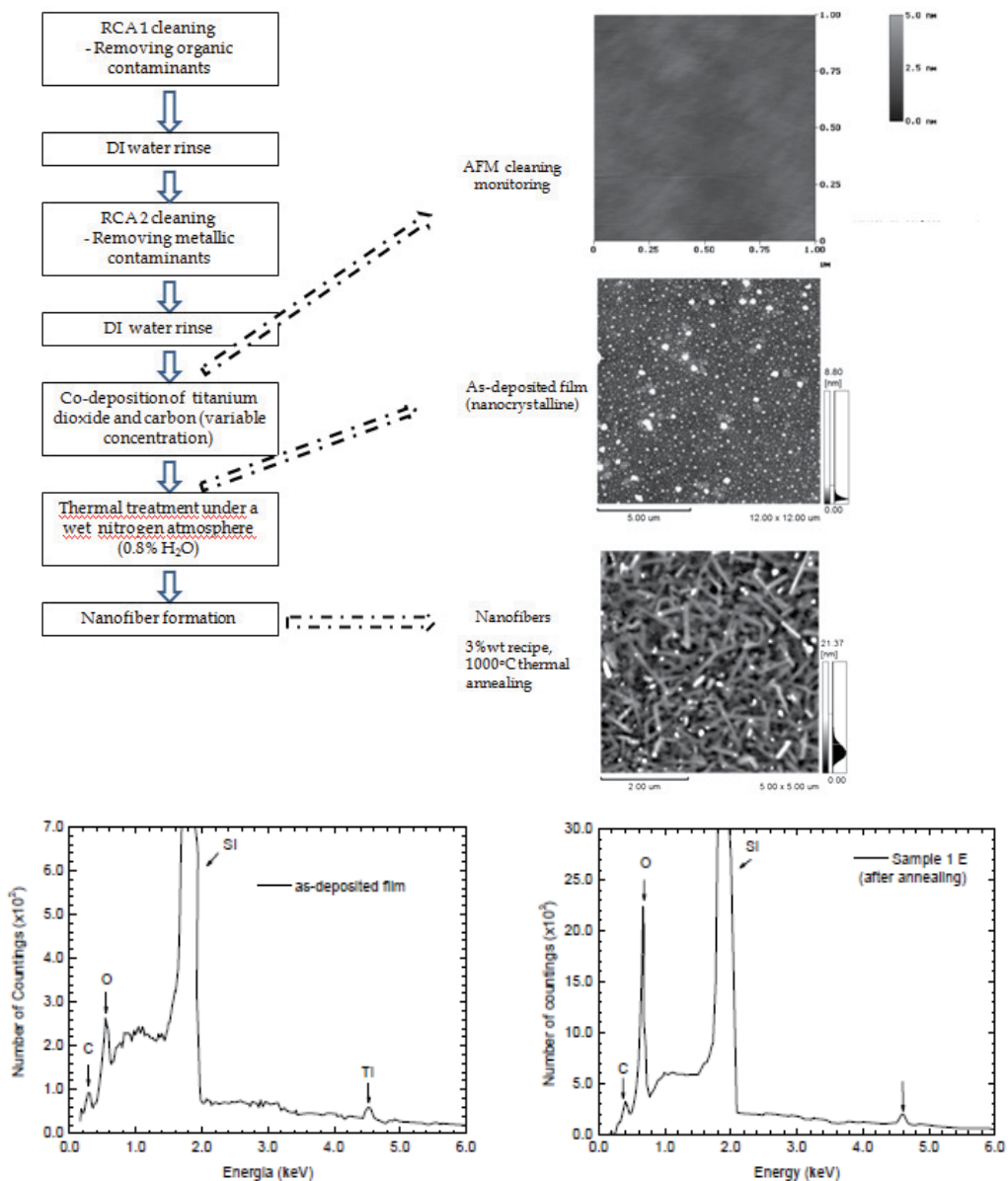
Fig. 2. Brief scheme of the sample preparation and the monitoring analysis: surface morphology by AFM technique and elemental analysis by EDS technique. The EDS spectra are not normalized; and therefore, only qualitative.

5. Producing meshes of Ti_3O_5 nano and microfibers

It is well known that is not easy to obtain titanium oxide nanowires by thermal treatment of Ti on Si, because $TiSi_2$ phases are favored over the nucleation of titanium dioxide nanowires in an inert gas or under high vacuum (Wu et. al., 2005), (Xiang et. al., 2005). In case of TiO_2 on Si, only when the high vacuum or inert gas was replaced by an oxygen-rich gas, TiO_2 nanowires could be formed on Si (Bennett et. al., 2002).

Figure 3a shows the obtained XRD spectra of titanium oxide thin films doped with 1.5%wt and 3.0%wt of carbon, respectively, and annealed at 700ºC (1G), 900ºC (1Fx and 1F) and 1000ºC (1Ex and 1E). The annealed films are primarily amorphous with a low content of crystalline Ti_3O_5 and rutile, except for the sample 1E where the higher crystallinity is demonstrated by high intensity peaks (about 772 times higher than the lowest intensity found for sample 1G) and for sample 1G where Ti_3O_5 was not be identified. However, when temperature reaches an intermediate value for the 3%wt carbon recipe, about 900ºC (as for sample 1F), the intensity of Ti_3O_5 and rutile increased in the amorphous film. On the other hand, for films doped with 1.5%wt of carbon recipe, only crystalline phase of Ti_3O_5 was observed at 700-900ºC, while Ti_3O_5 and rutile are observed at 1000ºC. .

Figure 3b is an ampliation of the XRD pattern shown in figure 3a of sample 1E, with the scale of the intensity reduced and, and with 2θ varying from 55 to 58 degrees when annealing to view the high intensity peaks and the peak deconvolution. It could be demonstrated that region is composed by three superposed peaks: Ti_3O_5 (<-5 1 2> and <-6 0 1>) and rutile (<220>), respectively.

Fig. 3. (a) Typical XRD spectra for the 3%wt recipe: samples 1G (700ºC), 1F (900ºC) and 1E (1000ºC), and for the 1.5%wt recipe: samples 1Fx (900ºC) and 1Ex (1000ºC); (b) ampliation of the most intense peaks of sample 1E (1000ºC) (dashed region of figure 3 a) and peak deconvolution, detailing the superposed peaks.

All of the crystalline orientations for Ti$_3$O$_5$ fitted well with the XRD patterns of λ-Ti$_3$O$_5$ (Monoclinic, C2/m E, a = 9.757Å, b = 3.802Å, c = 9.452Å) (Grey & Madsen, 1994). In addition, TiO$_{2-x}$C$_x$ was also identified with the aid of XRD powder patterns , which is an evidence that carbon occupies positions in the crystalline phase of the titanium dioxide (interstitial and substitutional) and introduces defects, electron and hole trapping centers because of the presence of carbon and carbonate-type species (Reyes-Garcia et. al., 2008). Therefore, after annealing at 1000^{0}C (sample 1E), the structure becomes predominantly crystalline, being formed by λ-Ti$_3$O$_5$ and rutile with carbon incorporation.

In order to shed further light on the influence of the carbon content, film morphology was evaluated by dynamic mode technique (AFM of Shimadzu). Figure 4 shows the obtained AFM images of nano- and micro-fibers prepared by annealing at different temperatures in wet N$_2$ (0.8%H$_2$O) for 3 wt%-doped TiO$_2$ thin films on a silicon substrate: a) top view of sample 1G; b) the correspondent statistics performed for figure 5 a); c) top view of sample 1F; d) top view of sample 1E; e) 3D view of sample 1E and (f) the correspondent statistics for figure 4d.

As a result of the performed analysis, the average RMS roughness of the as-deposited film was (2.3$\pm$0.5)nm and increased to (10$\pm$2)nm after annealing at 700°C in nitrogen+water vapor, being about four times higher. The observed "islands", as shown in Figure 4(a), presenting a diameter range of 19.05nm and 158.6nm.

On the other hand, as the temperature increases to 900°C, a threshold temperature, the morphology starts evoluting from small "islands" to micro scale meshes of fibers, with length varying from 0.79μm to 2.06μm and widths lower than 0.400μm (range: 0. 100 to 0.400μm). In this case, the RMS roughness decreased to (5.8$\pm$0.7)nm (Figure 4(c)) and, in place of "islands", needle-like nanofibers and embedded fibers were formed on the surface and below it.

Finally, after annealing at 1000°C, the film morphology was completely changed, as shown in Figure 4d (top view) and in figure 4e (3D view). In this case, micro scale meshes of fibers randomly distributed were observed with length ranging from 0.1 to 1.1μm (shown in figure 4 f) and average width of (0.170$\pm$20) μm. Also, the average RMS roughness decreased from (5.8$\pm$0.7)nm to (3.3$\pm$0.2)nm.

In contrast, when the carbon concentration was decreased below 2%wt, nano- and microfibers were not observed (AFM images not shown) on the samples prepared by annealing at different temperatures (700-1000^{0}C) in pure N$_2$ or wet N$_2$ (0.8%H$_2$O).

Figure 5a shows the FTIR analysis of C-doped TiO$_2$ samples1.5%wt (1F$_x$ and 1E$_x$) and 3.0%wt (1G, 1F and 1E) that have been annealed at 700°C, 900°C and 1000°C. A broad absorption peak at 1096cm^{-1} and this peak represents Si-O-Si stretching bond, while the Si-O-Si bending peak is also shown at 820cm^{-1} (Yakovlev et. al., 2000) and (Erkov et. al., 2000), both can be associated to silicon oxidation during the thermal annealing in water vapor atmosphere. Also, Ti-O-Ti stretching vibration of the rutile phase was observed at 614.4cm^{-1} for all samples (Yakovlev et. al., 2000) and (Erkov et. al., 2000), corroborating the XRD analysis, where a change in the cristallinity was demonstrated, evoluting from an armophous structure to a crystalline one (rutile). The higher intensity of this band is likely to be due to the increase in the amount of rutile when the carbon content is higher (3%wt). For this carbon content, Ti-O stretching at 736.5cm^{-1} (Yakovlev et. al., 2000) progressively increases as the annealing temperature increases from 700°C to 1000°C, which indicates progressive transition from an amorphous TiO$_2$ to a crystalline structure of λ-Ti$_3$O$_5$ and rutile. In addition, a band is observed at 781 cm^{-1} only for sample 1E, which was annealed at 1000°C, as shown in detail in figure 5b. Richiardi et al.(Richiardi et. al., 2001) shows this

band to be due to symmetric stretching of Ti-O-Si and Si-O-Si bonds, which corroborates a quantitative mixture of SiO_2 and TiO_2 at the interface; where TiO_2 is more likely rutile since it is at the interface as established by Raman analysis (not shown).

(a)

(b)

(c)

(d)

(e)

(f)
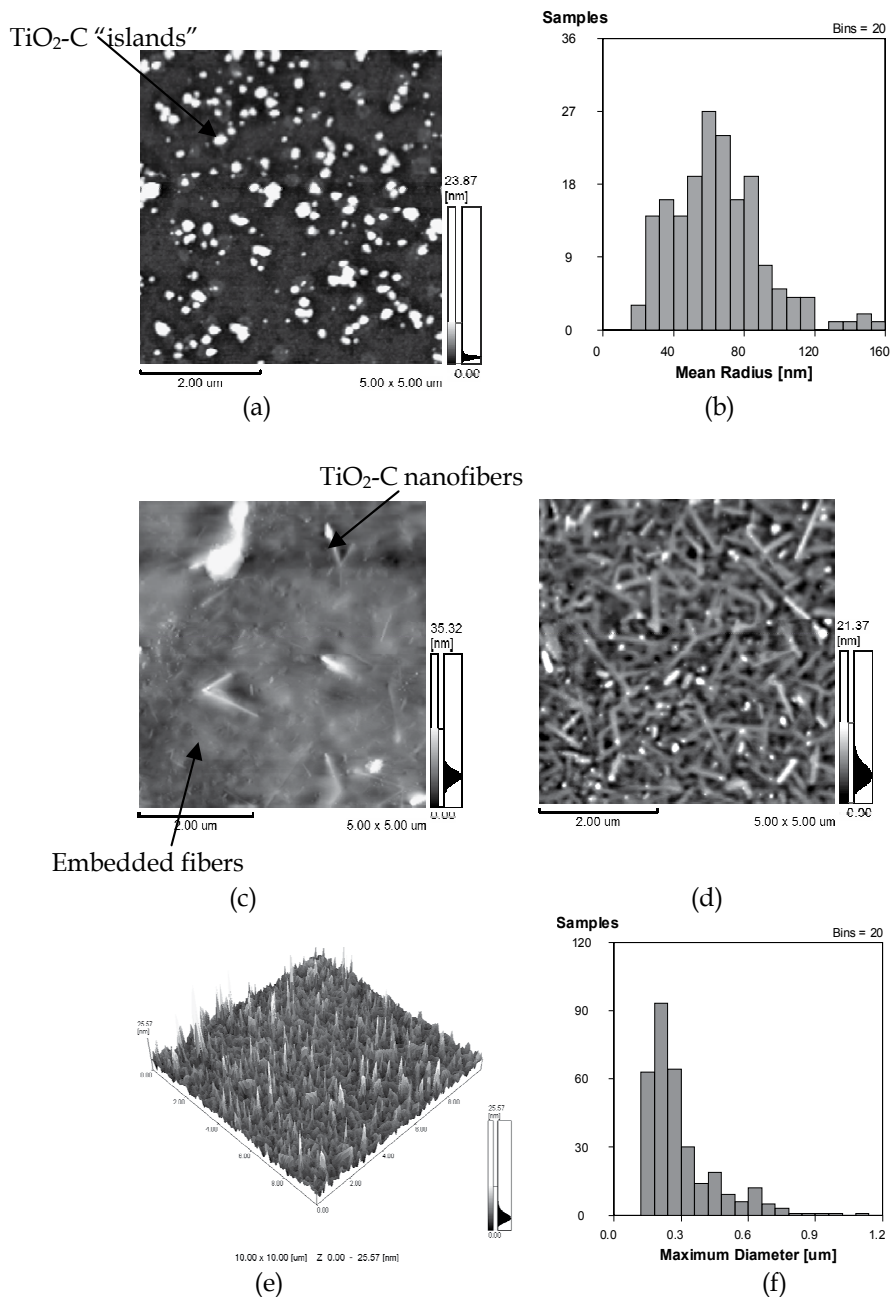
Fig. 4. Typical dynamic-mode AFM images for: (a) sample 1G annealed at 700°C; (b) statistics of (a); (c) sample 1F annealed at 900°C; (d) sample 1E (top view); (e) sample 1E (3D view) and (f) statistics of (d).
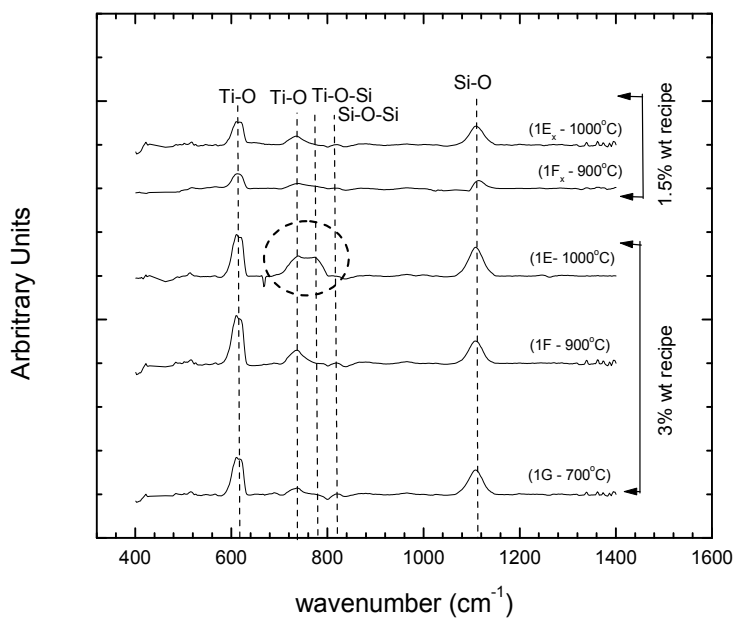
(a)
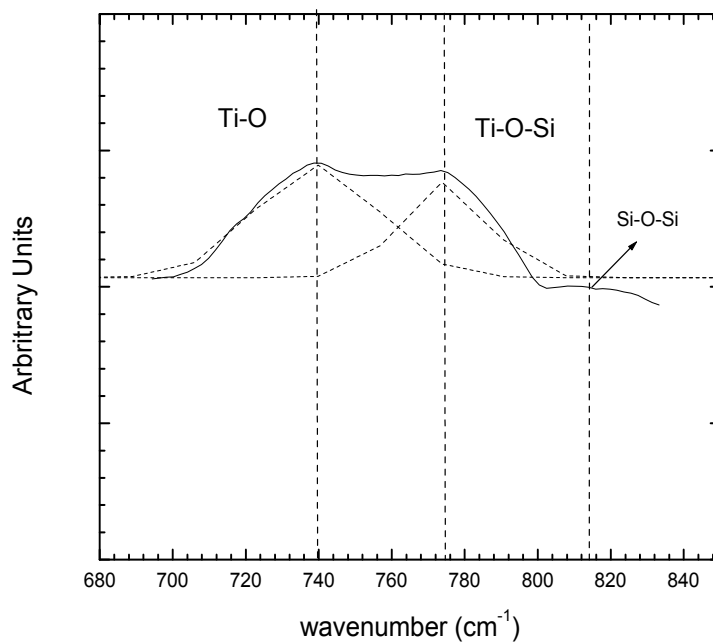
(b)

Fig. 5. a) Typical FTIR spectra as function of the wave number for the 3%wt recipe: samples
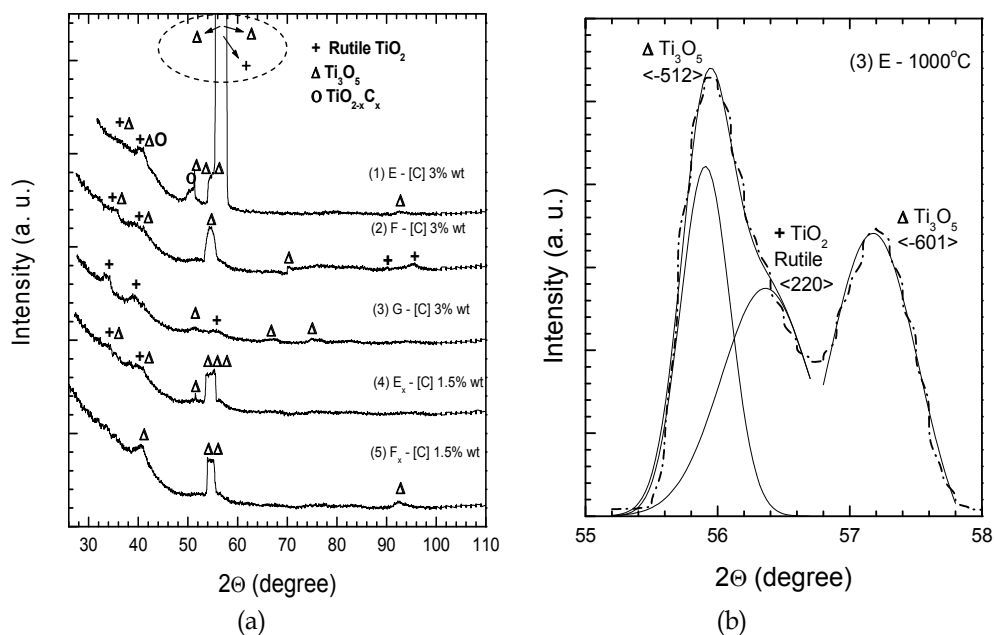1G (700°C), 1F (900°C) and 1E (1000°C), and for the 1.5%w recipe: samples 1F$_x$ (900°C) and
1E$_x$ (1000°C) and b) larger view of FTIR curve.

Aiming to evaluate stoichiometry and the carbon content after thermal treatments, the aerial concentrations of oxygen and titanium were obtained from Rutherford Backscattering Spectrometry (RBS) by fitting rump-code simulation (Climent-font et. al., 2002) to the experimental spectra. Using the extracted aerial concentrations (cm^{-2}), stoichiometry of the titanium oxide was determined admitting a weighted composition of $aTiO_x + bSiO_2$, where a, b and x are calculated parameters. The carbon content was obtained by EDS analysis because the detection limit was lower than the value reported to RBS analysis (Wuderlich et. al., 1993). Also, EDS has sufficient sensitivity to distinguish carbon content of 1.5%wt from 3.0wt% (detection limit of about 0.1wt%) analysis (Wuderlich et. al., 1993). Figure 6 illustrates the experimental RBS spectrum and the fitted simulation for the sample 1E.

Table 2 presents the average concentration of carbon [C], the stoichiometry and the aerial silicon-oxide concentration [SiO_2] extracted from the EDS and RBS analyses according to the procedure described in the experimental section.

For the 3.0%wt carbon concentration in table 2, the SiO_2-layer thickness ranged from 16.2 nm ($\approx 7.5 \times 10^{16}$ atoms/cm^2) to 19.4 nm ($\approx 9.0 \times 10^{16}$ atoms/cm^2) for temperatures varying from 700°C to 1000°C. In this case, as predicted by the band at 1096 cm^{-1}, the higher the temperature, the higher the aerial silicon oxide concentration, which is consistent with the increase of the band at 1096 cm^{-1} in Figure 5. However, the oxygen stoichiometric coefficient of TiO_x decreased from 2.0 to 1.7 (see table 1) when the temperature was increased from 700 to 900°C. Assuming the presence of crystalline Ti_3O_5 and rutile, as illustrated by the XRD results, $TiO_{1.70}$ fits well with 25% TiO_2 and 75% Ti_3O_5 at 1000°C. Moreover, TiO_2 is consistent with predominantly amorphous TiO_2 at 700°C (sample 1G), as illustrated by the XRD results. Finally, $TiO_{1.85}$ (sample 1F) fits well with 75% TiO_2 and 25% Ti_3O_5 at 900°C (sample 1F) and is also consistent with a predominantly amorphous TiO_2, as illustrated by the XRD results.
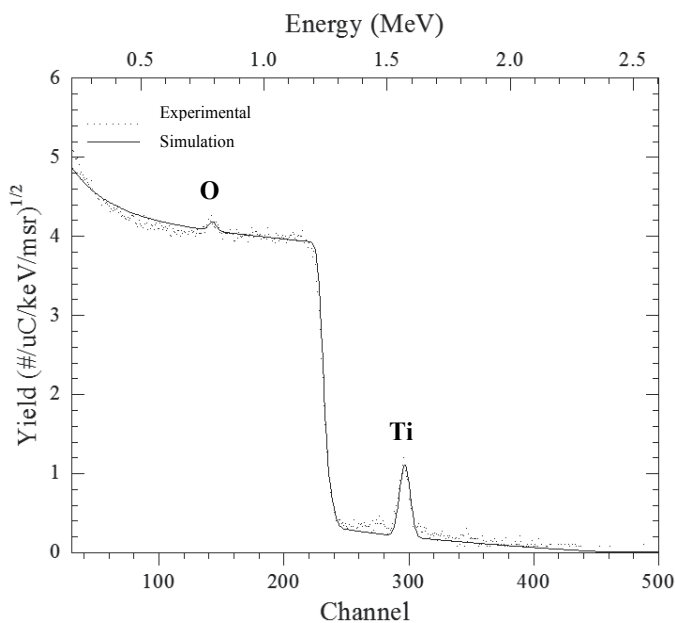
Fig. 6. Typical RBS spectrum of the sample 1E (3%w recipe).

For the 1.5%wt carbon concentration in table 2 the oxygen stoichiometric coefficient is close to 1.80 for the thermal treatments of 900°C and 1000°C. In this case, TiO$_{1.80}$ fits well with 66% TiO$_2$ and 33% Ti$_3$O$_5$, which is consistent with a predominantly amorphous TiO$_2$ with a low concentration of Ti$_3$O$_5$, as illustrated by the XRD results. In the latter case (sample 1Ex), the diffusion of the oxygen species might have been prevented, if compared to sample 1E, possibly due to a denser bulk of TiO$_2$ at 1000°C, which might have also slightly decreased the growth rate of the SiO$_2$ layer (Koch, 2002) .

Recipe	Sample	Temperature (°C)	[C] (%wt)	Stoichiometry	[TiO$_x$] (10^{16}/cm^2)	[SiO$_2$] (10^{16}/cm^2)
3.0%wt	1G	700	3.4±1.2	TiO$_{2.00}$	4.3	7.5
	1F	900	3.2±0.9	TiO$_{1.85}$ = 0.75TiO$_2$ + 0.25 Ti$_3$O$_5$	7.0	8.0
	1E	1000	3.4±0.6	TiO$_{1.70}$ =0.25TiO$_2$ + 0.75 Ti$_3$O$_5$	5.7	9.0
1.5%wt	1F$_X$	900	1.5±0.4	TiO$_{1.80}$ = 0.66TiO$_2$ + 0.33 Ti$_3$O$_5$	4.3	8.0
	1E$_X$	1000	1.7±0.2	TiO$_{1.80}$ = 0.66TiO$_2$ + 0.33 Ti$_3$O$_5$	3.6	8.5

Table 2. Average concentration of carbon [C] as obtained from EDS and, stoichiometry and aerial silicon oxide concentration [SiO$_2$] after fitting rump-code simulation to the experimental spectra using weighted compositions of aTiO$_x$ + bSiO$_2$. TiOx layer is divided into two different layers rutile TiO$_2$ and Ti$_3$O$_5$ according to XRD spectra from figure 3, except for sample G where rutile TiO$_2$ is dominant.

Figures 7a and 7b show the diffuse reflectance spectra and the solar spectrum for AM1.5G (ASTMG173) (Stem, 2007) and (ASTM, 2005), respectively. Figure 7a allow to infer that it is evident that the film annealed at 700°C has a less significant amount of absorption in the visible region with the absorption band limited at a wavelength below 460 nm. In this case, titanium oxide is predominantly amorphous, and the literature corroborates this limited band below 460 nm (Wang et. al., 2007). However, when the annealing temperature was increased to 900°C or 1000°C, samples 1F and 1E adsorbed a much larger light fraction in the visible region, which can be attributed to a structural change of the samples associated with a phase transition to rutile, TiO$_{2-x}$C$_x$ and Ti$_3$O$_5$. In this case, both positions, substitutional and interstitial, carbon significantly impacts the optical properties in the range of 500 to 800 nm because of the formation of complex midgap states (Reyes-Garcia et. al., 2008) and (Wang et. al., 2007).

(a)

(b)
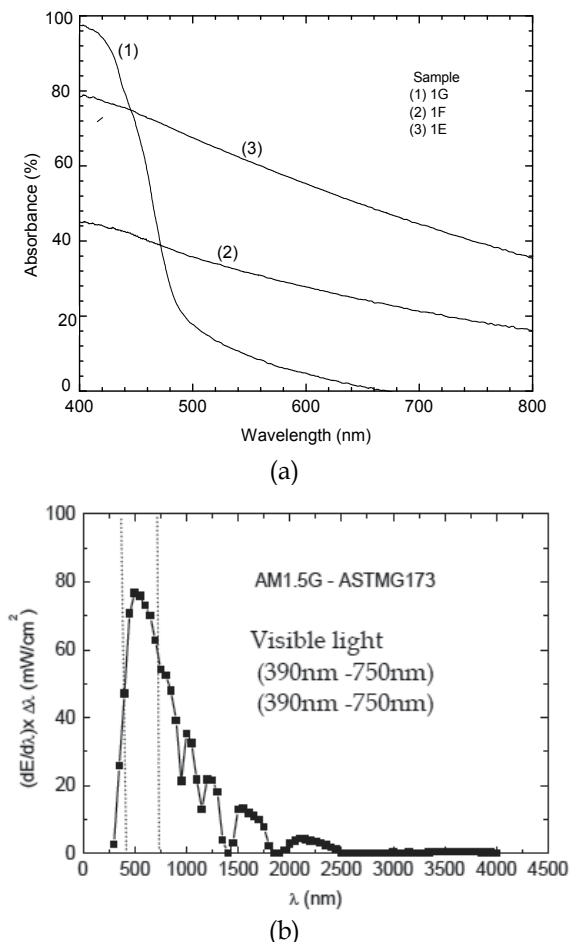
Fig. 7. (a) Absorbance curves as function of wavelength for samples processed with the 3%wt carbon recipe (1G, 1F and 1E). Their correspondent optical band-gap extracted from the curve is also presented. (b) Solar spectral irradiance as function of the wavelength, λ (nm) for AM1,5G spectrum (ASTM G173-03) (Stem, 2007), (ASTM, 2005).

Aiming at evaluating the photo catalytic properties of the developed material, the photoluminescence spectrum were obtained as function of the wavelength. Figure 8(a) shows the room temperature photoluminescence (PL) emission of the samples 1G(700°C), 1F (900°C) and 1E(1000°C) in which the vertical scale of the intensity was normalized using the silicon peak at 515nm for the three spectra. Based on this normalization, the PL emission of the samples 1G and 1F are significantly lower in area compared to sample 1E. In addition, figures 8b, 8c and 8d show the obtained spectrum for each studied case and peaks deconvolutions based on Gaussian distributions, respectively.

Basically, three characteristic band peaks are obtained: a) sample 1G: at approximately 2.2eV and 2eV; b) sample 1F: at approximately 2.2eV and 1.9eV and c) sample 1E: at approximately 2.2eV, 2.0eV and 1.9eV; which are close to one another and they are distant from the optical band gap reported on rutile (3.05eV) (Wang et. al., 2009) and on Ti_3O_5 (4.04eV) (Wouter et. al., 2007). On the other hand, Enache et al. (Enache et. al., 2004) report

that PL can reveal the nature of the defects involved in C-doped titanium oxides, showing that the broad peak at ~ 2.0eV is correlated to the amount of disorder due to the increase in the number of defects, oxygen vacancies or titanium interstitials (Enache et. al., 2004). Meanwhile, the broadband at ~1.90eV is believed to be associated to the presence of ionic point defects, or to excitons bound to these defects (Enache et. al, 2004) and the broadband at ~2.2 eV is attributed to self-trapped excitons (Enache et. al., 2004).
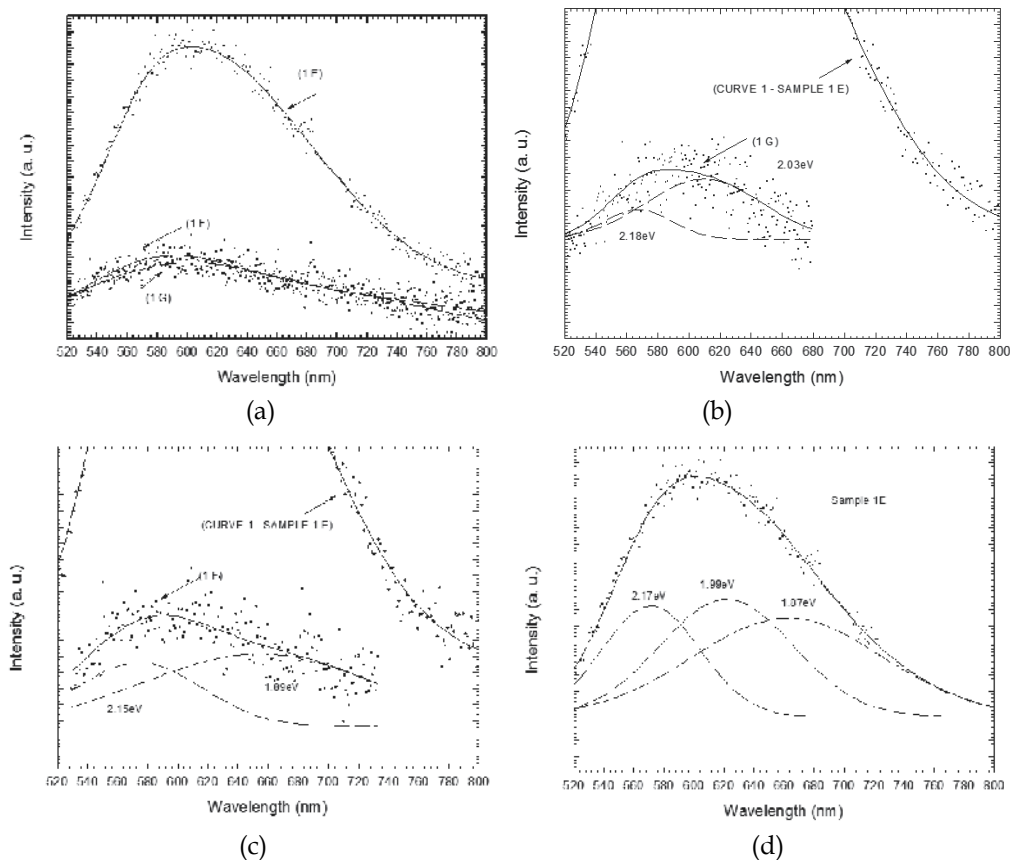
Fig. 8. PL measurements as wafunction of the wavelength: a) for the samples 1E, 1F and 1G; and peak deconvoution for samples b) 1E; c) 1F and d) 1G.

Thus, analyzing the deconvolutions (figures 8b, 8c and 8d) it can be observed that in figure 8 (b), sample G has as dominant the band centered at 2.0eV (about 63.8%) and a minor band centered at about 2.2eV, representing about 36.2% of total area. According to XRD spectra presented at figure 3a, the sample G is practically amorphous presenting small peaks associated to rutile TiO$_2$, thus it can be inferred that band peak at ~ 2.0eV to the number of defects, oxygen vacancies or titanium interstitials in rutile TiO$_2$ (as discussed item) mainly due to carbon doping and the band center at 2.2eV, attributed to some to self-trapped excitons (Enache et. al., 2004).

However, as the hydrothermal temperature annealing increases to 900ºC (sample 1F), the nanofibers started to be formed, and XRD peaks corresponding to Ti$_3$O$_5$ become dominant and the band corresponding to ~ 2.0eV (tentatively associated to rutile TiO$_2$) practically

vanishes. In this sample, the band centered at 2.2 eV (some to self-trapped excitons) is about 35.6% of the total area, practically equal the one presented for sample 1G. Meanwhile, the start of nanofibers formation promoted the generation of a new band, compared to sample G spectrum, centered at about 1.9eV (about 64.4% of the total area) being believed to be associated to of ionic point defects, or to excitons bound to these defects (Enache et. al., 2004). These defects might be provenient from the vacancies produced by carbon doping; however, this fact needs further investigation afterwards.

As the temperature goes to 1000oC the nanofibers are formed, and two high intensity peaks were identified in XRD spectrum, rutile TiO_2 and Ti_3O_5. Analyzing the deconvolution of PL spectrum of sample 1E, three bands could be identified, being centered at 2.2eV, 2.0eV and 1.9eV, representing about 21.4%, 34.5% and 44.1% of total area, respectively. The band centered at 2.2eV, initially associated to some to self-trapped excitons in samples 1G and 1F, had its area increased significantly, about three times than for the other cases. On the other hand, the band centered at 2.0eV, that was vanished in the beginning of the nanofibers formation (sample F), became intense with the increase in the amount of disorder due to the random distribution of nano- and microfibers, which can promote increasing of the density of defects, oxygen vacancies and titanium interstitials on carbon doped rutile TiO_2 and λ-Ti_3O_5 (Monoclinic, C2/m E, a = 9.757Å, b = 3.802Å, c = 9.452Å). However, it should be pointed out that this disorder is not correlated to the cristallinity of the film as demonstrated by XRD spectra. The mentioned disorder also promoted an increase in the broadband centered at ~1.90eV, as mentioned previously, believed to be associated to the presence of ionic point defects, or to excitons bound to these defects.

In order to compare the peak areas of the studied PL spectrum, obtained based on the peak deconvolution presented at figure 8, the normalized areas for each samples are presented as functions of the characteristical band, 1.90eV, 2.00 eV and 2.20eV in figure 9. Analyzing this figure, it can be easily identified the growth of the three bands for sample 1E for the three characteristic bands.
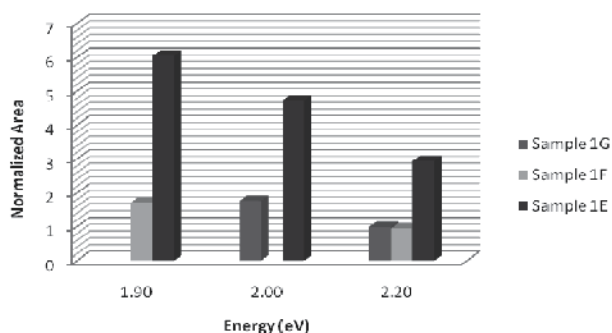
Fig. 9. Normalized areas for each studied sample as function of the normalized areas resulting from the peak deconvolution presented at figure 8.

6. Inferring about the reaction mechanisms to form the nanofibers

In order to infer a possible reaction mechanism model for producing nanofibers for the technique, the system can be divided into three groups: a) rutile carbon doped reactions; b) carbothermal reaction; c) TiO_2 behavior under nitrogen atmosphere and d) TiO_2 behavior under water vapor (an oxygen atmosphere (Richards, 2002) and hydrogen atmosphere), as presented at Table 3. The required energy to form reactions or the Gibbs potentials is

presented. Thus, the reactions that present a negative free energy are expected to occur spontaneously and the positive ones require adsorption of energy. Therefore, only the most probable or spontaneously reactions will be considered (the most negative Gibbs potential).

According to Valentini et. al.(Valentini et. al., 2005), the reactions that might occur in rutile titania and the correspondent required energy are represented for the equations (1)-(3) in table 3. Equation (1) stands for pure rutile material and (2)-(3) for carbon-doped titanium, occupying interstitial and substitutional positions, respectively. The energy required to interstitial reaction to occur is associated to the sum of the required energies to break the C-O and Ti-O bonds, while the required energy to substitutional reactions to occur is most probably associated to the tendency of carbon atoms trap electrons from the oxygen vacancy.

However, when high annealing temperatures are considered, carbothermal reactions (Sen et. al., 2011) and the interaction between TiO_2/Si (Richards, 2002) also become important. In particular, in carbothermal reaction, titanium dioxide is believed to react with carbon in order to obtain Ti_3O_5 and CO (equation (4)) in table 3. On the other hand, as the adopted atmosphere for the annealings in the proposed technique of this chapter consists of wet Nitrogen (0.8% water vapor), the dominant reactions between the interface TiO_2/Si are the ones obtained for nitrogen atmosphere, equation (5), so that Ti_3O_5 and SiO_2 are products of the expected reactions, as for the carbothermal reaction.

Focusing on the small percentage of water vapor present at the annealing atmosphere, it can be inferred that the water vapor dissociates at oxygen and hydrogen. Thus, all most probable reactions on TiO_2/Si interface point out to form Ti_3O_5, corroborating the XRD spectrum, AFM and FTIR spectra presented in the figures 3, 4 and 5.

Another point to be considered is that the hydrogen present in the atmosphere are expected to promote a kind of a redox reaction (Iowaki, 1983), when the hydrogen penetrates the film, forming oxygen vacancies and electrons are trapped as shown at equation (8). On the other hand, hydrogen is also adsorbed on neighboring oxygen, forming a hydroxyl group and Ti_3^+ that is not removed from surface, as shown in equation (9).
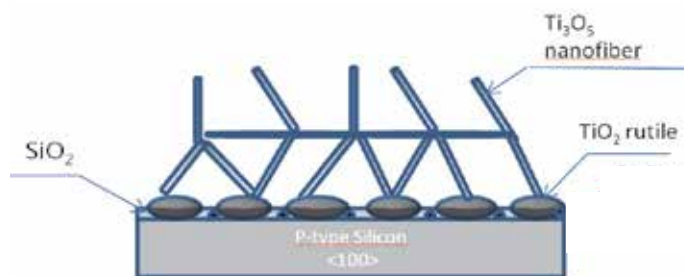
Fig. 10. Inferred scheme about nanofibers formation.

In order to understand how nano- and microfibers are formed on the silicon substrate, a schematic mechanism is proposed and illustrated in Figure 10. Initially, the amorphous TiO_2 would change from the amorphous to rutile phase, the carbon presence is believed to favor rutile phase (Binh, 2011). Rutile subsequently reacts with Si to form Ti_3O_5 (equations (4) and (5)). When the heating budget and carbon concentration are larger enough, Ti_3O_5 nano- and microfibers are formed to reach minimum free energy. The reactions presented in table 3 compete against each other to reach the minimum value for Gibbs potential, G_o. The equilibrium structure based on the competition of strain energy and surface energy would be either nanowires, or nanofibers.

		E(eV)
Carbon doping rutile titania (Valentini et. Al., 2005)	$TiO_2(s) \rightarrow TiO_{2-x} + xV_o + x/2\,O_2(g)$ (pure material) (1)	4.4
	$TiO_2C_x(s) \rightarrow TiO_{2-x}C_x(s) + xV_o + x/2\,O_2(g)$ (interstitial) (2)	2.4
	$TiO_{2-x}C_x(s) \rightarrow TiO_{2-2x}C_x(s) + xV_o + x/2\,O_2(g)$ (substitutional) (3)	2.4
Carbothermal Reactions (Sen et. al., 2011)	$3TiO_2 + C \rightarrow Ti_3O_5 + CO$ (4)	G_o (kJ) -156.9
TiO₂/ Si under nitrogen atmosphere (Richards, 2002)	Possible TiO₂/Si Reactions	G_o (kJ)
	$6TiO_2 + Si \rightarrow 2Ti_3O_5$ (5)	-156.9
TiO₂/ Si under oxygen atmosphere (Richards, 2002)	Possible TiO₂/Si Reactions	G_o (kJ)
	$3TiO_2 + O_2 \rightarrow Ti_3O_5 + 3/2 O_2$ (6)	398.1
	$TiO_2 + O_2 + Si \rightarrow TiO_2 + SiO_2$ (7)	-961.5
TiO₂ under hydrogen Atmosphere (Iowaki, 1983),		

Table 3. Possible involved reactions for the obtaining of the nanofiber.

7. Conclusions

In this chapter a review about the methods for producing nanofibers were presented and a new process for achieving the λ-Ti3O5 nano- and microfibers from C-doped TiO_2 thin films was also presented. Initially, the condition to form the nanofibers needs carbon (3%wt) as precursor seed followed by thermal treatment in nitrogen+water vapor (0.8%wt) environment at 1000°C during 120min. In this case, microscale meshes of fibers randomly distributed were observed with length ranging from 0.1 to 1.1μm and average width of (170±20)nm. The nano- and microfibers formation was characterized at different temperatures, including the initial stages at 900°C. From Raman and FTIR Spectroscopy techniques, it was shown that rutile is an inner layer located at the interface mesh/Si that is away from the surface so that the meshes of nano- and microfibers are predominantly composed of λ-Ti_3O_5 grown from the reaction with Si to form Ti_3O_5 and SiO_2. On the other hand, it was noteworthy that the microscale mesh of nano- and microfibers showed increased photoluminescence compared to amorphous TiO_2 with a broad peak in the visible

if compared with samples built up of carbon-doped rutile titanium dioxide and samples with the nanofibers at the initial stage.

8. Acknowledgements

9. References

Sauvage, F; Di Fonzo, F.; Bassi, A. L.; Casari, C. S.; Russo, V.; Divitini, G.; Ducati, C.; Bottani, C. E.; Comte, P.; and Graetzel, M. (2010), Hierarchical TiO$_2$ Photoanode for Dye-Sensitized Solar Cells, *Nanoletters*, Vol. 10, pp 2562-2567.

Lin, H.; Wang, Wen-li; Liu, Yi-zhu and Li, Jian-bao (2009). Review article: New Trends for Solar Cell Development and Recent Progress of Dye Sensitized Solar Cells, Frontiers of Materials Science in China, Vol. 3, Nº 4, pp. 345-352.

Kim, H.; Bae, S. and Bae, D., (2010) Synthesis and Characterization of Ru Doped TiO$_2$ Nanoparticles by A Sol-Gel and A Hydrothermal Process, *Advances in Technology of Materials and Materials Processing*, Vol. 12, Nº 9, pp 1-6.

Wenger, S. (2010) Strategies to optimizing dye-sensitized solar cells: organic sensitizers, tandem device structures, and numerical device modeling, Ph. D. Thesis, École Polytechnique Fédérale de Lausanne.

Kong, F.; Dai, S., and Wang, K. (2007); Review of recent progress in Dye-sensitized solar cells, *Advances in OptoElectronics*, Vol. 2007, pp. 1-13.

Hafez, H.; Lan, Z.; Li, Q.; Wu, J. (2010); Review: High efficiency dye-sentized solar cell based on novel TiO$_2$ nanorod/nanoparticle bilayer electrode. *Nanotechnology, Science and Applications*, Vol. 3, Nº 1, pp. 45-51.

Pagliaro, M.; Palmisano, G. and Ciriminna, R. (2009); Working principles of dye-sensitized solar cells and future applications *Photovoltaics International journal*, Vol. 2, pp. 47 – 50.

Fieggemeier, E. and Hagfeldt, A. (2004), Are dye sensitized nano-structured solar cells stable? An overview of device testing and component analyses, *International Journal of Photoenergy*, V. 06, pp. 127-140.

Wang, P.; Zakeeruddin, S. M.; Moser, J. E.; Nazeeruddin, M. K.; Sekiguchi, T. and Gratzel, M., (2003). A stable quasi-solid-state dye-sensitized solar cell with an amphilic ruthenium sensitizer and polymer gel electrolyte. *Nature Materials*, Vol. 2, pp. 402-407.

Ou, Hsin-Hung and Lo, Shang-Lien (2007) Review of titania nanotubes synthesized via the hydrothermal treatment: Fabrication, modification, and application. *Sep Purif Technol,* Vol. 58, pp 179–191.

Suzuki Y and Yoshikawa S. (2004). Synthesis and thermal analyses of TiO$_2$-derived nanotubes prepared by hydrothermal method. *Journal of Materials Research*, Vol.. 19, pp. 982-985.

Kim, I.; Gwak, J.; Han, S.; Singh, K. (2007), Synthesis of Pd or Pt/titanate nanotube and its application to catalytic type hydrogen gas sensor, *Sensors and Actuators B,* Vol. 128, pp. 320-325.

Varghese, O. K.; Gong, D.; Paulose, M.; Ong, K. G. Mand Grimes, C. A., (2003), Hydrogen sensing using titania nanotubes, *Sensors and Actuators B*, Vol. 93, pp. 338-344.

Chen, X. and Mao, S. S. (2007), Titanium Dioxide Nanomaterials: Synthesis, Properties, Modifications, andApplications,*Chem. Rev*., Vol. 107, pp. 2891-2959.

Nuansing, W.; Ninmuang, S.;Jaremboon, W.; Maensiri, S.; Seraphin, S. (2006), Structural characterization and morphology of electrospun TiO_2 nanofibers, *Materials Science and Engineering B*, Vol. 131, № 1-3, pp. 147-155.

Park, S. J.; Chase, G. G.; Jerong, K. and Kim, H. Y. (2010), Mechanical Properties of titania nanofiber mats fabricated by electropsinning of sol-gel precursor, *J. Sol-gel Technol.*, Vol. 54, pp. 188-194.

D. Valentini, D.; Pacchioni, G.; Selloni, A. (2005), Theory of carbon doping of titanium dioxide, *Chem. Matter*., Vol 17, pp. 6656-6665.

Kukovecz, A.; Hodos, M.; Horváth, E. ; Radnóczi, G.; Kónya, Z.; and Kiricsi, I. (2005). Oriented Crystal Growth Model Explains the Formation of Titania Nanotubes, *The Journal of Physical Chemistry B Letters*, Vol. 109, № 38, pp. 17781–17783.

Puma, G. L.; Bono, A.; Krishnaiah, D.; Collin, J. G. (2008). Preparation of titanium dioxide photocatalyst loaded onto activated carbon support using chemical vapor deposition: A review paper, *Journal of Hazardous Materials*, Vol. 157, № 2-3, pp. 209-219.

Yamamoto, S.; Bluhm, H.; Andersson, K.; Ketteler, G.; Ogasawara, H.; Salmeron, M. and Nilsson, A. (2008); In situ x-ray photoelectron spectroscopy studies of water on metals and oxides at ambient conditions; *Journal of Physics: Condensed Matter*, Vol. 20, No 18, pp. 184025.

Khan, MA; Han, DH; Yang, OB (2009). Enhanced photoresponse towards visible light in Ru doped titania nanotube. *Applied Surface Science*. Vol. 255, pp. 3687-3690.

Zhang, H.; Li, X. and Chen, G. (2010); chapter Fabrication of Photoelectrode Materials, Electrochemistry for the Enviroment, Springer New York, ISBN 978-0-387-68318-8, pp. 475-513.

Reyes-Garcia, A.; Sun, Y.; Reyes-GLL , K. R. and Raftery, D. (2009), Solid-state NMR and EPR analysis of carbon doped titanium dioxide photocatalystis ($TiO_{2-x}C_x$), *Solid State Nuclear Magnetic Resonance in Catalysi*s, Vol. 35, № 2, pp. 74-81.

Konstantinova, E. A.; Kokorin, A. I.; Saktivel, S.; Kisch, H. and Lips, K. (2007); Carbon-doped titanium dioxide: visible light photocatalysis and EPR investigation; *Transformation and storage of solar Energy*, Vol. 61, № 12, pp. 810-814.

Suzuki Y and Yoshikawa S. (2004). Synthesis and thermal analyses of TiO_2-derived nanotubes prepared by hydrothermal method. *Journal of Materials Research*, Vol.. 19, pp. 982-985.

Chen, Huei-Siou; Su, C.; Chen, Ji-Lian; Yang, Tsai-Yin; Hsu, Nai-Mu; and Li, Wen-Ren (2011), Preparation and Characterization of Pure Rutile TiO_2 Nanoparticles for Photocatalytic Study and Thin Films for Dye-sensitized Solar cells, *Journal of nanomaterials*, Vol. 2011, № 1, pp. 1 – 8.

Wu, Z.; Dong, F.; Zhao, W.; Wang, H.; Liu, Y. and Guan, B. (2009); The fabrication and characterization of novel carbon doped TiO_2 nanotubes, nanowires and nanorods with high visible light photocatalytic activity; *Nanotechnology*, Vol. 20, No 23, p. 235701.

Tryba, B. (2008), Increase of the photocalaytic activity of TiO_2 by carbon and iron modifications – review article, International Journal of Photoenergy, Vol. 2008, Article ID 721824, pp.1-15.

Dai, Z. R.; Gole, J. L.; Stout, J. D. and Wang, Z. L. (2002), Tin Oxide Nanowires, Nanoribbons, and Nanotubes; *J. Phys. Chem. B*, Vol. 106, N° 6, pp 1274–1279.

Yin, Y.; Zhang, G. and Xia, Y. (2002), Synthesis and Characterization of MgO Nanowires through a Vapor-Phase Precursor Method, *Adv. Func. Mater.*, Vol. *12*, pp.293-298.

Pan, Z. W., Dai, Z.R., and Wang, Z.L. (2002), Lead oxide nanobelts and phase transformation induced by electron beam irradiation, *Appl. Phys. Lett.*, Vol. 80, pp. 309-311.

Wu, J. M.; Shin, H. C. and Wu, W. T. (2005), Growth of TiO$_2$ nanorods by two-step thermal evaporation, *J. Vac. Sci. Technol. B*, Vol. 23, pp. 2122 – 2126.

Xiang, B., Wang, Q. X.; Zhang, X. Z.; Liu, L. Q.; Xu, J. and Yu., D. P. (2005), Synthesis and field emission properties of TiSi$_2$ nanowires *Appl. Phys. Lett. 86*, pp. 243103/1-243103/3 issue 24

Bennett, P. A.; Ashcroft, B.; He,Z. and Tromp, R. M. (2002), Growth dynamics of titanium silicide nanowires observed with low-energy electron microscopy, *J. Vac. Sci. Technol. B*, Vol. 20, pp. 2500-2504.

Wang, C. C.; Yu, C.-Y.; Kei, C. C.; Lee, C. T. and Perng, T. P. (2009); Formation of TiO$_2$ nanowires on silicon directly from nanoparticles, *Nanotechnology*, Vol. 20, pp. 1-6.

Sen, W.; Xu, B. q.; Yang, B.; Sun, H.-y.; Song, J.-x.; Wan, H.-l. and Dai, Y.-n. (2011), Preparation of TiC powders by carbothermal reduction method in vacuum, *Transactions of Nonferrous Metals Society of China* , Vol. 21, N° 1, pp 185-190.

Swift, G. A. and Koc, R. (1999), Formation studies of TiC from carbon coated TiO$_2$, *Journal of Materials Science*, Vol. 34 , pp. 3083 – 3093.

Bavykin, D. V.; Friedrich, J. M. and Walsh, F. C. (2006); Protonated titanates and TiO$_2$ nanostructured nanomaterials: synthesis, properties and applications, Vol. 18, N° 21, pp. 2807-2824.

Bavyjkin, D. V. and Walsh, F. C. (2009); Elongated titanate nanostructures and their applications; *European Journal of Inorganic Chemistry*, Vol. 2009, N° 8, pp. 977-997.

Santos Filho, S. G.; Hasenak, C. M.; Sanay, L. C. and Mertens, P. (1995); A less critical cleaning procedure for silicon wafer using diluted HF dip and boiling in isopropyl alcohol as final step; *J. Eletrechemical Soc.*, Vol. 142, N° 3, pp. 902 – 907.

Stem, N.; Santos Filho, S. G. (2010); Carbon-Modified Titanium Dioxide Deposited by E-Beam Aiming Hydrogen Sensing. *In: 25th Symposium on Micreoelectronics Technology and Devices, 2010, São Paulo. 25th Symposium on Micreoelectronics Technology and Devices (ECS Transactions)*). New Jersey, USA : Pennington, Vol. 31, pp. 433-439.

Stem, N.; Chinaglia E. F.; Santos Filho, S. G. (2011); Ti$_3$O$_5$ nano- and microfibers prepared via annealing of C-doped TiO$_2$ thin films aiming at solar cell and photocatalysis applications. *In: 26th Symposium on Microelectronics Technology and Devices (ECS Transactions). New Jersey, USA: Pennington, 2011.*

Stem, N.; Chinaglia E. F.; Santos Filho, S. G. (2011). Microscale meshes of Ti$_3$O$_5$ nano- and microfibers prepared via annealing of C-doped TiO$_2$ thin films. *Materials Science & Engineering. B, Solid-State Materials for Advanced Technology*, DOI: 10.1016/ j.mseb.2011.06.013, available on line.

Kern, W. (1990); The evolution of silicon wafer technology, *The Journal of Eletrochemical Society*, Vol. 137, N° 6, pp.1887-1892.

Reinhardt, K. A. and Wern. K (2008); Handbook of Silicon Wafer Cleaning Technology, Materials Science and Process Technology Series. 2nd Edition, Willian Andrew.

Shannon, R. D. (1964), Phase transformation studies in TiO_2 supporting different defect mechanisms in vacuum-reduced and hydrogen-reduced rutile. *J Appl Phys*, Vol. 35, pp. 3414–3416.

Liu, H.; Zhang, Y.; Li, R.; Cai, M.; Sun, X. (2010), A facile route to synthesize titanium oxide nanowires via water-assisted chemical vapor deposition *J. Nanopart. Res.* (2010) DOI 10.1007/s11051-010-0041-0.

Grey, I. E.; Li, C.; Madsen, I. C. (1994) Phase Equilibria and Structural Studies on the Solid Solution $MgTi_2O_5$-Ti_3O_5 *Journal of Solid State Chemistry*, Vol. 113, Nº 1, pp. 62-73.

Yakovlev, V. V.; Scarel, G.; Aita, C. R. and Mochizuki, S. (2000), Short-range order in ultrathinfilm titanium dioxide studied by Raman spectroscopy, *Appl. Phys. Lett.*, Vol. 76, Nº 9, pp. 1107-1109.

Erkov, V. G.; Devyatova, S. F.; Molodstova, E. L.; Malsteva, T. V.; and Yanovskii, U. A. (2000). Si-TiO_2 interface evolution at prolonged annealing in low vacuum or N_2O ambient Applied Surface Science, Vol. 166, Nº 1, pp. 51–56.

Climent-font, A; Watjen, U. and Bax, H. (2002); Quantitative RBS analysis using RUMP. On the accuracy of the He stopping in Si Nuclear Instruments and Methods in Physics Research, Section B, Vol. 71, pp. 81-86.

G. Richiardi, Al Damin, S. Bordiga, C. Lamberti, G. Spanó, F, Rivetti and A. Zecchina (2001), *J. Am. Chem. Soc.*, Vol. 123, 11409-11419.

Wuderlich, W.; Foitzik, A. H.; and Heuer, A. H. (1993); On the Quantitative EDS Analysis of Low Carbon Concentrations in Analytical TEM; *Ultramicroscopy*, Vol. 49, pp. 220 - 224.

Koch, Carl C. (2002). Nanostructured Materials - Processing, Properties and Potential Applications.. William Andrew Publishing/Noyes.New York, USA, ISBN 0-815514514.

ASTM G-173-03, Standard Table for reference solar spectrum irradiance direct normal and hemisphericalon 37º tilted surface, avaible at www.astm.org, accessed January 2005.

Stem, N. (2007), Células solares de silício de alto rendimento: otimizações teóricas e implementações experimentais utilizando processos de baixo custo, PhD Thesis, Escola Politécnica de Engenharia Elétrica da Universidade de São Paulo, http://www.teses.usp.br/teses/disponiveis/3/3140/tde-02042008-113959/fr.php.

Wang, X.; Meng, S.; Zhang, X.; Wang, H.; Zhong, W. and Du, Q. (2007). Multi-type carbon doping of TiO_2 photocatalyst, Chem. Phys. Lett., Vol. 444, pp. 292-296.

Sakthivel, S. and Kisch, H. (2003), Daylight Photocatalysis by Carbon-Modified Titanium Dioxide. *Angewandte Chemie International Edition*, Vol. 42, Nº 40, pp. 4908–4911.

Wouters, Y.; Galerie, A. and Petit, J-P. (2007), Photoelectrochemical study of oxides thermally grown on titanium in oxygen or water vapor atmospheres, *Journal of the Electrochemical Society*, Vol. 154, Nº 10, pp. C587-C592.

Enache, C. S.; Schoonman, J. S. and De Krol, R. V. (2004), The Photoresponse of Iron- and Carbon-Doped TiO_2 (Anatase) Photoelectrodes, *J. Electroceramics*, Vol. 13, Numbers 1-3, pp. 177-182.

Richards, B. S. (2002), Novel Uses of Titanium Dioxide for Silicon Solar Cells, *Ph.D. Thesis*, University of New South Wales.

Iowaki, T. (1983). Studies of the surface of titanium dioxide. Part 5.—Thermal desorption of hydrogen, *J. Chem. Soc., Faraday Trans. 1*, Vol. 79, pp. 137-146.

Dang, Binh H.Q.; Rahman, Mahfujur; MacElroy, J. M. Don (2011). Conversion of amorphous TiO_2 coatings into their crystallineform using a novel microwave plasma treatment. *Surface and Coatings Technology*, Article in Press

Dye Sensitized Solar Cells - Working Principles, Challenges and Opportunities

Khalil Ebrahim Jasim
Department of Physics, University of Bahrain
Kingdom of Bahrain

1. Introduction

Even before the industrial revolutions human life quality is greatly affected by the availability of energy. The escalated and savage consumption of conventional sources of energy are leading to forecasted energy and environmental crises. Renewable energy sources such as solar energy are considered as a feasible alternative because *"More energy from sunlight strikes Earth in 1 hour than all of the energy consumed by humans in an entire year."*(Lewis, 2007). Facilitating means to harvest a fraction of the solar energy reaching the Earth may solve many problems associated with both the energy and global environment (Nansen, 1995). Therefore, intensive research activities have resulted in attention-grabbing to the different classes of organic and inorganic based solar cells. A major study by IntertechPira stated that "The global Photovoltaic (PV) market, after experiencing a slow period, is expected to double within the next five years, reaching US$ 48 billion. Wafer-based silicon will continue as the dominant technology, but amorphous thin-film and Cadmium Telluride (CdTe) technologies will gain ground, and are expected to account for a combined 22% of the market by 2014" (www.intertechpira.com).

A solar cell is a photonic device that converts photons with specific wavelengths to electricity. After Alexandre Edmond Becquerel (French physicist) discovered the photoelectrochemical (photovoltaic) effect in 1839 (Becquerel, 1839) while he was investigating the effect of light on metal electrodes immersed in electrolyte, research in this area continued and technology developed to produce many types and structures of the materials presently used in photovoltaic (PV) technology. First and second generations photovoltaic cells are mainly constructed from semiconductors including crystalline silicon, III-V compounds, cadmium telluride, and copper indium selenide/sulfide (Hara & Arakawa, 2003; Hoffert, 1998; Zhao et al., 1999). Low cost solar cells have been the subject of intensive research work for the last three decades. Amorphous semiconductors were announced as one of the most promising materials for low cost energy production. However, dye sensitized solar cells DSSCs emerged as a new class of low cost energy conversion devices with simple manufacturing procedures. General comparison between semiconductor based solar cells and dye sensitized solar cells is presented in Table 1.

Incorporation of dye molecules in some wide bandgap semiconductor electrodes was a key factor in developing photoelecrochemical solar cells. Michael Gratzel and coworkers at the Ecole Polytechnique Federale de Lausanne (Gratzel, 2003; Nazerruddin et al., 1993; O' Regan & Gratzel, 1991) succeeded for the first time to produce what is known as "Gratzel Cell" or

the dye sensitized solar cell (DSSC) to imitate photosynthesis -the natural processes plants convert sunlight into energy- by sensitizing a nanocrystalline TiO_2 film using novel Ru bipyridl complex. In dye sensitized solar cell DSSC charge separation is accomplished by kinetic competition like in photosynthesis leading to photovoltaic action. It has been shown that DSSC are promising class of low cost and moderate efficiency solar cell (see Table 2 and Figure 1) based on organic materials (Gratzel, 2003; Hara & Arakawa, 2003).

	Semiconductor solar cells	DSSC
Transparency	Opaque	Transparent
Pro-Environment (Material & Process)	Normal	Great
Power Generation Cost	High	Low
Power Generation Efficiency	High	Normal
Color	Limited	Various

Table 1. Comparison between semiconductor based solar cell and the dye sensitized solar cell DSSC.

In fact, in semiconductor p-n junction solar cell charge separation is taken care by the junction built in electric field, while in dye sensitizes solar cell charge separation is by kinetic competition as in photosynthesis (Späth et al., 2003). The organic dye monolayer in the photoelectrochemical or dye sensitized solar cell replaces light absorbing pigments (chlorophylls), the wide bandgap nanostructured semiconductor layer replaces oxidized dihydro-nicotinamide-adenine-dinucleotide phosphate (NADPH), and carbon dioxide acts as the electron acceptor. Moreover, the electrolyte replaces the water while oxygen as the electron donor and oxidation product, respectively (Lagref. et al., 2008; Smestad & Gratzel, 1998). The overall cell efficiency of dye sensitized solar cell is found to be proportional to the electron injection efficiency in the wide bandgap nanostructured semiconductors. This finding has encouraged researchers over the past decade. ZnO_2 nanowires, for example, have been developed to replace both porous and TiO_2 nanoparticle based solar cells (Law et al., 2005). Also, metal complex and novel man made sensitizers have been proposed (Hasselmann & Meyer, 1999; Isalm et al., 2000; Yang et al., 2000). However, processing and synthesization of these sensitizers are complicated and costly processes (Amao & Komori 2004; Garcia et al., 2003; Hao et al., 2006; Kumara et al., 2006; Polo & Iha, 2006; Smestad, 1998; Yanagida et al., 2004). Development or extraction of photosensitizers with absorption range extended to the near IR is greatly desired. In our approach, the use of natural dye extracts, we found that our environment provides natural, non toxic and low cost dye sources with high absorbance level of UV, visible and near IR. Examples of such dye sources are Bahraini Henna (*Lawsonia inermis* L.) and Bahraini raspberries (Rubus spp.). In this work we provide further details about the first reported operation of Henna (*Lawsonia inermis* L.) as a natural dye sensitizer of TiO_2 nanostructured solar cell (Jasim & Hassan, 2009; Jasim et al. in press 2011). We have experienced the usefulness of commercialized dye sensitized solar cell kits such as the one provided by Dyesol™ to "illustrates how interdisciplinary science can be taught at lower division university and upper division high school levels for an understanding of renewable energy as well as basic science concepts." (Smestad, 1998; Smestad & Gratzel 1998) Furthermore, it aids proper training and awareness about the role of nanotechnology in modern civilization.

Classification	η [%]	Area[a] [cm^2]	V_{oc} [V]	J_{sc} [mA cm^{-2}]	FF [-]	Test center[b] (and date)	Producer
Silicon							
Si (crystalline)	24.7±0.5	4.00 (da)	0.706	42.2	0.83	Sandia (3/99)	UNSW PERL
Si (multicrystalline)	19.8±0.5	1.09 (ap)	0.654	38.1	0.80	Sandia (2/98)	UNSW/Eurosolare
Si (thin film transfer)	16.6±0.4	1.02 (ap)	0.645	32.8	0.78	FhG ISE (7/01)	U. Stuttgart
III–V cells							
GaAs (crystalline)	25.1±0.8	3.91 (t)	1.022	28.2	0.87	NREL (3/90)	Kopin
GaAs (thin film)	23.3±0.7	4.00 (ap)	1.011	27.6	0.84	NREL (4/90)	Kopin
GaAs (multicrystalline)	18.2±0.5	4.01 (t)	0.994	23.0	0.80	NREL (11/95)	RTI
InP (crystalline)	21.9±0.7	4.02 (t)	0.878	29.3	0.85	NREL (4/90)	Spire
Polycrystalline thin film							
CuInGaSe$_2$ (CIGS)	18.4±0.5	1.04 (t)	0.669	35.7	0.77	NREL (2/01)	NREL
CdTe	16.5±0.5	1.13 (ap)	0.845	26.7	0.76	NREL (9/01)	NREL
Amorphous/microcrystalline Si							
Si (nanocrystalline)	10.1±0.2	1.20 (ap)	0.539	24.4	0.77	JQA (12/97)	Kaneka
Photoelectrochemical cells							
Nanocrystalline dye	11.0±0.5	0.25 (ap)	0.795	19.4	0.71	FhG ISE (12/96)	EPFL, LPI
Nanocrystalline dye (submodule)	4.7±0.2	141.4 (ap)	0.795	11.3	0.59	FhG ISE (2/98)	INAP
Multijunction cells							
GaInP/GaAs	30.4	4.0 (t)	2.488	14.22	0.86	JQA (4/96)	Japan Energy
GaInP/GaAs/Ge	28.7±1.4	29.93 (t)	2.571	12.95	0.86	NREL (9/99)	Spectrolab
GaAs/CIS (thin film)	25.8±1.3	4.00 (t)				NREL (11/89)	Kopin/Boeing
a Si/CIGS (thin film)	14.6±0.7	2.40 (ap)	–	–	–	NREL (6/88)	ARCO

Table 2. Confirmed terrestrial cell efficiencies measured under the global AM 1.5 spectrum (1000 W · m^{-2}) at 25 °C. [a] (ap)=aperture area; (t)=total area; (da)=designated irradiance area. [b] FhG-ISE=Fraunhofer-Institute for Solar Energy system; JQA = Japan Quality Assurance (From Green & Emery, 2002).

In this chapter, we overview some aspects of the historical background, present, and anticipated future of dye sensitized solar cells. Operation principle of the dye sensitized solar cell is explained. Some schemes used in preparation and assembly of dye sensitized solar cell are presented with few recommendations that might lead to better performance and stability of the fabricated cell. The structural, optical, electrical, and photovoltaic performance stability of DSSC are discussed. The performance of nanocrystalline solar cell samples can be appreciably improved by optimizing the preparation technique, the class of the nanostructured materials, types of electrolyte, and high transparent conductive electrodes. Challenges associated with materials choice, nanostructured electrodes and device layers structure design are detailed. Recent trends in the development of
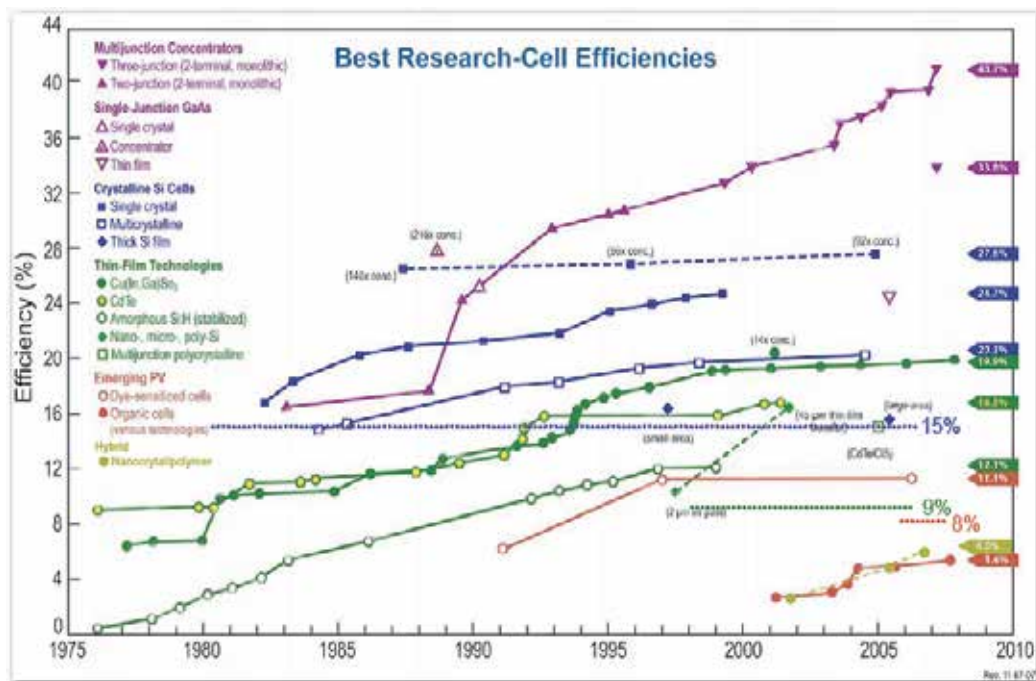
Fig. 1. Reported best research cell efficiencies (Source: National Renewable Laboratory, 2007). The Overall peak power production of dye sensitized solar cell represents a conversion efficiency of about 11%.

nano-crystalline materials for DSSCs technology are introduced. Manufacturability and different approaches suggested for commercialization of DSSC for various applications are outlined. We believe that the availability of efficient natural dye sensitizers, flexible and ink-printable conductive electrodes, and solid state electrolyte may enhance the development of a long term stable DSSCs and hence the feasibility of outdoor applications of both the dye sensitized solar cells and modules.

2. Structure of dye sensitized solar cell

The main parts of single junction dye sensitized solar cell are illustrated schematically in Figure 2. The cell is composed of four elements, namely, the transparent conducting and counter conducting electrodes, the nanostructured wide bandgap semiconducting layer, the dye molecules (sensitizer), and the electrolyte. The transparent conducting electrode and counter-electrode are coated with a thin conductive and transparent film such as fluorine-doped tin dioxide (SnO_2).

2.1 Transparent substrate for both the conducting electrode and counter electrode
Clear glass substrates are commonly used as substrate because of their relative low cost, availability and high optical transparency in the visible and near infrared regions of the electromagnetic spectrum. Conductive coating (film) in the form of thin transparent conductive oxide (TCO) is deposited on one side of the substrate. The conductive film ensures a very low electric resistance per square. Typical value of such resistance is 10-20 Ω
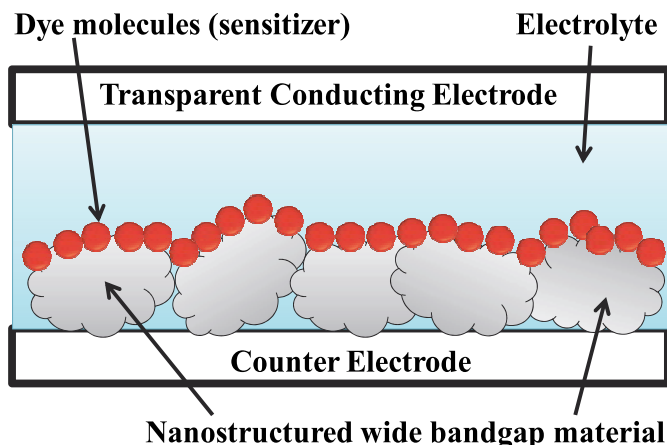
Fig. 2. Schematic of the structure of the dye sensitized solar cell.

per square at room temperature. The nanostructured wide bandgap oxide semiconductor (electron acceptor) is applied, printed or grown on the conductive side. Before assembling the cell the counter electrode must be coated with a catalyzing layer such as graphite layer to facilitates electron donation mechanism to the electrolyte (electron donor) as well be discussed later.

One must bear in mind that the transparency levels of the transparent conducting electrode after being coated with the conductive film is not 100% over the entire visible and near infrared (NIR) part of the solar spectrum. In fact, the deposition of nanostructured material reduces transparency of the electrode. Figure 3 shows a typical transmittance measurement (using dual beam spectrophotometer) of conductive glass electrode before and after being coated with nanostructured TiO_2 layer.
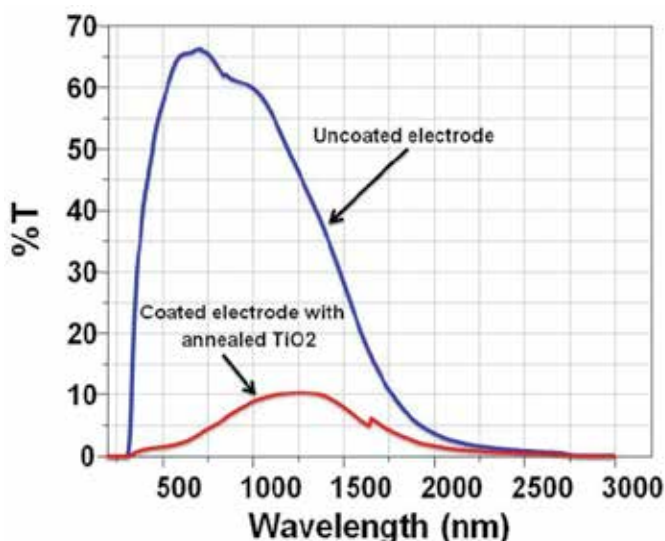
Fig. 3. Transmittance of conductive glass electrode before and after being coated with nanostructured TiO_2 layer.

2.2 Nanostructured photoelectrode

In the old generations of photoelectrochemeical solar cells (PSC) photoelectrodes were made from bulky semiconductor materials such as Si, GaAs or CdS. However, these kinds of photoelectrodes when exposed to light they undergo photocorrosion that results in poor stability of the photoelctrochemical cell. The use of sensitized wide bandgap semiconductors such as TiO_2, or ZnO_2 resulted in high chemical stability of the cell due to their resistance to photocorrosion. The problem with bulky single or poly-crystalline wide bandgap is the low light to current conversion efficiency mainly due to inadequate adsorption of sensitizer because of limited surface area of the electrode. One approach to enhance light-harvesting efficiency (LHE) and hence the light to current conversion efficiency is to increase surface area (the roughness factor) of the sensitized photoelectrode.

Due to the remarkable changes in mechanical, electrical, magnetic, optical and chemical properties of nanostructured materials compared to its phase in bulk structures, it received considerable attention (Gleiter, 1989). Moreover, because the area occupied by one dye molecule is much larger than its optical cross section for light capture, the absorption of light by a monolayer of dye is insubstantial. It has been confirmed that high photovoltaic efficiency cannot be achieved with the use of a flat layer of semiconductor or wide bandgap semiconductor oxide surface but rather by use of nanostructured layer of very high roughness factor (surface area). Therefore, Gratzel and his coworkers replaced the bulky layer of titanium dioxide (TiO_2) with nonoporous TiO_2 layer as a photoelectrode. Also, they have developed efficient photosensitizers (new Ru complex, see for example Figure 16) that are capable of absorbing wide range of visible and near infrared portion of the solar spectrum and achieved remarkable photovoltaic cell performance (Nazerruddin et al., 1993; O' Regan & Gratzel, 1991; Smestad & Gratzel, 1998). Nanoporusity of the TiO_2 paste (or colloidal solution) is achievable by sintering (annealing) of the deposited TiO_2 layer at approximately 450 °C in a well ventilated zone for about 15 minutes (see Figure 4). The high porosity (>50%) of the nanostructured TiO_2 layer allows facile diffusion of redox mediators within the layer to react with surface-bound sensitizers. Lindström et al. reported "A method for manufacturing a nanostructured porous layer of a semiconductor material at room temperature. The porous layer is pressed on a conducting glass or plastic substrate for use in a dye-sensitized nanocrystalline solar cell." (Lindström et al., 2001)
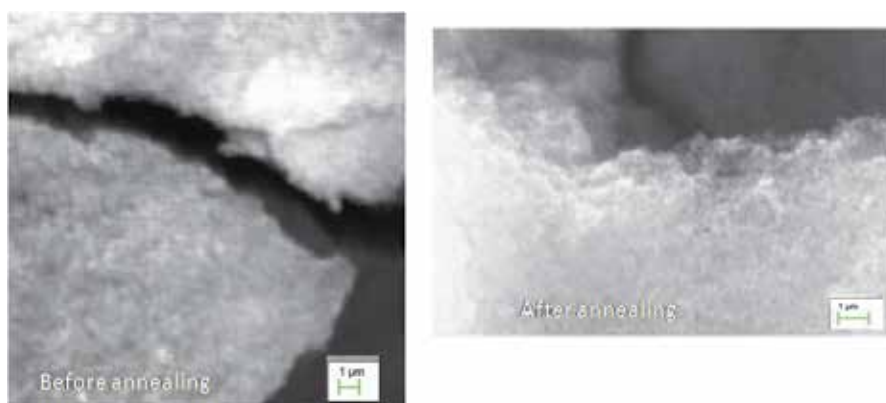
Fig. 4. Scanning electron microscope (SEM) images for TiO_2 photoelectrode before and after annealing it at about 450°C for 15 minutes.

Because it is not expensive, none toxic and having good chemical stability in solution while irradiated, Titanium dioxide has attracted great attention in many fields other than nanostructured photovoltaics such as photocatalysts, environmental purification, electronic devices, gas sensors, and photoelectrodes (Karami, 2010). The preparation procedures of TiO_2 film is quite simple since it is requires no vacuum facilities. Nanostructured TiO_2 layers are prepared following the procedure detailed in (Hara & Arakawa, 2003; Nazerruddin et al., 1993; O' Regan & Gratzel, 1991; Smestad, 1998) "A suspension of TiO_2 is prepared by adding 9 ml of nitric acid solution of PH 3-4 (1 ml increment) to 6 g of colloidal P25 TiO_2 powder in mortar and pestle. While grinding, 8 ml of distilled water (in 1 ml increment) is added to get a white- free flow- paste. Finally, a drop of transparent surfactant is added in 1 ml of distilled water to ensure coating uniformity and adhesion to the transparent conducting glass electrode. The ratio of the nitric acid solution to the colloidal P25 TiO_2 powder is a critical factor for the cell performance. If the ratio exceeds a certain threshold value the resulting film becomes too thick and has a tendency to peel off. On the other hand, a low ratio reduces appreciably the efficiency of light absorption" (Jasim & Hassan, 2009). Our group adopted the Doctor blade method to deposit TiO_2 suspension uniformly on a cleaned (rinsed with ethanol) electrode plate. The TiO_2 layer must be allowed to dry for few minutes and then annealed at approximately 450°C (in a well ventilated zone) for about 15 minutes to form a nanoporous, large surface area TiO_2 layer. The nanostructured film must be allowed to cool down slowly to room temperature. This is a necessary condition to remove thermal stresses and avoid cracking of the glass or peeling off the TiO_2 film.
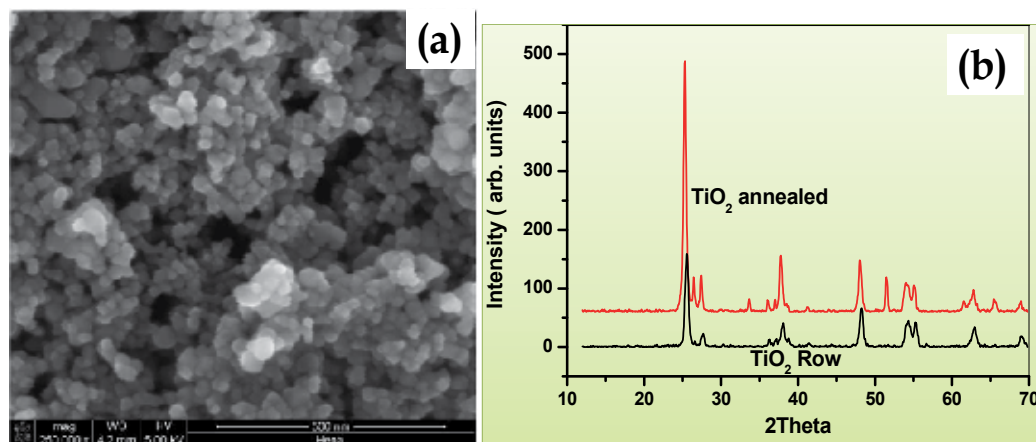
Fig. 5. (a) Scanning electron microscope (SEM) images and (b) XRD for TiO_2 photoelectrod before and after being annealed.

Scanning electron microscopy SEM (see Figure 5-a) or X-ray diffraction measurements (XRD) (see Figure 5-b) is usually used to confirm the formation of nanostructured TiO_2 layer. Analysis of the XRD data (shown in Figure 5-b) confirmers the formation of nanocrystalline TiO_2 particles of sizes less than 50 nm (Jasim & Hassan, 2009). The nanoporous structure of the TiO_2 layer suggests that the roughness factor of 1000 is achievable. In other words, a 1-cm^2 coated area of the conductive transparent electrode with nanostructured TiO_2 layer actually possessing a surface area of 1000 cm^2 (Hara & Arakawa, 2003). The formation of nanostructured TiO_2 layer is greatly affected by TiO_2 suspension

preparation procedures as well as by the annealing temperature. We found that a sintered TiO$_2$ film at temperatures lower than the recommended 450°C resulted in cells that generate unnoticeable electric current even in the μA level. Moreover, nanostructured TiO$_2$ layer degradation in this case is fast and cracks form after a short period of time when the cell is exposed to direct sunlight. Recently Zhu et al. investigated the effects of annealing temperature on the charge-collection and light-harvesting properties of TiO$_2$ nanotube-based dye-sensitized solar cells (see Figure 6) and the reported "DSSCs containing titanium oxide nanotube (NT) arrays films annealed at 400 °C exhibited the fastest transport and slowest recombination kinetics. The various structural changes were also found to affect the light-harvesting, charge-injection, and charge-collection properties of DSSCs, which, in turn, altered the photocurrent density, photovoltage, and solar energy conversion efficiency" (Zhu et al. 2010).
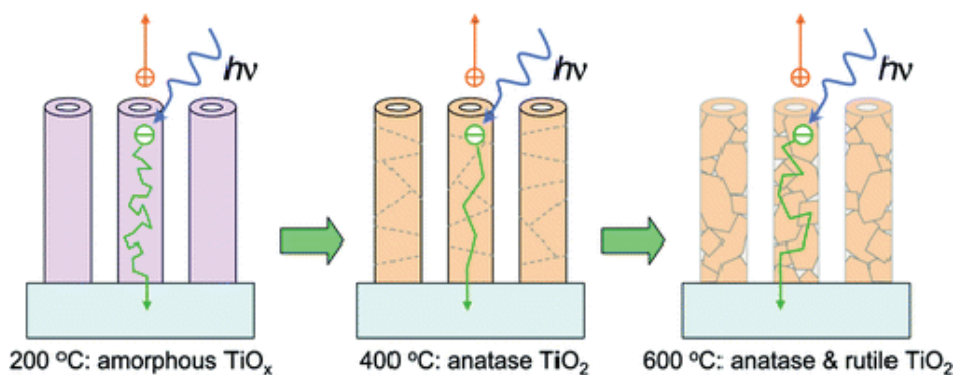
Fig. 6. Schematic illustration of the effects of annealing temperature on the charge-collection and light-harvesting properties of TiO$_2$ nanotube-based dye-sensitized solar cells (From Zhu et al., 2010).

One of the important factors that affect the cell's efficiency is the thickness of the nanostructured TiO$_2$ layer which must be less than 20 μm to ensure that the diffusion length of the photoelectrons is greater than that of the nanocrystalline TiO$_2$ layer. TiO$_2$ is the most commonly used nanocrystalline semiconductor oxide electrode in the DSSC as an electron acceptor to support a molecular or quantum dot QD sensitizer is TiO$_2$ (Gratzel, 2003). Other wide bandgap semiconductor oxides is becoming common is the zinc oxide ZnO$_2$. ZnO$_2$ possesses a bandgap of 3.37 eV and a large excitation binding energy of 60 meV. Kim *et al.* reported that the nanorods array electrode showed stable photovoltaic properties and exhibited much higher energy conversion efficiency (Kim et al., 2006). Another example, Law and coworkers have grown by chemical bath deposition ZnO$_2$ nanowires 8-μm long with 100 nm diameters as photoelectrod (see Figure 7) the efficiency of a ZnO$_2$ nanowire photoelectrode DSSC is about 2.4%. This low efficiency level compared to that of nanostructured TiO$_2$ photoelectrode DSSC is probably due to inadequate surface area for sensitizer adsorption (Baxter et al., 2006; Boercker et al., 2009; Law et al., 2005). Other research groups suggested that the growth of longer, thinner, denser ZnO$_2$ nanowires is a practical approach to enhance cell efficiency (Guo et al., 2005). Investigations show that ZnO$_2$ nanorod size could be freely modified by controlling the solution conditions such as temperature, precursor concentration, reaction time, and adopting multi-step growth. Nanorod structured photoelectrode offers a great potential for improved electron transport.

It has been found that the short circuit current density and cell performance significantly increase as nanorods length increases because a higher amount of the adsorbed dye on longer nanorods, resulting in improving conversion efficiency (Kim et al. 2006).

Because titanium dioxide is abundant, low cost, biocompatible and non-toxic (Gratzel & Hagfeldt, 2000), it is advantageous to be used in dye sensitized solar cells. Therefore, nanotube and nanowire-structured TiO_2 photoelectrode for dye-sensitized solar cells have been investigated (Mor et al., 2006; Pavasupree et al., 2005; Pavasupree et al., 2006; Shen et al., 2006; Suzuki et al., 2006). Moreover; SnO_2, or Nb_2O_5 employed not only to ensure large roughness factor (after nanostructuring the photoelectrode) but also to increase photgenerated electron diffusion length (Bergeron et al., 2005; Sun et al. 2006). Many studies suggest replacing nanoparticles film with an array of single crystalline nanowires (rods), nanoplants, or nanosheets in which the electron transport increases by several orders of magnitude (Kopidakis et al., 2003; Law et al., 2005; Noack et al., 2002; Tiwari & Snure, 2008; Xian et al., 2006). Incorporation of vertically aligned carbon nanotube counter electrode improved efficiency of TiO_2/anthocyanin dye-Sensitized solar cells as reported by Sayer et al. They attributed the improvement to "the large surface area created by the 3D structure of the arrays in comparison to the planar geometry of the graphite and Pt electrodes, as well as the excellent electrical properties of the CNTs." (Sayer et al., 2010).
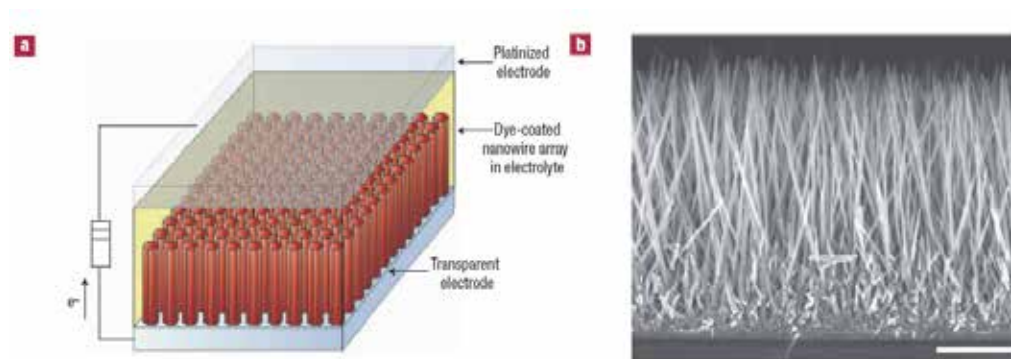
Fig. 7. (a) Schematic illustration of the ZnO nanowire dye sensitized solar cell, light is incident through the bottom electrode, and (b) scanning electron microscopy cross-section of a cleaved nanowire array. The wires are in direct contact with the transparent substrate, with no intervening particle layer. Scale bar, 5-μm (From Law et al., 2005).

2.3 Photosensitizer

Dye molecules of proper molecular structure are used to sensitized wide bandgap nanostructured photoelectrode. Upon absorption of photon, a dye molecule adsorbed to the surface of say nanostructured TiO_2 gets oxidized and the excited electron is injected into the nanostructured TiO_2. Among the first kind of promising sensitizers were Polypyridyl compounds of Ru(II) that have been investigated extensively. Many researches have focused on molecular engineering of ruthenium compounds. Nazeeruddin et al. have reported the "black dye" as promising charge transfer sensitizer in DSSC. Kelly, et.al studied other ruthenium complexes $Ru(dcb)(bpy)_2$ (Kelly, et al 1999), Farzad et al. explored the $Ru(dcbH_2)(bpy)_2(PF_6)_2$ and $Os(dcbH_2)(bpy)_2-(PF6)_2$ (Farzad et al., 1999), Qu et al. studied cis-$Ru(bpy)_2(ina)_2(PF_6)_2$ (Qu et al., 2000) , Shoute et al.

investigated the *cis*-Ru(dcbH$_2$)$_2$(NCS) (Shoute et al., 2003), and Kleverlaan et al. worked with OsIII-bpa-Ru (Kleverlaan et al 2000). Sensitizations of natural dye extracts such as shiso leaf pigments (Kumara et al., 2006), Black rice (Hao et al., 2006), Fruit of calafate (Polo and Iha, 2006), Rosella (Wongcharee et al., 2007), Natural anthocyanins (Fernando et al., 2008), Henna (*Lawsonia inermis* L.) (Jasim & Hassan, 2009; Jasim et al., in press 2011), and wormwood, bamboo leaves (En Mei Jin *et al.,* 2010) have been investigated and photovoltaic action of the tested cells reveals some opportunities. Calogero et al. suggested that "Finding appropriate additives for improving open circuit voltage V$_{OC}$ without causing dye degradation might result in a further enhancement of cell performance, making the practical application of such systems more suitable to economically viable solar energy devices for our society." (Calogero et al., 2009)
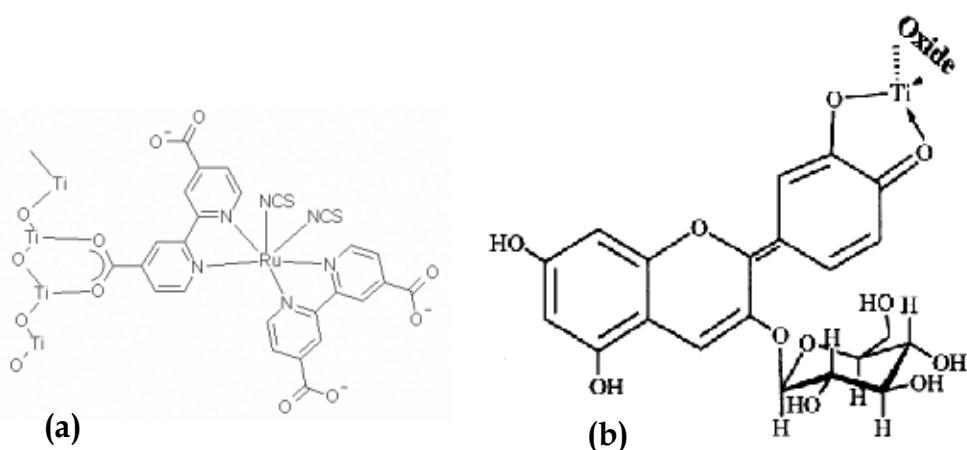
Fig. 8. (a) Ruthenium based red or "N3" dye adsorbed onto a titanium dioxide surface (from Martinson et al., 2008), and (b) Proposed structure of the cyanin dye adsorbed to one of the titanium metal centers on the titanium dioxide surface (From Smestad, 1988).

Gratzel group developed many Ru complex photosensitizers (examples are shown in Figure 16). One famous example is the *cis*-Di(thiocyanato)bis(2,2'-bipyridyl)-4,4'-dicarboxylate) ruthenium(II), coded as N3 or N-719 dye it has been an outstanding solar light absorber and charge-transfer sensitizer. The red dye or N3 dye (structure is shown in Figure 8-a and Figure 16) is capable of absorbing photons of wavelength ranging from 400 nm to 900 nm (see Figure 16) because of metal to ligand charge transfer transition. Theoretical Study of new ruthenium-based dyes for dye sensitized solar cells by Monari et al., states "The UV/vis absorption spectra have been computed within the time-dependent density functional theory formalism. The obtained excitation energies are compared with the experimental results." (Monari et al., 2011) In fact, for dye molecule to be excellent sensitizer, it must possess several carbonyl (C=O) or hydroxyl (-OH) groups capable of chelating to the Ti$^{(IV)}$ sites on the TiO$_2$ surface as shown in Figure 8 (Tennakone et al., 1997). Extracted dye from California blackberries (Rubus ursinus) has been found to be an excellent fast-staining dye for sensitization, on the other hand, dyes extracted from strawberries lack such complexing capability and hence not suggested as natural dye sensitizer (Cherpy et al., 1997; Semistad & Gratzel, 1998; Semistad, 1988).
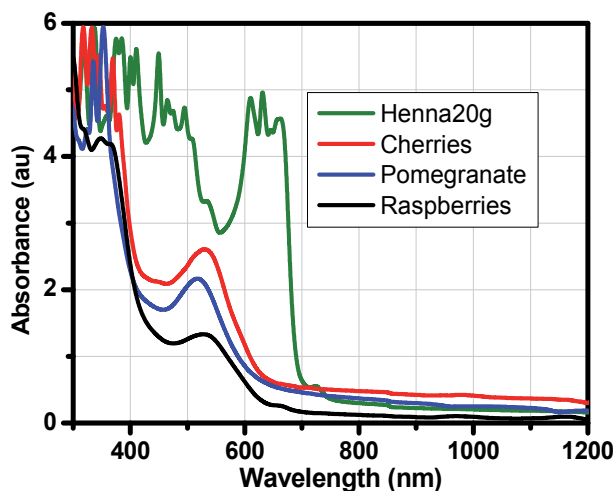
Fig. 9. Measured absorbance of some extracted natural dyes in methanol as solvent.

Commercialized dye sensitized solar cells and modules use ruthenium bipyridyl–based dyes (N3 dyes or N917) achieved conversion efficiencies above 10% (Nazerruddin, et al., 1993). However, these dyes and those chemically engineered are hard to put up and are expensive (Cherepy et al., 1997). Therefore, in attempt to develop green solar cells; our group at the University of Bahrain used Soxhlet Extractor in the extraction of natural dye solutions from abundant natural dye sources such as Bahraini Henna (*Lawsonia inermis* L.), Yemeni Henna, pomegranate, raspberries, and cherries after being dried(Jasim, submitted for publication 2011). We used methanol as solvent in each extraction process. The absorbance of the extracted dye solution has been measured using dual beam spectrophotometer (see Figure 9). Different concentrations of Henna (*Lawsonia inermis* L.) extracts have been prepared from the original extract. The light harvesting efficiency (LHE) for each concentration has been calculated from the absorbance (see Figure 10). The light harvesting efficiency is given as:

$$LHE(\lambda) = \left(1 - 10^{-A(\lambda)}\right) \times 100 \qquad (1)$$

where A (λ) is the absorbance of the sample at specific wavelength.

The absorbance and hence the LHE increases with concentration of dye extract. Also, as shown in Figure 10, as Henna extract concentration increases the absorbance increases and covers broader range of wavelengths.

Since not all photons scattered by or transmitted through the nanocrystalline TiO_2 layer get absorbed by a monolayer of the adsorbed dyes molecules, the incorporation of energy relay dyes might help enhancing the light harvesting efficiency. A remarkable enhancement in absorption spectral bandwidth and 26% increase in power conversion efficiency have been accomplished with some sensitizers after energy relay dyes have been added (Harding et al., 2009). Metal free organic sensitizers such as metal free iodine reported by Horiuchi et al. demonstrated remarkable high efficiency "The solar energy to current conversion efficiencies with the new indoline dye was 6.51%. Under the same conditions, the N3 dye was 7.89%" (Horiuchi et al., 2004). Semiconductor quantum dots QDs are nanostructured crystalline semiconductors where quantum confinement effect due to their size results in
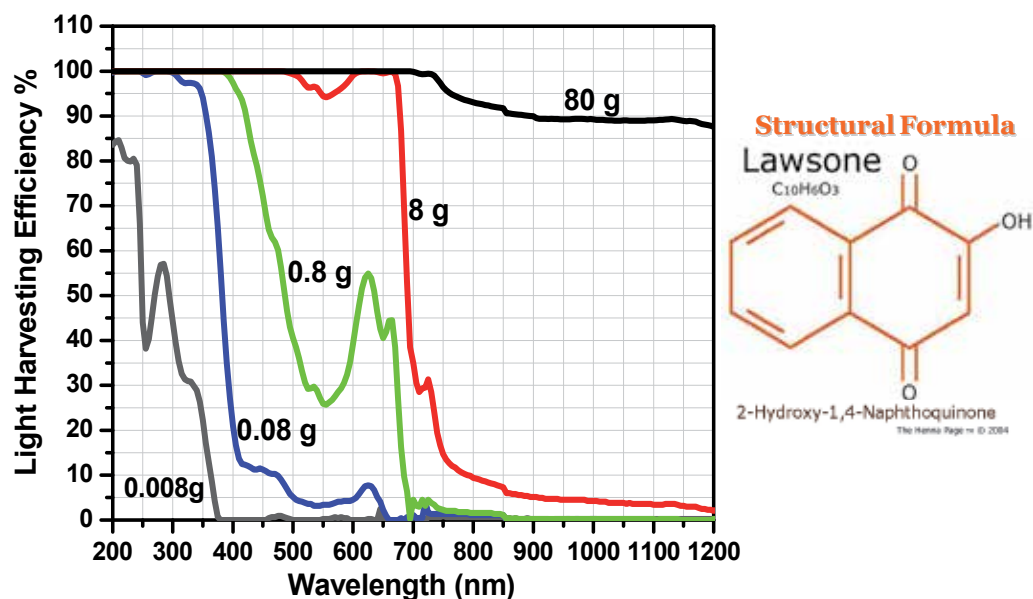
Fig. 10. Light harvesting efficiency of Henna extract at different concentrations. Data are given in grams of Henna powder per 100 ml of methanol as solvent. Also, shown the structural formula of Lawsone molecule that is responsible for the characteristic color of Henna (From www.hennapage.com).

remarkable optical linear and nonlinear behaviors. Excitonic absorption edge of quantum dots is size dependent as shown in Figure 11 for lead sulfide PbS quantum dots suspended in toluene. It is anticipated that quantum dots are alternatives of dyes as light-harvesting structures in DSSC. Light absorption produces excitons or electron-hole pairs. Excitons have an average physical separation between the electron and hole, referred to as the Exciton Bohr Radius. Usually, Bohr radius is greater the QD diameter (e.g., for PbS Boher radius is 20 nm) leading to quantum confinement effect (discrete energy levels = artificial molecule). Excitons dissociate at the QD TiO_2 interface. The electron is subsequently injected in the semiconductor oxide conduction band, while the hole is transferred to a hole conductor or an electrolyte. Efficient and rapid hole injection from PbS QDs into triarylamine hole conductors has been demonstrated, and IPCE (Incident Photon to Current Conversion Efficiency) values exceeding 50% have been obtained. QDs have much higher optical cross sections than molecular sensitizers, depending on their size. However, they also occupy a larger area on the surface of the nanostructured photoelectrode, decreasing the QD concentration in the film. Thus, the value of the absorption length is similar to that observed for the dye-loaded nanostructured photoelectrode. Investigations show that multiple excitons can be produced from the absorption of a single photon by a QD via impact ionization if the photon energy is 3 times higher than its band gap (Ellinson et al., 2005; Nozik, 2004; Nozik, 2005). The issue to be confronted is to find ways to collect the excitons before they recombine get lost in the cell.

Unlike dyes that absorb over relatively narrow region, semiconductor quantum dots such as PbS (see Figure 11-b) absorb strongly all photons with energy greater than the bandgap,

thus a far higher proportion of light can be converted into useful energy using nanocrystals compared to dyes. Perhaps most important, dyes are disgracefully unstable and tend to photobleach over a relatively short amount of time. Quantum dots prepared with a properly designed outer shell are very stable and hence long lasting solar cells without degradation in performance are feasible. Quantum dots-sensitized solar cell produces quantum yields greater than one due to impact ionization process (Nozik, 2001). Dye molecules cannot undergo this process. Solar cells made from semiconductor QDs such as CdSe, CdS, PbS and InP showed a promising photovoltaic effect (Hoyer & Konenkamp, 1995; Liu & Kamat 1993; Plass et al., 2002; Vogel & Weller 1994; Zaban et al., 1998; Zweible & Green, 2000). Significant successes have been achieved in improving the photo-conversion efficiency of solar cells based on CdSe quantum dote light harvesters supported with carbon nanotube this is accomplished by incorporating carbon nanotubes network in the nanostructured TiO_2 layer, and accordingly assisting charge transport process network (Hasobe et al., 2006; Robel et al., 2005). Consequently, appreciable improvement in the photo-conversion efficiency of the DSSC is attainable. Recently Fuke et al., reported CdSe quantum-dot-sensitized solar cell with ~100% internal quantum efficiency. A significant enhancement in both the electron injection efficiency at the QD/TiO_2 interface and charge collection efficiency at the QD/electrolyte interface" were achieved (Fuke et al., 2010).
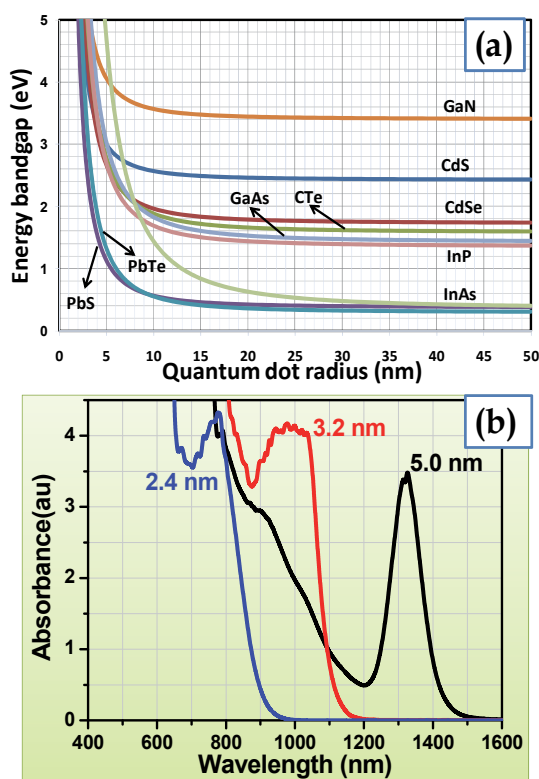
Fig. 11. (a) Calculated energy gap of some semiconductor quantum dots using the effective mass- approximation -model and (b) measured absorbance of PbS quantum dots suspended in toluene of three different sizes (radius).

2.4 Redox electrolyte

Electrolyte containing I^-/I_3^- redox ions is used in DSSC to regenerate the oxidized dye molecules and hence completing the electric circuit by mediating electrons between the nanostructured electrode and counter electrode. NaI, LiI and R_4NI (tetraalkylammonium iodide) are well known examples of mixture of iodide usually dissolved in nonprotonic solvents such as acetonitrile, propylene carbonate and propionitrile to make electrolyte. Cell performance is greatly affected by ion conductivity in the electrolyte which is directly affected by the viscosity of the solvent. Thus, solvent with lower viscosity is highly recommended. Moreover, counter cations of iodides such as Na^+, Li^+, and R_4N^+ do affect the cell performance mainly due to their adsorption on nanostructured electrode (TiO_2) or ion conductivity. It has been found that addition of *tert*-butylpyridine to the redoxing electrolyte improves cell performance (Nazeeruddin et al., 1993) (see Figure 19). Br^-/Br_3^- redox couple was used in DSSCs and promising results were obtained. The V_{oc} and I_{sc} increased for the Eosin Y-based DSSC when the redox couple was changed from I^-/I_3^- to Br^-/Br_3^- (Suri & Mehra, 2006).

The redoxing electrolyte needs to be chosen such that the reduction of I_3^- ions by injection of electrons is fast and efficient (see Figure 13). This arise from the fact that the dependence of both hole transport and collection efficiency on the dye-cation reduction and I^-/I_3^- redox efficiency at counter electrodes are to be taken into account (Yanagida, 2006). Besides limiting cell stability due to evaporation, liquid electrolyte inhibits fabrication of multi-cell modules, since module manufacturing requires cells be connected electrically yet separated chemically (Matsumoto et al., 2001; Tennakone et al., 1999). Hence, a significant shortcoming of the dye sensitized solar cells filled with liquid state redoxing electrolyte is the leakage of the electrolyte, leading to reduction of cell's lifespan, as well as the associated technological problems related to device sealing up and hence, long-term stability (Kang, *et al.*, 2003). Many research groups investigate the use of ionic liquids, polymer, and hole conductor electrolytes (see Figure 12) to replace the need of organic solvents in liquid electrolytes. Despite the reported relative low cell's efficiency of 4–7.5% (device area < 1 cm²) , these kind of electrolyte are promising and may facilitate commercialization of dye sensitize solar modules (Kawano, et al., 2004; Kuang et al., 2006; Schmidt-Mende & Gratzel, 2006; Wang et al., 2004).

Addition of polymer gel to quasi-solidify electrolytes has been investigated by many research groups (Ren et al., 2001; Kubo et al., 2001; Nogueira et al., 2001). It has been found that the addition of Poly(viny1idene fluoride-co-hexafluoropropylene) to the KI/I_2 electrolyte has improved both the fill factors and energy conversion efficiency of the cells by about 17% (Kang, et al., 2003). Gel electrolytes also are very attractive from many perspectives such as: Efficiency is a compromise between electrolyte viscosity and ionic mobility; gelled ionic liquids have an anomalously high ionic mobility despite their high viscosity, and particularly for realization of monolithic arrays inter-cell sealing (Wang, et al., 2005). Innovative classes of electrolytes such as p-type, polymeric conductor, PEDOT or PEDOT:TMA, which carries electrons from the counter electrode to the oxidized dye encouraging further investigations to optimize and/or design new ones. Recently one of the first systematic study of charge transport and recombination in solid state dye sensitized solar cell SDSCs using conjugated polymer hole transporter has been reported by Zhang et al., in this investigation organic indoline dye D131 as the sensitizer and poly(3-hexylthiophene) (P3HT) as the hole transporter a power conversion efficiency of 3.85% have been recorded. Therefore, this class of solar cells is expected to represent one of the most efficient SDSCs using polymeric hole transporter (Zhang et al, 2011).
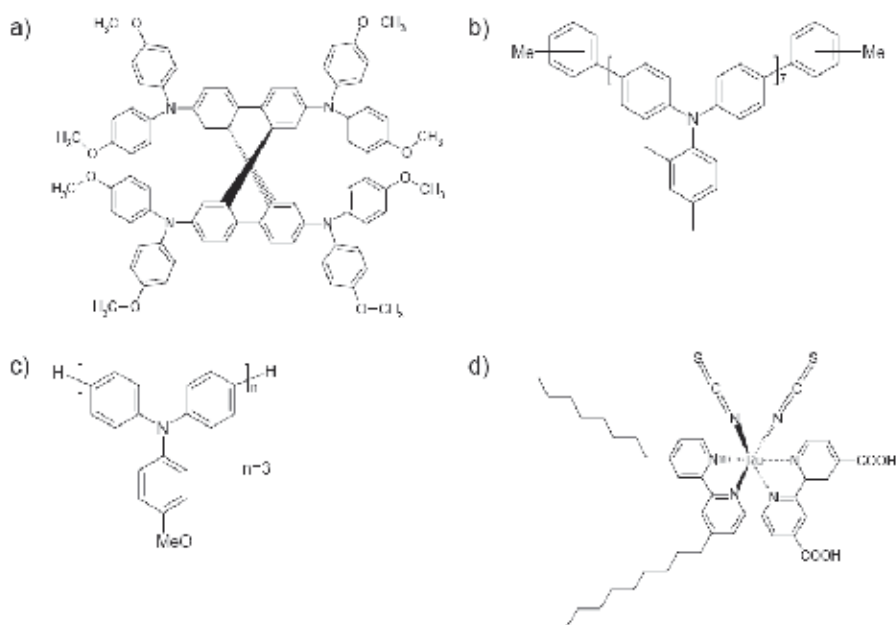
Fig. 12. (a) Chemical structure of the hole-conductor spiro-OMeTAD resulted in cells energy conversion efficiency η = 4%, (b) Chemical structure of AV-DM resulted in cells with η = 0.9%, (c) Structure of AV-OM. resulted in cells with η = 2%, (d) Structure of the Z907 dye used for all solar cells as sensitizer of the nanostructured TiO$_2$ film (From Schmidt-Mende & Gratzel, 2006).

3. How dye sensitized solar cell works

In this section we overview the following: Process during which light energy get converted to electric one, photovoltaic performance, charge injection, charge transport in the nanostructured electrode, charge recombination, and cell dark current.

3.1 Operating principle of dye sensitized solar cell

Nanocrystalline TiO$_2$ is deposited on the conducting electrode (photoelectrode) to provide the necessary large surface area to adsorb sensitizers (dye molecules). Upon absorption of photons, dye molecules are excited from the highest occupied molecular orbitals (HOMO) to the lowest unoccupied molecular orbital (LUMO) states as shown schematically in Figure 13. This process is represented by Eq. 2. Once an electron is injected into the conduction band of the wide bandgap semiconductor nanostructured TiO$_2$ film, the dye molecule (photosensitizer) becomes oxidized, (Equation 3). The injected electron is transported between the TiO$_2$ nanoparticles and then extracted to a load where the work done is delivered as an electrical energy, (Equation 4). Electrolytes containing I$^-$/I$_3^-$ redox ions is used as an electron mediator between the TiO$_2$ photoelectrode and the carbon coated counter electrode. Therefore, the oxidized dye molecules (photosensitizer) are regenerated by receiving electrons from the I$^-$ ion redox mediator that get oxidized to I$_3^-$ (Tri-iodide ions). This process is represented by Eq. 5. The I$_3^-$ substitutes the internally donated electron

with that from the external load and reduced back to I^- ion, (Equation 6). The movement of electrons in the conduction band of the wide bandgap nanostructured semiconductor is accompanied by the diffusion of charge-compensating cations in the electrolyte layer close to the nanoparticle surface. Therefore, generation of electric power in DSSC causes no permanent chemical change or transformation (Gratzel, 2005).

$$S + photon \rightarrow S* \qquad\qquad \text{(2) Excitation process}$$

$$S* + TiO_2 \rightarrow e^-_{(TiO_2)} + S^+ \qquad\qquad \text{(3) Injection process}$$

$$e^-_{(TiO_2)} + C.E. \rightarrow TiO_2 + e^-_{(C.E)} + electrical\,energy \quad \text{(4) Energy generation}$$

$$S^+ + \frac{3}{2}I^- \rightarrow S + \frac{1}{2}I_3^- \qquad\qquad \text{(5) Regeneration of dye}$$

$$\frac{1}{2}I_3^- + e^-_{(C.E.)} \rightarrow \frac{3}{2}I^- + C.E. \qquad\qquad \text{(6) e- Recapture reaction}$$
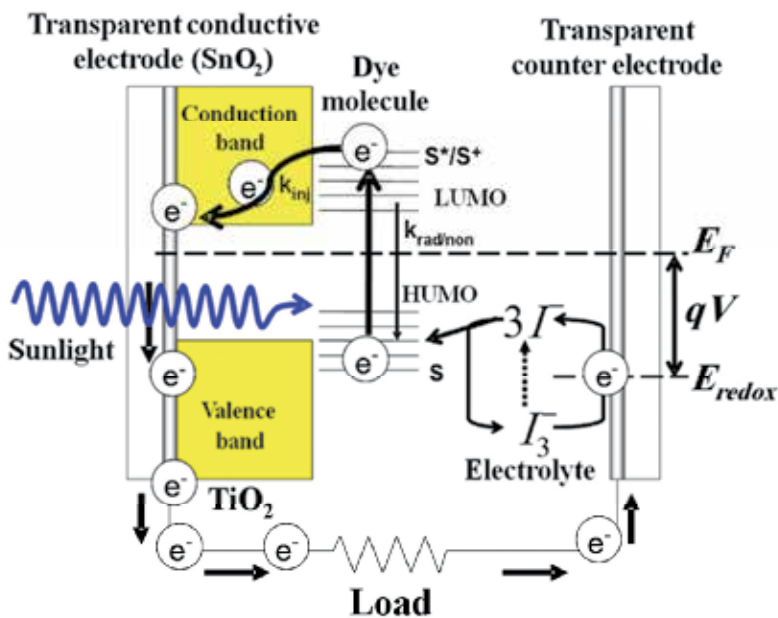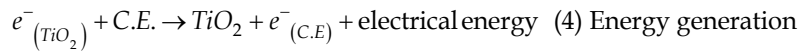
Fig. 13. Schematic illustration of operation principle of dye sensitized solar cell.

As illustrated in Fig. 13, the maximum potential produced by the cell is determined by the energy separation between the electrolyte chemical potential (E_{redox}) and the Fermi level (E_F) of the TiO₂ layer. The small energy separation between the HOMO and LUMO ensures absorption of low energy photons in the solar spectrum. Therefore, the photocurrent level is dependent on the HOMO-LUMO levels separation. This is analogous to inorganic

semiconductors energy bandgap (E_g). In fact, effective electron injection into the conduction band of TiO_2 is improved with the increase of energy separation of LUMO and the bottom of the TiO_2 conduction band. Furthermore, for the HOMO level to effectively accept the donated electrons from the redox mediator, the energy difference between the HOMO and redox chemical potential must be more positive (Hara & Arakawa, 2003).

3.2 Photovoltaic performance

Figure 14 presents examples of the I-V characteristics of natural dye sensitized solar cell NDSSC with Bahraini Henna (*Lawsonia inermis* L.), pomegranate, Bahraini raspberries, and cherries. We found that nature of the dye and its concentration has a remarkable effect on the magnitude of the collected photocurrent. Under full solar spectrum irradiation with photon flux $I_0 = 100$ mW/cm² (Air Mass 1.5), the photon energy –to- electricity conversion efficiency is defined as (Gratzel, 2003):

$$\eta = \frac{J_{sc} \times V_{oc} \times FF}{I_0} \tag{7}$$

where J_{sc} is the short circuit current, V_{oc} the open circuit voltage, and FF is the fill factor of the solar cell which is calculated by multiplying both the photocurrent and voltage resulting in maximum electric power delivered by the cell.
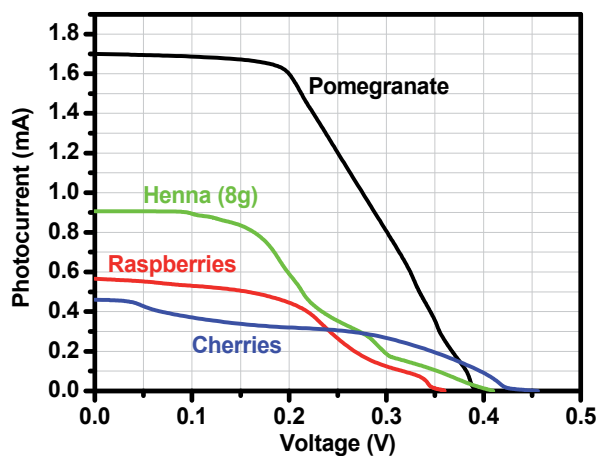
Fig. 14. Photocurrent vs. voltage curves obtained for nanostructured TiO_2 photoelectrodes sensitized with some extracted natural dyes (Jasim, submitted for publications).

Table 3 shows the electrical properties of some assembled NDSSCs. Photocurrent and voltage drop on a variable load have been recorded instantaneously while the cell is exposed to direct sun illumination. Due to light reflection and absorption by the conductive photoelectrode and the scattering nature of the nanostructured TiO_2, the measured transmittance of the photoelectrode (see Figure 3) shows an average of 10% of the solar spectrum (Air Mass 1.5) may reach the sensitizers. Since TiO_2 past is applied on the conductive electrode using doctor blade method the effective area of the irradiated part of the cell is 1.5 cm × 2 cm. Despite the variation of Bahraini Henna extract concentration the cells produced almost the same open circuit voltage V_{oc}. On the other hand, the short circuit

current I_{sc} varies with Henna extract concentration. Highly concentrated Bahraini Henna extracts results in non-ideal I-V characteristics even though it possesses 100% light harvesting efficiency in the UV and in the visible parts of the electromagnetic spectrum. The dye concentration was found to influence remarkably the magnitude of the collected photocurrent. High concentration of Henna extract introduces a series resistance that ultimately reduces the generated photocurrent. On the other hand, diluted extracts reduces the magnitude of the photocurrent and cell efficiency. (Jasim et al, 2011).

Dye	V_{oc} (V)	I_{sc} (mA)	FF	% η
Bahraini Henna 80g	0.426	0.368	0.246	0.128
Bahraini Henna 8g	0.410	0.906	0.363	0.450
Bahraini Henna 0.8g	0.419	0.620	0.330	0.286
Yameni Henna 84g	0.306	0.407	0.281	0.117
Yameni Henna 21g	0.326	0.430	0.371	0.174
Yameni Henna 4.2g	0.500	0.414	0.276	0.191
Cherries in Methanol	0.305	0.466	0.383	0.181
Cherries in Methanol+ 1% HCL	0.301	0.463	0.288	0.134
Pomegranate	0.395	1.700	0.481	1.076
Raspberries	0.360	0.566	0.455	0.309

Table 3. Electrical properties of some assembled natural dye sensitized solar cells NDSSCs (From Jasim et al, 2011; Jasim, submitted for publications).
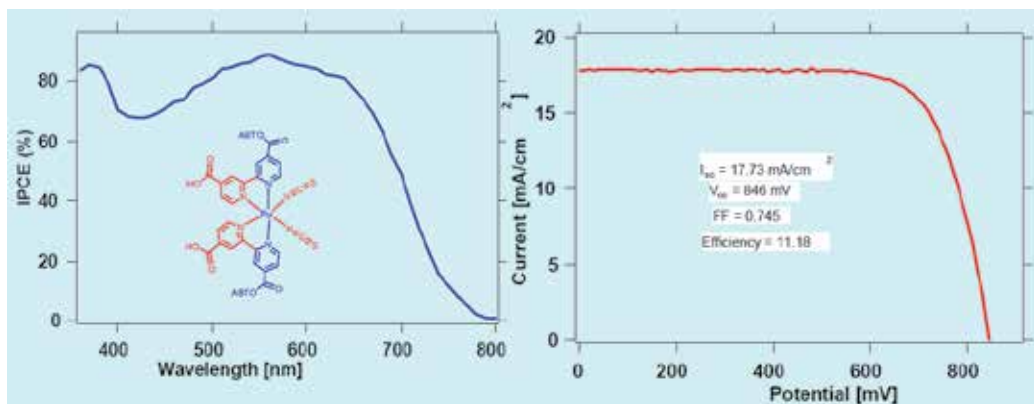
Fig. 15. Photovoltaic performance of DSSC laboratory cell (a) Photo current action spectrum showing the monochromatic incident photon to current conversion efficiency (IPCE) as function of light wavelength obtained with the N-719 sensitizer. (*b*) *Photocurrent density – voltage* curve of the same cell under AM 1.5 standard test conditions. (From Nazeeruddin et al., 2005).

Gratzel and coworkers reported cell efficiency of 10.4% using black dye (RuL′(NCS)$_3$ complexes) and as shown in Figure 15, cells with solar to electric power conversion efficiency of the DSSC in full AM 1.5 sun light validated by accredited PV calibration laboratories has reached over 11% (Chiba et al., 2006). Jiu et al., (Jiu, et al., 2006) have

synthesized highly crystalline TiO_2 nanorods with lengths of 100-300 nm and diameters of 20-30 nm. The rod shape kept under high calcination temperatures contributed to the achievement of the high conversion efficiency of light-to-electricity of 7.29%. Reported efficiencies of nanostructured ZnO_2 photoelectrodes based cells are encouraging and many research groups are dedicating their efforts to provide cells with efficiency close to that reported for sensitized nanostructured TiO_2 photoelectrodes.

The short circuit current magnitude affects directly the incident photon-to-current conversion efficiency IPCE which is defined using the photoresponse and the light intensity as:

$$IPCE(\lambda) = \frac{1240(eV.nm) \times J_{sc}(\mu A / cm^2)}{\lambda(nm) \times I(\mu W / cm^{-2})} \tag{8}$$

where λ is the wavelength of the absorbed photon and I is the light intensity at wavelength λ. Figures 15 and 16 present IPCE examples of some commonly used sensitizers by Gratzel and coworkers.
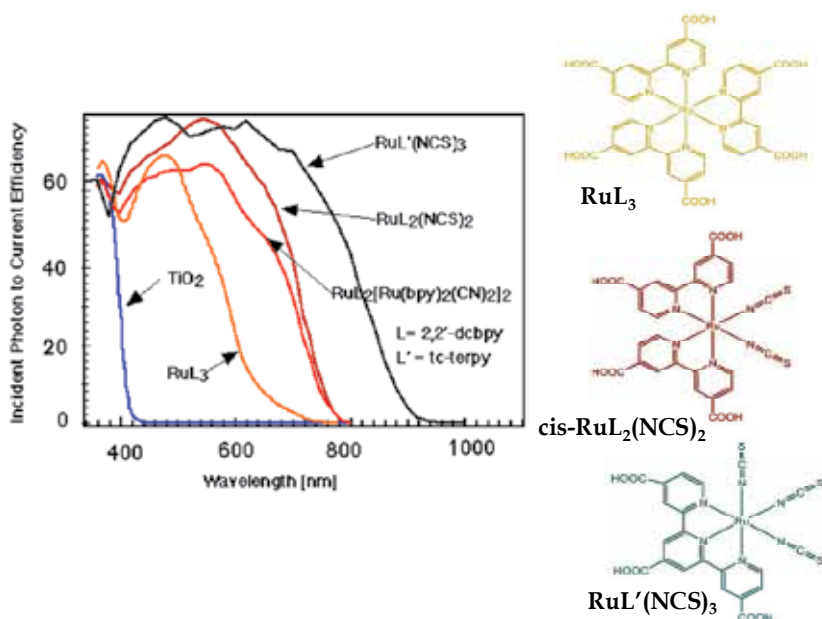
Fig. 16. Spectral response (IPCE) of dye-sensitized solar cell for different dyes compared with the spectral response of bare TiO_2 electrode and the ideal IPCE curve for a single bandgap device (From http://dcwww.epfl.ch/icp/ICP-2/solarcellE.html. and Gratzel et al., 2005).

In terms of light harvesting efficiency LHE, quantum yield of electron injection quantum yield Φ_{inj}, and collection efficiency η_c of the injected electrons at the back contact IPCE is given by:

$$IPCE = LHE \times \Phi_{inj} \times \eta_c \tag{9}$$

Therefore, IPCE equals the LHE if both Φ_{inj} and η_c are close 100%. However, Charge injection from the electronically excited sensitizer into the conduction band of the nanostructured wide bandgap semiconductor is in furious competition with other radiative and non-radiative processes. Due to electron transfer dynamics (see Figure 17), if electron injection in the semiconductor is comparable to, or slower than, the relaxation time of the dye, Φ_{inj} will be way below 100%. This can be deduced from the definition of the quantum yield Φ_{inj} (Cherepy et al., 1997):

$$\Phi_{inj} = \frac{k_{inj}}{k_{inj} + k_{rad} + k_{nrad}} \tag{10}$$

The quantum yield approaches 100% only when the radiative and nonradiative rates (k_{rad}, k_{nrad}) (paths shown in Figure 13) are much smaller than the injection rate k_{inj}. The rate constant for charge injection k_{inj} is given by Fermi golden rule (Gratzel, 2001; Hara & Arakawa, 2003):

$$k_{inj} = \left(\frac{4\pi^2}{h}\right) |V|^2 \rho(E) \tag{11}$$

where h is Planck's constant, $|V|$ is the electron-coupling matrix element and $\rho(E)$ is the density of electronic acceptor states in the conduction band of the semiconductor. Equation (11) assumes that electron transfer from the excited dye molecules into the semiconductors is activationless and hence exhibits a temperature-independent rate. Some representative examples of electron injection rate constants k_{inj} and electronic coupling matrix elements $|V|$ measured by laser flash photolysis for some sensitizers adsorbed onto nanocrystalline TiO_2, t_f and Φ_{tnj} (the excited-state lifetime and the injection quantum yield, respectively) are presented in Table 4 (Gratzel, 2001; Hara & Arakawa, 2003). The shown values of $|V|$ on Table 4 credited to the degree of overlapping of photosensitizer excited states wavefunction and the conduction band of the nanostructured photoelectrode. The distance between the adsorbed sensitizer and the nanostructured photoelectrode affect the value of the electronic coupling matrix elements.

Sensitizers	k_{inj} [s^{-1}]	$|V|$ [cm^{-1}]	t_f [ns]	Quantum yield
$Ru^{II}(bpy)_3$	2×10^5	0.04	600	0.1
$Ru^{II}L_3$ (H_2O)	3×10^7	0.3	600	0.6
$Ru^{II}L_3$ (EtOH)	4×10^{12}	90	600	1.0
$Ru^{II}L_2(NCS)_2$	10^{13}	130	50	1.0
Coumarin-343	5×10^{12}	100	10	1.0
Eosin-Y	9×10^8	2	1	0.4

Table 4. Electron injection rate constants k_{inj} and electronic coupling matrix elements $|V|$ measured by laser flash photolysis for various sensitizers adsorbed onto nanocrystalline TiO_2. In the sensitizers column, L stands for the 4,4'-dicarboxy-2,2'-bipyridyl ligand and bipy for 2,2'-bipyridyl (From Gratzel, 2001).

Advantages of tandem structure have been investigated both theoretically and experimentally as approaches to improve the photocurrent of DSSC (Durr et al., 2004). "The

tandem structured cell exhibited higher photocurrent and conversion efficiency than each single DSSC mainly caused by its extended spectral response." (Kubo et al., 2004)

3.3 Charge injection, transport, recombination, and cell dark current

Kinetics of electron injection into the semiconductor photoelectrod after being excited from the photosensitizer has been investigated by many researchers using time-resolved laser spectroscopy (Hara & Arakawa, 2003). It has been found that both the configuration of the photosensitizer material and the energy separation between the conduction band level of the wideband gap semiconductor and the LUMO level of the photosensitizer are greatly affecting the electron transfer rate to the wideband gap semiconductor. Figure 17 shows a schematic illustration of kinetics in the DSSC. The shown arrows indicate excitation of the dye from the HOMO to the LUMO level, relaxation of the exited state (60 ns), electron injection from the dye LUMO level to the TiO_2 conduction band (50 fs -1.7 ps), recombination of the injected electron with the hole in the dye HOMO level (ns -ms), recombination of the electron in the TiO_2 conduction band with a hole (I_3^-) in the electrolyte (10 ms), and the regeneration of the oxidized dye by I^- (10 ns). (Hagfeldt & Gratzel, 2000).
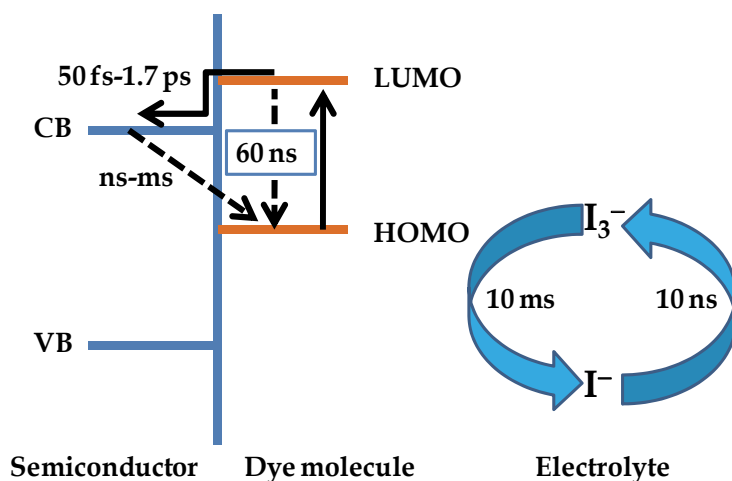
Fig. 17. Schematic illustration of kinetics in the DSSC, depicted from Hagfeldt & Gratzel, 2000.

It has been confirmed that electron injection from the excited dye such as the N_3 dye or $RuL_2(NCS)_2$ complex into the TiO_2 conduction band (CB) is a very fast process in femtosecond scale. The reduction of the oxidized dye by the redox electrolyte's I⁻ ions occur in about 10^{-8} seconds. Recombination of photoinjected CB electrons with oxidized dye molecules or with the oxidized form of the electrolyte redox couple (I_3^- ions) occurs in microseconds (Hara & Arakawa, 2003). To achieve good quantum yield, the rate constant for charge injection should be in the picosecond range. In conclusion, Fast recovery of the sensitizer is important for attaining long term stability. Also, long-lasting charge separation is a very important key factor to the performance of solar cells. Thus, new designs for larger conjugated dye-sensitizer molecules have been reported by investigators ,for example, Haque et al., (Haque et al., 2004) studied hybrid supermolecules that are efficiently retard the recombination of the charge-separated state and therefore assure enhanced energy

conversion efficiency by extending the lifetime of light-induced charge-separated states as illustrated in Figure 18, "Hybrid supermolecule: This is the structure of the redox triad that gave the most efficient charge separation in the report by Haque and colleagues . The triad is made of a ruthenium complex anchored to nanocrystalline TiO$_2$ (the electron acceptor) and covalently linked to polymeric chains of triphenyl-amine groups (the electron donor). Arrows represent the direction of the electron transfer process. The first step of the electron transfer is the light-induced excitation of the chromophore (process 1). Following this an electron is readily injected from the sensitizer excited state into the conduction band of the TiO$_2$ semiconductor (process 2). The direct recombination of primarily separated charges (process 3) would degrade the absorbed energy into heat. In this supermolecule this is avoided through the fast reduction of the ruthenium by the linked triphenyl-amine electron donor groups (process 4). The secondary recombination process (process 5) between the injected electron and the oxidized amine radical is made increasingly slow because the positive charge can hop from one triphenylamine function to the adjacent one along the chain (process 6) and the hole moves away from the TiO$_2$ surface. The overall photo-initiated process thus results in unidirectional electron flow from the end of the polymeric chains to the oxide (from right to left) and a very long-lived charge-separated state" (Moser, 2005).

In TiO$_2$ nanoparticle DSSCs, the electrons diffuse to the anode by hopping 103-106 times between particles (Baxter et al., 2006). With each hop there is a considerable probability of recombination of the photoexcited electron with the electrolyte since both the diffusion and recombination rates are on the order of milliseconds. Hence, this allows recombination to limit the cell efficiency. On the other hand, nanowire or tube structured photoelectrode (e.g., ZnO$_2$) provide a direct path (express highway) to the anode, leading to increased diffusion rate without increasing the recombination rate and thus increases cell efficiency.
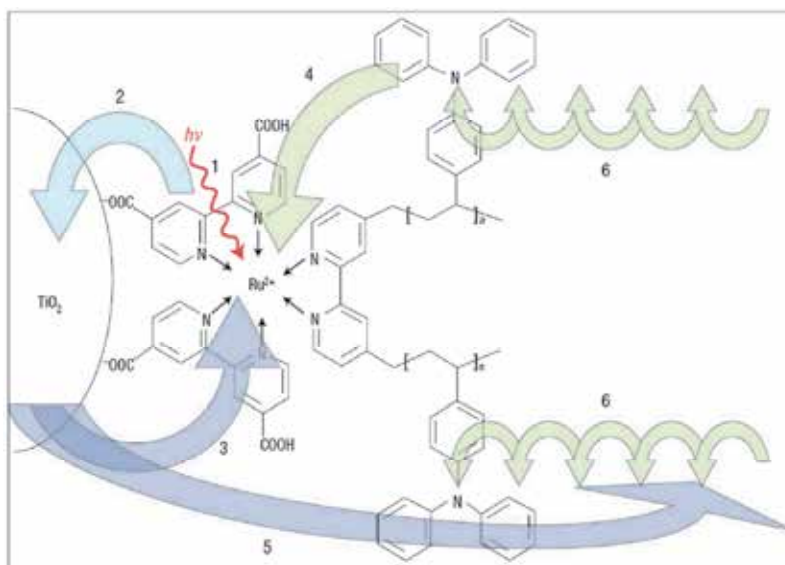
Fig. 18. Schematics of the hybrid supermolecule. The supersensitizer molecule adsorbed to a nanostructured TiO$_2$ surface promise to improve the photovoltaic conversion efficiency of dye sensitized solar cell (From Moser, 2005).

Dark current in DSSC is mainly due to the loss of the injected electron from nanostructured wide bandgap semiconductor (say TiO_2) to I_3^- (the hole carrier in solution electrolyte). Thus, it is a back reaction that must be eliminated or minimized. Reduction of dark current enhances the open circuit voltage of the cell, this can be deduced from the following general equation of solar cell relating the open circuit voltage V_{OC} to both the injection current I_{inj} and dark current I_{dark}:

$$V_{OC} = \frac{k_B T}{q} \ln\left(\frac{I_{inj}}{I_{dark}} + 1 \right) \tag{12}$$

where k_B is the Boltzmann constant, T is the absolute temperature of the cell, and q is the magnitude of the electron charge. In fact, dark current mainly occurs at the TiO_2/electrolyte interface where no photosensitizer got adsorbed. One successful way to suppress dark current is to use one of pyridine derivatives (e.g., tert-butylpyridine TBP) as coadsorbates on the nanostructured TiO_2 surface. Figure 19 shows the current–voltage characteristics obtained for NKX-2311-sensitized TiO_2 solar cells (Hara et al., 2003).
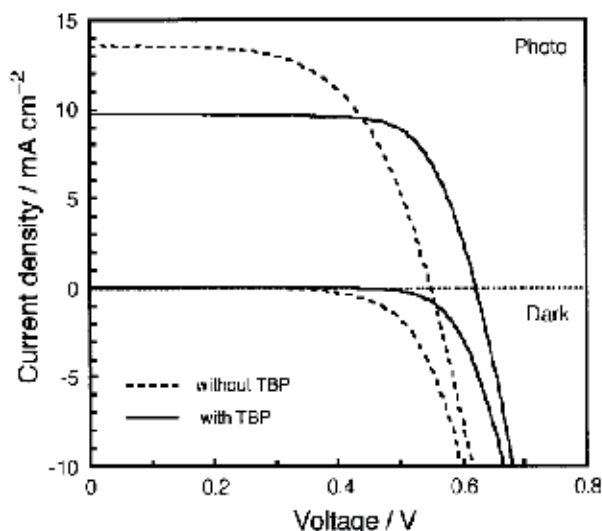
Fig. 19. Current–voltage curves obtained for NKX-2311-sensitized TiO_2 solar cells in an electrolyte of 0.6M DMPImI–0.1M LiI–0.05M I2 in methoxyacetonitrile: (– – –) without TBP, (—) with 0.5M TBP (From Hara et al., 2003).

4. Applications of DSSC

Because of the physical nature of the dye sensitized solar cells, inexpensive, environment-friendly materials, processing, and realization of various colors (kind of the used sensitizing dye); power window and shingles are prospective applications in building integrated photovoltaics BIPV. The Australian company Sustainable Technologies International has produced electric-power-producing glass tiles on a large scale for field testing and the first building has been equipped with a wall of this type (see for example, Figure 20-a). The availability of lightweight flexible dye sensitized cells or modules are attractive for

applications in room or outdoor light powered calculators, gadgets, and mobiles. Dye sensitized solar cell can be designed as indoor colorful decorative elements (see Figure 20-b). Flexible dye sensitized solar modules opens opportunities for integrating them with many portable devices, baggage, gears, or outfits (Pagliaro et al., w w w. pv- te ch.org) (see Figure 20-c and Figure 20-d). In power generation, dye sensitized modules with efficiency of 10% are attractive choice to replace the common crystalline Si-based modules. In 2010 Sony announced fabrication of modules with efficiency close to 10% and hence opportunity of commercialization of DSSC modules is attainable.
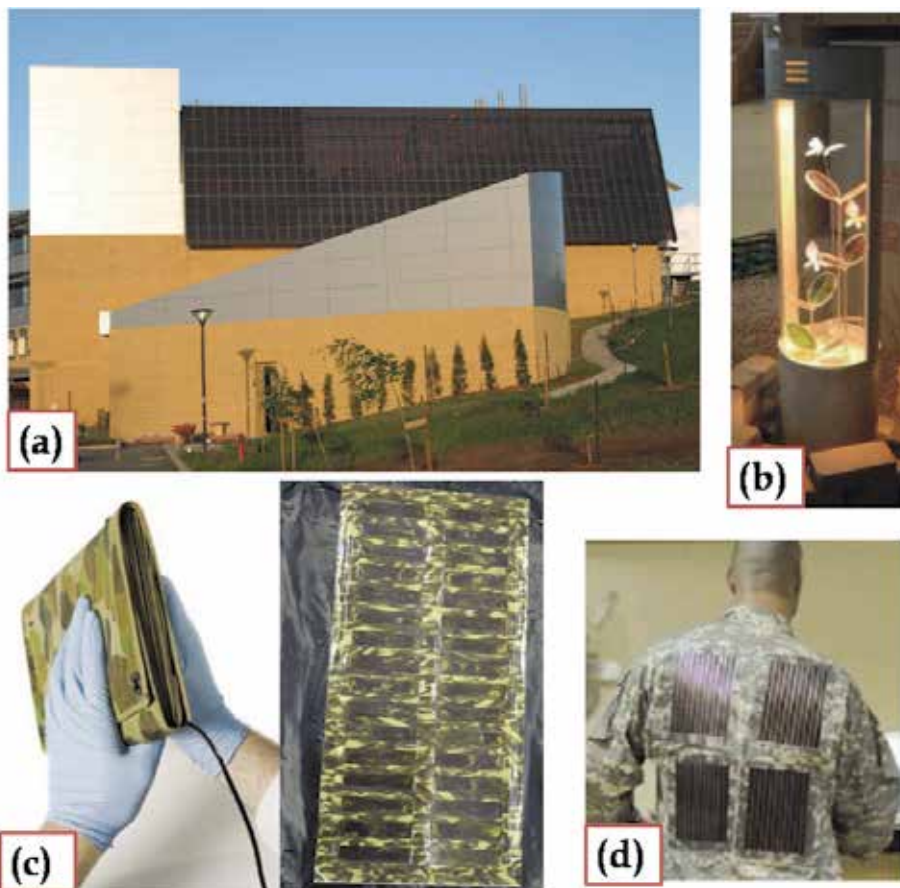
Fig. 20. Application examples of dye sensitized solar cells and modules: (a) 200 m2 of STI DSSC panels installed in Newcastle (Australia)– the first commercial DSSC module (http://www.sta.com.au/index.htm), (b) indoor ornament of dye sensitized solar cells leaves (AISIN SEIKI CO.,LTD), (c) flexible DSSC-based solar module developed by Dyesol (http://www.dyesol.com), and (d) jacket commercialized by G24i (http://www.g24i.com).

5. Commercialization of DSSC

Commercialization of dye sensitized solar cells and modules is taking place on almost all continents (Lenzmann & Kroon, 2007). In Asia, specifically in Japan: IMRA-Aisin

Seiki/Toyota, Sharp, Toshiba, Dai Nippon, Peccell Technologies. In Australia: Dyesol. In USA Konarka. G24i in UK, and Solaronix in Switzerland. G24i has announced a DSC module production of 25MW capacity in 2007 in Cardiff, Wales (UK), with extension plans up to 200MW by the end of 2008 (http://www.g24i.com). The success of many labs and companies such as ASIAN and Toyota Central R & D Labs., INC. (see Figure 21) to demonstrate various sizes and colors in a series-connected dye solar cell module in many international exhibitions and conferences reflects the potential role of dye sensitized solar cells systems in the PV technology. In fact, Toyota has installed in their dream house walls a similar kind of DSSCs panels shown in Figure 21-b.
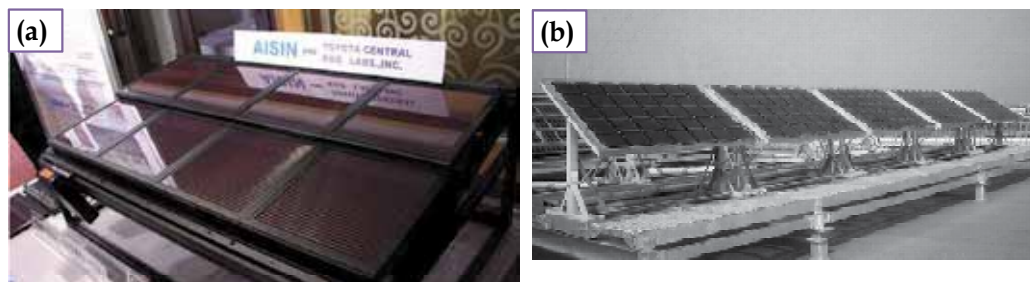
Fig. 21. (a) An example of DSSC module for outdoor application (Fromhttp://kuroppe.tagen.tohoku.ac.jp/~dsc/cell.html) and (b) Outdoor field tests of DSSC modules produced by Aisin Seiki in Kariya City. Note the pc-Si modules in the second row. (From Gratzel article at http://rsta.royalsocietypublishing.org/content/365/1853/993.full#ref-3).

Glass substrate is robust and sustains high temperatures, but it is fragile, nonflexible, and pricey when designed for windows or roofs. Flexible DSSCs have been intensively investigated. Miyasaka et. al. (Miyasaka & Kijitori, 2004) used the ITO (indium tin oxide) coated on PET (polyethylene terephatalate) as the substrate for DSSCs. Generally, the conducting glass is usually coated with nanocrystallineTiO$_2$ and then sintered at 450°C-500°C to improve the electronic contact not only between the particles and support but also among the particles. Plastics films have a low ability to withstand heat. The efficiency of plastic-based dye sensitized solar cells is lower than that of using glass substrate (η = 4.1%, J_{sc}= 9.0mA/cm^2, V_{oc} = 0.74V, FF = 0.61) because of poor necking of TiO$_2$ particles. Kang et al., (Kang et al.2006), used the stainless steel as the substrate for photoelectrode of DSSCs (see Figure 22). The cell illuminated through the counter electrode due to the non-penetration of light through metal substrate. In their system, the SiOx layer was coated on stainless steel (sheet resistance ~ 1 mΩ per square) and separated ITO from stainless steel, for preventing photocurrent leakage from stainless steel to the electrolyte. The constructed cells resulted in J_{sc} = 12 mA/cm^2, V_{oc} = 0.61 V, FF = 0.66, and η = 4.2 %. Recently, Chang et al. fabricated flexible substrate cell that produced conversion efficiency close to 2.91%. The photoelectrode substrates are flexible stainless steel sheet with thickness 0.07mm and titanium (Ti) sheet with thickness 0.25mm (Chang et al., 2010). Also, the reported approach by Yen et al. in developing a low temperature process for the flexible dye-sensitized solar cells using commercially available TiO$_2$ nanoparticles (such as P25) is interesting since it yielded a conversion efficiency of 3.10% for an incident solar energy of 100 mW/cm^2 (Yen et al. 2010). Because Titanium has extremely high corrosion resistance, compared with stainless steel, Titanium is still the privileged substrate material.
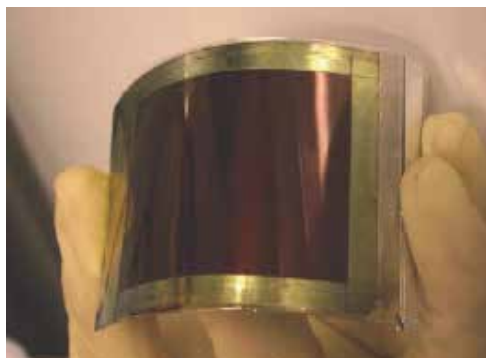
Fig. 22. A prototype of a flexible dye sensitized solar cell using stainless steel substrate (From Kang et al., 2006).

Availability of nonvolatile electrolyte is another issue toward commercialization of single or multi-junction modules. Polymer (solid) electrolyte, hole conductor, and solidified ionic liquids are solvent free choices with high electronic conductivity and chemical stability (Wang et al., 2005.) The key to high power heterojunction DSSC is to increase the effective diffusion length of electron within the nanostructured electrode by increasing the mobility of hole conductor or the extinction coefficient of the sensitizer to ensure more efficient light harvesting action. Since heat and UV light degrade cells performance, development of heat sink and optimized low cost UV coating is a must for outdoor applications. The successes in development of flexible substrate, solid electrolyte, and spectrally broad absorption range inexpensive nontoxic dyes will potentially open the possibility of role-to-role mass production of dye sensitized solar cells and modules (see Figure 23). Molecular engineering of efficient and stable organic sensitizers is an open invitation for many research groups, the successes in this area is expected to advance production and commercialization of DSSC (Kim et al., 2006).
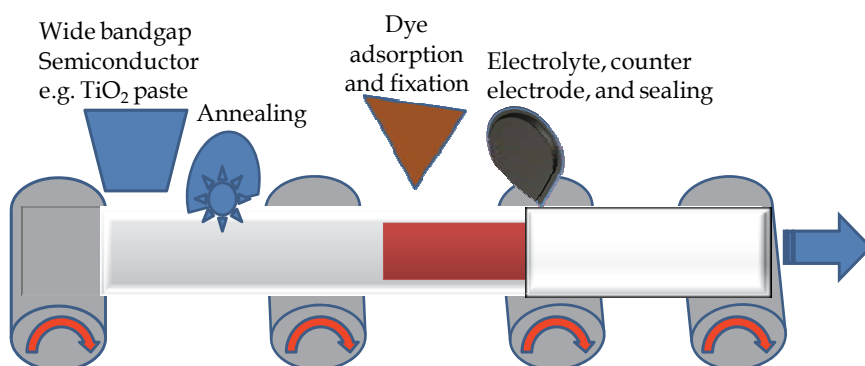
Fig. 23. Schematic of role-to-role manufacturing of flexible dye sensitized solar cells.

6. Conclusions

In This chapter we have discussed one example of the third generation solar cells, called photoelectrochemical cell and now called nanocrystalline dye sensitized solar cells DSSC or Gratzel cell. Nanocrystalline dye sensitized solar cell DSSC is classified as a low cost,

environmental friendly, and capable of being highly efficient cell mainly due to materials, charge carriers generation and transport within the cell structure. The nanostructured dye-sensitized solar cell (DSSC) is going to provide economically credible alternative to present day p–n junction photovoltaics. In fact, dye sensitized solar cell are green solar cell mimicking the green leave. In dye sensitized solar cell electricity is generated as a result of electron transfer due to photoexcitation of dye molecules adsorbed to nanostructured wide bandage material photoelectrode. The oxidized dye molecules regenerated by gaining electrons from electrolyte which is reduced by the electrons reaching the counter-electrode of the cell. In dye sensitized solar cells light absorption is separated from carrier transport. From educational point of view, since nanostructured dye sensitized solar cell DSSC is mimicking photosynthesis in plants, it provides an interdisciplinary context for students learning the basic principles of biological extraction, chemistry, physics, environmental science and electron transfer.

The requirements of practical sensitizers are: broad band and high level absorption of visible and near infrared region of the electromagnetic spectrum, exhibit thermal and photochemical stability, definitely chelating to the semiconductor oxide surface and inject electrons into the conduction band with a quantum yield of unity, and owning suitable ground- and excited state redox properties. Investigations of solvent free electrolyte such as polymer based, and ionic liquid are promising. In order to commercialize dye sensitized solar cell in low power applications, flexible DSSCs have been intensively investigated. The solar to electric power conversion efficiency of the DSC in full AM 1.5 sun light validated by accredited PV calibration laboratories has reached over 11 % and modules with efficiency close to 10% has been exhibited in 2010. Nanowires and quantum dots QDSSCs may be a promising solar cell design.

The search for green sources or generators of energy is considered one of the priorities in today's societies and occupies many policy makers' agendas. We at the University of Bahrain are the first to start the investigation of Dye sensitized solar cells DSSCs in the Arabian Gulf. Dye sensitized solar cells using natural organic dies were prepared using low cost materials and natural dyes. Sensitization of wide gap oxides semiconductor materials was accomplished with the growth of nanocrystalline TiO_2. The natural dyes extracted from Henna (*Lawsonia inermis* L.), pomegranate, cherries, and raspberries (Rubus spp.). We found that the nanocrystalline material based solar cell system exhibits an excellent optical absorption parameters for visible and near infrared portion of the electromagnetic spectrum. The performance of natural dye extract sensitized nanocrystalline solar cells can be appreciably enhanced by optimizing preparation technique, using different types of electrolyte, reported additives, and sealing.

In short, compared to Si based solar cells dye sensitized solar cells are of low cost and ease of production, their performance increases with temperature, possessing bifacial configuration - advantage for diffuse light, have transparency for power windows, color can be varied by selection of the dye, invisible PV-cells based on near-IR sensitizers are feasible, and they are outperforms amorphous Si. Moreover, DSSC shows higher conversion efficiency than polycrystalline Si in diffuse light or cloudy conditions. It is believed that nanocrystalline photovoltaic devices are becoming viable contender for large scale future solar energy converters.

7. Acknowledgments

8. References

Amao, Y. & Komori, T. (2004). Bio-photovoltaic conversion device using chlorine-e_6 derived from chlorophyll from *Spirulina* adsorbed on a nanocrystalline TiO_2 film electrode. *Biosensors Bioelectronics*, Vol. 19, Issue 8, pp. 843-847.

Baxter, J.B; Walker, A.M; van Ommering, K. & Aydil, E.S. (2006). Synthesis and characterization of ZnO nanowires and their integration into dye-sensitized solar cells . *Nanotechnology*, Vol. 17, Issue 11, pp. S 304-S 312.

Becquerel, A. E. (1839). Mčmoire sur les effets électriques produits sous l'influence des rayons solaires. *C. R. Acad. Sci. Paris*, Vol. 9, pp. 561-567.

Bergeron, B.V.; Marton, A.; Oskam, G. & Meyer, G.J. (2005). Dye-Sensitized SnO_2 Electrodes with Iodide and Pseudohalide Redox Mediators. J. Phys. Chem. B, Vol, 109, pp.935-943.

Boercker, J.E; Schmidt, J.B. & Aydil, E.S. (2009). Transport Limited Growth of Zinc Oxide Nanowires. Cryst. Growth, Vol. 9 (6), pp 2783–2789.

Calogero, G.; Di Marco,G.; Caramori, S.; Cazzanti, S.; Roberto Argazzi, R. and Bignozzi, C.A. (2009). Natural dye senstizers for photoelectrochemical cells. *Energy Environ. Sci.*, Vol. 2, Issue 11, pp. 1162-1172.

Chang, H.; Chen, T.L.; Huang, K.D.; Chien, S.H. & Hung, K.C. (2010). Fabrication of highly efficient flexible dye-sensitized solar cells. *Journal of Alloys and Compounds*, Vol. 504, Issue 2, pp. S435-S438.

Cherepy, N.J.; Smestad, G.P.; Gratzel, M. & Zhang, J.Z. (1997). Ultrafast Electron Injection: Implications for a Photoelectrochemical Cell Utilizing an Anthocyanin Dye-Sensitized TiO_2 Nanocrystalline Electrode. *J. Phys. Chem. B*, Vol. 101, pp. 9342-9351.

Chiba, Y.; Islam, A.; Watanabe, Y; Komiya, R.; Koide, N. & Han, L. (2006). Dye-sensitized solar cells with conversion efficiency of 11.1%. *Japanese Journal of Applied Physics, Part 2: Letters & Express Letters* , Vol. 45, pp. 24-28.

Durr M.; Bamedi A.; Yasuda A. & Nelles G. (2004). Tandem dye-sensitized solar cell for improved power conversion efficiencies. *Appl. Phys. Lett*., Volume 84 (17), pp. 3397-3399.

Ellinson, R.; Beard, M.; Johnson, J.; Yu, P.; Micic, O.; Nozik, A.; Shabaev, A.; and Efros A. (2005). Highly Efficient Multiple Exciton Generation in Colloidal PbSe and PbS Quantum Dots, *Nano Letters*, Vol. 5, No. 5, pp. 865-871.

Farzad, F.; Thompson, D. W.; Kelly, C. A.; and Meyer, G. J. (1999). Competitive Intermolecular Energy Transfer and Electron Injection at Sensitized Semiconductor Interfaces. *J. Am. Chem. Soc.*, Vol. 121, pp. 5577-5578.

Fernando, J.M.R.C. & Senadeera G.K.R. (2008). Natural anthocyanins as photosensitizers for dye-sensitized solar devices. *Current Science*, Vol. 95, No. 5, pp. 663-666.

Garcia, C.G., Polo, A.S. and Iha, N.Y. (2003). Fruit extracts and ruthenium polypyridinic dyes for sensitization of TiO_2 in photoelectrochemical solar cells. *J. Photochem. Photbiol. A(Chem.)*, Vol. 160 (1-2), pp. 87-91.

Gleiter, H. (1989). Nanocrystalline materials. *Prog. Mater. Sci.*, Vol. 33, pp. 223-315.

Gratzel, M. & Hagfeldt, A. (2000). Molecular Photovoltaics. *Acc. Chem. Res*, Vol. 33, pp. 269-277.

Gratzel, M. (2001). Molecular photovoltaics that mimic photosynthesis. *Pure Appl. Chem.*, Vol. 73, No. 3, pp. 459–467.

Gratzel, M., (2003). Dye-sensitized solar cells. *Journal of Photochemistry and Photobiology C: Photochemistry Reviews* 4, pp. 145–153.

Gratzel, M. (2005). Solar Energy Conversion by Dye-Sensitized Photovoltaic Cells. *Inorg. Chem.*, Vol. *44*, pp. 6841-6851.

Green, M. A.; Emery, K. Solar Cell Efficiency Tables 19, *Prog. Photovolt.: Res. Appl.* 2002; 10:55-61.

Guo, M.; Diao, P.; Wang, X. & Cai, S. (2005). The effect of hydrothermal growth temperature on preparation and photoelectrochemical performance of ZnO nanorod array films. *Journal of Solid State Chemistry*, Vol., 178, pp. 3210-3215.

Hao, S.; Wu, J.; Huang, Y. & Lin, J. (2006). Natural dyes as photosensitizers for dye-sensitized solar cell. *Sol. Energy*, Vol. 80, Issue 2, pp. 209-214.

Hara, K. & Arakawa, H. (2003). Dye-sensitized Solar Cells, In: Handbook of Photovoltaic Science and Engineering, A. Luque and S. Hegedus, (Ed.), Chapter 15, pp. 663-700, John Wiley & Sons, Ltd, ISBN: 0-471-49196-9.

Hara, K.; Tachibanaa, Y.; Ohgab, Y.; Shinpob, A.; Sugab, S.; Sayamaa,K.; Sugiharaa, H. & Arakawaa, H. (2003). Dye-sensitized nanocrystalline TiO_2 solar cells based on novel coumarin dyes. *Solar Energy Materials & Solar Cells*, Vol. 77, pp. 89–103.

Haque,S.A.; Handa,A.; Katja,P.; Palomares,E.; Thelakkat, M. & Durrant, J.R. (2005). Supermolecular control of charge transfer in dye-sensitized nanocrystalline TiO_2 films: towards a quantitative structure-function relationship. *Angewandte Chemie International Edition*, Vol. 44, pp. 5740-5744.

Harding, H.E.; Hoke, E.T.; Armistrong, P.B.; Yum, J.; Comte, P.; Torres, T.; Frechet, J.M.J.; Nazeeruddin, M.K.; Gratzel, M. & McGehee, M.D. (2009). Increased light harvesting in dye-sensitized solar cells with energy relay dyes. *Nature Photonics*, Vol. 3, pp. 406-411.

Hasobe, T.; Fukuzumi, S. & Kamat, P.V. (2006). Organized Assemblies of Single Wall Carbon Nanotubes and Porphyrin for Photochemical Solar Cells: Charge Injection from Excited Porphyrin into Single-Walled Carbon Nanotubes. *Journal of Physical Chemistry B,* Vol.110 (50), pp. 25477–25484.

Hasselmann, G. & Meyer, G. (1999). Sensitization of Nanocrystalline TiO2 by Re(I) Polypyridyl Compounds . *J. Phys. Chem.*, Vol. 212, pp. 39-44.

Hirata, N.; Lagref, J.; Palomares, E.J.; Durrant, J.R.; M. Khaja Nazeeruddin, Gratzel,M. & Di Censo, *D. (2004).* Supramolecular Control of Charge-Transfer Dynamics on Dye-sensitized Nanocrystalline TiO_2 Films . *Chem. Eur. J.* Vol. 10, Issue 3, pp. 595–602.

Hoffert, M.I; Caldeira, K.; Jain, A.K.; Haites,E.F.; Harvey, L.D.; Potter, S.D.; Schlesinger, M.E.; Schneider, S.H.; Watts, R.G.; Wigley, T.M. & Wuebbles, D.J. (1998). Energy implications of future stabilization of atmospheric CO_2 content. *Nature* , Vol. 395, pp. 881-884.

Horiuchi,T.; Hidetoshi Miura,H.; Sumioka, K. & Satoshi Uchida, S. (2004). High Efficiency of Dye-Sensitized Solar Cells Based on Metal-Free Indoline Dyes. *J. Am. Chem. Soc.*, Vol. *126* (39), pp 12218–12219.

Hoyer, P. & Könenkamp, R., (1995). Photoconduction in porous TiO₂ sensitized by PbS quantum dots. *Appl. Phys. Lett. Vol.* 66, Issue 3, pp. 349-351.

Islam, A.; Hara, K.; Singh, L. P.; Katoh, R.; Yanagida, M.; Murata, S.; Takahashi, Y.; Sugihara, H. & Arakawa, H. (2000) *Chem. Lett.*, pp. 490-491.

Jasim, K. E. & Hassan, A.M. (2009). Nanocrystalline TiO₂ based natural dye sensitised solar cells. *Int. J. Nanomanufacturing*, Vol. 4, Nos. 1/2/3/4, pp.242–247.

Jasim, K. E.; Al Dallal, S. & Hassan, A.M. (2011). Natural dye-sensitised photovoltaic cell based on nanoporous TiO₂, *Int. J. Nanoparticles*,(in press 2011).

Jasim, K. E; Al Dallal, S. & Hassan, A.M. (2011). HENNA (*Lawsonia inermis* L.) DYE-SENSITIZED NANOCRYSTALINE TITANIA SOLAR CELL. *J. Nanotechnology*, submitted for publication.

Jasim, K. E. (2011). Natural Dye-Sensitized Solar Cell Based On Nanocrystalline TiO₂. *Sains Mallaysiana*, submitted for publication.

En Mei Jin; Kyung-Hee Park; Bo Jin; Je-Jung Yun, & Hal-Bon Gu (2010). Photosensitization of nanoporous TiO₂ films with natural dye. Phys. Scr,.Vol. 2010, Issue T139, pp. 014006.

Jiu, J., Wang, F., Isoda, S., and Adachi, M. (2006). *J Phys Chem B Condens Matter Mater Surf Interfaces Biophys.*, Vol. 110(5), pp. 2087-2092

Kang, M.G., Park, N-G., Kim, K-M., Ryu, K.S., Chang S.H. & Kim, K.J. (2003). Highyl efficient polymer gel electrolytes for fye-sensitized solar cells. *3rd World Conference on Phorovolroic Emru Conversion . May 11-18, 2003 Osnh, Japan.*

Kang , M.; Park, N.; Ryu, K.; Chang, S. & Kim, K. (2006). A 4.2% efficient flexible dye-sensitized TiO2 solar cells using stainless steel substrate. *Solar Energy Materials & Solar cells*, Vol. 90, pp. 574-581.

Karami, A. (2010). Synthesis of TiO₂ Nano Powder by the Sol-Gel Method and Its Use as a Photocatalyst. *J. Iran. Chem. Soc.*, Vol. 7, pp. S154-S160.

Kawano, R.; Matsui, H.; Matsuyama, C.; Sato, A.; Susan, Md. A. B.H.; Tanabe, A. & Watanabe, M. (2004). High performance dye-sensitized solar cells using ionic liquids as their electrolytes. *Journal of Photochemistry and Photobiology A*, Vol. 164, no. 1–3, pp. 87–92.

Kelly, C. A.; Thompson, D. W.; Farzad, F. & Meyer, G. J. (1999). Excited State Deactivation of Ruthenium(II) Polypyridyl Chromophores Bound to Nanocrystalline TiO₂ Mesoporous Films. ,*Langmuir*, Vol. *15*, pp. 731-734.

Kim, K.S.; Kang, Y.S.; Lee, J.H.; Shin, Y.J.; Park, N.G.; Ryu, K.S. & Chang, S.H. (2006). Photovoltaic properties of nano-particulate and nanorod array ZnO electrodes for dye-sensitized solar cell. *Bull Korean Chem. Soc*, Vol. 27, pp. 295-298.

Kim,S.; Lee, J.K.; Kang, S.O.; Ko, J.J.; Yum, J.H.; Fantacci, S.; De Angelis, F.; Di Censo, D.; Nazeeruddinand, Md. K. & Graetzel, M., (2006). Molecular Engineering of Organic Sensitizers for Solar Cell Applications. *J. Am. Chem, Soc*, Vol. 128,pp. 16701-16707.

Kleverlaan, C. J.; Indelli, M. T.; Bignozzi, C. A.; Pavanin, L.; Scandola, F. & Hasselmann, Meyer, G. J. (2000*). Stepwise Photoinduced Charge Separation in Heterotriads: Binuclear Rh(III) Complexes on Nanocrystalline Titanium Dioxide. *J. Am. Chem. Soc.*, Vol. 122, pp. 2840-2849.

Kopidakis, N.; Benkstien, K.D.; van de Lagemaat, J. & Frank, A.J. (2003). *J. Phys. Chem. B*, Vol, 107, pp. 11307.

Kuang, D.; Wang, P.; Ito, S.; Zakeeruddin, S.M. & Gratzel, M. (2006). Stable mesoscopic dye-sensitized solar cells based on tetracyanoborate ionic liquid electrolyte. *Journal of the American Chemical Society*, Vol. 128, no. 24, pp. 7732–7733.

Kubo, W.; Murakoshi, K.; Kitamua, T.; Yoshida, S.; Haruki, M.; Hanabusa, K.; Shirai, H.; Wada, Y., & Yanagida, S. (2001). Quasi-Solid-State Dye-Sensitized TiO_2 Solar Cells: Effective Charge Transport in Mesoporous Space Filled with Gel Ele, . *J Phys. Chem. B*, Vol. 105, Issue 51, pp. 12809-12812.

Kubo, W.; Sakamoto, A.; Kitamura, T.; Wada, Y. & Yanagida, S. (2004). Dye-sensitized solar cells: improvement of spectral response by tandem structure, *Journal of Photochemistry and Photobiology A: Chemistry* ,Vol.164, pp. 33–39.

Kumara, G.R.A., Kanebo, S., Okuya, M., Onwaona-Agyeman, B., Konno, A., and Tennakone, K. (2006) . *Sol. Enrgy Mater. Sol. Cells*, Vol. 90, pp.1220.

Lagref, J.J.; Nazeeruddin, M.K., & Graetzel, M. (2008). Artificial photosynthesis based on dye-sensitized nanocrystalline TiO_2 solar cells, *INORGANICA CHIMICA ACTA*, Vol. 361, Issue 3, pp.735-745.

Law, M.; Greene, L. E.; Johnson, J. C.; Saykally, R. & Yang, P. D. (2005). Nanowire dye-sensitized solar cells. *Nature Materials, Vol. 4*, 455-459.

Lenzmann, F.O. & Kroon, J.M. (2007). Recent Advances in Dye-Sensitized Solar Cells, *Advances in OptoElectronics* , Volume 2007, Article ID 65073.

Lewis, N. S. (2007). Toward Cost-Effective Solar Energy Use. *Science*, Vol *315*, pp. 798-801.

Lindström, H.; Holmberg, A.; Magnusson, E.; Malmqvist, L. & Hagfeldt, A. (2001). A new method to make dye-sensitized nanocrystalline solar cells at room temperature, *Journal of Photochemistry and Photobiology A: Chemistry*, Vol. 145, pp. 107–112.

Liu, D. and Kamat, P.V. (1993). Photoelectrochemical behavior of thin cadmium selenide and coupled titania/cadmium selenide semiconductor films. *J. Phys. Chem.* Vol. 97, pp. 10769-10773.

Martinson, A. B. F.; Hamann, T. W.; Pellin, M. J. & Hupp, J. T. (2008). New Architectures for Dye-Sensitized Solar Cells. *Chem. – Eur. J.*, Vol. 14, 4458– 4467.

Matsumoto, M.; Wada, Y.; T. Kitamura, T.; Shigaki, K.; Inoue, T.; Ikeda, M. and Yanagida, S. (2001). Fabrication of solid-state dye-sensitized TiO_2 solar cell using polymer electrolyte. *Bull. Chem. Soc. Japan*, vol. 74, pp. 387-393.

Miyasaka, T. & Kijitori, Y. (2004). Low-temperature fabrication of dye-sensitized plastic electrodes by electrophoretic preparation of mesoporous TiO2 layers. *J. Electrochem. Soc.*, Vol. 151(11), pp. A1767-A1773.

Monari, A.; Assfeld, X.; Beley, M. & Gros, P.C. (2011). Theoretical Study of New Ruthenium-Based Dyes for Dye-Sensitized Solar Cells. *J. Phys. Chem. A*, Vol.*115* (15), pp. 3596–3603.

Mor, G.K.; Shankar, K.; Paulose, M.; Varghese, O.K. & Grimes, C.A. (2006). Use of Highly-Ordered TiO_2 Nanotube Arrays in Dye-Sensitized Solar Cells. *Nanoletters*, Vol., 6, Issue 2, p.215-218.

Moser, J.-E. (2005). Solar Cells Later rather than sooner, *Nature materials*, Vol. 4, pp. 723-724.

Nansen, R. (1995). S u n Power: The Global Solution for the Coming Energy Crisis s. Ocean Press, ISBN-10: 0964702118, Washington, USA.

Nazerruddin, M.K; Kay, A.; Ridicio, I.; Humphry-Baker, R.; Mueller, E.; Liska, P.; Vlachopoulos, N. & Gratzel, M. (1993). *J. Amer. Chem. Soc.* Vol. 115, pp. 6382-6390.

Nazeeruddin, M. K.; De Angelis, F.; Fantacci, S.; Selloni, A.; Viscardi, G.;Liska, P.; Ito, S.; Takeru, B., & Graetzel, M. (2005). Combined Experimental and DFT-TDDFT Computational Study of Photoelectrochemical Cell Ruthenium Sensitizers. *J. Am. Chem. Soc*, Vol. 127(48), pp. 16835-16847.

Noack, V., Weller, H., & Eychmuller, A. (2002). J. Phys. Chem. B, Vol. 106, pp. 8514.

Nogueira, A.F.; De Paoli, M.A.; Montanan, I.; Monkhouse, R. & Durrant, I. (2001). J. *Phys. Chem. B, Vol.* 105, pp. 7417.

Nozik, A.J. (2001). Quantum Dot Solar Cells. *Annu. Rev. Phys. Chem. Vol.* 52, pp. 193-231.

Nozik, A. J. (2004). Quantum dot solar cells. *Next Gener. Photovoltaics*, pp. 196-222.

Nozik, A. J. (2005). Exciton multiplication and relaxation dynamics in quantum dots: applications to ultrahigh-efficiency solar photon conversion. *Inorg. Chem*. Vol. 44,pp. 6893–6899.

O'Regan B. & Gratzel, M. (1991). A low cost, high-efficiency solar cell based on dye-sensitized colloidal TiO2 films. *Nature*; Vol. 353, pp. 737–739.

Pagliaro, M.; Palmisano, G., & Ciriminna,R. (2008). Working principles of dye-sensitised solar cells and future applications,third print edition of *Photovoltaics International journal*, w w w.pv- te ch.org.

Pavasupree, S.; Suzuki, Y.; Yoshikawa, S., & Kawahata, R. (2005). Synthesis of Titanate, TiO$_2$(B), and AnataseTiO$_2$ Nanofibers from Natural Rutile Sand, *J. Solid State Chem*, Vol. 178 (10), pp. 3110-3116.

Pavasupree, S.; Ngamsinlapasathian, S.; Nakajima, M.; Suzuki, Y., & Yoshikawa, S. (2006). Synthesis, characterization, photocatalytic activity and dye-sensitized solar cell performance of nanorods/nanoparticles TiO2 with mesoporous structure, *Journal of Photochemistry and Photobiology A: Chemistry*, Vol. 184. pp 163–169.

Plass, R.; Pelet, S.; Krueger, J., & Gratzel, M. (2002). Quantum Dot Sensitization of Organic-Inorganic Hybrid Solar Cells, *Phys. Chem. B*, Vol. 106 (31), pp. 7578 -7580.

Polo, A.S., and Iha, N.Y. (2006). Blue sensitizers for solar cells: natural dyes from Calafate and Jaboticaba. *Sol. Enrgy Mater. Sol. Cells*, Vol. 90, pp.1936-1944.

Qu, P.; Thompson, D. W., & Meyer, G. J. (2000). Temperature Dependent, Interfacial Electron Transfer from Ru(II) Polypyridyl Compounds with Low Lying Ligand Field States to Nanocrystalline Titanium Dioxide. *Langmuir*, Vol. 16, pp. 4662-4671.

Ren, Y.; Zhang, Z.; Gao, E.; Fang, S., & Cai, S. (2001). A dye-sensitized nanoporous TiO$_2$ photoelectrochemical cell with novel gel network polymer electrolyte. *J. Appl. Electochem.*,Vol. 31, pp. 445-447.

Robel, I.; Bunker, B. A. & Kamat, P. V. (2005). Single-walled carbon nanotube-CdS nanocomposites as light-harvesting assemblies: Photoinduced charge-transfer interactions, *Adv. Mater.*, 17, 20, pp. 2458-2463..

Sayer, R. A.; Hodson, S.L. & Fisher, T.S. (2010). Improved Efficiency of Dye-Sensitized Solar Cells Using a Vertically Aligned Carbon Nanotube Counter Electrode, *J. Sol. Energy Eng*, Vol. 132, Issue 2, 021007 (4 pages).

Schmidt-Mende, L. & Gratzel, M. (2006). TiO$_2$ pore-filling and its effect on the efficiency of solid-state dye-sensitized solar cells, *Thin Solid Films 500*, pp. 296–301.

Shen, Q., Katayama, K., Sawada, T., Yamaguchi, M., and Toyoda, T. (2006). Optical Absorption, Photoelectrochemical, and Ultrafast Carrier Dynamic Investigations of TiO$_2$ Electrodes Composed of Nanotubes and Nanowires Sensitized with CdSe Quantum Dots, *Japanese Journal of Applied Physics*, Vol. 45, No. 6B, pp. 5569-5574.

Shoute, L. C. T., & Loppnow, G. R. (2003). Excited-state Metal-to-Ligand Charge Transfer Dynamics of a Ruthenium(II) Dye in Solution and Adsorbed on TiO2 Nanoparticles from Resonance Raman Spectroscopy. *J. Am. Chem. Soc.*, Vol.125, pp.15636-15646.

Smestad, G.P. (1998). Education and solar conversion: Demonstrating electron transfer, *Sol. Energy Mater. Sol. Cells*, Vol. 55, pp. 157-178.

Smestad, G.P. & Gratzel, M. (1998). Demonstrating Electron Transfer and Nanotechnology: A Natural Dye-Sensitized Nanocrystalline Energy Converter, *Journal of Chemical Education*, Vol. 75 No. 6, pp. 752-756.

Späth, M., Sommeling, P. M., van Roosmalen, J. A. M., Smit, H. J. P., van der Burg, N. P. G., Mahieu, D. R., Bakker, N. J. & Kroon, J. M. (2003). Reproducible Manufacturing of Dye-Sensitized Solar Cells on a Semi-automated Baseline, *Prog. Photovolt: Res. Appl.* Vol. 11, pp. 207-220.

Suri, P., Panwar, M., & Mehra, R. (2007). Photovoltaic performance of dye-sensitized ZnO solar cell based on Eosin-Y photosensitizer, Materials Science-Poland, Vol. 25, No. 1, pp. 137-144.

SSun, J.Q.; Wang, J.S.; Wu, X.C.; Zhang, G.S.; Wei, J.Y.; Zhang, S.Q.; Li, H. & Chen, D.R. (2006). Novel Method for High-Yield Synthesis of Rutile SnO_2 Nanorods by Oriented Aggregation. *Crystal Growth & Design*, Vol., 6, Issue 7, pp.1584-1587.

Suzuki, Y.; Ngamsinlapasathian, S.; Yoshida, R., & Yoshikawa, S. (2006). Partially nanowires-structured porous TiO2 electrode for dye-sensitized solar cell. *Central Euro. J. Chem.*, Vol. 4 (3), pp. 476 -488.

Tennakone, K.; Kumara, G.; Kottegota, I. & Wijayantha, K. (1997). The photostability of dye-sensitized solid state photovoltaic cells: factors determining the stability of the pigment in n-TiO2/Cyanidin/p-CuI cells. *Semicond. Sci. Technol.* Vol. 12, pp. 128.

Tennakone, K.; Perera, V.P.S; Kottegoda, I.R.M. & Kumara, G. (1999). Dye-sensitized solid state photovoltaic cell based on composite zinc oxide/tin (IV) oxide films, *J. Phys. D-App. Phys.*, Vol. 32, No. 4, pp. 372.

Tiwari, A., & Snure, M. (2008). Synthesis and Characterization of ZnO Nano-Plant-Like Electrodes. *Journal of Nanoscience and Nanotechnology*, Vol. 8, pp. 3981-3987.

Vogel, R. & Weller. H. (1994). Quantum-Sized PbS, CdS, AgzS, Sb&, and Bi& Particles as Sensitizers for Various Nanoporous Wide- Bandgap Semiconductors. *J. Phys. Chem. Vol.* 98, pp. 3183-3188.

Wang, P., Zakeeruddin, S.M., Moser, J.,-E., Humphry-Baker, R., and Gratzel, M. (2004). "A solvent-free, SeCN-/(SeCN)3− based ionic liquid electrolyte for high-efficiency dye-sensitized nanocrystalline solar cells," *Journal of the American Chemical Society*, vol. 126, no. 23, pp. 7164–7165.

Wang, P.; Klein, C.; Humphry-Baker, R.; Zakeeruddin, S. M. & Gratzel, M. (2005). Stable >= 8% efficient nanocrystalline dye-sensitized solar cell based on an electrolyte of low volatility. *Appl. Phys. Lett.* Vol. 86 (12), pp. Art. No.123508.

Wongcharee, K.; Meeyoo, V. & Chavadej, S. (2007). Dye-sensitized Solar Cell Using Natural Dye Extract From Rosslea and Blue Pea Flower . *Sol. Enrgy. Mater. Sol. Cells*, Vol. 91 (7), pp. 566-571.

www.g24i.com

www.intertechpira.com

Xiang, J.H., Zhu, P.X., Masuda, Y., Okuya, M., Kaneko, S. & Koumoto, K. (2006). Flexible solar-cell from zinc oxide nanocrystalline sheets self-assembled by an in-situ electrodeposition process. *J. Nanosci. Nanotechnol.* Vol. 6 (6), pp. 1797-1801.

Yanagida, S., (2006). Recent research progress of dye-sensitized solar cells in Japan. *C. R. Chemie*. Vol. 9, pp. 597-604.

Yang, M., Thompson, D., and Meyer, G. (2000). Dual Sensitization Pathways of TiO_2 by $Na_2[Fe(bpy)(CN)_4]$. *Inorg. Chem*. Vol. 39, pp. 3738-3739.

Yanagida, S., Senadeera, G.K.R., Nakamura, K., Kitamura, T., & Wada, Y. (2004). Polythiophene-sensitized TiO_2 solar cells. *J. Photohem. Photbiol. A*, Vol. 166, pp. 75-80.

Yen, W.; Hsieh, C.; Hung, C.; Hong-Wen Wang, H., & Tsui, M. (2010). Flexible TiO2 Working Electrode for Dye-sensitized Solar Cells. *Journal of the Chinese Chemical Society*, Vol 57, pp.1162-1166.

Zaban, A.; Micic, O.I.; Gregg, B.A. & Nozik, A.J. (1998). Photosensitization of Nanoporous TiO_2 Electrodes with InP Quantum Dots. *Langmuir, Vol.* 14 (12), pp. 3153-3156.

Zhang, W.; Zhu, R.; Li, F.; Qing Wang, Q. & Bin Liu, B. (2011). High-Performance Solid-State Organic Dye Sensitized Solar Cells with P3HT as Hole Transporter. J. Phys. Chem. C, Vol. 115 (14), pp 7038–7043.

Zhu, K.; Neale, N.R.; Halverson, A.F.; Kim, J.Y. & Frank, A.J. (2010). Effects of Annealing Temperature on the Charge-Collection and Light-Harvesting Properties of TiO_2 Nanotube-Based Dye-Sensitized Solar Cells. J. Phys. Chem. C, Vol. 114 (32), pp 13433–13441.

Zhao, J.; Wang, A. & Green, M.A. (1999). 24.5% Efficiency Silicon PERT Cells on MCZ Substrates and 24.7% Efficiency PERL Cells on FZ Substrates. *Progress in Photovoltaics*, Vol. 7, pp. 471-474.

Zweibel, K. & Green, M.A. (ed.) (2000). *Progress in Photovoltaics: Research and Applications*, Volume 8, Issue 1, pp. 171 – 185, John Wiley & Sons, Ltd;

Shape Control of Highly Crystallized Titania Nanorods for Dye-Sensitized Solar Cells Based on Formation Mechanism

Motonari Adachi[1,4], Katsuya Yoshida[2], Takehiro Kurata[2],
Jun Adachi[3], Katsumi Tsuchiya[2], Yasushige Mori[2] and Fumio Uchida[4]
[1]*Research Center of Interfacial Phenomena, Faculty of Science and Engineering,
Doshisha University, 1-3 Miyakodani, Tatara, Kyotanabe,*
[2]*Department of Chemical Engineering and Materials Science,
Doshisha University, 1-3 Miyakodani, Tatara, Kyotanabe,*
[3]*National Instituite of Biomedical Innovation, 7-6-8 Asagi Saito, Ibaraki,*
[4]*Fuji Chemical Co., Ltd., 1-35-1 Deyashikinishi-machi, Hirakata,*
Japan

1. Introduction

Utilization of solar energy - the part transmitted to the earth in the form of light- relies on how effectively it can be converted into the form of electricity. In this regard, dye-sensitized solar cells have attracted recent attention as they are expected to offer the possibility of inexpensive yet efficient solar energy conversion. The performance of dye-sensitized solar cells depends critically on a constituent nanocrystalline wide-band-gap semiconductor (usually titania, TiO_2, nanoparticles) on which a dye is adsorbed. The electrical and optical properties of such nanoparticles are often dependent on their morphology and crystallinity in addition to size, and hence, it is essential to be able to control the particle size, shape, their distributions and crystallinity (Empedocles et al., 1999; Nirmal & Brus, 1999; Manna et al., 2000), which requires an in-depth understanding of the mechanisms of nucleation and growth as well as such processes as aggregation and coarsening.

Among the unique properties exhibited by nanomaterials, the movement of electrons and holes in semiconductor materials is dominated mainly by the well-known quantum confinement, and the transport properties related to phonons and photons are largely affected by the size, geometry, and crystallinity of the materials (Alivisatos, 1996a, 1996b; Murray et al., 2000; Burda et al., 2005). Up to now, various ideas for morphological control were introduced (Masuda & Fukuda, 1995; Masuda et al., 1997; Lakshmi et al., 1997a, 1997b; Penn & Banfield, 1998; Banfield et al., 2000; Peng et al., 2000; Puntes et al., 2001; Pacholski et al., 2002; Tang et al., 2002, 2004; Peng, 2003; Scher et al., 2003; Yu et al., 2003; Cao, 2004; Cheng et al., 2004; Cui et al., 2004; Garcia & Tello, 2004; Liu et al., 2004; Pei et al., 2004; Reiss et al., 2004; Song & Zhang, 2004; Wu et al., 2004; Yang et al., 2004; Zhang et al., 2004) based on: (1) a mixture of surfactants used to bind them selectively to the crystallographic faces for CdS (Scher et al., 2003), (2) monomer concentration and ligand effects for CdSe (Peng et al., 2000), (3) growth rate by controlling heating rate for $CoFe_2O_4$ (Song & Zhang, 2004), (4)

biological routes in peptide sequence for FePt (Reiss et al., 2004), (5) controlled removal of protecting organic stabilizer for CdTe (Yu et al., 2003; Tang et al., 2002, 2004), (6) anodic alumina used as a template (Masuda & Fukuda, 1995; Masuda et al., 1997), and (7) the "oriented attachment" mechanism for nanoparticles (Penn & Banfield, 1998; Banfield et al., 2000). A number of methods have been developed to control the shape of nanocrystals on the basis of these ideas.

Titanium dioxide has a great potential in alleviating the energy crisis through effective utilization of solar energy with photovoltaics and water splitting devices, and is believed to be the most promising material for the electrode of dye-sensitized solar cells (Fujishima & Honda, 1972; Fujishima et al., 2000; Hagfeldt & Grätzel, 2000; Grätzel, 2000, 2001, 2004, 2005; Nazeeruddin et al., 2005). To further pursue this potential in terms of its morphology in dispersion, we have synthesized highly crystallized nanoscale "one-dimensional" titania materials such as titania nanowires having network structure (Adachi et al., 2004) and titania nanorods (Jiu et al., 2006), which were confirmed to provide highly efficient dye-sensitized solar cells (Adachi et al., 2007, 2008; Kurata et al., 2010).

Extremely high crystalline features of nanorods can be perceived in the images of high-resolution transmission electron microscopy (Yoshida et al., 2008; Kurata et al., 2010) as shown in Fig. 1. A highly magnified, high-resolution transmission electron microscopy image (Fig. 1b) demonstrates a well-regulated alignment of titanium atoms in crystalline anatase structure with essentially no lattice defects. The TiO_2 anatase (101) face, (-101) face, and (001) face are clearly observed; a specific feature definitely captured and to be noted is that the nanorod edge is sharply demarcated by the kinks consisting of (101) and (-101) planes. Such bare anatase crystal with atomic alignment - anatase TiO_2 crystals not covered with amorphous or additional phases around the edge or rim - is extremely important, when used as the materials for the electrodes, to achieve high performance for electrons transport and dye adsorption in the dye-sensitized solar cells. The longitudinal direction of the nanorod is along the *c*-direction, and the lattice spacing of 0.95 nm for the (001) plane and that of 0.35 nm for the {101} plane agree quite well with the corresponding values recorded in JCPDS. Such visual evidence strongly supports that the electron transport rate in the titania nanorods is expected to be very rapid, bringing highly efficient dye-sensitized solar cells through the use of the titania nanorods as the materials for the electrodes.

So far we have attained the power conversion efficiency ranging from 8.52% (Kurata et al., 2010) to 8.93% (Yoshida et al., 2008) using these nanorods as the electrode of dye-sensitized solar cells. In order to realize further improvement in conversion efficiency, we need to investigate the ways to control the shape as well as size of these nanorods by maintaining the extremely high crystalline feature of the nanorods. To accomplish the proper control of size and shape of nanorods, we examined the formation processes of nanorods under the most suitable condition for making nanorods, which is called "standard condition" hereafter, the results of which were detailed in a published work (Kurata et al., 2010).

In this chapter we first present the formation processes of titania nanorods under the standard condition in reasonable depth (Kurata et al., 2010). We then present the effects of both the concentrations of reactants, especially ethylenediamine, and the temperature-change strategy on the formation processes of nanorods. Based on all these findings, shape and size control of highly crystallized titania nanorods was proposed and carried out, leading to high-aspect-ratio, longer titania nanorods with highly crystallized state being successfully synthesized. We finally present that high dispersion of titania nanorods having highly crystallized state can be attained with the help of acetylacetone.
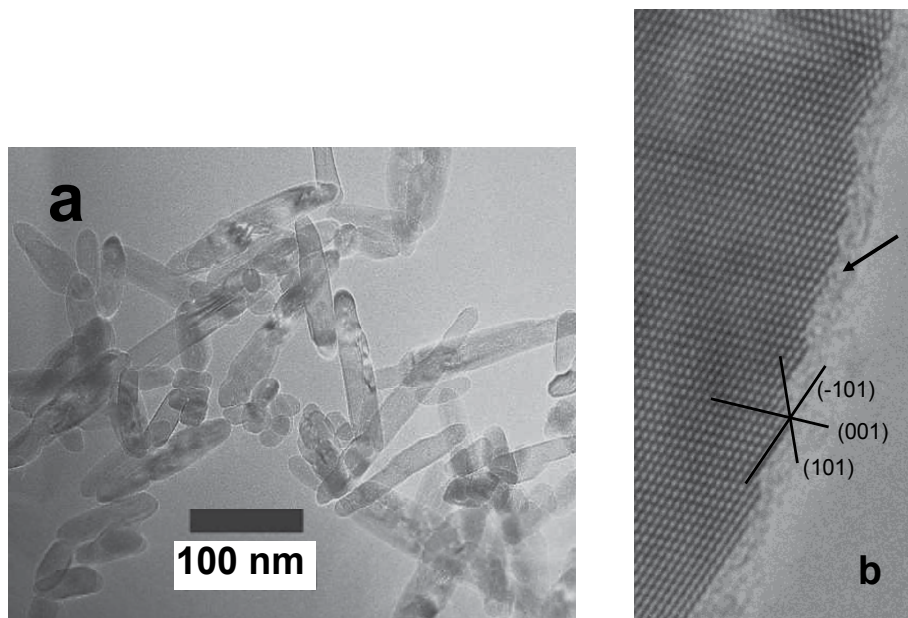
Fig. 1. Transmission electron microscopy images of highly crystallized titania nanorods covered with dye: (a) low-magnification image of titania nanorods, and (b) high-resolution image near the edge of a titania nanorod with dye coverage indicated by the arrow.

2. Experimental

The experimental procedure under the standard condition has been described in detail in our previous papers (Jiu et al., 2006; Kurata et al., 2010). Here, we summarize the essential part of the standard procedure and describe the modifications made on it. First, a 10-wt% aqueous solution of blockcopolymer F127 [(PEO)$_{106}$-(PPO)$_{70}$-(PEO)$_{106}$] was prepared using deionized pure water (Millipore Milli-Q). Cetyltrimethylammonium bromide was dissolved in the F127 solution at 308 K with a fixed concentration of cetyltrimethylammonium bromide, 0.055 M. In some modified cases the synthesis was carried out under no cetyltrimethylammonium bromide conditions. Ethylenediamine was added as a basic catalyst and also as a shape director (Sugimoto et al., 2003). The concentration of ethylenediamine was 0.25 M in the standard condition; in the modified conditions, the ethylenediamine concentration was varied from 0 to 0.5 M in order to examine its effects. After a transparent solution was obtained, tetraisopropyl orthotitanate (0.25 M) was added into the solution with stirring. This solution was stirred for half a day in the standard condition. The solution including white precipitates obtained by hydrolysis and condensation reactions of tetraisopropyl orthotitanate was then transferred into a Teflon autoclave sealed with a crust made of stainless steel, and reacted at 433 K for a desired period.

In the modified cases with temperature strategy, the reaction temperature was reduced during the preparation from 433 to 413 K to investigate its effects on the reaction mechanism. When acetylacetone was used to modify tetraisopropyl orthotitanate by binding acetylacetone to Ti atoms of tetraisopropyl orthotitanate, the transparent solutions were obtained after one-week stirring before hydrothermal reaction. The reaction product

obtained under the hydrothermal condition at a desired time was washed by isopropyl alcohol and deionized pure water, followed by separating the reaction product by centrifugation (Kokusan H-40F). After the washing, the obtained sample was dried in vacuum for 24 h (EYELA Vacuum Oven VOS-450-SD). To gain additional insight into the underlying mechanism for the transition from amorphous-like structure to titania anatase crystalline structure in the early stage of the reaction, changes in shape and crystalline structure of reaction products upon calcination at 723 K for 2 h were observed and measured.

3. Results and discussion

3.1 Formation processes under standard condition

First of all, the formation processes under the standard condition are described prior to comparing the experimental results and discussing the effects of various modifications on those under the modified conditions. Typical transmission electron microscopy images of reaction products at 0.5, 2, 3.5, 4, 6, and 24 h under the standard condition (Kurata et al., 2010) are shown in Fig. 2. At 0.5 h, only a film-like structure was observed. At 2 h, the shape of reaction products was still mostly film-like, while some deep-black wedge-shaped structure partly appeared. At 3.5 h, the main structure was still film-like, with uneven light and dark patches recognized. At 4 h, however, only rod-shaped products were observable, signifying that the film-like shape with amorphous-like structure changed to nanorod-shaped titania in a time interval between 3.5 and 4 h. After 6 h, only nanorod shape was observed. The morphology was observed to change very slowly with time after 6 h.
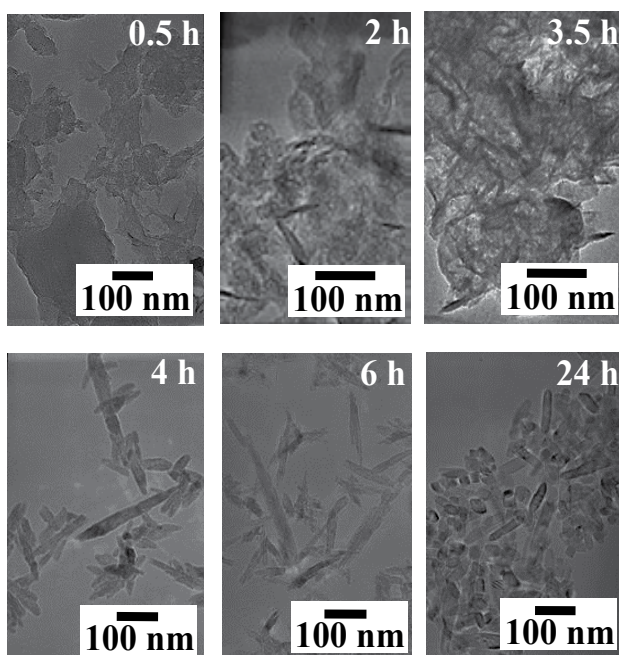
Fig. 2. Transmission electron microscopy images of reaction products at 0.5, 2, 3.5, 4, 6, and 24 h under standard condition (Kutata et al., 2010).
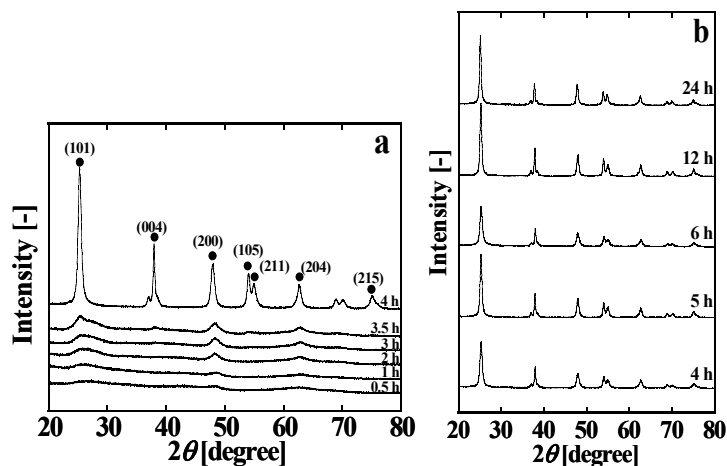
Fig. 3. Variation in X-ray diffraction spectra of reaction products: (a) from 0.5 to 4 h, (b) from 4 to 24 h.

Fig. 3 shows the variation in X-ray diffraction spectra (a) from 0.5 to 4 h and (b) from 4 to 24 h under the standard condition (Kurata et al., 2010), i.e., 0.25-M tetraisopropyl orthotitanate, 10-wt% F127, 0.055-M cetyltrimethylammonium bromide, 0.25-M ethylenediamine, and at 433 K. In the initial stage of reaction, X-ray diffraction spectra showed almost no clear peak, indicating the TiO_2 formed was amorphous. From 2 to 3.5 h, tiny and broad anatase peaks appeared, but the main structure of titania was still amorphous-like. During 3.5 to 4 h interval, a drastic change in the X-ray diffraction spectrum was detected, signifying the evolution from amorphous-like to clear anatase crystalline structure. From 4 to 24 h, X-ray diffraction spectra showed no appreciable changes.

In order to investigate the underlying process for the transition from amorphous-like structure to titania anatase crystalline structure in the early stage of the reaction, variations in shape and crystalline structure of reaction products upon calcination at 723 K for 2 h were utilized by Kurata et al. (2010). Fig. 4 shows the structural change from amorphous to anatase phase at 0.5 h after calcination, and the amorphous-like structure at 2 and 3.5 h also changing to anatase phase. At 4 h, the anatase crystalline structure was already formed before calcination. After 6 h, the X-ray diffraction patterns obtained before calcination almost completely coincided with those after calcination, indicating that crystalline structure before calcination did not change upon calcination owing to the highly crystallized state already achieved prior to calcination.

Transmission electron microscopy images of reaction products at reaction times of 0.5, 2, 3.5, 4, 6, and 24 h after calcination at 723 K for 2 h (Kurata et al., 2010) are shown in Fig. 5. Titania anatase nanoparticles with diameter around 10 nm were identifiable for the reaction products obtained at 0.5 h upon the calcination. While the product obtained at 1 h also changed to nanoparticles, the product obtained at 2 h changed to a mixture of nanoparticles and nanorods on the calcination. Similarly, a mixture of nanoparticles and nanorods were obtained for the product of 3.5 h upon the calcination. The fraction of rods at 3.5 h increased in comparison with that at 2 h. The nanorods formation could thus be claimed to be attributed to the growth of nuclei with anatase-like structure on the calcination. X-ray diffraction spectra before the calcination at 2 and 3.5 h were quite different from those of highly crystallized titania anatase at 6 and 24 h.
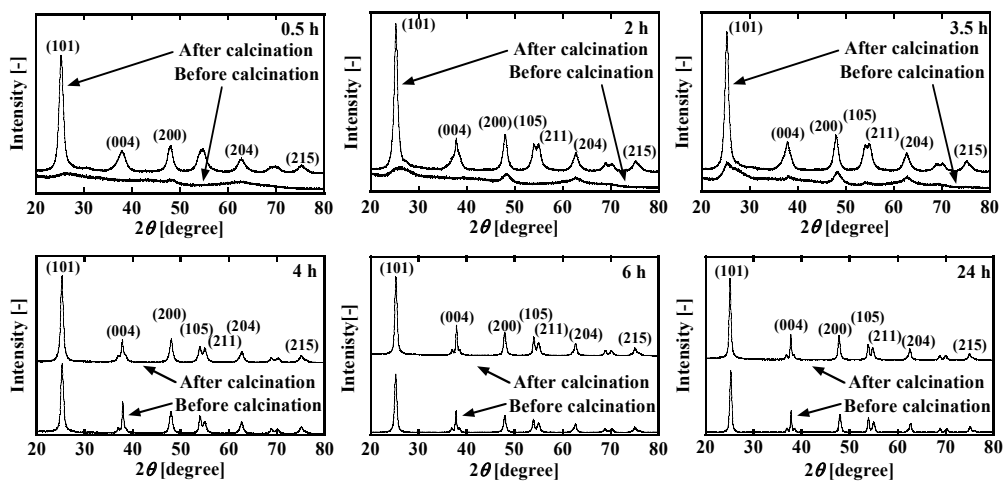
Fig. 4. Variation in X-ray diffraction patterns of reaction products upon calcination at 723 K for 2 h for the samples obtained at reaction times of 0.5, 2, 3.5, 4, 6, and 24 h.

The peak at 48.3 deg corresponding to (200) plane (2θ = 48.1 deg) in anatase phase was clearly observable and larger than those at 37.7 and 63 deg corresponding to (004) and (204) planes. Furthermore, no peak is observable at 38.6 deg, which corresponds to characteristic peak of (11) plane of Lepidocrocite (two-dimensional titania crystal). Therefore, the crystalline structure generated from film-like amorphous phase is inferred to be very thin two-dimensional anatase crystal.
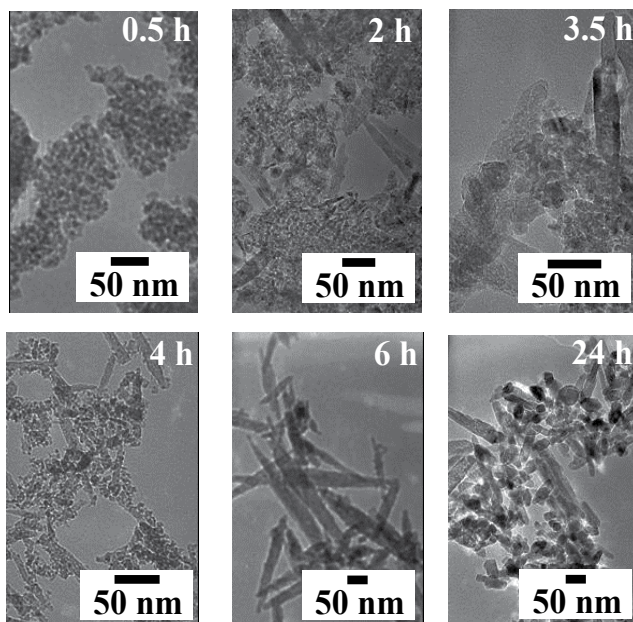
Fig. 5. Transmission electron microscopy images of reaction products obtained at 0.5, 2, 3.5, 4, 6, and 24 h after calcination at 723 K for 2 h.

The intensity ratio of (004) peak to (200) peak in X-ray diffraction spectra is shown in Fig. 6 as a function of the reaction time before and after calcination (Kurata et al., 2010). The almost zero ratio was obtained from 0.5 to 2 h in the absence of calcination, indicating that ordering of amorphous titania from random connection to crystal, evidenced partly in Fig. 2 and 3, occurred only in the film with no growth in the *c*-axis. The ratio, then, had increased progressively up to 0.38 at 3.5 h revealing slight growth in the *c*-axis, until the ratio attained a maximum rate of increase between 3.5 and 4 h duration, corresponding to the drastic change in the shape and crystalline structure of reaction products. Such an overwhelming increase in the intensity ratio (004)/(200) indicates that the phase transition from amorphous-like phase to anatase phase can bring about significant growth in the *c*-axis. The highest value was obtained at 4 h and slightly decreased with time, asymptotically approaching a constant of ~1.2 after 6 h. After calcination, the ratio gradually increased from 0.5 up to 6 h, and then reached a constant value, which was identical to the value obtained before calcination. These two distinctive trends shown in Fig. 6 signify that the crystalline structure of nanorods did not change on calcination, maintaining the intensity ratio at the same asymptotic level (~1.2) before and after calcination.
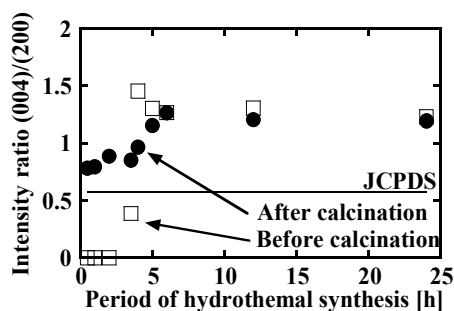
Fig. 6. Intensity ratio of (004) peak to (200) peak in X-ray diffraction spectra with reaction time under conditions before and after calcination.

3.2 Effects of ethylenediamine concentration and temperature change on the formation processes of nanorods

We investigated the effects of both ethylenediamine concentration and temperature change on the formation processes of nanorods. In particular, their mechanistic contributions to size and shape control of highly crystallized titania nanorods were inferred, together with the results of formation processes under standard condition mentioned above.
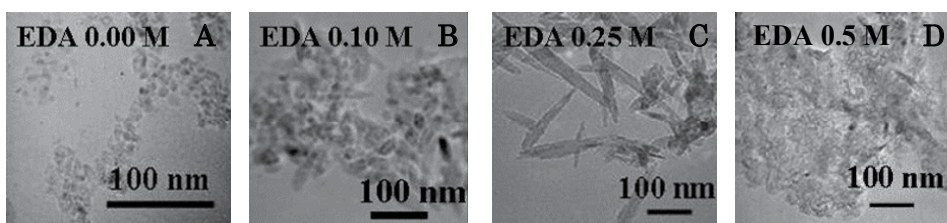
Fig. 7. Transmission electron microscopy images of reaction products synthesized at different ethylenediamine concentrations by hydrothermal method. Reaction conditions: 433 K, 6 h. "EDA" designates ethylenediamine.

Fig. 7 shows the effects of ethylenediamine concentration on the morphology of reaction products at 433 K for 6 h. When the ethylenediamine concentration was 0, titania particles with aspect ratio of roughly unity were formed. As the concentration was changed from 0 to 0.1 M, the morphology of titania shifted from particulate to a mixture of particles and rods. As the concentration reached 0.25 M (i.e., the value used under the standard condition, and thus as expected), only nanorods were observed to form, while at an ethylenediamine concentration as high as 0.5 M the observed products appeared to be unexpectedly film-like titanate. The corresponding X-ray diffraction spectra for the given series of samples are shown in Fig. 8. When the ethylenediamine concentration was 0 M, typical anatase peaks were obtained where (004) peak has a lower height than (200) peak, matching the spherical shape observed in Fig. 7A. When the ethylenediamine concentration was 0.25 M, a clear anatase spectrum was observed with higher (004) peak in comparison to (200) peak, signifying the formation of titania nanorods. For 0.1-M ethylenediamine concentration an intermediate spectrum between those of 0 and 0.25 M was observed due to the formation of particle-rod mixture as discussed above (see Fig. 7B). When the concentration became 0.5 M, a weak amorphous-like spectrum was obtained, corresponding to the observation of film-like structure in Fig. 7D. All these results signify that there should exist an optimum ethylenediamine concentration for controlling the rate of formation of titania nanorods at $\approx$ 0.25 M, above which - specifically at as high as 0.5 M - the reaction rate tends to slow down; that is, the morphological transition would be delayed. Such inference could be made by referring the morphology transformation as depicted in Fig. 2 under the standard condition with 0.25-M ethylenediamine.
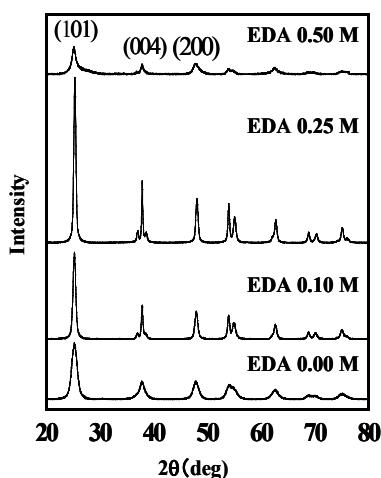
Fig. 8. X-ray diffraction spectra of the same samples shown in Fig. 7.

To further investigate the formation processes of titania nanorods at this high ethylenediamine concentration of 0.5 M, we carried out a series of experiments for evaluating the time course of the formation processes; the results are shown in Fig. 9. Film-like structure was observed up to 6 h as stated above; after 8 h, however, only rod shape was identifiable, signifying that the transformation from the amorphous film-like structure to the anatase titania nanorods has been almost completed by this time. Fig. 10 shows transmission electron microscopy and high-resolution transmission electron microscopy images of the

reaction product obtained at 45 h. Ordered alignment of titania atoms in anatase structure can be clearly perceived, indicating the formation of highly crystallized titania anatase nanorods.
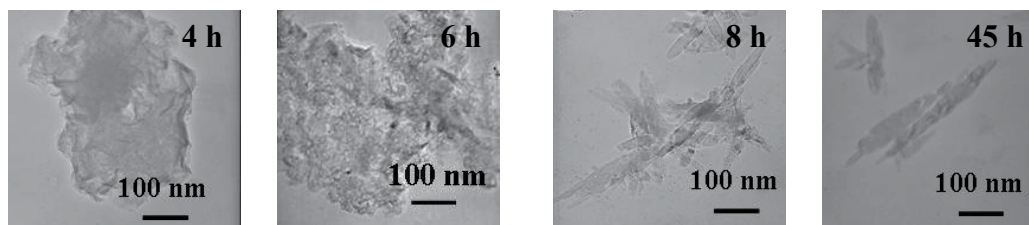
Fig. 9. Transmission electron microscopy images of reaction products obtained at different reaction times for 0.5-M ethylenediamine concentration. The rest of reaction conditions are the same as in the standard condition.

The effect of temperature change/reduction was examined by obtaining the time course of the formation processes at 413 K based on scanning electron microscopy images and X-ray diffraction measurements; the results are shown in Figs. 11 and 12, respectively. As shown in Fig. 11, the film-like structure was still observed at even 36 h. The X-ray diffraction spectrum obtained at 36 h shows no significant peaks, i.e., amorphous-like phase formation, which was observed under the standard condition at only up to 3.5 h (see Fig. 3a). Therefore, the reaction rate at 413 K became significantly slower. From scanning electron microscopy images, coexistence of titania nanorods and film was observed until 56 h, which was never recognized at the standard reaction temperature 433 K. It was after 64 h that only titania nanorods were finally observed. The scanning electron microscopy image obtained at 64 h shows a wide distribution in length of nanorods from roughly 10 to 600 nm, implying that nucleation and growth of nanorods would proceed concurrently because of the slow reaction rate at 413 K. The X-ray diffraction spectrum at 48 h, on the other hand, shows anatase peaks, though each peak height is not high. The peak height increases gradually with time up to 64 h. This observation suggests again the coexistence of amorphous-like films and titania nanorods. The peak height becomes higher with an increase in the fraction of titania nanorods up to 64 h.
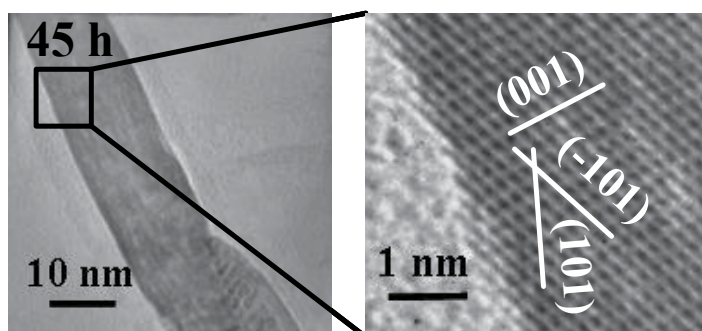
Fig. 10. Transmission electron microscopy and high-resolution transmission electron microscopy images of reaction product obtained at 45 h under 0.5-M ethylenediamine.
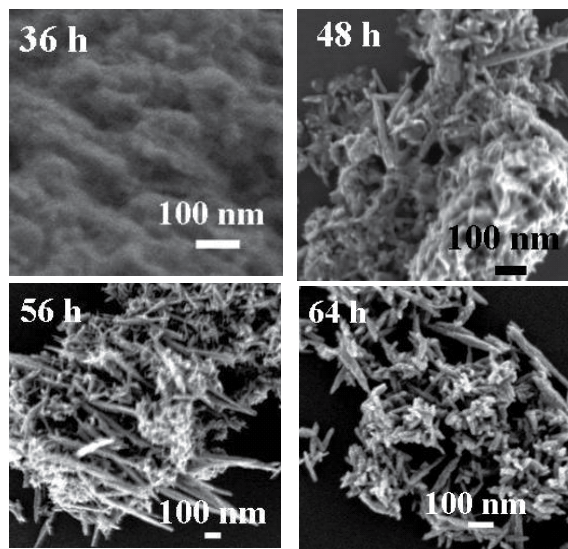
Fig. 11. Scanning electron microscopy images of reaction products obtained under the condition of 413 K at various times.
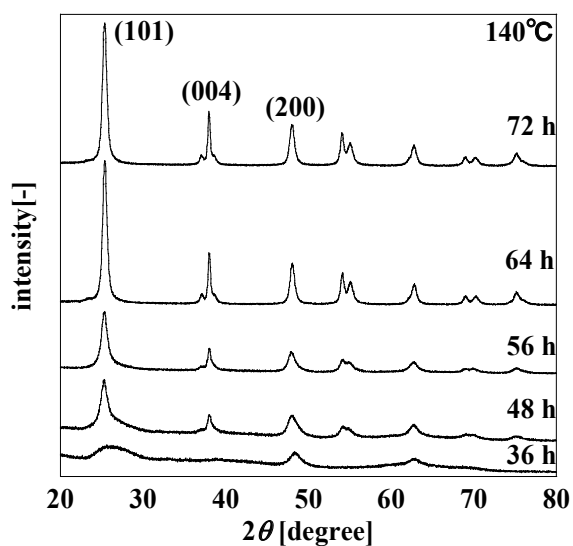
Fig. 12. X-ray diffraction patterns of the same reaction products of Fig. 11.

The observations and measurements made on temperature change described above are summarized in Fig. 13. At 413 K, the reaction is slow, resulting in concurrence of nucleation and growth of nanorods. At 433 K, on the other hand, the reaction occurs rapidly, resulting in 1) the prevalence of nucleation almost exclusively in the amorphous phase in the early reaction stage, 2) a drastic change from amorphous phase to crystalline titania anatase nanorods, and 3) no concurrence of nucleation and growth of nanorods. These findings should give some hints for the strategy for size and shape control.
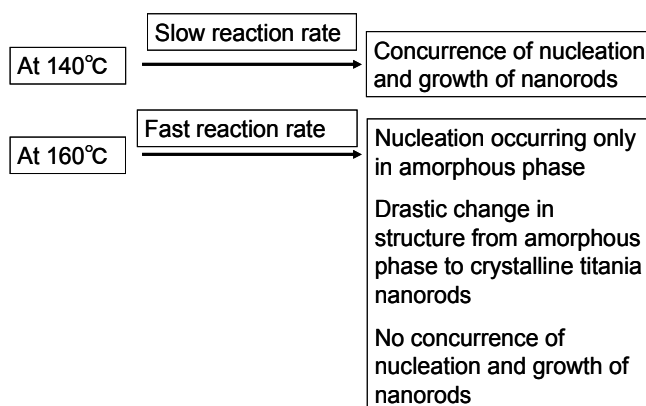
Fig. 13. Effects of reaction temperature on characteristics of formation processes at 413 K and 433 K.

3.3 Strategy for shape and size control of highly crystallized titania nanorods

The proposed strategy is given in Fig. 14. Nuclei are to be generated at a higher temperature 433 K in the early stage of reaction. These nuclei formed coincidently are to be reacted at a reduced temperature 413 K under hydrothermal conditions without further nucleation. Then, growth of rather uniform-sized and shaped nanorods is expected, in the aid of high concentration of ethylenediamine in effectively reducing their nucleation rate. In addition, we can also use the effectiveness of acetylacetone in obtaining good dispersion of nanorods (to be discussed later).
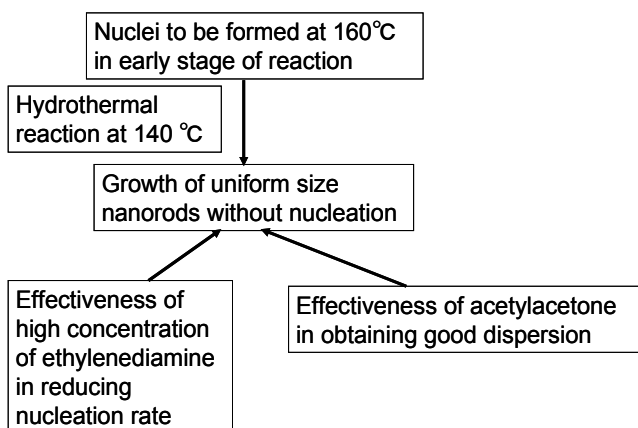
Fig. 14. Strategy for size and shape control of titania nanorods.

The specific preparation procedures are as follows. The even formation of nuclei was attempted at 433 K under the standard condition via the hydrothermal reaction for 2 h before being cooled down to room temperature. Ethylenediamine was then added to have

its concentration be 0.5 M for selectively reducing nucleation rate. Formation reaction with these precursory nuclei was successively carried out at 413 K under the hydrothermal condition for 52 h; the reaction conditions are in the following: 0.25-M tetraisopropyl orthotitanate, 10-wt% F127, 0.055-M cetyltrimethylammonium bromide and 0.5-M ethylenediamine. A transmission electron microscopy image of thus obtained nanorods is shown in Fig. 15. Over 800-nm long, high-aspect-ratio nanorods were indeed obtained. In comparison to the nanorods images for 433 K at 24 h shown in Fig. 2 and those for 413 K at 64 h in Fig. 11, the nanorods obtained based on the proposed shape-control strategy were certainly improved in terms of morphological uniformity, despite the presence of some shorter nanorods, which stems from the not completely avoidable occurrence of nucleation during the formation reaction.
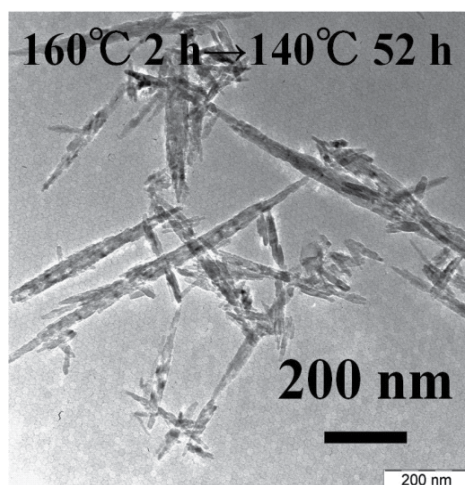
Fig. 15. Transmission elecron microscopy image of shape-controlled nanorods prepared based on the strategy given in Fig. 14.

3.4 Highly dispersed titania nanorods obtained with the help of acetylacetone

The effect of addition of acetylacetone was examined separately. In the experiments the same moles of acetylacetone and tetraisopropyl orthotitanate were mixed with each other to make a 1:1 complex. The complex was added to an aqueous solution of 10-wt% F127 containing 0.3-0.5 M ethylenediamine but no cetyltrimethylammonium bromide. The solution was stirred for one week at room temperature. The solution became transparent after 1-week stirring, which was never observed in the absence of acetylacetone. Adding acetylacetone thus must have a critical effect on particle dispersion. An example of nanorods thus obtained is shown in Fig. 16 (top) under the condition of 0.3-M ethylenediamine. Very good dispersion of titania nanorods was attained, and highly crystallized state is obvious as demonstrated in the high-resolution image in Fig. 16 (bottom). Since acetylacetone is known to adsorb on the surface of titania anatase crystal (Connor et al., 1995), adsorbed acetylacetone molecules could prevent aggregation of titania nanorods, resulting in such good dispersion. Also, since acetylacetone is expected to affect the formation mechanism, utilization of acetylacetone might improve the shape-control scheme of nanorods.
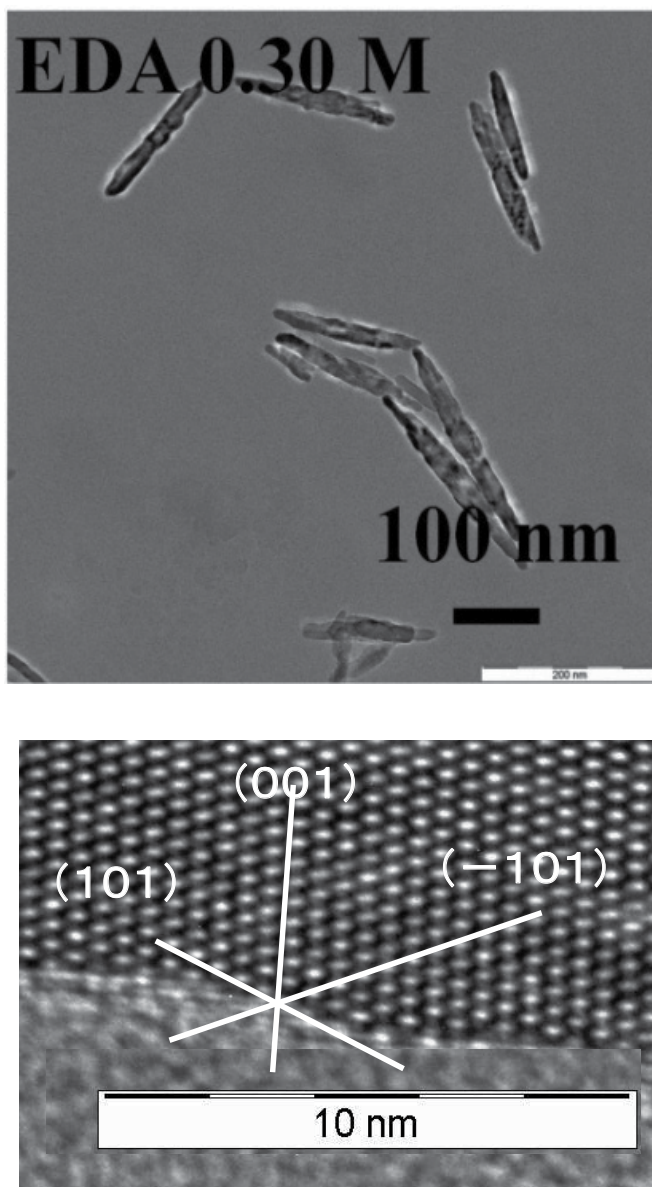
Fig. 16. Highly dispersed titania nanorods obtained with the help of acetylacetone (top) and highly crystallized feature of the nanorods demonstrated by high-resolution transmission electron microscpy image (bottom).

3.5 Application for dye-sensitized solar cells

The application of highly crystallized titania nanorods for making dye-sensitized solar cells was already reported (Yoshida et al., 2008; Kurata et al., 2010). A titania electrode made of titania nanorods was successfully fabricated as follows. The complex electrodes were

prepared by the repetitive coating-calcining process: 3 layers of titania nanoparticles (Jiu et al., 2004, 2007) were first coated on FTO conducting glass, followed by 7 layers of mixed gel composed of titania nanorods and P-25. High light-to-electricity conversion efficiencies of 8.52 to 8.93% were achieved as exemplified in Fig. 17. We are now trying to get much higher power conversion efficiency by utilizing the shape-controlled, highly crystallized titania nanorods with high dispersion as a titania electrode of dye-sensitized solar cells.

J_{sc}=14.7 mA/cm^2
V_{oc}=0.771 V
FF=0.750
Efficiency=8.52 %
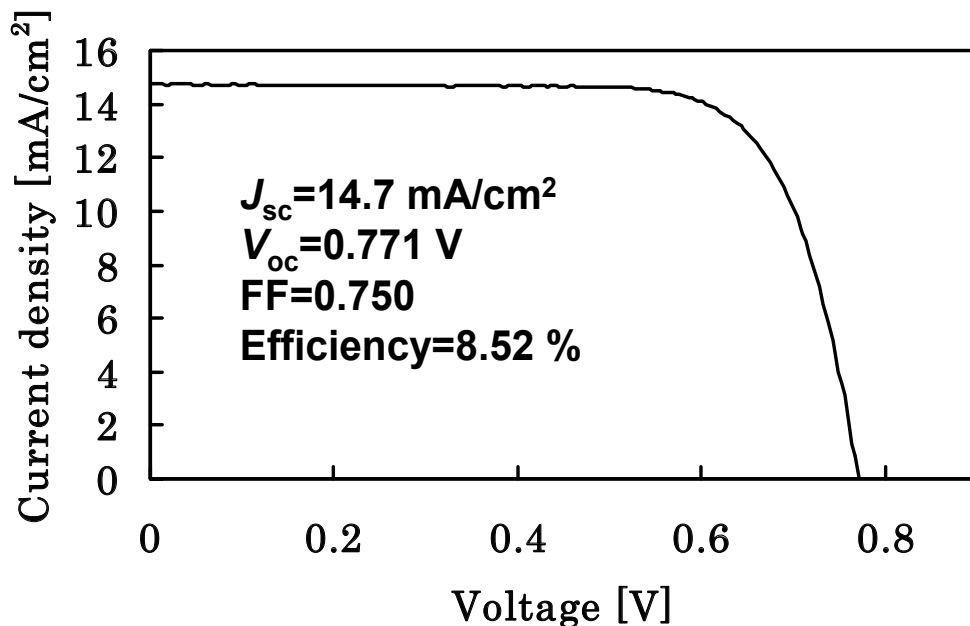
Fig. 17. I-V curve for complex dye-sensitized solar cell electrode consisting of highly crystallized titania nanorods, P-25, and titania nanoparticles.

4. Conclusions

The formation processes of highly crystallized titania nanorods were revealed in detail under 10-wt% F127, 0.25-M tetraisopropyl orthotitanate, 0.055-M cetyltrimethylammonium bromide, 0.25-M ethylenediamine, and 433 K (standard) conditions.

Strategy for shape and size control of highly crystallized titania nanorods was proposed through the findings obtained by examining the effects of both ethylenediamine concentration and temperature change on the formation processes of titania nanorods. Over 800-nm long and high-aspect-ratio, highly crystallized titania nanorods were successfully synthesized following the proposed strategy.

5. References

Adachi, M. Jiu, J. & Isoda, S. (2007). Synthesis of morphology-controlled titania nanocrystals and application for dye-sensitized solar cells. *Current Nanoscience*, 3, pp. 285-295

Adachi, M. Jiu, J. Isoda, S. Mori, Y. & Uchida, F. (2008). Self-assembled nanoscale architecture of TiO_2 and application for dye-sensitized solar cells. *Nanotechnology. Science and Applications*, 1, pp. 1-7

Adachi, M. Murata, Y. Takao, J. Jiu, J. Sakamoto, M. & Wang, F. (2004). Highly efficient dye-sensitized solar cells with titania thin film electrode composed of network structure of single-crystal-like TiO_2 nanowires made by "Oriented Attachment" mechanism. *J. Am. Chem. Soc.*, 126, pp. 14943-14949

Adachi, M. Sakamoto, M. Jiu, J. Ogata, Y. & Isoda, S. (2006). Determination of parameters of electron transport in dye-sensitized solar cells using electrochemical impedance spectroscopy. *J. Phys. Chem. B* 110, pp. 13872-13880

Alivisatos, A. P. (1996a). Semiconductor Clusters, Nanocrystals, and Quantum Dots. *Science*, 271, pp. 933-937

Alivisatos, A. P. (1996b). Perspectives on the physical chemistry of semiconductor nanocrystals. *J. Phys. Chem.*, 100, pp. 13226-13239

Banfield, J. F. Welch, S. A. Zhang, H. Ebert, T. T. & Penn, R. L. (2000). Aggregation-based crystal growth and microstructure development in natural iron oxyhydroxide biomineralization products. *Science*, 289, pp. 751-754

Burda, C. Chen, X. Narayanan, R. & El-Sayed, M. A. (2005). Chemistry and properties of nanocrystals of different shapes. *Chem. Rev.*, 105, pp. 1025-1102

Cao Y. C. (2004) Synthesis of square gadolinium-oxide nanoplates. *J. Am. Chem. Soc.*, 126, pp. 7456-7457

Cheng, B. Rusell, J. M. Shi, W. Zhang, L. & Samulski, E. T. (2004). Large-scale, solution-phase growth of single-crystalline SnO_2 nanorods. *J. Am. Chem. Soc.*, 126, pp. 5972-5973

Connor, P. A.. Dobson, K. D & McQuillan: A. J. (1995). New sol-gel attenuated total reflection infrared spectroscopic method for analysis of adsorption at metal oxide surface in aqueous solution. Chelation of $TiO2$, $ZrO2$, and $Al2O3$ surfaces by catechol, 8-quinolinol, and acetylacetopne. *Langmuir*, 11, pp. 4193-4195

Cui, Y. Bjork, M. T. Liddle, J. A. Sonnichsen, C. Boussert, B. & Alivisatos, A. P. (2004). Integration of colloidal nanocrystals into lithographically patterned devices. *Nano Lett.*, 4, pp. 1093-1098

Empedocles, S. A. Neuhauser, R. Shimizu, K. & Bawendi, M. G. (1999). Photoluminescence from single semiconductor nanostructures. *Adv. Mater.*, 11, pp. 1243-1256

Fabregat-Santiago, F. Bisquert, J. Palomares, E. Kuang, D. Zakeeruddin, S. M. & Grätzel, M. (2007). Correlation between photovoltaic performance and impedance spectroscopy of dye-sensitized solar cells based on ionic liquid: *J. Phys. Chem. C*, 111, pp. 6550-6560

Fujishima, A. & Honda, K. (1972). Electrochemical photolysis of water at a semiconductor electrode. *Nature*, 238, pp. 37-38

Fujishima, A. Rao, T. N. & Tryk, D. A. (2000). Titanium dioxide photocatalysis. *J. Photpchem. Photobio. C*, 1, pp. 1-21

Fukuda, K. Ebina, Y. Shibata, T. Aizawa, T. Nakai, I. & Sasaki, T. (2007) Unusual crystallization behaviors of anatase nanocrystallites from a molecularly thin titania

nanosheet and its stacked forms: Increase in nucleation temperature and oriented growth. *J. Am. Chem. Soc.*, 129, pp. 202-209.

Garcia, R. & Tello, R. (2004). Size and shape controlled growth of molecular nano-structures on silicon oxide templates. *Nano Lett.*, 4, pp. 1115-1119

Grätzel, M. (2000). Photovoltaic performance and long-term stability of dye-sensitized meosocopic solar cells. *C. R. Chemie.*, 9, pp. 578-583

Grätzel, M. (2001). Photoelectrochemical cells. *Nature*, 414, pp. 338-344

Grätzel, M. (2004). Conversion of sunlight to electric power by nanocrystalline dye-sensitized solar cells. *J. Photpchem. Photobio. A: Chemistry*, 164, pp. 3-14

Grätzel, M. (2005). Solar Energy Conversion by Dye-Sensitized Photovoltaic Cells. *Inorg. Chem.*, 44, pp. 6841-6851

Hagfeldt, A. & Grätzel, M. (2000). Molecular photovoltaics. *Acc. Chem. Res.*, 33, pp. 269-277

Jiu, J. Isoda, S. Adachi, M. & Wang, F. (2007). Preparation of TiO2 nanocrystalline with 3-5 nm and application for dye-sensitized solar cell. *J. Photochem. Photobio. A: Cemistry*, 189, pp. 314-321

Jiu, J. Isoda, S. Wang, F. & Adachi, M. (2006). Dye-sensitized solar cells based on a single-crystalline TiO2 nanorod film. *J. Phys. Chem. B*, 110, pp. 2087-2092

Jiu, J. Wang, F. Sakamoto, M. Takao, J. & Adachi, M. (2004). Preparation of nanocrystaline TiO_2 with mixed template and its application for dye-sensitized solar cells. *J. Electrochem. Soc.,* 151, pp. A1653-A1658

Kurata, T. Mori, Y. Isoda, S. Jiu, J. Tsuchiya, K. Uchida, F. & Adachi, M. (2010). Characterization and formation process of highly crystallized single crystalline TiO_2 nanorods for dye-sensitized solar cells. *Current Nanoscience*, 6, pp. 269-276

Lakshmi, B. B. Dorhout, P. K. & Martin, C. R. (1997a). Sol-gel template synthesis of semiconductor nanostructures. *Chem. Mater.*, 9, pp. 857-862

Lakshmi, B. B. Dorhout, P. K. & Martin, C. R. (1997b). Sol-gel template synthesis of semiconductor oxide micro- and nanostructures. *Chem. Mater.*, 9, pp. 2544-2550

Liu, C. Wu, X. Klemmer, T. Shukla, N. Yang, X. Weller, D. Roy, A. G. Tanase, M.& Laughlin, D. (2004). Polyol process synthesis of monodispersed fept nanoparticles. *J. Phys. Chem. B*, 108, pp. 6121-6123

Manna, L. Scher, E. C. & Alivisatos, A. P. (2000). Synthesis of soluble and processable rod-, arrow-, teardrop-, and tetrapod-shaped CdSe nanocrystals. *J. Am. Chem. Soc.*, 122, pp. 12700-12706

Masuda, H. & Fukuda, K. (1995). Ordered Metal nanohole arrays made by a two-step replication of honeycomb structures of anodic alumina. *Science*. 268, pp. 1466-1468

Masuda, H. Yamada, H. Satoh, M. Asoh, H. Nakao, M. & Tamamura, T. (1997) Highly ordered nanochannel-array architecture in anodic alumina. *Appl. Phys. Lett.*, 71, pp. 2770-2772

Murray, C. B. Kagan, C. R. & Bawendi, M. G. (2000). Synthesis and characterization of monodisperse nanocrystals and close-packed nanocryatal assemblies. *Annu. Rev. Mater. Sci.*, 30, pp. 545-610

Nazeeruddin, M. K. De Angelis, F. Fantacci, S. Selloni, A. Viscardi, G. Liska, P. Ito, S. Bessho, T. & Graetzel, M. (2005) Combined experimental and DFT-TDDFT computational

study of photoelectrochemical cell ruthenium sensitizers. *J. Am. Chem. Soc.*, 127, pp. 16835-16847

Nirmal, M. & Brus, L. (1999). Luminescence photophysics in semiconductor nanocrystals. *Acc. Chem. Res.*, 32, pp. 407-414

Pacholski, C. Kornowski, A. & Weller, H. (2002). Self-assembly of ZnO: From nanodots to nanorods. *Angew. Chem. Int. Ed.*,. 41, pp. 1188-1191

Pei, L. Mori, K. & Adachi, M. (2004). Formation process of two-dimensional networked gold nanowires by citrate reduction of $AuCl_4^-$ and the shape stabilization. *Langmuir*, 20, pp. 7837-7843

Peng, X. (2003) Mechanisms for the shape-control and shape-evolution of colloidal semiconductor nanocrystals. *Adv. Mater.*, 15, pp. 459-463

Peng, X. G. Manna, L. Yang, W. D. Wickham, J. Scher, E. Kadavanich, A. & Alivisatos, A. P. (2000). Shape control of CdSe nanocrystals. *Nature*, 404, pp. 59-61

Penn, R. L. & Banfield, J. F. (1998). Morphology development and crystal growth in nanocrystalline aggregates under hydrothermal conditions: insights from titania. *Science*, 281, pp. 969-971

Puntes, V. F. Krishnan, K. M. & Alivisatos, A. P. (2001). Colloidal nanocrystal shape and size control: The case of cobalt. *Science*, 291, pp. 2115-2117

Reiss, B. D. Mao, C. Solis, D. J. Ryan, K. S. Thomson, T. & Belcher. (2004). A. M. Biological routes to metal alloy ferromagnetic nanostructures. *Nano Lett.*, 4, pp. 1127-1132

Scher, E. C. Soc, R. Manna, L.& Alivisatos, A. P. (2003). Shape control and applications of nanocrystals. *Phil. Trans. R. Soc.* Lond. A, 361, pp. 241-257

Song, Q. & Zhang, Z. J. Shape control and associated magnetic properties of spinel cobalt ferrite nanocrystals, J. (2004). *Am. Chem. Soc.*, 126, pp. 6164-6168

Sugimoto, T. Zhou, X. & Muramatsu, A. (2003). Synthesis of uniform anatase TiO_2 nanoparticles by gel–sol method 4. Shape control. *J. Colloid Interface Sci.*, 259, pp. 53-61

Tang, Z. Kotov, N. A. & Giersig. M. (2002). Spontaneous Organization of single CdTe nanoparticles into luminescent nanowires. *Science*, 297, pp. 237-240

Tang, Z. Ozturk, B. Wang, Y. & Kotov. N. A. (2004). Simple preparation strategy and one-dimensional energy transfer in CdTe nanoparticle chains. *J. Phys. Chem. B*, 108, pp. 6927-6931

Wu, G. Zhang, L. Cheng, B. Xie, T. & Yuan, X. (2004). Synthesis of Eu_2O_3 nanotube arrays through a facile sol-gel template approach. *J. Am. Chem. Soc.*, 126, pp. 5976-5977

Yang, D. Wang, R. Zhang, J. & Liu, Z. (2004). Synthesis of nickel hydroxide nanoribbons with a new phase: A solution chemistry approach. *J. Phys. Chem. B,* 108, pp. 7531-7533

Yoshida, K. Jiu, J. Nagamatsu, D. Nemoto, T. Kurata, H. Adachi, M. & Isoda, S. (2008). Structure of TiO2 Nanorods formed with doiuble surfactants, *Molecular crystals and liquid crystals.* 491, pp. 14-20

Yu, W. W. Wang, Y. A. & Peng, X. (2003). Formation and stability of size-, shape-, and structure-controlled cdte nanocrystals: Ligand effects on monomers and nanocrystals. *Chem. Mater.*, 15, pp. 4300-4308

Zhang, H. Sun, J. Ma, D. Bao, X. Klein-Hoffmann, A. Weinberg, G. Su, D. & Schlogl, R. (2004). Unusual mesoporous SBA-15 with Parallel channels running along the short axis. *J. Am. Chem. Soc.*, 126, pp. 7440-7441

Dye-Sensitized Solar Cells Based on Polymer Electrolytes

Mi-Ra Kim, Sung-Hae Park, Ji-Un Kim and Jin-Kook Lee
Department of Polymer Science & Engineering, Pusan National University,
Jangjeon-dong, Guemjeong-gu, Busan,
South Korea

1. Introduction

Dye-sensitized solar cells (DSSCs) using organic liquid electrolytes have received significant attention because of their low production cost, simple structure and high power conversion efficiency [1-5]. Recently, the power conversion efficiencies of DSSCs using Ruthenium complex dyes, liquid electrolytes, and Pt counter electrode have reached 10.4 % (100 mW/cm², AM 1.5) by Grätzel group [6]. However, the important drawback of DSSCs using liquid electrolyte is the less long-term stability due to the volatility of the electrolyte contained organic solvent. In the viewpoint for commercialize, durability is a crucial component. Then, gel electrolytes are being investigated to substitute the liquid electrolytes [7-10]. One way to make a gel electrolyte is to add organic or inorganic (or both) materials. In the past decades, many studies have been carried out on this kind of gel electrolyte, and great progress has been achieved [11-12]. The advantages of them include; limited internal shorting, leakage of electrolytes and non-combustible reaction products at the electrode surface existing in the gel polymer electrolytes [13-14]. However, because of their complicated preparing technology and poor mechanical strength, they cannot be used in commercial production [15-16]. To overcome this problem, the polymer membrane is soaked in an electrolyte solution that has been examined [17-19].

To prepare the polymer membrane for polymer electrolyte, a number of processing techniques such as drawing [20], template synthesis [21-22], phase separation [23], electrospinning [24], etc. have been used. Among of these, the electrospinning technology is a simple and low-cost method for making ultra-thin diameter fibers. This technique, invented in 1934, makes use of an electrical field that is applied across a polymer solution and a collector, to force a polymer solution jet out from a small hole [25]. When the diameters of polymer fiber materials are shrunk of micrometers to submicrons or nanometers, several amazing characteristics appear such as a very large surface area to volume ratio, flexibility in surface functionalities, and superior mechanical performance compared to any other known forms of this material [26]. In recent years, the electrospinning method has gained greater attention. A vastly greater number of synthetic and natural polymer solutions were prepared with electrospun fibers, such as poly(ethylene oxide) (PEO) in distilled water [27], polyurethane in N,N-dimethylformamide (DMF) [28], poly(ε-caprolactone) (PCL) in acetone [29], PVDF in acetone/ N,N-dimethylacetamide (DMAc) (7:3 by weight) [30], and regenerated cellulose in 2:1(w/w) acetone/DMAc [31].

Many applications of electrospun fibers were also studied. In addition, this technique is highly versatile and allows the processing of not only many different polymers into polymeric nanofibers, but also the co-processing of polymer mixtures, mixtures of polymers, and low molecular weight nonvolatile materials, etc [13,32].

2. Principle

2.1 Dye-sensitized solar cells (DSSCs)
2.1.1 History of DSSCs

The history of the sensitization of semiconductors to light of wavelength longer than that corresponding to the band gap has been presented elsewhere [33,34]. It is an interesting convergence of photography and photo-electrochemistry, both of which rely on photo-induced charge separation at a liquid–solid interface. The silver halides used in photography have band gaps of the order of 2.7–3.2 eV, and are therefore insensitive to much of the visible spectrum, just as is the TiO_2 now used in these photo-electrochemical devices.

The material has many advantages for sensitized photochemistry and photo-electrochemistry: it is a low cost, widely available, non-toxic and biocompatible material, and as such is even used in health care products as well as domestic applications such as paint pigmentation. The standard dye at the time was *tris*(2,2′-bipyridyl-4,4′-carboxylate) ruthenium(II), the function of the carboxylate being the attachment by chemisorption of the chromophore to the oxide substrate. Progress thereafter, until the announcement in 1991 of the sensitized electrochemical photovoltaic device with a conversion efficiency at that time of 7.1% under solar illumination, was incremental, a synergy of structure, substrate roughness and morphology, dye photophysics [35] and electrolyte redox chemistry. That evolution has continued progressively since then, with certified efficiency now over 10%.

2.1.2 Structure and working principles of DSSCs

The DSSC consists of the following staffs (Fig. 1). (1) transparent conductive oxide glass (F-doped SnO_2 glass (FTO glass), (2) Nanoporous TiO_2 layers (diameter ; 15-20 nm), (3) dye monolayer bonded to TiO_2 nano-particles, (4) electrolytes consisting of I^- and I_3^- redox species, (5) platinum, (6) a counter electrode.

A schematic presentation of the operating principles of the DSSC is given in Fig. 2. At the heart of the system is a mesoscopic oxide semiconductor film, which is placed in contact with a redox electrolyte or an organic hole conductor. The choice of material has been TiO_2 (anatase) although alternative wide hand gap oxides such as ZnO, and Nb_2O_5 have also been investigated. Attached to the surface of the nanocrystalline film is a monolayer of the sensitizer. Photo-excitation of the latter results in the injection of an electron into the conduction band of the oxide. The dye is regenerated by electron donation from the electrolyte, usually an organic solvent containing a redox system, such as the iodide/ triiodide couple. The regeneration of the sensitizer by iodide intercepts the recapture of the reduction of the conduction band electron by the oxidized dye. The iodide is regenerated in turn by triiodide at the counter electrode when the circuit is completed via electron migration through the external load.
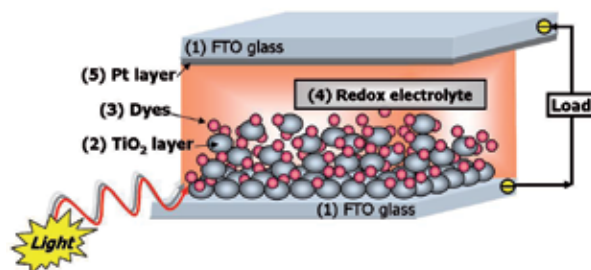
Fig. 1. A schematic presentation of a cross-section structure of the DSSC.
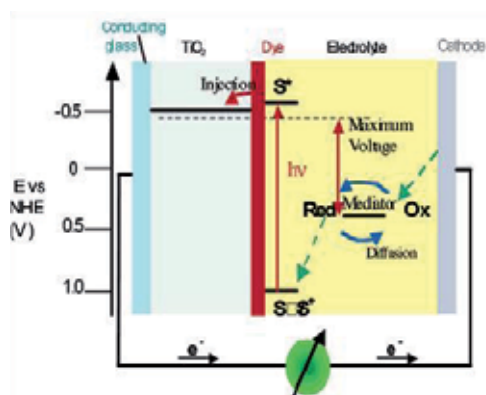
Fig. 2. A schematic presentation of the operating principles of the DSSC.

$$TiO_2/S + h\nu \rightarrow TiO_2/S^* \tag{I}$$

$$TiO_2/S^* \rightarrow TiO_2/S^+ + e_{cb} \tag{II}$$

$$TiO_2/S^+ + e_{cb} \rightarrow TiO_2/S \tag{III}$$

$$TiO_2/S^+ + (3/2)I^- \rightarrow TiO_2/S + (1/2)I_3^- \tag{IV}$$

$$(1/2)I_3^- + e_{(pt)} \rightarrow (3/2)I^-, \; I_3^- + 2e_{cb} \rightarrow 3I^- \tag{V}$$
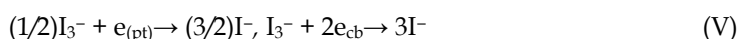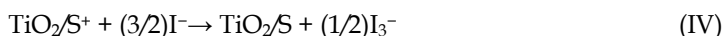
Light absorption is performed by a monolayer of dye (S) adsorbed chemically at the semiconductor surface and excited by a photon of light (Eq. (I)). After having been excited (S*) by a photon of light, the dye-usually a transition metal complex whose molecular properties are specifically for the task is able to transfer an electron to the semiconductor (TiO₂) by the injection process (Eq. (II)). The efficiency of a DSSC in the process for energy conversion depends on the relative energy levels and the kinetics of electron transfer processes at the liquid junction of the sensitized semiconductor/electrolyte interface. For efficient operation of the cell, the rate of electron injection must be faster than the decay of the dye excited state. Also, the rate of rereduction of the oxidized dye (dye cation) by the electron donor in the electrolyte (Eq. (IV)) must be higher than the rate of back reaction of the injected electrons with the dye cation (Eq. (III)), as well as the rate of reaction of injected electrons with the electron acceptor in the electrolyte (Eq. (V)). Finally, the kinetics of the reaction at the counter electrode must also guarantee the fast regeneration of charge mediator (Eq. (V)), or this reaction could also become rate limiting in the overall cell performance [36-39].

2.1.3 Present DSSC research and development

2.1.3.1 Sensitizer (Dye)

The ideal sensitizer for a single junction photovoltaic cell converting standard global AM 1.5 sunlight to electricity should absorb all light below a threshold wavelength of about 920 nm. In addition, it must also carry attachment groups such as carboxylate or phosphonate to firmly graft it to the semiconductor oxide surface. Upon excitation it should inject electrons into the solid with a quantum yield of unity. The energy level of the excited state should be well matched to the lower bound of the conduction band of the oxide to minimize energetic losses during the electron transfer reaction.

Its redox potential should be sufficiently high that it can be regenerated via electron donation from the redox electrolyte or the hole conductor. Finally, it should be stable enough to sustain about 108 turnover cycles corresponding to about 20 years of exposure to natural light.
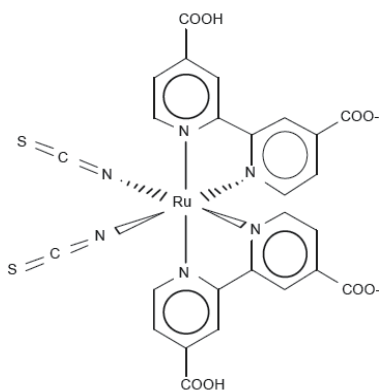
Fig. 3. Chemical structure of the N3 ruthenium complex used as a charge transfer sensitizer in DSSCs.

The best photovoltaic performance both in terms of conversion yield and long-term stability has so far been achieved with polypyridyl complexes of ruthenium and osmium. Sensitizers having the general structure $ML_2(X)_2$, where L stands for 2,2′-bipyridyl-4,4′-dicarboxylic acid M is Ru or Os and X presents a halide, cyanide, thiocyanate, acetyl acetonate, thiacarbamate or water substituent, are particularly promising. Thus, the ruthenium complex *cis*-$RuL_2(NCS)_2$, known as N3 dye, shown in Fig. 3 has become the paradigm of heterogeneous charge transfer sensitizer for mesoporous solar cells.

2.1.3.2 Mesoporous oxide film development

When the dye-sensitized nanocrystalline solar cell was first presented, perhaps the most puzzling phenomenon was the highly efficient charge transport through the nanocrystalline TiO_2 layer. The mesoporous electrodes are very much different compared to their compact analogs because (i) the inherent conductivity of the film is very low; (ii) the small size of the nanocrystalline particles does not support a built-in electrical field; and (iii) the electrolyte penetrates the porous film all the way to the back-contact making the semiconductor/electrolyte interface essentially three-dimensional. Charge transport in mesoporous systems is under keen debate today and several interpretations based on the Montrol Scher model for random displacement of charge carriers in disordered solids [40]

have been advanced. However, the "effective" electron diffusion coefficient is expected to depend on a number of factors such as trap filling and space charge compensation by ionic motion in the electrolyte. Therefore, the theoretical and experimental effort will continue as there is a need for further in depth analysis of this intriguing charge percolation process. The factors controlling the rate of charge carriers percolation across the nanocrystalline film are presently under intense scrutiny. Intensity modulated impedance spectroscopy has proved to be an elegant and powerful tool [41,42] to address important questions related to the characteristic time constants for charge carrier transport and reaction dynamics in DSSCs. On the material science side, future research will be directed towards synthesizing structures with a higher degree of order than the random fractal-like assembly of nanoparticles shown in Fig. 4. A desirable morphology of the films would have the mesoporous channels or nanorods aligned in parallel to each other and vertically with respect to the transparent conducting oxide (TCO) glass current collector. This would facilitate pore diffusion, give easier access to the film surface avid grain boundaries and allow the junction to be formed under better control.
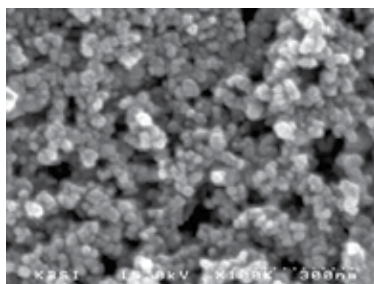
Fig. 4. Scanning electron micrograph of a sintered mesoscopic TiO_2 film supported on an FTO glass. The average particle size is 20 nm.

One approach to fabricate such oxide structures is based on surfactant templates assisted preparation of TiO_2 nanotubes as described in recent paper by Adachi et al. [43]. The hybrid nanorod-polymer composite cells developed by Huynh et al. [44] have confirmed the superior photovoltaic performance of such films with regards to random particle networks.

2.1.3.3 Polymer electrolytes

The polymer-based material is generally produced in a thin-film configuration by casting or spin-coating techniques. Polymer electrolytes are composed by alkaline salts (e.g. lithium or sodium salts) dissolved in a high molar mass polyether host (e.g. poly(ethylene oxide) (PEO) or poly(propylene oxide) (PPO)) [45]. In polymer electrolytes, the polymer matrix should be an efficient solvent for the salt, capable of dissociating it and minimizing the formation of ion pairs. The solubility of the salt relies on the ability of the electron donor atoms in the polymer chain to coordinate the cation through a Lewis type acid–base interaction. This interaction also depends on the lattice energy of the salt and the structure of the host polymer. The mechanism for ionic motion in polymer electrolytes results from a solvation–desolvation process along the chains that occurs predominantly in the amorphous polymer phase. Since the ionic motion is strictly correlated with the segmental motion of the polymer chains, the ionic conductivity increases with increasing chain mobility. The ionic conductivity is also a function of the number of charge carriers in the polymer matrix. However, above a limiting high salt concentration the segmental motion of the polymer chains is reduced due to an "ionic cross-linking" which decreases ionic conductivity [46].

2.1.4 Characteristics of DSSCs

There are several factors for characterization of DSSCs below; (See Fig. 5).

2.1.4.1 Incident photon-to current efficiency (IPCE)

The Incident Photon-to-Current Efficiency (IPCE), also called external quantum efficiency, is defined as the number of electrons generated by light in the external circuit divided by the number of incident photons as a function of excitation wavelength. It is expressed in Eq. (1) [47]. A high IPCE is a prerequisite for high-power photovoltaic applications, which depends on the sensitizer photon absorption, excited state electron injection. And electrons transport to the terminals.

$$IPCE = [(1.25 \times 10^3) \times \text{photocurrent density}(mAcm^{-2})] \times [\text{Wavelength}(nm) \times \text{photon flux } (Wm^{-2})]^{-1} \quad (1)$$

2.1.4.2 Open-circuit voltage (V_{oc})

If there is no external circuit, the incoming photons will still create hole-electron pairs and they will still travel downhill to the layers, but they will pile up there because there is no external wire. The number of carriers leaking back is equal to the number being generated by the incoming light, an equilibrium voltage has been reached. This is called the open-circuit voltage (V_{oc}). In DSSCs, V_{oc} is defined by the difference between Fermi level of TiO_2 and redox potential of electrolyte [10].
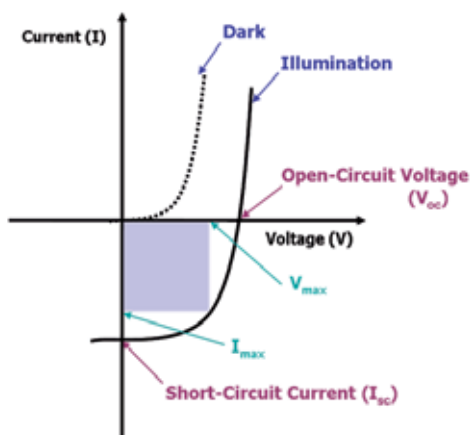
Fig. 5. Several factors for characterization of DSSC.

2.1.4.3 Short-circuit current (I_{sc}) and Short-circuit current density (J_{sc})

If the external circuit is simply a wire and has no appreciable resistance, the current that flows is the short-circuit current (I_{sc}) and is directly related to the number of photons of light being absorbed by the cell. Short-circuit current density (J_{sc}) is short-circuit current per active area.

2.1.4.4 Fill factor (FF)

The fill factor (FF) is obtained by diving the product of current and voltage measured at the power point (maximum output power P_{max}) by the product of short-circuit current and the open-circuit voltage. The power point is the maximum product of the cell voltage and the photocurrent obtained on the I-V curve.

$$P_{max} = I_{max} \times V_{max} = FF \times I_{sc} \times V_{oc} \quad (2)$$

$$FF = P_{max} / I_{sc} \times V_{oc} \tag{3}$$

2.1.4.5 Power conversion efficiency

The power conversion efficiency (η) of the dye-sensitized solar cell is determined by the photocurrent density measured at short-circuit, V_{oc}, the FF of the cell, and the intensity of the incident light (P_i) as shown in follow equation.

$$\eta = I_{sc} \times V_{oc} \times FF / P_i \tag{4}$$

Sometimes the use of the ratio of the maximum power output (P_{max}) to the incident power input (P_{in}), defined as

$$\eta = P_{max} / P_{in} = I_{sc} \times V_{oc} \times FF / P_{in} \tag{5}$$

2.1.5 Advantages and disadvantages of DSSCs

The major advantage of the concept of dye sensitization is the fact that the conduction mechanism is based on a majority carrier transport as opposed to the minority carrier transport of conventional inorganic cells. This means that bulk or surface recombination of the charge carriers in the TiO_2 semiconductor cannot happen. Thus, impure starting materials and a simple cell processing without any clean room steps are permitted, yet resulting in promising power conversion efficiencies of 7 - 11% and the hope of a low-cost device for photoelectrochemical solar energy conversion. On the other hand impure materials can result in a strongly reduced lifetime of the cells. The most important issue of the dye-sensitized cells is the stability over the time and the temperature range which occurs under outdoor conditions. Although it could be shown, that intrinsic degradation can considerably be reduced, the behavior of the liquid electrolyte under extreme conditions is still unknown. For a successful commercialization of these cells, the encapsulation/sealing, the coloration and the electrolyte filling has to be transferred into fully automated lines including the final closure of the filling openings. Therefore, a significant effort is taken in order to replace the liquid electrolyte by a gel electrolyte, a solid-state electrolyte or a p-type conducting polymer material.

2.2 Electrospinning
2.2.1 History of electrospinning method

The process of using electrostatic forces to form synthetic fibers, known as electrospinning, has been known for over 100 years. From 1934 to 1944, Formhals published a series of patents [25,48,49,50], describing an experimental setup for the production of polymer filaments using an electrostatic force. A polymer solution, such as cellulose acetate, was introduced into the electric field. It was not until 1934, when Formhals patented a process, that electrospinning truly surfaced as a valid technique for sinning small-diameter fibers. In 1952, Vonnegut and Neubauer were able to produce streams of highly electrified uniform droplets of about 0.1mm in diameter [51]. They invented a simple apparatus for the electrical atomization. In 1955, Drozin investigated the dispersion of a series of liquids into aerosols under high electric potentials [52]. Formhals studied for a better understanding of the electrospinning process; however, it would be nearly 30years before Taylor would publish work regarding the jet forming process. In 1969, Taylor published his work examining how the polymer droplet at the end of a capillary behaves when an electric field is applied [53]. In his studies he found that the pendant droplet develops into a cone (now

called the Taylor cone) when the surface tension is balanced by electrostatic forces. In 1971, Baumgarten made an apparatus to electrospun acrylic fibers with diameters in the range of 0.05-1.1 microns [54]. Since 1980s and especially in recent years, the electrospinning process has regained more attention probably due to interest in nanotechnology, as ultrafine fibers or fibrous structures of various polymers with diameters down to submicrons or nanometers can be easily fabricated with this process. One of the most important applications of traditional micro-size fibers, especially engineering fibers such and carbon, glass, and Kevlar fivers is to be used as reinforcements in composite developments [55]. In addition to composite reinforcement, other application fields based on electrospun polymer nanofibers, such as medical prosthesis [55-57], filtration, cosmetics [59], tissue engineering [60], liquid crystal device [61], electromagnetic shielding and photovoltaic device [62], have been steadily extended especially in recent years.

2.2.2 Principles of electrospinning method

Fig. 6 shows the schematic diagram of the electrospinning method. There are basically three components to fulfill this process: a high voltage supplier, a capillary tube with a pipette or needle of a small diameter, and a metal collecting screen. A typical electrospinning setup consists of a capillary through which the liquid to be electrospun is forced; a high voltage source with positive or negative polarity, which injects charge into the liquid; and a grounded collector. Once it has been ejected out of the metal needle with a small hole, the polymer solution was introduced into the electric field. The polymer filaments formed between two electrodes bearing electrical charges of opposite polarity. Before the polymer solution reach the collector, the polymer solution jet evaporates or solidifies, and is collected as an interconnecting web of small fibers. One of these electrodes was placed into the solution and the other onto a collector (Fig. 7).
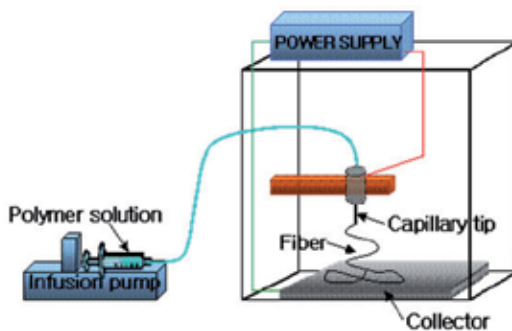
Fig. 6. Schematic diagram of the electrospinning method.

2.2.3 Ideal targets of electrospun nanofibers

As long as a polymer can be electrospun into nanofibers, ideal targets would be in that: (1) the diameters of the fibers be consistent and controllable, (2) the fiber surface be defect-free or defect-controllable, and (3) continuous single nanofibers be collectable. However researches so far have shown that there three targets are by no means easily achievable [26].

2.2.4 Processing parameters

There are a number of processing parameters that can greatly affect fiber formation and structure. The parameters are polymer concentration, applied voltage, flow rate, tip to

collector distance (TCD) and Solvent volatility. Furthermore, all parameters can influence the formation of bead defects.

2.2.4.1 Polymer concentration

The polymer concentration determines the spinnability of a solution, namely whether a fiber forms or not. The solution must have a high enough polymer concentration for chain entanglements to occur; however the solution cannot be either too dilute or too concentrated. If the solution is too dilute then the fibers break up into droplets before reaching the collector due to the effects of surface tension. However, if the solution is too concentrated then fibers cannot be formed due to the high viscosity, which makes it difficult to control the solution flow rate through the capillary. Thus, an optimum range of polymer concentrations exists in which fibers can be electrospun when all other parameters are held constant. A higher viscosity results in a larger fibers diameter [53, 63]. When polymers dissolve in a solvent, the solution viscosity is proportional to the polymer concentration. Thus, the higher the polymer concentration the larger the resulting nanofiber diameters will be.

2.2.4.2 Applied voltage

The strength of the applied electric field controls formation of fibers from several microns in diameter to tens of nanometers. Deitzel et al. examined a polyethylene oxide (PEO)/water system and found that increases in applied voltage altered the shape of the surface at which the Taylor cone and fiber jet were formed [64]. At lower applied voltages the Taylor cone formed at the tip of the drop; however, as the applied voltage was increased the volume of the drop decreased until the Taylor cone was formed at the tip of the capillary, which was associated with an increase in bead defects seen among the electrospun fibers (Fig.8). Moreover, another parameter which affects the fiber diameter to a remarkable extent is the applied voltage. In general, a higher applied voltage ejects more fluid in a jet, resulting in a larger fiber diameter [27].

2.2.4.3 Flow rate

Polymer flow rate also has an impact of fiber size, and additionally can influence fiber porosity as well as fiber shape. In the Taylor's work, they realized that the cone shape at the tip of the capillary cannot be maintained if the flow of solution through the capillary is insufficient to replace the solution ejected as the fiber jet [53]. They demonstrated that both fiber diameter and pore size increase with increasing flow rate. Additionally, at high flow rates significant amounts of bead defects were noticeable, due to the inability of fibers to dry completely before reaching the collector [60].
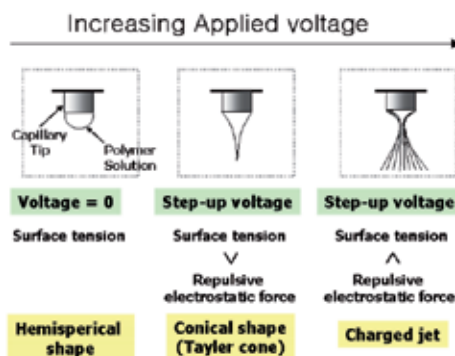
Fig. 7. Effect of varying the applied voltage on the formation of the Taylor cone.

2.2.4.4 Tip to collector distance (TCD)

The distance of between capillary tip and collector can also influence fiber size by 1-2 orders of magnitude. Additionally, this distance can dictate whether the end result is electrospinning or electrospraying. Doshi and Reneker found that the fiber diameter decreased with increasing distances from the Taylor cone [65].

2.2.4.5 Solvent volatility

Choice of solvent is also critical as to whether fibers are capable of forming, as well as influencing fiber porosity. In order for sufficient solvent evaporation to occur between the capillary tip and the collector a volatile solvent must be used. As the fiber jet travels through the atmosphere toward the collector a phase separation occurs before the solid polymer fibers are deposited, a process that is greatly influenced by volatility of the solvent. Zhao et al. examined the structural properties of 15 wt % of poly(Vinylidene Fluoride) nanofibers with different volume ratios in DMF/Acetone [66]. When DMF was used as the solvent without acetone, bead-fibers were found. When 9:1 DMF/acetone was used a s the solvent in the polymer solution, beads in the electrospun almost disappeared. Furthermore, the ultafine fibers without beads demonstrated clearly when the acetone amount in the solution increased to 20 %. Acetone is more volatile than DMF. Furthermore, the changes of solution properties by the addition of acetone could probably improve the electrospun membrane morphology and decrease the possibility of bead formation.

3. Results

3.1 Preparation of electrospun poly(vinylidene fluoride-hexafluoropropylene) (PVDF-HFP) nanofibers

Generally, in the electrospinning method, the changing of the parameters had a great effect on fiber morphology. To prepare the electrospun PVDF-HFP nanofiber films with the suitable morphology, we prepared the electrospun PVDF-HFP nanofiber films by several parameters such as the applied voltage(voltage supplier: NNC-ESP100, Nano NC Co., Ltd.), the tip-to-collector distance (TCD), and the concentration of the PVDF-HFP. First, the PVDF-HFP was dissolved in acetone/DMAc (7/3 weight ratio) for 24 hours at room temperature. Then, we prepared the electrospun PVDF-HFP nanofibers by the electrospinning method with different parameters. The applied voltage was ranged from 8 to 14 kV, TCD was varied from 13 to 21 cm, and the concentration of PVDF-HFP varied from 11 to 17 wt %. On all occasions, we used a syringe pump (781100, Kd Scientific) to control the flow rate of the polymer solution, the solution flow rate was 2 ml/h.

In the electrospinning method, the changing of the polymer concentration had a great effect on fiber morphology. To investigate the influence of polymer concentrations on the electrospun PVDF-HFP nanofibers, we prepared the PVDF-HFP nanofibers. When the polymer concentration were varied from 11 wt% to 17 wt%, TCD and applied voltages were 15 cm and 14 kV, respectively. Over the polymer solution of 19 wt% and below the polymer solution of 9 wt%, the nanofibers did not form. Fig. 8 shows the surface images of the electrospun PVDF-HFP nanofibers observed by FE-SEM and the diameter distributions of nanofibers. The increase of the polymer concentration resulted in an increase of the average fiber diameter of the electrospun PVDF-HFP nanofibers. In particular, the PVDF-HFP nanofiber, which was prepared from 15 wt% of polymer concentration showed a highly regular morphology with an average diameter of 800 - 1000 nm.
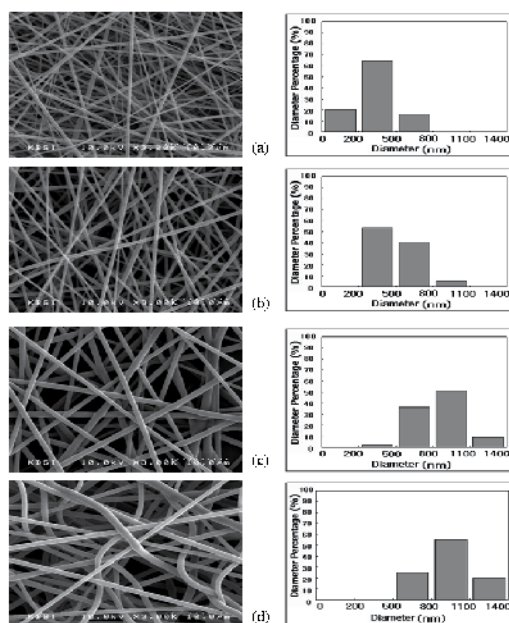
Fig. 8. FE-SEM images of electrospun PVDF-HFP nanofibers with different polymer concentrations (Applied voltage = 14 kV, TCD = 15 cm, flow rate = 2 ml/h) and their diameter distributions: (a) 11 wt%, (b) 13 wt%, (c) 15 wt%, (d) 17 wt%.
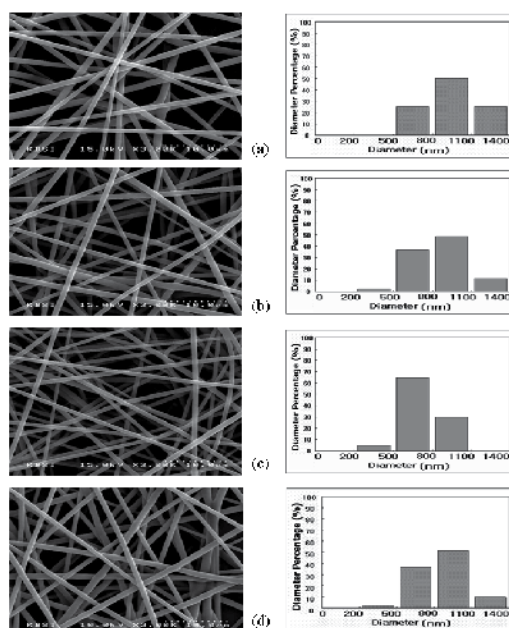
Fig. 9. FE-SEM images of electrospun PVDF-HFP nanofiber with different applied voltages (TCD = 15 cm, polymer concentration = 15 wt%, flow rate = 2 ml/h) and their diameter distributions: (a) 8 kV, (b) 10 kV, (c) 12 kV, (d) 14 kV.
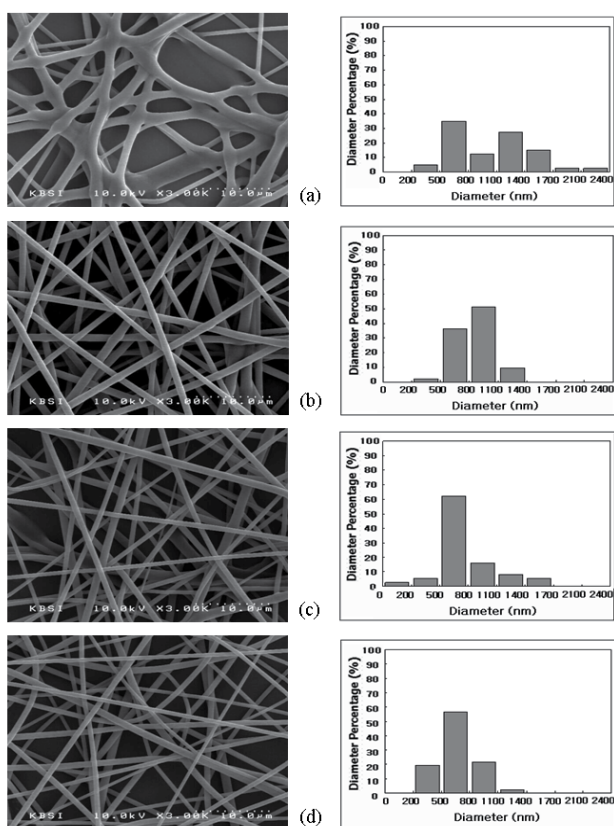
Fig. 10. FE-SEM images of electrospun PVDF-HFP nanofibers with different TCDs (Applied voltage = 14 kV, polymer concentration = 15 wt%, flow rate = 2 ml/h) and their diameter distributions: (a) 13 cm, (b) 15 cm, (c) 17 cm, (d) 19 cm.

To investigate the effect of applied voltage, experiments were carried out when the applied voltage was varied from 8 kV to 14 kV, TCD and polymer concentrations were held at 15 cm and 15 wt%, respectively. The morphologies of electrospun PVDF-HFP nanofibers prepared are shown in Fig. 9.

In addition, we prepared the electrospun PVDF-HFP nanofibers when the TCD was varied from 13 cm to 19 cm, applied voltage and polymer concentrations were held at 14 kV and 15 wt%, respectively. The morphologies of prepared electrospun PVDF-HFP nanofibers prepared are shown in Fig. 10. When the TCD was just close below 13 cm, irregular fiber morphology was formed, because the polymer jet arrived at the collector before the solidification. Therefore, we were able to optimize the preparation condition at an applied voltage of 14 kV, a polymer concentration of 15 wt%, and TCD of 15 cm to obtain the regular PVDF-HFP nanofibers.

As the changing of such parameters in the electrospinning method, the diameter and the morphology of the nanofibers fabricated were changed. At the condition of the 15 wt% of PVDF-HFP polymer solution, 14 kV of the applied voltage, 15 cm of the TCD and 2 ml/h of the flow rate, the nanofibers of the electrospun PVDF-HFP films showed extremely regular morphology with diameter of average 0.8 ~ 1.0 μm.

3.2 Characterizations of PVDF-HFP nanofibers

The pore size, the volume fraction and interconnectivity of pore domain, and the type of porous polymer matrix will determine the uptake and the ion conductivity of the electrolyte [63]. To investigate the effect of porous polymer matrix, the spin-coated PVDF-HFP film was also fabricated by using conventional spin-coating method, and measured the ionic conductivity under the same condition. The ionic conductivity of the spin-coated PVDF-HFP film was 1.37×10^{-3} S/cm, and this value showed lower value than the electrospun PVDF-HFP nanofiber film.

To measure the uptake and the porosity of the electropsun PVDF-HFP nanofiber films from electrolyte solution, the electropsun PVDF-HFP nanofiber films were taken out from the electrolyte solution after activation and excess electrolyte solution on the film surface was wiped.

The electrolyte uptake (U) was evaluated according to the following formula:

$$U = [(m-m_0)/m_0] \times 100\%$$

where m and m_0 are the masses of wet and dry of the electrospun nanofiber films, respectively.

The porosity (P) of the electrospun nanofibers was calculated from the density of electrospun PVDF-HFP nanofibers (ρ_m, g/cm^3) and the density of pure PVDF-HFP (ρ_p = 1.77 g/cm^3):

$$P \text{ (vol.\%)} = (1 - \rho_m/\rho_p) \times 100$$

The density of the electrospun PVDF-HFP nanofibers was determined by measuring the volume and the weight of the electrospun PVDF-HFP nanofibers. The uptake and the porosity of the electrospun PVDF-HFP nanofiber film was obtained 653±50 % and 70±2.3 %, respectively, regardless the diameter and the morphology of nanofibers prepared with various parameters.

3.3 Fabrications of DSSCs devices using PVDF-HFP nanofibers

We prepared the DSSC devices, sandwiched with working electrode using TiO$_2$ impregnated dyes and counter electrode using a platinum (Pt, T/SP) electrode as two electrodes. The DSSC device was fabricated using this following process. The TiO$_2$ pastes (Ti-Nanoxide, HT/SP) were spread on a FTO glass using the doctor blade method and calcinated at 500 $^\circ$C. The sensitizer Cis-di(thiocyanato)-N,N-bis(2,2'-bypyridil-4.4'-dicarboxylic acid)ruthenium (II) complex (N3 dye) was dissolved in pure ethanol in a concentration of 20 mg per 100 ml of solution. The FTO glass deposited TiO$_2$ was dipped in an ethanol solution at 45 $^\circ$C for 18 hours. The electospun PVDF-HFP nanofibers or the spin-coated PVDF-HFP film were cut by 0.65 cm × 0.65 cm after drying, and put on the TiO$_2$ adsorbed the dyes, the electrolyte solution was dropped above them, and dried in a dry oven at 45 $^\circ$C for 2 hours to evaporate wholly the solvent. To compare with the electrospun PVDF-HFP nanofiber films, the conventional spin-coating method was used for making a spin-coated PVDF-HFP film. In all cases, the thickness of the electrospun PVDF-HFP nanofibers and spin-coated PVDF-HFP film were 30±1 μm by using digimatic micrometer. The electrolyte was consisted of 0.10 M of iodine (I$_2$), 0.30 M of 1-propyl-3-methylimidazolium iodide (PMII), and 0.20 M of tetrabutylammonium iodide (TBAI) in the solution of ethylene carbonate (EC)/ propylene carbonate (PC)/ acetonitrile (AN) (8:2:5

v/v/v). The Pt pastes were spread on a FTO glass using the doctor blade method and calcinated at 400 ºC.

3.4 Photovoltaic properties of the DSSC devices using PVDF-HFP nanofibers

The DSSC devices using several different electrospun PVDF-HFP nanofibers on various parameters were fabricated and their photovoltaic characteristics are summarized in Table 1 – 3. I-V curves of the DSSC devices using them are shown in Fig. 11. The concentration of the PVDF-HFP solution was 15 wt% in acetone/DMAc (7/3 by weight ratio). The photovoltaic characteristics of the DSSC devices were measured by using Solar Simulator (150 W simulator, PEC-L11, PECCELL) under AM 1.5 and 100 mW/cm^2 of the light intensity.
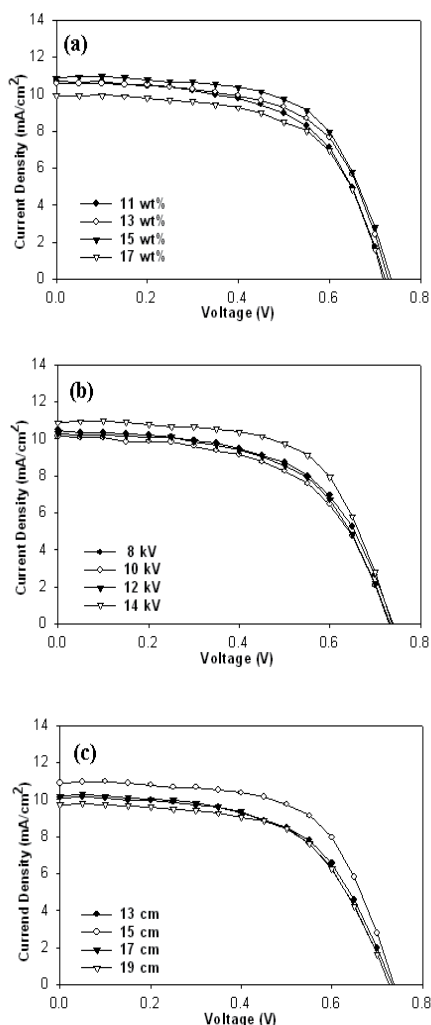
Fig. 11. I-V curves of DSSC devices using electrospun PVDF-HFP nanofibers under illumination at AM 1.5 condition: (a) different polymer concentrations, (b) different applied voltages, (c) different TCDs.

Polymer concentration (wt.%)	V_{OC} (V)	J_{SC} (mA/cm²)	FF	η (%)
11	0.74	10.88	0.60	4.78
13	0.73	10.57	0.62	4.78
15	0.74	10.89	0.63	5.02
17	0.72	9.92	0.62	4.41

Table 1. Photovoltaic performances of DSSC devices using electrospun PVDF-HFP nanofibers on different polymer concentrations

Applied voltage (kV)	V_{OC} (V)	J_{SC} (mA/cm²)	FF	η (%)
8	0.74	10.50	0.57	4.41
10	0.73	10.10	0.56	4.17
12	0.74	10.30	0.58	4.35
14	0.74	10.88	0.63	5.02

Table 2. Photovoltaic performances of DSSC devices using electrospun PVDF-HFP nanofibers on different applied voltages

TCD (cm)	V_{OC} (V)	J_{SC} (mA/cm²)	FF	η (%)
13	0.73	10.10	0.58	4.30
15	0.74	10.88	0.63	5.02
17	0.73	10.20	0.57	4.23
19	0.73	9.72	0.60	4.21

Table 3. Photovoltaic performances of DSSC devices using electrospun PVDF-HFP nanofibers on different TCDs

Type	V_{OC} (V)	J_{SC} (mA/cm²)	FF	η (%)
Electrospun PVDF-HFP nanofiber film	0.75	12.3	0.57	5.21
Spin-coated PVDF-HFP film	0.67	3.87	0.55	1.43

Table 4. Photovoltaic characteristics of DSSC devices using electrospun PVDF-HFP nanofiber film and spin-coated PVDF-HFP film in polymer electrolytes

The active area of the DSSC devices measured by using a black mask was 0.25 cm². The V_{OC}, J_{SC}, FF, and η of the DSSC device using the spin-coated PVDF-HFP film were 0.67 V, 3.87 mA/cm², 0.56, and 1.43 %, respectively. The η of DSSC device using the spin-coated PVDF-HFP film was lower than it of the DSSC device using electrospun PVDF-HFP nanofiber films, because of the decrease of J_{SC}, and all data are summarized in Table 4 and their I-V curves are shown in Fig. 12. This result seemed that because the porosity of the electrospun PVDF-HFP nanofibers is higher than it of the spin-coated PVDF-HFP film, ion transfer occurred well and regular nanofiber morphology helped to transfer ion produced by redox

mechanism, therefore, overall power conversion efficiency of DSSC devices using the electrospun PVDF-HFP nanofiber films was higher than that of the DSSC device using spin-coated PVDF-HFP film. However, the minute change of nanofibers diameter was influenced little on power conversion efficiency.
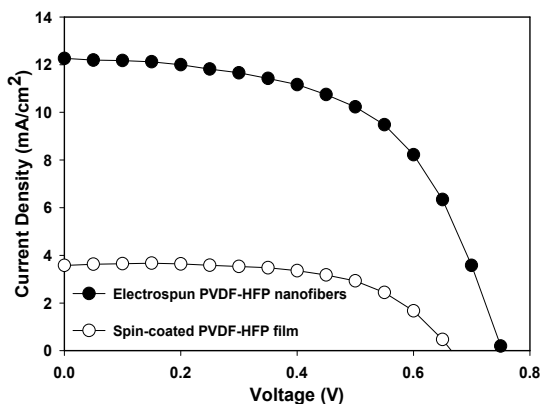
Fig. 12. I-V curves of the DSSC devices using electrospun PVDF-HFP nanofibers and spin-coated PVDF-HFP film.

3.5 Effect of electrolyte in the electrospun PVDF-HFP nanofibers on DSSC

The photovoltaic performance of DSSC devices using the electrospun PVDF-HFP nanofibers showed remarkable improved results compared to DSSC devices using the spin-coated PVDF-HFP film. To prove these results, the interfacial charge transfer resistances were investigated by the EIS measurement. The EIS data were measured with impedance analyzer at same condition using FTO/TiO_2/electrolyte/Pt/FTO cells, and fitted by Z-MAN software (WONATECH) and Echem analyst (GAMRY). The Nyquist plots of the FTO/TiO_2/electrolyte/Pt/FTO cells and charge transfer resistances are shown in Fig. 13 and Table 5, respectively. The equivalent circuit of DSSC devices is shown in Fig. 14. The R_S, $R1_{CT}$ and $R2_{CT}$ were series resistance, the charge transfer resistance of Pt/electrolyte interface, and the charge transfer resistance of TiO_2/electrolyte interface, respectively. The $R2_{CT}$ of the DSSC device using the spin-coated PVDF-HFP film was similar to that of the DSSC device using the electrospun PVDF-HFP nanofibers. However, the R_S and $R1_{CT}$ of the DSSC device using the spin-coated PVDF-HFP film were higher than those of the DSSC device using the electrospun PVDF-HFP nanofibers. These results showed that the spin-coated film has a higher resistance than the electropun nanofibers, and poor I^-/I^{3-} activity between Pt and electrolyte affected to the low value of the J_{SC}. As a result, the η of the DSSC device using the spin-coated PVDF-HFP film showed low value.

Type	R_S (Ω)	$R1_{CT}$ (Ω)	$R2_{CT}$ (Ω)
Electrospun PVDF-HFP nanofibers	21.70	11.01	11.07
Spin-coated PVDF-HFP film	31.87	25.02	14.37

Table 5. The series resistances (R_S), the charge transfer resistance of the Pt/electrolyte ($R1_{CT}$) and TiO_2/electrolyte ($R2_{CT}$) in the DSSC devices under AM 1.5 by the EIS measurement
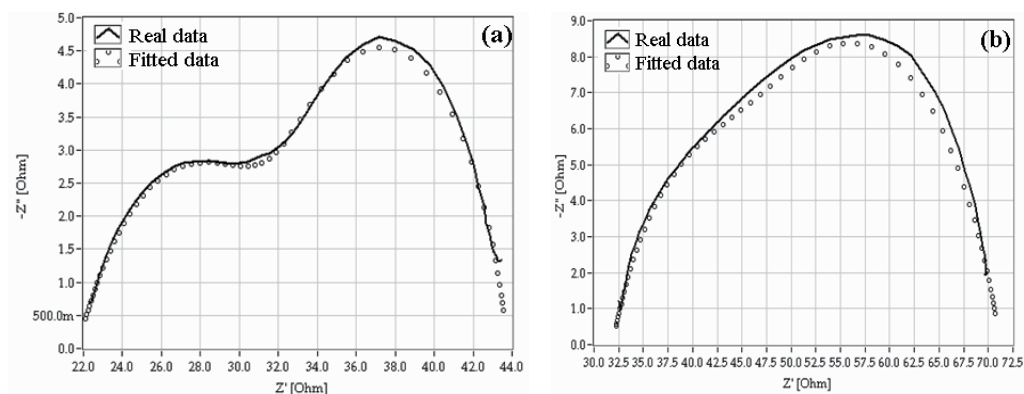
Fig. 13. Nyquist plots the $FTO/TiO_2/electrolyte/Pt/FTO$ device using (a) electrospun PVDF-HFP nanofiber film electrolyte, and (b) spin-coated PVDF-HFP film electrolyte.
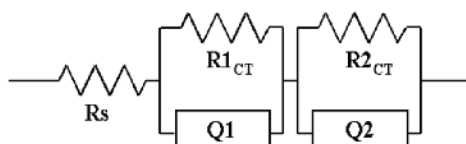
Fig. 14. The equivalent circuit of the DSSC device. (R_S: Series resistance, $R1_{CT}$: charge transfer resistance of Pt/electrolyte, $R2_{CT}$: charge transfer resistance of TiO_2/electrolyte, Q1 and Q2: constant phase element)
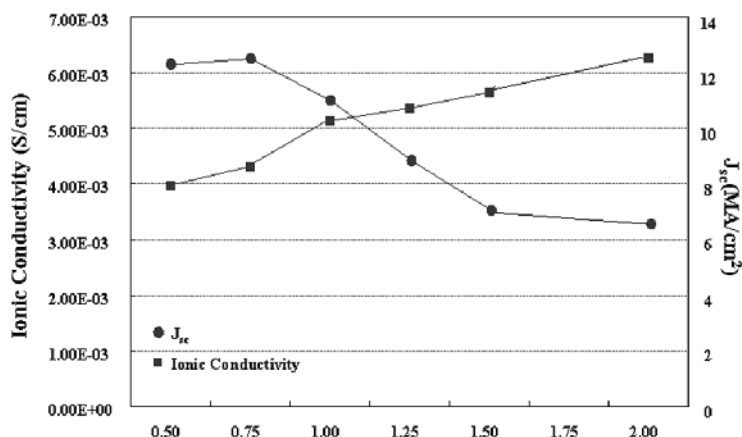
Fig. 15. Ionic conductivities of electrospun PVDF-HFP nanofiber films and J_{sc} of DSSC devices using electrospun PVDF-HFP nanofiber films with mole ratio of iodine to TBAI.

In addition, to investigate the photovoltaic effect of I_2 concentrations on DSSC using the electrospun PVDF-HFP nanofiber, we prepared $FTO/TiO_2/Dye/Electrolyte/Pt/FTO$ devices with various mole ratios of I_2 to TBAI in electrolyte solutions. In Table 6, as the increase of the I_2 concentration in electrolyte, the ionic conductivity of the electrospun

PVDF-HFP nanofiber films increased, while the photocurrent density of the DSSC devices using the electrospun PVDF-HFP nanofibers electrolyte decreased. The relationship between the ionic conductivity the electrospun PVDF-HFP nanofiber films and the photocurrent density of the DSSC devices are illustrated in Fig. 15 and I-V curves are shown in Fig. 16. In general, the photocurrent density of DSSC using the liquid electrolyte is proportionate to the ionic conductivity in electrolyte. From these results, we found that the photocurrent density and the efficiency on DSSC using the electrospun PVDF-HFP nanofibers electrolyte are not necessarily proportionate to the ionic conductivity in electrolyte.
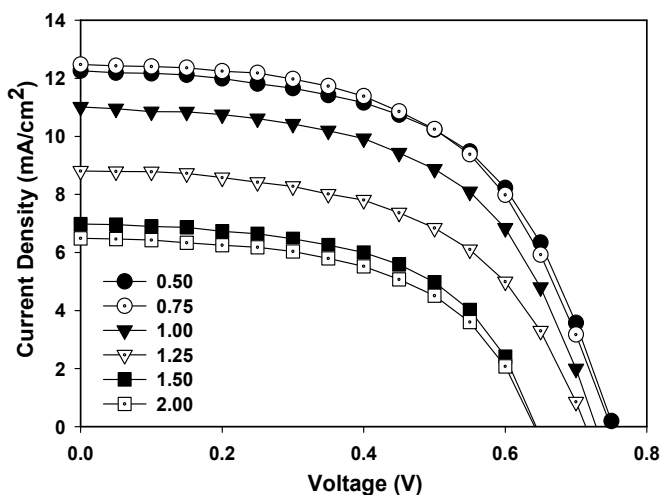
Fig. 16. The I-V curves of the DSSC devices using electrospun PVDF-HFP nanofibers with mole ratio of iodine to TBAI.

4. Future outlooks

During the rebirth of polymer electrospining over the past decade the applicability of electrospun fibers has become apparent across many fields. This highly adaptable process allows the formation of functional fibrous membranes for applications such as tissue engineering, drug delivery, sensor, cosmetic and photovoltaic devices. Electrospun nanofibers offer an unprecedented flexibility and modularity in design. Improvements in strength and durability, and their incorporation in composite membranes, will allow there scaffolds to compete with existing membrane technology. Currently, the research field of electrospnning is ripe with functional materials from resorbable cells to ceramic solid-phase catalyst and continued research interest is expected to improve most areas of full cells and photovoltaic cells.

5. Acknowledgement

6. References

Adachi, M.; Murata, Y.; Okada, I. & Yoshikawa, S. (2003). Formation of Titania Nanotubes and Applications for Dye-Sensitized Solar Cells. *Journal of the Electrochemical Society*, Vol. 150, No. 8, pp. G488-G493, ISSN 0013-4651

Amadelli, R.; Argazzi, R.; Bignozzi, C. A. & Scandola, F. (1990). Design of antenna-sensitizer polynuclear complexes. Sensitization of titanium dioxide with [Ru(bpy)2(CN)2]2Ru(bpy(COO)2)22. *Journal of the American Chemical Society*, Vol. 112, No. 20, pp. 7099-7103, ISSN 0002-7863

Anton, Formhals (1934). Process and apparatus for preparing artificial threads. US Patent 1,975,504.

Anton, Formhals (1939). Method and apparatus for spinning. US Patent 2160962

Anton, Formhals (1940). Artificial thread and method of producing same. US Patent 2187306

Anton, Formhals (1944). Method and apparatus for spinning. US Patent 2349950

Armand, M. (1990). Polymers with Ionic Conductivity. *Advanced Materials*, Vol. 2, No. 6-7, pp. 278-286, ISSN 1521-4095

Asano, T.; Kubo, T. & Nishikitani, Y. (2004). Electrochemical properties of dye-sensitized solar cells fabricated with PVDF-type polymeric solid electrolytes. *Journal of Photochemistry and Photobiology A: Chemistry*, Vol. 164, No. 1-3, pp. 111-115, ISSN 1010-6030

Bach, U.; Lupo, D.; Comte, P.; Moser, J. E.; Weissortel, F.; Salbeck, J.; Spreitzer, H. & Gratzel, M. (1998). Solid-state dye-sensitized mesoporous TiO2 solar cells with high photon-to-electron conversion efficiencies. *Nature*, Vol. 395, No. 6702, pp. 583-585, ISSN 0028-0836

Baumgarten, P. K. (1971). Electrostatic spinning of acrylic microfibers. *Journal of Colloid and Interface Science*, Vol. 36, No. 1, pp. 71-79, ISSN 0021-9797

Berry, John P. (Wirral, GB2) (1990). Electrostatically produced structures and methods of manufacturing. US Patent 4965110

Bornat, A. L., GB2) (1987). Production of electrostatically spun products. US Patent 4689186

Cao, J. H.; Zhu, B. K. & Xu, Y. Y. (2006). Structure and ionic conductivity of porous polymer electrolytes based on PVDF-HFP copolymer membranes. *Journal of Membrane Science*, Vol. 281, No. 1-2, pp. 446-453, ISSN 0376-7388

Caruso, R. A.; Schattka, J. H. & Greiner, A. (2001). Titanium Dioxide Tubes from Sol–Gel Coating of Electrospun Polymer Fibers. *Advanced Materials*, Vol. 13, No. 20, pp. 1577-1579, ISSN 1521-4095.

Chand, S. (2000). Review Carbon fibers for composites. *Journal of Materials Science*, Vol. 35, No. 6, pp. 1303-1313, ISSN 0022-2461

Deitzel, J. M.; Kleinmeyer, J.; Harris, D. & Tan, N. C. B. (2001). The effect of processing variables on the morphology of electrospun nanofibers and textiles. *Polymer*, Vol. 42, No. 1, pp. 261-272, ISSN 0032-3861

Deitzel, J. M.; Kleinmeyer, J.; Harris, D. & Tan, N. C. B. (2001). The effect of processing variables on the morphology of electrospun nanofibers and textiles. *Polymer*, Vol. 42, No. 1, pp. 261-272, ISSN 0032-3861.

Demir, M. M.; Yilgor, I.; Yilgor, E. & Erman, B. (2002). Electrospinning of polyurethane fibers. *Polymer*, Vol. 43, No. 11, pp. 3303-3309, ISSN 0032-3861

Dloczik, L.; Ileperuma, O.; Lauermann, I.; Peter, L. M.; Ponomarev, E. A.; Redmond, G.; Shaw, N. J. & Uhlendorf, I. (1997). Dynamic Response of Dye-Sensitized Nanocrystalline Solar Cells: Characterization by Intensity-Modulated Photocurrent

Spectroscopy. *The Journal of Physical Chemistry B*, Vol. 101, No. 49, pp. 10281-10289, ISSN 1520-6106

Doshi, J. & Reneker, D. H. (1995). Electrospinning process and applications of electrospun fibers. *Journal of Electrostatics*, Vol. 35, No. 2-3, pp. 151-160, ISSN 0304-3886

Drozin, V. G. (1955). The electrical dispersion of liquids as aerosols. *Journal of Colloid Science*, Vol. 10, No. 2, pp. 158-164, ISSN 0095-8522

Feng, L.; Li, S.; Li, H.; Zhai, J.; Song, Y.; Jiang, L. & Zhu, D. (2002). Super-Hydrophobic Surface of Aligned Polyacrylonitrile Nanofibers. *Angewandte Chemie International Edition*, Vol. 41, No. 7, pp. 1221-1223, ISSN 1521-3773

Grätzel, M. (2004). Conversion of sunlight to electric power by nanocrystalline dye-sensitized solar cells. *Journal of Photochemistry and Photobiology A: Chemistry*, Vol. 164, No. 1-3, pp. 3-14, ISSN 1010-6030

Hagfeldt, A. & Gratzel, M. (1995). Light-Induced Redox Reactions in Nanocrystalline Systems. *Chemical Reviews*, Vol. 95, No. 1, pp. 49-68, ISSN 0009-2665

Hagfeldt, A. & Grätzel, M. (2000). Molecular Photovoltaics. *Accounts of Chemical Research*, Vol. 33, No. 5, pp. 269-277, ISSN 0001-4842

Hohman, M. M.; Shin, M.; Rutledge, G. & Brenner, M. P. (2001). Electrospinning and electrically forced jets. II. Applications. *Physics of Fluids*, Vol. 13, No. 8, pp. 2221-2236, ISSN 1070-6631

Hou, H. Q.; Jun, Z.; Reuning, A.; Schaper, A.; Wendorff, J. H. & Greiner, A. (2002). Poly(p-xylylene) nanotubes by coating and removal of ultrathin polymer template fibers. *Macromolecules*, Vol. 35, No. 7, pp. 2429-2431, ISSN 0024-9297

Hu Y. J.; Chen B.; Yuan Y. (2007). Preparation and Electrochemical Properties of Polymer Li-ion Battery Reinforced by non-woven Fabric. *J. Cent. South Univ.Technol, Vol. 14, No. 1*, pp. 47-49, ISSN 1005-9784

Huang, H. T. & Wunder, S. L. (2001). Ionic conductivity of microporous PVDF-HFP/PS polymer blends. *Journal of the Electrochemical Society*, Vol. 148, No. 3, pp. A279-A283, ISSN 0013-4651

Huang, Z.-M.; Zhang, Y. Z.; Kotaki, M. & Ramakrishna, S. (2003). A review on polymer nanofibers by electrospinning and their applications in nanocomposites. *Composites Science and Technology*, Vol. 63, No. 15, pp. 2223-2253, ISSN 0266-3538

Huynh, W. U.; Dittmer, J. J. & Alivisatos, A. P. (2002). Hybrid Nanorod-Polymer Solar Cells. *Science*, Vol. 295, No. 5564, pp. 2425-2427, ISSN 0036-8075

Jeong, Y.-B. & Kim, D.-W. (2004). Cycling performances of Li/LiCoO2 cell with polymer-coated separator. *Electrochimica Acta*, Vol. 50, No. 2-3, pp. 323-326, ISSN 0013-4686

Kalyanasundaram, K. & Grätzel, M. (1998). Applications of functionalized transition metal complexes in photonic and optoelectronic devices. *Coordination Chemistry Reviews*, Vol. 177, No. 1, pp. 347-414, ISSN 0010-8545

Kelly, C. A. & Meyer, G. J. (2001). Excited state processes at sensitized nanocrystalline thin film semiconductor interfaces. *Coordination Chemistry Reviews*, Vol. 211, No. 1, pp. 295-315, ISSN 0010-8545

Kim, D. W. & Sun, Y. K. (2001). Electrochemical characterization of gel polymer electrolytes prepared with porous membranes. *Journal of Power Sources*, Vol. 102, No. 1-2, pp. 41-45, ISSN 0378-7753

Kim, D. W.; Kim, Y. R.; Park, J. K. & Moon, S. I. (1998). Electrical properties of the plasticized polymer electrolytes based on acrylonitrile-methyl methacrylate copolymers. *Solid State Ionics*, Vol. 106, No. 3-4, pp. 329-337, ISSN 0167-2738

Kim, J. R.; Choi, S. W.; Jo, S. M.; Lee, W. S. & Kim, B. C. (2005). Characterization and properties of P(VdF-HFP)-based fibrous polymer electrolyte membrane prepared

by electrospinning. *Journal of the Electrochemical Society*, Vol. 152, No. 2, pp. A295-A300, ISSN 0013-4651

Komiya, R.; Han, L.; Yamanaka, R.; Islam, A. & Mitate, T. (2004). Highly efficient quasi-solid state dye-sensitized solar cell with ion conducting polymer electrolyte. *Journal of Photochemistry and Photobiology A: Chemistry*, Vol. 164, No. 1-3, pp. 123-127, ISSN 1010-6030

Liu, H. & Hsieh, Y.-L. (2003). Surface methacrylation and graft copolymerization of ultrafine cellulose fibers. *Journal of Polymer Science Part B: Polymer Physics*, Vol. 41, No. 9, pp. 953-964, ISSN 1099-0488

M. Armand, in: J.R. MacCallum, C.A. Vincent (Eds.). (1987). Current state of PEO-based electrolyte *Polymer Electrolyte Reviews-1*, Elsevier Applied Science, London

Ma P. X.; Zhang R. (1999). *Synthetic nano-scale fibrous extracellular matrix*. pp. 60-72, John Wiley

Martin, C. R. (1996). Membrane-Based Synthesis of Nanomaterials. *Chemistry of Materials*, Vol. 8, No. 8, pp. 1739-1746, ISSN 0897-4756

McEvoy, A. J. & Grätzel, M. (1994). Sensitisation in photochemistry and photovoltaics. *Solar Energy Materials and Solar Cells*, Vol. 32, No. 3, pp. 221-227, ISSN 0927-0248

Meyer, G. J. (1997). Efficient Light-to-Electrical Energy Conversion: Nanocrystalline TiO2 Films Modified with Inorganic Sensitizers. *Journal of Chemical Education*, Vol. 74, No. 6, pp. 652l, ISSN 0021-9584

Michot, T.; Nishimoto, A. & Watanabe, M. (2000). Electrochemical properties of polymer gel electrolytes based on poly(vinylidene fluoride) copolymer and homopolymer. *Electrochimica Acta*, Vol. 45, No. 8-9, pp. 1347-1360, ISSN 0013-4686

Nazeeruddin, M. K.; Kay, A.; Rodicio, I.; Humphry-Baker, R.; Mueller, E.; Liska, P.; Vlachopoulos, N. & Graetzel, M. (1993). Conversion of light to electricity by cis-X2bis(2,2'-bipyridyl-4,4'-dicarboxylate)ruthenium(II) charge-transfer sensitizers (X = Cl-, Br-, I-, CN-, and SCN-) on nanocrystalline titanium dioxide electrodes. *Journal of the American Chemical Society*, Vol. 115, No. 14, pp. 6382-6390, ISSN 0002-7863

Nelson, J. (1999). Continuous-time random-walk model of electron transport in nanocrystalline TiO_{2} electrodes. *Physical Review B*, Vol. 59, No. 23, pp. 15374, ISSN 1098-0121

Nogueira, A. F. & De Paoli, M.-A. (2000). A dye sensitized TiO2 photovoltaic cell constructed with an elastomeric electrolyte. *Solar Energy Materials and Solar Cells*, Vol. 61, No. 2, pp. 135-141, ISSN 0927-0248

Ondarçuhu, T. & Joachim, C. (1998). Drawing a single nanofibre over hundreds of microns. *EPL (Europhysics Letters)*, Vol. 42, No. 2, pp. 215, ISSN 0295-5075

O'Regan, B. and M. Gratzel (1991). A low-cost, high-efficiency solar cell based on dye-sensitized colloidal TiO2 films. *Nature*, Vol.353, No.6346, pp. 737-740, ISSN 0028-0836

Péchy, P.; Renouard, T.; Zakeeruddin, S. M.; Humphry-Baker, R.; Comte, P.; Liska, P.; Cevey, L.; Costa, E.; Shklover, V.; Spiccia, L.; Deacon, G. B.; Bignozzi, C. A. & Grätzel, M. (2001). Engineering of Efficient Panchromatic Sensitizers for Nanocrystalline TiO2-Based Solar Cells. *Journal of the American Chemical Society*, Vol. 123, No. 8, pp. 1613-1624, ISSN 0002-7863

Reneker, D. H.; Kataphinan, W.; Theron, A.; Zussman, E. & Yarin, A. L. (2002). Nanofiber garlands of polycaprolactone by electrospinning. *Polymer*, Vol. 43, No. 25, pp. 6785-6794, ISSN 0032-3861

Senecal, Kris (N. Smithfield, RI, US); Samuelson, Lynne (Marlborough, MA, US); Sennett, Michael (Sudbury, MA, US); Schreuder-gibson, Heidi (Holliston, MA, US) (2006). Conductive (electrical, ionic, and photoelectric) polymer membrane articles, and method for producing same. US Patent 7109136

Sill, T. J. & von Recum, H. A. (2008). Electrospinning: Applications in drug delivery and tissue engineering. *Biomaterials*, Vol. 29, No. 13, pp. 1989-2006, ISSN 0142-9612

Smith, Daniel J. (Stow, OH); Reneker, Darrell H. (Akron, OH); Mcmanus, Albert T. (San Antonio, TX); Schreuder-gibson, Heidi L. (Holliston, MA); Mello, Charlene (Rochester, MA); Sennett, Michael S. (Sudbury, MA) (2004). Electrospun fibers and an apparatus therefor. US Patent 6753454

Stephan, A. M.; Nahm, K. S.; Anbu Kulandainathan, M.; Ravi, G. & Wilson, J. (2006). Poly(vinylidene fluoride-hexafluoropropylene) (PVdF-HFP) based composite electrolytes for lithium batteries. *European Polymer Journal*, Vol. 42, No. 8, pp. 1728-1734, ISSN 0014-3057

Stergiopoulos, T.; Arabatzis, I. M.; Katsaros, G. & Falaras, P. (2002). Binary Polyethylene Oxide/Titania Solid-State Redox Electrolyte for Highly Efficient Nanocrystalline TiO2 Photoelectrochemical Cells. *Nano Letters*, Vol. 2, No. 11, pp. 1259-1261, ISSN 1530-6984

Sze S M. (1981). *Physics of Semiconductor Devices* (New York : Wiley) p 264

Taylor, G. (1969). Electrically Driven Jets. *Proceedings of the Royal Society of London. Series A, Mathematical and Physical Sciences*, Vol. 313, No. 1515, pp. 453-475, ISSN 0080-4630

van de Lagemaat, J.; Park, N. G. & Frank, A. J. (2000). Influence of Electrical Potential Distribution, Charge Transport, and Recombination on the Photopotential and Photocurrent Conversion Efficiency of Dye-Sensitized Nanocrystalline TiO2 Solar Cells: A Study by Electrical Impedance and Optical Modulation Techniques. *The Journal of Physical Chemistry B*, Vol. 104, No. 9, pp. 2044-2052, ISSN 1520-6106

Vonnegut, B. & Neubauer, R. L. (1952). Production of monodisperse liquid particles by electrical atomization. *Journal of Colloid Science*, Vol. 7, No. 6, pp. 616-622, ISSN 0095-8522

Wang, P.; Zakeeruddin, S. M. & Grätzel, M. (2004). Solidifying liquid electrolytes with fluorine polymer and silica nanoparticles for quasi-solid dye-sensitized solar cells. *Journal of Fluorine Chemistry*, Vol. 125, No. 8, pp. 1241-1245, ISSN 0022-1139

Wang, P.; Zakeeruddin, S. M.; Moser, J. E.; Nazeeruddin, M. K.; Sekiguchi, T. & Gratzel, M. (2003). A stable quasi-solid-state dye-sensitized solar cell with an amphiphilic ruthenium sensitizer and polymer gel electrolyte. *Nat Mater*, Vol. 2, No. 6, pp. 402-407, ISSN 1476-1122

Watanabe, M.; Kanba, M.; Matsuda, H.; Tsunemi, K.; Mizoguchi, K.; Tsuchida, E. & Shinohara, I. (1981). High lithium ionic conductivity of polymeric solid electrolytes. *Die Makromolekulare Chemie, Rapid Communications*, Vol. 2, No. 12, pp. 741-744, ISSN 0173-2803

Waters, Colin M. (Tattingstone, GB2); Noakes, Timothy J. (Selbourne, GB2); Pavey, Ian (Fernhurst, GB2); Hitomi, Chiyoji (Tsokuba, JP) (1992). Liquid crystal devices. US Patent 5088807

Zhizhen Zhao, Jingquing Li, Xiaoyan Yuan Xing Li, Yuanyuan Zhang, Jing Sheng. (2005). *journal of Applied Polmer Scence, 97*, 466-474. Zhao, Z. Z.; Li, J. Q.; Yuan, X. Y.; Li, X.; Zhang, Y. Y. & Sheng, J. (2005). Preparation and properties of electrospun poly(vinylidene fluoride) membranes. *Journal of Applied Polymer Science*, Vol. 97, No. 2, pp. 466-474, ISSN 0021-8995

Development of Dye-Sensitized Solar Cell for High Conversion Efficiency

Yongwoo Kim[1] and Deugwoo Lee[2]
[1]Korea Industrial Complex Corporation
[2]Pusan National University
Korea

1. Introduction

The Solar cell energy is presently promising because of oil inflation, fuel exhaustion, global warming, and space development. Many advanced countries rapidly develop the solar cell energy under a nation enterprise. Particularly, dye-sensitized solar cell (DSC), the 3rd generation solar cell, has low-cost of manufactures about 1/3~1/5 times compared with the silicon solar cell, which encourages the research globally.

Dye-sensitized Solar Cell (DSC) is evaluated to be low-cost technology as the manufacturing DSC is more inexpensive 5 times than producing Silicon Solar Cell. Currently, the best conversion efficiency is 11%, the tile-shaped modules are being produced in STI, Austria. Moreover the efficiency to increase over 15% and the process of fabricating DSC for commercialization are attempted to be highly researched.

Recently, production of nano-particles becomes available due to development of nano-technologies. Since they have broad contact area comparing to the existing compound materials being generally used and increased mechanical, thermal and electrical characteristics, etc., they are attracting public attention as a new material to implement various functions. Especially, nano-tube has more excellent mechanical and electrical characteristics than normal particle type materials. And it is known that the smaller its diameter, i.e. aspect ratio, is, the better its characteristics are. Accordingly a lot of researches related to nano-compound materials have been being progressed nationally and internationally (Gojny et al., 2003; Jijima, 1991; Chang et al., 2001).

It is new methods to improve light conversion efficiency using several approaches such as nanocrystalline CNT/TiO_2 hybrid material, reflect mirror with micro pyramid structure, and concentrating light with Fresnel lens.

Figure.1 shows the operational principle and structure of dye sensitized cell. If visible rays are absorbed by n-type nano particles TiO_2 that dye molecules are chemically absorbed on the surface, the dye molecules generate electron-hole pairs, and the electron were injected into the conduction band of semiconductor's oxides. These electrons that are injected into the semiconductor's oxide electrode generate current through each nano particles' interfaces. The holes that are made from dye molecules are deoxidized by receiving electrons, thus causing the dye-sensitized cells begin to work (Zhang et al., 2010).
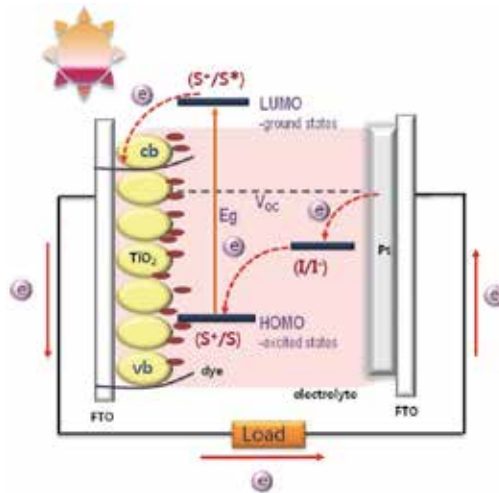
Fig. 1. A schematic representation of the construction of a DSSC
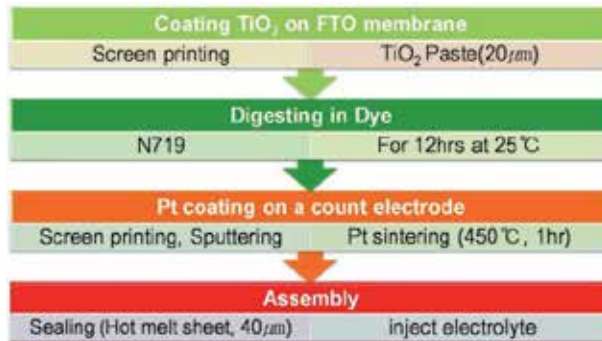
Fig. 2. Process of manufacturing DSSC

We applied screen printing method on FTO membrane to TiO_2 paste in 20μm. Coated working electrode membrane was sintered at 450°C and digested them into dye (N719) for about 12 hours.
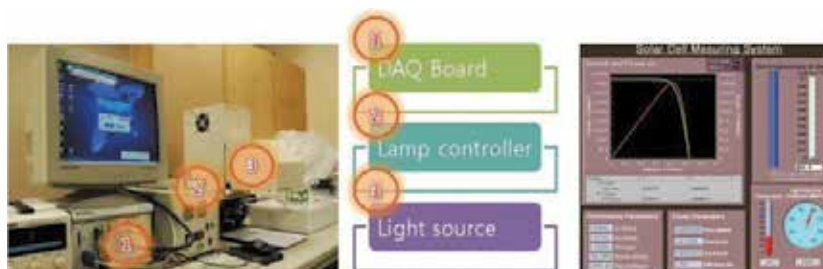
Fig. 3. Measurement system and program

In order to understand efficiency increase of solar cells due to coating method, we compared individual efficiencies using solar cell simulator. Measuring efficiency of solar cells had been progressed under AM (air mass) 1.5 conditions (1sun, 100mW/cm²).

2. A study of photocatalyst of the TiO$_2$ thin film with acid dispersed CNT

As one of major variables of dye-sensitized solar cell, the dye absorbed light energy transits from ground state to excited state and gets electron injection. Electrons are injected in a very fast speed of femtosecond or picoseconds unit and oxidized dye is renewed within several nanoseconds. On the other hand, since rejoining speed that the electron becomes dissolved into electrolyte via surface state is slow such as micro seconds or milliseconds and most of photons are injected semiconductor conduction band, those electrons that are not injected meet holes again to be restored and decrease efficiency of solar cell. If we utilize CNT that is advantageous for electrical and thermal conduction as a compound material, we can increase electron injection speed than rejoining speed and increase efficiency of dye-sensitized solar cells through movement of more electrons.

Since multi walled carbon nanotube (MWCNT) is a material to well transfer electricity and heat, it can function as a basic electrode. Nanotubes function as electrodes to penetrate into broad TiO$_2$ surface mutually and assist extracting charge carriers efficiently from dye layer. Since these electrodes are very clear under longer wavelength, they are advantageous for solar light spectrums.

This study utilizes CNT that is advantageous for electrical and thermal conduction as a compound material so that surface resistance between clear electrodes and dye layer decreases, electron injection speed can be increased more than the rejoining speed of electrons and efficiency of dye-sensitized solar cell can be also increased through movement of more electrons. In order to perform the task, this study will composite nano-crystal TiO$_2$ with sol-gel technique (Tracey et al., 1998), establish optimal thin film formation conditions through identification of correlation between permeability and conductivity by manufacturing distributed CNT through acid treatment and compound thin film, and perform characteristics assessment by applying it to solar cells upon surface resistance between dye layer and FTO.

Dye-sensitized solar cell is a device to apply photosynthesis principle of the plant by combining pigments to absorb light energy within chloroplast with polymer and applying them to the solar cell. Dye-sensitized solar cell basically consists of dye polymer to absorb solar light, semiconductor compound having broad band gap serving as n-type semiconductor, electrolyte serving as p-type semiconductor, relative electrode for catalysis, and clear electrode to permeate solar light. Dye-sensitized solar cell is composed of semiconductor nanoparticles where dye absorbs solar energy and separation/transfer of generated electrons are diffused upon electron concentration difference. Processes to generate and transfer electrons play an essential role to determine performance of the cells. Firstly entering time of excited electrons from the dye into TiO$_2$ should be shorter than that of joining with holes and being exterminated. Normally entering time of electron is very fast in femtoseconds through picoseconds and oxidated dye is renewed within several nanoseconds (Tachibana et al., 1996).

2.1 Composition of TiO$_2$

Manufacturing methods of TiO$_2$ for photocatalyst generally includes hydro thermal method (Chen et al., 1995), sedimentation method (Ellis et al., 1989; Lee et al., 2000), sol-gel technique (Ding et al., 1995; Johnson, 1985; Hwang & Kim, 1995), CVD method (Lee et al., 1999), etc. Hydro thermal method that may get mainly powder materials has complex equipment and difficult for continuous work, while sedimentation method allows easy

production but it has disadvantages cohesion between particles, powder with possibility of uneven composition, and difficulties for fineness as bulk materials from sintering and harmonization of crystalline. Comparing to them, sol-gel technique has advantages to allow easy acquisition of TiO_2 powder for photocatalyst with even composition relatively simply and low temperature composition available.

2.2 CNT dispersion

Carbon nanotube exists as a form of bundle or cohesion body due to strong van der Waals forces between tubes as like interaction between graphite plates. This cohesion phenomenon obstructs formation of 3-dimensional network structure in manufacturing compound to increase electrical or mechanical properties. It is an important technology to disperse carbon nanotube and release individual strand, as it increases functional efficiency. Dispersion methods of carbon nanotube can be classified into mainly mechanical dispersion, dispersion using strong acid, dispersion with solution, etc. Firstly, dispersion using strong acids is to agitate with composition of nitric acid and hydrochloric acetone at 130°C for 6h or using composition of sulfuric acid and hydrochloric acid. Dispersing with solution is to melt carbon nanotubes through surface active agents such as SDS (sodium dodecyl sulfate), Triton X-100, LDS, etc. The most various mechanical dispersion methods include supersonic treatment by mixing acetone and methanole, or using ball milling method to minimize length and diameter distribution of carbon nanotubes. Others include dispersions with grinding process using mortars, abrasion process, high shear strength using liquid, etc.

2.3 Experiment method and conditions
2.3.1 Production and coating of CNT/TiO₂

TTIP that is used for this study generates photocatalyst TiO_2 under low temperature heating conditions but it has a disadvantage fast hydrolysis with air or small moisture due to very string reactivity. So we had made even chelate compound by adding AcAc into the ethanol solution and severely agitating it for 30 minutes at room temperature using agitator in order
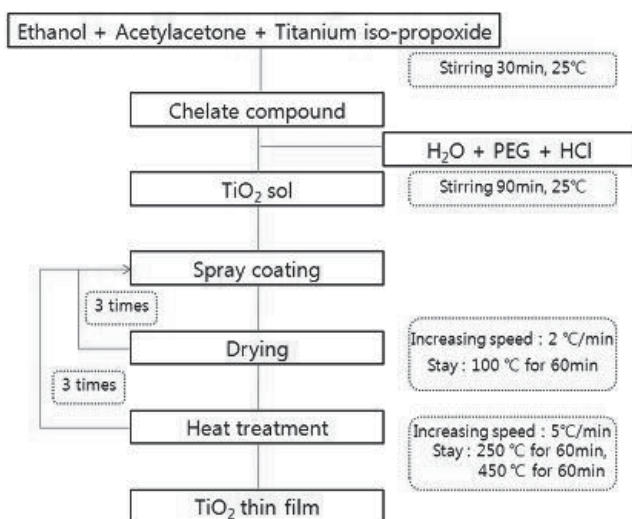
Fig. 4. Process of fabricating TiO_2 Thin Film

to control hydrolysis speed of TTIP. And we have prepared water solution by melting HCl 0.15 mole catalyst for stability of sol and PEG 0.5 mole adhesion to increase osculation with plate to be coated into 50mole distilled water and drop it into the chelate compound. At the moment, it is possible to manufacture yellow clear sol by severely agitating and reacting chelate compound at room temperature for 90min.

For dispersion of CNT, we mixed 60% nitric acid and distilled water in 1:3 volume ratio and severely agitated it at 130°C for 6h. After acid treatment, we mixed a lot of distilled water, apply ultra sonication and continued to neutralize it using PTFE thin film filter with 1um in diameter until it has been neutralized.

In order to understand permeability and electrical characteristics of composited TiO_2 sol and dispersed CNT by concentrations, we have mage mixture solution by establishing variables with Volume% concentrations 0.5, 2.5, 5 and 10.

This study with TiO_2 thin film manufacturing method using sol-gel technique has an advantage to allow applying various processes such as dip-coating method, spinning method, Spray, etc. As spray coating out of them has advantages such as uniform thickness, various compositions to manufacture films by mixing solutions, no big influence from viscosity of solution comparing to spinning method, and available coating without influences from patterned plate, plate surface energy or roughness. It is considered that it is the most appropriate for commercialization as it allows easy manufacture and application of broad area plate.

2.3.2 Manufacture of Dye-sensitized solar cell

We applied composited CNT/TiO_2 to screen printing on FTO plate to coat about 3μm in thickness and coated TiO_2 paste from Dyesol in 15μm. Then we could increase the whole efficiency of cells by decreasing surface resistance between TiO_2 layer absorbed with dye and FTO plate and assisting movement of electrons. Fig. 3 shows coated plated by CNT concentrations, from which we can see that these plates with high content of CNT have thicker colours. We sintered them at 450°C and digested them into dye (N719) for about 24 hours. We coated platinum onto FTO plate with relative electrode and sintered it at 450°C. We sealed prepared 2 plates with Hot melt sheet having about 60μm in thickness and completed them by injecting electrolyte.
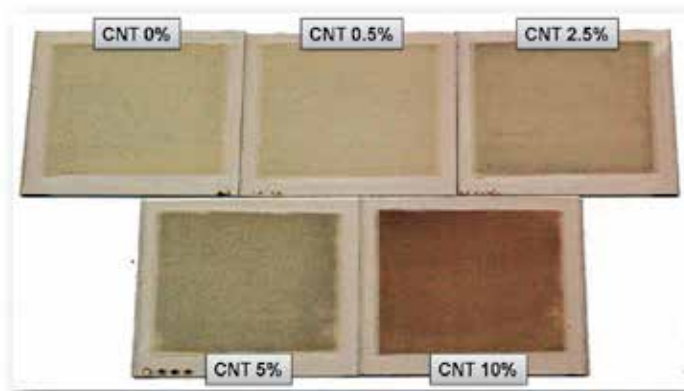
Fig. 5. Feature of CNT/TiO_2 thin film by screen-printing

2.4 Conclusion and considerations
2.4.1 Change of permeability upon CNT concentration
In order to check permeability and electrical characteristics of CNT by concentrations, We coated glass plate with about 5μm in thickness using spray technique, and produced TiO_2 thin film by increasing temperature and sintering it at 450°C for 1 hour. Fig. 6(a) shows composited CNT/TiO_2 thin film surface with very small and even particle. In case of (b), it shows thin film surface of TiO_2 paste from Dyesol with uneven large particles but very excellent porosity. From the results of measurements for permeability of each thin film, as CNT content increases, permeability drops straight and reaches only 10% when concentration becomes 5, 10%.
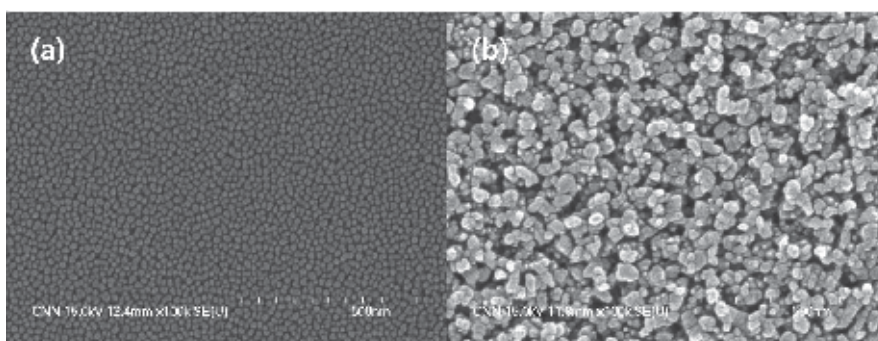
Fig. 6. SEM images of CNT/TiO_2 (a) and TiO_2 paste(b)
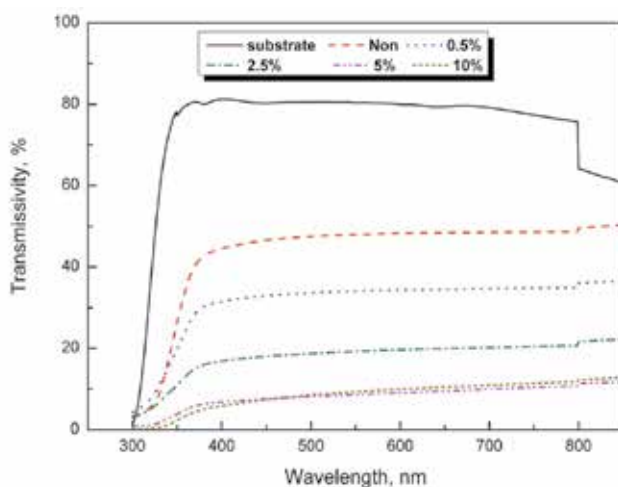
Fig. 7.Transmissivity of TiO_2 layers

2.4.2 Change of surface resistance upon CNT concentration
Fig. 8 shows measurement results of surface resistances upon CNT concentrations. It shows a graph acquired upon each condition by increasing voltage from -1V to 1V by 50mV interval. As CNT concentration with excellent electrical characteristics increases and surface resistance becomes low, it is considered that it would be advantageous for transfer of electrons separated from the dye.
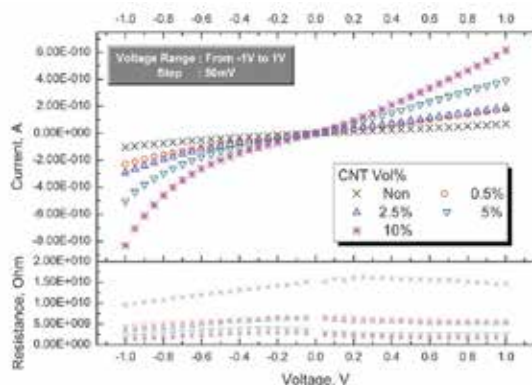
Fig. 8. I-V curve and resistance of TiO$_2$ layers

2.4.3 Efficiency change of Dye-sensitized solar cell upon CNT concentration

Fig. 9 shows I-V and P-V curve of CNT 0.5% indicating the highest energy efficiency out of CNT concentrations. Efficiency can be calculated from output power by estimating voltage (V_{mp}) and current (I_{mp}) to achieve the maximum output from I-V curve when strength of solar light becomes input power.
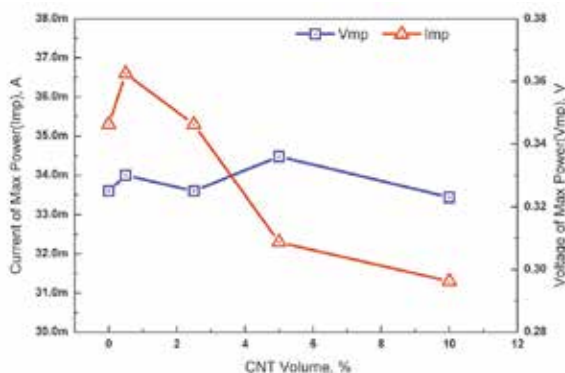
Fig. 9. I-V and P-V curve of DSC with CNT 0.5%
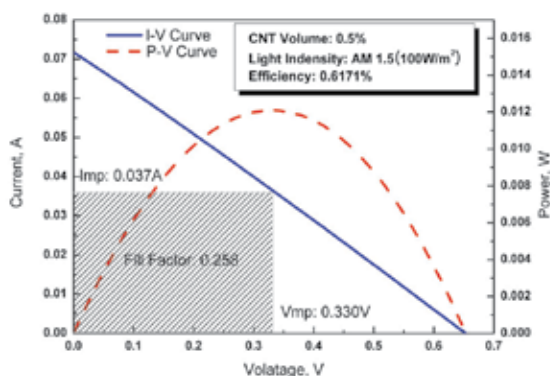
Fig. 10. I_{mp} and V_{mp} of DSC of each CNT volume

In order to confirm if movement of electrons increases according to content of CNT within CNT/TiO$_2$ compound material, we compared V$_{mp}$ and Imp values upon each condition on Fig. 10. V$_{mp}$ values refer to voltage values when solar cell performs the maximum power, and CNT contents show relatively even values throughout the whole areas. In case of Imp, we can see that it shows high value on very low CNT content such as 0.5%. It means that a lot of electrons are transferred comparing to no CNT, in spite of low generation of electrons due to low permeability. Under high CNT content, such as 5, 10%, we can see that generated electrons are small as surface resistance is low but permeability is low.

2.5 Conclusions

This study has confirmed efficiency of solar cells upon impact of permeability and surface resistance by manufacturing CNT/TiO$_2$ compound material to increase transfer of electrons separated from dye layer using sol-gel technique as a variable having effect on efficiency of dye-sensitized solar cell and applying in to the solar cells.

- It was possible to develop CNT/TiO$_2$ compound material to remarkably reduce surface resistance of solar cells and increase efficiency of them and acquire the highest efficiency at 0.5% Vol concentration of CNT.
- It is concluded that as CNT concentration increases, surface resistance becomes low with excellent electrical characteristics, but the solar cells reacting against solar light receive large influence from permeability.
- High permeability increases voltage of solar cells and CNT/TiO$_2$ compound material with low surface resistance effectively transfers electrons generated from the dye, so they contribute to increase of the current.
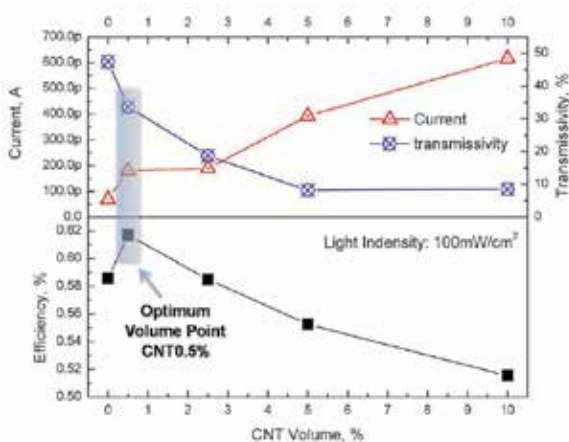
Fig. 11. Determine of optimum CNT volume of DSC

3. The recovery of light with a reflector of microstructures

We have studied a reflector recovering the loss light for improvement conversion efficiency of DSC. One of methods to increase efficiency of dye-sensitized solar cell is to expand surface area of semiconductor oxide such as TiO$_2$. Since dye polymer has high efficiency when it is absorbed on the semiconductor as a single molecule layer, solar light absorption becomes larger as the surface area of the semiconductor on which dye polymer is absorbed

is wide. Consequently efficiency of the cell is improved as TiO_2 particles are small and porousness is high. This study has researched that the dye produces electrons as much as possible using a method to lengthen scattering distance by reflecting entered solar light rather than expanding surface area of the oxide.

The reflector angle was determined by optical analysis program. Micro pyramid patterns with the 112.6° were processed using the ultra precision shaping machine in order to maximize the conversion efficiency due to increasing light distance. In addition, a comparative study carried out about the conversion efficiency. We made the DSC that is attached reflector with mirror angle 112.6° below. We measured conversion efficiency of solar cell by solar simulator that can irradiate 100mW/cm² (1Sum, AM 1.5).
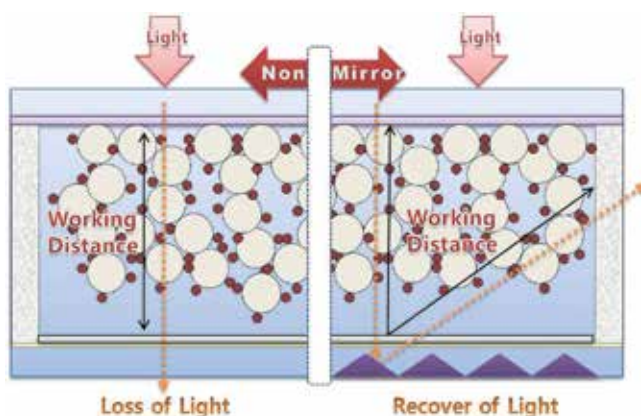
Fig. 12. Scheme of DSC with reflector

As a result of this experiment, the DSC with micro pyramid mirror improves efficiency about 2% against the DSC with black plate. Reflected light can cross more dye of TiO_2 Layer. Therefore, Voltage of maximum power (V_{mp}) increases other reflector with different mirror angle.

We propose a new method to improve light conversion efficiency using a reflector to collect light being lost from permeation through the dye-sensitized solar cell. The goals of this study are to

- Fabrication of reflector with microstructure
- Improve working distance of scattering light
- Control mirror angle by optimum design
- Improve photoelectric efficiency with micro pyramid arrayed mirror

3.1 Light simulation

We designed a micro reflector to lengthen scattering distance of reflected solar light on the dye layer of dye-sensitized solar cell using light analysis program.

In order to maximize light scattering distance of dye layer, we allowed value of Light Angle (θ_l) to be the maximum so that reflected light can be spread out widely on the dye layer. Light Angle and Mirror Angle (θ_m) are indicated on Figure 13. We measured Light Angle according to aspect ratio of height and width of micropattern of the reflector, and determined Mirror Angle when this value became the maximum. Result values of analysis according to Aspect Ratio values are indicated on Table 1 and Figure 14.
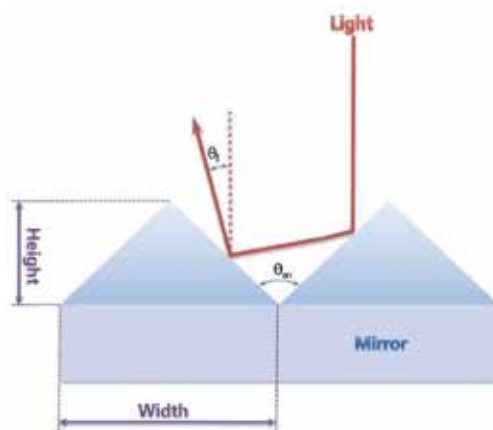
Fig. 13. Scheme of light path and mirror angle
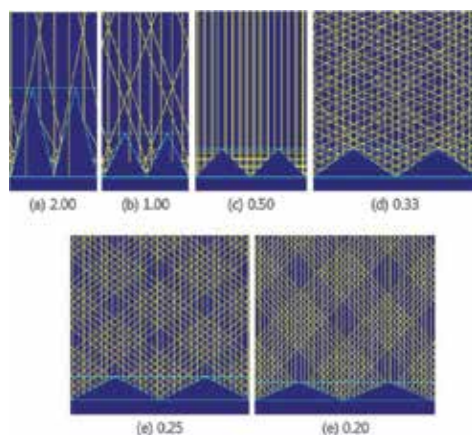
Fig. 14. Simulation results pursuant to aspect ratio

Aspect Ratio	Height [μm]	Width [μm]	Mirror Angle [degree]	Light Angle [degree]	Working distance [μm]
2	50	25	28.8	11.6	40.8
1	50	50	53.2	21.2	42.9
0.5	50	100	90.0	0.0	40
0.33	50	150	112.6	67.5	104.5
0.25	50	200	126.9	53.6	67.4
0.2	50	250	136.4	43.8	55.4

Table 1. Results of light simulation

The results of light analysis said that when Aspect Ratio was 0.33 and Mirror Angle was 112.6°, Light Angle had max value of 67.5°. At the moment, considering that thickness of dye layer of dye-sensitized solar is 40μl, solar light can meet the largest amount of dye with about 104.5μm of scattering distance.
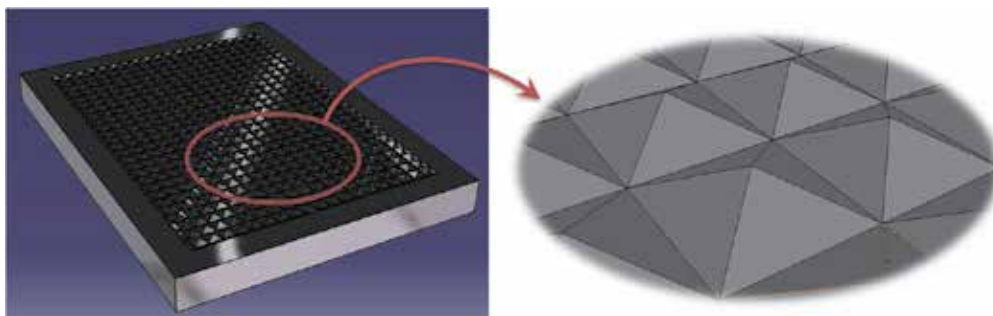
Fig. 15. Modelling of microstructure arrayed mirror

3.2 Fabrication of a reflector

In case of creating micropatterns on the material through micro cutting using single crystal diamond tool, pattern dimensions such as height, width and length of the micropattern depend on shape, cutting depth and feeding amount of the machining tool. In case of shaping machining of material using single crystal diamond having a certain tool angle, its sectional shape has 3-dimensional structure of pyramid shape. In order to machine pyramid shape, process consisted of machining one axis with diamond shaping machining and machining other axis by rotating table by 90° (Kim, 2005).
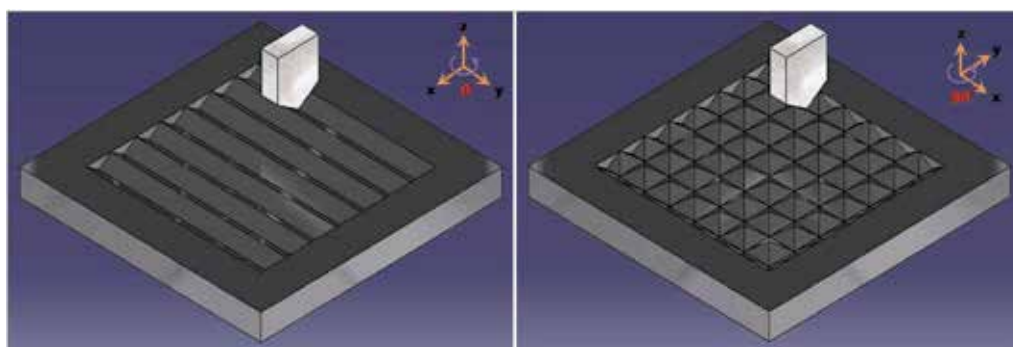
Fig. 16. Tool path of Pyramid shape

For machining sample, Oxygen Free Copper (OFHC copper) to be mostly used for general reflector mirror, etc. has been used. From the results of light analysis, a single crystal diamond bite with s112.6° of tool angle to maximize Light Angle has been used. Cutting length was total 50μm with 5μm steps, and feeding interval was 100μm. Height of mound of machined material was about 33.35μm. After machining, material was washed with supersonic wave to remove micro burr or chip, etc. generated from machining, treated with acid for about 15 seconds with fluoric acid and coated with gold through electrolytic plating. Micropattern machining experiment had been performed using commercial super precision machine. Shape of micro machined sample had been measured using SEM. Figure 18 shows pyramid shaped reflector machined by shaping machine and has 100μm width and 33.35μm height with tetrahedron shape. There was burr generated at the bottom of micro machined work that would be created during 90°rotation machining. It is considered to study machining conditions of cutting amount and feeding speed.
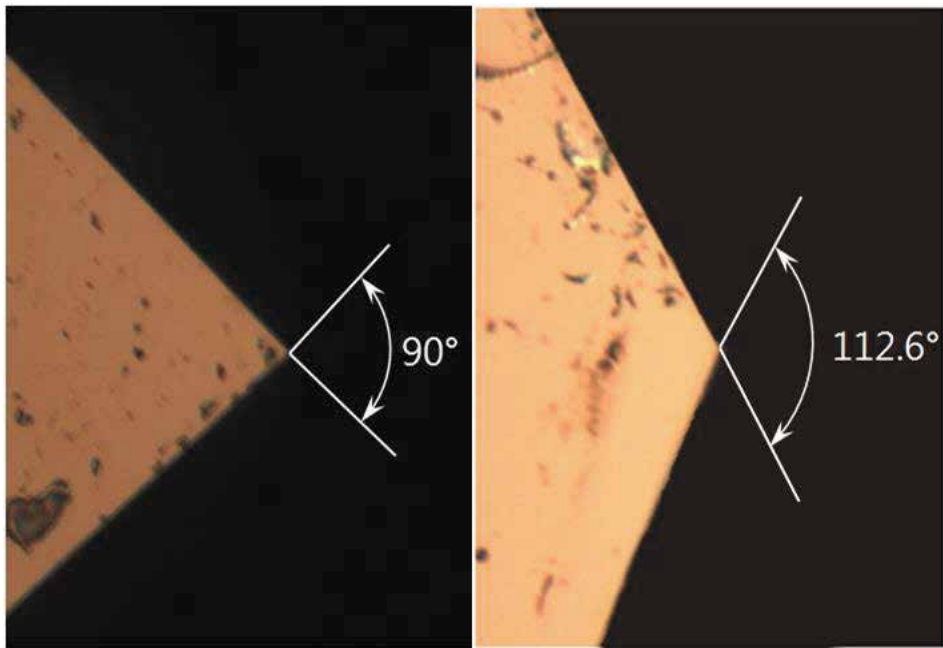
Fig. 17. Images of single diamond tool
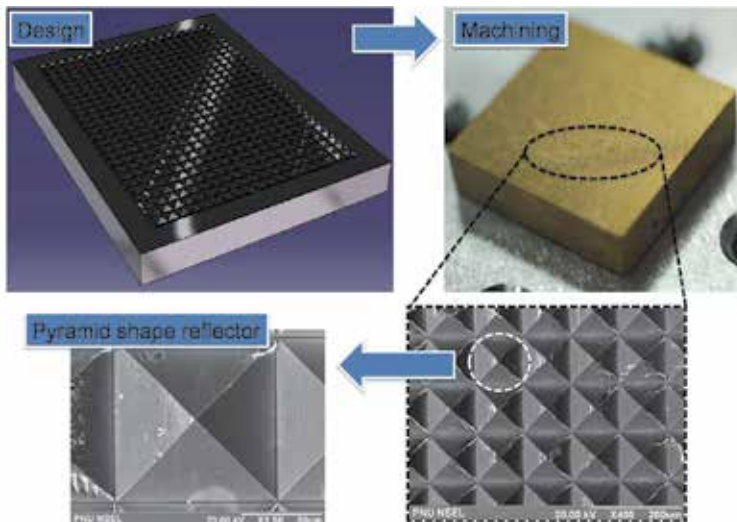
Fig. 18. Machined pattern for reflector

3.3 Results

We made DSC by handmade which of size is 11mm x 4mm. It is smaller area than my precedent study that obtains about 0.5% of efficiency. And size of mirror also becomes smaller before. Figure 19 shows I-V and P-V line diagram in order to measure efficiency of the cell by attaching a black plate at the bottom of dye-sensitized solar cell, pass-through of light in figure 20, and pyramid shaped reflector in figure 21.
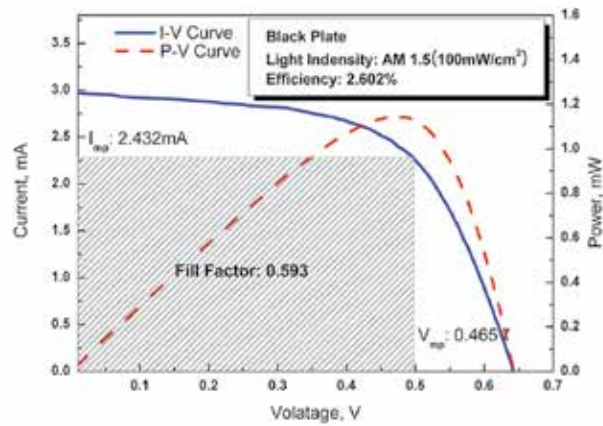
Fig. 19. I-V and P-V curve based on black plate
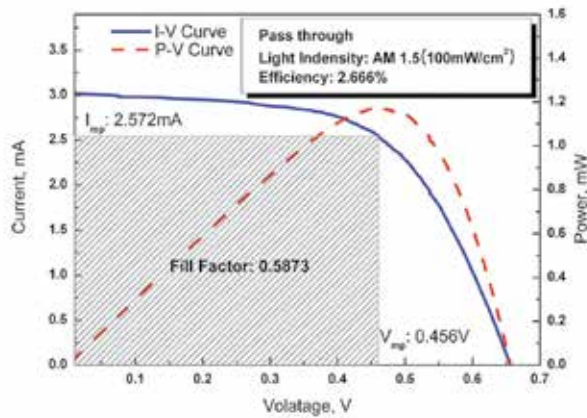
Fig. 20. I-V and P-V curve without a reflector
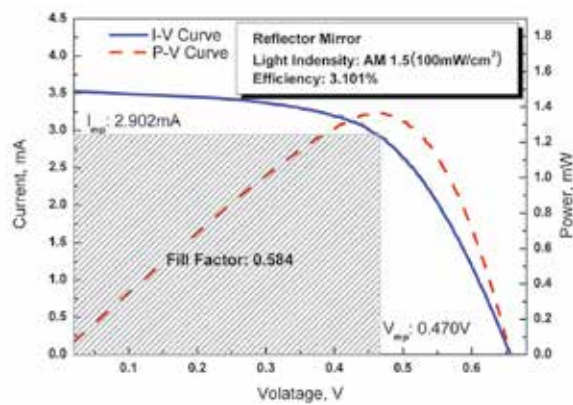
Fig. 21. I-V and P-V curve based on micro pyramid pattern reflector

3.4 Conclusions

This study machined micropatterned micro reflector and measured conversion efficiency of solar cell in order to increase efficiency of dye-sensitized solar cell. Its results are summarized as follows:
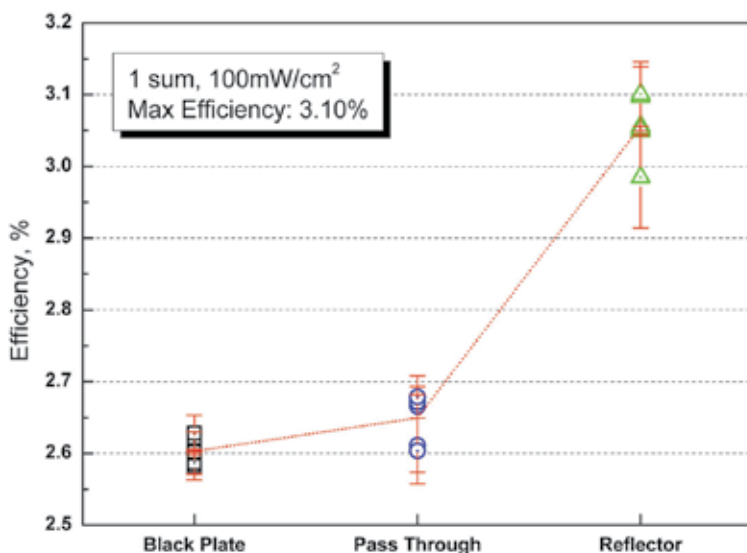
Fig. 22. Comparison of efficiency of different reflector

It was possible to get the optimal reflection angle 112.6° to increase conversion efficiency through reflector to collect lost light passing through dye-sensitized solar cell by performing light analysis.

When using reflector with pyramid shape, it was confirmed that it could get higher energy conversion efficiency by about 17% than a black plate

In case of micro pyramid reflector, maximized inclination to lengthen distance to meet dye layer of TiO_2 had maximized max power current (I_{mp}) and brought about entire efficiency improvement, different from vertical reflection.

4. Photovoltaic performance of Dye-sensitized solar cell by concentrating sunlight

One of method that can be improved efficiency of solar cell is concentrating light. Various factors influence the production of electricity from solar cells such as solar radiation, solar cell installation angle, direction, shade, solar cell module temperature. Among these, solar cell installation angle, direction, and shade have almost no influence on the system performance once the solar cell system is installed unless artificial external effects are given because they are determined when the solar cell system is designed and installed. After installation, the performance of a solar cell system varies greatly by the solar radiation reaching the module surface and the surface temperature. The higher the solar radiation, the higher the efficiency of the solar cell becomes. Due to the nature of the solar cell module, the power production increases in proportion to the solar radiation, and the power generation

increases as the surface temperature of the solar cell module increases. Therefore, we can improve the performance of solar cell modules by compulsorily increasing the solar cell module temperature through solar concentration.

This study intended to develop solar cell module that can maximize the efficiency of unit cells of dye-sensitized solar cell (DSSC) by maximizing solar concentration and minimizing solar loss while analyzing and improving the factors that influence the efficiency of DSSC.

In this study, and was concentrated by Fresnel lens. High temperature heat on concentration can decrease efficiency of solar cell so as cooling radiator was installed. Maximum concentrating ratio was 26 times of 1sun (2.6W/cm²). When the solar energy of High density was illuminated on a DSC, It was confirmed that temperature and concentrating ratio affect efficiency of DSC.
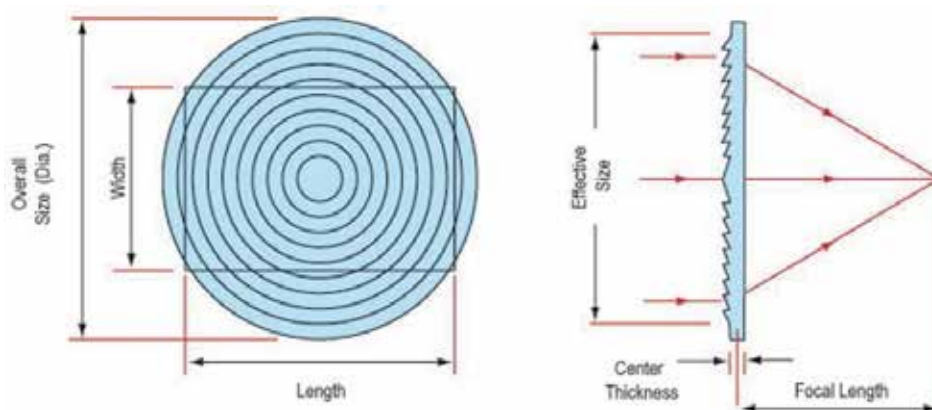
Fig. 23. Structure of Fresnel lens

Contents	Value
Grooves/Inch	100
Size H x L (inches)	5.0 x 5.0
Effective Size (inches)	Φ 4.0
Effective Focal Length (inches)	2.8
Center Thickness (inches)	0.06
Transmission (%)	92(wavelength 400~1100nm)

Table 2. Specifications of Fresnel lens

When high density light is illuminated in the DSC using concentrating lens, conversion efficiency is reached up to 16.11%. The enhancement in overall device efficiency is a result of increased open circuit potential and short circuit current. If coolant system is used, it can help guarantee of stable performance of a high efficiency of DSC at 45°C.
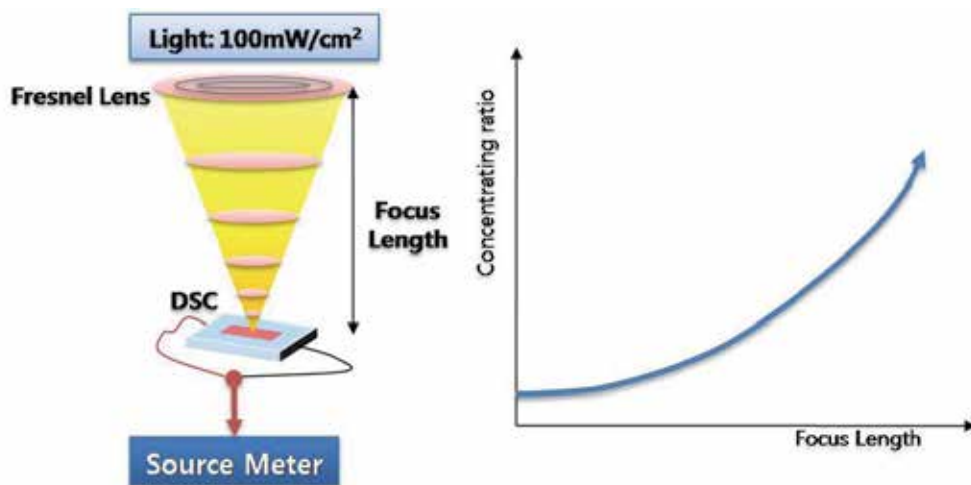
Fig. 24. Schematic of concentrating DSC

4.1 Evaluation of solar cell performance by changing temperature

High temperature is generated when solar energy is concentrated to improve energy conversion efficiency. Performance drops due to sealing problems such as the leakage and evaporation of electrolytes resulting from the changes in the volume of volatile electrolytes and the increase of vapour tension (Kim, 2007). To solve this problem, many efforts are being made to achieve performance reliability such as replacement of liquid electrolytes with solid electrolytes, development of new materials for sealing, and the performance of thermal stability tests (Fischer et al., 1997). Performance varies greatly by the surface temperature and the solar radiation that reaches the cell surface of a solar cell. The higher the solar radiation, the higher power production becomes, and the performance of a solar cell varies by surface temperature. In this study, the effects of the changing cell temperature on the efficiency of solar cells, and the optimum conditions for thermal stability in solar concentration and the production of solar cell module were investigated.
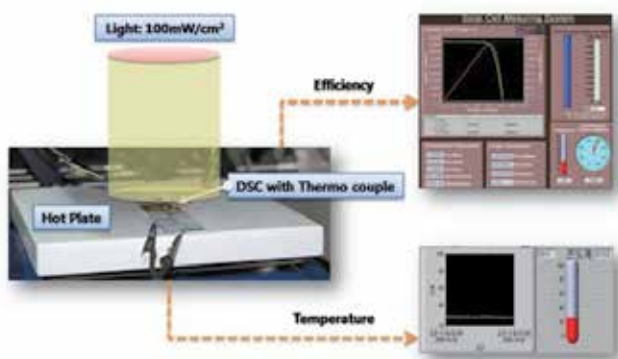
Fig. 25. Schematic design of measurements

Figure 25 shows a schematic diagram of a device for measuring the changes in the efficiency of DSSC according to changing temperature. A hot plate was used as a heat source, and a

resin epoxy was used for sealing to prevent the leakage and evaporation of electrolytes due to exposure to high temperature. To examine the cell efficiency under changing temperature, a thermocouple for measuring temperature was attached to the DSSC. For this thermocouple, the K-type from Omega was used. The change in the efficiency of the solar cell was measured while the temperature was varied from 35°C to 65°C in 5°C steps.

4.2 Performance evaluation of the solar cell by solar concentration rate

The solar cell device was fabricated in such a way to obtain high efficiency by increasing the energy density through solar concentration. The lens for solar concentration was a Fresnel lens with the conventional curved surface of the lens replaced by concentric grooves, and fine patterns were formed on the thin, light plastic surface. Each groove has a refracting surface like a very small prism with a fixed focal distance and a low aberration. Because the lens is thin, it has a low loss from light absorption. A high groove density provides high image quality and a low groove density increases efficiency.
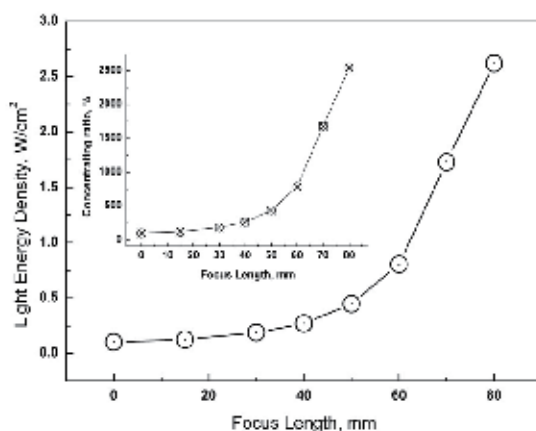
Fig. 26. Energy density due to focus length of Fresnel lens

The focal distances of the Fresnel lens were defined as 15, 30, 40, 50, 60, 70, and 80mm. A power meter was used to measure the concentrated energy density to determine the solar concentration rate for each focal distance. If was found that the energy density increased exponentially as the focal distance increased. As shown in Figure 26, the solar concentration rate at the highest focal distance was approx. 26 times (2.619W/cm^2) the 1sun (100mW/cm^2) condition.

4.3 Results

Figure 27 shows the results of the efficiency of the DSSC measured by different cell temperatures with the solar intensity of 1sun (AM 1.5, 100mW/cm^2). The cell efficiency increased as the cell temperature increased and abruptly dropped from 45°C.

Figure 28 shows the maximum output, maximum output current (I_{mp}) and voltage (V_{mp}) at various temperatures as percentages of the values at 35°C to determine the factors influencing cell efficiency and output. It shows I-V line diagrams comparing the changes of I_{SC} and V_{OC} at different cell temperature. I_{SC} increased as the cell temperature increased and dropped from 55°C while V_{OC} decreased as the temperature increased.
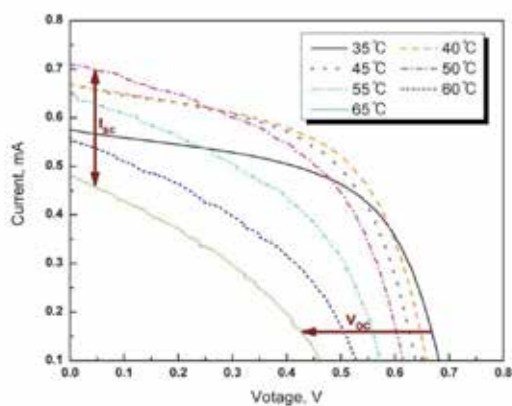
Fig. 27. Comparison of I-V curve due to temperature change
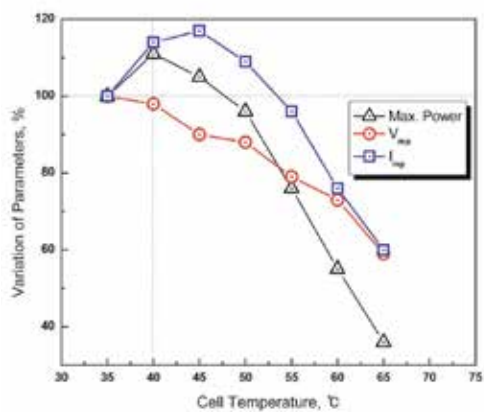
Fig. 28. Performance changes due to temperature change
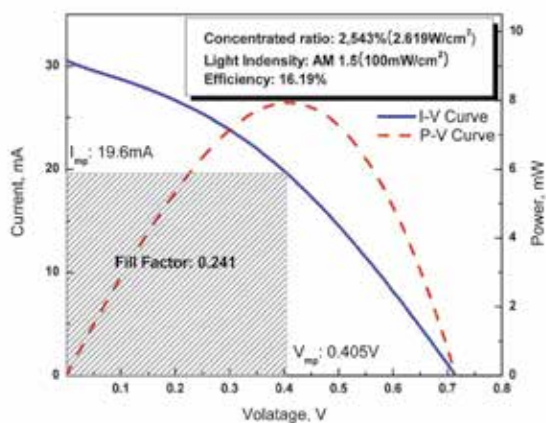
Fig. 29. I-V curves of DSC due to Focus length

The changing efficiency of the DSSC by solar concentration rate was measured at varying focal distances with the prepared lens and stage. Figure 29 shows the I-V line diagrams for each solar concentration rate. When the focal distance was 80mm and the solar concentration was at the maximum of 2,543%, the cell efficiency was 16.2%.
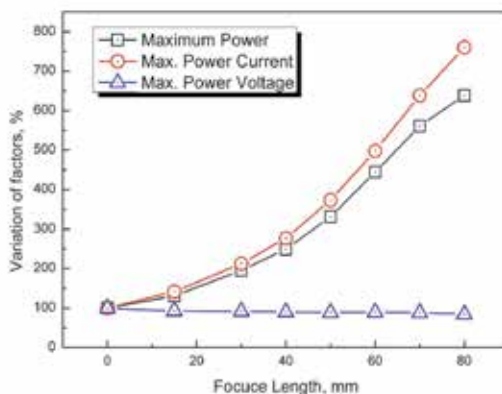
Fig. 30. Performance changes due to focus length

Figure 30 shows the maximum output for each focal distance and the voltage and current changes in percentages at the maximum output to determine the factors influencing efficiency improvement. The maximum output increased as the solar concentration rate increased, indicating cell efficiency improvement. It was found that the increase of current (I_{mp}) by solar concentration had a direct influence.

4.4 Conclusions
This study investigated the changes in efficiency when concentrated solar radiation with high energy density was applied to DSSC to determine the factors influencing efficiency.

- Imp increased as the cell temperature increased and dropped from 45°C while V_{mp} decreased as temperature increased.
- The efficiency of DSSC at changing temperatures was investigated when high heat was generated by solar concentration, and the highest efficiency was obtained at 45°C. As temperature increased over this value, the cell efficiency dropped sharply. Thus, a cooling device is essential when manufacturing a power generation system using solar concentration.
- The high energy density obtained by solar concentration increased the efficiency of DSSC by 6.4 times on average and up to 16.1% by absolute value. Because current density can be increased by solar concentration, it is possible to implement solar cells with a high output.

5. Concentrating system of Dye-sensitized solar cell with a heat exchanger

Conversion efficiency of solar cell is the key point for reducing price to manufacture products. The efficiency is expected to be improved by using the concentrator system, because lost energy density of concentrator system increase in proportion to quantity of concentration.

In this study, the conversion efficiency is expected to be improved by concentrating light which has high energy density through the concentrating lens. In this process, DSC will emit heat at high temperature and make defection like evaporation and leaks of an electrolyte. To protect this problem, we have discussed the way to ensure steady cells by developing the system available to return the heat of the high temperature.

Cell of temperature was maintained 30°C at 1sun(100mW/cm²) condition, Concentrated light density was 2.6W/cm² that is about 26suns. The cell is measured for 480 minutes because it is generally running for 8 hours during a day. On average, the conversion efficiency of the cell is 13. 24%. Finally we conform that the solar cell using concentration system with a heat exchange is available to steady and highly improve the conversion efficiency.

5.1 Concentrating system with a heat exchanger

The dye-sensitized solar cell with concentrated light generates high heat from concentrated light with high density and results in defections such as leakage of electrolyte, evaporation, etc. In order to prevent them, the researcher has installed a cooler under the solar cell and executed stability test. The stability test has a meaning to confirm efficiency change and ensure performance reliability of the cell when they have been exposed to the light for a long time. Figure 31 shows apparatus and conditions used for this test. Efficiencies have been acquired for a certain time period by keeping temperature of the cell at 30°C using the cooler and radiating light with 2.6W/cm² that is 25.4 times of the maximum light concentration under 1sun. Measurement time was 480 minutes considering that the number of hours when the solar cell can be operated during daytime on clean weather us 8 hours.
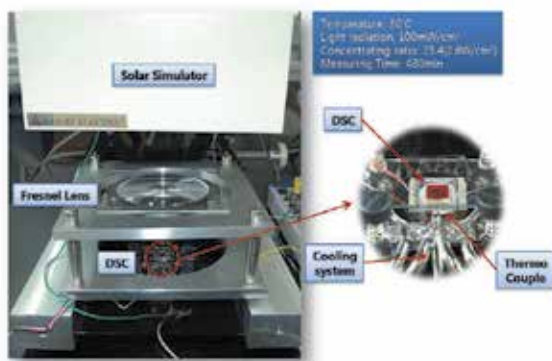
Fig. 31. Equipment for thermal stability test

5.2 Results

In order to measure efficiency change of the dye-sensitized solar cell upon change of light concentration coefficient, efficiencies have been measured according to focal distances using the prepared lens and stage. Figure 32 shows I-V curve of the solar cell upon light concentration coefficients. When the light concentration coefficient is a maximum of 2,543% at 80mm of focal distance, efficiency of the cell showed 16.2%.

Figure 33 shows efficiency changes of the dye-sensitized solar cell for 480 minutes in a graph. As the measurement was started and time passed, the efficiency was linearly reduced

and showed 11.5% after 480 minutes, reduced by 25.6% comparing to 15.4% of initial efficiency. It is considered that it could perform 13.2% of average efficiency over the entire time period. Consequently, it is possible to realize a stable and high efficient solar cell with light concentration utilizing the cooler.
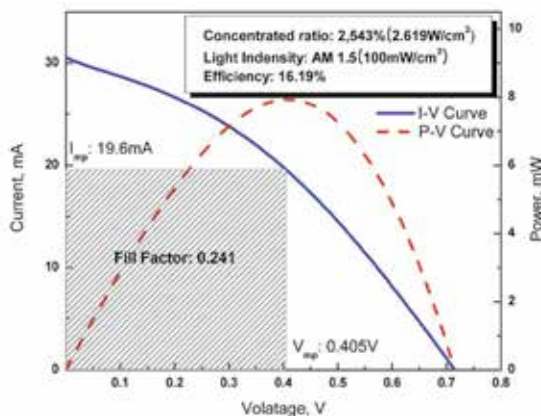
Fig. 32. I-V curves of DSC on Focus length 80mm
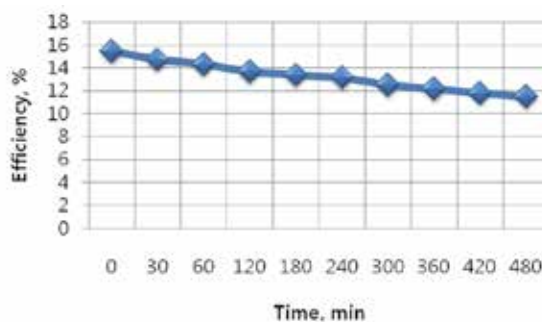
Fig. 33. Efficiency change of DSC due to time

5.3 Conclusion
When concentrating light through the Fresnel lens that has less light loss with thinner than normal lens and may increase energy density with small aberration against focus, it was possible to confirm a maximum light concentration coefficient at 80mm of focal distance.
When keeping a certain temperature (about 30°C) using the cooler, it was possible to get average 13.2% efficiency for 8 hours using the condenser lens. This shows that it would be possible to realize the high efficient dye-sensitized solar cell by making light concentration and cooling system in a module.
Light concentration is mostly advantageous as a practical technology of the high efficient dye-sensitized solar cell. In addition, it is possible to increase comprehensive energy use rate by progressing power generation and heating at the same time as a cogeneration pattern using the high heat generated from light concentration. This has applied light concentration and cooling on the basis of a single cell, but it would be possible to get the higher efficiency from fabrication cost per unit area and operation of the circulation system such as motor, etc. if it will be extended to a large area in a form of a power plant.

6. Acknowledgment

This chapter is composed to be based on my thesis of doctorate and proceedings of conferences.

7. References

Gojny, F. H., Nastalczyk, J., Roslaniec Z., & Sculte, K. (2003). Surface Modified Multi-walled Carbon Nanotubes in CNT/Epoxy-composites, *Chemistry Physical Letters*, Vol. 370, Issues 5-6, pp. 820-824, ISSN:0009-2614

Jijima, S. (1991). Helical Microtubules of Graphitic Carbin. *Nature*, Vol. 354, pp. 56-58 , ISSN:0028-0836

Chang, H., Lee, J., Lee, S., & Lee, Y.(2001). Adsorption of NH_3 and NO_2 Molecules on Carbon-nanotubes, *Applied Physical Letters*, Vol. 79, No. 23, pp. 3863-3865, ISSN:0003-6951

Zhang, J., Yang, G., Sun, Q., Zheng, J., Wang, P., Zhu, Y., & Zhao, X. (2010). The improved performance of dye sensitized solar cells by bifunctional aminosilane modified dye sensitized photoanode. *Journal of Renewable and Sustainable Energy,* Vol. 2, Issue 1, p. 10 , ISSN:1941-7012

Tracey, S., M. Hodgson, S. N. B., Ray, A. K., & Ghassernlooy, Z. (1998). The Role and Interaction of Process Parameters on The Nature of Alkoxide Derived Sol-gel Films. *Journal of Materials Processing Technology*, Vol. 77, pp. 86-94, ISSN:0924-0136

Tachibana, Y. Moser, J. E. Graltzel, M. Klug, D. R. and Durrant ,J. R. (1996). Subpicosecond Interfacial Charge Separation in Dye-Sensitized Nanocrystalline Titanium Dioxide Films. *J. Phys. Chem.* Vol. 100, pp.20056-20062, ISSN: 0022-3654

Chen, Q., Qian, Y., Chen, Z., Zhou, G., & Zhang, Y. (1995). Preparation of TiO_2 Powder with Different Morphologies by An Oxidation-hydrothermal Combination Method. *Materials Letters*, Vol. 22, Issues 1-2, pp.77-80, ISSN: 0167-577X

Ellis, S. K., & McNamara, E. P. Jr. (1989). Powder Synthesis Research at CAMP. *American Ceramic Society bulletin,* Vol. 68, No. 5, pp. 988-991 , ISSN: 0002-7812

Lee, B. M., Shin, D. Y., & Han, S. M. (2000). Synthesis of Hydrous TiO_2 Powder by Dropping Precipitant Method and Photocatalytic Properties. *Journal of Korean Ceramic Society*, Vol. 37,pp. 308-313.

Ding, X. Z., Qi, Z. Z., & He, Y. Z. (1995). Study of the room temperature ageing effect on structural evolution of gel-derived nanocrystalline titania powders. *Journal of Materials Science Letters*, Vol. 15, No. 4, pp.320-322 , ISSN:0059-1650

Johnson, D. W. Jr. (1985). Sol-gel Processing of Ceramics and Glass. *American Ceramic Society bulletin*, Vol. 64, No. 12, pp.1597-1602, ISSN: 0002-7812

Hwang, K. S., & Kim, B. H. (1995). A Study on the Characteristics of TiO_2 Thin Films by Sol-gel Process. *Journal of Korean Ceramic Society*, Vol. 32, pp.281-288

Lee, H. Y., Park, Y. H., & Ko, K. H. (1999). Photocatalytic Characteristics of TiO_2 Films by LPMOCVD. *Journal of Korean Ceramic Society*, Vol. 36, pp.1303-1309

Kim, S. W. (2005). *Die machining with micro tetrahedron patterns array using the ultra precision shaping machine* , PhD. Thesis of Pusan National University

Kim, J. H. (2007). Dye-Sensitized Solar Cell. *News & Information for Chemical Engineers*, Vol. 25, No. 4, p.390

Fischer, J. E., Dai, H., Thess, A., Lee, R., Hanjani, N. M., Dehaas, D. L., & Smalley, R. E. (1997). Metallic resistivity in crystalline ropes of single-wall carbon nanotubes. Physical Review B, Vol. 55, No. 8, pp.4921-4924, ISSN: 0163-1829

Effective Methods for the High Efficiency Dye-Sensitized Solar Cells Based on the Metal Substrates

Ho-Gyeong Yun[1*], Byeong-Soo Bae[2], Yongseok Jun[3] and Man Gu Kang[1]

[1]Convergence Components & Materials Research Lab., Electronics and Telecommunications Research Institute (ETRI), Daejeon,
[2]Lab. of Optical Materials and Coating (LOMC), Dep. of Materials Science and Eng. KAIST, Daejeon
[3]Interdisciplinary School of Green Energy, Ulsan National Institute of Science, Ulsan,
Republic of Korea

1. Introduction

A nano porous dye-sensitized solar cell (DSSC) has been widely studied since its origin by O'Regan and Grätzel.[1] By virtue of many sincere attempts, a conversion efficiency of more than 11%[2] and long-term stability[3] has been achieved using a DSSC with F-doped SnO_2 layered glass (FTO-glass). However, relatively low conversion efficiency of the DSSC, compared with the crystalline Si (24.7%) or thin film CIGS (19.9%), restricts its further applications so far.[4] In order to improve the conversion efficiency of the DSSC, continuous attempts have been made in the past decades. Researchers have concentrated their attention on the working or counter electrode materials, synthesizing dye, additives of the electrolytes, nano-structures for enhancing light scattering and so on.[5-9] However, there have been few reports on the interface between nano-crystalline electrode material and current collecting substrates, in particular on the DSSC with thin and light-weight metal substrates. A DSSC with thin and lightweight substrate could extend its application. However, widely used conductive-layer-coated plastic films such as indium doped tin oxide (ITO) coated polyethylene terephthalate (PET) or polyethylene naphthalate (PEN) film degrade at the TiO_2 sintering temperature of approximately 500 °C. Furthermore, thermal treatment of TiO_2 particles below plastic degeneration temperature causes poor necking of TiO_2 particles, resulting in a low conversion efficiency.[10] Several methods have been tried in order to answer to this problem, such as hydrothermal crystallization,[11] electrophoretic deposition under high DC fields,[12] and low temperature sintering.[13] However, these methods did not show the fundamental solution for the low necking problem. For better attempts, instead of plastic film, previous study has proposed thin metal foil as a substrates.[14-16] A thin metal foil can be a excellent alternative to conductive-layer-coated plastic films, because temperature limitation due to substrate could be eliminated.
Focusing on the characteristics of the interface between nano-sized TiO_2 and metal substrates, this chapter describes several effective methods for the high efficiency DSSCs

based on metal substrates. Briefly, we report a increased light-to-electricity conversion efficiency and decreased electrical resistance of DSSC with the roughened StSt substrate.[17] In addition, an acid treatment of the Ti substrates for nanocrystalline TiO_2 photo-electrode prior to thermal oxidation significantly improved the optical and electrochemical behaviors at the same time, resulting in a highly increased performance in terms of all performance factors, i.e. V_{oc}, J_{sc}, FF, and efficiency.[18] Finally, a synergistic effect of vertically grown TiO_2 nano tube (TiO_2 NT) array and TiO_2 nano powder (TiO_2 NP) would also be introduced.[19] Detailed experimental procedures are not described in this chapter, because they are well explained in the references.

2. StSt and Ti substrates for photo-electrodes of the DSSCs

Considering the work function of the metals, promising metal substrates for DSSCs are Ti, StSt, tungsten (W) and Zinc (Zn)[14] because the work function determine the contact types, i.e. ohmic contact or schottky contact. In case of the n-type semiconductor such as TiO_2, the work function of the metal should be lower than that of semiconductor, ohmic contact. Furthermore, in the metals such as Ti, StSt, W, and Zn, the oxide layer produced by thermal treatment play important roles in the cell properties.[16] However, during thermal treatment, Al, Co, and etc generate insulating oxide layer, which make it insulator. Ti is most desirable metal substrate of the DSSCs because the thermally oxidized layer might have very similar structure with the nano-crystalline TiO_2 layer. The almost same electrochemical impedance of the W with the Ti was also reported. Under the assumption that most of the oxide layer is WO_3, the conduction band energy level of the W locates only 0.15 V below the one of TiO_2, as shown in Fig. 1[16] When the mutual disposition of energy levels is considered, the conduction band energy levels of the facing semiconductor metal oxides overlap.[20, 21] This overlapping does not significantly block the charge carriers flow, and no noticeable increase of the resistance has been reported.[16] However, W is not a common but rare metal. In the case of the StSt, some higher electrochemical impedance than Ti was reported due to conduction band energy level mismatch. However, StSt is most common and cost-effective material for the substrates of the DSSCs. Therefore, Ti and StSt are most frequently focused at the realization of the DSSCs on the metal substrates.[22-26]
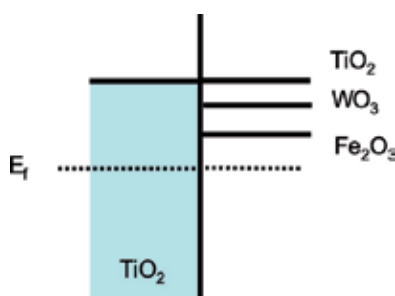
Fig. 1. Diagram of the conduction band edges of the semiconductor metal oxides. © The Electrochemical Society[16].

3. StSt substrate: effect of increased surface area[17]

The injection process used in the DSSC does not introduce a hole, i.e. minority carriers, in the TiO_2, only an extra electron.[27] On the contrary, as majority carriers and minority

carriers, electrons and holes co-exist in *p-n* junction type solar cell, causing high electron/hole recombination rate. Therefore, in order to decrease the emitter recombination as much as possible, point-contact solar cells were introduced.[28, 29] In this paragraph, however, we report increased conversion efficiency and decreased electrical resistance of DSSCs with the roughened StSt substrates. Sulfuric acid-based solutions are effective StSt pickling reagents.[30] Additives, such as hydrated sodium thiosulphate and propargyl alcohol, endowed the StSt with pores and increased the surface area.[31] Under the atomic force microscope (AFM) analysis, the actual surface area of the roughened StSt substrates were measured to be a 23.6% increase. (Fig. 2)
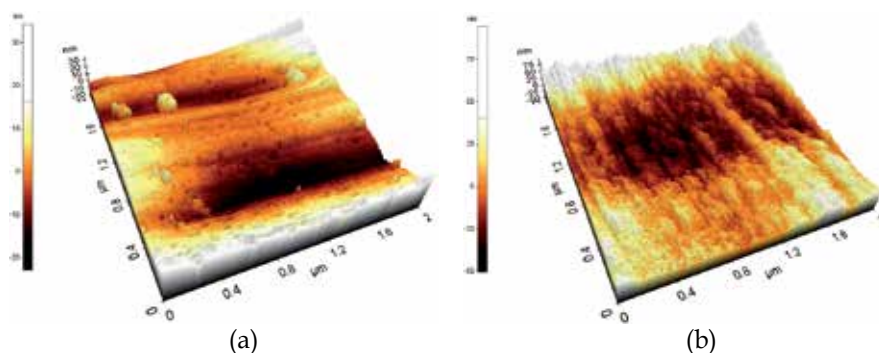
Fig. 2. AFM images of StSt surface (a) before and (b) after roughening process. © American Institute of Physics[17].
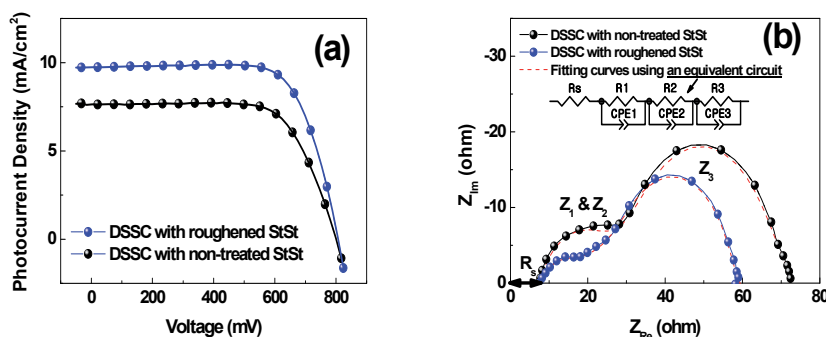
Fig. 3. Under AM 1.5 irradiation (100 mW/cm^2) with a xenon lamp. (a) *J-V* curves of DSSC with nontreated StSt substrates and roughened StSt substrates. (b) Electrochemical impedance spectra measured at the frequency range of 10^{-1}–10^6 Hz and fitting curves using an equivalent circuit model including three CPEs. © American Institute of Physics[17].

The *J-V* characteristics of the DSSCs with non-treated and roughened StSt substrates are shown in Fig. 3. (a). After roughening, the conversion efficiency and J_{sc} of the DSSC increased 33% and 27% respectively. However, open circuit voltage (V_{oc}) and fill factor (*FF*) remained nearly constant. V_{oc} changed from 800 mV to 807 mV and *FF* varied from 70.3% to 72.4% after roughening. To identify the cause of the increased J_{sc} and efficiency, electrochemical impedance spectra were measured in the frequency range of 10^{-1} to 10^6 Hz

and the resistance from electrochemical impedance spectra was estimated using the equivalent circuit model including 3 constant phase elements (CPEs). (Fig. 3. (b)) Even though there were small differences in R_2 and R_3 after roughening, R_1 was reduced from 17.1 to 3.9. The largely reduced R_1 clearly comes from the reduced electrical resistance of the TiO_2/StSt interface because R_1 represents the electrical resistance at this interface.[32] Considering the same electrical resistance between the TiO_2 particles and the interface with the Pt/electrolyte in DSSCs with both non-treated and roughened substrates, the small difference of R_2 after roughening is expected result. The value of R_3 is closely related to the reverse electron transfer from TiO_2 to the electrolyte.[32] In detail, as the number of electrons returning to the electrolyte increases, the arc of Z_3 increases. Therefore, the fact that R_3 remains unchanged after roughening clearly indicates that the increased electrical contact area does not cause an increase in reverse electron transfer.

4. Ti substrate: a simple surface treating method[18]

In this paragraph, we report that acid (HNO_3-HF) treatment of the titanium (Ti) substrate for the photo-electrode significantly improved the efficiency of DSSCs. Prior to spreading the TiO_2 paste, the Ti substrates were chemically treated with HNO_3-HF solution. As shown in Fig. 4 (a) and (b), HNO_3-HF treatment caused sharp steps at the grain boundaries, due to different etching rates of dissimilar crystal structures between the grains and the grain boundaries.[33] Fig. 5 (a) ~ (c) shows the cross-sectional scanning transmission electron microscopy (STEM) images of the Ti substrates. On the outermost surface, the non-treated Ti substrate exhibited a finer-grained structure. This suggests that the outermost surface of the Ti substrate was composed of finer-grained disordered Ti, which resulted from the thermo-mechanical manufacturing process.[34] However, treatment of the Ti substrate with the HNO_3-HF solution completely removed this finer-grained disordered region. Furthermore, the thermally oxidized layer of the non-treated substrate was much thicker and more variable than that of the HNO_3-HF-treated substrates. (Fig. 5 and 6) In the field emission transmission electron microscope (FE-TEM) analysis, the oxidized layer of the non-treated Ti substrate, which was produced by oxygen diffusion to the finer-grained disordered region, showed a disordered grain structure, i.e. a low degree of crystallinity. However, the oxide layer of HNO_3-HF-treated Ti substrates, which was developed by the oxygen diffusion into the normally-grained Ti substrate, was almost a single crystal. The corresponding X-ray diffraction (XRD) patterns also showed that the HNO_3-HF treatment had produced a variation on the phase and crystallinity of a thermally oxidized layer.
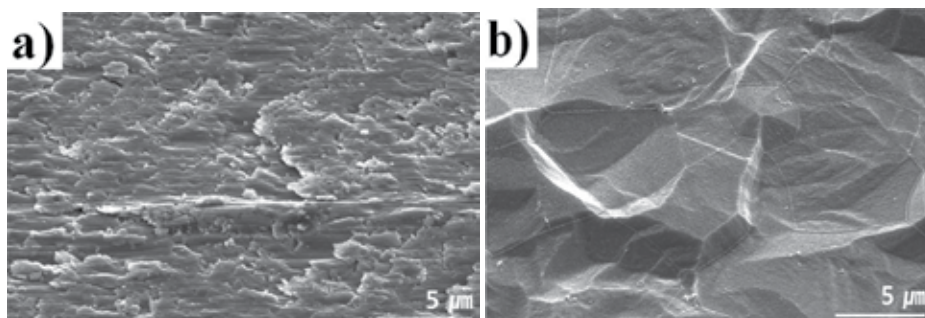
Fig. 4. SEM images of the Ti surface before thermal annealing: (a) non-treated, (b) HF-HNO3 treated. © WILEY-VCH Verlag GmbH & Co. KGaA, Weinheim[18].
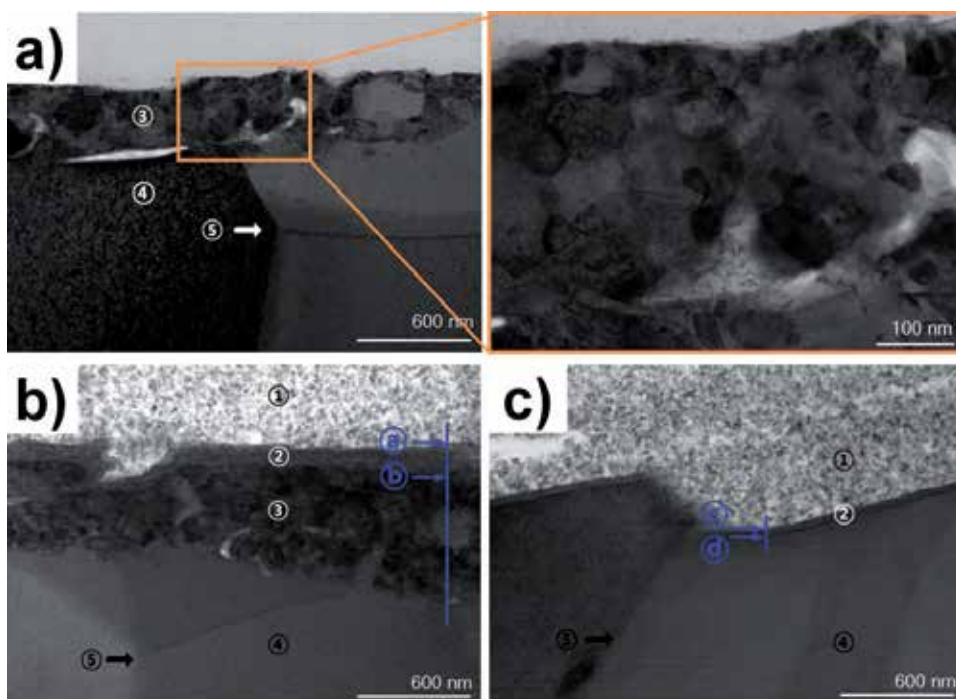
Fig. 5. Cross-sectional STEM images of Ti substrates (a) untreated substrate before thermal annealing, including a magnified view of the finer grained disordered region, (b) untreated substrate after thermal annealing at 550 °C for 30 min, (c) HF-HNO₃-treated substrate after thermal annealing. Note: ① sintered TiO_2 particles, ② thermally oxidized Ti, ③ finer-grained disordered Ti, ④ normally grained Ti, ⑤ normal grain-boundaries of Ti. © WILEY-VCH Verlag GmbH & Co. KGaA, Weinheim[18].
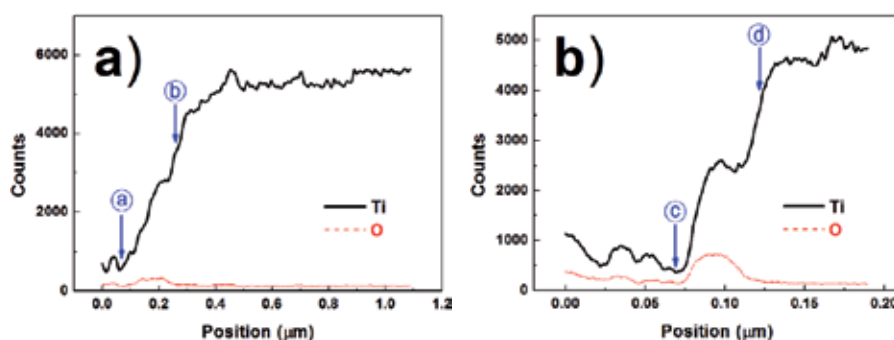
Fig. 6. EDX graph of (a) a line-scan shown in Fig. 5 (b), (b) a line-scan shown in Fig. 5 (c). © WILEY-VCH Verlag GmbH & Co. KGaA, Weinheim[18].
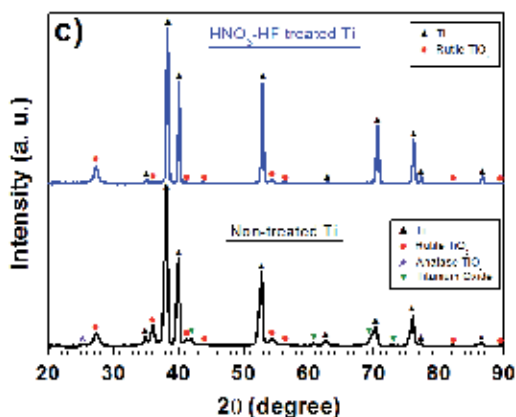
Fig. 7. By use of a 2θ scan method, XRD patterns of non-treated and HNO₃-HF-treated Ti substrates after thermal annealing at 550 °C for 30 min. © WILEY-VCH Verlag GmbH & Co. KGaA, Weinheim[18].

As shown in Fig. 7, the thermally oxidized layer of the non-treated Ti substrate exhibited various oxide forms including anatase TiO_2, rutile TiO_2, and titanium oxide. However, only rutile TiO_2 was observed in the oxide layer of the HNO₃-HF-treated Ti substrate.

The variation of the microstructures influenced the optical and electrochemical behaviour at the same time resulting in highly increased efficiency, 9.20%. (Fig. 8 (d)) Fig. 8 (a) shows the optical reflection of the Ti. The HNO₃-HF-treated substrate exhibited a significantly increased optical reflection. The low and flat reflection behavior of the non-treated Ti substrates could be attributed to the thick and non-uniform thickness of the oxide layer and the inferior optical reflectance at the inner metal surface.[35, 36] In the evaluation of the illumination intensity effect on the performance factors, the V_{oc} and J_{sc} exhibited logarithmic and linear dependence respectively. However, FF decreased under stronger illumination intensity. These consequences suggest that the improved performance of the DSSC with the HNO₃-HF-treated substrate cannot be attributed to the enhanced optical reflection alone. Rather, the greater part of this improvement could be attributed to a reduced back reaction of the electrons with I_3^- ions at the interface of the conductive substrate and electrolyte because the thickness of the nano crystalline TiO_2 layer is about 15μm. For a device with a > 10 μm thick TiO_2 layer, performance increases due to reflection are restricted to wavelengths above 580 nm where the absorption of the N719 dye is weak.[15]

The blocking layer (compact TiO_2) at the interface of the TiO_2 particles/conductive substrates has been studied[37, 38] and several groups concluded that recombination occurs predominantly near the conductive substrate and not across the entire TiO_2 film.[39] In the DSSCs with metal substrates, the oxidized layer is naturally formed at the interface of the TiO_2 particles/conductive substrate during thermal annealing. However, it seems that the low quality oxidized layer induced poor blocking behavior of the DSSCs with the non-treated Ti substrates. The recombination kinetics were investigated by the evaluation of the rate of photovoltage decay. The rate of photovoltage decay is inversely proportional to the lifetime of the photoelectron in the DSSCs, and the lifetime of the electron is inversely proportional to the rate of recombination.[40] The HNO₃-HF treatment of the Ti substrates strongly influenced the rate of the photovoltage decay. (Fig. 8 (b)) The electron recombination may lead to a lowering of the photocurrent, but also to a decrease in the

photovoltage by lowering the quasi-Fermi level for the electrons under illumination due to a kinetic argument.[41, 42] Furthermore, the *FF* is a measure of the increase in recombination (decrease in photocurrent) with increasing photovoltage.[43] If the improved optical reflection at the substrate were a dominant element of enhanced performance, the V_{oc} and *FF* would restrictively increase and decrease respectively. An obviously possible cause for the significantly improved performance is decreased recombination at the interface of the TiO_2/conductive substrate after HNO_3-HF treatment.
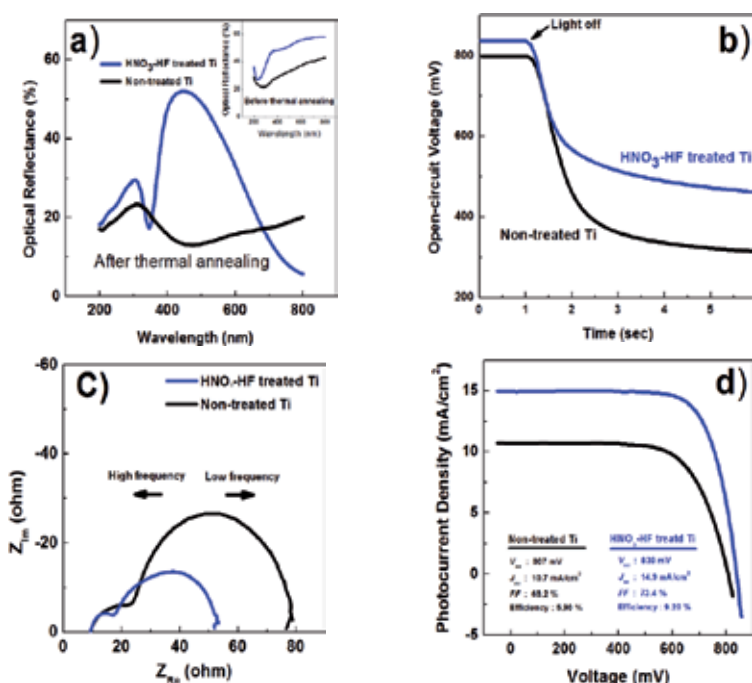
Fig. 8. (a) Optical reflectance of Ti substrates measured with UV-VIS-NIR spectro-photometers combined with an integrated sphere before and after thermal annealing at 550 °C for 30 min. Baseline calibration was performed with a standard specimen composed of polytetrafluoroethylene (PTFE). (b) open-circuit voltage decay measurement, (c) electrochemical impedance spectra, and (d) J-V curves of DSSC with non-treated and HNO_3-HF-treated Ti substrates. © WILEY-VCH Verlag GmbH & Co. KGaA, Weinheim[18].

As shown in Fig. 8 (c), electrochemical impedance also improved after HNO_3-HF treatment. The 1st semicircle is closely related to charge transfer at the counter electrode and/or electrical contact between conductive substrate/TiO_2 or TiO_2 particles.[22] The relatively small size of the 1st semicircles (high frequency range) in the cell with the HNO_3-HF-treated substrate indicated a reduced electrical resistance, i.e. improved contact at the TiO_2/Ti interface accordingly. Furthermore, the size of the 2nd semicircle (low frequency range) was also largely decreased. The 2nd semicircle is related to the recombination of electrons with I_3^-.[14] Under the assumption that the micro-structures of the oxidized layers determine the blocking ability, the significantly decreased size of the 2nd semicircle could be attributed to a highly decreased charge recombination by virtue of improved micro-structure after HNO_3-HF treatment of the Ti substrate.

5. Hybrid substrate: TiO₂ NP on the TiO₂ NT grown Ti substrates[19]

In the case of DSSCs based on metal substrates, light illumination should come from a counter electrode, i.e., back illumination. Therefore, the light scattering layer,[9] which enhances the optical path length, should be located between 20 nm sized TiO_2 nano-particles (NPs) and conductive substrates. This structure causes poor adhesion due to the large particle size of the scattering layer. Considering slow recombination and light scattering,[44] TiO_2 nano-particles has been incorporated on the short TiO_2 nano-tube grown Ti substrates. The preparation of photo-electrode is completed by four steps: ① anodization of a Ti foil for the formation of short TiO_2 NT arrays, ② doctor blading of TiO_2 NP included paste on the TiO_2 NT formed Ti substrates, ③ thermal treatment of the photo-electrode prepared by step ① & ②, ④ dye coating. In our approach, therefore, the fabrication time and length of TiO_2 NT could be minimized without diminishing, rather increasing, the surface area of the photo-electrode.
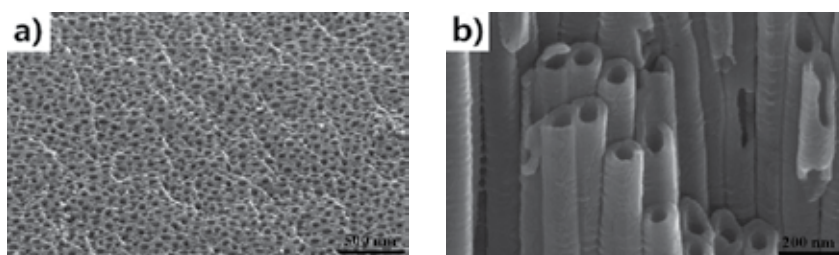
Fig. 9. SEM images of the TiO_2 NT fabricated Ti for 30 min anodizing (a) surface and (b) cross-section. © The Royal Society of Chemistry[19].

Out of several fabrication method of the TiO_2 NT such as electrochemical anodizing,[45] hydrothermal synthesis,[46] and template-assisted synthesis,[47] anodizing is a relatively simple approach for the preparation of optimized TiO_2 NT.[48] Anodizing at 50 V in a solution of ethylene glycol containing ammonium fluoride (NH_4F) resulted in the formation of regular TiO_2 NT arrays. (Fig. 9) When the anodizing was performed for 30 min, the tube diameter and wall thickness were estimated to be about 100 and < 50 nm, respectively. The lengths of the TiO_2 NT layers were controlled by the anodizing time. When the anodizing was performed for 15, 30, and 60 min, the lengths of the TiO_2 NTs were 1.53, 4.36, and 8.17 μm, respectively. TiO_2 NT and TiO_2 NP bonded well following thermal annealing at 550 °C for 30 min. (Fig. 10)
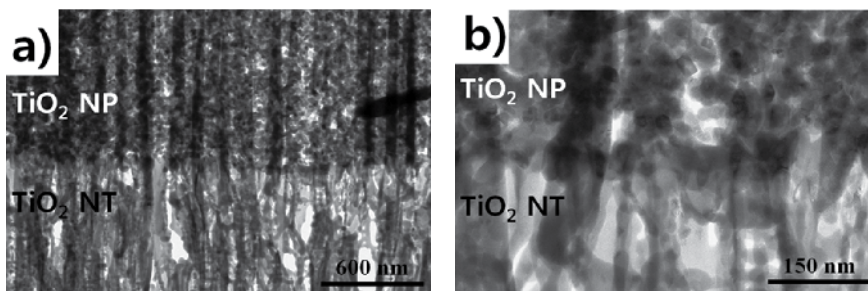
Fig. 10. Cross-sectional TEM images of (a) interface between TiO_2 NP and TiO_2 NT (b) magnified view of (a). © The Royal Society of Chemistry[19].

As is same with the previous paragraph, the TiO_2 NP film was made 15 μm thick, because that was the size that allowed DSSCs to exhibit optimal performance. When the thickness of the TiO_2 NP was more than 15 μm, the DSSC with TiO_2 NP on the Ti substrate (TiO_2 NP/Ti) exhibited a lowered performance because the thick TiO_2 layer (> 15 μm) provided additional electron recombination sites, resulting in a decreased open-circuit voltage (V_{oc}) and fill factor (FF).[49] However, a performance of the DSSCs with TiO_2 NP+NT/Ti increased continuously with increasing TiO_2 NT thickness up to 30 min anodized TiO_2 NT. (Fig. 11 (a)) This difference between the DSSC with TiO_2 NP+NT/Ti and the DSSC with TiO_2 NP/Ti can be attributed to the TiO_2 NT having an electron recombination that was reduced by comparison with the TiO_2 NP. The electron lifetime in the TiO_2 NT was longer than that in the TiO_2 NP because of the electron-recombination suppression from the reduction in electron-hopping across the inter-crystalline contacts between the grain boundaries.[50] As is described in the previous paragraph, optical transmission is restricted to wavelengths > 570 nm for a device with a TiO_2 layer that is more than 10 μm thick, resulting in a restricted increase in J_{sc}.[15] However, strong internal light scattering within the TiO_2 NTs elongated the path length of the long-wavelength incident light to promote the capture of photons by the dye molecules.[44] Despite a surface area of the DSSC with TiO_2 NP on 30-min-anodized TiO_2 NT/Ti that was smaller than that of DSSC with 20 μm thick TiO_2 NP/Ti, the increased J_{sc} could also be a result of stronger light scattering effects.

The reduced electron recombination at the interface of the TiO_2 NT/electrolyte was also represented in an electrochemical impedance measurement (Fig. 11 (b)). Under the assumption that the TiO_2 NT is superior to TiO_2 NP in the interfacial contact with Ti substrates due to the *in-situ* fabrication process, the largely reduced size of the 1st semicircle in a DSSC with TiO_2 NP+NT/Ti could be a result of the reduced electrical resistance at the interfacial contact. However, the size of the 2nd semicircle (low frequency range) was almost the same. The 2nd semicircle represents the recombination of injected electrons to the TiO_2 film with electrolyte.[51] Furthermore, the DSSCs with TiO_2 NP/Ti and TiO_2 NP+NT/Ti exhibited a similar rate of photovoltage decay, which is proportional to the rate of recombination (Fig. 11 (c)). The overall TiO_2 film in the DSSC with TiO_2 NP+NT/Ti was thicker than that of the DSSC with TiO_2 NP/Ti due to the introduction of the TiO_2 NT layer at the interface of the TiO_2 NP and Ti substrate. Therefore, it seems that the small variation in the 2nd semicircle in the electrochemical impedance spectra and the rate of photovoltage decay can be attributed to the slow recombination characteristics of the TiO_2 NT.
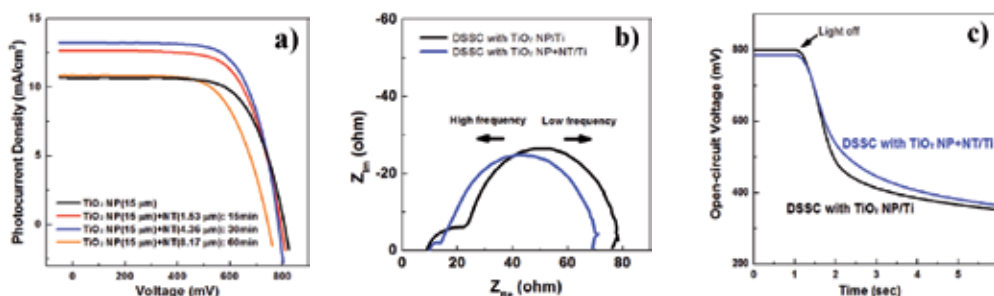
Fig. 11. (a) *J–V* characteristics of the DSSC with TiO_2 NP/Ti and TiO_2 NP + NT/Ti. (b) Electrochemical impedance spectra in frequencies ranging from 10^{-1} to 10^6 Hz. (c) Open-circuit voltage decay measurement. © The Royal Society of Chemistry[19].

6. Conclusion

Several methods for the high efficiency DSSCs based on the metal substrates have been introduced. In the case of the StSt substrate, the solar cell performance was significantly improved by the roughening process, which enhances electrical contact by roughening the substrates. In addition, when a Ti substrate was treated with an acid solution, both the surface morphology and the crystalline structure of the thermally oxidized layer were varied, resulting in the simultaneous improvements in V_{oc}, J_{sc} and FF. Finally, the DSSCs with TiO$_2$ NP + NT/Ti were prepared for the synergistic effect of vertically grown TiO$_2$ NTand TiO$_2$ NP films. The slow electron recombination at the interface of the TiO$_2$ NT/electrolyte and the light scattering effect might have simultaneously contributed to DSSC performance, resulting in the improved Jsc and conversion efficiency with only a negligible effect on the V_{oc} and FF.

7. Acknowledgements

8. References

[1] B. O'Regan, M. Grätzel, *Nature* 353, 737 (1991)

[2] M. K. Nazeerudden, P. Pechy, T. Renouard, S. M. Zakeeruddin, B. R. Humphry, P. Comte, P. Liska, L. Cevey, E. Costa, V. Shklover, L. Spiccia, G. B. Deacon, C. A. Bignozzi, M. Grätzel, *J. Am. Chem. Soc.* 123, 1613 (2001)

[3] P. Wang, S. M. Zakeeruddin, J. E. Moser, K. Nazeeruddin, T. Sekiguchi, M. Grätzel, *Nat. Mat.* 2, 402 (2003)

[4] M. A. Green, K. Emery, Y. Hishikawa, W. Warta, *Progress in Photovoltaics* 17, 320 (2009)

[5] Y. J. Kim, M. H. Lee, H. J. Kim, G. Lim, Y. S. Choi, N. -G. Park, K. Kim, W. I. Lee, *Adv. Mater.* 21, 3668 (2009)

[6] A. Nattestad, A. J. Mozer, M. K. R. Fischer, Y. –B. Cheng, A. Mishra, P. Bäuerle, U. Bach, *Nature Mater.* 9, 31 (2010)

[7] F. Gao, Y. Wang, J. Zhang, D. Shi, M. Wang, R. Humphry-Baker, P. Wang, S. M. Zakeerudding, M. Grätzel, *Chem. Commun.* 2635 (2008)

[8] M. Wang, X. Li, H. Lin, P. Pechy, S. M. Zakeeruddin, M. Grätzel, *Dalton Trans.* 10015 (2009)

[9] S. Ito, S. M. Zakeeruddin, R. Humphry-Baker, P. Liska, R. Charvet, P. Comte, M. K. Nazeeruddin, P. Péchy, M. Takata, H. Miura, S. Uchida, M. Grätzel, *Adv. Mater.* 18, 1202 (2006)

[10] C. Y. Jiang, X. W. Sun, K. W. Tan, G. Q. Lo, A. K. K. Kyaw, D. L. Kwong, *Appl. Phys. Lett.* 92, 143101 (2008)

[11] D. Zhang, T. Yoshida, H. Minoura, *Adv. Mater.* 15, 814 (2003)

[12] D. Mattews, A. Kay, M. Grätzel, *Aust. J. Chem.* 47, 1869 (1994)

[13] C. Longo, A. F. Nogueira, M. A. De Paoli, H. Cachet, *J. Phys. Chem. B* 106, 5925 (2002)

[14] M. G. Kang, N. G. Park, K. S. Ryu, S. H. Chang, K. J. Kim, *Sol. Energy Mater.Sol. Cells* 90, 574 (2006)

[15] Y. Jun, J. Kim, M. G. Kang, *Sol. Energy Mater. Sol. Cells* 91, 779 (2007)

[16] Y. Jun, M. G. Kang, *J. Electrochem. Soc.* 154, B68 (2007)

[17] H. -G. Yun , Y. Jun , J. Kim , B. -S. Bae , M. G. Kang , *Appl. Phy. Lett.* 93, 133311 (2008)

[18] H. -G. Yun , B. -S. Bae, M. G. Kang , *Advanced Energy Materials* 1, 1 (2011)

[19] H. -G. Yun , J. H. Park , B. -S. Bae , M. G. Kang , *J. Mater. Chem.* 21, 3558 (2011)

[20] M. K. Kang, N. G. Park, S. R. Kwang, H. C. Soon, K. J. Kim, *Chem. Lett.* 34, 804 (2005)

[21] H. H. Kung, H. S. Jarrett, A. W. Sleight, A. Ferretti, *J. Appl. Phys.* 48, 2463 (1977)

[22] J. H. Park, Y. Jun, H. –G. Yun, S. –Y. Lee, M. G. Kang, *J. of Electrochem. Soc.* 155, F145 (2008)

[23] H. Lindström, A. Holmberg, E. Magnusson, S. Lindquist, L. Malmqvist, A. Hagfeldt, *Nano Lett.* 1, 97 (2001)

[24] S. Uchida, M. Tomiha, H. Takizawa, M. Kawaraya, *J. of Photochem. and Photobio. A: Chem* 164, 93 (2004)

[25] T. Miyasaka, Y. Kijitori, *J. of Electrochem. Soc.* 151, A1767 (2004)

[26] M. Dürr, A. Schmid, M. Obermaier, S. Rosselli, A. Yasuda, G. Nells, *Nature Mat.* 4, 607 (2005)

[27] J. N. Hart, Y. -B. Cheng, G. P. Simon, L. Spiccia, *J. of Nanoscience and Nanotech.* 8, 2230 (2008)

[28] T. Markvat, L. Castaner, Solar Cells: Materials, Manufacture and Operation, Elsevier Science, Oxford, 377 (2005)

[29] R. M. Swanson, S. K. Beckwith, R. A. Crane, W. D. Eaides, Y. O. Kwark, R. A. Sinton, S. E. Swiiwiun, *IEEE Trans. on Elec. Dev.* 31, 5 (1984)

[30] A. Tamba, N. Azzerri, *J. App. Electrochem.* 2, 175 (1972)

[31] S. E. Hajjaji, M. E. Alaoui, P. Simon, A. Guenbour, A. Ben Bachir, E. Puech-Costes, M. T. Maurette, L. Aries, *Sci. and Tech. of Adv. Mat.* 6, 519 (2005)

[32] T. Hoshikawa, M. Yamada, R. Kikuchi, K. Eguchi, *J. Electrochem. Soc.* 152, E68 (2005)

[33] J. Lichtscheidl, K. J. Hartig, N. Getoff, C. Tauschnitz, G. Nauer, *Z. Naturforsch. A* 36a , 727 (1981)

[34] P. R. F. Barnes, L. K. Randeniya, P. F. Vohralik, I. C. Plumb, *J. Electrochem. Soc.* 154 , H249 (2007)

[35] G. Jerkiewicz, H. Strzelecki, *Langmuir* 12, 1005 (1996)

[36] J. –L. Delplancke, M. Degrez, A. Fontana, R. Winand, *Surface Tech.* 16 , 153 (1982)

[37] J. Xia, N. Masaki, K. Jiang, S. Yanagida, *Chem. Commun.* 138 (2007)

[38] B. Peng, G. Jungmann, C. Jäger, D. Haarer, H.-W. Schmidt, M. Thelakkat, *Coord. Chem. Rev.* 248, 1479 (2004)

[39] K. Zhu, E. A. Schiff, N. -G. Park, J. V. D. Lagemaat, A. J. Frank, *Appl. Phys. Lett.* 80, 685 (2002)

[40] A. Zaban, M. Greenshtein, J. Bisquetr, *Chem. Phys. Chem* 4, 859 (2003)

[41] Hagfeldt, M. Grätzel, *Chem, Rev.* 95, 49 (1995)

[42] Kumar, P. G. Santangelo, N. S. Lewis, *J. Phys. Chem.* 96, 834 (1992)

[43] D. Cahen, G. Hodes, M. Grätzel, J. F. Guillemoles, I. Riess, *J. Phys. Chem. B* 104, 2053 (2000)

[44] K. Zhu, N. R. Neale, A. Miedaner, A. J. Frank, *Nano Lett.* 7, 69 (2007)

[45] D. Gong, C. A. Grimes, O. K. Varghese, W. C. Hu, R. S. Singh, Z. Chen, E. C. Dickey, *J. Mater. Res.* 16, 3331 (2001)

[46] T. Kasuga, M. Hiramatsu, A. Hoson, T. Sekino, K. Niihara, *Langmuir* 14, 3160 (1998)

[47] P. Hoyer, *Langmuir* 12, 1411 (2006)
[48] G. K. Mor, K. Shankar, M. Paulose, O. K. Varghese, C. A. Grimes, *Nano Lett.* 5, 191 (2005)
[49] R. Kato, A. Furube, A. V. Barzykin, H. Arakawa, M. Tachiya, *Coord. Chem. Rev.* 248, 1195 (2004)
[50] C.-J. Lin, W.-Y. Yu, S.-H. Chien, *Appl. Phys. Lett.* 93, 133107 (2008)
[51] T. Hoshikawa, M. Yamada, R. Kikuchi, K. Eguchi, J. Electrochem. Soc. 152, E68 (2005)

Dye Solar Cells: Basic and Photon Management Strategies

Lorenzo Dominici[1,2] et al.[*]
[1]Centre for Hybrid and Organic Solar Energy Centre (CHOSE), Dept. of Electronic Eng.,
Tor Vergata University of Rome, Roma
[2]Molecular Photonics Laboratory, Dept. of Basic and Applied Physics for Eng.,
SAPIENZA University of Rome, Roma
Italy

1. Introduction

After the introduction in 1991 by B. O'Regan and M. Grätzel, Dye Solar Cells (DSCs) have reached power conversion efficiency values over small area device as high as 11%. Being manufactured with relatively easy fabrication processes often borrowed from the printing industry and utilizing low cost materials, DSC technology can be considered nowadays a proper candidate for a large scale production in industrial environment for commercial purposes.

This scenario passes through some challenging issues which need to be addressed such as the set-up of a reliable, highly automated and cost-effective production line and the increase of large area panels performances, in terms of efficiency, stability and life-time of the devices.

In this work, an overview of the most utilized DSCs materials and fabrication techniques are highlighted, and some of the most significant characterization methods are described. In this direction, different approaches used to improves devices performances are presented.

In particular, several methods and techniques known as Light Management (LM) have been reported, based to the ability of the light to be confined most of the time in the cell structure. This behavior contributes to stimulate higher levels of charge generation by exploiting scattering and reflection effects.

The use of diffusive scattering layers (SLs), nanovoids, photonic crystals (PCs), or photoanodes co-sensitization approaches consisting in the use of two Dyes absorbing in two different parts of the visible range, have been demonstrated to be effective strategies to carry out the highest values of device electrical parameters.

Finally, to increase the light path inside the DSCs active layer, the use of refractive element on the topside (a complementary approach to SL) has been shown a promising possibility to further improve the generated photocurrent.

[*]Daniele Colonna[1], Daniele D'Ercole[1], Girolamo Mincuzzi[1], Riccardo Riccitelli[3], Francesco Michelotti[2], Thomas M. Brown[1], Andrea Reale[1] and Aldo Di Carlo[1]
1 Centre for Hybrid and Organic Solar Energy Centre (CHOSE), Dept. of Electronic Eng., Tor Vergata University of Rome, Roma, Italy
2 Molecular Photonics Laboratory, Dept. of Basic and Applied Physics for Eng., SAPIENZA University of Rome, Roma, Italy
3 DYERS srl, Roma, Italy

2. Material and processing for dye solar cell technology

Since the introduction and development of the dye-sensitized solar cell (DSC) (O'Regan & Graetzel, 1991) several efforts have been made to optimize the materials involved in the photo-electrochemical process and to improve the light conversion efficiency of the device (Hagfeldt & Graetzel, 1995), by exploiting a low cost production process based on simple fabrication methods, similar to those used in printing processes.

2.1 Dye solar cells architecture and working principle

In Fig. 1 the basic configuration of a Dye Solar Cell (DSC) is sketched (Chappel et al., 2005). Amongst the main elements of this electrochemical photovoltaic device is a mesoporous nanocrystalline Titanium Dioxide (nc-TiO$_2$) film deposited over a transparent and conductive layer coated glass (in particular Soda Lime or Borosilicate). As alternative to the nc-TiO$_2$, other large band-gap semiconductors (such as ZnO, Nb$_2$O$_5$, and SrTiO$_3$) can be utilized as well as flexible and plastic (PET or PEN) substrates are a valid options in substitution of the glass. Generally, the nc-TiO$_2$ film thickness is fixed to a value comprised between few microns to few tens of microns and the substrates conductivity is provided by a transparent conducting oxide (TCO) coating. Fluorine doped tin oxide (SnO$_2$:F), FTO is the most commonly used (although Tin doped Indium Oxide (In$_2$O$_3$:SnO$_2$) ITO is frequently found onto plastic substrates) since enables low cost massive production of substrates showing a sheet resistance as low as 8 Ωcm^{-2} (Solaronix®).

On the surface of the TiO$_2$, a monolayer of visible light harvesting dye molecules is adsorbed resulting in the TiO$_2$ visible light sensitizing. A wide variety of dye molecules, included naturals dyes extracted from fruits flowers or leaves, have been proposed and tested (Polo et al., 2004; Kalyanasundaram & Graetzel, 1998). At the moment metallorganic ruthenium complexes containing anchoring groups such as carboxylic acid, dihydroxy, and phosphonic acid on pyridyl ligands show the best performances. Largely diffused are in particular dyes commonly named as N3, black dye, N719 and Z907, which enable fabrication of highly performing devices (Kroon et al., 2007; Nazeeruddin et al., 2005; Z. S. Wang et al., 2005).
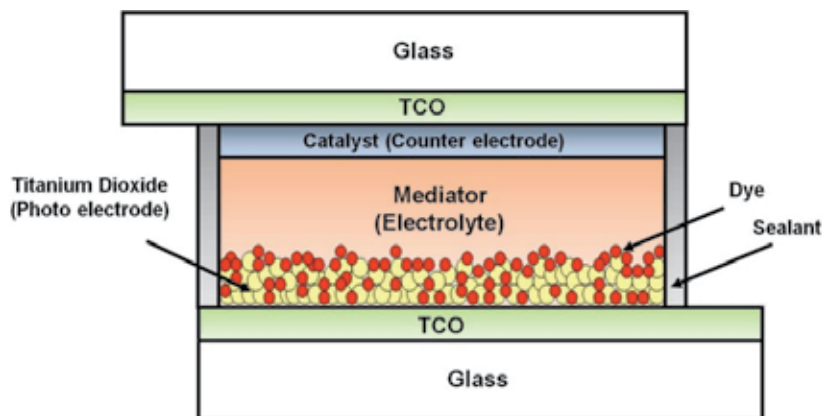
Fig. 1. Dye Solar Cell Structure. Basic cell's constituent are a transparent conductive substrate (TCO) coated glass and over it a nc-TiO$_2$ layer sensitized by a monolayer of adsorbed dye (photo-electrode), a red-ox mediator and, finally a catalyst (Pt) coated conductive substrate (counter-electrode).

It is worth to point out that the nc-TiO$_2$ mesoporous morphology (Fig. 2), for a film thickness of 10 μm, leads to an effective surface area about 1000 times larger as compared to a bulk TiO$_2$ layer, allowing for a significantly large number of sites offered to the dye sensitizer (Chen & Mao, 2007).
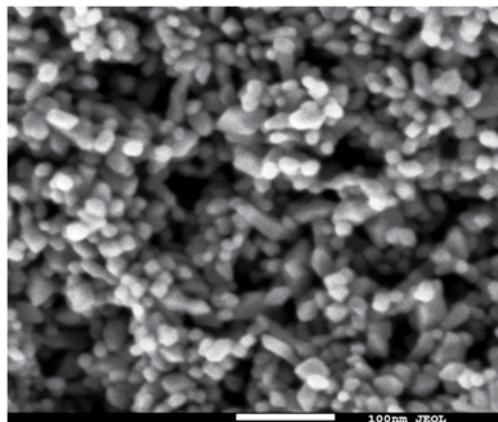
Fig. 2. A SEM image of nc-TiO$_2$ film utilized for Dye Solar Cells fabrication is shown. Although is possible to distinguish each nanoparticles (with a diameter of around 20 nm) large aggregates are evident resulting in a characteristic meso-porous morphology (Mincuzzi et al., 2011).

The conductive substrate together with the dye sensitized film form the cell photo-electrode. The dye sensitized film is placed in contact with a red-ox mediator electrolyte or an organic hole conductor material. The former is obtained solving a red-ox couple (such for instance the ions I$_3^-$/ I$^-$ or Co$^{(III)}$/Co$^{(II)}$) in a solvent such as 3-me-thoxypropionitrile (MPN), acetonitrile (ACN) or valeronitrile (VN). Finally the device is completed with a counter-electrode generally composed of a transparent and conductive substrate on which a Pt film of few tens of nanometers is deposited for red-ox catalysis purpose. The two electrodes and the red-ox electrolyte mediator are sealed together, evoking the characteristic picture of a sandwich-like structure. The most diffused sealants are thermoplastic gaskets typically made of Surlyn® (i.e. random copolymer poly(ethylene-co-methacrylic acid) – EMAA), Bynel® (modified ethylene acrylate polymer) or alternatively vitreous pastes or glass frits.

Additionally, an optional light scattering layer made of particles with diameter of few hundreds of nanometers may be applied on top of the TiO$_2$ film in order to increase the photons optical path (transmitted light will be in fact back scattered into the nc-TiO$_2$ layer) and therefore the light harvesting (Hore et al., 2006). Although it has been demonstrated that this plays a beneficial role, a scattering layer leads to an opaque (not transparent) DSC device preventing the possibility of the use of the panel for building integration (as an active window for instance), one of the most interesting features and applications of DSC technology.

The working principle of DSC can be readily explained in terms of the electrons kinetics process and electrons transfer reactions taking place into the cell as a consequence of photon absorption. Fig. 3 shows the energy diagram and electrons transfer paths involved in a DSC.
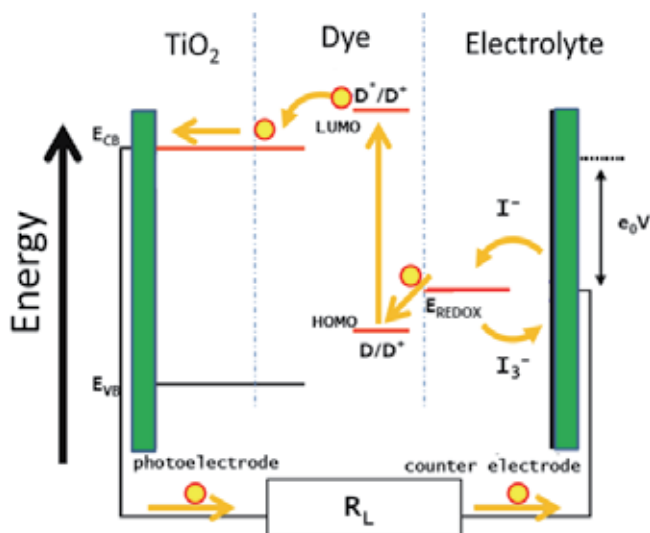
Fig. 3. DSC working principle: the absorption of a photon by a Dye molecule in its ground state D induce the transition to the excited state D*. The injection of an e- into the TiO$_2$ conduction band occurs, resulting in the Dye oxidation D+. The e- diffuse into the TiO$_2$ reaching an external circuit and a load R$_L$ where electrical power is produced. Successively it is reintroduced into the cell by the counter electrodes and regenerate the oxidized Dye D+ utilizing a redox couple as mediator.
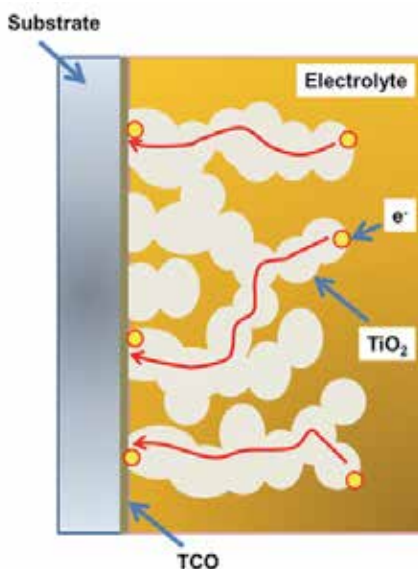
Fig. 4. The diffusion paths of the injected photon into the nc-TiO$_2$ conduction band are sketched. The nc-TiO$_2$ film sintering process promotes the electromechanical bonding between the nanoparticles facilitating the charge diffusion process in terms of increment of the intra-particles hopping rate.

By absorption of a photon, a dye molecule is set to the excited state D* from its ground state D. It follows that an electron is promoted from the highest occupied molecular orbital (HOMO) to the lowest unoccupied molecular orbital (LUMO) and then rapidly injected into the conduction band (E_{CB}) of the TiO_2. The dye molecule is then oxidized (D^+) whilst an hole is injected into the electrolyte. Charge transport occurs in the conduction band of the TiO_2 by pure diffusion of electrons percolating through the interconnected nc-TiO_2 particles to the FTO electrode (see Fig. 4). No electronic drift has been detected and electric fields in the TiO_2 are screened by the cations in the electrolyte, which penetrate the nano-scale pores of the TiO_2 (Van de Lagemaat et al., 2000).

Upon reaching the TCO electrode, the electrons are conducted to the counter-electrode via the external load (R_L) generating electrical power. Catalyzed by the platinum on the counter-electrode, the electrons are accepted by the electrolyte. This means, that the holes in the electrolyte (the I_3^-) recombine with electrons to form the negative charge carriers,

$$I_3^- + 2e\text{-} \rightarrow 3I^-$$
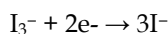
By diffusion, the negative charge (I^-) is transported back with the aim to reduce the oxidized dye molecule (D^+). Triiodide (I_3^-) is formed and the electrical circuit is closed:

$$2D^+ + 3I^- \rightarrow I_3^- + 2D$$
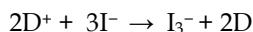
Therefore, in DSC device charge separation and charge transport occur in different media spatially separated. Apparently the device generates electric power from light without suffering any permanent chemical transformation. Nevertheless, going in deep toward a device realistic and detailed modeling, processes involving current losses have to be included and remarked.

When a photon is absorbed, a dye molecule is set in an excited state S*, the back relaxation (or back reaction) into its ground state S may also occur, preventing the injection of an electron into the TiO_2 (see Fig. 5). As shown by Nazeeruddin et al. (Nazeeruddin et al., 1993) the injection process has a much larger probability to occur resulting in a characteristic injection time in the range of fs -ps, which is more than 1000 times faster than back relaxation (about 10 ns) straightforwardly negligible.

As reported above, electrons injected into the conduction band of the TiO_2 diffuse through the TiO_2 film toward the FTO anode contact. The electron transport into the mesoporous nc-TiO_2 film can be modelled as a combination of two mechanisms electron hopping between sites and multiple trapping/detrapping (Bisquert et al., 2009). In the latter case, electrons spend part of their time immobilized in trap sites from which they are excited thermally back to the conduction band. Nevertheless, during their transit, there is a significant probability that an electron recombine (and be lost) with the oxidized dye molecule S^+, before the dye reduction caused by the electrolyte. We are facing, nonetheless, to a process with a characteristic time of several hundreds of nanoseconds resulting 100 times slower than the reduction induced by the electrolyte (~10 ns) (Hagfeldt & Graetzel, 1995).

Instead, electrons injected into the TiO_2 conduction band may, during the diffusion, more often recombine with the holes in the electrolyte, i.e. I_3^-. This constitutes the most significant electron loss mechanism in the DSC and it can be asserted that the electrons transport by diffusion in the nc-TiO_2, and their recombination with the electrolyte are the two competing processes in the DSC technology, affecting the device efficiency of electrons collection (Peter & Wijayantha, 2000). It is important to point out that, although the triiodide concentration in

a DSC should be small for this reason, it should be high enough as to provide right amount of recombination for the electrons at the Pt counter-electrode. If this is not the case, the maximum current of the DSC will be diffusion-limited, i.e. cut by the diffusion of triiodide.
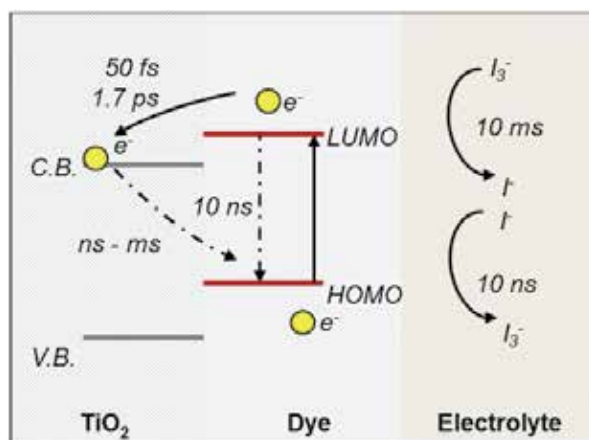
Fig. 5. Electron losses processes taking place into a DSC are shown. Also shown are the characteristic time relative to each of the considered processes.

Finally, it should be noted, that TiO$_2$ is a semiconductor with a large band gap of 3.2 eV, corresponding to a wavelength of λ=390 nm. Accordingly, visible light is not absorbed by the TiO$_2$ film. Direct absorption by UV-light is unwanted, since the created holes in the valence band of the TiO$_2$ are highly reactive and tends to produce the so called side reactions in the mediators, highly destructive for the long life time of the cell (Hinsch et al., 2001).

2.2 Dye solar cells fabrication

One of the main advantages connected with the DSC technology is the possibility to easily implement the fabrication steps involved, often borrowed from the printing industry, processing abundant materials with a relative low mass production costs (Di Carlo et al., 2008).

Differently from others photovoltaic technologies (those Si-based for instance) which are more mature and produced in an industrial environment according to well established procedures (Ito et al., 2007), for DSC a standard fabrication procedure is yet to be defined. Nevertheless the following steps are widely reported in literature, they strongly represent a prerequisite list to define and set-up an eventual industrial DSC pilot production line:

a - Cleaning of transparent and conductive substrates. Is generally carried out sonicating the substrates successively in solvents like acetone and ethanol for few minutes. In the case of glass substrates, this step may be further accomplished by firing the substrates in furnace or oven, in order to burn out the organic compound and preserve the subsequent processes.

b - TiO$_2$ film deposition. To obtain a mesoporous nc-TiO$_2$ film, from few micron up to few tens of microns thick, various techniques are adopted. One of the more diffused consists in preparing a colloidal paste composed of TiO$_2$ nanoparticles, organic binders, and solvents (Ito et al., 2007) and deposit it by various printing techniques such as screen printing, slot dye coating, gravure coating, flexographic printing, doctor blade and spray casting.

According to the printing technique performed, the composition of the paste and its recipe may observe some slight variation. For instance, in the case of automatic screen printer, it is recommendable to use TiO_2 pastes containing printing oil such as terpineol in order to facilitate the deposition process and a solvent like ethanol to optimize the deposition process for doctor blade technique. Also utilized are techniques such as spin coating, sputtering and electro deposition (Chen & Mao, 2007). It is interesting to point out that with the use of a layout or a mask it is possible to deposit the colloidal nc-TiO_2 layer according to a given pattern or shape.

Different authors have also shown the possibility to fabricate Dye Solar Cells utilizing TiO_2 films made with ordered nanostructures such as nanotubes, nanowires or nanorods (Chen & Mao, 2007). In these cases colloidal pastes are not anymore considered and furthers techniques are utilized. It is important to mention amongst the others, chemical vapor deposition, physical vapor deposition, sonochemical method and microwave method (Chen & Mao, 2007).

c - TiO_2 sintering. After the colloidal TiO_2 paste is deposited, a thermal treatment more often indicated as annealing, firing or sintering is required. In fact it is possible, via heat, to get rid of solvents and organic binders contained into the paste and in the meaning time to promote an electromechanical bonding intra-particles and between particles and the underlying substrate. This step clearly has a huge bearing on the film morphology and porosity which in turn determines the cells performances. At the end of the sintering process, a trade off is required between the necessity to guarantee a good electromechanical bonding and the requirement to keep a large porosity maximizing the sensitized surface area. Conventionally an optimum, depending on the paste composition, is obtained applying the photo-anodes (before the dye adsorption) to an increasing ramp temperature in an oven, furnace or hotplate with a final ~ 30 min step at 450–500 °C (Mincuzzi et al., 2009).

Although this procedure guarantees the fabrication of DSCs with good performances (included cells having the highest efficiency ever reported of approximately 12% over small area (Nazeeruddin et al., 2005; Buscaino et al., 2007)) it shows nevertheless some drawbacks. Since the nc-TiO_2 is heated with the substrate the mentioned conventional procedure is unsuitable for plastic substrates. For similar reasons DSC would not be integrated on the same substrate with others optoelectronic devices which would be destroyed by the high temperature. Oven and furnace are energetically expensive increasing the payback energy of the whole fabrication process. Finally, at 450–500°C conductive glass substrates could bend irregularly, preventing the possibility to fabricate large area DSC devices.

Alternative procedures have been proposed with the aim to overcome some of the mentioned drawbacks. For instance there have been several attempts to produce the TiO_2 film via low-temperature sintering suitable for plastic substrates (100–150°C) by utilizing a binder free colloidal TiO_2 paste. However, the devices with low-temperature sintered films were found to exhibit lower efficiencies than those with high-temperature sintered films. Pichot et al. (Pichot et al., 2000) have fabricated a flexible TiO_2 electrode that was spin coated onto indium–tin oxide (ITO)-coated PET substrates from an organic-free nc-TiO_2 colloidal suspension and then sintered at low temperature (100 °C) for 24 h. However, the overall device efficiency was relatively low (1.22%) under 1-sun illumination (100mW/cm²). A mechanical compression of a surfactant free colloidal TiO_2 paste onto an ITO/PET substrate at room temperature has been demonstrated as an alternative sintering method for making plastic-based DSCs at temperatures between 25 °C and 120 °C. Utilizing this method,

conversion efficiencies approaching 3% under 100 mW/cm^2 were reported (Lindstrom et al., 2002). Zhang et al. have developed a low-temperature chemical method for the fabrication of mesoporous TiO$_2$ films grown on ITO/PET substrates at 100 °C using a hydrothermal synthesis with conversion efficiency of 2.3% under 1-sun illumination. However, this process is only capable of partial crystallization of the starting Ti salts, and thus might require a subsequent high-temperature (450 °C) heat treatment (D. Zhang et al., 2003). Also several optical methods have been proposed including the use of I.R. lamps (Pan et al., 2009; H. Kim et al., 2006; Watson et al., 2010; Uchida et al., 2004) treatments. Nevertheless all the mentioned attempts produced solar cells with limited efficiencies compared to cells where standard high temperature sintering is carried out.

d - Dyeing. The nc-TiO$_2$ sensitization by dye adsorption (or dyeing) is carried out following two different strategies. In a case, sintered films are soaked with the substrate in a solution of ethanol and dye for a time period varying from around 10h to around 1h, depending on the dye solution temperature which correspondingly could be fixed in the range from T ambient to maximum T=80°C (which is ethanol evaporation temperature). Successively, TiO$_2$ films and substrates are rinsed in ethanol.

In the other case, devices are first sealed by means of a glass frit (see the step 6 below) and then dyeing is carried out fluxing the ethanol/dye solution through the gap between the electrodes. This second procedure has been introduced by the group of Fraunhofer ISE (Hinsch et al., 2008).

e - Pt deposition and thermal treatment. A crucial step in devices fabrication is to obtain a catalyst layer showing an effective catalytic activity. The main catalyst layer is a thin layer of Pt (some tenths on nanometers thick). Although the Pt layer could be obtained by sputtering, more frequently it is generally attained after thermal processing or curing of a Pt based precursor paste or solution which has been previously deposited by screen printing, doctor blade, spin coating or other printing techniques over the counter-electrode substrate. A Pt-based catalytic precursor paste composition suitable for printing technique is obtained mixing an organic compound (e.g. terpineol), a binder or stabilizer (e.g. ethyl-cellulose) and a precursor (e.g. hexachloroplatinic acid H$_2$PtCl$_6$) (Khelashvili et al., 2006).

A less viscous alternative, suitable for brush processing or spin coating, consists of an hexachloroplatinic acid solution in 2-propanol (Gutierrez-Tauste et al., 2005).

The cure of the catalytic precursor layer is conventionally carried out utilizing an oven, furnace or hot plate in order to treat the layer to a curing temperature with a final step of 5 – 30 minutes at 400 – 500°C (Kroon et al., 2007; Solaronix®). Whilst an effective Pt-precursor curing is guaranteed by this conventional procedure, nonetheless, the required high processing temperature induces some drawbacks already mentioned and listed in the case of nc-TiO$_2$ sintering. Kim et al. (S. S. Kim et al., 2006) also reported on Pt counter-electrodes prepared by means of direct current and pulse current electro-deposition methods, which are relatively simple and low cost processes.

Moreover these techniques are hardly scalable on large area devices. Alternatively, other materials than Pt, processed at low temperature (<150 °C) could be considered. As reported by Murakami et al., use of Carbon Black could be a valid and low cost alternative, and a small area cell showing power conversion efficiency exceeding 9% has been reported (Murakami & Graetzel, 2008). The same authors reported also a cell with catalyst layer made of Polymeric material such as PEDOT. Saito et al. and Suzuki et al. reported the application of a chemically produced conducting polymer and carbon nanotubes used as counter-electrode (Saito et al., 2002; Suzuki et al., 2003; Saito et al., 2004). Although the fabrication

cost can be decreased in these cases, the conversion efficiency is still relatively low compared to a cell with a Pt based counter-electrode.

f - Device sealing. Ideally, device sealing should be long lasting, minimize as much as possible H_2O infiltration (detrimental for the dye), O_2 infiltration (it induces dye photo-catalysis) and electrolyte leakage, the principal cause of module contacts corrosion (Okada & Tanabe, 2006). The sealant has to be Pb free because Pb degassing results to be an hurdle for the Pt catalytic activity (Sastrawan et al., 2006). Find a sealing material and procedure fully satisfying all the mentioned requirement is still an open issue for the DSC technology.

Nevertheless, as already mentioned, two different strategies are generally adopted for this purpose, by using thermoplastic gaskets, or glass frits. In the first case the sealing is attained by thermal pressing the two electrodes with the gasket between them. Alternatively a lead-free glass frit paste is deposited between the two electrodes and then heated until it melts sealing the device (Sastrawan et al., 2006). The melting temperature varies upon the glass frit paste composition, although it generally exceed 400 °C. Whilst in the first case the process can be carried out having the photo-electrode already dye sensitized, this is prevented in the last case since the high temperature necessary for the glass frit melting will damage the dye molecules. As reported in the step 4, for this reason dyeing is in this case carried out by fluxing the dye solution (Hinsch et al., 2008).

g - Electrolyte injection. Finally, by back vacuum technique, electrolyte is injected into the sealed device through an hole drilled into one of the substrates. The hole is on end stopped by means of a glass patch. Further possibilities consist in fluxing the electrolyte (Hinsch et al., 2008) or in printing (before the device sealing) a previously gelificated redox mediator (P. Wang et al., 2003).

2.3 Large area devices

Large area dye solar cell devices are obtained interconnecting unit cells to form modules which could in turn be interconnected to realize a panel. The individual cells must not only be insulated from each other electrically (and this is performed via TCO laser scribing), but also electrolytically otherwise photo-induced electrophoresis would occur.
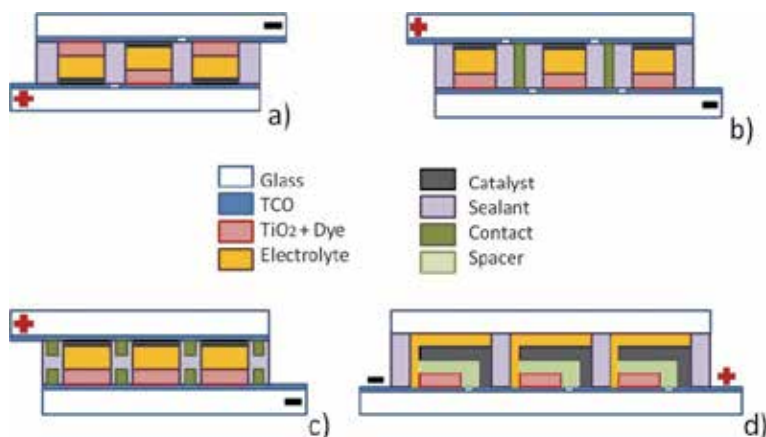
Fig. 6. Different architectures of Dye Solar Cells. Four different strategies are sketched: w-series interconnection (a), z-series interconnection (b), parallel interconnection (c), and monolithic-series design (d).

Furthermore, the electrical interconnections must be protected against the highly corrosive activity performed by electrolyte. As shown in Fig. 6 various interconnection architectures have been proposed for the modules, namely parallel, monolithic, z-series and w-series. Examples of modules obtained following different connections strategies are discussed in the literature (Tulloch, 2004) and disclosed in the following patents (Kay, 1995; Okada & Tanabe, 2006; Tulloch & Skryabin, 2006; Arakawa et al., 2007).

It is considered in particular modules to increase the voltage output cells which are connected together via either z-series or w-series schemes. In z-series design unit cells are sealed and connected by means of conductive vertical interconnections. The advantages of this design are an high voltage output and facility for eventual pre- and post-treatment of the electrodes. The disadvantage, is the risk of a fill factor lowering resulting from the series resistance of the interconnection. A crucial aspect regards the fabrication and realization of thermally stable vertical interconnections. Such interconnections need also to be protected from the corrosion eventually caused by the red-ox electrolyte leakage, which could compromise the modules performance and its working life time. An efficient and reliable interconnection strategy for z-series architecture modules is a still open technological challenge while some solutions have been proposed and disclosed in the following patents (Tulloch & Skryabin, 2006; Ezaki et al., 2006).

Differently from the z-series the w scheme avoids to interconnect altogether by juxtaposing cells facing in one direction with cells facing the opposite direction i.e. that have photo-electrode/counter-electrodes in opposite alternation and still requires separation of the cells by an effective sealing. This interconnection designs, is particularly attractive because the modules are potentially scalable to large dimensions avoiding the successive step of interconnection and integration of separate cells into a panel drastically simplifying the fabrication process compared to crystalline silicon panels. In DSCs the cells and interconnects can be integrated together by simple printing processes. Furthermore w-series design has advantages in simplicity and avoids the reduction in fill factor resulting from additional resistance of series interconnects, especially when the modules operate at high temperatures, but has some manufacturing and performance weaknesses. In manufacturing of this design, it is necessary that the counter-electrode and photo-electrode have to be processed on the same substrate. When conventional fabrication methods are utilized, this introduces processing complexities in deposition, curing, pre and post curing treatments of the cells materials in particular for the TiO_2 and catalyst precursor paste.

The design of a monolithic DSC (Vesce et al., 2011) is a planar-connected device with an only conductive glass, formed by a triple-layer sintered at once (Meyer et al., 2009) or together (Pettersson et al., 2007). The multilayer structure is typically composed by: a mesoporous TiO_2 working layer, a spacer/scattering layer and a counter-electrode layer. The spacer layer is often formed by ZrO_2 or rutile-TiO_2, while the counter-electrode layer is usually composed by Pt, Au, carbon or a mixture of these (Murakami & Graetzel, 2008). In order to obtain the maximum advantages from the monolithic architecture, some researcher reports the application of a quasi-solid gel electrolyte (non-volatile electrolyte) deposited by printing methods like blade-coating or screen-printing technique instead of an electrolyte processing by liquid injection (volatile electrolyte) (P. Wang et al., 2003).

For all types of serial DSC architectures, single cells must be insulated and serial connected causing a complex fabrication process, high serial resistance and a strong precision in order to maintain the ohmic contact (L. Wang et al., 2010). In contrast, a simple fabrication process is used to fabricate large scale parallel design DSC modules. In this architecture, (Tulloch,

2004), the grids utilizing conductive fingers to collect current are printed on the two substrates separately. Nowadays, the researchers that work on this design are devoting to find alternative materials solutions for the grid since Ag, Au, Cu, Al, and Ni are all easy to be corroded by the iodide electrolyte (Goldstein et al., 2010). Moreover, new coatings like polymer or glass frits are successfully applied in parallel DSC module design.

Having in mind the materials, strategies and fabrication processes aforementioned, various research groups (CHOSE, ISE Fraunhofer, KIST, NREL) and companies (3GSolar, G24i, Sony, Fujikura) have shown DSC panels and large area devices utilizing fabrication process which could be potentially integrated into an automatic production line.

Nevertheless, the scale up of DSC devices over large area for industrial and commercial purpose, poses some scientific and technological challenges. In particular, it is important to mention the reduction of the series resistance (Dai et al., 2005), strictly related to the increasing of the performance, stability and working life time of large area modules (P. Wang et al., 2003; Sommeling et al., 2004; Kuang et al., 2007), and the setting-up of a highly automated and energetically efficient fabrication process (Somani et al., 2005; Meyer et al., 2007; Mincuzzi et al., 2009).

3. Characterization techniques

The typical parameters to characterize a PV device belong also to DSCs performance. However, different technologies often imply different attentions to perform the measurement. Parameters like short circuit current, open circuit voltage, fill factor and power conversion efficiency, are extracted from the photo-current/voltage characteristic (J-V curve). This measurement can be fundamentally performed in two ways: in dark conditions (without illumination) and with illumination. In the last case, we are able to extract all the parameters. Illuminating with white light, the J-V curve represents an integrate response of the cell to all the wavelengths simultaneously. The standard test conditions (STC) correspond to power density of 1 sun (100mW/cm^2), light spectrum of an air mass 1.5 global (AM1.5G) and working temperature of 25°C.

Incident Photon-to-electron Conversion Efficiency (IPCE) measurements, on the other hand, quantify how many incident photons at a single wavelength are converted in extracted electrons at the electrodes. It strictly depends on the optical and electrical properties of the cell. In particular, it can be decomposed in the product of three main terms: light harvesting efficiency (LHE), injection efficiency (η_{inj}) and collection efficiency (η_{col}) (Halme et al., 2008; Barnes et al., 2008). The first is reduced by optical phenomena, such as reflections, transmission and competitive absorption, while injection and collection efficiencies depend on electrical mechanisms at widely different time scales. The injection counts how many excited electrons are transferred from dye molecules to titanium dioxide film. It is the fastest process in the cell, with characteristic times from femto to pico-seconds, measured by means of pump-probe techniques (Koops & Durrant, 2008).

The collection efficiency says how many injected electrons into the titanium dioxide film reach the electrodes. It can be evaluated by many different techniques, among which photovoltage decay (Walker et al., 2006), intensity modulated photovoltage spectroscopy (IMVS), intensity modulated photocurrent spectroscopy (IMPS) (Schlichthorl et al., 1999) and electrochemical impedance spectroscopy (EIS) (Q. Wang et al., 2005). The slowest process in the cell is the ionic diffusion in the electrolyte, which can be studied by EIS as well.

3.1 I-V characteristics and IPCE spectra

I-V characteristics and IPCE spectra can be related each other. Actually, from the complete IPCE spectra, it is possible to calculate the short circuit current that one should measure under solar simulator in the following way:

$$J_{SC}(\lambda) = \int_{\lambda 1}^{\lambda 2} IPCE(\lambda) P_{STC}(\lambda) \frac{\lambda}{1240} d\lambda \qquad (1)$$

with $P_{STC}(\lambda)$ the spectral density at standard test conditions and λ the wavelength in nm. This calculation is an important check that should be always performed to control the measurement accuracy. Many factors can influence the deviation of the current measured under solar simulator from the value calculated by equation (1). In particular, according to the solar simulator class, the spectrum can considerably differ from AM1.5 conditions (Ito et al., 2004). Because the calculation is performed at AM1.5, an overestimation or an underestimation can occur. It mainly depends on the light harvesting efficiency of the cell or more simply from the absorption coefficient of dye molecules. A good way to overcome this discrepancy consists in estimating the mismatch factor (M) (Seaman, 1982). It considers the spectral responses of the test and reference cells and the spectral irradiance of the solar simulator (while AM1.5 is known). It can vary a lot among various kind of cells (it is close to unity for silicon solar cells). In Fig.1 the calculated and the measured currents for dye solar cells with different dyes are put in relation. Different dyes mean different absorption spectra, and consequently a variation of the mismatch factor. Although a linear relation is obtained, the angular coefficient is different from one. Moreover, to make the things more complicated, there is the dependence of dye solar cells response from the level of illumination. So, as it will be clear soon, to relate the results from IPCE and J-V measurements is important to be in the same light intensity conditions. It means that also IPCE spectra should be acquired at 1 sun condition.
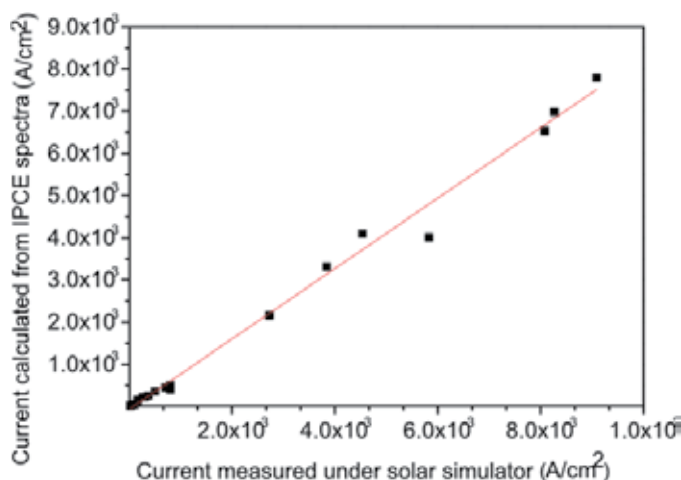
Fig. 7. Density Current measured under solar simulator and calculated by IPCE spectra are put in relation for cells with different dye molecules. A perfect agreement would give an angular coefficient m equal to one. In this case we have m=(0.83±0.02) and an adjusted R-square of 0.992.

Actually, DSC photovoltaic characterization is critical. Performing J-V curve, the direction of scan as well the delay time during the measurement must be chosen accurately otherwise different results can be obtained. One of the most important reason for these different behaviors is due to strong capacitance effects presented in this kind of device (Koide & Han, 2004). The main consequence is the long constant time of this kind of cells (in the order of some seconds) with respect to other technologies. An overestimation of short circuit current can be carried out, in particular when small area cells are characterized. In this case, the device area is generally larger than the active area, and, when illuminated, a considerable amount of light not impinging onto the active area can be redirected to it (light piping effect) (Ito et al., 2006). According to the simulator class, the beam divergence can amplify this effect. To overcome it, an appropriate opaque mask must be applied onto the external surface front glass. Then, particularly for large area devices, or for devices delivering high current, the external bad contacts can strongly influence the measurement. Good contacts can be obtained with bus bars applied by screen-printing technique.

On the other hand, IPCE measurement on dye solar cells is a critical issue as well. IPCE measurements can be performed in two ways, applying a direct (DC) or an alternate (AC) method. The first one is the classical way to acquire IPCE spectra, while the second one consists in illuminating the cell with white light (also called bias light) simultaneously with the monochromatic component. The bias light acts as a sort of polarization of the cell, increasing its response, besides the fact that, in this way, the cell can be put under conditions closer to the working ones. The current due only to monochromatic light (we say monochromatic current) is discriminated from the current due to the bias light, by using a coherent detection. It means that the monochromatic light is modulated at a certain frequency and by a lock-in amplifier, only the current modulated at the same frequency will be detected.
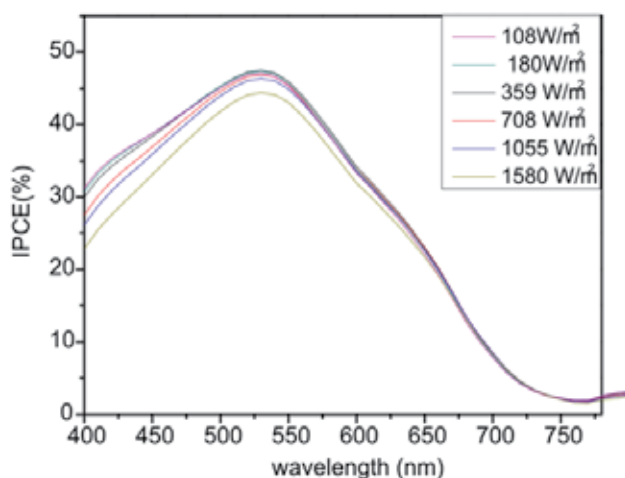
Fig. 8. IPCE spectra in function of the bias light illumination. A clear dependence from the light power density is shown. In the legend, the bias light power density is shown.

There are mainly two effects affecting IPCE when we illuminate with different power density conditions: the trap filling effect and the electrolyte ions mobility. While the first affects negatively the IPCE spectra at low light level conditions, the second comes into play at high light density reducing the solar cell response as well. For trap filling we mean the ability to occupy the states inside the titanium dioxide gap, close to the conduction band edge. These levels are centers of recombination for the electron in conduction band. At single wavelength, the filling is not efficient, reducing the cell response (see Fig. 8). It has been verified that the application of a bias light can be simulated in the DC method, if the intensity of the monochromatic light is high (Sommeling et al., 2000). On the other hand, at high intensity the electrolyte ions could be not able to regenerate effectively the homo level of the dye. This effect is dramatically enhanced when we use $Co^{(II)}$-$Co^{(III)}$ as redox couple.

Aware of the dependence from light intensity, to control the measurement accuracy under solar simulator, it is mandatory to perform IPCE acquisition at the same conditions.

Different dynamics are present in the photovoltaic mechanism of a dye solar cell. In presence of illumination, however, only the slowest process will dominate. The result is that the dye solar cell response is really slow. The modulation of the monochromatic light should be less than 1 Hz, taking into account that it should be verified every time different materials are involved (in particular the electrolyte and the titanium dioxide film employed).
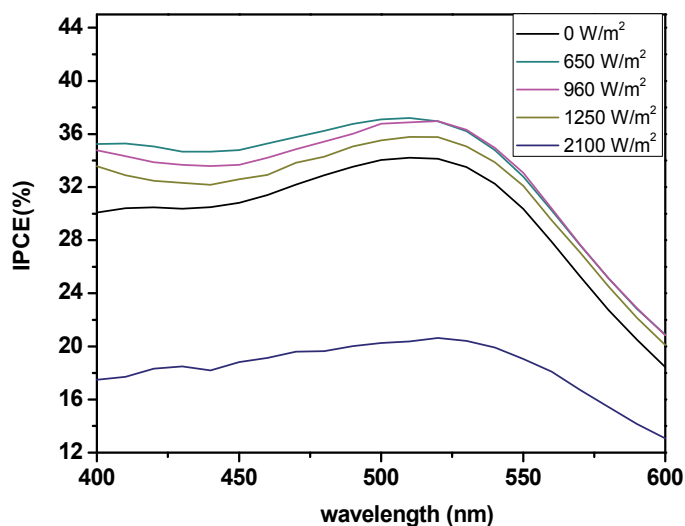
Fig. 9. IPCE spectra in function of the bias light illumination for a dye solar cell with $Co^{(II)}$-$Co^{(III)}$ as redox couple. A decrease of the signal intensity at high intensity levels has been measured.
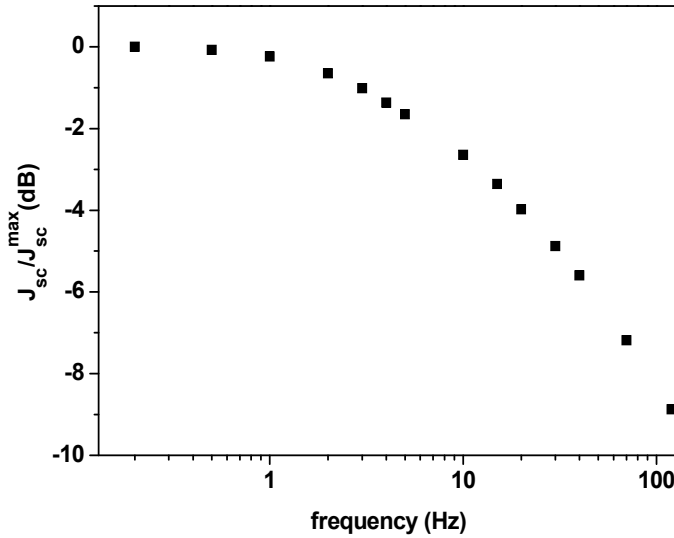
Fig. 10. DSC response in function of light frequency modulation. In the y-axis, photocurrent appears as a ratio (in decibel) with respect to the maximum current at the lower frequency. The response of a DSC is slow if compared to silicon technology.

IPCE spectra take in account many different phenomena that we can distinguish in two main categories: optical and electrical ones. In particular IPCE depends on the ability of the cell to harvest the light. Photon management techniques try to improve just this factor. The light harvesting efficiency of the cell can be calculated starting from spectrophotometric measurements. A simple optical model of the geometry allows the estimation of this quantity, that is the electrons generated compared to the incident photons. In a simplified scheme, assuming a Lambert-Beer behavior, we can model the light harvesting efficiency when the light impinges onto the front side of the cell in the following way:

$$LHE(\lambda) = T_{TCO}(\lambda) \cdot \frac{\alpha_{dye}}{\alpha} \cdot \left(1 - e^{-\alpha d}\right) \tag{2}$$

where T_{TCO} is the transmittance of the transparent conductive oxide, α is the absorption coefficient of the entire film and α_{dye} is the absorption coefficient due to the dye molecules. This is, obviously, a simple approach, where second-order reflectance terms are not considered. Measuring IPCE and estimating LHE, we are actually able to obtain information about injection and collection efficiencies just making the following ratio:

$$APCE(\lambda) = \eta_{inj}\eta_{col} = \frac{IPCE(\lambda)}{LHE(\lambda)} \tag{3}$$

where APCE stands for Absorbed Photon to Current conversion Efficiency and it is the product between injection and collection efficiencies.
Making the measurements illuminating both sides of the cells in different times, an estimation of the collection efficiency, the diffusion length (L_D) and the injection efficiency, has been demonstrated under strict conditions (Halme et al., 2008; Barnes et al., 2008).
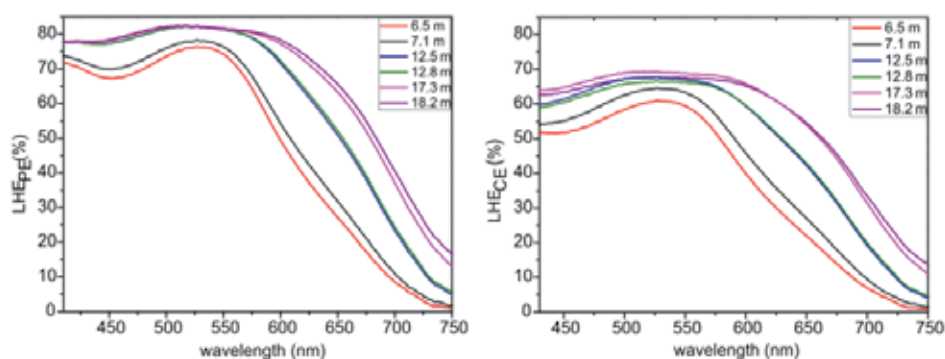
Fig. 11. Light Harvesting Efficiency for cells with different thicknesses illuminating from photo- (on the left) and counter- electrode (on the right) sides.

In Fig. 11, estimation of LHE for different thicknesses of the titanium dioxide film for both directions of illumination has been reported. As intuitive, LHE from counter electrode side is typically less than in the case of front side because of the generation profile inside the titania layer and the electrolyte absorption, mostly in the wavelength range under 500 nm.

4. Photon management

The typical paths followed to increase the performances of DSCs are linked to their main components, i.e., to improve the mesoporous nanocrystalline titania (nc-TiO$_2$), to find new dyes or dye combinations and to improve the ionic electrolyte. Approaches to enhance efficiency are also being followed which belong to a wide strategy of photon management. The dye management itself acting on the dye properties may be considered inside the panorama of photon management (Park, 2010). It consists in a multiple dyes co-sensitization in order to enlarge photonic response via panchromatic absorption, hence to increase efficiency. There have been already proposed works focalizing on the panchromatic feature of a dye solar cell (Ogura et al., 2009; Yum et al., 2007; Park, 2010). The way to get improvement is by the use of two (up to three) dyes adsorbed on the nanocrystalline titania that are responsible for broad spectral response of the device. The development of organic sensitizers (C101 etc.) (C.-Y. Chen et al., 2007; Abbotto et al., 2008) led to very high levels of efficiency. More in general, photon management consists in the ability to confine light in the dye solar cell to stimulate high levels of charge enforced by scattering and reflection effects. At the same time, this should be coupled to decreasing the recombination of charge mostly at the interface nanocrystalline TiO$_2$/electrolyte. Indeed, it is known that the top performances of DSC devices are reached by keeping in mind also all the parasitic and recombination effect and the way to minimize them. For example, in order to quench the recombination at FTO/electrolyte interface and to facilitate the injection between the dye LUMO and the TiO$_2$ conduction band, it can be used a photoanodes treatment by a titanium tetrachloride (TiCl4) solution (Vesce et al., 2010). Then, the transparent layer of titania (average particle diameter 15-20 nm) can be covered or added by larger scattering particles (150-400 nm in size) (Usami, 1997; Arakawa et al., 2006; Colonna et al., 2010) causing the random reflection of the light back into the cell (Mie scattering). Indeed, the most common way of photon management consists in the development of diffuse scattering layers (SLs) capable to be used as incoherent back mirrors for the incoming light passing through the cell

and otherwise not converted into current. In 1997 (Usami, 1997) a theoretical work by A. Usami proposed the use of a scattering layer onto the nc-TiO$_2$ layer and a rutile thin layer between the glass and TCO conductive film. This implies a very effective enhancement of the light collected into the cell, but also means that the DSC remains opaque. Nowadays, the scattering layers (Hore et al., 2006; Arakawa et al., 2006), centers (Hore et al., 2005) and superstructures (Chen et al., 2009; Q. F. Zhang et al., 2008) are well known and routinely used (Graetzel, 2005). Despite other approaches to the problem of increasing DSC performances while maintaining light transmittance (Colodrero et al., 2009a; Ogura et al., 2009) the record of performance for a DSC is obtained by the use of diffuse SLs (Nazeeruddin et al., 2005; Arakawa et al., 2006). To confer order to the scattered light, Miguez proposed the selective mirror for DSC (Colodrero et al., 2009a) made out from colloidal TiO$_2$ suspensions (Wijnhoven & Vos, 1998; Colodrero et al., 2008). They consist in photonic crystals (PCs) (Yip et al., 2008; Colodrero et al., 2009b), introduced either inside the titania layer or on its backside (Nishimura et al., 2003; Mihi et al., 2006), currently under an intense experimentation. Scheme in Fig. 12 resumes some of the light management approaches for conversion efficiency improvement.
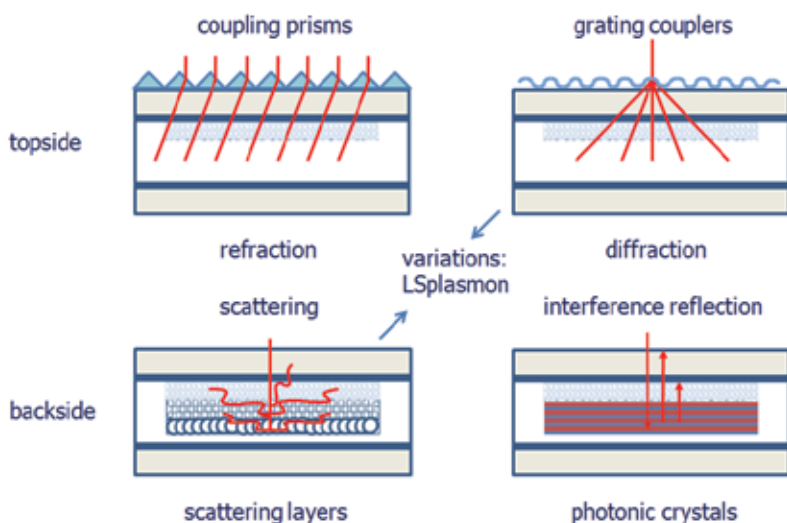
Fig. 12. Photon management basic approaches.

Some of these techniques will be described in the following sub-sections. In both SLs and PCs techniques of photon management, the increased light path in the active layer (e.g., by scattering or interferential confinement), will enhance the light harvesting efficiency (LHE). Even the reflection can be exploited to call into play of photons otherwise lost from the cell, as in V-shaped or folded solar cells (Tvingstedt et al., 2008; Zhou et al., 2008). In the waveguide DSC (Ruhle et al., 2008) a coupling prism let the light enter beyond the condition of total reflection at the glass plates/air interface without letting it to escape. Plasmonic solar cells (Tvingstedt et al., 2007; Catchpole & Polman, 2008) may represent another kind of photon management for field enhancement (near-field) or scattering by surface plasmon polaritons (mostly localized on metallic nanoparticles). Other

configurations involve field enhancement plus diffraction from metallic subwavelength arrays (Hagglund et al., 2008; Pala et al., 2009; Ding et al., 2011). An increased optical path may be obtained in principle also by dielectric diffraction or refraction (Dominici et al., 2010). Structuring the top side with a dielectric surface texturing, either nanometric or micrometric (Tvingstedt et al., 2008), could achieve the additional (diffracted) light rays or a larger inclination of (refracted) path (respectively by using of grating couplers or microprisms and microspheres for example).

4.1 Co-sensitization

The co-sensitization of nc-titania anodes approach consists in the use of two or more dyes anchored on the same substrate (Chen et al., 2005; Shah et al., 1999). It has been considered with particular attention to some organic dyes having complementary spectral response in the red with respect to the ruthenium-based dyes (largely used for standard DSC), such as squaraine (SQ1) (Clifford et al., 2004), cyanine (Pandey et al., 2010), phthalocyanine (Ono et al., 2009), hemicyanine (Cid et al., 2007). Indeed in other studies the co-sensibilization approach has shown high device performances toward red and violet as well in the electromagnetic spectrum (Yao et al., 2003; Kuang et al., 2007; Yum et al., 2007, 2008; Chen et al., 2005; Clifford et al., 2004). The scope of co-sensitization is to enlarge the absorbance spectrum of the cell toward the Near Infra Red (NIR), thus to increase the Incident Photon to Current Efficiency (IPCE) by enhancing the LHE (*Light Harvesting Efficiency*) and the efficiency of injection inside the TiO_2 (see IPCE section).

Here have been investigated the co-sensitization effects by using two conventional Ru-based dyes, the N719 and the Z907, together with a second one that is a typical Dye for dye lasers (HWSands). With respect to other co-sensitization approaches it has been shown the improvement of performances without losses when the dyes are both anchored to TiO_2. This means that the behavior of photocurrent and efficiency is summed not linearly, i.e. more than the sum of each single dye performance cells.

The most important fact to take into account in this approach is that the dye does not reach the saturation point, i.e. maximum allowed absorbance and hence maximum performances. What done is the immersion by using the first ruthenium dye followed by the second one for a determined time. In fact by setting properly the dipping time there have get enhanced performances with respect to 'one dye system DSC'. It should be noted that the immersion time far from the saturation of the titania layer for the ruthenium dyes implies technological reasons. In fact in Building Integrated Photovoltaic (BIPV), to which DSC are devoted, the transparency is a central factor. A saturated working electrode will be slightly opaque, while by using a second dye absorbing toward the red together with the unsaturated one is possible to keep an acceptable level of transparency and efficiency.

Experimental spectra were acquired with the integrating sphere of a Spectrophotometer by using the undyed titanium dioxide substrate as reference. The working electrode's absorbance saturates after some hours for N719 and Z907 depending on the thickness of TiO_2 and dye concentration whereas for SDA is found that the saturation time is of the order of 15-30 minutes for both thicknesses investigated and has been also observed a photo-cleavage due to TiO_2. In the figure below are reported absorbance of N719 on nc-TiO_2 at different times and the photocatalisys of NIR dye.

The optical response of the double dye is enlarged up to 700nm due to the presence of near IR dye. It should be noted that prolonged dipping time in the SDA solution will cause a displacement towards the N719 molecules already attached on the TiO_2 surface; in fact MLCT (Metal to Ligand Charge Transfer) band absorption of N719 (3h) decreases after 15 minutes dipping in SDA. The same trend is kept also for 30 and 45 minutes (see Fig. 14).
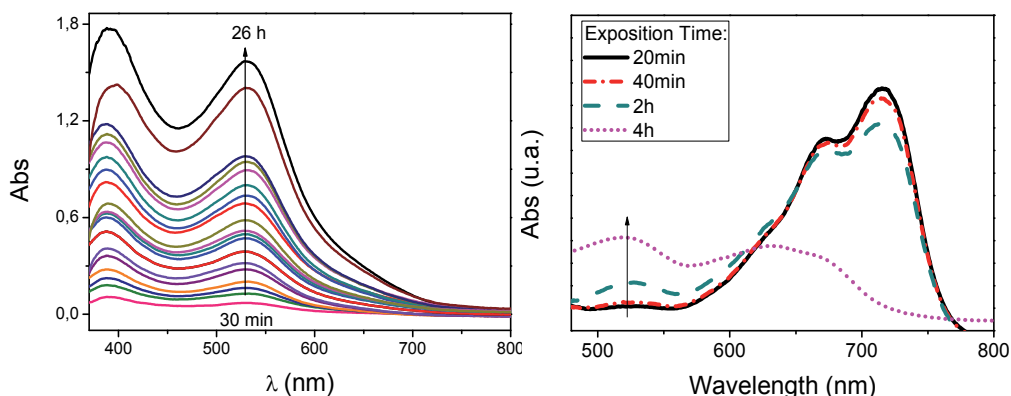
Fig. 13. (Left) Absorbance of nc-titania dyed with N719 (30 min up to 26 hours) and (right) photo-cleavage of SDA due to the TiO$_2$.
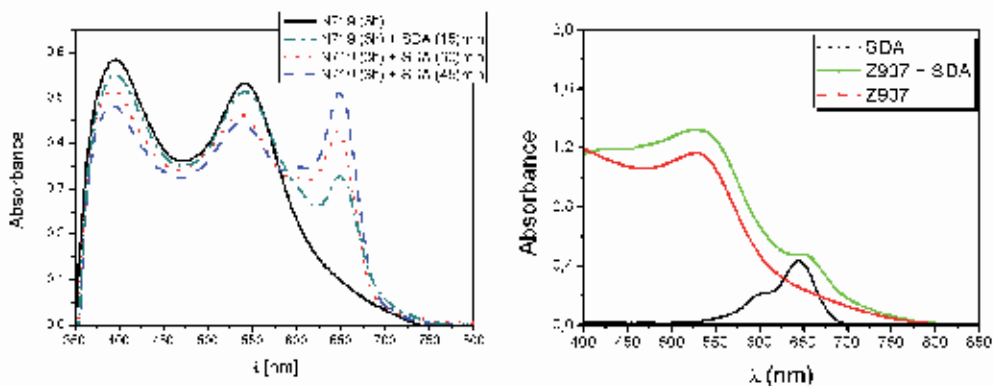
Fig. 14. Left: Co-sensitized spectra of the SDA1570 dye together with N719 on nanocrystalline titania substrates (6 µm) along with single dye absorbance. Several dipping times were chosen to show the decreasing peak of the N719 due to SDA1570 effect. Right: Co-sensitized spectra of the SDA1570 dye together with Z907 on nanocrystalline titania substrates (12 µm) along with single dye absorbance.

There is the gradual detaching of the N719 molecules from the titania due to the SDA environment. In this process it should be considered the equilibrium constants of the process involving initially the N719-TiO$_2$ photoelectrode in EtOH solution of SDA. The latter molecules act on the substrate by mass action due to the concentration gradient. The SDA molecule acts for N719 detaching from the TiO$_2$ surface. This depends mainly on the concentration of SDA solution, on the temperature, and the time. Finally there will be reached a dynamical equilibrium in which the number of SDA entering molecules on titania is equal to the same detaching molecules. Since such configuration is undesired, the finding of the optimal adsorbing point by both N719 and SDA molecules is central factor.

For completeness the action of SDA on dyed N719 PEs and *vice versa*, immersed up to 18 hours on titania was investigated (see figure 15, right). It is found that SDA is not able to detach all the N719 molecules, consequently the absorbance has almost the same trend for

15 minutes and 18 hours of SDA on saturated (18 h) N719 PE. The N719 instead shows an increasing of the absorbance passing from 15 minutes to 18 hours when alone (figure 15, left); moreover the attachment dynamic of N719 is very slow if compared to SDA. On the contrary it can be seen that the N719 environment for a saturated SDA photoelectrode is deleterious for the latter, being completely cancelled (figure 15, dot curve). It can be noted that the maximum absorbance of N719-SDA PEs is almost the same for 15 minutes and 18 hours of SDA immersion meaning that the affinity of SDA to the N719 saturated titania is limited.
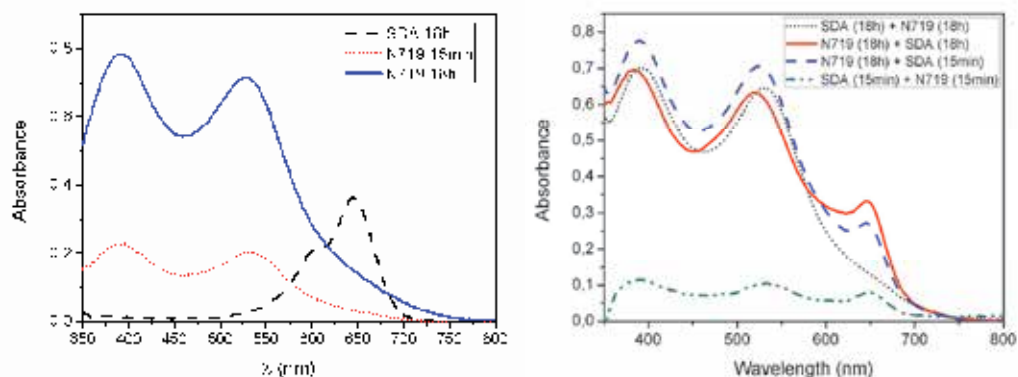
Fig. 15. Absorbance of 6 micrometers titania PEs in several dye adsorption configurations; (left) single dye TiO$_2$ attachment and (right) saturation conditions.

A similar study for Z907 + SDA system has been carried out; the transparent 12 micrometers thick TiO$_2$ PE was dipped in Z907 (0.3 mM) for 5 hours, while SDA for 30 minute steps. In this case, due to the ability of the thicker PE to generate an higher current with respect to the previous case, the electric performances are notably higher than N719 (Fig. 16).
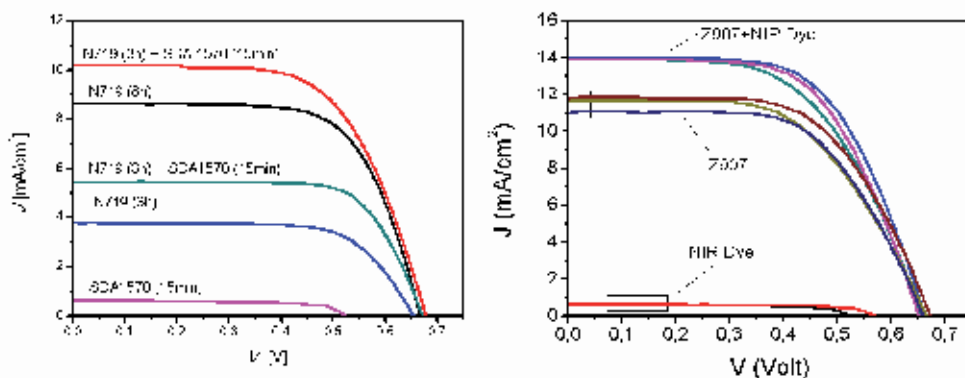
Fig. 16. J-V curves for N719-SDA (left) and Z907-SDA (right) co-sensitized systems. The lowest curve is due to the SDA sensitizer alone (labeled NIR in the right plot). It can be seen that the contribution of SDA is very small when compared to the N719 or Z907 current generation, but it becomes very important when the ruthenium dye is already and partially attached to the surface.

In this case, by taking into account that the Z907 Ruthenium-based dye has hydrophobic chains, we shall consider that (relatively) prolonged dipping times are required by the SDA to attach efficiently to the Z907 dyed titania PEs. This explains the small absorbance seen in figure 1 where the Z907 (5h) is immersed for thirty minutes in SDA solution.

The cells assembled by using the above photoanodes arrangements have been tested under a sun simulator (AM1.5) at 0.1Wcm^{-2} of illumination density of power. It is found that for N719-SDA system (at different dipping times) the co-sensitized cell outperform the single dye, having unexpected Jsc generation and efficiency. The same trend, but with higher values, has been found for Z907-SDA arrangement.

The Internal Photon to Current Conversion Efficiency confirms the above trends showing a zone of generation at the SDA excitation energy (650-660 nm).
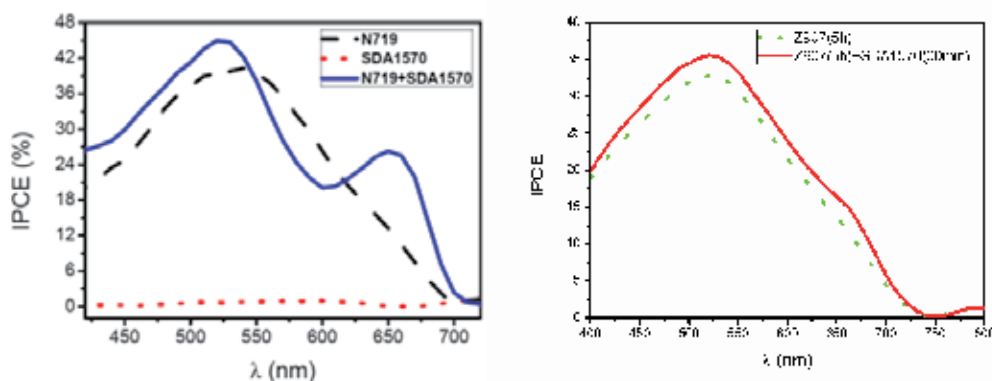
Fig. 17. IPCE results of the studied systems. In the case of N719-SDA couple the SDA pick is well identified at 660, whereas in the Z907-SDA only a small increasing of the IPCE figure is registered.

The immersion of the partially N719-sensitized photoanode in a SDA solution induces the saturation of the remaining free TiO$_2$ surface and at the same time a partial displacement of the already attached N719/Z907 molecules, creating a sort of "self-organization" of the two molecules that improves the cell performance, limiting the energy loss due to excitonic interaction between homologue molecules. This seems to be confirmed by IPCE measured. It shows in fact that photocurrent for the co-sensitized cell has a relative maximum in the wavelength region of maximum absorbance of SDA1570 confirming that it acts as an absorber on the TiO$_2$ but not as carrier generator in the cell when anchored alone to the titania. Instead, if attached together with N719 a major contribution in charge collection starts. Moreover the N719 active spectra in the co-sensitized device is blue shifted and narrower than that in the non co-sensitized device. Such a molecular organization effect can justify the fact that SDA1570 alone is not a sensitizer, while together with N719 it becomes a sensitizer for DSCs (Colonna et al., 2011a).

4.2 Diffusive scattering layers

The use of larger titania particles dispersed or added in layers on the nc-TiO$_2$ slab of a dye solar cell has been proven to be the best arrangement for high performance DSC (Nazeeruddin et al., 2005). The scheme of a DSC having a thin slab of opaque titania

particles (~ 150-400 nm) onto the transparent one in several configuration is depicted in Fig. 18. The optimal diameter of the transparent nc-titania particles is about 15-20 nm; during the sintering process at nearly 500°C, the particles create the mesoscopic structure and the effective surface of the TiO$_2$ electrode is increased by up to 10^3 factor with respect to the apparent area. In this way when the dye is adsorbed there are up to 1000 monolayers of dye in the cell for charge generation (Ferber & Luther, 1998). The pores in the layers have the better diameter for electrolyte infiltration and diffusion. If the TiO$_2$ particles are too small, the pores are not large enough for the dye and the electrolyte infiltration. Finally the larger the size particles the smaller is the internal surface, hence poor charge generation.
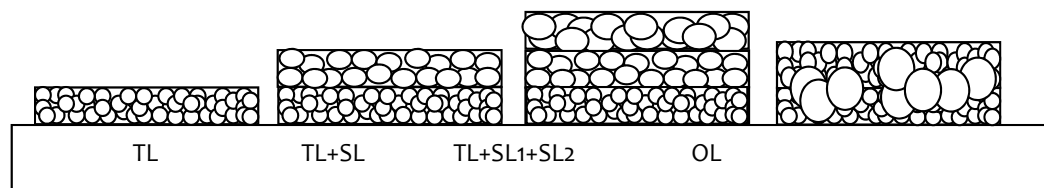
Fig. 18. From left to right hand: few micrometers nc-TiO$_2$ (~ 15-20nm); single scattering layer (d ~ 100nm) on the previous; double scattering layer with upper one having d > 200nm particle size; dispersion of small and large diameter TiO$_2$ particles. TL = Transparent layer, SL = Scattering Layer, OL = Opaque Layer.

Due to the opacity of scattering titania particles placed onto the transparent nc-TiO$_2$ the incident light passes through the nanocrystalline dyed titania, then it encounters the diffusive slab of bigger particles and is resent back to the PE finally. The average size of the scattering particles can be tailored to be between 60 and 500 nm, whereas the layer thickness can vary between 3-4 and 20 micrometers (Arakawa et al., 2006; Koo et al., 2008).

It should be considered that by doubling the thickness of nanocrystalline transparent titania the photocurrent will not be doubled because the difference in transmittance decreases with increasing wavelength, that is, little difference at wavelength ranging from 650 nm to 800 nm. For this reason, a TiO$_2$ film having only nanocrystalline particles cannot improve photocurrent density significantly by increasing the film thickness (Park, 2010). For this reason the random effect of a diffusive layer can enhance the reflectivity back to the cell by increasing the incident light path length and therefore the absorption, thus the LHE. All the works based on such strategy have been based on *A. Usami* (Usami, 1997) studies to demonstrate that with a simple model for multiple scattering the best configuration can be obtained with particles which size is a fraction of the incoming wavelength. *Usami* considered that Mie scattering theory is a rough approximation if scattering particles are not spherical and for multiple scattering. To take them into account some corrections have to be introduced. The exact solution of scattering of light by a particle is obtained by Mie theory, along with the dependence on particle size, absorption index, uniform dispersion of the particles, sufficient particle condensation for effective electron transfer and sufficient opening for the adsorption of the sensitizers (Arakawa et al., 2006; Park, 2010).

It has been found that the optimal scattering matching condition is obtained for kd/π = 0.7 ~ 1.6. Since the wave vector is given by k = 2π/λ, this condition implies that it exists an interval of wavelengths and size scattering particles for best improvement condition.

For this study it has been investigated firstly the absorption, i.e. A = 1 - T - R, of substrates taking into account the reflections of the device. In this way can be understood the spectral

area in which the diffusive layers can efficiently operate. In the figure below can be seen the absorption of nc-TiO₂ of 6 and 12 μm along with the SLs effect. It should be noted that the growth of 1 or 2 diffusive slabs of the same particle diameter creates the same absorption to the PE.

For quantitative estimation on the cell performance the study the IPCE trend of the cell is required in order to see explicitly the enhancement factor. This is because the absorption curve does not take into consideration the final device arrangement, that is the current generated by itself. On the right plot of the figure are shown reflectance spectra (diffuse and specular) due to transparent or scattering particles, in a normal configuration. Typically the SL can enhance the photocurrent to very high percentage because of the random reflection. Indeed it can be seen that almost all the reflected light by the scattering layer is intercepted by the dye pigment up to 600 nm. Therefore the absorption A of the cell will be increased as the IPCE.
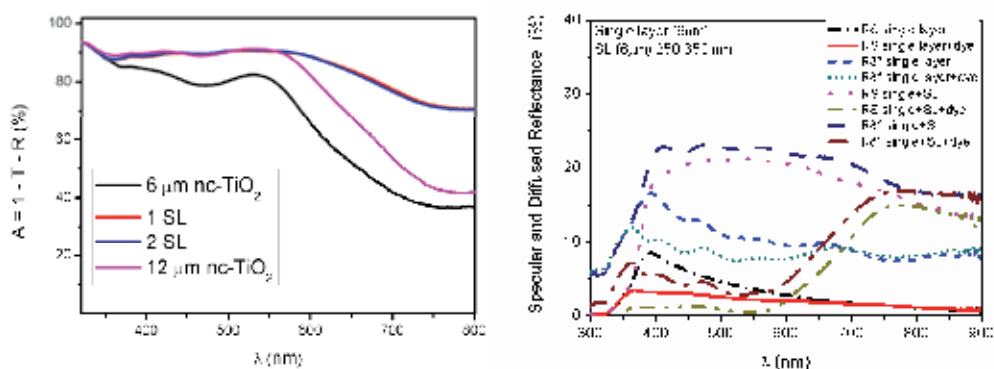
Fig. 19. (Left) Absorption of nc-TiO₂ dyed electrodes and the same covered by one or two diffusive scattering layers. (Right) Diffuse and specular reflectance of the 6 μm titania added by the dye (N719) and not.
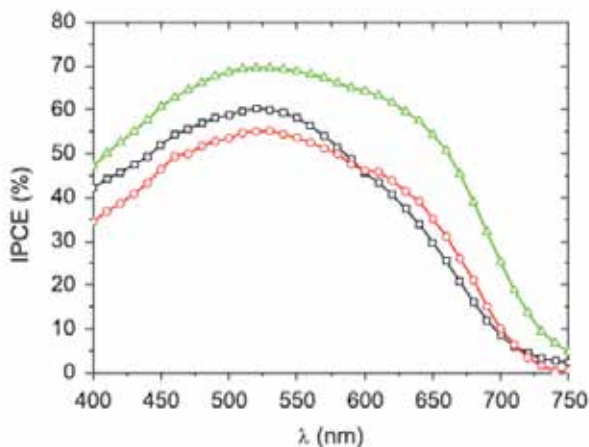
Fig. 20. External Quantum Efficiency of a standard DSC along with two scattering arrangements.

Tipically the IPCE curves have the shape reported in the following figure. In that case thicknesses for both transparent and opaque layers are reported in table 1 (Colonna et al., 2010). The enhancement in the zone over the dye pick has been simply obtained, confirming the idea followed from the above discussion (Usami, 1997).

The electrical values registered are shown in the table. The photocurrent reaches an increment > 45% by using a scattering layer with the same size of the transparent slab, whereas it is quenched by a thicker scattering layer (~ 22 μm).

Finally it is instructive to evaluate the enhancement factor due to the ratio between IPCE$_{SL}$ and IPCE$_{St-DSC}$. The region of the actual enhancement due to the scattering layer is centered at over 700 nm.
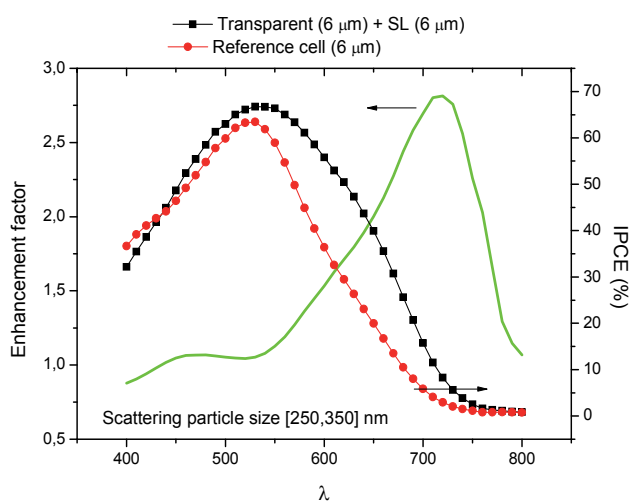
Fig. 21. Single IPCEs for transparent and SL arrangement and enhancement factor due to the SL.

Cell	TiO$_2$ (μm)	Jsc (mA/cm^2)	Voc (mV)	ff (%)	η (%)
A	12	13.7	710	61	5.93
B	12 + 12	20.2	719	59	8.55
C	12 + 12 + 10	14.4	766	59	6.53

Table 1. Arrangement of photoelectrodes and electric performances of standard DSC (st-DSC) along with scattering structure integrated.

In conclusion the use of larger titania particles for light scattering within the dye sensitized solar cell has been investigated in terms of enhancement in the red region of the spectrum. It has been found that for particular arrangements the photocurrent improvement can reach unprecedented results (Colonna et al., 2010).

4.3 Photonic crystals

One Dimension Photonic Crystals (1DPC) within the DSC assembly represent probably the most important field for future development of the field for several reasons soon described. Up until 2008 it was known from some authors that the integration with inverse opals

(3DPC) could be possible but mechanisms arising in that dye solar cell is different from the one described in the rest of the section since it is coherent scattering effect (Nishimura et al., 2003; Halaoui et al., 2005; Lee et al., 2008; Mihi & Miguez, 2005; Mihi et al., 2006, 2008). The combination of one dimension photonic crystal (1DPCs) layers made by using colloidal solution of SiO$_2$ and TiO$_2$ in the dye solar cell technology has been introduced by *S. Colodrero* and *H. Miguez* at CSIC in 2008 as a new powerful tool for DSC technology (Colodrero et al., 2008). They demonstrated the physical properties of the photonic crystal stack in terms of modes of the light once has passed through the multilayer assembly (Colodrero et al., 2009a; Colodrero et al., 2009b; Lozano et al., 2010). The materials integrated on the nc-TiO$_2$ is composed by alternating SiO$_2$ (n$_{SiO2}$ ~ 1,5) and TiO$_2$ (n$_{TiO2}$ ~ 2,5). The periodic arrangement of layers creates patterns of waves interfering in a range of wavelength depending on the thicknesses of each layer when the light is reflected. This imply that the DSC-PCs based can generate a gain with respect to a standard DSC because both the incoming polychromatic light stimulates transitions (standard process) and the reflected PC's band is sent back into the cell. Moreover the arrangement of silica-titania bi-layers creates a periodic refractive index responsible of the photonic band, causing the structural color of the photoanode (Calvo et al., 2008). The Bragg's law implies that the reflected wavelength due to an *optical thickness* of n$_1$d$_1$ + n$_2$d$_2$ is:

$$\lambda_B = 2(n_1 d_1 + n_2 d_2) \tag{4}$$

where the factor 2 refers to the double verse (in and out) of the optical path. The emission photonic band can be calculated by considering the Distributed Bragg Reflector (DBR) used for waveguides. In this case the *photonic stop band* is given by the formula:

$$\Delta\lambda_B = \frac{4\lambda_B}{\pi} asin\left[\frac{n_2 - n_1}{n_1 + n_2}\right] \tag{5}$$

where λ_B derives from the (1). This band represents the optical range of reflected wavelength on the alloy and for the materials used in this study for example with a λ_B = 650 nm, the $\Delta\lambda_B$ is ca. 200 nm (see figure 2). The intensity of the reflectance is given by:

$$R = \left[\frac{(n_0)(n_2)^{2N} - (n_S)(n_1)^{2N}}{(n_0)(n_2)^{2N} + (n_S)(n_1)^{2N}}\right]^2 \tag{6}$$

where n$_0$, is the refractive indexes of the entering medium, n$_1$, n$_2$ the indexes of the alternating materials and finally n$_s$ the index of the exit material. N is the number of the bi-layers creating the structure.

The PC can be created with a simple reliable procedure (Colodrero et al., 2008) giving the possibility to tailor the optical thickness by varying the operative settings of deposition. It consists in the growth of layers by spin coating technique. The final result is the creation of an stack of porous layers. Due to the porosity itself the electrolyte can infiltrate in the pores where it modifies the dielectric constant, hence causing the variation of refractive index of the layer stack and the reflectance Bragg's peak is consequently red shifted according to the Eq. (4). Therefore the reflectance of the complete DSC device will present reflection at wavelengths corresponding to the previous reported in figure plus a shift to the red because of refractive index variation. The reflection will enhance electrical and optical characteristics

of the standard cell by conferring selective photocurrent enhancement. Indeed the IPCE shows well defined improvement zones corresponding to the reflected range of light.
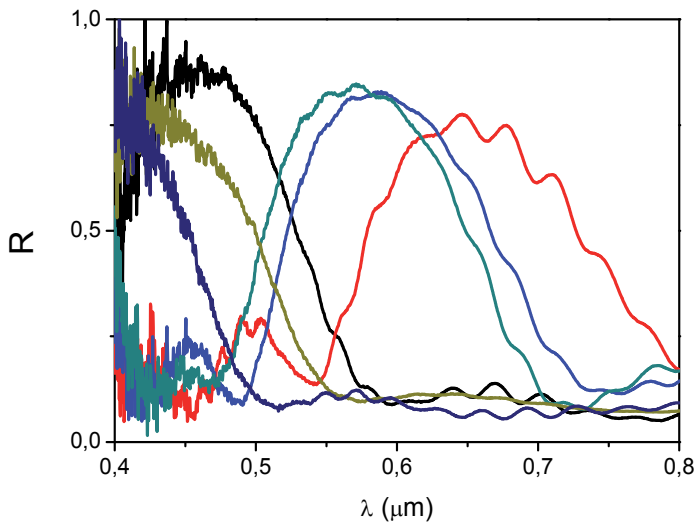
Fig. 22. Reflectance on nc-TiO$_2$ PEs containing SiO$_2$/TiO$_2$ bi-layers measured by FTIR.
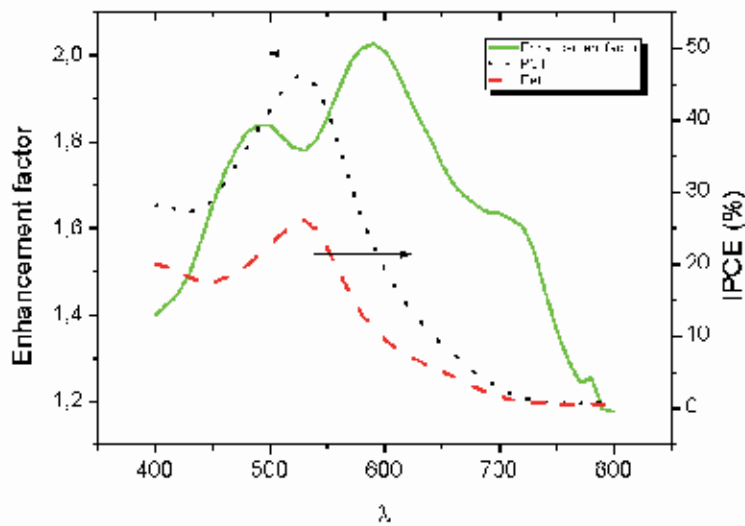
Fig. 23. IPCE enhancement factor calculated by the ratio between the PC integrated and the standard DSC.

The last point is of importance in this development because not only the cell will have high performances, but also a structural coloration will arise independently of the dye color. Finally the important consideration is that the 1DPC-DSC keeps the transparency, meaning that such DSC branch can be further explored for BIPV applications (Colonna et al., 2011b).

4.4 Angular refractive path

Recently (Colonna et al., 2010; Dominici et al., 2010) a strong enhancement of short circuit photocurrent I_{SC} by varying the angle of incidence of a monochromatic laser beam was shown for DSCs. A light path lengthening is active, supposedly, due to the typical features of the absorbing (titania) layer in the semitransparent DSC. I.e., its (relatively) low refractive index n and absorption coefficient a which offer margin improvement for an Angular Refractive Path (ARP) factor to increase the LHE. Indeed, an external oblique incidence θ_a of light corresponds to an oblique angle of propagation θ_{eff} inside the sensitized titania too. The lower the effective index n_{eff} the larger the internal angle θ_{eff}. When $a \cdot h$ is low, an inclination of the propagation line inside the active layer allows to lengthen the path and further absorb light beyond the inherent limit of the native thickness h. Evidence of the ARP factor depends both on the thickness of the cell and the wavelength, plus the eventual use of a coupling prism. The prism allows indeed to reach larger angles of propagation. According to theory, the ARP is shown to be more effective for thinner cells and at wavelengths where the dye molecules absorb less, while the use of the prism enhances it further. The ARP may also explain why DSCs under diffuse illumination work better than other PV technologies, giving hints for new concepts in design of more efficient DSCs.

In order to present evidence of such effect, we initially propose three simple configurations in Fig. 24. The same cell is firstly illuminated in an EQE (i.e., IPCE) setup at $\theta=00°$ (normal incidence) retrieving the quantum efficiency spectrum. Then the DSC is rotated and illuminated at a $\theta=45°$ angle of incidence. Hence, for the same angle in air (between the light beam and the normal to the cell) a coupling prism is used (half cube, BK7 glass prism). In this last case a matching index oil (n=1.66) is used between the prism (n=1.515) and the glass substrate (n=1.59).
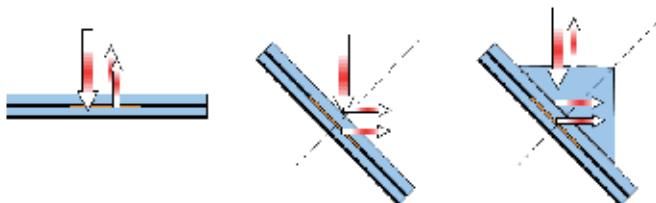
Fig. 24. Three simple configurations to test the refractive angular path. They correspond to normal incidence ($\theta=00°$) without prism, oblique incidence ($\theta=45°$) without prism and oblique incidence ($\theta=45°$) with prism. To keep the light spot always wholly inside the active area means to have constant impinging power. The external reflections are represented together with reflection from the active layer.

The spectra registered in the wavelength range 400-650nm appear in Fig. 25, from bottom to top following the order of their presentation. There is a certain enhancement deriving from the use of an oblique incidence, further pushed up by the use of the prism. Such enhancement can be represented by normalizing the last two curves to the first one. It presents two main features. Firstly, where the EQE (hence, absorption) is high the enhancement has got a local minimum and vice-versa. This feature is expected as introduced on the basis of the ARP theory, discussed more in detail in the following. Secondly, there is a certain monotonic increase of the enhancement with wavelength. This may derive from a λ dispersion of the refractive index of the porous titania.
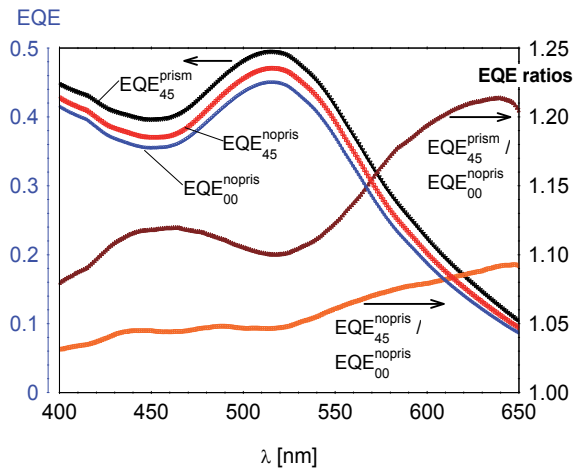
Fig. 25. Measured EQE for three simple configurations on a thin (3μm) DSC. The three configurations correspond to normal incidence (θ=00°) without prism, oblique incidence (θ=45°) without prism and oblique incidence (θ=45°) with prism. The light spot is always wholly inside the active area (impinging power is constant). The enhancement ratios are retrieved normalizing the last two curves to the first one.
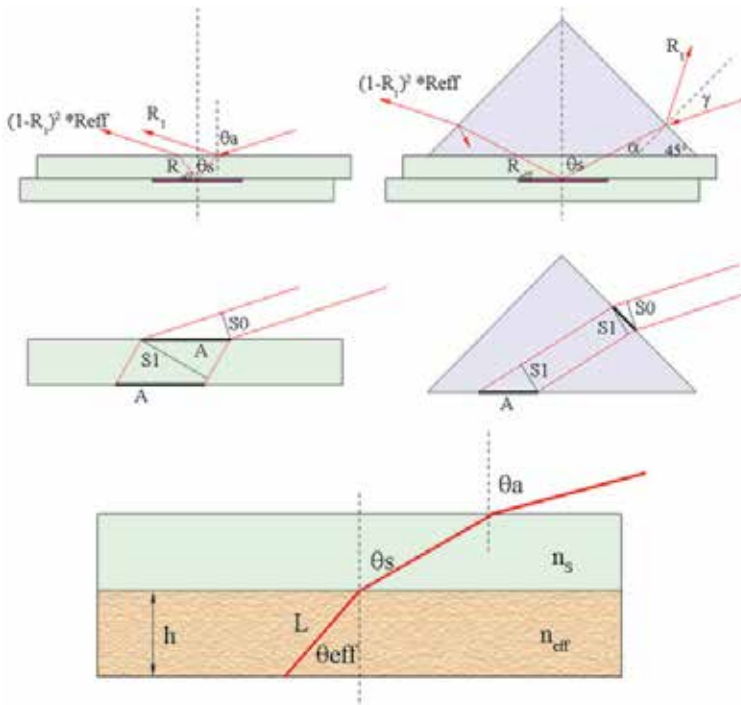
Fig. 26. Mechanism of the three main angular factors in the case of bare device and prism coupling. The considered effects are external reflectivity, projection of the active area and angular refractive path.

Now, the refractive term which we call ARP is not the only acting. Usually angular effects are known as detrimental on the output of photovoltaic devices. This is mainly due to a geometrical factor. When the cell is rotated in a wider light beam, the angular reduction of cross section seen by the cell reduces the collected power according to the *cosine law* (Balenzategui & Chenlo, 2005). Under a sun-simulator, such an effect does not allow to evaluate the other three angular factors we are interested in, since these are important at large angles but are screened by the convolution with the *cosine* term. With the laser, taking care that the spot size of the illuminating beam is always fully contained inside the active area, the impinging power is constant. Hence, the photocurrent measured for each incidence angle is directly proportional to the conversion efficiency and there is no need to take into account the *cosine law*. Instead, we will discuss in the following three other angular factors that are still acting on the photocurrent. These are the external air glass reflectance, the variation of the light intensity and the term of refraction ARP. A schematic of their action mechanism is drawn in the Fig. 26, for without and with coupling prism. The same external angle in air θ_a (considered between the light ray and the normal to the cell substrate) converts in two different angles of propagation inside the substrate θ_s for the bare DSC and with prism. Respectively: $\theta_s=asin(sin\theta_a/n_s)$; $\theta_s=45°-a=45°-asin(sin\gamma/n_s)= 45°-asin[sin(45°-\theta_a)/n_s]$. For simplicity we have used Snell law considering the same refractive index for the prism and the substrate n_s. At the same time, the reflection at their interface may be neglected. The first row of Fig. 26 represent the relevant angles and reflectance. What we consider here is the external air glass reflectance R_1 (in the figure) which varies with the incidence angle. The other one R_{eff} is the reflectance from the active layer (more precisely, multilayer stack). This can be used in attenuated total reflection (ATR) or different setups to study the internal layers but is not of interest here. In the following the external reflectance will be considered by using instead the term of transmittance $T(\theta)=1-R_1(\theta)$. The second row of the Fig. 26 represents the projection area A of the beam over the active area, respect to its external cross section S_0. The projection area affects, together with the transmittance, the light intensity over the titania $I(\theta)\propto T(\theta)/A(\theta)$. Finally, the last row represents the light path L inside the active layer which may be expressed using Snell law again, $L=h/cos\theta_{eff}=h/cos[asin(n_s sin\theta_s/n_{eff})]$. We are indicating the refractive index of the titania layer as an effective index n_{eff} since the nanoporous nature of the titania. It is anchored with dye molecules and its porosity filled with the electrolyte. Hence, according to a Bruggemann effective medium approximation, n_{eff} should be somewhat in between the index of a bulk titania (in anatase phase) and the electrolyte one (mainly due to its solvent).

To represent such angular factors for both bare DSCs and DSC plus prism, we prefer using the internal angle in glass, θ_s. The transmittance $T(\theta)$ term is well known by the Fresnel law which can be applied for both bare DSC and prism configurations. For the bare cell, T appears symmetrical when representing it versus both positive and negative angles of incidence (-90°≤θ_a≤+90° => -40°<θ_s<+40°). The same doesn't hold for the prism and the same full θ_a range converts in an asymmetrical different θ_s range (+05°<θ_s<+85°, when considering a single prism side as the entrance one). In such case, the T factor is a limiting one only for very larger positive angles. In the case of using an adequate emi-cylindrical prism (instead that the half cube one) T would be constant across a full range of θ_s. It should be noted that experimentally, the two ranges cannot be fully explored. At grazing angle the cross section of the substrate or the prism side becomes too small. The variation of the projection area has been represented as S_0/A, retrieved by means of geometrical considerations from the previous Fig. 26 and Snell law once more. In the case of the bare cell such factor follows a

cosine law. Finally, we plot the angular refractive path as $L=h/cos\theta_{eff}=h/cos[asin(n_s sin\theta_s/n_{eff})]$
for different indexes of the titania layer. The lower the n_{eff} the larger the inclination of the
rays, hence the lengthening of the path. The ARP factor depends on θ_{eff} and appears the
same for the two configurations, when representing it towards the internal angle θ_s.
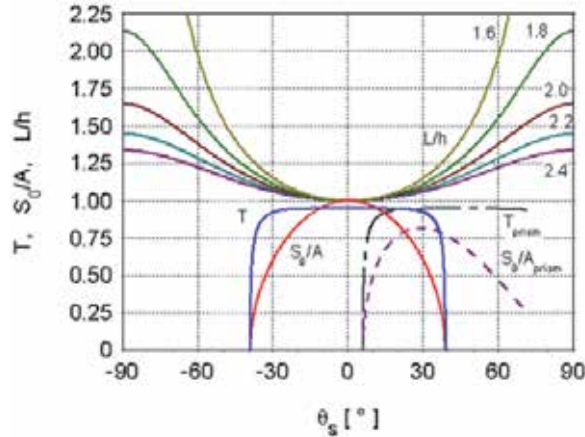
Fig. 27. Computed analytical forms of the three different angular factors that affect I_{SC}.
Normalized projection section S_0/A of the beam over the titania (bare cell, bottom central,
and with prism, bottom right). Transmitted light power T at the external air/glass interface
without (middle central) and with prism (middle right), for the case of unpolarized light.
Normalized light path L/h for five different effective indexes of the titania/electrolyte phase
(top curves, from bottom to top n_{eff} = 2.4, 2.2, 2.0, 1.8 and 1.6).
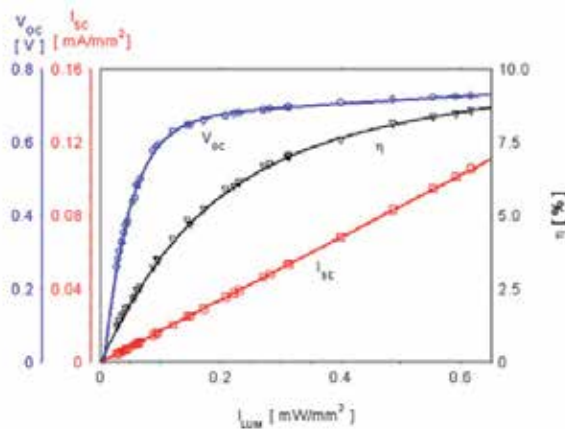
Fig. 28. Main parameters of a DSC measured versus the light intensity at λ=545nm and
normal incidence. The I_{SC} could be fitted to a linear curve, while the V_{OC} and the power
efficiency η to an exponential plus a linear. The light spot from a lamp was about 8mm² .

In the Fig. 27 the computed variation of the three factor are represented. Using a simple
approximation of a Lambert Beer exponential absorption in the sensitized titania, we may
write the quantum efficiency as:

$$EQE = LHE \cdot IQE = T\left(\theta_s\right) \cdot [1 - e^{-\alpha L(\theta_s)}] \cdot \eta_{inj}\eta_{col} \qquad (7)$$

The effect of the second mechanism, the projection area and its influence on the intensity, may be supposed to potentially affect the internal quantum efficiency IQE via one or both of its subterms, the injection η_{inj} and collection η_{col} efficiencies (Trupke et al., 2000). Since the T factor is well known, and we are mainly interested in the refractive path, the effect of the intensity yet unknown needs to be quantified or cleared out in some other way. In the Fig. 28 we report measurements of the main parameters of a standard DSC (thick, h=12μm) towards the intensity I_{LUM} of a monochromatic beam (λ=545nm), at normal incidence (θ_s=0°). The short circuit current I_{SC} keeps linear in the full used range. Hence, in such range there is no apparent dependence of the EQE on the intensity. The following angular measurements were executed with a light intensity which remains inside the I_{LUM} range of Fig. 28.

The Fig. 29 presents angular measurements on thick and thin cells at a wavelength (λ=633nm) where EQE is quite low, about one third of the maximum. The two central curves are the measurements on a standard DSC (thick, h=12μm). The lowest of the two (M-shaped) represents the bare EQE while the upper one (U-shaped) is the EQE normalized to the transmittance T (top solid line, blue on line). As it can be observed the resulting normalized EQE is monotonically increasing with the module of the angle θ. It could be fitted by using the refractive term $1-e^{-ah/cos[asin(n_s sin\theta_s/n_{eff})]}$ retrieving an effective index of n_{eff} = 2.21.
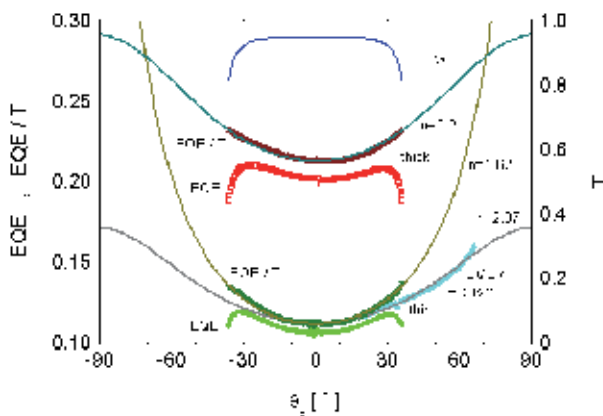
Fig. 29. EQE measured on thick and thin DSCs at λ=633nm. All normalized curves could be fitted to the angular path (Lambert-Beer as a function of the angle). The retrieved effective indexes depend on the specific cell and for a given cell also upon using or not the prism. This may be due to different TiO_2 porosities and thicknesses and to single cell disuniformity.

Experimentally, the symmetry of the curves indicate a proper alignment of the light beam with respect to the axis of rotation. The two bottom central curves represent similar measurements on a thin (h=3μm) cell. In this case, a larger angular enhancement could be seen, considered both in absolute and in percentage values. This is expected since the lower h. The fit with the refractive term is rather good, but the retrieved n_{eff} = 1.62 is much lower than the previous one on the thick cell. This could be ascribed to real differences in the titania layer porosity, but the difference appears to be too large. Another physical effect may be taken into consideration. Increasing the angle, and so the path lengthening, means to effectively absorb photons and generate charges closer to the photoelectrode. So the

electrolyte ions should pass through a longer percolation path across the nanoporous titania. This supposedly influences the collection efficiency η_{col} in a different way between thick and thin cells. An outlook of this work is to investigate such potential effect with electrochemical impedance spectroscopy (EIS) measurements at different angles of incidence.

The bottom curve on the right is the normalized EQE when using the coupling prism on the thin cell. Also now we fitted (somewhat less well at large angles) with the refractive path, but the refractive index is still different (n_{eff} = 2.07) and this time on the same cell. Such aspect is not good and will require further investigations in the future, to reach a good agreement between measurements on the bare cell and the prism case. Experimentally, when excluding the intensity factor, a further issue could be still influencing. Indeed, if spatial disuniformity of the layer is present (hence, of EQE across the active area), the enlargement of the beam projection with the angle could affect the angular trend by sampling regions with different EQE. This could partially explain the observed differences and indicate the importance of having DSCs with a very uniform titania layer for the angular measurements. Another outlook for future implementation is the execution of measurements with also an emi-cylindrical prism and the correlation of the results obtained with all the three coupling elements (bare cell, half-cube prism, emi-cylindrical prism).

5. Conclusions

The technology of the dye solar cells offers nowadays a quite assessed typical configuration. Yet, different strategies are currently under study for increasing the stability and lifetime, but also for the improvement of the energy conversion efficiency. Among such techniques, acting on the main components of the DSCs remains almost a must issue. Traditionally, modifying the titania properties, looking for different fabrications or semiconductors, together with the research of new dyes and electrolytes, still seem a very wide action field, too wide to make sure previsions but surely promising in the actual energetic panorama. Besides, approaches derived from nano photonic and plasmonic technology are being integrated in the dye solar cells with more complex schemes to further improve efficiency in a wide sense of photon management. In such a context, the present work investigated the use of scattering layers, double dye co-sensitization, photonic crystals and also angular refractive path. Till now, the use of diffusive scattering layers led to the best performances. Typical size of the used opaque particles (150 to 400 nanometers) causes along all the wavelengths a reflectance of the non absorbed light back into the cell. Quantitatively the effect caused the improvement of a relative 47% in photocurrent and over 40% in efficiency. The co-sensitization technique was approached by using the conventional Red Dye together with the SDA1570 typically used for dye laser systems. The co-sensitization procedure was showed to be effective, putting into evidence non-linear effects by synergic mechanisms. The performance of co-sensitized cells outperform the sum of those with the single dyes. The immersion of the partially N719-sensitized photoanode in a SDA solution induces the saturation of the remaining free TiO_2 surface and at the same time a partial displacement of the already attached N719 molecules, organizing the two molecules in such a way which limits the energy losses due to the excitonic interactions between homologue molecules. Despite the lower efficiency (~20%) of the co-sensitized DSCs with respect to standard ones, transparency is gained (doubled), confirming as an effective strategy for BIPV applications. The integration of photonic crystals into the DSC for structural coloration represents one of the most engaging results. In fact, despite the color created by the silica/titania multilayer grown onto the nanocrystalline TiO_2 together with the color conferred by the dye itself, the cell is able to enhance the photocurrent and efficiency because of interferential reflections.

Variously colored DSCs were fabricated with the proper designs of the photonic crystals. The PCs schemes led to ca. 60% enhancement in efficiency and ca. 50% in *Jsc*, on thin DSCs, with 3 micrometers thick nc-TiO$_2$ titania. Also in this case the devices are quite transparent, conferring other important properties / instruments to DSC, i.e. for the building integration. The differences between SLs and PCs arrangements have to be ascribed to their basic issues. Photonic Crystals allow selective reflections based on their structural order, while SLs rely on a random configuration. Hence, PCs effect results in well defined enhancements corresponding to the reflected bands, whereas the typically used SLs lead to an increased absorption at the longer wavelengths with a tailoring at the shorter ones. Finally, the PCs are capable to confer a color independent from the dye color and mostly important keeping a good DSCs transparency; the SLs instead are affected by losing DSCs transparency at all. One main contribution of this work has been to realize and discuss state-of-the-art implementations of all these techniques, which actually are largely studied in the literature. Besides them, also an apparently minor feature was investigated responding to a very basic concept of photon management. The application of an angular setup to illuminate DSCs, allowed to quantify the response of the cells to oblique incidence of light. Apart from the power loss due to the reduction of cross section according to the cosine law, the IPCE rises. The bare cells present a maximum in IPCE at an angle of incidence in between 50° and 60°. This happens although the reflectance of the external air/glass interface grows with angle. Such a feature is ascribed to a photon path lengthening, i.e., an angular refractive path. Upon using a coupling prism two main advantages are obtained. The cut-off in the external transmittance can be overcome and at the same time larger internal angles can be achieved. A simplified yet robust model, based on Fresnel reflectance, Snell law of refraction and Lambert-Beer absorption is able to fit the angular dependencies of the quantum efficiency. The model depends on the effective refractive index of the mesoporous titania layer, which can be set as a fit parameter together with the optical absorbance. Hence, the angular IPCE allows also an investigation of the internal active layer, even though simplified at this stage. The enhancement is active due to the typical features of the thin absorbing titania layer, i.e., its refractive index and absorption coefficient, which offer margin improvements for a ray propagating obliquely to be more absorbed. Hence, it depends on the wavelength, thickness and porosity of the titania layer, but also, for example, on the electrolyte refractive index too. From a photon management point of view, the angular effect has in common with the SLs and PCs to be more effective on thin DSCs and at wavelength where they absorbs less. Unfortunately, its disadvantage is to suffer from the reduction of cross section and power. Nevertheless, it can still give suggestions on structuring DSCs working at normal incidence, and, it cannot be excluded also its potential use in proper new designs of thin films DSCs.

6. References

Abbotto, A.; Barolo, C.; Bellotto, L.; De Angelis, F.; Graetzel, M.; Manfredi, N.; Marinzi, C.; Fantacci, S.; Yum, J.-H. & Nazeeruddin, Md. K. (2008). Electron-rich heteroaromatic conjugated bipyridine based ruthenium sensitizer for efficient dye sensitized solar cells. *Chemical Communications* 42, 5318-5320, doi:10.1039/b900208a

Arakawa, H.; Yamaguchi, T.; Takeuchi, A. & Agatsuma, S. (2006). Efficiency Improvement of Dye-Sensitized Solar Cell by Light Confined Effect, *Conference Record of the IEEE 4th WCPEC*, 1, 36-39, ISBN 1-4244-0017-1, Waikoloa, Hawaii, USA, May 7-12, 2006, doi:10.1109/WCPEC.2006.279340

Arakawa, H.; Yamaguchi, T.; Takeuchi, A.; Okada, K.; Ezure, T. & Tanabe, N. (2007). Solar Cells Module. *JP2007012377 (A)*

Balenzategui, J. L. & Chenlo, F. (2005). Measurement and analysis of angular response of bare and encapsulated silicon solar cells. *Solar Energy Materials and Solar Cells* 86, 1, 53-83, doi:10.1016/j.solmat.2004.06.007

Barnes, P. R. F.; Anderson, A. Y.; Koops, S. E.; Durrant, J. R. & O'Regan, B. C. (2008). Electron injection efficiency and diffusion length in dye-sensitized solar cells derived from incident photon conversion efficiency measurements. *Journal of Physical Chemistry C* 113, 1126-1136

Bisquert, J.; Fabregat-Santiago, F.; Mora-Sero, I.; Garcia-Belmonte, G. & Gimenez, S. (2009). Electron Lifetime in Dye-Sensitized Solar Cells: Theory and Interpretation of Measurements. *Journal of Physical Chemistry C* 113, 40, 17278–17290, doi:10.1021/jp9037649

Buscaino, R.; Baiocchi, C.; Barolo, C.; Medana, C.; Graetzel, M., Nazeeruddin, Md. K. & Viscardi, G. (2007). A mass spectrometric analysis of sensitizer solution used for dye-sensitized solar cell. *Inorganica Chimica Acta* 361, 798–805

Calvo, M. E.; Colodrero, S.; Rojas, T. C.; Anta, J. A.; Ocaña, M. & Míguez, H. (2008). Photoconducting Bragg Mirrors based on TiO2 Nanoparticle Multilayers. *Advanced Functional Materials* 18, 18, 2708-2715, doi:10.1002/adfm.200800039

Catchpole, K. R. & Polman, A. (2008). Plasmonic solar cells. *Optics Express* 16, 26, 21793-21800, doi:10.1364/OE.16.021793

Chappel, S.; Grinis, L.; Ofir, A. & Zaban, A. (2005). Extending the Current Collector into the Nanoporous Matrix of Dye Sensitized Electrodes. *Journal of Physical Chemistry B* 109, 1643-1647, doi:10.1021/jp044949+

Chen, C.-Y.; Wu, S.-J.; Wu, C.-G.; Chen, J.-G.; Ho, K.-C. New ruthenium complexes containing oligoalkylthiophene-substituted 1,10-phenanthroline for nanocrystalline dye-sensitized solar cells. *Advanced Functional Materials* 17, 1, 29–36

Chen, D.; Huang, F.; Cheng, Y.-B. & Caruso, R. A. (2009). Mesoporous Anatase TiO2 Beads with High Surface Areas and Controllable Pore Sizes: A Superior Candidate for High-Performance Dye-Sensitized Solar Cells. *Advanced Materials* 21, 21, 2206–2210

Chen, X. & Mao, S. S. (2007). Titanium Dioxide Nanomaterials: Synthesis, Properties, Modifications, and Applications. *Chemical Reviews* 107, 7, 2891−2959, doi:10.1021/cr0500535

Chen, Y.; Zeng, Z.; Li, C.; Wang, W.; Wang X. & Zhang, B. (2005). Highly efficient co-sensitization of nanocrystalline TiO2 electrodes with plural organic dyes. *New Journal of Chemistry* 29, 773-776, doi:10.1039/b502725j

Cid, J.-J.; Yum, J.-H.; Jang, S.-R.; Nazeeruddin, M. K.; Martinez-Ferrero, E.; Palomares, E.; Ko, J.; Graetzel, M. & Torres, T. (2007). Molecular Cosensitization for Efficient Panchromatic Dye-Sensitized Solar Cells. *Angewandte Chemie International Edition* 46, 44, 8358–8362, doi:10.1002/anie.200703106

Clifford, J. N.; Palomares, E.; Nazeeruddin, M. K.; Thampi, R.; Grätzel, M. & Durrant, J. R. (2004). *Journal of American Chemical Society* 126, 18, 5670-5671, doi:10.1021/ja049705h

Colodrero, S.; Ocaña, M. & Míguez, H. (2008). Nanoparticle-based one-dimensional photonic crystals. *Langmuir* 24, 9, 4430-4434

Colodrero, S.; Mihi, A.; Anta, J. A.; Ocaña, M. & Míguez, H. (2009a). Experimental demonstration of the mechanism of light harvesting enhancement in Photonic-Crystal-Based Dye-Sensitized Solar Cells. *Journal of Physical Chemistry C* 113, 4, 1150-1154

Colodrero, S.; Mihi, A.; Haggman, L.; Ocaña, M.; Boschloo, G.; Hagfeldt, A. & Míguez, H. (2009b). Porous One-Dimensional Photonic Crystals Improve the Power-Conversion Efficiency of Dye-Sensitized Solar Cells. *Advanced Materials* 21, 7, 764-770

Colonna, D.; Dominici, L.; D'Ercole, D.; Brunetti, A.; Michelotti, F.; Brown, T. M.; Reale, A. & Di Carlo, A. (2010). *Superlattice and Microstructures* 47, 197-201

Colonna, D.; Colodrero, S.; Miguez, H.; Di Carlo, A. (2011). Introducing structural color in dye sensitized solar cells by using photonic nanostructures: interplay between conversion efficiency and optical properties. [in print]

Colonna, D.; Capogna, V.; Lembo, A.; Reale, A.; Brown, T. M. & Di Carlo, A. (2011). Efficient co-sensitization of nanocrystalline titania photo-anodes of Dye-Sensitized Solar Cells. [in print]

Dai, S.; Wang, K.; Weng, J.; Sui, Y.; Huang, Y.; Xiao, S.; Chen, S.; Hu, L.; Kong, F.; Pan, X.; Shi, C. & Guo, L. (2005). Design of DSC panel with efficiency more than 6%. *Solar Energy Materials and Solar Cells* 85, 447–455

Di Carlo, A.; Reale, A.; Brown, T. M.; Cecchetti, M.; Giordano, F.; Roma, G.; Liberatore, M.; Mirruzzo, V. & Conte, V. (2008). Smart Materials and Concepts for Photovoltaics: Dye Sensitized Solar Cells, In: *Smart Materials for Energy, Communications and Security*, I.A. Luk'yanchuk & D. Mezzane, (Ed.), 97-126, Springer, ISBN 978-1-4020-8795-0 (Print), 978-1-4020-8796-7 (Online), Dordrecht, The Netherlands, doi:10.1007/978-1-4020-8796-7

Ding, I-K.; Zhu, J.; Cai, W.; Moon, S.-J.; Cai, N.; Wang, P.; Zakeeruddin, S. M.; Graetzel, M.; Brongersma, M. L.; Cui, Y. & McGehee, M. D. (2011). Plasmonic Dye-Sensitized Solar Cells. *Advanced Energy Materials* 1, 52-57

Dominici, L.; Vesce, L.; Colonna, D.; Michelotti, F.; Brown, T. M.; Reale, A. & Di Carlo, A. (2010). Angular and prism coupling refractive enhancement in dye solar cells. *Applied Physics Letters* 96, 103302, doi:10.1063/1.3328097

Ezaki, S.; Gonda, I.; Okuyama, Y.; Takashima, A. & Furusaki, K. (2006). Dye Sensitized Solar Cells. *JP2006294423 (A)*

Ferber, J. & Luther, J. (1998). Computer simulations of light scattering and absorption in dye-sensitized solar cells. *Solar Energy Materials and Solar Cells* 54, 1-4, 265-275

Goldstein, J.; Yakupov, I. & Breen, B. (2010). Development of large area photovoltaic dye cells at 3GSolar. *Solar Energy Materials and Solar Cells* 94, 4, 638-641

Graetzel, M. (2005). Solar energy conversion by dye-sensitized photovoltaic cells. *Inorganic Chemistry* 44, 20, 6841-6851

Gutierrez-Tauste, D.; Zumeta, I.; Vigil, E.; Hernandez-Fenollosa, M. A.; Domenech, X. & Ayllon, J. A. (2005). New low-temperature preparation method of the TiO2 porous photoelectrode for dye-sensitized solar cells using UV irradiation. *Journal of Photochemistry and Photobiology A: Chemistry* 175, 165-171 doi:10.1016/j.jphotochem.2005.04.031

Hagfeldt, A. & Graetzel, M. (1995). Light-Induced Redox Reactions in Nanocrystalline Systems. *Chemical Reviews* 95, 1, 49-68, doi:10.1021/cr00033a003

Hägglund, C.; Zäch, M. & Kasemo, B. (2008). Enhanced charge carrier generation in dye sensitized solar cells by nanoparticle plasmons. *Applied Physics Letters* 92, 1, 013113, doi:10.1063/1.2830817

Halaoui, L. I.; Abrams, N. M. & Mallouk, T. (2005). Increasing the conversion efficiency of dye-sensitized TiO2 photoelectrochemical cells by coupling to photonic crystals. *Journal of Physical Chemistry B*, 109, 13, 6334-6342

Halme, J.; Boschloo, G.; Hagfeldt, A. & Lund, P. (2008). Spectral Characteristics of Light Harvesting, Electron Injection, and Steady-State Charge Collection in Pressed TiO2 Dye Solar Cells. *Journal of Physical Chemistry C* 112, 5623-5637, doi:10.1021/jp711245f

Hinsch, A.; Kroon, J. M.; Kern, R.; Uhlendorf, I.; Holzbock, J.; Meyer, A. & Ferber, J. Long-term stability of dye-sensitised solar cells (2001). *Progress in Photovoltaics: Research and Applications* 9, 6, 425–438, doi:10.1002/pip.397

Hinsch, A.; Behrens, S.; Berginc, M.; Bönnemann, H.; Brandt, H.; Drewitz, A.; Einsele, F.; Faßler, D.; Gerhard, D.; Gores, H.; Haag, R.; Herzig, T.; Himmler, S.; Khelashvili, G.; Koch, D.; Nazmutdinova, G.; Opara-Krasovec, U.; Putyra, P.; Rau, U.; Sastrawan, R.; Schauer, T.; Schreiner, C.; Sensfuss, S.; Siegers, C.; Skupien, K.; Wachter, P.; Walter, J.; Wasserscheid, P.; Würfel, U. & Zistler, M. (2008). Material Development for Dye Solar Modules: Results from an Integrated Approach. *Progress in Photovoltaics: Research and Applications* 16, 6, 489–501

Hore, S.; Nitz, P.; Vetter, C.; Prahl, C.; Niggemann, M. & Kern, R. (2005). Scattering spherical voids in nanocrystalline TiO2 - enhancement of efficiency in dye-sensitized solar cells. *Chemical Communications* 15, 2011-2013, doi:10.1039/B418658N

Hore, S.; Vetter, C.; Kern, R.; Smit, H. & Hinsch, A. (2006). Influence of scattering layers on efficiency of dye-sensitized solar cells. *Solar Energy Materials and Solar Cells* 90, 9, 1176-1188, doi:10.1016/j.solmat.2005.07.002

Ito, S.; Matsui, H.; Okada, K.; Kusano, S.; Kitamura, T.; Wada, Y. & Yanagida, S. (2004). Calibration of solar simulator for evaluation of dye-sensitized solar cells. *Solar Energy Materials and Solar Cells* 82, 3, 421-429, doi:10.1016/j.solmat.2004.01.030

Ito, S.; Nazeeruddin, M.; Liska, P.; Comte, P.; Charvet, R.; Pechy, P.; Jirousek, M.; Kay, A.; Zakeeruddin, S. & Graetzel, M. (2006). Photovoltaic Characterization of Dye-sensitized Solar Cells: Effect of Device Masking on Conversion Efficiency. *Progress in photovoltaics: research and applications* 14, 7, 589-601

Ito, S.; Chen, P.; Comte, P.; Nazeeruddin, M. K.; Liska, P.; Pechy, P. & Graetzel, M. (2007). Fabrication of screen-printing pastes from TiO2 powders for dye-sensitised solar cells. *Progress in photovoltaics: research and applications,* 15, 6, doi:10.1002/pip.768

Kalyanasundaram, K. & Graetzel, M. (1998). Applications of functionalized transition metal complexes in photonic and optoelectronic devices. *Coordination Chemistry Reviews* 177, 1, 347-414

Kay, A. (1995). Dye-stabilised photovoltaic cell module. *DE4416247 (A1)*

Khelashvili, G.; Behrens, S.; Weidenthaler, C.; Vetter, C.; Hinsch, A.; Kern, R.; Skupien, K.; Dinjus, E. & Bonnemann, H. (2006). Catalytic platinum layers for dye solar cells: A comparative study. *Thin Solid Films*, 511–512, 342–348, doi:10.1016/j.tsf.2005.12.059

Kim, C.; Lior, N. & Okuyama, K. (1996). Simple mathematical expressions for spectral extinction and scattering properties of small size-parameter particles, including examples for soot and TiO2. *Journal of Quantitative Spectroscopy and Radiative Transfer* 55, 3, 391-411, doi:10.1016/0022-4073(95)00160-3

Kim, H.; Auyeung, R. C. Y.; Ollinger, M.; Kushto, G. P.; Kafafi, Z. H. & Piqué, A. (2006). Laser-sintered mesoporous TiO2 electrodes for dye-sensitized solar cells. *Applied Physics A: Materials Science & Processing* 83, 1, 73-76, doi:10.1007/s00339-005-3449-0

Kim, S. S.; Nah, Y. C.; Noh, Y. Y.; Jo, J. & Kim, D. Y. (2006). Electrodeposited Pt for cost-efficient and flexible dye-sensitized solar cells. *Electrochimica Acta*, 51, 3814–3819, doi:10.1016/j.electacta.2005.10.047

Koide, N. & Han, L. (2004). Measuring methods of cell performance of dye-sensitized solar cells. *Review Of Scientific Instruments* 75, 9, 2828-2831, doi:10.1063/1.1784556

Koo, H. J.; Park, J.; Yoo, B.; Yoo, K.; Kim, K. & Park, N. G. (2008). Size-dependent scattering efficiency in dye-sensitized solar cell. *Inorganica Chimica Acta* 361, 3, 677-683

Koops, S. E. & Durrant, J. R. (2008). Transient emission studies of electron injection in dye sensitised solar cells. *Inorganica Chimica Acta* 361, 3, 663-670

Kroon, J. M.; Bakker, N. J.; Smit, H. J. P.; Liska, P.; Thampi, K. R.; Wang, P.; Zakeeruddin, S. M.; Grätzel, M.; Hinsch, A.; Hore, S.; Würfel, U.; Sastrawan, R.; Durrant, J. R.; Palomares, E.; Pettersson, H.; Gruszecki, T.; Walter, J.; Skupien, K. & Tulloch, G. E. (2007). Nanocrystalline dye-sensitized solar cells having maximum performance. *Progress in Photovoltaics: Research and Applications* 15, 1, 1-18, doi:10.1002/pip.707

Kuang, D.; Walter, P.; Nuesch, F.; Kim, S.; Ko, J.; Comte, P.; Zakeeruddin, S. M.; Nazeeruddin, M. K. & Graetzel, M. (2007*). Co-sensitization of Organic Dyes for Efficient Ionic Liquid Electrolyte-Based Dye-Sensitized Solar Cells. *Langmuir* 23, 10906-10909, doi: 10.1021/la702411n

Lee, S.-H. A.; Abrams, N. M.; Hoertz, P. G.; Barber, G. D.; Halaoui, L. I. & Mallouk, T. E. (2008). Coupling of Titania Inverse Opals to Nanocrystalline Titania Layers in Dye-Sensitized Solar Cells. *Journal of Physical Chemistry B* 112, 46, 14415–14421

Lindström, H.; Magnusson, E.; Holmberg, A.; Södergren, S.; Lindquist, S.-E. & Hagfeldt, A. (2002). A new method for manufacturing nanostructured electrodes on glass substrates. *Solar Energy Materials and Solar Cells* 73, 91, doi:10.1016/S0927-0248(01)00114-3

Lozano, G.; Colodrero, S.; Caulier, O.; Calvo, M. E. & Miguez, H. (2010). Theoretical Analysis of the Performance of One-Dimensional Photonic Crystal-Based Dye-Sensitized Solar Cells. *Journal of Physical Chemistry C* 114, 8, 3681–3687

Meyer, T.; Martineau, D.; Azam, A. & Meyer, A. (2007). All Screen Printed Dye Solar Cell, *Proceeding of SPIE* 6656, 665608.1-665608.11, ISBN 978-0-8194-6804-8, San Diego, California, USA, August 28-30, 2007

Meyer, T.; Scott, M.; Martineau, D.; Meyer, A. & Cainaud, Y. (2009). Turning the dye solar cell into a product, *3rd International Conference Industrialization of DSC, DSC-IC 09*, Nara, Japan, April 22-24, 2009

Mihi, A. & Miguez, H. (2005). Origin of Light-Harvesting Enhancement in Colloidal-Photonic-Crystal-Based Dye-Sensitized Solar Cells. *Journal of Physical Chemistry B* 109, 15968-15976

Mihi, A.; López-Alcaraz, F. J. & Míguez, H. (2006). Full spectrum enhancement of the light harvesting efficiency of dye sensitized solar cells by including colloidal photonic crystal multilayers. *Applied Physics Letters* 88, 193110

Mihi, A.; Calvo, M.; Anta, J. A. & Miguez, H. (2008). Spectral Response of Opal-Based Dye-Sensitized Solar Cells. *Journal of Physical Chemistry C* 112, 1, 13-17

Mincuzzi, G.; Vesce, L.; Reale, A.; Di Carlo, A. & Brown, T. M. (2009). Efficient sintering of nanocrystalline titanium dioxide films for dye solar cells via raster scanning laser *Applied Physics Letters* 95, 103312, doi:10.1063/1.3222915

Mincuzzi, G.; Vesce, L.; Liberatore, M.; Reale, A.; Di Carlo, A. & Brown, T. M. (2011). Dye Laser Sintered TiO_2 Films for Dye Solar Cells Fabrication: an Electrical, Morphological and Electron Lifetime Investigation. *IEEE Transaction on Electron Devices*, doi:10.1109/TED.2011.2160643 [in print]

Murakami, T. N. & Graetzel, M. (2008). Counter electrodes for DSC: Application of functional materials as catalysts. *Inorganica Chimica Acta* 361, 572–580

Nazeeruddin, M.; Kay, A.; Rodicio, I.; Humphry-Baker, R.; Muller, E.; Liska, P.; Vlachopoulos, N. & Graetzel, M. (1993). Conversion of light to electricity by cis-X2bis(2,2'-bipyridyl-4,4'-dicarboxylate)ruthenium(II) charge-transfer sensitizers (X = Cl-, Br-, I-, CN-, and SCN-) on nanocrystalline titanium dioxide electrodes. *Journal of the American Chemical Society* 115, 14, 6382, doi:10.1021/ja00067a063

Nazeeruddin, M. K.; De Angelis, F.; Fantacci, S.; Selloni, A.; Viscardi, G.; Liska, P.; Ito, S.; Takeru, B. & Graetzel, M. (2005). Combined Experimental and DFT-TDDFT

Computational Study of Photoelectrochemical Cell Ruthenium Sensitizers. *Journal of the American Chemical Society* 127, 16835-16847, doi:10.1021/ja052467l

Nishimura, S.; Abrams, N.; Lewis, B. A.; Halaoui, L. I.; Mallouk, T. E.; Benkstein, K. D.; Van de Lagemaat, J. & Frank, A. J. (2003). Standing wave enhancement of red absorbance and photocurrent in dye-sensitized titanium dioxide photoelectrodes coupled to photonic crystals. *Journal of the American Chemical Society* 125, 20, 6306-6310

Ogura, R. Y.; Nakane, S.; Morooka, M.; Orihashi, M.; Suzuki, Y. & Noda, K. (2009). High-performance dye-sensitized solar cell with a multiple dye system. *Applied Physics Letters* 94, 073308, doi:10.1063/1.3086891

Okada, K. & Tanabe, N. (2006). Dye-Sensitized Solar cell and its manufacturing method. *JP2006236960 (A)*

Ono, T.; Yamaguchi, T. & Arakawa, H. (2009). Study on dye-sensitized solar cell using novel infrared dye. *Solar Energy Materials and Solar Cells* 93, 831–835

O'Regan, B. & Graetzel, M. (1991). A low-cost, high-efficiency solar cell based on dye-sensitized colloidal TiO2 films. *Nature* 353, 737-740, doi:10.1038/353737a0

Pan, H.; Ko, S. H.; Misra, N. & Grigoropoulos, C. P. (2009). Laser annealed composite titanium dioxide electrodes for dye-sensitized solar cells on glass and plastics. *Applied Physics Letters* 94, 071117, doi:10.1063/1.3082095

Pala, R. A.; White, J.; Barnard, E.; Liu, J. & Brongersma, M. L. (2009). Design of Plasmonic Thin-Film Solar Cells with Broadband Absorption Enhancements. *Advanced Materials* 21, 1-6

Pandey, S. S.; Inoue, T.; Fujikawa, N.; Yamaguchi, Y. & Hayase, S. (2010). Substituent effect in direct ring functionalized squaraine dyes on near infra-red sensitization of nanocrystalline TiO2 for molecular photovoltaics. *Journal of Photochemistry and Photobiology A: Chemistry* 214, 2-3, 269-275

Park, N.-G. (2010). Light management in dye-sensitized solar cell. *Korean Journal of Chemical Engineering* 27, 2, 375-384, doi:10.2478/s11814-010-0112-z

Peter, L. M. & Wijayantha, K. G. U. (2000). Electron transport and back reaction in dye sensitised nanocrystalline photovoltaic cells. *Electrochimica Acta* 45, 28, 4543-4551, doi:10.1016/S0013-4686(00)00605-8

Pettersson, H.; Gruszecki, T.; Bernhard, R.; Häggman, L.; Gorlov, M.; Boschloo, G.; Edvinsson, T.; Kloo, L. & Hagfeldt A. (2007). The monolithic muticell: A tool for testing material components in dye-sensitized solar cells, *Progress in Photovoltaics: Research and Applications* 15, 113-121

Pichot, F.; Pitts, J. R. & Greg, B. A. (2000). Low-Temperature Sintering of TiO2 Colloids: Application to Flexible Dye-Sensitized Solar Cells. *Langmuir*, 16, 13, 5626–5630, doi:10.1021/la000095i

Polo, A. S.; Itokazu, M. K. & Murakami Iha, N. Y. (2004). Metal complex sensitizers in dye-sensitized solar cells. *Coordination Chemistry Reviews* 248, 1343-1361 doi:10.1016/j.ccr.2004.04.013

Rühle, S.; Greenwald, S.; Koren, E. & Zaban, A. (2008). Optical Waveguide Enhanced Photovoltaics. *Optics Express* 16, 26, 21801-21806, doi:10.1364/OE.16.021801

Saito, Y.; Kitamura, T.; Wada, Y. & Yanagida, S. (2002). Application of Poly(3,4-ethylendioxythiophene) to Counter Electrode in Dye-Sensitized Solar Cells. *Chemistry Letters* 31, 10, 1060, doi:10.1246/cl.2002.1060

Saito, Y.; Kubo, W.; Kitamura, T.; Wada, Y. & Yanagida, S. (2004). I-/I-3(-) redox reaction behavior on poly(3,4-ethylenedioxythiophene) counter electrode in dye-sensitized solar cells. *Journal of Photochemistry and Photobiology A: Chemistry* 164, 1-3, 153-157, doi:10.1016/j.jphotochem.2003.11.01

Sastrawan, R.; Beier, J.; Belledin, U.; Hemming, S.; Hinsch, A.; Kern, R.; Vetter, C.; Petrat, F. M.; Prodi-Schwab, A.; Lechner, P. & Hoffmann, W. (2006). A glass frit-sealed dye solar cell module with integrated series connections. *Solar Energy Materials and Solar Cells* 90, 11, 1680-1691

Schlichthorl, G.; Park, N. G. & Frank, A. J. (1999). Evaluation of the Charge-Collection Efficiency of Dye-Sensitized Nanocrystalline TiO2 Solar Cells. *Journal of Physical Chemistry B* 103, 5, 782-791, doi:10.1021/jp9831177

Seaman, C. H. (1982). Calibration of solar cells by the reference cell method—The spectral mismatch problem. *Solar Energy* 29, 4, 291-298, doi:10.1016/0038-092X(82)90244-4

Shah, A.; Torres, P.; Tscharner, R.; Wyrsch, N. & Keppner, H. (1999). Photovoltaic Technology: The Case for Thin-Film Solar Cells. *Science* 285, 5428, 692-698

Solaronix S.A., April 2011 prod. spec. retrieved from http://www.solaronix.com/products/

Somani, P. R.; Dionigi, C.; Murgia, M.; Palles, D.; Nozar, P. & Ruani, G. (2005). Solid-state dye PV cells using inverse opal TiO2 films. *Solar Energy Materials and Solar Cells* 87, 513–519

Sommeling, P. M.; Rieffe, H. C.; van Roosmalen, J. A. M.; Schönecker, A.; Kroon, J. M.; Wienke, J. A. & Hinsch, A. (2000). Spectral response and IV-characterization of dye-sensitized nanocrystalline TiO2 solar cells. *Solar Energy Materials and Solar Cells* 62, 4, 399-410, doi:10.1016/S0927-0248(00)00004-0

Sommeling, P. M.; Späth, M.; Smit, H. J. P.; Bakker, N. J. & Kroon, J. M. (2004). Long-term stability testing of dye-sensitized solar cells. *Journal of Photochemistry and Photobiology A: Chemistry* 164, 137–144

Suzuki, K.; Yamaguchi, M.; Kumagai, M. & Yanagida, S. (2003). Application of Carbon Nanotubes to Counter Electrodes of Dye-sensitized Solar Cells. *Chemistry Letters* 32, 1, 28-29

Trupke, T.; Würfe, P. & Uhlendorf, I. (2000). Dependence of the Photocurrent Conversion Efficiency of Dye-Sensitized Solar Cells on the Incident Light Intensity. *Journal of Physical Chemistry B*, 104, 48, 11484–11488, doi:10.1021/jp001392z

Tulloch, G. E. (2004). Light and energy-dye solar cells for the 21st century. *Journal of Photochemistry and Photobiology A: Chemistry* 164, 1-3, 209-219, doi:10.1016/j.jphotochem.2004.01.027

Tulloch, G. E. & Skryabin, I. L. (2006). Photoelectrochemical devices. *KR20060035598 (A)*

Tvingstedt, K.; Persson, N.-K.; Inganäs, O.; Rahachou, A. & Zozoulenko, I. V. (2007). Surface plasmon increase absorption in polymer photovoltaic cells. *Applied Physics Letters* 91, 113514, doi:10.1063/1.2782910

Tvingstedt, K.; Dal Zilio, S.; Inganäs, O. & Tormen, M. (2008). Trapping light with micro lenses in thin film organic photovoltaic cells. *Optics Express* 16, 26, 21608-21615

Uchida, S.; Tomiha, M.; Masaki, N.; Miyazawa, A. & Takizawa, H. (2004). Preparation of TiO2 nanocrystalline electrode for dye-sensitized solar cells by 28 GHz microwave irradiation. *Solar Energy Materials and Solar Cells* 81, 135–139, doi:10.1016/j.solmat.2003.08.020.

Usami, A. (1997). Theoretical study of application of multiple scattering of light to a dye-sensitized nanocrystalline photoelectrichemical cell. *Chemical Physics Letters* 277, 1-3, 105-108, doi:10.1016/S0009-2614(97)00878-6

Van de Lagemaat, J.; Park, N. G. & Frank, A. J. (2000). Comparison of Dye-Sensitized Rutile - and Anatase-Based TiO2 Solar Cells. *Journal of Physical Chemistry B* 104, 2044-2052, doi:10.1021/jp994365l

Vesce, L.; Riccitelli, R.; Soscia, G.; Brown, T. M.; Di Carlo, A. & Reale, A. (2010). Optimization of nanostructured titania photoanodes for dye-sensitized solar cells:

Study and experimentation of TiCl$_4$ treatment. *Journal of Non-Crystalline Solids* 356, 37-40, 1958-1961

Vesce, L.; Riccitelli, R.; Orabona, A.; Brown, T. M.; Di Carlo, A. & Reale, A. (2011). Fabrication of Spacer and Catalytic Layers in Monolithic Dye-sensitized Solar Cells. *Progress in Photovoltaics: Research and Applications* [in print]

Walker, A. B.; Peter, L. M.; Lobato, K. & Cameron, P. J. (2006). Analysis of photovoltage decay transients in dye-sensitized solar cells. *Journal of Physical Chemistry B* 110, 50, 25504-25507

Wang, L.; Fang, X. & Zhang, Z. (2010). Design methods for large scale dye-sensitized solar modules and the progress of stability research. *Renewable and Sustainable Energy Reviews* 14, 3178-3184

Wang, P.; Zakeeruddin, M.; Moser, J. E.; Nazeeruddin, M. K.; Sekiguchi, T. & Graetzel, M. (2003). A stable quasi-solid-state dye sensitized solar cell with an amphiphilic ruthenium sensitizer and polymer gel electrolyte. *Nature Materials* 2, 402-407

Wang, Q.; Moser, J. E. & Graetzel, M. (2005). Electrochemical impedance spectroscopic analysis of dye-sensitized solar cells. *Journal of Physical Chemistry B* 109, 31, 14945-14953

Wang, Z. S.; Yamaguchi, T.; Sugihara, H. & Arakawa, H. (2005). Significant Efficiency Improvement of the Black Dye-Sensitized Solar Cell through Protonation of TiO2 Films. *Langmuir*, 21, 4272-4276, doi:10.1021/la050134w

Watson, T.; Mabbett, I.; Wang, H.; Peter, L. & Worsley, D. (2010). Ultrafast near infrared sintering of TiO2 layers on metal substrates for dye-sensitized solar cells. *Progress in Photovoltaics: Research and Applications*, [in print], doi:10.1002/pip.1041

Wijnhoven, J. E. G. J. & Vos, W. L. (1998). Preparation of Photonic Crystals Made of Air Spheres in Titania. *Science* 281, 5378, 802-804, doi:10.1126/science.281.5378.802

Yao, Q-H.; Meng, F.-S.; Li, F.-Y.; Tian, H. & Huang, C.-H. (2003). Photoelectric conversion properties of four novel carboxylated hemicyanine dyes on TiO2 electrode. *Journal of Materials Chemistry* 13, 5, 1048–1053, doi:10.1039/B300083B

Yip, C.-H.; Chiang, Y.-M. & Wong, C.-C. (2008). Dielectric Band Edge Enhancement of Energy Conversion Efficiency in Photonic Crystal Dye-Sensitized Solar Cell. *Journal of Physical Chemistry C* 112, 23, 8735-8740

Yum, J-H.; Walter, P.; Huber, S.; Rentsch, D.; Geiger, T.; Nuesch, F.; De Angelis, F.; Graetzel, M. & Nazeeruddin, M. K. (2007). Efficient Far Red Sensitization of Nanocrystalline TiO2 Films by an Unsymmetrical Squaraine Dye. *Journal of American Chemical Society* 129, 34, 10320-10321, doi:10.1021/ja0731470

Yum, J.-H.; Moon, S. J.; Humphry-Baker, R.; Walter, P.; Geiger, T.; Nuesch, F.; Graetzel, M. & Nazeeruddin, M. K. (2008). Effect of coadsorbent on the photovoltaic performance of squaraine sensitized nanocrystalline solar cells. *Nanotechnology* 19, 42, 424005, doi:10.1088/0957-4484/19/42/424005

Zhang, D.; Yoshida, T. & Minoura, H. (2003). Low-Temperature Fabrication of Efficient Porous Titania Photoelectrodes by Hydrothermal Crystallization at the Solid/Gas Interface. *Advanced Materials* 15, 10, 814-817, doi:10.1002/adma.200304561

Zhang, Q. F.; Chou, T. P.; Russo, B.; Jenekhe, S. A. & Cao, G. Z. (2008). Polydisperse Aggregates of ZnO Nanocrystallites: A Method for Energy-Conversion-Efficiency Enhancement in Dye-Sensitized Solar Cells. *Advanced Functional Materials* 18, 11, 1654-1660, doi:10.1002/adfm.200701073

Zhou, Y.; Zhang, F.; Tvingstedt, K.; Tian, W. & Inganäs, O. (2008). Multifolded polymer solar cells on flexible substrates. *Applied Physics Letters* 93, 033302, doi:10.1063/1.2957995

Ordered Semiconductor Photoanode Films for Dye-Sensitized Solar Cells Based on Zinc Oxide-Titanium Oxide Hybrid Nanostructures

Xiang-Dong Gao, Cai-Lu Wang, Xiao-Yan Gan and Xiao-Min Li
State Key Lab of High Performance Ceramics and Superfine Microstructures, Shanghai Institute of Ceramics, Chinese Academy of Sciences, Shanghai, P. R. China

1. Introduction

Dye-sensitized solar cell (DSC) is a new type solar cell based on the photoelectric conversion occurred at the organic dye-semiconductor nanoparticle interface. DSC has attracted great research interests due to its high efficiency for energy conversion (11%) and low production cost compared with the traditional Si based photovoltaic cell (O'Regan et al., 1991; Grätzel et al., 2001). In confront of the huge difficulties in propelling the conversion efficiency of DSC up to 15% or higher, very recently, significant research efforts have been redirected to the optimization of photoanode, while others are stick to seeking better sensitizer or solid electrolytes (Mor et al., 2006a; Grätzel et al., 2006; Li et al., 2006; Zhang et al., 2011).

The photoanode is the kernel component of DSC assuming two major functions, supporting dye molecules, and transporting photo-induced electrons to the bottom electrode. Traditionally, the photoanode is the nanoporous thick film (15-20 um in thickness) consisted of TiO_2 nanoparticles, characterized by the disordered nature (Figure 1a). The electron transport in this disordered network of TiO_2 film is rather difficult due to two factors: (1) The presence of a large quantity of electron traps at the nanostructured TiO_2/electrolyte interface, such as the intrinsic defect sites (e.g. oxygen defects or surface states) and the grain boundaries, which may influence the interfacial charge-transfer kinetics. (2) The tortuosity of the electron path in the photoanode formed via the calcinations at high temperature, which may hinder the free transport of electron and increase the electron-hole recombination rate. In contrast, the ideal photoanode film (Figure 1b) should be built up by very thin (10-20 nm) and long (10-20 um) semiconductor nanowire array, possessing no surface states, which should exhibit the total photoelectric conversion efficiency of 24% based on the widely used black dye (N719) and I^2/I^{3-} electrolyte system. However, limited by the current fabrication technology level, it is extremely difficult to realize this photoanode film in a short term. Therefore, the development of some practical measures to optimize the photoanode is fundamentally important. The photoanode film can be optimized further from two aspects, to enhance electron gathering and transporting efficiency and to inhabit the charge recombination at the same time. Figure 1c illustrates the schematic of the hybrid photoanode structure, using 1D ZnO nanowire as the major path for the electron transportation, and using 0D TiO_2 nanoparticles as the supporting framework of dye molecules. By using two kinds of nanostructures assuming two different functions of

the photoanode, the efficiency of the hybrid photoanode is expected to improve compared with the traditional nanoparticle-based photoanode.
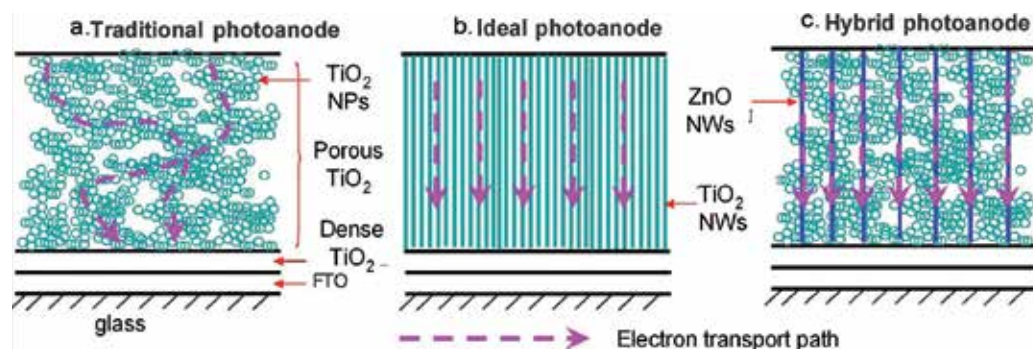
Fig. 1. Schematic of the electron transporting path in the traditional, ideal, and hybrid photoanode. NPs: Nanoparticles; NWs: Nanowires.

Many efforts have been devoted to construct photoanodes of DSCs using ordered semiconductor nanostructures such as nanowires, nanotubes or hierarchical structures. In 2005, M. Law et al. first demonstrated the photoanode film built by a dense array of oriented and crystalline ZnO nanowires (Law et al., 2005). The direct electrical pathways provided by the nanowires ensured the rapid collection of carriers generated throughout the device, and a full Sun efficiency of 1.5% was demonstrated, limited primarily by the surface area of the nanowire array. G. K. Mor et al. reported highly ordered transparent TiO_2 nanotube arrays (6-nm pore diameter, 17-nm wall thickness, and 360-nm length) as the photoanode, which were grown perpendicular to a fluorine-doped tin oxide-coated glass substrate by anodic oxidation of a titanium thin film (Mor et al., 2006b). Although the electrode was only 360-nm-thick, the generated photocurrent was 7.87 mA/cm^2, with a photocurrent efficiency of 2.9%, indicating the great potential of the ordered photoanode. K. Zhu et al. investigated the dynamics of electron transport and recombination in DSCs incorporating oriented TiO_2 nanotube arrays from electrochemically anodized Ti foils, and proved that the nanotube-based DSCs had significantly higher charge-collection efficiencies than the nanoparticle-based counterparts (Zhu et al., 2007). S H Kang et al. developed chemically synthesized TiO_2 nanorod based photoanodes (Kang et al., 2008). These nanorod-based DSCs showed improved photovoltaic properties (6.2 % versus 4.3 % for nanoparticle-based DSCs) owing to the characteristics of slightly enhanced electron transport and predominantly degraded charge recombination. W. Zhang et al. used mesoporous TiO_2 nanofibers with a high surface area of 112 m^2 /g prepared by electrospinning technique as the photoanode, and demonstrated the conversion efficiency of 1.82% in solid-state DSCs (Zhang et al., 2010). Recently, C. S. Rustomji et al. designed and constructed photoanodes based on new 3-D configurations of TiO_2 nanotubes, which, unlike prior nanotube-based cells where tubes were grown vertically in a 2-D array, consisted of tubes that extended radially in a 3-D array from a grid of fine titania wires (Rustomji et al., 2010). Its overall efficiency reached 5.0%, and the incident photon-to-current efficiency exceeds 60% over a broad part of the visible spectrum. S. Guldin et al. presented a material assembly route toward double-layer photoanode of DSCs, by coupling a high-surface mesoporous underlayer with an optically and electrically active three-dimensionally periodic TiO_2 photonic crystal overlayer (Guldin et al., 2010). In contrast to earlier studies, the double layer structure exhibited porosity at the mesoporous and the microporous length scales as well as pore and electronic connectivity at

all levels. This construct enabled effective dye sensitization, electrolyte infiltration and charge collection from both the mesoporous and the photonic crystal layers.

Apart from various ordered TiO_2 nanostructures, ZnO has also been widely investigated as an alternative of TiO_2 to construct the photoanode of DSCs. For example, E. Hosono et al. pyrolyzed upright-standing sheets of layered hydroxide zinc carbonate, and obtained upstanding nanocrystalline ZnO films with the *c*-axis parallel to the substrate (Hosono et al., 2005). The corresponding DSCs possessed the conversion efficiency of 3.9%, much higher than the regular efficiency level of ~2% at that time (Rensmo et al., 1997). C. K. Xu et al. reported the photoanode using ultralong ZnO nanowires with up to 33 μm thick sensitizing films while maintaining high electron collection efficiency, which resulted in greatly improved performance (from 1.1% to 2.1%) compared to previously reported ZnO nanowire-based DSCs (Xu et al., 2010). J. X. Wang et al. used porous hierarchical disklike ZnO nanostructure fabricated via a simple low-temperature hydrothermal method as the photoanodes, and achieved improved photovoltaic performance (2.49%) compared with that of the ZnO nanowire arrays owing to the enlarged surface area and natural electron collection routes of ZnO hierarchical nanostructures (Wang et al., 2010). A. B. F. Martinson et al. introduced high surface area ZnO nanotube photoanodes templated by anodic aluminum oxide in DSCs via atomic layer deposition technique, providing a direct path for charge collection over tens of micrometers thickness (Martinson et al., 2007). Compared to similar ZnO-based devices, ZnO nanotube cells show exceptional photovoltage and fill factors, in addition to power efficiencies up to 1.6%. G Z Cao's group took the hierarchically popcorn-ball structured ZnO film as the photoanode, and attained the efficiency improvement from 0.6% to 3.5%, and finally 5.4%, by inducing light scattering within the photoelectrode films via the aggregation of ZnO nanocrystallites, thus demonstrating the huge potential of ZnO nanostructures in realizing DSCs with high efficiency (Chou et al., 2007; Zhang et al., 2008).

In parallel with photoanode films consisted by merely one type of material (ZnO, TiO_2, nanoparticles, nanowires, or nanotubes), the hybrid photoanode represents another important research trend, which is usually built by two or more materials or morphologies. Due to the obvious advantages of the hybrid photoanode including the improved interfacial structure/charge separation, the direct electron transporting path, and the vast possibilities to tune the microstructure and photoelectrochemical properties of the photoanode, this research trend has been gaining more and more interests. For example, K. M. Lee et al. incorporated multi-wall carbon nanotube in low-temperature fabricated TiO_2 photoanode, with the efficiency improvement of 20% (0.1% CNT), which may be resulted from retarded charge recombination between injected electrons and electron acceptors in the redox electrolyte (Lee et al., 2008). P. Brown et al. studied the single-wall carbon nanotube (SWCNT)/TiO_2 hybrid system, and proved that SWCNT support networks can be incorporated into mesoscopic TiO_2 films to improve the charge transport in DSCs (Brown et al., 2008). While no net increase in power conversion efficiency was obtained, an increase in photon-to-current efficiency (IPCE) represented the beneficial role of the SWCNT as a conducting scaffold to facilitate charge separation and charge transport in nanostructured semiconductor films. S. Pang et al. incorporated ZnO nanorods with different sizes into TiO_2 nanoparticle-based photoanode, and improved the conversion efficiency by 15% (Pang et al., 2007). They attributed the improved efficiency to the faster charge carrier transport rate, the decreased recombination, and the higher V_{oc}. B. Tan et al. used the composites of anatase TiO_2 nanoparticles and single-crystalline anatase TiO_2 nanowires as electrodes to fabricate DSCs, which possessed the advantages of both building blocks, i.e., the high surface area of

nanoparticle aggregates and the rapid electron transport rate and the light scattering effect of single-crystalline nanowires (Tan et al., 2006). An enhancement of power efficiency from 6.7% for pure nanoparticle cells to 8.6% for the composite cell with 20 wt% nanowires was achieved, showing that employing nanoparticle/nanowire composites represented a promising approach for further improving the efficiencies of DSCs. C. H. Ku et al. reported ZnO nanowire/nanoparticle composite photoanodes with different nanoparticle-occupying extents (Ku et al., 2008). Aligned ZnO nanowires were grown on the seeded FTO substrate using an aqueous chemical bath deposition (CBD) first, and then, growth of nanoparticles among ZnO NWs by another base-free CBD was preceded further for different periods. The corresponding DSCs showed an efficiency of 2.37%, indicating the good potential of the hybrid nanostructures in ordered photoanodes.

Apart from the direct blending of two different semiconductor components as mentioned above, the coating technique has also been applied widely to create the hybrid photoanodes. M. Law et al. developed photoanodes constructed by ZnO nanowires arrays coated with thin shells of amorphous Al_2O_3 or anatase TiO_2 by atomic layer deposition (Law et al., 2006). They found that, while alumina shells of all thicknesses acted as insulating barriers that improve cell open-circuit voltage only at the expense of a larger decrease in short-circuit current density, titania shells in thickness of 10-25 nm can cause a dramatic increase in V_{OC} and fill factor with little current falloff, resulting in a substantial improvement in overall conversion efficiency (2.25%). They attributed the improved performance to the radial surface field within each nanowire that decreases the rate of recombination. K. Park et al. described a ZnO-TiO_2 hybrid photoanode by coating ultrathin TiO_2 layer by atomic layer deposition on submicrometer-sized aggregates of ZnO nanocrystallites (Park et al., 2010). The introduction of the TiO_2 ultrathin layer increased both the open circuit voltage and the fill factor as a result of the suppressed surface charge recombination without impairing the photocurrent density, thus realizing more than 20% enhancement in the conversion efficiency from 5.2% to 6.3%. S. H. Kang et al. examined effects of ZnO coating on the anodic TiO_2 nanotube array film on the conversion efficiency (Kang et al., 2007). Compared with the solid-sate cells consisted of an anodic TiO_2 film as the working electrode under backside illumination, an almost 20% improvement from the ZnO coating was achieved (from 0.578% to 0.704%), which can be attributed to the suppressed electron flow to the back-direction and the enhanced open-circuit voltage.

Despite considerable effects in this area, however, the record efficiency of 11% for DSCs is not surpassed by these new type cells, due to the complexity of both the nanoporous photoanode and the cell structure of DSCs. Much comprehensive and in-depth work related to this topic is required.

In this chapter, we focused on the ordered photoanode film built up by two semiconductor materials, zinc oxide (ZnO) and titanium oxide (TiO_2). Three type of ZnO nanostructures were selected, including the nanowire array (grown by the hydrothermal method), the nanoporous disk array grown on FTO substrate, and the nanoporous disk powder (transformed from the solution-synthesized zinc-based compound $ZnCl_2.[Zn(OH)_2]_4.H_2O$). Different types of TiO_2 nanoparticles were used, including commercial nanoparticles P25 & P90 (Degauss Co., Germany), and home-made hydrothermal TiO_2 nanoparticles, which have been widely used in producing traditional high-efficiency DSCs. Two kinds of preparation technique of ZnO-TiO_2 hybrid film were used according to the status of ZnO nanostructures (array or powder). The microstructure, optical and electrical properties of the hybrid film were investigated, and the performance of corresponding DSCs was measured and

compared with results of traditional cell. In special, the emphasis was placed on the controlling method of the microstructure of ZnO-TiO$_2$ hybrid films, and on the electron transporting mechanism in the hybrid films.

2. ZnO nanowire array/TiO$_2$ NPs hybrid photoanodes

In this section, two types of ZnO nanowire (NW) array were selected, i.e., dense and sparse NW array, with an aim to examine the effects of the distribution density of NW on the microstructure and photoelectrochemical properties of the hybrid cells. For the dense NW array, the ultrasonic irradition was used to promote the penetration of TiO$_2$ nanoparticles in the interstice of ZnO NWs.

2.1 Hybrid photoanodes based on dense ZnO NW array

ZnO nanowire (NW) arrays were grown on ZnO-seeded fluorinated tin oxide (FTO, 20 Ω/□) substrates by chemical bath deposition method. ZnO seed layer was prepared by sol–gel technique. ZnO NW arrays were obtained by immersing the seeded substrates upside-down in an aqueous solution of 0.025 mol/L zinc nitrate hydrate and 0.025 mol/L hexamethylenetetramine (HMT) in a sealed beaker at 90 °C for 12 h. After the deposition of ZnO NW, TiO$_2$ nanoparticles (NPs) were coated on ZnO NW by dipping the substrate into a well-dispersed TiO$_2$ suspension containing 0.5 g TiO$_2$ NPs (P25), 20 µL acetyl acetone, 100 µL Triton X-100 in 10 mL distilled water and 10 mL ethanol with 20 µL acetic acid. To facilitate the attachment and the gap filling of TiO$_2$ NPs into the interstices of ZnO NWs, the ultrasonic irradiation generated from a high-density ultrasonic probe (Zhi-sun, JYD-250, Ti alloy-horn, 20–25 kHz) was applied to TiO$_2$ suspension. The working mode was adjusted to work for 2 seconds and idle for 2 seconds, with the repetition of 99 cycles. The electrodes were then withdrawn at a speed of 3 cm per minute, dried, and sintered at 450 °C for 30 min in air. Figure 2 gave the schematic for the fabrication of the hybrid ZnO NW array/TiO$_2$ photoanopde.

For DSCs fabrication, ZnO NW based electrodes were immersed in a 0.5 mmol/L ethanol solution of N719 for 1 h for dye loading. The sensitized electrode was sandwiched with platinum coated FTO counter electrode separated by a hot–melt spacer (100 µm in thickness, Dupont, Surlyn 1702). The internal space of the cell was filled with an electrolyte containing 0.5 mol/L LiI, 0.05 mol/L I$_2$, 0.5mo/L 4-tertbutylpyridine, and 0.6 mol/L 1-hexyl-3-methylimidazolium iodide in 3-methoxypropionitrile solvent. The active cell area was typically 0.25 cm^2.
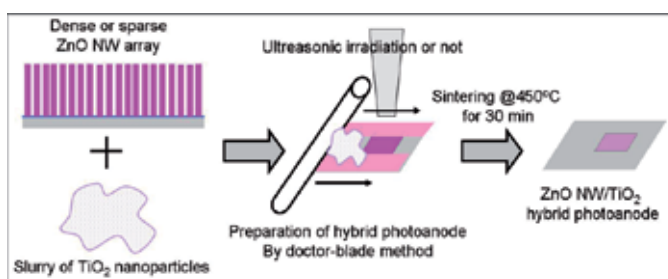
Fig. 2. Schematic of the preparation process of ZnO NW array/TiO$_2$ nanoparticles hybrid photoanode. NW: Nanowire.
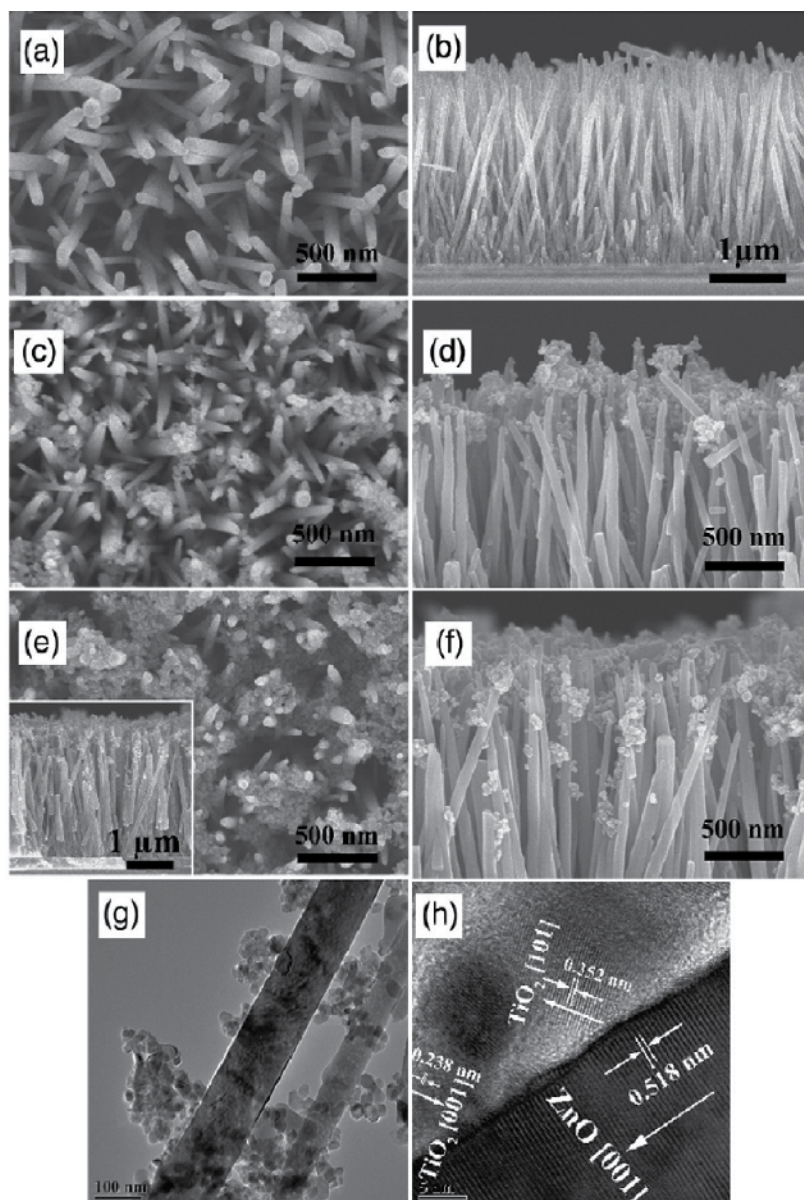
Fig. 3. FESEM images of ZnO NW arrays (a)–(b), hybrid ZnO NW/TiO₂ NP photoanodes prepared without (c)–(d), and with (e)–(f) the ultrasonic treatment. (g) Low and (f) high-resolution TEM images of the hybrid photoanodes prepared with ultrasonic treatment. (Reproduced from Ref. (Gan et al., 2007))

Figure 3 showed the top and side-view SEM images of ZnO NWs grown on FTO substrate and ZnO-TiO₂ hybrid photoanode film with/without ultrasonic treatment. Results indicate that, for ZnO nanowire array with a density of ~3.3×10⁹ cm⁻² and an average diameter of 80 nm and length of 3 μm, TiO₂ slurry with relatively high viscosity is difficult to penetreate into the inner pore of ZnO nanowires. As can be seen from Fig.3 c and d, only a small

amount of TiO_2 NPs were covered on the side surface of NWs and most of the NPs sit on the top of NWs without filling in the inner gaps. When the ultrasonic irradiation was applied, the coverage of NPs on the side surface of NWs was significantly improved (Fig. 3 e-h), and TiO_2 NPs were uniformly infiltrated into the interstices of NWs rather than stuck to the top of NWs. The cavitation in liquid–solid systems induced by the ultrasonic irradiation bears intensive physical effects, which can promote the transfer of TiO_2 NPs and drive them infiltrating into the gaps of NPs.

Figure 4 (left) showed the absorption spectra of the N719-sensitized ZnO NW, and hybrid ZnO NW/TiO_2 NP electrodes prepared with and without ultrasonic treatment, respectively. The absorption peak at around 515 nm, which corresponded to metal to ligand charge transfer (MLCT) in N719 dye (Nazeeruddin et al., 1993), significantly increased for the hybrid electrodes as compared to that of the pure ZnO NW electrode, proving that the dye-loading content is apparently increased upon the combination of ZnO NW with TiO_2 NPs. Besides, the hybrid electrode prepared with ultrasonic treatment showed an increase in the absorption in the wavelength range of 400–800 nm compared with that without ultrasonic treatment, indicating the higher surface area and the enriched light harvesting property by filling more TiO_2 NPs into the interstices between ZnO NWs with the assistance of ultrasonic irradiation.

Figure 4 (right) illustrated I–V characteristics of DSCs based on pure ZnO NWs and ZnO/TiO_2 hybrid photoanodes. Results show that the short-circuit current density (I_{sc}) and the conversion efficiency (η) of ZnO NWs based cell can be dramatically improved by incorporating TiO_2 NPs, which can be ascribed to the increase in the surface area and the dye loading quantity. However, the open-circuit voltage (V_{oc}) and the fill-factor (FF) of the hybrid DSCs decreased compared to those of pure ZnO NW DSC, which may be resulted from the increased interfaces and surface traps in the hybrid photoanode which may act as the recombination center under illumination. For the hybrid photoanode prepared with ultrasonic treatment, its I_{sc}, V_{oc}, FF, and η was 3.54 mA/cm², 0.60 V, 0.37, and 0.79%, respectively, indicating an approximately 35% improvement of the overall conversion efficiency compared with the photoanode without ultrasonic treatment. This improvement may originate from the enhanced light harvesting and the better attachment of TiO_2 NPs to ZnO NWs resulted from the efficient pore filling induced by the ultrasonic irradiation treatment.
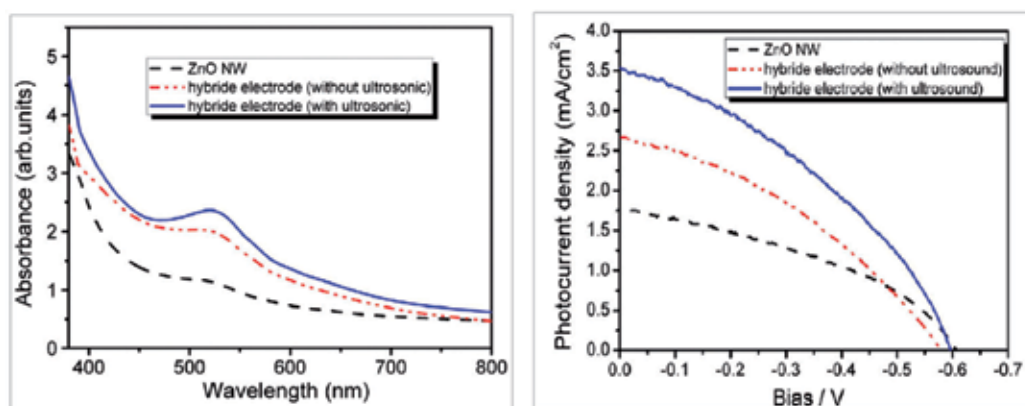
Fig. 4. The absorption spectra (left) of N719-sensitized ZnO NW arrays, and hybrid ZnO NW/TiO_2 NP photoanodes prepared without and with ultrasonic treatment, and I–V characteristics of corresponding DSCs (right). (Reproduced from Ref. (Gan et al., 2007))

In summary, these results indicate that, for the hybrid films combining dense ZnO NW array and TiO$_2$ NPs, the crucial aspect is to make TiO$_2$ NPs contained in the slurry penetrate into the deep interstice of ZnO NWs. The application of ultrasonic irradiation or other external fields may be helpful for the penetration of TiO$_2$ NPs, which usually result in the increase of the photoelectrochemical performance of the hybrid cells. However, it seems that the full filling of TiO$_2$ in the dense NW array is very difficult based on the current technique. So it is meaningful to develop the sparse nanowire array or other forms of TiO$_2$ NPs, to realize the good combination of ZnO NW array and TiO$_2$ NPs.

2.2 Hybrid photoanodes based on sparse ZnO NW array

In this section, ZnO NW array with sparse density was integrated with TiO$_2$ NPs, to form the hybrid photoanode. The growth of sparse ZnO NW array was realized by reducing the pH value of the precursor via the chemical bath deposition (CBD) method. The substrates and the experimental parameters were similar to those of dense one except the concentration of Zn^{2+} and HMT (both 0.02 mol/L), and the pH value (2.0-3.0).

TiO$_2$ slurry was prepared following the method in Ref (Ito et al., 2008), and the mass ratio of TiO$_2$, ethyl cellulose, and terpineol was 18 : 9 : 73. Due to the acid-dissolute nature of ZnO materials, the pH value of TiO$_2$ slurry should be controlled neutral or weak alkaline.

The preparation of the hybrid film based on sparse ZnO NW array was similar to that of dense array, as described in Section 2.1. The sensitization of the film was carried out in N719 dye solution dissolved in a mixture of acetonitrile and tertbutyl alcohol (volume ratio, 1:1) for 20-24 hours at room temperature. The fabrication of the cells was similar to the procedure described in Section 2.1, with the electrolyte composition of 0.6 M BMII, 0.03 M I$_2$, 0.10 M guanidinium thiocyanate and 0.5 M 4-tertbutylpyridine in a mixture of acetonitrile and valeronitrile (volume ratio, 85:15).

Figure 5 gave SEM images of sparse ZnO NW on the surface and cross section. It can be seen that the density of ZnO nanowire on FTO substrate is much sparser than the dense ZnO NW (Figure 3 a&b). But with the decrease of the density, the diameter of ZnO NW increases greatly, up to several micrometers.

The hybrid cell based on the sparse ZnO NW array exhibited the conversion efficiency of 2.16%, lower than the TiO$_2$ NPs-based cell (2.54%) as illustrated in Figure 6. The decreased efficiency of the hybrid cell is mainly resulted from the reduced photocurrent density compared with the TiO$_2$ cell, while the open voltage keeps unchanged and the fill factor improved from 0.06 to 0.078. The open-circuit voltage decay (OCVD) analysis (Figure 6) indicated that the hybrid film exhibits longer decay time when the illumination is turned off, indicating lower recombination rate between photo-induced electrons and holes. We believe that the obviously reduced photocurrent density may be related to the reduced surface area induced by the incorporation of large size ZnO nanowires, which may resulted in the reduced dye loading content. So the improvement in the efficiency of DSCs via the integration of sparse ZnO NW array and TiO$_2$ NPs is possible, as long as the size of ZnO nanowire can be reduced to tens of nanometers. However, limited by the current technology level of ZnO nanowire array, it is not an easy task to grow ZnO NW array both sparse and thin enough for the application in the hybrid photoanodes of DSCs.

In summary, we have successfully prepared the hybrid photoanode film using sparse ZnO
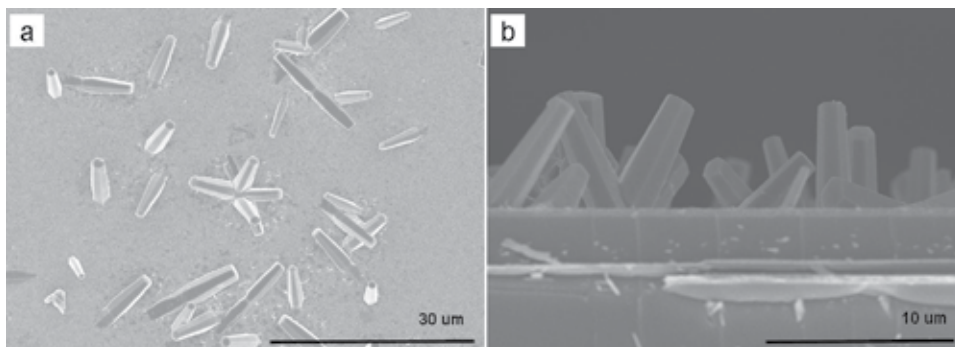
Fig. 5. FESEM images of sparse ZnO NW array on the surface (a) and the cross section (b).
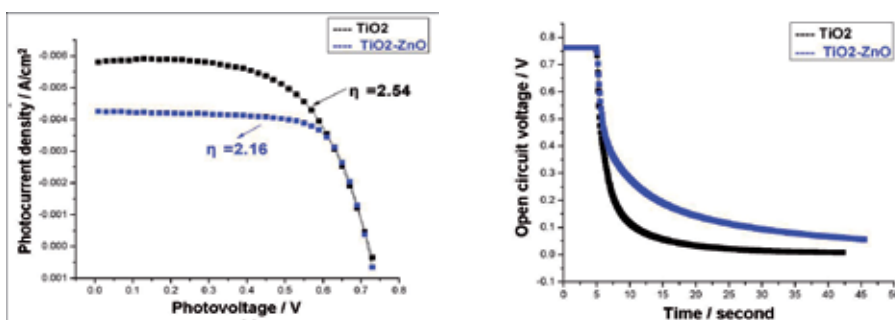
Fig. 6. I-V curves (left) and open-circuit voltage decay (OCVD) curves (right) of TiO_2 NPs-based cell and ZnO–TiO_2 hybrid cells based on sparse ZnO NW array under AM 1.5 illumination (100 mW/cm²). The active area is 0.27 cm² for all cells.

NW array and TiO_2 NPs. Although the total efficiency of the hybrid cell was lower than the TiO_2 NPs-based cell, the obvious improvement in the fill factor and the reduction in the recombination rate were observed. The reduced efficiency was mainly related to the decreased photocurrent density originated from the large-size ZnO NW. The further chance to improve the efficiency of ZnO NW based hybrid cell may reside in the realization of ZnO NWs with both sparse density and thin diameter.

3. ZnO nanoporous disk array/TiO$_2$ NPs hybrid photoanodes

In this section, an alternative ZnO nanostructure was used to prepare hybrid photoanode film, i.e., ZnO disk array possessing nanoporous feature. Compared with the traditional ZnO NW, the thickness of ZnO disk is lower and the surface area is higher. Thus higher effect in improving the conversion efficiency of DSCs can be expected.

ZnO nanoporous disk array was transformed from the disk of a layered zinc-based compound – simonkollite ($ZnCl_2.[Zn(OH)_2]_4.H_2O$, brief as ZHC) via calcinations. Conductive FTO glass coated by a thin TiO_2 layer (deposited by the hydrolysis of 40 mM $TiCl_4$ aqueous solution at 70ºC) was used as the substrate. Typically, ZHC disk was prepared by CBD method. Aqueous solutions of 20 ml $ZnCl_2$ (0.2 mol/l), 20 ml hexamethylenetetramine (HMT) (0.2 mol/l), and 40 ml ethanol were mixed in a beaker and heated to 70ºC in oven for 2 hours. After washing with H_2O and ethanol carefully, ZHC nanodisk array deposited on TiO_2/FTO substrate was sintered in air at 500ºC for 4 hours, to convert ZHC to ZnO nanoporous disk.

TiO$_2$ NPs slurry was prepared by grinning TiO$_2$ commercial nanoparticles (P90, Degauss Co.) 0.5 g, H$_2$O 2.5g, PEG 20000 0.25 g in porcelain mortar. The ZnO-TiO$_2$ hybrid film was prepared by the doctor blade method, and the ZnO nanoporous disk array grown on TiO$_2$/FTO substrate was used. To achieve a specific thickness of the film, two layers of TiO$_2$ slurry were applied. The dried hybrid cell was sintered at 450ºC in air for 30 minutes.

The sensitization of photoanode films and the fabrication of the cells were similar to those described in Section 2.1, except that the sensitizing time was prolonged to 24 hours.

Figure. 7(a) illustrated SEM images of ZHC nanodisk array deposited on TiO$_2$/FTO substrate. It can be seen that as-deposited ZHC exhibit rather regular hexagonal disk shape, with the size of ~ 10 um. The distribution of ZHC disks on substrate is sparse, satisfying the "low-content" requirement of ZnO in the hybrid photoanode film. After annealing at 500ºC, ZHC disks were transformed into ZnO with typical nanoporous structure (as shown in Figure 7(b)), while the sheet structure (~100 nm in thickness) was maintained. Figure 7 (c) and (d) showed SEM images of the hybrid films based on this sparse nanoporous ZnO disk array. We can see that the morphology of the hybrid film on the surface and the cross section was rather smooth and uniform, with little difference from the traditional pure TiO$_2$ film (Gao, 2007). In addition, ZnO sheet like structures can not be found in either the surface or the cross section due to the low content of ZnO in the hybrid film.
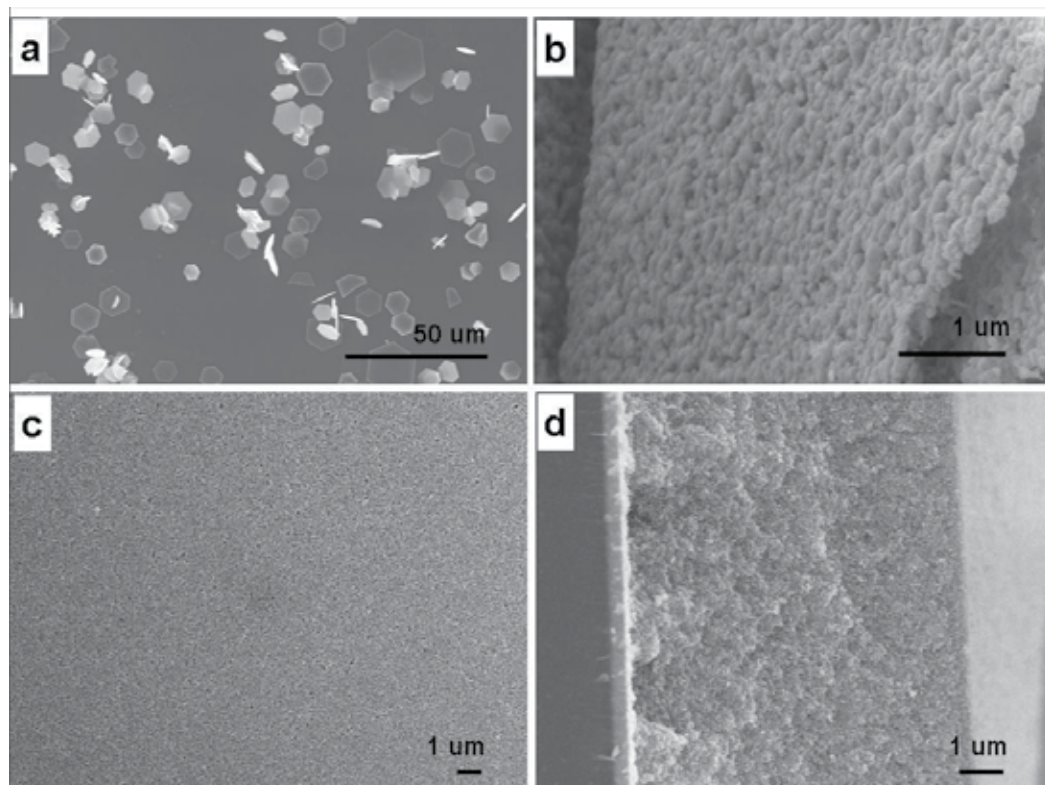
Fig. 7. FESEM images of (a) ZHC disk array and (b) ZnO nanoporous disk transformed from ZHC via calcinations at 500ºC; FESEM images of ZnO-TiO$_2$ hybrid film based on sparse nanoporous ZnO disk array. (c) Surface and (d) cross section.

Figure 8 (left) gave the optical transmittance spectra of FTO substrate, pure TiO_2 film and the hybrid film. Results indicate that in the wavelength rage of 470-800 nm, the hybrid film possesses relatively lower transmittance than the pure TiO_2 film, while in the wavelength band of 300-470 nm, the transmittance of the hybrid film is higher. The reduced transmittance in the higher wavelength band of the hybrid film may be related to the scattering effects of the large ZnO disk in the film. In view of the maximum absorption of N719 dye molecules located at ~ 525 nm (Figure 4), the scattering of ZnO nanoporous disks to the incident light has positive influence on the performance of the hybrid cells. The reduced transmittance in the lower band of the pure TiO_2 film may be related to the increased agglomeration of TiO_2 NPs, which can induce the larger secondary particles and the higher scattering effects in the lower wavelength range. In contrast, the presence of large-size ZnO sheet may reduce the agglomeration phenomena to some extent, thus exhibiting higher transmittance.

Figure 8 (right) gave I-V curves of pure TiO_2 NPs cell and ZnO nanodisk array – TiO_2 NPs hybrid cell under AM 1.5 illumination (100 mW/cm²). It can be seen that the cell based on the hybrid film possesses much higher photocurrent density than TiO_2 NPs cell, increasing from 7.84 mA/cm² to 11.70 mA/cm². Also the improvements in the photovoltage and the fill factor of the hybrid cell are observed. As a result, the total conversion efficiency changes from 3.07% to 5.19%, increased by up to 60%.
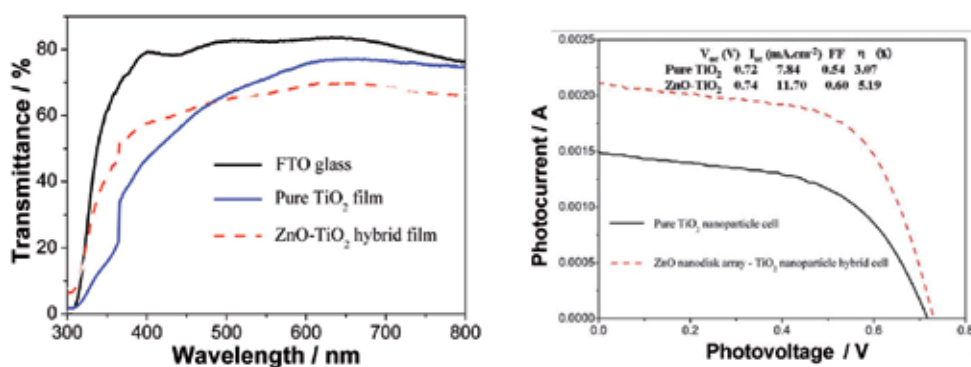
Fig. 8. The optical transmittance spectra (left) of pure TiO_2 NPs film and ZnO-TiO_2 hybrid film deposited on FTO substrate; I-V curves (right) of pure TiO_2 NPs cell and ZnO nanodisk array – TiO_2 NPs hybrid cell under AM 1.5 illumination (100 mW/cm²). The active area is 0.27 cm² for pure TiO_2 cell and 0.18 for ZnO-TiO_2 hybrid cell.

The reason for the efficiency improvement in the hybrid cell compared with NPs-based cell was analyzed by AC impedance under the illumination condition and open-circuit voltage decay (OCVD) analysis under the dark condition.

Figure 9 (left) showed Nyquist plots of the hybrid and pure photoanode, and the lower table gave the simulation results according to the physical model given in the inset. Two arcs can be clearly identified in the Nyquist plot for each sample. The left (high frequency) arc corresponds to the charge transfer process at the Pt counter electrode (R_{ct1}). The right large arc arises from the charge transport at the TiO_2/dye/electrolyte interface (R_{ct2}). The right small arc is related to the Warburg diffusion process of I^-/I_3^- in the electrolyte, which is not discussed in this work. The overall series resistance of the cell (R_s) is the resistance measured when electrons are transported through the device in the high-frequency range exceeding 10^5

Hz. By simulated calculation following the equivalent circuit, we can obtain the calculated value of R_s, R_{ct1}, and R_{ct2} for each sample. Results show that the hybrid film exhibits obviously lower R_s, R_{ct1}, and R_{ct2} than the pure TiO_2 film, indicating that the overall series resistance, the resistance at the Pt/electrolyte interface and at the TiO_2/dye/electrolyte interface in the hybrid cell is lower than the traditional TiO_2 NPs cell.

Figure 9 (right) showed OCVD curves of the hybrid and pure photoanode. While the pure TiO_2 cell exhibits rapid voltage decrease after the turning off of the illumination, the hybrid cell has much slower decay behavior, indicating that the photo-induced electron-hole recombination rate in the hybrid film is lower than the pure TiO_2 cell.

We believe the reduced overall resistance, the interfacial resistance and the electron-hole recombination rate is responsible for the obvious improvement in the total conversion efficiency in the hybrid cell.

In brief, we prepared ZnO-TiO_2 hybrid photoanode film based on sparse ZnO nanoporous disk array grown on TiO_2/FTO substrate. Though the obvious change in the microstructure of the film could not be observed, the hybrid film possessed increasing scattering effects in the wavelength range of 470-800 nm, which was beneficial to the light absorption of the dye molecules. Also the integration of ZnO nanoporous disk into TiO_2 NPs film resulted in the decrease of the overall series resistance and the resistance at the Pt/electrolyte interface and at the TiO_2/dye/electrolyte interface. As a result, the conversion efficiency was improved by 60%, indicating the great potential of the sparse ZnO nanoporous disk array in the field of hybrid DSC photoanodes.

	R_s (Ω)	CPE_{ct1} ($\mu FS^{\alpha-1}$)	R_{ct1} (Ω)	α_{ct1}	CPE_{ct2} ($\mu FS^{\alpha-1}$)	R_{ct2} (Ω)	α_{ct2}
Pure TiO_2	18.54	6.45E-5	17	0.63	0.00176	46.50	0.78
ZnO-TiO_2	12.21	1.55E-4	12	0.60	0.00243	28.00	0.82
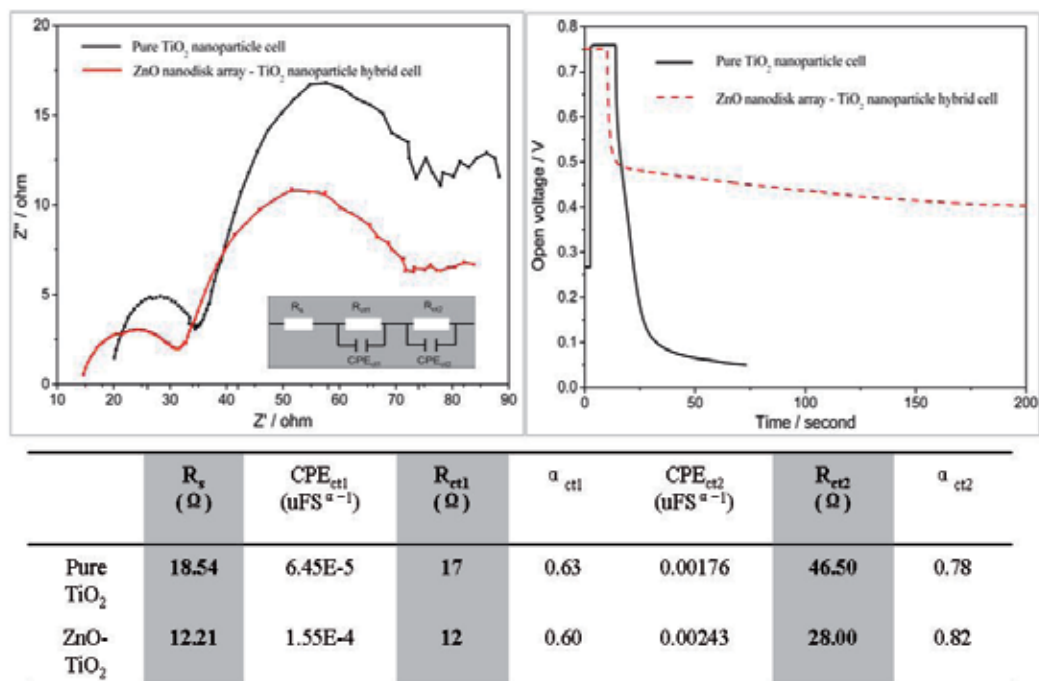
Fig. 9. Nyquist plots (left) and open-circuit voltage decay plots of pure TiO_2 NPs cell and ZnO nanodisk array – TiO_2 NPs hybrid cell. The attached table illustrates EIS parameters calculated from the given equivalent circuit.

4. ZnO nanoporous disk powder/TiO$_2$ NPs hybrid photoanodes

The disadvantage for the hybrid photoanode between ZnO array (both the nanoporous disk array and the nanowire array) and TiO$_2$ NPs lies in the difficulties in controlling the precise content of ZnO in the hybrid film, which is a crucial parameter for any composite material. Also, the distribution of ZnO array in the hybrid film may be not uniform, and difficult to control. Therefore, in this section, we attempted to blend ZnO nanoporous disk in the powder form into TiO$_2$ slurry, and prepared a uniform hybrid film via the doctor-blade technique. By this method, we can examine the effects of ZnO content in the hybrid film on the microstructure and properties of photoanode, and find an optimal composition for ZnO-TiO$_2$ hybrid photoanodes.

The powder of ZnO nanoporous disks was synthesized by the pyrolysis of chemical bath deposited ZHC nanodisks. Two types of TiO$_2$ NPs were selected, i.e., the commercial P25 TiO$_2$ and the hydrothermal TiO$_2$ NPs following the procedure described in Ref (Ito et al., 2008).

4.1 Hybrid photoanodes based on P25 TiO$_2$ NPs

Layered ZHC was prepared by the chemical bath deposition method. Typically, aqueous solutions of 20 ml ZnCl$_2$ (0.2 mol/l), 20 ml hexamethylenetetramine (HMT) (0.2 mol/l), and 40 ml ethanol were mixed together and heated to 70°C in oven for 2 hours, resulting in the white precipitation of ZHC. After centrifuging and drying, the powders were annealed at 500°C in a tube furnace in air for 18 hours to convert ZHC into ZnO.

Film electrodes for DSCs were deposited onto FTO substrate via TiO$_2$ or TiO$_2$/ZnO slurry by the doctor blade technique. For P25 TiO$_2$ NPs, the TiO$_2$ slurry was prepared using the mixed suspension of TiO$_2$ NPs (P25) (0.5 g) and PEG-1000 (0.25 g). The TiO$_2$/ZnO hybrid electrodes were made by using the mixed suspension of P25, PEG and ZnO disk powder, with the weight percentages of ZnO being 0 (S1), 0.5% (S3) and 1% (S2). The electrodes were sintered at 450°C for 120 min. The detail preparation process of the hybrid film was illustrated in Figure 10.
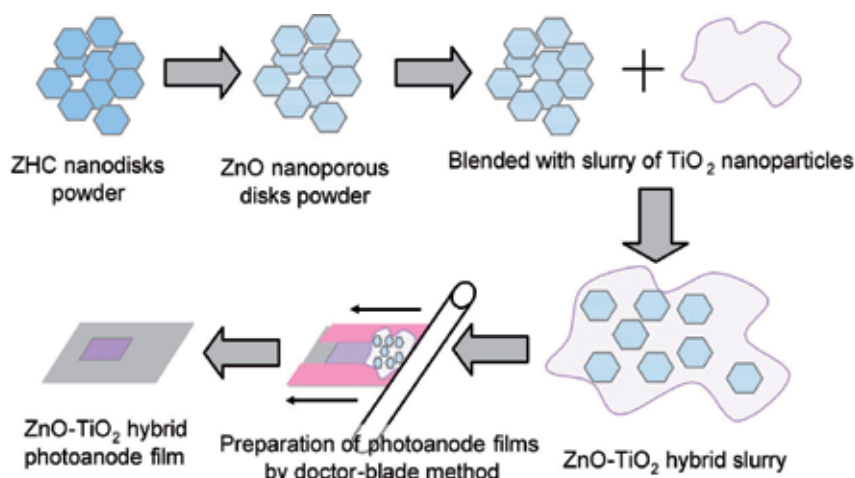
Fig. 10. Schematic of the preparation process of ZnO/TiO$_2$ hybrid photoanodes based on nanoporous ZnO disk powder and TiO$_2$ nanoparticles.
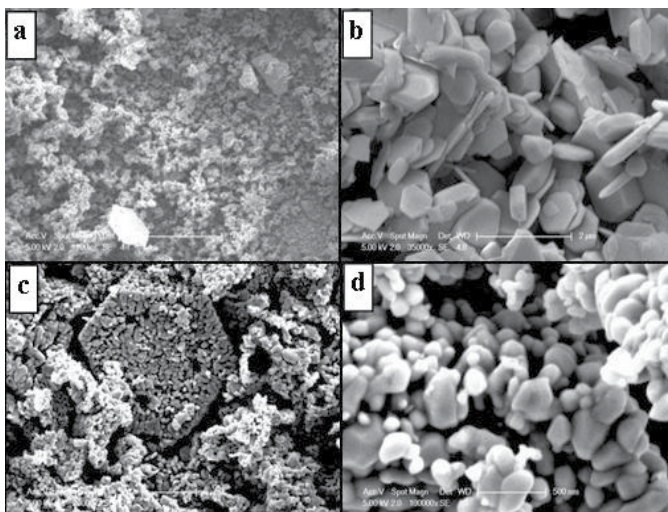
Fig. 11. SEM images of as-prepared ZHC powders and ZnO nanoporous disk after annealing at 500°C: (a) Low magnification morphology of ZHC powder; (b) Typical ZHC disks; (c) Low magnification morphology of ZnO nanoporous disks; (d) Enlarged view of nanoporous structure. (Reproduced from Ref (Gao et al., 2009))
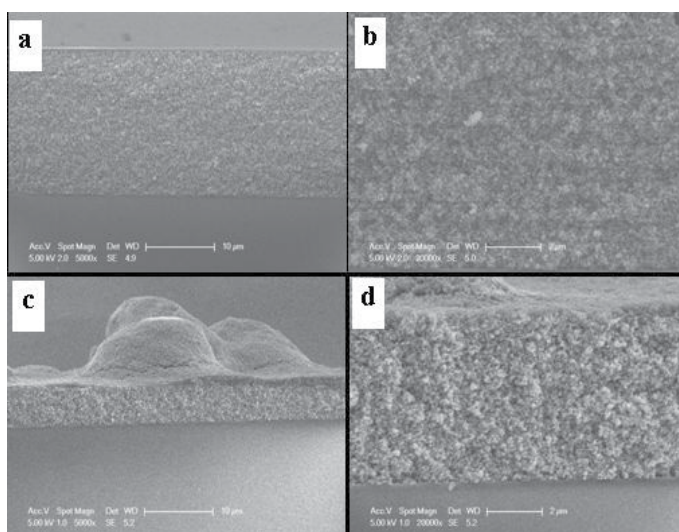
Fig. 12. SEM images of the cross section of TiO_2 film (a-b) and $ZnO-TiO_2$ hybrid film (c-d) prepared on glass substrate. (a) and (c): low magnification; (b) and (d): high magnification. (Reproduced from Ref (Gao et al., 2009))

The annealed electrodes were stained by N719 dye by soaking them in a 0.5 mmol/l solution of N719 for 12 hours. FTO glass substrates were coated by Pt catalyst layer by decomposing $H_2PtCl_6·6(H_2O)$ at 400°C, and were used as the counter electrode. The working electrode and the counter electrode were cohered together by surlyn 1702 hot melt foil. The electrolyte, consisted of 0.05 M I_2, 0.1 M LiI and 0.5 M tertbutylpyridine in acetonitrile, was filled into the cell from the hole in the counter electrode.

Figure 11 gave SEM images of as-prepared ZHC disks and nanoporous ZnO disks obtained by sintering. As-prepared ZHC possesses obvious disk-like feature, with the side length of 500-1000 nm and the thickness of 100-300 nm in average. After annealing, ZnO disks with the nanoporous feature were obtained, with the pore size ranging from 50-200 nm. In addition, the linking between neighboring ZnO particles in each disk can be clearly observed, which is expected to provide good electron transport in DSCs.

Figure 12 showed the cross-section morphologies of the pure TiO_2 film and $1\%ZnO/TiO_2$ hybrid film. While the pure TiO_2 film shows a uniform surface morphology and typical nanoporous structure with a thickness of ~20 μm, the hybrid film possesses a rough surface with large humps of ~10 μm (Fig.12 c) and lower thickness (~6 μm). The results indicate that even a small amount of ZnO powder blended in TiO_2 slurry can change the microstructure and thickness of the film electrodes significantly, which may be related to the change of the slurry viscosity during the preparation process. The presence of large ZnO particles (several μm in size) in the hybrid slurries may hamper the free flow of the TiO_2 slurry, thus resulting in the formation of large humps on the surface and the higher internal roughness

The optical transmittance spectra (Figure 13 (left)) of the TiO_2 and ZnO/TiO_2 hybrid films shows that both the pure and hybrid films exhibit strong scattering effects on the incident light in the visible and near infrared band. Compared with the pure TiO_2 film electrode, the hybrid film electrodes show much lower transmittance in the wavelength range of 500-1100 nm, indicating that a very small amount of ZnO disks can exert significant effects on the optical properties of the photoanode.

	R_s (Ω.cm^{-2})	CPE_{ct1} (uFcm^{-2} S^{a-1})	R_{ct1} (Ω cm^{-2})	a_{ct1}	CPE_{ct2} (uFcm^{-2} S^{a-1})	R_{ct2} (Ω cm^{-2})	a_{ct2}
S1	14.69	49.65	74.46	0.85	311.2	108.10	0.71
S2	13.00	223.10	57.59	0.82	8.36	26.29	0.89
S3	13.51	229.00	56.99	0.84	31.22	27.28	0.76
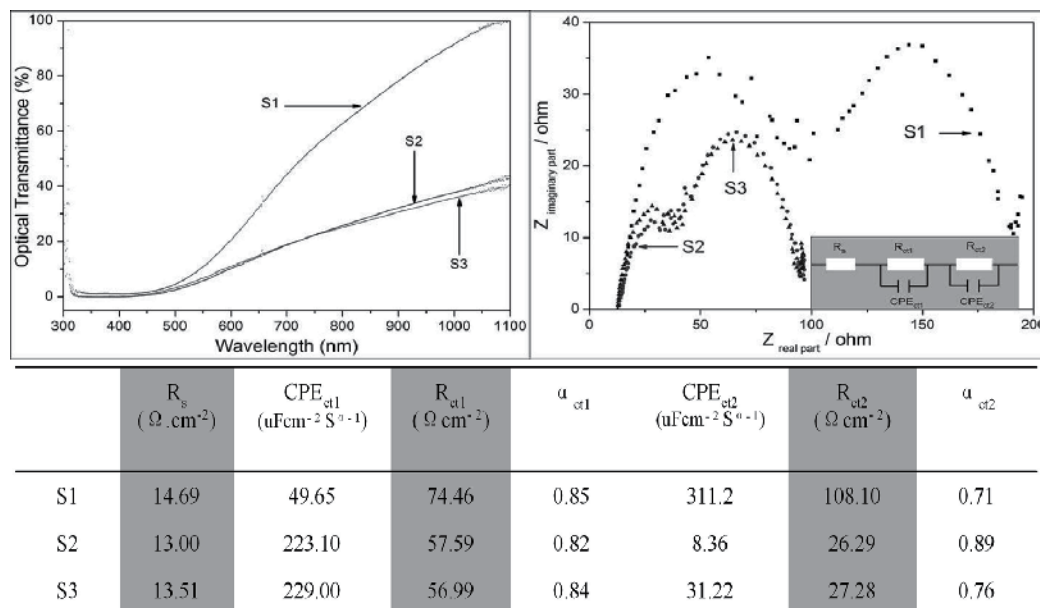
Fig. 13. Optical transmittance (left) of TiO_2 film (S1) and ZnO/TiO_2 hybrid film on FTO glass substrate, with ZnO percentage of 1% (S2) and 0.5% (S3), and electrochemical impedance spectra (right) of the DSCs based on TiO_2 electrode (S1) and $ZnO-TiO_2$ hybrid electrodes (S2 and S3). The attached table illustrates EIS parameters calculated from the given equivalent circuit. (Reproduced from Ref (Gao et al., 2009))

Figure 13 (right) showed the impedance spectra of DSCs using TiO_2 and ZnO/TiO_2 hybrid photoanodes. Results show that, both hybrid cells exhibit lower R_s, R_{ct1}, and R_{ct2} than those of the pure TiO_2 cell (S1), indicating that the incorporation of ZnO in the photoanode can decrease the overall series resistance of device significantly and facilitate the interfacial charge transport in both Pt/electrolyte and TiO_2/dye/electrolyte interface. The reason for this improvement may be the combination of the high electron transport nature of one-dimensional ZnO materials (Martinson et al., 2006), the large particle size and the network structure of ZnO disk.

Figure 14 revealed I-V curves of DSCs with TiO_2 and ZnO-TiO_2 hybrid films. The overall efficiencies of three cells are in the order of S3>S2>S1. While the cell using pure TiO_2 electrode (S1) exhibits the lowest efficiency of 1.1%, the cells with 0.5% and 1% ZnO-TiO_2 hybrid electrodes show higher efficiency of 2.7% and 2.3%, improved by 145% and 109%, respectively. Two hybrid cells exhibit similar V_{oc} but significantly higher I_{sc} and higher fill factor than pure TiO_2 cell, indicating that the improvement in the photocurrent density and fill factor is the main reason for the efficiency improvement. Also, the concentration of ZnO in the hybrid film should be no higher than 1% in this case, which is consistent with our previous observation in the hybrid film based on the sparse ZnO nanoporous disk array (Section 3) and results of other researchers on the DSCs with ZnO nanorod-TiO_2 hybrid electrode (Kang et al., 2007).
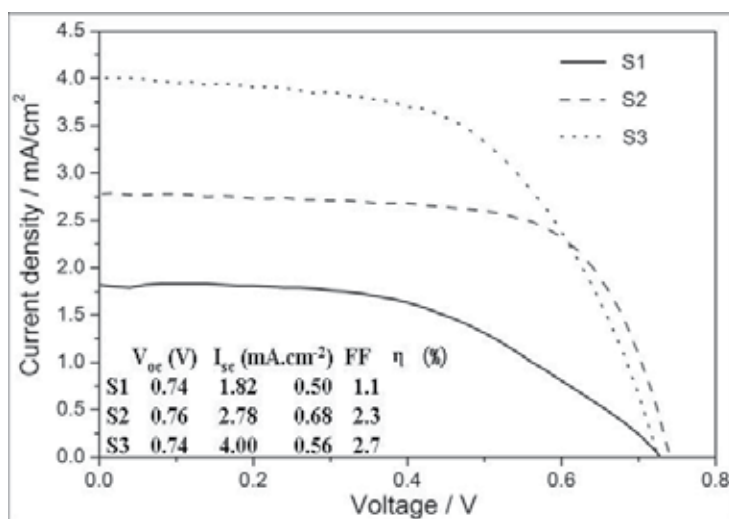
Fig. 14. The I–V characteristic curves of DSCs based on TiO_2 electrode (S1) and ZnO/TiO_2 hybrid electrode with ZnO percentage of 1% (S2) and 0.5% (S3). (Reproduced from Ref (Gao et al., 2009))

In summary, we have successfully demonstrated that ZnO nanoporous disk prepared from layered zinc based compound ZHC can be used to improve the efficiency of TiO_2 photoanodes effectively. The direct incorporation of ZnO nanodisk powder into TiO_2 slurry combined with the doctor-blade technique was proved an effective way to prepare the hybrid films. Results showed that even a small amount of ZnO incorporation in the TiO_2 film (≤1%) can significantly influence the microstructure, optical and electrical properties. The rougher inner microstructure, the enhanced light-scattering effect on the visible and

infrared light region, and the higher interfacial charge-transport rate were responsible for the improved efficiency in the hybrid photoanodes when compared with the pure TiO_2 film.

4.2 Hybrid photoanodes based on hydrothermal TiO_2 NPs

In this section, TiO_2 hydrothermal NPs were used as the source of TiO_2 for the preparation of the hybrid film. ZnO-TiO_2 hybrid slurry was prepared by adding specific amount of ZnO nanoporous disk powder into TiO_2 NPs slurry. TiO_2 NPs were prepared via the hydrothermal method and the slurry containing TiO_2 (18% by weight), ethyl cellulose (9%) and terpineol (73%) was prepared following Ref (Ito et al., 2008). ZnO nanoporous disk powder with the weight percentage of 0.5%-2% (compared with TiO_2) was blended into the slurry before the evaporation of ethanol via rotate-evaporator. Due to the acid-dissolute nature of ZnO materials, the pH value of TiO_2 slurry should be controlled at neutral or weak alkaline range.

ZnO-TiO_2 hybrid photoanodes were prepared by the doctor-blade technique using the hybrid slurry. Conductive FTO glass coated by a thin TiO_2 layer (deposited by the hydrolysis of 40 mM $TiCl_4$ aqueous solution at 70ºC) was used as the substrate. The sensitization of the photoanode film and the fabrication of the cells were similar to the procedure described in Section 2.2.

	V_{oc} (V)	I_{sc} (mA.cm^{-2})	FF	η (%)
0.5%ZnO-TiO_2	0.81	5.19	0.68	2.84
1.0%ZnO-TiO_2	0.805	5.52	0.66	2.94
2.0%ZnO-TiO_2	0.89	3.52	0.62	1.94
0.5%ZnO-TiO_2 with ZnO coated	0.79	4.56	0.63	2.29
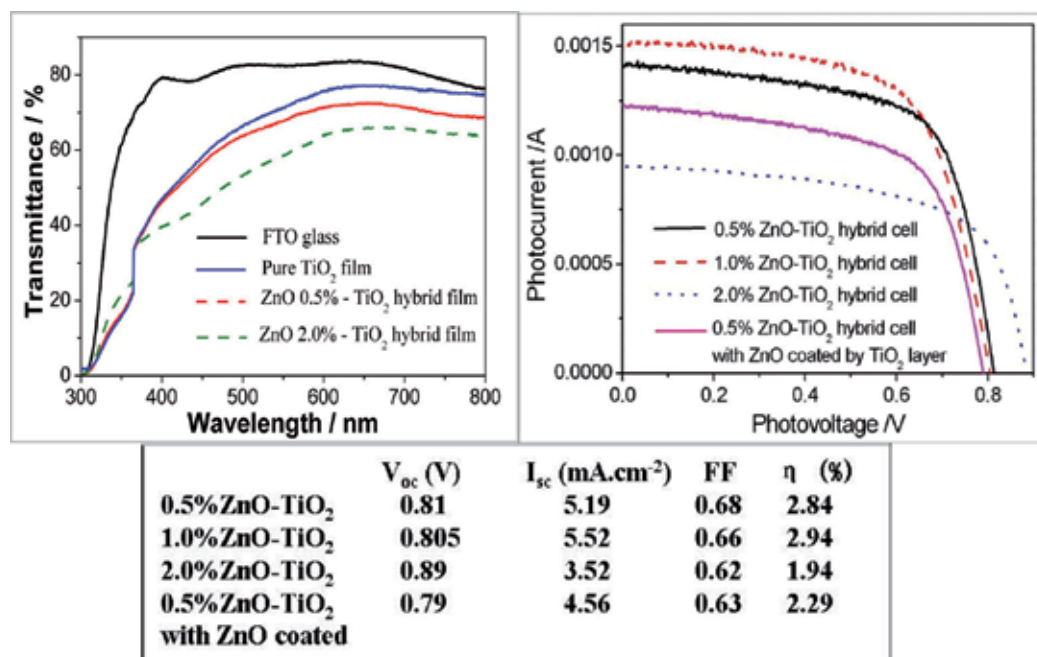
Fig. 15. Optical transmittance (left) of ZnO-TiO_2 hybrid film deposited on FTO substrate, and I-V curves (right) of ZnO – TiO_2 hybrid cells based on different ZnO contents (0.5-2% by weight) under AM 1.5 illumination (100 mW/cm²). The active area is 0.27 cm² for all cells.

SEM analysis (not shown here) indicates that the microstructure of the hybrid film was similar to that of pure TiO_2 film, different from the results in P25 slurry (Section 4.1). We think this difference may be resulted from the solvent of the slurry. In P25 based hybrid

slurry, water is the dispersant, and the presence of large-size ZnO disk may exert significant influences on the viscosity of the slurry, thus modifying the microstructure of the hybrid film. In the hydrothermal TiO$_2$ hybrid slurry, organic terpineol was used as the dispersant, which possessed much higher viscosity than water. So the presence of a very small percentage of ZnO disks in the slurry had only minor influences on the viscosity and other physical properties of the hybrid slurry. Correspondingly, the microstructure of the hybrid film differed little from the pure one.

Figure 15 (left) showed optical transmittance spectra of ZnO-TiO$_2$ hybrid film deposited on FTO substrate. Different from microstructure results, the hybrid films exhibit obviously lower transmittance than the pure TiO$_2$ film in the visible-near infrared wavelength, which can be ascribed to the scattering effects of ZnO disks dispersed uniformly in the film. As mentioned above, this scattering behavior is beneficial to the absorption of N719 dye molecules. Also the hybrid film with 2% ZnO exhibits higher scattering effects than the one with 0.5% ZnO.

I-V curves given in Figure 15 (right) indicate that the photoanode with 1% ZnO possesses the highest efficiency compared with 0.5% ZnO and 2% ZnO hybrid films. While the cell parameters of the cells based on 0.5% and 1%ZnO are similar, the cell with 2%ZnO shows much less photocurrent density, which may account for the main fall in the efficiency. Also we were trying to coat a thin TiO$_2$ layer on ZnO nanoporous disk before its incorporation into TiO$_2$ slurry via the sol-gel method. Results show that this coating is not helpful in this case, maybe resulted from the reduced surface area in ZnO nanoporous disk due to TiO$_2$ coating. Further and in-depth investigation in this direction is required.

	R_s (Ω)	CPE_{ct1} (uFS$^{\alpha-1}$)	R_{ct1} (Ω)	α_{ct1}	CPE_{ct2} (uFS$^{\alpha-1}$)	R_{ct2} (Ω)	α_{ct2}
(a)	17.1	0.0015	10.0	0.7	0.004	21.5	0.9
(b)	19.4	0.003	6.5	0.7	0.0185	19.1	0.9
(c)	17.5	0.0025	14.0	0.7	0.008	44.0	0.85
(d)	18.8	0.0015	9.0	0.7	0.004	30.0	0.9
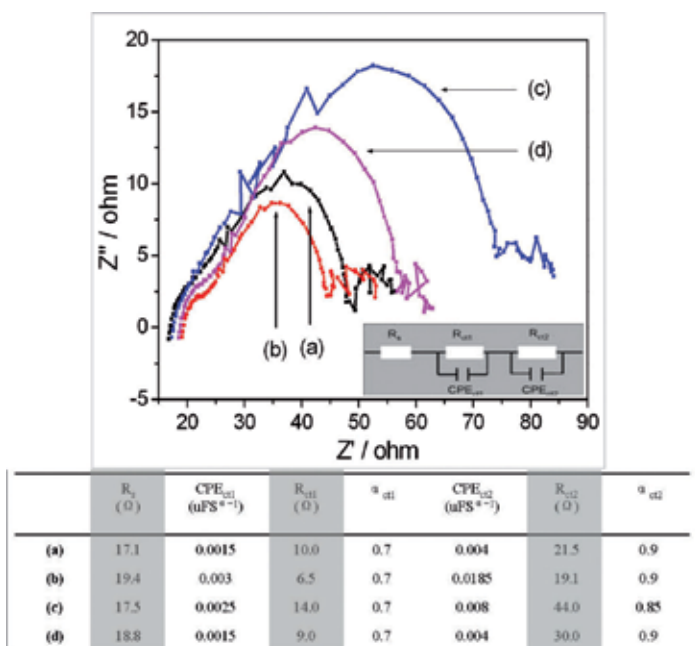
Fig. 16. Nyquist plots of ZnO nanodisk – TiO$_2$ NPs hybrid cells with ZnO content in hybrid slurry by weight of (a) 0.5%, (b) 1.0%, (c) 2.0%), and (d) 0.5% (ZnO disks were coated by a thin TiO$_2$ layer via sol-gel technique). The table illustrates EIS parameters calculated from the given equivalent circuit.
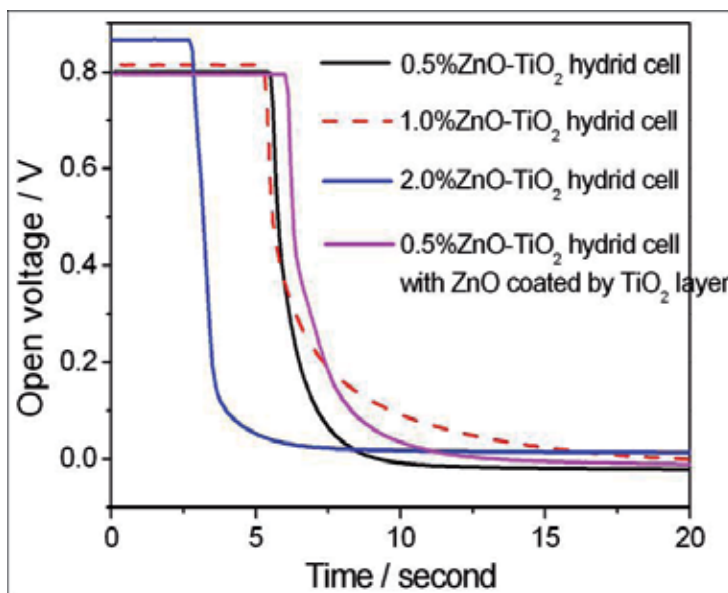
Fig. 17. Open-circuit voltage decay plots of ZnO nanodisk – TiO$_2$ NPs hybrid cells with different ZnO content in hybrid slurry by weight (0.5%-2.0%).

Figure 16 illustrated Nyquist plots of ZnO-TiO$_2$ hybrid cells obtained from EIS analysis. From the results of simulation, we can see that the hybrid cell with 1%ZnO content possesses the lowest resistance at Pt/electrolyte interface and at TiO$_2$/dye/electrolyte interface. The resistance at two interfaces increases when the content of ZnO in hybrid film is either lower or higher than 1%. In special, for the hybrid film with 2% ZnO content, the resistance at both interfaces is higher than that of film with 1% or 0.5% ZnO content. Also for the film with 0.5% ZnO coated with a thin TiO$_2$ layer, the resistance at the TiO$_2$/dye/electrolyte interface and the overall series resistance were increased, thus resulted in the reduction in the total conversion efficiency. In general, we can derive a linear relationship between the interfacial resistance obtained from EIS analysis and the overall conversion efficiency of the hybrid cell.

Figure 17 showed OCVD plots of the hybrid cell with different ZnO content. Results show that 1%ZnO-TiO$_2$ hybrid cell exhibits the slowest voltage decay rate among all four cells, indicating the lower recombination rate, which is consistent with its high conversion efficiency. Also the coating of a thin TiO$_2$ layer on ZnO nanoporous disk via sol-gel technique can slightly improve the recombination properties of the hybrid cell, which is beneficial to the improvement of the efficiency. However, other consequences induced by the coating, possibly the blocking of the nanopore and the decrease of the surface area, resulted in the reduction of the overall efficiency at last.

For ZnO-TiO$_2$ hybrid cell, it is important to discuss the effects of the treatment of the photoanode film in TiCl$_4$ aqueous solution. ZnO is intrinsically an amphoteric oxide, which can be dissolved in TiCl$_4$ aqueous solution with the strong acid nature. So it should be very careful in treating ZnO-TiO$_2$ hybrid films in TiCl$_4$ solutions. Figure 18 illustrated I-V curves of TiO$_2$ and ZnO-TiO$_2$ film with and without TiCl$_4$ treatment. Results show that the

incorporation of ZnO into TiO_2 can improve the efficiency from 3.5% to 3.98% before the $TiCl_4$ treatment. However, after the treatment, the efficiency of the hybrid film decreases to 3.2%, while the efficiency of the pure TiO_2 film increases to 6.38%. The dissolution of ZnO dispersed uniformly in the hybrid film may be underlying reason for the efficiency reduction. On the other hand, the $TiCl_4$ treatment is a very powerful method to improve the efficiency of the pure TiO_2 cell. So it is necessary to develop an alternative treatment method in a neutral aqueous solution, which has minor influence on the structure of ZnO. Other methods may be also helpful including the protective coating technique on ZnO nanoporous disks by thin TiO_2 layer which can resist the corrosion of acid. However, when the protective coating technique is adopted, one has to be careful in avoiding the blocking of the nanopore present in ZnO nanostructures.

In summary, this section discussed the preparation of ZnO-TiO_2 hybrid photoanode films based on ZnO nanoporous disk powder and hydrothermal TiO_2 NPs. An optimal ZnO content of ~1% in the hybrid film was observed, with the total conversion efficiency of ~2.94%. While the efficiency improvement in the hybrid cell was realized when compared with the pure TiO_2 film when no $TiCl_4$ treatment was performed, the decrease in the efficiency in the hybrid film after the $TiCl_4$ treatment indicated the sensitivity of the hybrid system. The development of other treatment methods suitable for ZnO-TiO_2 hybrid system or other protective means may afford the further direction in this field.
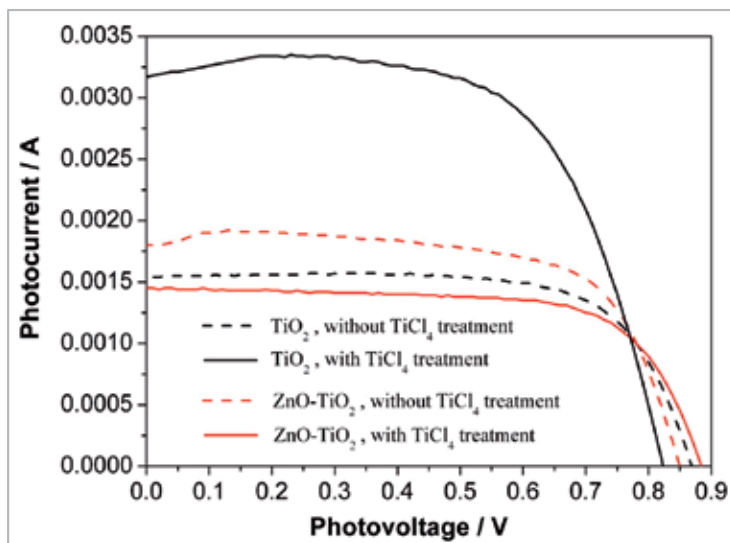
Fig. 18. I-V curves of TiO_2 NPs-based cell and ZnO–TiO_2 hybrid cells under AM 1.5 illumination (100 mW/cm²), illustrating the effects of $TiCl_4$ treatment.

5. Conclusion

In summary, the chapter started with a general review on the ordered TiO_2 and ZnO photoanode and the hybrid photoanode, outlining a brief picture on the status of the ordered photoanode in the field of DSCs. Then focusing on the ZnO-TiO_2 hybrid photoanodes, four type of ZnO nanostructure (including dense and sparse nanowire array, sparse nanoporous disk array, and nanoporous disk powder) and three type of TiO_2 nanoparticles (including P25, P90, and home-made hydrothermal nanoparticles) were used to prepare various hybrid films. Results show that, in general, the integration of ZnO with TiO_2 is a powerful means to improve the efficiency of the photoanode of DSCs, with the improvement up to 150%. However, one has to take great care in realizing the ideal hybrid structures. The content of ZnO in the hybrid film has to be maintained at a low level (e.g. ~1% by weight) in order to obtain a positive effect, which means that sparse and thin nanowire array or nanodisk array instead of the dense array is preferred. Also great care has to be taken during the $TiCl_4$ treatment of the ZnO-TiO_2 hybrid photoanode or the protective coating of ZnO nanostructures, preventing the destruction to the microstructure of ZnO nanostructures. Though at the current stage the overall conversion efficiency of the hybrid cell has not overpassed the highest level of the pure TiO_2 cell, it represents a very powerful and important technical route to optimize the microstructure and the performance of the ordered photoanode. We believe, by the continuous efforts of the forthcoming researchers, the hybrid semiconductor photoanodes with ordered structures will eventually shed the light to the DSCs with the breakthrough efficiency.

6. Acknowledgment

7. References

Brown, P.; Takechi, K. & Kamat, P. V. (2008). Single-Walled Carbon Nanotube Scaffolds for Dye-Sensitized Solar Cells. *J. Phys. Chem. C,* Vol. 112, No. 12, pp. 4776-4782.

Chou, T. P.; Zhang, Q. F.; Fryxell, G. E. & Cao, G. Z. (2007). Hierarchically Structured ZnO Film for Dye-Sensitized Solar Cells with Enhanced Energy Conversion Efficiency. *Adv. Mater.,* Vol. 19, No. 18, pp. 2588-2592.

Gan, X. Y.; Li, X. M.; Gao, X. D.; Zhuge, F. W. & Yu, W. D. (2007). ZnO Nanowire/TiO_2 Nanoparticle Photoanodes Prepared by the Ultrasonic Irradiation Assisted Dip-coating Method. *Thin Solid Films.* Vol. 518, No. 17, pp. 4809–4812.

Gao, X. D.; Li, X. M.; Yu, W. D.; Qiu, J. J. & Gan, X. Y. (2007). Preparation of Nanoporous TiO_2 Thick Film and Its Photoelectrochemical Properties Sensitized by Merbromin. *J. Inorg. Mater.,* Vol. 22, No.6, pp. 1079-1085.

Gao, X. D.; Gao, W.; Yan, X. D.; Zhuge, F. W.; Bian, J. M. & Li, X. M. (2009). ZnO Nanoporous Disk-TiO$_2$ Nanoparticle Hybrid Film Electrode For Dye-Sensitized Solar Cells. *Funct. Mater. Lett.*, Vol. 2, No.1, pp. 27-31.

Grätzel M. (2001). Photoelectrochemical cells. *Nature,* Vol. 414, No. 6861, pp. 338-344.

Grätzel M. (2006). Photovoltaic Performance and Long-Term Stability of Dye-Sensitized Mesoscopic Solar Cells. *C. R. Chimie,* Vol. 9, No. 5/6, pp. 578-583.

Guldin, S.; Huttner, S.; Kolle, M.; Welland, M. E.; Muller-Buschbaum, P.; Friend, R. H.; Steiner, U. & Te´treault N. (2010). Dye-Sensitized Solar Cell Based on a Three-Dimensional Photonic Crystal. *Nano Lett.*, Vol. 10, No. 7, pp. 2303–2309.

Hosono, E.; Fujihara, S.; Honma, I. & Zhou, H. (2005). The Fabrication of an Upright-Standing Zinc Oxide Nanosheet for Use in Dye-Sensitized Solar Cells. *Adv. Mater.*, Vol. 17, No. 17, pp. 2091–2094.

Ito, S; Murakami, T. N.; Comte, P.; Liska, P.; Grätzel, C.; Nazeeruddin, M. K. & Grätzel M. (2008). Fabrication of Thin Film Dye Sensitized Solar Cells with Solar to Electric Power Conversion Efficiency Over 10%. *Thin Solid Films*, Vol. 516, No. 14, pp. 4613-4619.

Kang, S. H.; Kim, J. Y.; Kim, Y.; Kim, H. S. & Sung, Y. E. (2007). Surface Modification of Stretched TiO$_2$ Nanotubes for Solid-State Dye-Sensitized Solar Cells. *J. Phys. Chem. C,* Vol. 111, No. 26, pp. 9614-9623

Kang, S. H.; Choi, S. H.; Kang, M. S.; Kim, J. Y.; Kim, H. S.; Hyeon, T. & Sung, Y. E. (2008). Nanorod-Based Dye-Sensitized Solar Cells with Improved Charge Collection Efficiency. *Adv. Mater.*, Vol. 20, No.1, pp. 54 -58.

Ku, C. H.; Yang, H. H.; Chen, G. R. & Wu, J. J. (2008). Wet-Chemical Route to ZnO Nanowire-Layered Basic Zinc Acetate/ZnO Nanoparticle Composite Film. *Cryst. Growth Des.*, Vol. 8, No. 1, pp. 283-290.

Law, M.; Greene, L. E.; Johnson, J. C.; Saykally, R. & Yang P. (2005). Nanowire dye-sensitized solar cells. *Nature Materials,* Vol. 4, No. 6, pp. 455-459.

Law, M.; Greene, L. E.; Radenovic, A.; Kuykendall, T.; Liphardt, J. & Yang, P. (2006). ZnO-Al$_2$O$_3$ and ZnO-TiO$_2$ Core-Shell Nanowire Dye-Sensitized Solar Cells. *J. Phys. Chem. B,* Vol. 110, No. 45, pp. 22652-22663.

Lee, K. M.; Hu, C. W.; Chen, H. W. & Ho, K. C. (2008). Incorporating Carbon Nanotube in a Low-Temperature Fabrication Process for Dye-Sensitized TiO$_2$ Solar Cells. *Solar Energy Materials & Solar Cells,* Vol. 92, No. 12, pp. 1628-1633.

Li, B.; Wang, L. D.; Kang, B.; Wang, P. & Qiu, Y. (2006). Review of Recent Progress in Solid-State Dye-Sensitized Solar Cells. *Sol. Energy Mater. Sol. Cells,* Vol. 90, No. 5, pp.549-573.

Martinson, A. B. F.; McGarrah, J. E.; Parpia, M. O. K. & Hupp, J. T. (2006). Dynamics of Charge Transport and Recombination in ZnO Nanorod Array Dye-sensitized Solar Cells. *Phys. Chem. Chem. Phys.*, Vol. 8, No. 40, pp. 4655-4659.

Martinson, A. B. F.; Jeffrey, J. W.; Elam, W.; Hupp, J. T. & Pellin, M. J. (2007). ZnO Nanotube Based Dye-Sensitized Solar Cells. *Nano Lett.*, Vol. 7, No. 8, pp. 2183-2187.

Mor, G. K.; Varghese, O. K.; Paulose, M.; Shankar, K. & Grimes C. A. (2006a). A Review on Highly Ordered, Vertically Oriented TiO_2 Nanotube Arrays: Fabrication, Material Properties, and Solar Energy Applications. *Sol. Energy Mater. Sol. Cells,* Vol. *90*, No. 14, pp. 2011-2075.

Mor, G. K.; Shankar, K.; Paulose, M.; Varghese, O. K. & Grimes, C. A. (2006b). Use of Highly-Ordered TiO_2 Nanotube Arrays in Dye-Sensitized Solar Cells. *Nano Lett.,* Vol. 6, No. 2, pp. 215-218.

Nazeeruddin, M. K.; Kay, A.; Rodicio, I.; Humpbry-Baker, R.; Müller, E.; Liska, P.; Vlachopoulos, N. & Grätzel, M. (1993). Conversion of Light to Electricity by Cis-X2bis(2,2'-bipyridyl-4,4'-dicarboxylate) Ruthenium(II) Charge-Transfer Sensitizers (X = Cl-, Br-, I-, CN-, and SCN-) on Nanocrystalline Titanium Dioxide Electrodes. *J. Am. Chem. Soc.,* Vol. 115, No.14 , pp. 6382-6390.

O'Regan B. & Grätzel M. (1991). A Low-Cost, High-Efficiency Solar Cell Based on Dye-Sensitized Colloidal TiO_2 Films. *Nature,* Vol. *353*, No. 6346, pp. 737-740.

Pang, S.; Xie, T.; Zhang, Y.; Wei, X.; Yang, M.; Wang, D. & Du, Z. (2007). Research on the Effect of Different Sizes of ZnO Nanorods on the Efficiency of TiO_2-Based Dye-Sensitized Solar Cells. *J. Phys. Chem. C,* Vol. 111, No. 49, pp. 18417-18422.

Park, K.; Zhang, Q.; Garcia, B. B.; Zhou, X. Y.; Jeong, Y. H. & Cao, G. Z. (2010). Effect of an Ultrathin TiO_2 Layer Coated on Submicrometer-Sized ZnO Nanocrystallite Aggregates by Atomic Layer Deposition on the Performance of Dye-Sensitized Solar Cells. *Adv. Mater.,* Vol. 22, No. 21, pp. 2329–2332.

Rensmo, H.; Keis, K.; Lindstrom, H.; Sodergren, S.; Solbrand, A.; Hagfeldt, A. & Lindquist, S. E. (1997). High Light-to Energy Conversion Efficiencies for Solar Cells Based on Nanostructured ZnO Electrodes. *J. Phys. Chem. B.,* Vol. 101, No. 14, pp. 2598-2601.

Rustomji, C. S.; Frandsen, C. J.; Jin, S. & Tauber, M. J. (2010). Dye-Sensitized Solar Cell Constructed with Titanium Mesh and 3-D Array of TiO_2 Nanotubes. *J. Phys. Chem. B,* Vol. 114, No. 45, pp. 14537–14543.

Tan, B. & Wu, Y. Y. (2006). Dye-Sensitized Solar Cells Based on Anatase TiO_2 Nanoparticle/Nanowire Composites. *J. Phys. Chem. B,* Vol. 110, No. 32, 15932-15938.

Wang, J. X.; Wu, C. M. L.; Cheung, W. S.; Luo, L. B.; He, Z. B.; Yuan, G. D.; Zhang, W. J.; Lee, C. S. & Lee, S. T. (2010). Synthesis of Hierarchical Porous ZnO Disklike Nanostructures for Improved Photovoltaic Properties of Dye-Sensitized Solar Cells. *J. Phys. Chem. C,* Vol. 114, No. 31, pp. 13157–13161.

Xu, C. K.; Shin, P.; Cao, L. L. & Gao, D. (2010). Preferential Growth of Long ZnO Nanowire Array and Its Application in Dye-Sensitized Solar Cells. *J. Phys. Chem. C,* Vol. 114, No. 1, pp. 125–129.

Zhang, Q.; Chou, T.; Russo, B.; Jenekhe, S. & Cao, G. (2008). Aggregation of ZnO Nanocrystallites for High Conversion Efficiency in Dye-Sensitized Solar Cells. *Angew. Chem. Int. Edt.*, Vol. 47, No. 13, pp. 2402-2406.

Zhang, W.; Zhu, R.; Ke, L.; Liu, X. Z.; Liu, B. & Ramakrishna S. (2010). Anatase Mesoporous TiO_2 Nanofibers with High Surface Area for Solid-State Dye-Sensitized Solar Cells. *Small,* Vol. 6, No. 19, pp. 2176–2182.

Zhang Q. F. & Cao G. Z. (2011). Nanostructured Photoelectrodes for Dye-Sensitized Solar Cells. *Nano Today*, Vol. 6, No. 1, pp. 91-109.

Zhu, K.; Neale, N. R.; Miedaner, A. & Frank, A. J. (2007). Enhanced Charge-Collection Efficiencies and Light Scattering in Dye-Sensitized Solar Cells Using Oriented TiO_2 Nanotubes Arrays. *Nano Lett.,* Vol. 7, No. 1, pp. 29-74.

Photo-Induced Electron Transfer from Dye or Quantum Dot to TiO$_2$ Nanoparticles at Single Molecule Level

King-Chuen Lin and Chun-Li Chang
Department of Chemistry, National Taiwan University, Taipei 106,
Institute of Atomic and Molecular Sciences, Academia Sinica, Taipei 106,
Taiwan

1. Introduction

Dye-sensitized solar cell (DSSC) has attracted wide attention for the potential application to convert sunlight into electricity. Organic dyes blended with TiO$_2$ nanoparticles (NPs) have been recognized as important light harvesting materials especially in the visible spectral range (Hara et al., 2002; Bisquert et al., 2002; Gratzel, 2001; Ferrere & Gregg, 2001; Hagfeldt & Gratzel, 2000; Cahen et al., 2000). The functional materials are assembled in a sandwiched type to undergo photon-induced current process. Following photoexcitation, the embedded dye molecules may lead to electron transfer (ET) to the TiO$_2$ conduction band. The injected electron flows through the semiconductor network and the external load to the counter electrode. At the counter electrode, the oxidized dye is reduced by electron donation from an electrolyte, and then the circuit becomes complete. The electron transfer kinetics in most dye/TiO$_2$ systems is as rapid as in the time regime of femtosecond to several hundred picoseconds. The injected electrons are localized in either subband or surface states of TiO$_2$ semiconductor. A fraction of the electrons, detrapped thermally from the reduced semiconductor, may possibly undergo recombination with the oxidized dye molecules. Such a back ET process takes place slowly from subnanoseconds to several milliseconds. An efficient solar cell deign should control lowering the rate of back electron transfer to prolong the lifetimes of charge-separated states. Therefore, characterizing kinetics of the forward and backward ET may be conducive to facilitating the working efficiency of a solar cell design.

Among a variety of DSSC designs, Grätzel and coworkers have applied ruthenium-based dyes adsorbed on the TiO$_2$ thin film, thereby achieving a very high power-conversion efficiency >11% (Gratzel, 2003, 2005). Despite a much lower efficiency in comparison, quantum dots (QDs) adopted recently to substitute for dyes have been popularly investigated including PbS (Plass et al., 2002; Ju et al., 2010), InAs (Yu et al., 2006), CdSe (Lee & Lo, 2009; Fan et al., 2010), CdS (Baker & Kamat, 2009; Lee & Lo, 2009), and PbSe (Luther et al., 2008; Choi et al., 2009). QDs have potential to be an alternative as electron donors (Robel et al., 2006; Kamat, 2008), for their unique properties such as size-dependent tunable energy gap (Yu et al., 2003; Kamat, 2008), a broad absorption band with large absorption cross sections (Yu et al., 2003), and multiple exciton generation (Yu et al., 2003; Luther et al., 2007; Kim et al., 2008; Sambur et al., 2010). When QDs absorb a photon to form an electron-hole

pair, the electrons may have chance to transfer to an accepting species such as TiO$_2$, if the conduction band edge of QDs is tuned higher than the conduction band of TiO$_2$ (Robel et al., 2006; Yu et al., 2006; Kamat, 2008). Like the DSSC mechanism, kinetic behavior of ET between QDs and TiO$_2$ is one of the key roles to achieve a high energy-conversion efficiency. The bulk measurements yield ensemble-averaged information and sometimes could mask or overlook specific phenomena occurring at the sensitizer-semiconductor interfaces. For instance, conformation change and reorientation of the adsorbate structure feasibly induce the fluctuation of fluorescence decay times for ET processes, but such detailed dynamical complexity can not be visualized in ensemble experiments (Moerner & Fromm, 2003; Michalet et al., 2006). As a result, single molecule spectroscopy (SMS) has emerged as a powerful tool for investigating the dynamic processes of excited molecules in heterogeneous surrounding (Xie & Dunn, 1994; Garcia-Parajo et al., 2000; Moerner & Fromm, 2003; Michalet et al., 2006; Gaiduk et al., 2007). Analysis of fluorescence intermittency observed in SMS, or called on/off blinking phenomena, has been widely studied to unveil the dynamic behaviors of triplet state (Yip et al., 1998; Veerman et al., 1999; Kohn et al., 2002), molecular reorientation (Ambrose et al., 1994), energy transfer (VandenBout et al., 1997; Cotlet et al., 2005; Flors et al., 2007), spectral diffusions (Xie & Dunn, 1994; Kulzer et al., 1997), and electron transfer (Holman & Adams, 2004; Bell et al., 2006; Wang et al., 2009; Chen et al., 2010). This chapter is confined to understand ET dynamics of either dyes or QDs adsorbed on the TiO$_2$ NPs thin film at a single molecule level.

By taking advantage of the SMS merits, the IFET phenomena of oxazine 1 dye and CdSe/ZnS core/shell QD adsorbed individually on the TiO$_2$ NPs surface are demonstrated. We acquired fluorescence trajectories of single dye molecule, characteristic of "on" and "off" blinking with time, in which the intensity fluctuation is attributed to the interfacial electron transfer (IFET) behavior. The fluorescent dye molecule lies in an off-blinking state when its electron moves to the TiO$_2$ NPs conduction band. While the electron transfers back to the oxidized state, the dye molecule blinks on again following photoexcitation. Discrete fluorescence intensity jumps between "on" and "off" level are analyzed by using autocorrelation function. The "on" and "off" lifetimes and the subsequent rate constants of forward and backward ET are then determined. On the other hand, the fluorescence lifetimes of QDs are measured as an alternative determination for the ET rate constants. QDs with different sizes are adopted for demonstration. We apply time-correlated single-photon counting (TCSPC) to measure fluorescence lifetimes among a quantity of QDs for each size. The fluorescence lifetime becomes shorter and the resultant "off" time is prolonged with decreased size of QDs. The off-time and on-time probability densities are then estimated and fitted appropriately. With the aid of Marcus model, theoretical ET rate constants are calculated for comparison and the ET process may thus be gained insight.

2. Experimental

2.1 Apparatus

All single molecule experiments were performed with a confocal fluorescence microscope. For the single dye (or QD) experiments, a single-mode pulsed laser at 630 nm (or 375 nm), with a repetition rate of 10 MHz (or 5 MHz) and pulsed duration of 280 ps (or 300 ps), was used as the excitation source. The beam collimated with a pair of lenses was spectrally filtered with an excitation filter before entering an inversed microscope. An oil immersion objective (100x, NA1.40) was used both to focus the laser beam onto the sample, prepared

on the surface of a glass coverslip, and to collect fluorescence from the sample. The excitation intensity of the pulsed beam was constantly measured to be 40 - 210 W/cm^2 right on the top of the bare coverslip throughout the experiments. The fluorescence, after transmitting through a dichroic mirror, was refocused by a tube lens (200 mm focal length) onto an optical fiber (62.5 μm diameter) which was coupled to an avalanche photodiode (APD) detector with a 175 μm active area. Here the fiber serves as a pinhole to reject out-of-focus light. The fluorescence signal may also be reflected simultaneously to a charge-coupled device (CCD) by a beamsplitter. A notch filter (6<OD) or a combination of bandpass filters were positioned in front of the detector to remove excitation background. Given the wide-field images with a CCD detector, each fluorescent single molecule was readily moved to an illuminated position using a x-y positioning stage. The fluorescence lifetime of single molecule was measured by TCSPC with a TimeHarp 200 PCI-board (PicoQuant). The data were stored in a time-tagged time-resolved mode, which allowed recording every detected photon and its individual timing information. By taking into account deconvolution of the instrument response function (SymPhoTime by PicoQuant), the TCSPC curve was analyzed by single exponential tail-fit.

2.2 Material preparation

The TiO₂ precursor was prepared by a sol-gel process. 72 mL of 98% Titanium(IV) isopropoxide was added to 430 mL of 0.1 M nitric acid solution which was then stirred and heated to 85 °C for 8 h. The colloid, as filtered from the cooled mixture, was heated again in an autoclave at five temperatures of 180, 200, 220, 240, and 260 °C for 12 h to grow TiO₂ NPs. The TiO₂ colloid was concentrated to 13 wt%, followed by addition of a 30 wt% (with respect to TiO₂) of polyethylene glycol to prevent from cracking during drying.

To prepare for the thin film, 40-50 μL of 0.65% TiO₂ NPs aliquot was spin-coated on a cleaned coverslip. The same process was repeated four times to ensure TiO₂ well coated over the coverslip. After drying in the air for 30 min, the film was heated to 450 °C at a rate of 20 °C/min, and remained for 30 min before cooling to the room temperature. The phase and the size of TiO₂ NPs were characterized by using scanning electron microscopy. A drop of 30 μL of 0.1 nM oxazine 1 dye in methanol solution or 35 μL of 4 - 200 pg/L QDs in toluene solution was spin-coated over the TiO₂ NPs surface, and then put on the sample stage of microscope for fluorescence measurement.

3. Fluorescence intermittency and electron transfer by single dye molecule

3.1 Fluorescence lifetimes

As shown in Fig.1, the TiO₂ NPs thin film was well covered over the coverslip to ensure that the oxazine 1 dye may be fully adsorbed on the TiO₂ surfaces. The enlarged images displayed the NPs size about ~20 nm. Fig.2 shows absorption spectra of oxazine 1 solution in the presence (or absence) of TiO₂ NPs by means of ensemble measurements. The absorption cross section reaches as large as ~3.5×10^{-16} cm^2 at 630 nm. The fluorescence yield is 0.11 in ethanol as the solvent and increases to 0.19 in ethylene glycol (Sens & Drexhage, 1981). When the dye in methanol solution is diluted from 10^{-6} to 10^{-8} M, the spectral profile remains the same with a major peak and a minor shoulder. The spectra appear almost the same between the conditions with and without TiO₂ NPs involvement. The results suggest that the dimer contribution should be minor and negligible.
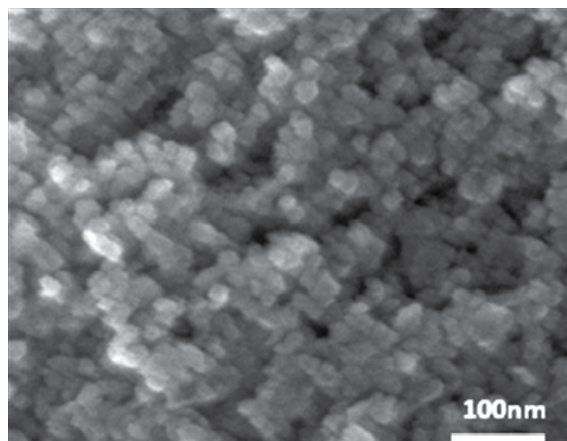
Fig. 1. Images of TiO_2 NPs thin film by using scanning electron microscopy. The average sizes of TiO_2 NP are about 20 nm for both films.

A 10^{-10} M of oxazine 1 dye solution was spin-coated on a bare or a TiO_2 NPs-coated coverslip. Fig.3(a) displays the fluorescence images of the single oxazine 1 molecules within a 24 μm x 24 μm area on the bare coverslip, as excited by a pulsed laser at 630 nm with excitation intensity of 39±2 W/cm². Each bright spot is attributed to a single molecular fluorescence. The diffraction-limited spot size is about ~650 nm. Fig.3(b) shows the background emissions of the TiO_2 NPs surface. Stray light scattered by the TiO_2 NPs causes background noise, which is however dimmer than those fluorescent spots from the dye molecules. Fig.3(c) shows the single molecular fluorescence images of dye molecules on TiO_2 NPs surface. The maximum fluorescence intensity reaches 650 counts acquired by a CCD within an integration time of 0.5 s. The fluorescent spots have different intensities resulting from variation of molecular orientation and micro-environments. The surface densities of fluorescent oxazine 1 on glass or TiO_2 coverslip are counted to be 0.088 or 0.085 per μm², respectively, with an uncertainty of ±10%. It is difficult to make a comparison with the surface density prepared initially, since a great amount of dye solution is sputtered away during the spin-coating process. The roughness of the TiO_2 NPs-coated coverslip may reduce the dye molecules from sputtering away to some extents, as compared to a smooth bare glass. Although the surface density of fluorescent spots is similar between them, some molecules in the excitation might be quenched by a faster IFET process before fluorescing and thus fail to be detected. The clefts or interstices in the TiO_2 film are probably ideal sites for effective IFET.

As shown in Fig.4(a), fluorescence decay of a single dye molecule on TiO_2 is obtained for the lifetime measurements by the TCSPC method. The decay curve is fitted to a single exponential function yielding a lifetime of 2.6 ns. In this manner, the lifetimes successively determined among 100 different oxazine 1 molecules are distributed in Fig.4(b), with an average value of 2.86±0.31 ns. The lifetime scattering reveals an inhomogeneous character among the dye molecules measured, because of variation of dipole orientation, transition frequency, and molecular polarization on the surface. In addition, the fluctuation of the lifetime is partially attributed to the power density variation which is about ±3%. For comparison, the average lifetimes over 100 oxazine 1 molecules are measured analogously to be 3.02±0.61 ns on the bare coverslip.
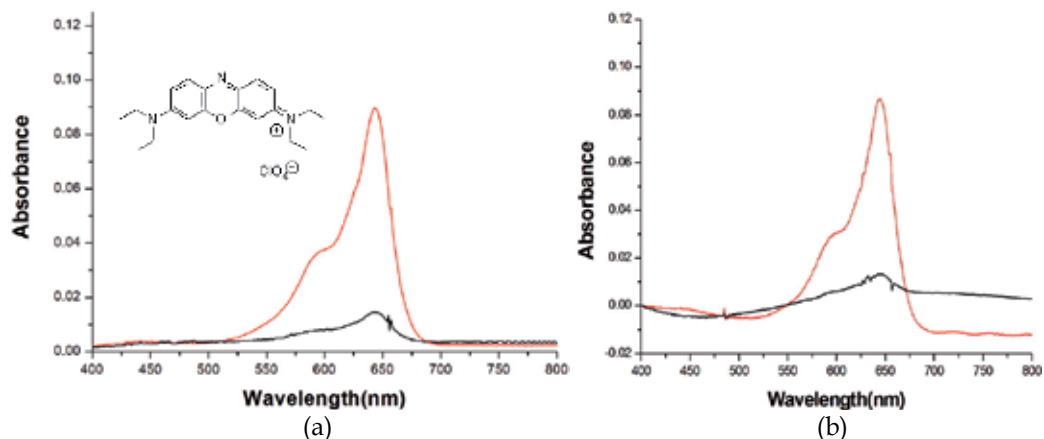
Fig. 2. (a) Absorption spectra of oxazine 1 dye in methanol solution with concentration of 1×10^{-6} (larger peak) and 1×10^{-8} M, respectively. Oxazine 1 structure is also displayed. (b) Absorption spectra of oxazine 1 methanol solution with concentration of 1×10^{-6} (larger peak) and 1×10^{-8} M, respectively, in the presence of TiO₂ NPs
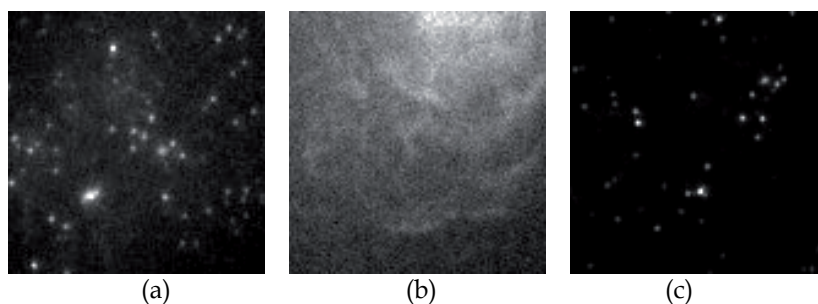
Fig. 3. Fluorescence images of (a) oxazine 1 molecules on bare coverslip, (b) TiO₂ NPs film without dye molecules involved, and (c) oxazine 1 molecules on TiO₂ NPs–coated coverslip.

Despite no statistical difference with the uncertainty considered, the average lifetime of the dye on the TiO₂ film is significantly smaller than that on the bare coverslip. While inspecting Fig.4(b), the asymmetric distribution shows more molecules lying on the side of shorter fluorescence lifetime. It suggests two points. First, some molecules might undergo even faster IFET process such that the excited state lifetimes become too short to be detected. Second, slight difference of the fluorescence lifetimes implies that most IFET processes should be slow and inefficient. The oxazine 1 molecule lacks effective anchoring groups like carboxylate in metal-polypyridine complexes to covalently bind the dye to the semiconductor (Oregan & Gratzel, 1991; Ramakrishna et al., 2005). These dye molecules randomly selected are anticipated to be physisorbed to the TiO₂ NPs surface or loosely trapped at the NPs interstices. However, that does not mean all interactions based on physisorption can not lead to efficient electron transfer. Some organic dyes such as cyanine or xanthene dyes incorporated in Langmuir-Blodgett films deposited on In₂O₃ or SnO₂ electrodes show very efficient electron transfer even without chemisorptions, due to a large free-energy difference between the lowest unoccupied molecular orbital (LUMO) of the dye

and the edge of the conduction band of the semiconductor(Arden & Fromherz, 1980; Biesmans et al., 1991; Biesmans et al., 1992).
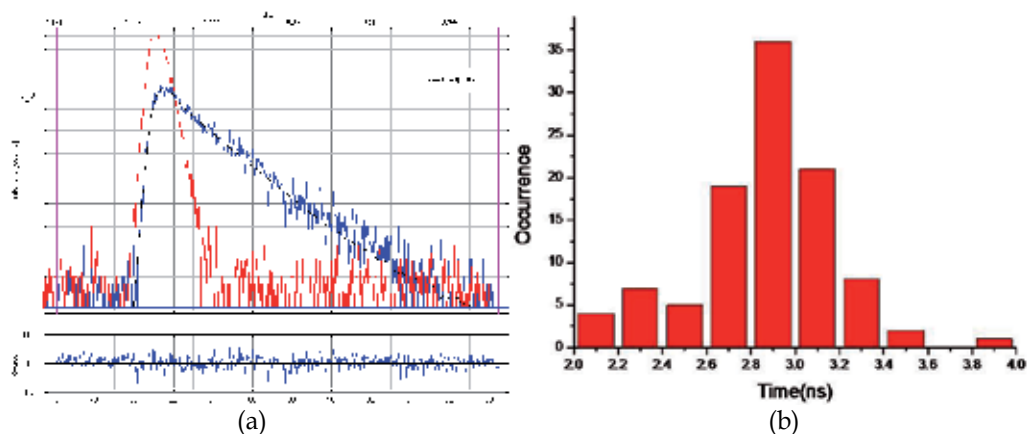
Fig. 4. (a) Fluorescence decay of single oxazine 1 molecule in the presence of TiO$_2$ NPs measured by using time-correlated single photon counting. The instrument response function gives a faster decay estimated to be 550 ps. (b) Distribution of excited state lifetimes among 100 single oxazine 1 molecules on the TiO$_2$ NPs surface, yielding an average lifetime of about 2.86 ns.

3.2 Fluorescence intensity trajectories

Fig.5(a) displays fluorescence intensity as a function of running time of a single oxazine 1 molecule on the bare coverslip with a 20 ms binning time to record the photon counts of emission. These time scales average out any faster fluorescence fluctuation or blinking of the dye molecules. The single-molecule trace shows a constant level of fluorescence intensity which then drops to the background in one step when photobleaching occurs. Wilkinson et al. reported the triplet state lifetime to be 14.5 μs for oxazine 1 in acetonitrile solution (Wilkinson et al., 1991), and a significantly longer lifetime is yet expected for the dye adsorbed on the solid film. A constant level of fluorescence intensity in Fig.5(a) implies that the prolonged lifetimes should be much shorter than the integration time adopted such that the triplet blinking may be smeared out. When 100 single molecules are sampled, about 70% display the trajectories like Fig.5(a). The remaining show blinks occasionally before photobleaching, in part because of photo-induced electron transfer to impurity sites of the glass coverslip. It is difficult to observe clearly triplet blinking of the single molecule caused by intersystem crossing. Instead, an average intensity of 5 counts/20 ms appears. The triplet state lifetime if assumed to be 14.5 μs amounts to 0.003 count, which is too weak to be resolved temporally.

As shown in Fig.6A(a), when the single-molecule fluorescence intensity trajectory of the dye molecules on the bare coverslip is slotted within 1 s-window, the fluorescence decay lifetimes are measured to be 3.63 ns and 3.59 ns for the time period of 54~55s and 266~267s, respectively (Fig.6A(b)). Alternatively, the lifetime fluctuation trajectory binned in 0.5 s-window gives rise to an average lifetime of 3.44±0.48 ns (Fig.6A(c)), which is consistent with that averaged over 100 molecules. These facts indicate that the fluorescence intensity fluctuation for oxazine 1 on glass is dominated by the radiative relaxation process from the singlet state.
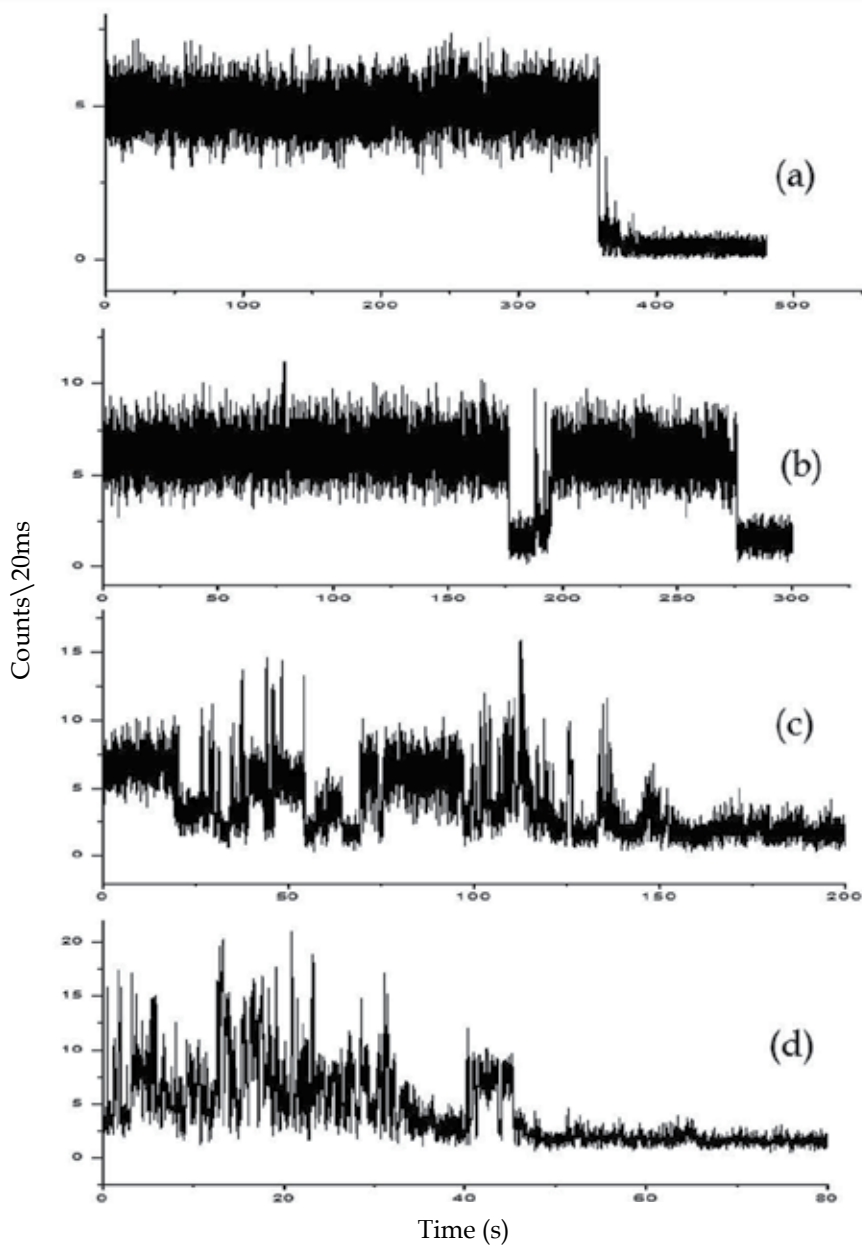
Fig. 5. Fluorescence trajectories recorded for single oxazine 1 molecules (a) on bare coverslip, and (b-d) on TiO₂ NPs-coated coverslip.
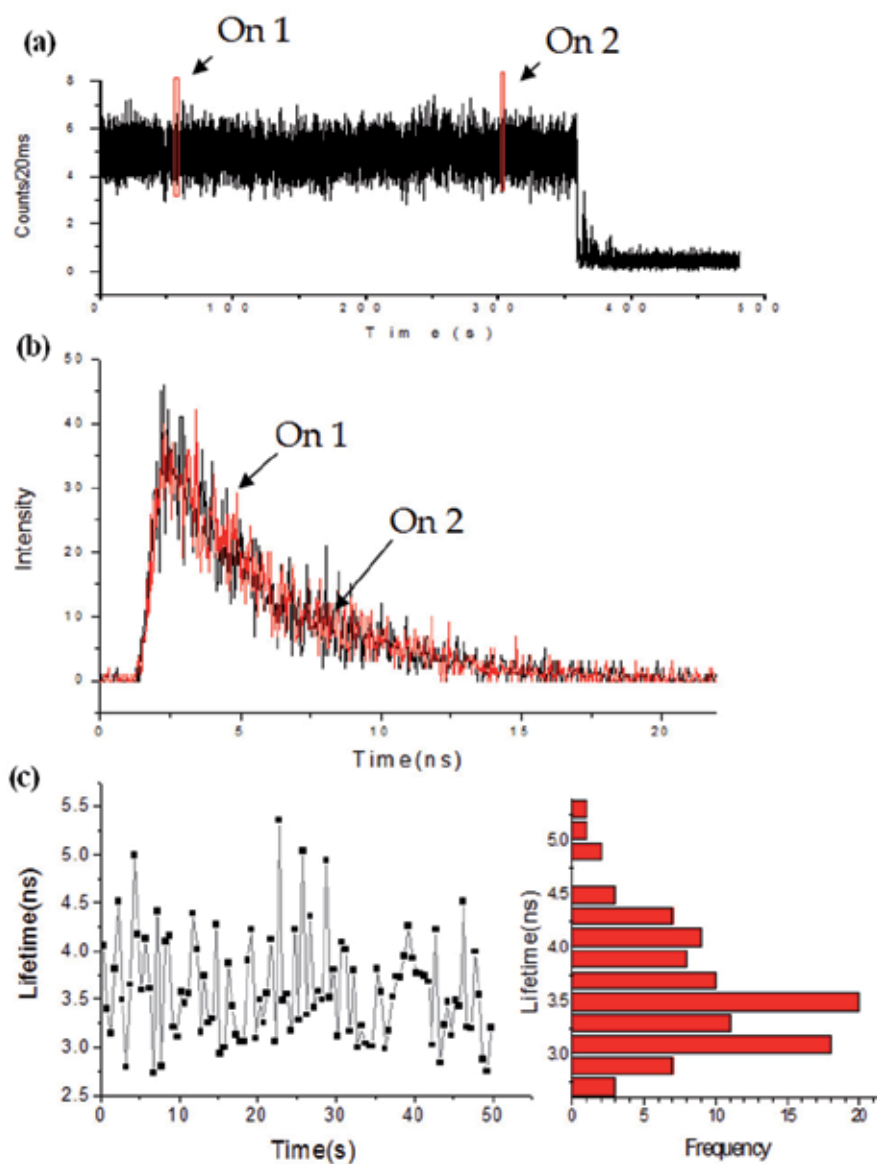
Fig. 6. (A) Single-molecule fluorescence decay profile of oxazine1 on bare glass. (a) The fluorescence intensity fluctuation slotted at 1 and 2 positions each within 1-s window. (b) Fluorescence decay profile for the 1 and 2 slots gives rise to the decay time of 3.63 ns and 3.59 ns, respectively. (c) The lifetime (binning window 0.5s) fluctuation trajectory (left), and the histogram for the lifetime trajectory from 0 to 50 s before photobleaching. The average lifetime is 3.44±0.48 ns.
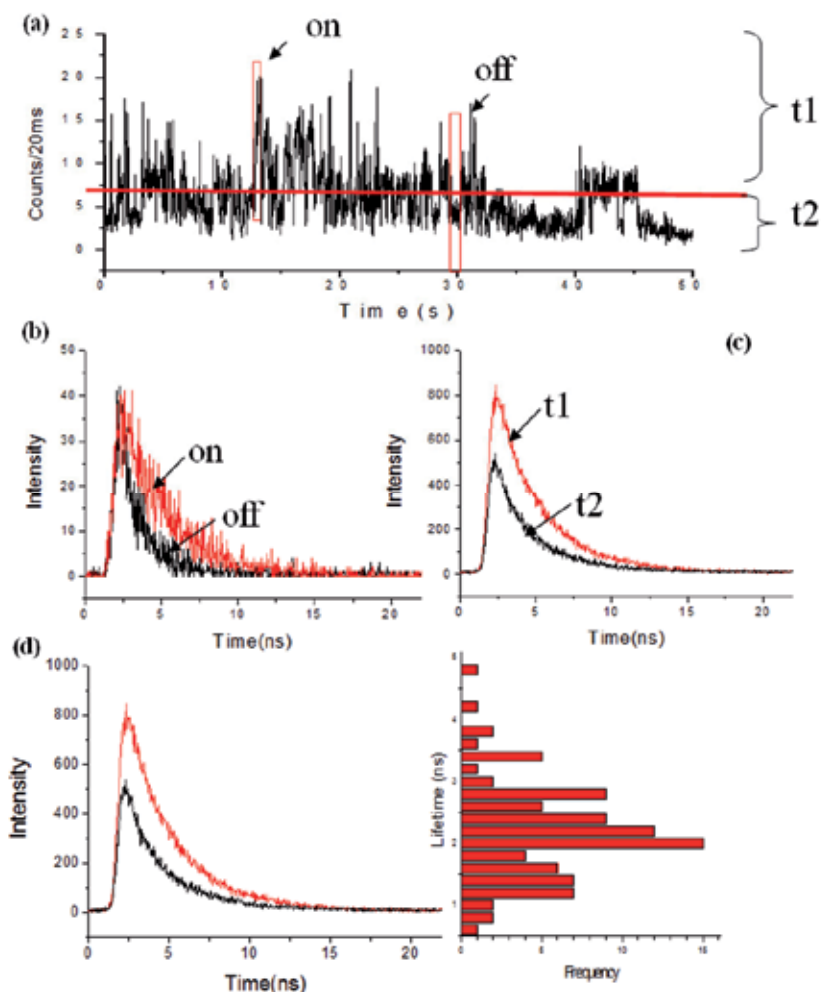
Fig. 6. (B) Single-molecule fluorescence decay profile of oxazine1 on TiO₂ NPs film. (a) The fluorescence intensity fluctuation slotted at one "on" position and the other "off" position. (b) Fluorescence decay profile for the "on" and "off" slots gives rise to the decay time of 2.93 and 1.26 ns, respectively. (c) Given a threshold set at 7 photocounts/20 ms, the emission trajectory is separated to higher level and lower level. Fluorescence decay profiles for high and low intensity have similar results as the "on" and "off" slots in (b). (d) The lifetime (binning window 0.5s) fluctuation in a range from 0.6 to 4.8 ns (left), and the histogram for the lifetime trajectory from 0 to 50 s before photobleaching.

On the other hand, Fig.5(b-d) show the fluorescence trajectories of individual dye molecules in the presence of TiO₂ NPs thin film ranging from several microseconds to seconds before photobleaching. These trajectories are classified into three types among 100 single dye molecules as sampled. About 20% of molecules yield the traces as in Fig.5(b), in which the interaction with TiO₂ NPs is weak such that the molecule fluoresces at most time. A 60% majority show the traces as in Fig.5(c), in which a stronger interaction is found and the "off" time becomes longer. The remaining 20% give the traces as in Fig.5(d), in which the

molecule stays longer at "off" time. The molecule in Fig.5(d) should have relatively active electron transfer such that the fluorescence process is suppressed.

Fig.5(d) is used as an example. The fluorescence intensity trajectory is slotted within a 500-photon binned window to select one "on" intensity and the other "off" intensity (Fig.6B(a)). Analyzing the fluorescence decay yields a result of 2.93 and 1.26 ns for the "on" (12.85~13.33 s slot) and "off" (29.15~30.20 s slot) lifetime, respectively (Fig.6B(b)). Given a threshold at 7 counts/20 ms, the fluorescence intensity is divided to higher level and lower level. The lifetime analysis of these two levels yields the results similar to those obtained in the above time slots. The "on" state shows a twofold longer lifetime than the "off" state (Fig.6B(c)). This fact indicates that the fluorescence intensity fluctuation is caused by both factors of reactivity, i.e., the fraction of IFET occurrence frequency (Wang et al., 2009), and rate of electron transfer. The fluorescence lifetimes analyzed within 0.5s-window fluctuate in a range from 0.6 to 4.8 ns, which is more widely scattered than those acquired on the bare glass (Fig.6B(d)). This phenomenon suggests existence of additional depopulation pathway which is ascribed to ET between oxazine1 and TiO_2. However, other contribution such as rotational and translational motion of the dye on the TiO_2 film can not be rule out without information of polarization dependence of the fluorescence.

3.3 Autocorrelation analysis

An autocorrelation function based on the fluorescence intensity trajectory is further analyzed. When the dye molecules are adsorbed on the TiO_2 NPs surface, a four-level energy scheme is formed including singlet ground, singlet excited, and triplet states of the dye molecule as well as conduction band of TiO_2. Upon irradiation with a laser source, the excited population may undergo various deactivation processes. Because the selected dye molecule has a relatively short triplet excursion, the fluorescence in the absence of TiO_2 film becomes a constant average intensity with near shot-noise-limited fluctuation, as displayed in Fig.5(a) (Haase et al., 2004; Holman & Adams, 2004). As a result, the system can be simplified to a three-level energy scheme.

As the ET process occurs, the fluorescence appears to blink on and off. The transition between the on and off states may be considered as feeding between the singlet and the conduction subspaces (Yip et al., 1998),

$$\text{On} \xrightleftharpoons[k_{on}]{k_{off}} \text{off} \,. \tag{1}$$
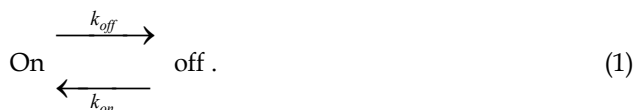
The on-state rate constant is equivalent to the backward ET rate constant from the conduction band, i.e.,

$$k_{on} = k_{bet\,,} \tag{2}$$

while the off-state rate constant corresponds to the excitation rate constant k_{ex} multiplied by the fraction of population relaxing to the conduction band, as expressed by

$$k_{off} = \frac{k_{et}}{k_{21} + k_{et}} k_{ex} \,. \tag{3}$$

Here, k_{21} is the relaxation rate constant from the excited singlet to ground state containing the radiative and non-radiative processes and k_{et} is the forward ET rate constant. k_{ex} is related to the excitation intensity I_o (units of erg/cm² s) by

$$k_{ex} = \sigma I_o / h\upsilon, \tag{4}$$

where σ is the absorption cross section and $h\upsilon$ is the photon energy. The average residence times in the on and off states correspond to the reciprocal of the feeding rate in the off and on states, respectively. That is, $\tau_{on} = 1/k_{off}$ and $\tau_{off} = 1/k_{on}$.

The rate constants in on-off transition may then be quantified by analyzing autocorrelation of fluorescence intensities (Holman & Adams, 2004). The normalized autocorrelation function is defined as the rate of detecting pairs of photons separated in time by an interval τ, relative to the rate when the photons are uncorrelated. It is expressed as

$$G(\tau) = \frac{< I(t)I(t+\tau) >}{< I(t) >^2} , \tag{5}$$

where I(t) is the fluorescence intensity at time t and τ is the correlation time. The bracketed term denotes the intensity average over time. When the population relaxation is dominated by the singlet decay, the autocorrelation function may be simplified to an exponential decay, i.e.,

$$G(\tau) = A + Be^{-k\tau}, \tag{6}$$

where A is an offset constant, B a pre-exponential factor, and k the decay rate constant. They are determined by fitting to the autocorrelation data. These parameters are explicitly related to the phenomena of on/off blinking due to the ET processes by,

$$k = k_{on} + k_{off} \tag{7}$$

and

$$\frac{B}{A} = \frac{k_{on}k_{off}(I_{on} - I_{off})^2}{(k_{on}I_{on} + k_{off}I_{off})^2} . \tag{8}$$

If $I_{on} >> I_{off}$, then the above equation is simplified to

$$\frac{B}{A} = \frac{k_{off}}{k_{on}} . \tag{9}$$

The forward and backward ET rate constants in the dye molecule-TiO₂ NPs system can thus be evaluated.

According to eq.5, Fig.7(a) shows that the autocorrelation result based on the fluorescence trajectory of the dye on glass (Fig.5(a)) appears to be noisy ranging from zero to microseconds. The dynamic information of the triplet state can not be resolved, consistent with the analyzed results of fluorescence decay times. When the dye molecule is on TiO₂, the fluorescence trajectory given in Fig.5(c) is adopted as an example for evaluation of the individual "on" and "off" times. As shown in Fig.7(b), the resulting autocorrelation function

is fitted to a single exponential decay, yielding a B/A value of 0.2 and k of 2.17 s^{-1}. Given the excitation rate constant k_{ex} of 2.2x10^4 s^{-1} (38.5 W/cm^2 was used) and the fluorescence decay k_{21} of 3.28x10^8 s^{-1} determined in the excited state lifetime measurement, k_{et} and k_{bet} are evaluated to be 5.4x10^3 and 1.8 s^{-1}, respectively, according to eqs.2,3,7, and 9. The IFET and back ET rate constants with the "on" and "off" times for the examples in Fig.5(b-d) are listed in Table 1. For comparison, the corresponding lifetime measurements are also listed. A more efficient IFET is apparently accompanied by a shorter excited state lifetime.

(a)   (b)
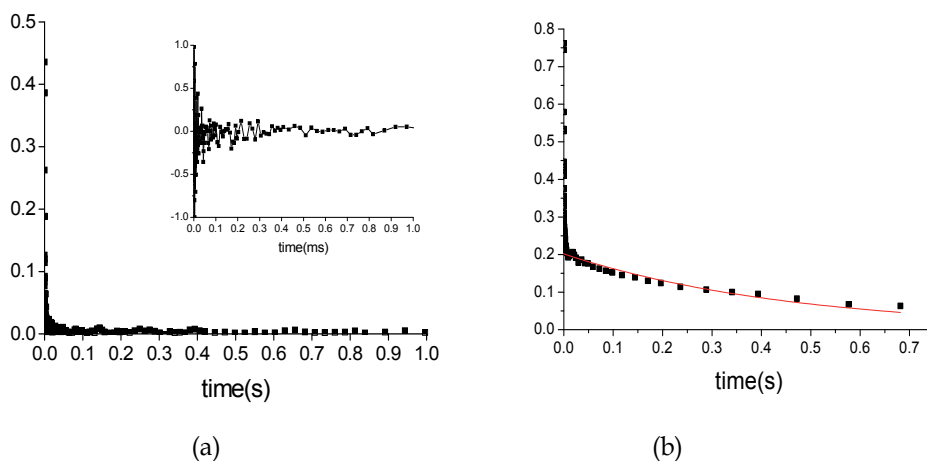
Fig. 7. Autocorrelation function of fluorescence intensity from single oxazine 1 molecules (a) on bare coverslip, (b) on TiO$_2$ NPs-coated coverslip. The inset in (a) is the enlarged trace within the range of 1 ms.

	Lifetime/ns	τ_{on} (s)	τ_{off} (s)	k_{et} (s^{-1})	k_{bet} (s^{-1})
A	4.0	-	-	-	-
B	3.4	86.02	1.43	1.6 x10^2	0.7
C	3.1	2.75	0.55	5.4 x10^3	1.8
D	2.9	0.49	0.08	3.2 x10^4	12.0

Table 1. The excited state lifetimes and kinetic data for the single-molecule traces shown in Fig. 6.

As with the above examples, 100 single dye molecules are successively analyzed. The resulting IFET and back ET rate constants are displayed in the form of histogram (Fig.8(a) and (b)), yielding a range of 10^2-10^4 and 0.1-10 s^{-1}, respectively. The distributions are fitted with an individual single-exponential function to yield an average value of (1.0±0.1)x10^4 and 4.7±0.9 s^{-1}, which are the upper limit of the IFET and back ET rate constants among these 100 single molecules analyzed, if the unknown contributions of rotational and translational motion are considered. The obtained average rate of electron transfer is much slower than the fluorescence relaxation. That is why no statistical difference of the fluorescence lifetimes of the dye is found between TiO$_2$ and bare coverslip. The ET rate constant distribution could be affected by different orientation and distance between dye molecule and TiO$_2$ NPs. The weak coupling between electron donor and acceptor may be caused by physisorption

between the dye molecule and the TiO$_2$ NPs or a disfavored energy system for the dye electron jumping into the conduction band of the semiconductor. The resulting ET quantum yield as small as 3.1x10^{-5} is difficult to be detected in the ensemble system. Nevertheless, such slow electron transfer events are detectable at a single molecule level as demonstrated in this work.

(a)   (b)
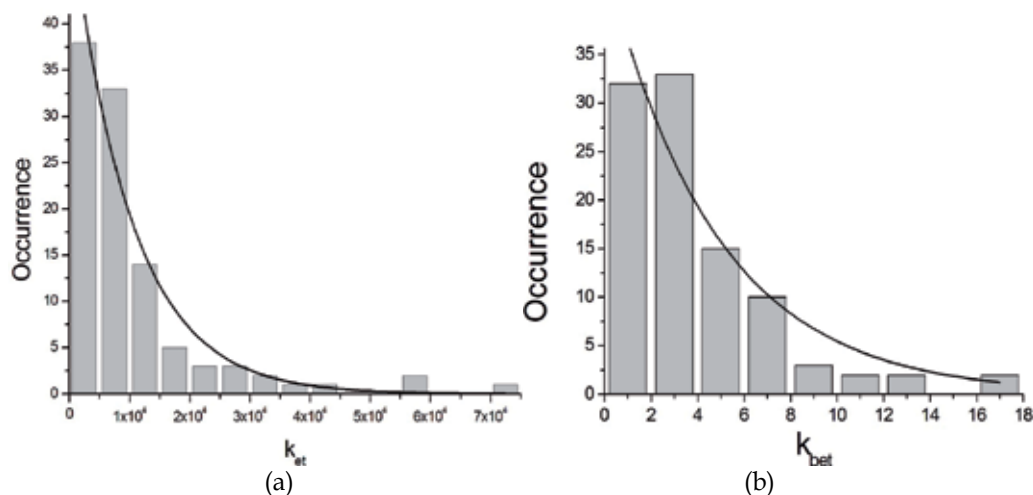
Fig. 8. The histograms of (a) k$_{et}$ and (b) k$_{bet}$ determined among 100 dye molecules. The average values of (1.0±0.1)x10^4 and 4.74 s^{-1} are evaluated by a fit to single-exponential function.
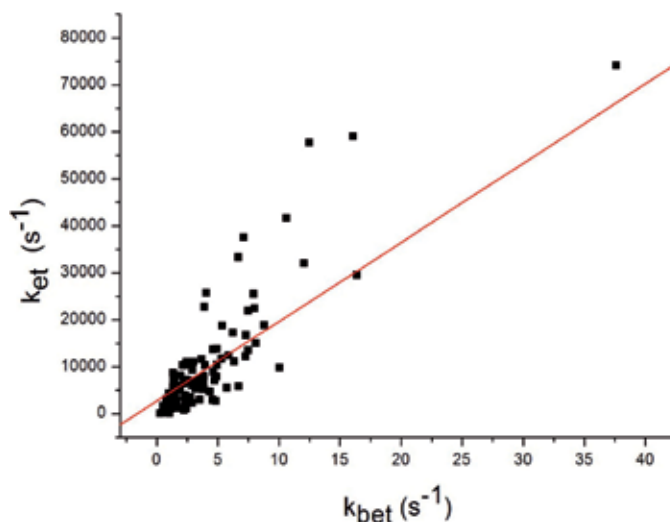
Fig. 9. A linear correlation between photo-induced electron transfer and back electron transfer rate constant.

The process of photo-induced ET involves charge ejection from the oxazine 1 LUMO (~2.38 ev) into a large energetically accessible density of states within the conduction band of

TiO$_2$(~4.4 ev), while the back ET involves thermal relaxation of electrons from the conduction band or from a local trap (energetically discrete states) back to the singly occupied molecular orbital (SOMO) of the oxazine 1 cation.[37] It is interesting to find a linear correlation with a slope of 1.7x10^3 between IFET and back ET rate constants, as shown in Fig.9. Despite difference of the mechanisms, k$_{bet}$ increases almost in proportion to k$_{et}$. Such a strong correlation between forward and backward ET rate constants suggests that for different dye molecules the ET energetics remains the same but the electronic coupling between the excited state of the dye molecules and the conduction band of the solid film varies widely (Cotlet et al., 2004). Both forward and backward ET processes are affected similarly by geometric distance and orientation between electron donor and acceptor.

4. Fluorescence intermittency and electron transfer by quantum dots

4.1 Fluorescence intermittency and lifetime determination

Three different sizes of CdSe/ZnS core/shell QDs were used. Each size was estimated by averaging over 100 individual QDs images obtained by transmission emission spectroscopy (TEM), yielding the diameters of 3.6±0.6, 4.6±0.7, and 6.4±0.8 nm, which are denoted as A, B, and C size, respectively, for convenience. Each kind was then characterized by UV/Vis and fluorescence spectrophotometers to obtain its corresponding absorption and emission spectra. As shown in Fig.10(a) and (b), a smaller size of QDs leads to emission spectrum shifted to shorter wavelength. From their first exciton absorption bands at 500, 544, and 601 nm, the diameter for the CdSe core size was estimated to be 2.4, 2.9, and 4.6 nm (Yu et al., 2003), respectively, sharing about 25-37% of the whole volume. In addition, given the band gaps determined from the absorption bands and the highest occupied molecular orbital (HOMO) potential of -6.12 ~ -6.15 Ev (Tvrdy et al., 2011), the LUMO potentials of QDs may be estimated to be -4.06, -3.86, and -3.67 eV along the order of decreased size.
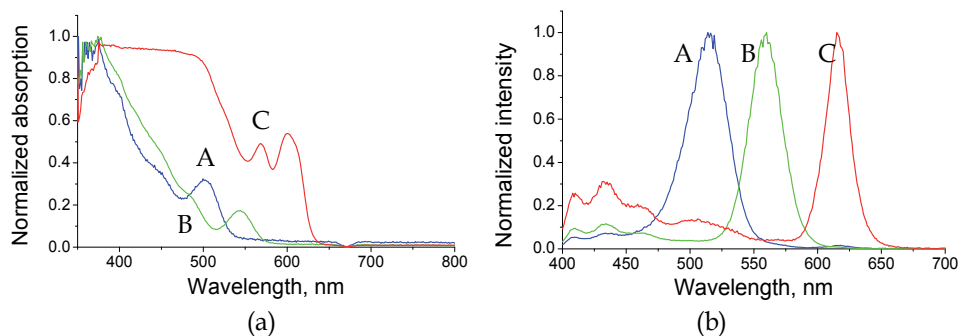
Fig. 10. (a) Absorption and (b) fluorescence spectra of QDs in toluene solution with excitation wavelength fixed at 375 nm. The maximum intensities for both spectra have been normalized. A, B, and C species have the diameters of 3.6, 4.6, and 6.4 nm, respectively.

Each size of QDs was individually spin-coated on bare and TiO$_2$ coverslip. Fig.11 shows an example for the photoluminescence (PL) images within a 24 μm x 24 μm area of the smallest QDs on the glass and TiO$_2$ NPs thin film, as excited at 375 nm. The surface densities of fluorescent QDs on TiO$_2$ were less than those on glass. Their difference becomes more significant with the decreased size of QDs.

(a)   (b)
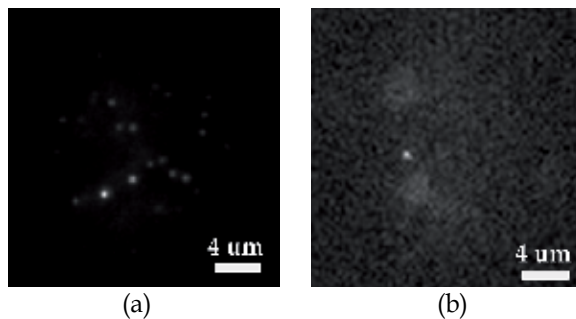
Fig. 11. The CCD images of QDs with the diameter of 3.6 nm at 4.5×10^{-11} g/L which was spin-coated on (a) glass and (b) TiO₂ film.
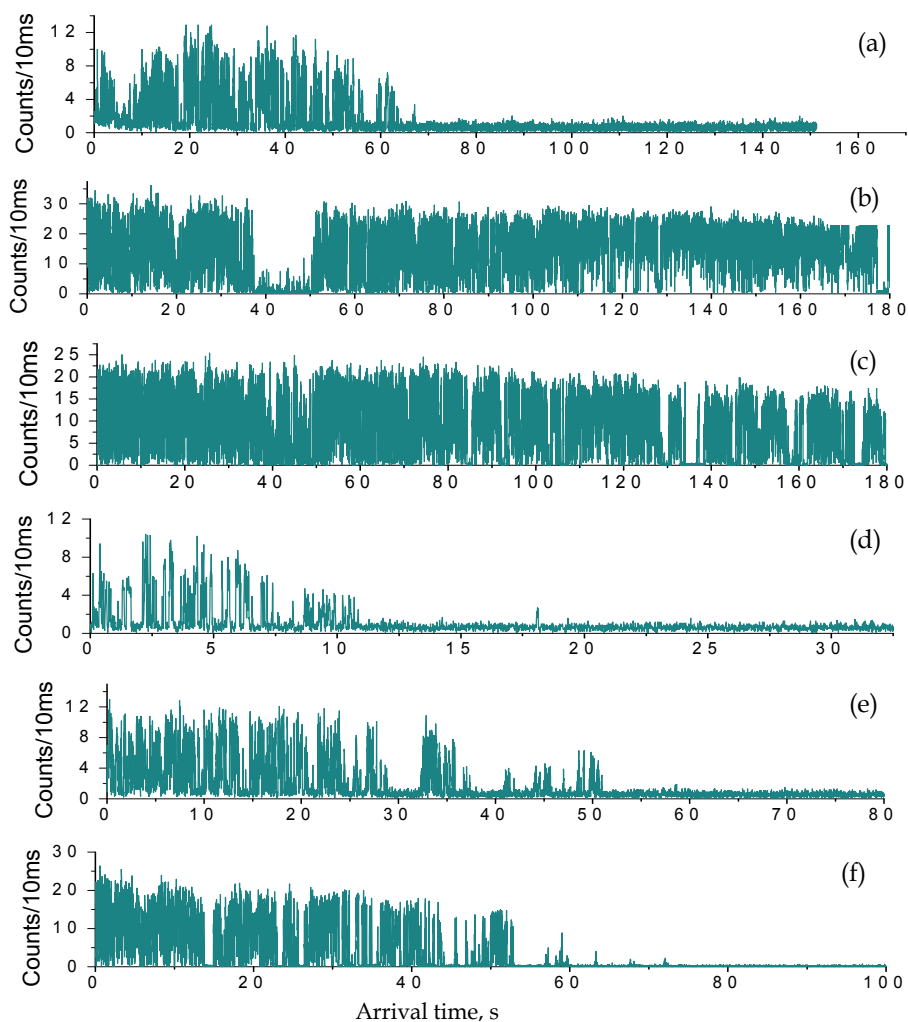
Fig. 12. The fluorescence trajectories of single QD with A, B, and C size adsorbed on (a,b,c) glass and (d,e,f) TiO₂ film. The order of increased size is followed from a to c and from d to f.

As a single bright spot was focused, the trajectory of fluorescence intensity was acquired until photobleaching. The trajectory is represented as a number of emitting photons collected within a binning time as a function of the arrival time after the experiment starts. Fig.12 shows the examples for the three sizes of QDs on glass and TiO_2. The bleaching time of the trajectory appears shorter with the decreased size of QDs, showing an average value of 9.4, 19.6, and 34.1 s on TiO_2, which are much shorter than those on glass. In addition, QDs on either surface are characterized by intermittent fluorescence. As compared to those on glass coverslip, QDs on TiO_2 endure shorter on-time (or fluorescing time) events but longer off-time events. This trend is followed along a descending order of size.

The photons collected within a binning time can be plotted as a function of delay time which is defined as the photon arrival time with respect to the excitation pulse. The fluorescence decay for a single QD is thus obtained. Each acquired curve can be applied to a mono-exponential tail-fit, thereby yielding the corresponding lifetime for a selected arrival time slot. For increasing single-to-noise ratio, the on-state lifetime is averaged over the entire trajectory. However, the off-state lifetime cannot be precisely estimated, because its signal is close to the background noise with limited number of photons collected. Fig.13 shows a single QD lifetime determined for different sizes on glass and TiO_2. A smaller size of QDs results in a shorter on-state lifetime on either surface. Given the same size of QDs, the lifetime on TiO_2 appears to be shorter than that on glass. Their lifetime difference increases with the decreased size. As reported previously (Jin et al., 2010a), the trajectories of fluorescence intermittency and lifetime fluctuation are closely correlated. A similar trend is also found in this work.
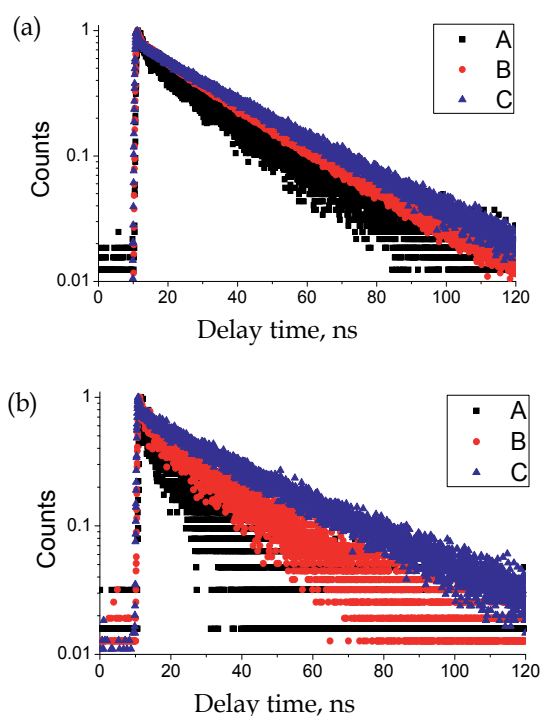
Fig. 13. The fluorescence decay, detected by the TCSPC method, for three types of QDs spin-coated on (a) glass and (b) TiO_2 film. The number of counts is normalized to unity.

Fig.14 shows the lifetime histograms among 20-90 single QDs for the three sizes on glass and TiO$_2$. The corresponding average lifetimes are listed in Table 2. As shown in Fig.14, the smallest QDs on TiO$_2$ have much less on-events than those on glass. For clear lifetime comparison of QDs adsorption between glass and TiO$_2$, each on-event distribution is normalized to unity. The Gaussian-like lifetime histogram has a wide distribution for both glass and TiO$_2$. The lifetime difference for the A type of QDs can be readily differentiated between these two surfaces. As listed in Table 2, their average lifetimes correspond to 19.3 and 14.9 s. In contrast, a tiny lifetime difference between 25.7 and 25.5 s for the C type of QDs is buried in a large uncertainty.
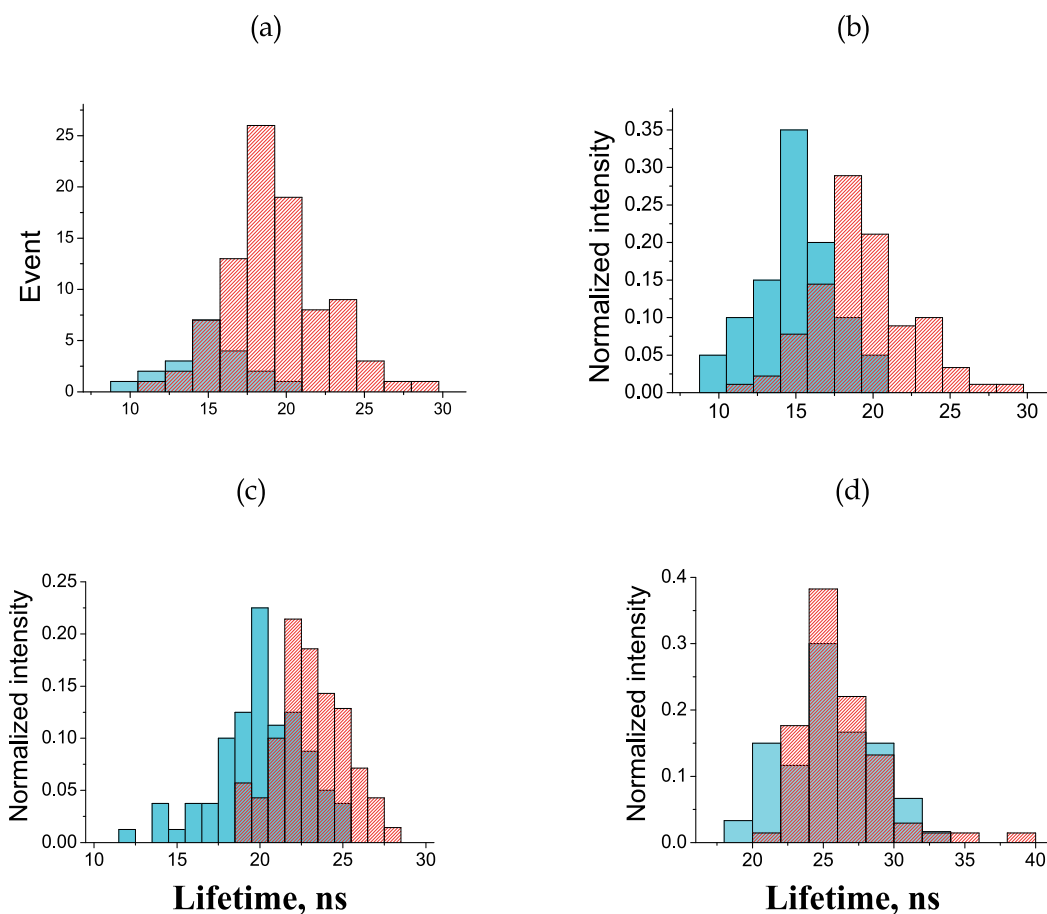
Fig. 14. The distributions of fluorescence lifetime for (a,b) QDs A and (c,d) QDs B and C. (a) comparison of on-event occurrence for QDs A between glass and TiO$_2$. (b,c,d) each area of distribution is normalized to unity. The lifetime distributions of QDs on glass and TiO$_2$ are displayed in red and blue, respectively.

Quantum Dots	Size	Substrate	Amount	Lifetime, ns
A	$3.6 \pm 0.6\ nm$	Glass	90	19.3 ± 3.2
		TiO_2 film	20	14.9 ± 2.4
B	$4.6 \pm 0.7\ nm$	Glass	70	22.6 ± 2.1
		TiO_2 film	80	19.6 ± 2.7
C	$6.4 \pm 0.8\ nm$	Glass	68	25.7 ± 2.2
		TiO_2 film	60	25.5 ± 3.2

Table 2. Size-dependence of on-state lifetimes of quantum dots (QDs) on glass and TiO_2 film which are averaged over a quantity of single QDs.

4.2 Interfacial electron transfer

Upon excitation at 375 nm, a QD electron is pumped to the conduction band forming an exciton. The energy gained from recombination of electron and hole will be released radiatively or nonradiatively. However, the excited electron may be feasibly scattered out of its state in the conduction band and be prolonged for recombination. The excited electron probably undergoes resonant tunneling to a trapped state in the shell or nonresonant transition to another trapped state in or outside the QD (Hartmann et al., 2011; Krauss & Peterson, 2010; Jin et al., 2010b; Kuno et al., 2001). The off state of QD is formed, as the charged hole remains. When a second electron-hole pair is generated by a second light pulse or other processes, the energy released from recombination of electron and hole may transfer to the charged hole or trapped electron to cause Auger relaxation. Its relaxation rate is expected to be faster than the PL rate. Given a QD with the core radius of 2 nm, the Auger relaxation rate was estimated to be 100 times larger than the radiative decay rate (Hartmann et al., 2011). The fluorescence fluctuation is obviously affected by the Auger relaxation process that is expected to be <100 ps.

As shown in Fig.12, the on-time events of fluorescence intermittency for QDs on TiO_2 are more significantly suppressed than those on glass. The shortened on events are expected to be caused by the ET from QDs to the TiO_2 film. The analogous phenomena have been reported elsewhere (Hamada et al., 2010; Jin & Lian, 2009). The more rapid the ET is, the shorter the on-state lifetime becomes. The fluorescence lifetime may be estimated by (Jin & Lian, 2009; Kamat, 2008; Robel et al., 2006)

$$\tau = \frac{1}{k_r + k_A + k_{ET}} \qquad (10)$$

where k_r, k_A, and k_{ET} denote intrinsic decay rate of radiation, Auger relaxation rate, and ET rate. When QD is adsorbed on glass, the ET rate is assumed to be zero. The fluorescence fluctuation is dominated by the Auger relaxation. Thus, given the lifetime measurements on both glass and TiO_2 and assumption of the same Auger relaxation rate, the ET rate constant from QDs to TiO_2 can be estimated by the reciprocal of the lifetime difference. The resulting ET rate constants are $(1.5\pm1.4)\times10^7$ and $(6.8\pm8.1)\times10^6$ s^{-1} for the QDs A and B, respectively. A large uncertainty is caused by a wide lifetime distribution. The ET rates depend on the QDs size. The smaller QDs have a twice larger rate constant. However, the ET rate constant for

the largest size cannot be determined precisely, due to a slight lifetime difference but with large uncertainty. The ET quantum yield Φ may then be estimated as 22.6 and 13.3% for the A and B sizes, respectively, according to the following equation,

$$\Phi = \frac{k_{ET}}{k_r + k_A + k_{ET}} = k_{ET}\tau \tag{11}$$

The larger QDs result in a smaller quantum yield.

In an analogous experiment, Jin and Lian obtained an average ET rate of 3.2×10^7 s^{-1} from CdSe/ZnS core/shell QDs with capped carboxylic acid functional groups (Jin & Lian, 2009). Their size was estimated to have core diameter of 4.0 nm based on the first exciton peak at 585 nm. While considering the size dependence, our result is about ten times smaller. It might be caused by the additional carboxylic acid functional groups which can speed up the ET rates.

Different from the method of lifetime measurement, autocorrelation of fluorescence intensities can be alternatively used to quantify the kinetic rate constants in on-off transition, as described in Section III.C (Chen et al., 2010). By analyzing exponential autocorrelation of fluorescence trajectory under a three-level energy system, the forward and back ET rate constants of single oxazine 1 dye/TiO₂ film were reported above (Chen et al., 2010). As the uncertainty was considered, there was no statistical difference of the lifetime measurements for the single dye adsorption between glass and TiO₂. Such a small ET activity can be indeed quantified by analyzing the autocorrelation function. Unfortunately, this method cannot be applied effectively to the QDs case, because the kinetic system involves multiple manifolds that make analysis more complicated.

The non-exponential fluorescence fluctuation was reported in single semiconductor QDs early in 1996 (Nirmal et al., 1996). To explain such fluorescence intermittency, Efros *et al.* (Efros & Rosen, 1997) proposed an Auger ionization model, in which an electron (hole) ejection outside the core QDs is caused by nonradiative relaxation of a bi-exciton. However, Auger ionization process would lead to a single exponential probability distribution of 'on' events, which is against the power-law distributions and the large dynamic range of time scale observed experimentally (Kuno et al., 2000, 2001). Nesbitt and coworkers later investigated the detailed kinetics of fluorescence intermittency in colloidal CdSe QDs and evaluated several related models at the single molecule level. They concluded that the kinetics of electron or hole tunneling to trap sites with environmental fluctuation should be more appropriate to account for the blinking phenomena (Kuno et al., 2001). Frantsuzov and Marcus (Frantsuzov & Marcus, 2005) further suggested a model regarding fluctuation of nonradiative recombination rate to account for the unanswered problem for a continuous distribution of relaxation times.

To compare the blinking activity for a single QD, probability density P(t) is defined to indicate the blinking frequency between the on and off states. The probability density P(t) of a QD at on or off states for duration time t may be calculated by(Kuno et al., 2001; Cui et al., 2008; Jin & Lian, 2009; Jin et al., 2010a)

$$P_i(t) = \frac{N_i(t)}{N_{i,tot}\Delta t_{av}} \tag{12}$$

where i denotes on or off states, N(t) the number of on or off events of duration time t, N_{tot} the total number of on or off events, and Δt_{av} the average time between the nearest neighbor events. The threshold fluorescence intensity to separate the on and off states is set at 3σ. σ is

the standard deviation of the background fluorescence intensity which can be fitted with a Gaussian function.

Fig.15 shows a fluorescence trajectory with a threshold intensity and its corresponding blinking frequency for a single QD (3.6 nm) on glass and TiO$_2$. The subsequent on-state and off-state probability densities accumulated over 10 single QDs for each species are displayed in Fig.16 and Fig.17, which show similar behavior as a single QD but with more data points to reduce uncertainty. The P(t) distribution at the on state for each size under either surface condition essentially follows power law statistics at the short time but deviates downward at the long time tails. The bending tail phenomena are similar to those reported (Tang & Marcus, 2005a, b; Cui et al., 2008; Peterson & Nesbitt, 2009; Jin et al., 2010a). These on-state distributions can be fitted by a truncated power law, as expressed by (Tang & Marcus, 2005a, b; Cui et al., 2008; Peterson & Nesbitt, 2009; Jin et al., 2010a)

$$P_i(t) = Dt^{-m_i} \exp(-\Gamma_i t) \qquad (13)$$

where D is the amplitude associated with electronic coupling and other factors, m$_i$ the power law exponent for the on state, and Γ the saturation rate. The truncated power law was developed by Marcus and coworkers for interpreting the blinking behavior of QD which was attributed to the ET process between a QD and its localized surface states (Tang & Marcus, 2005a, b). According to eq.13, the fitting parameters of m$_{on}$ and Γ_{on} are listed in Table 3. The QDs on TiO$_2$ apparently result in larger Γ values than those on glass. In addition, the trend is found that a smaller QD may have a larger Γ. As for m$_{on}$, the obtained range is from 0.70 to 0.93, smaller than 1.5 as expected by Marcus model (Tang & Marcus, 2005a, b; Cui et al., 2008). Such deviation for m$_{on}$ was also found by the Lian group in a similar experiment (Jin et al., 2010a; Jin et al., 2010b). Note that the power law distribution with a bending tail in the long time region is solely found at the on states. In contrast, the off-state probability density may be fit to a simple power law statistics expressed by,

$$P_i(t) = Et^{-m_i} \qquad (14)$$

where E is a scaling coefficient and m$_i$ is the power law exponent for the off state. A similar trend for both on- and off-state distributions was analogously found elsewhere (Cui et al., 2008; Peterson & Nesbitt, 2009). As listed in Table 3, the obtained m$_{off}$ yields a smaller value when QDs are adsorbed on TiO$_2$. They lie in the range of 1.6-2.1, which are consistent with those reported (Kuno et al., 2001; Cui et al., 2008; Peterson & Nesbitt, 2009).

The on-time saturation rate should be associated with the ET rate. According to Marcus model (Tang & Marcus, 2005a, b), the free energy curves of light emitting state and dark state can be represented by an individual parabola along a reaction coordinate, which is assumed to have the same curvature. Then, Γ_{on} can be related to the free energy change ΔG_{ET} based on the ET process. That is (Tang & Marcus, 2005a, b; Cui et al., 2008),

$$\Gamma_{on} = \frac{(\lambda + \Delta G_{ET})^2}{8 t_{diff} \lambda k_B T} \qquad (15)$$

where λ is the system reorganization energy, t$_{diff}$ the diffusion correlation time constant for motion on a parabolic energy surface, k$_B$ the Boltzmann constant, and T the absolute temperature. Given the conduction band of -4.41 eV for TiO$_2$ NPs and the LUMO potentials of QDs, -3.67 and -3.86 eV for the A and B sizes, respectively, the corresponding -ΔG_{ET} may
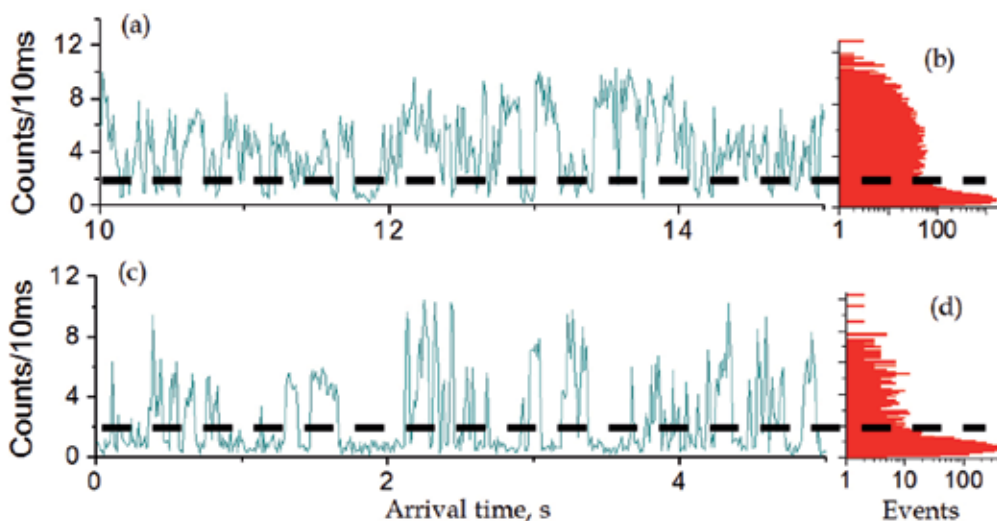
Fig. 15. The fluorescence trajectory and corresponding on/off blinking frequency distribution of single QD A on (a,b) glass and (c,d) TiO₂ film. The black lines denote the intensity thresholds to separate the on and off state which are set at a level 3σ above the background noise. σ is the standard deviation of background noise.
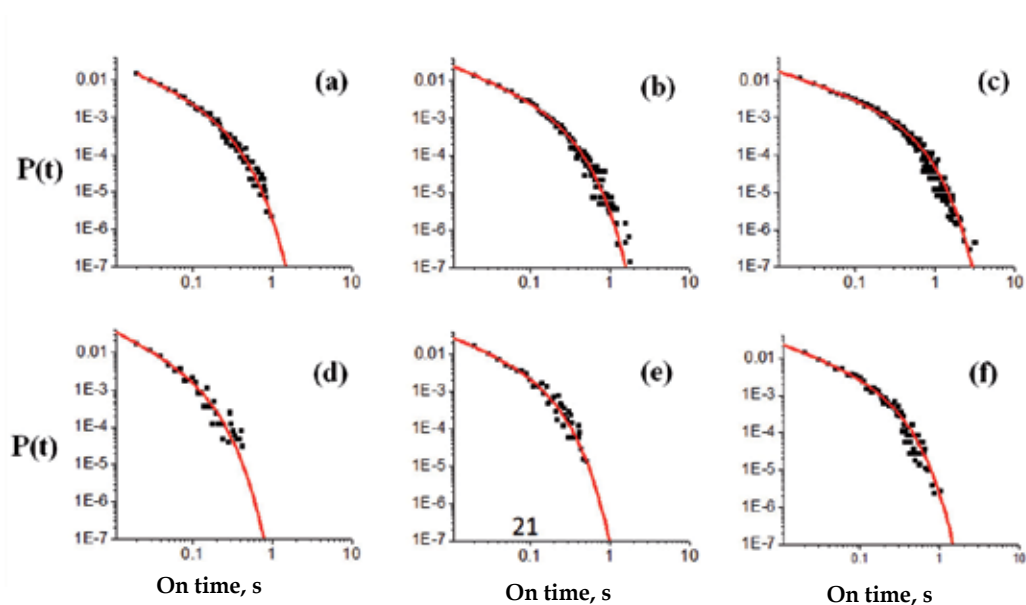
Fig. 16. The on-state probability density of 10 single QDs with A, B, and C size on (a,b,c) glass and (d,e,f) TiO₂ film. The order of increased size is followed from a to c and from d to f. The spots denote experimental data and lines denote simulation by truncated power law distribution.
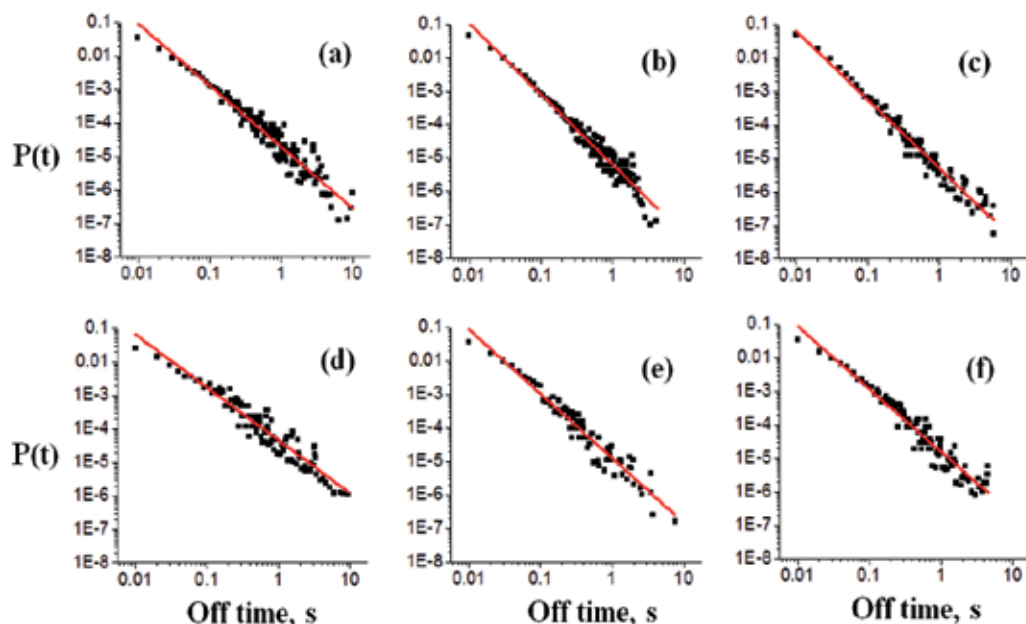
Fig. 17. The off-state probability density of 10 single QDs with A, B, and C size on (a,b,c) glass and (d,e,f) TiO$_2$ film. The order of increased size is followed from a to c and from d to f. The spots denote experimental data and lines denote simulation by power law distribution.

Quantum dots	Substrate	m_{on}	m_{off}	$1/\Gamma_{on}$, ms
A	Glass	0.910 ± 0.005	1.85 ± 0.04	181.9 ± 3.1
	TiO$_2$ film	0.925 ± 0.006	1.58 ± 0.05	75.7 ± 1.3
B	Glass	0.803 ± 0.002	2.07 ± 0.05	188.6 ± 1.9
	TiO$_2$ film	0.785 ± 0.005	1.91 ± 0.06	108.4 ± 2.1
C	Glass	0.699 ± 0.002	2.04 ± 0.04	355.4 ± 4.3
	TiO$_2$ film	0.760 ± 0.004	1.87 ± 0.05	172.0 ± 3.1

Table 3. The fitting parameters of 10 single quantum dots at the on state in terms of truncated power law distribution and off state in terms of power law distribution.
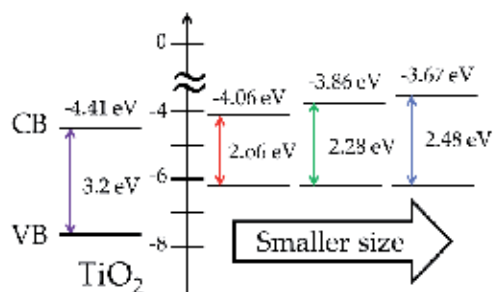
Fig. 18. The energy diagram of TiO$_2$ and QDs with A, B, and C size.

be estimated to be 0.74 and 0.55 eV. The related energy diagram is displayed in Fig.18. For a smaller QD, the larger conduction band gap between QD and TiO₂ can induce a larger driving force to facilitate the ET process (Tvrdy et al., 2011). If λ and t_{diff} remain constant, substituting ΔG_{ET} and Γ_{on} into eq.15 for different size of QDs yields λ to be 636 and -416 meV, of which only the positive value is meaningful.

4.3 Model prediction of electron transfer

In the following is the Marcus model which has been successfully used to describe the ET kinetics for the systems of organic dyes coupled to various metal oxides (She et al., 2005; Tvrdy et al., 2011),

$$k_{ET} = \frac{4\pi^2}{h} \int_{-\infty}^{\infty} \rho(E) |H(E)|^2 \frac{1}{\sqrt{4\pi\lambda k_B T}} \exp(\frac{(1+\Delta G+E)^2}{4\lambda k_B T})dE \tag{16}$$

where H(E) is the overlap matrix element, $\rho(E)$ the density of electron accepting states, h the Planck's constant, and ΔG the free energy change of the system, which is composed of three factors. They are (1) the energy change between initial and final electronic states, equivalent to ΔG_{ET} mentioned in eq.15, (2) the free energy difference between nonneutral donating and accepting species in the ET process, and (3) the free energy of coulombic interaction for electron and hole separation (Tvrdy et al., 2011). Among them, only ΔG_{ET} can be measured experimentally. Because of similarity as the work by the Kamat group (Tvrdy et al., 2011), the contributions of the second and third factors are referred to their work. That is,

$$\Delta G = \Delta G_{ET} + \frac{e^2}{2R_{QD}} + 2.2\frac{e^2}{\varepsilon_{QD}R_{QD}} - \frac{e^2}{4(R_{QD}+s)}\frac{\varepsilon_{TiO_2}-1}{\varepsilon_{TiO_2}+1} \tag{17}$$

where e is the elementary charge, R_{QD} and ε_{QD} are the radius and dielectric permittivity of the QD, ε_{TiO2} is the dielectric permittivity of TiO₂, and s is the separation distance between QD and TiO₂. Given s, assumed to be the same as reported (Tvrdy et al., 2011), and the data of ΔG_{ET}, R_{QD}, ε_{QD} and ε_{TiO2}, ΔG is estimated to be -0.22, -0.143, and -0.054 eV for the A, B, and C sizes of QDs, respectively. As compared to ΔG_{ET}, the driving force for moving electron from QD to TiO₂ is suppressed after taking into account the additional contributions in eq.17.

In a perfect semiconductor crystal, the density of unoccupied states $\rho(E)$ is given as (She et al., 2005; Tvrdy et al., 2011)

$$\rho(E) = V_o \frac{(2m_e^*)^{3/2}}{2\pi\hbar^3}\sqrt{E} \tag{18}$$

where V_o is the effective volume, known to be 34.9 Å³ for TiO₂ crystal, m_e^* the electron effective mass, equivalent to 10 m_0 (m_0 is the mass of free electron) (She et al., 2005), and $\hbar$ is h/2π. For a TiO₂ nanoparticle with high surface to volume ratio, the density of states in eq.18 requires modification by considering the defect states which are treated as a Gaussian distribution of width Δ. (She et al., 2005; Tvrdy et al., 2011) The modified density of states $\rho_D(E)$ is then expressed as

$$\rho_D(E) = \int_0^{\infty} \rho(E') \frac{1}{\Delta\sqrt{2\pi}} \exp(\frac{(E-E')^2}{2\Delta^2})dE' \tag{19}$$

Given a constant H(E), substituting eqs.18 and 19 into eq.16 yields an explicit relation between k_{ET} and ΔG.

As reported (She et al., 2005), when the dye/metal oxide system was surrounded by a buffer layer, the reorganization energy λ increases to 100-500 meV, because additional energy is required for system rearrangement. In this work, CdSe/ZnS QDs are spin-coated on the TiO$_2$ NPs film which is exposed to the air. The requirement of reorganization energy should be small. Therefore, the λ value of 636 meV in the estimate (eq.15) seems to be unreasonable. When ΔG_{ET} is replaced by ΔG, λ is obtained to be 178 and -248 meV based on eq.15. The selected λ of 178 meV is more acceptable than the one obtained with ΔG_{ET} substituted. The width Δ of defect states for the TiO$_2$ NPs is insensitive in the k_{ET} calculation by eq.16. We adopt the same Δ of 50 meV as reported (Tvrdy et al., 2011). Given H(E) assumed to have 0.83 cm^{-1} and the data of ΔG, λ, and Δ, k_{ET} is optimized to be 1.42x10^7, 6.80x10^6, and 1.86x10^6 s^{-1} for three increased sizes of QDs. The first two results agree very well with the experimental findings. The ET rate constant for the C type of QDs cannot be precisely determined experimentally, but may be estimated with the aid of model prediction.

For our system, CdSe/ZnS core/shell QDs are spin-coated on the TiO$_2$ thin film. Unlike this preparation procedure, Kamat and coworkers immersed TiO$_2$ film in the colloidal CdSe QDs solution to make a tight contact between donor and acceptor and then measured the electron transfer rates under a vacuum condition (Tvrdy et al., 2011). Therefore, the overlap matrix elements, H(E), which is associated with the coupling between electron donating and accepting states, must make difference. In our work, the core CdSe QD and TiO$_2$ have a loose contact and thus a smaller H(E) of 0.83 cm^{-1} is obtained. In contrast, a much larger value of 57 cm^{-1} was adopted by the Kamat group (Tvrdy et al., 2011). That is why the ET rates obtained herein are relatively slower by a factor of 10^4.

5. Concluding remarks

This chapter describes IFET induced by a single dye molecule or a single QD which is individually adsorbed on the TiO$_2$ NPs film. The fluorescence lifetimes determined among different single oxazine 1 dye molecules are widely spread, because of micro-environmental influence. These lifetimes are in proximity to those measured on the bare coverslip, indicative of the IFET inefficiency for those dye molecules sampled in this work. However, some molecules may proceed via very efficient IFET process, but fail to be detected. Due to a shorter triplet excursion, oxazine 1-TiO$_2$ NPs system is treated effectively as a three-level system upon irradiation. The exponential autocorrelation function may thus be analyzed to quantify the related kinetic rate constants in an on-off transition. The IFET processes are found to be inhomogeneous, with a rate constant varying from molecule to molecule. The reactivity and rate of ET fluctuation of the same single molecule are the main source to result in fluorescence intensity fluctuation. These phenomena, which are obscured in the ensemble-averaged system, are attributed to micro-environment variation for each single molecule. The oxazine 1 dye is apparently unsuitable for application to the DSSC design, because of its lower ET rates. Nevertheless, the single molecule spectroscopy provides a potential tool looking into the microscopic ET behaviors for different dye molecules to facilitate the working efficiency for the cell design. In addition, it is capable of detecting a low ET quantum yield, which is difficult to measure with conventional ensemble-averaged methods.

The second part of this chapter describes the ET from QDs to TiO₂ NPs film. The ET kinetics depends on the size of CdSe/ZnS QDs. The trajectories of fluorescence intermittency of three different sizes of QDs on glass and TiO₂ are acquired and the subsequent fluorescence lifetimes are determined. While assuming the lack of electron transfer for the QD on glass, the ET rates from QD to TiO₂ may be inferred in terms of reciprocal of the lifetime difference. The following trend is found: the smaller the size of QDs, the larger the ET rate constants. The distribution of off-time probability density versus the arrival time is fit to a simple power law statistics. However, the plot of on-time probability density can be characterized by a truncated power law distribution. Marcus's electron transfer model is employed to fit the bending tail behavior and to further calculate the ET rate constants, which show consistency with our experimental findings.

6. Acknowledgments

7. References

Ambrose, W. P., P. M. Goodwin, J. C. Martin & R. A. Keller (1994) Single-molecule Detection and Photochemistry on a Surface Using Near-field Optical excitation. *Physical Review Letters,* 72, 1, (Jan 1994), 160-163, 0031-9007

Arden, W. & P. Fromherz (1980) Photosensitization of Semiconductor Electrode by Cyanine Dye in Lipid Bilayer. *Journal of the Electrochemical Society,* 127, 2, 1980), 370-378, 0013-4651

Baker, D. R. & P. V. Kamat (2009) Photosensitization of TiO2 Nanostructures with CdS Quantum Dots: Particulate versus Tubular Support Architectures. *Advanced Functional Materials,* 19, 5, (Mar 2009), 805-811, 1616-301X

Bell, T. D. M., C. Pagba, M. Myahkostupov, J. Hofkens & P. Piotrowiak (2006) Inhomogeneity of electron injection rates in dye-sensitized TiO2: Comparison of the mesoporous film and single nanoparticle Behavior. *Journal of Physical Chemistry B,* 110, 50, (Dec 2006), 25314-25321, 1520-6106

Biesmans, G., M. Vanderauweraer, C. Cathry & F. C. Deschryver (1992) On the Photosensitized Injection of Electrons into SNO₂ from Cyanine Dyes Incorporated in Langmuir-Blodgett-Films. *Chemical Physics,* 160, 1, (Feb 1992), 97-121, 0301-0104

Biesmans, G., M. Vanderauweraer, C. Cathry, D. Meerschaut, F. C. Deschryver, W. Storck & F. Willig (1991) Photosensitized Electron Injection from Xanthene Dyes Incorporated in Langmuir-Blodgett-Films into SNO₂ Electrodes. *Journal of Physical Chemistry,* 95, 9, (May 1991), 3771-3779, 0022-3654

Bisquert, J., A. Zaban & P. Salvador (2002) Analysis of the mechanisms of electron recombination in nanoporous TiO2 dye-sensitized solar cells. Nonequilibrium steady-state statistics and interfacial electron transfer via surface states. *Journal of Physical Chemistry B,* 106, 34, (Aug 2002), 8774-8782, 1520-6106

Cahen, D., G. Hodes, M. Gratzel, J. F. Guillemoles & I. Riess (2000) Nature of photovoltaic action in dye-sensitized solar cells. *Journal of Physical Chemistry B,* 104, 9, (Mar 2000), 2053-2059, 1089-5647

Chen, Y. J., H. Y. Tzeng, H. F. Fan, M. S. Chen, J. S. Huang & K. C. Lin (2010) Photoinduced Electron Transfer of Oxazine 1/TiO2 Nanoparticles at Single Molecule Level by Using Confocal Fluorescence Microscopy. *Langmuir,* 26, 11, (Jun 2010), 9050-9060, 0743-7463

Choi, J. J., Y. F. Lim, M. B. Santiago-Berrios, M. Oh, B. R. Hyun, L. F. Sung, A. C. Bartnik, A. Goedhart, G. G. Malliaras, H. D. Abruna, F. W. Wise & T. Hanrath (2009) PbSe Nanocrystal Excitonic Solar Cells. *Nano Letters,* 9, 11, (Nov 2009), 3749-3755, 1530-6984

Cotlet, M., S. Masuo, G. B. Luo, J. Hofkens, M. Van der Auweraer, J. Verhoeven, K. Mullen, X. L. S. Xie & F. De Schryver (2004) Probing conformational dynamics in single donor-acceptor synthetic molecules by means of photoinduced reversible electron transfer. *Proceedings of the National Academy of Sciences of the United States of America,* 101, 40, (Oct 2004), 14343-14348, 0027-8424

Cotlet, M., T. Vosch, S. Habuchi, T. Weil, K. Mullen, J. Hofkens & F. De Schryver (2005) Probing intramolecular Forster resonance energy transfer in a naphthaleneimide-peryleneimide-terrylenediimide-based dendrimer by ensemble and single-molecule fluorescence spectroscopy. *Journal of the American Chemical Society,* 127, 27, (Jul 2005), 9760-9768, 0002-7863

Cui, S. C., T. Tachikawa, M. Fujitsuka & T. Majima (2008) Interfacial Electron Transfer Dynamics in a Single CdTe Quantum Dot-Pyromellitimide Conjugate. *Journal of Physical Chemistry C,* 112, 49, (Dec 2008), 19625-19634, 1932-7447

Efros, A. L. & M. Rosen (1997) Random telegraph signal in the photoluminescence intensity of a single quantum dot. *Physical Review Letters,* 78, 6, (Feb 1997), 1110-1113, 0031-9007

Fan, S. Q., B. Fang, J. H. Kim, J. J. Kim, J. S. Yu & J. Ko (2010) Hierarchical nanostructured spherical carbon with hollow core/mesoporous shell as a highly efficient counter electrode in CdSe quantum-dot-sensitized solar cells. *Applied Physics Letters,* 96, 6, (Feb 2010), 0003-6951

Ferrere, S. & B. A. Gregg (2001) Large increases in photocurrents and solar conversion efficiencies by UV illumination of dye sensitized solar cells. *Journal of Physical Chemistry B,* 105, 32, (Aug 2001), 7602-7605, 1089-5647

Flors, C., I. Oesterling, T. Schnitzler, E. Fron, G. Schweitzer, M. Sliwa, A. Herrmann, M. van der Auweraer, F. C. de Schryver, K. Mullen & J. Hofkens (2007) Energy and electron transfer in ethynylene bridged perylene diimide multichromophores. *Journal of Physical Chemistry C,* 111, 12, (Mar 2007), 4861-4870, 1932-7447

Frantsuzov, P. A. & R. A. Marcus (2005) Explanation of quantum dot blinking without the long-lived trap hypothesis. *Physical Review B,* 72, 15, (Oct 2005), 1098-0121

Gaiduk, A., R. Kuhnemuth, S. Felekyan, M. Antonik, W. Becker, V. Kudryavtsev, C. Sandhagen & C. A. M. Seidel (2007) Fluorescence detection with high time resolution: From optical microscopy to simultaneous force and fluorescence

spectroscopy. *Microscopy Research and Technique,* 70, 5, (May 2007), 433-441, 1059-910X

Garcia-Parajo, M. F., G. M. J. Segers-Nolten, J. A. Veerman, J. Greve & N. F. van Hulst (2000) Real-time light-driven dynamics of the fluorescence emission in single green fluorescent protein molecules. *Proceedings of the National Academy of Sciences of the United States of America,* 97, 13, (Jun 2000), 7237-7242, 0027-8424

Gratzel, M. (2001) Photoelectrochemical cells. *Nature,* 414, 6861, (Nov 2001), 338-344, 0028-0836

Gratzel, M. (2003) Dye-sensitized solar cells. *Journal of Photochemistry and Photobiology C-Photochemistry Reviews,* 4, 2, (Oct 2003), 145-153, 1389-5567

Gratzel, M. (2005) Mesoscopic solar cells for electricity and hydrogen production from sunlight. *Chemistry Letters,* 34, 1, (Jan 2005), 8-13, 0366-7022

Haase, M., C. G. Hubner, E. Reuther, A. Herrmann, K. Mullen & T. Basche (2004) Exponential and power-law kinetics in single-molecule fluorescence intermittency. *Journal of Physical Chemistry B,* 108, 29, (Jul 2004), 10445-10450, 1520-6106

Hagfeldt, A. & M. Gratzel (2000) Molecular photovoltaics. *Accounts of Chemical Research,* 33, 5, (May 2000), 269-277, 0001-4842

Hamada, M., S. Nakanishi, T. Itoh, M. Ishikawa & V. Biju (2010) Blinking Suppression in CdSe/ZnS Single Quantum Dots by TiO2 Nanoparticles. *Acs Nano,* 4, 8, (Aug 2010), 4445-4454, 1936-0851

Hara, K., H. Horiuchi, R. Katoh, L. P. Singh, H. Sugihara, K. Sayama, S. Murata, M. Tachiya & H. Arakawa (2002) Effect of the ligand structure on the efficiency of electron injection from excited Ru-phenanthroline complexes to nanocrystalline TiO2 films. *Journal of Physical Chemistry B,* 106, 2, (Jan 2002), 374-379, 1520-6106

Hartmann, T., V. I. Yudson & P. Reineker (2011) Model for the off-time distribution in blinking quantum dots. *Journal of Luminescence,* 131, 3, 2011), 379-381, 0022-2313

Holman, M. W. & D. M. Adams (2004) Using single-molecule fluorescence spectroscopy to study electron transfer. *ChemPhysChem,* 5, 12, (Dec 2004), 1831-1836, 1439-4235

Jin, S. Y., J. C. Hsiang, H. M. Zhu, N. H. Song, R. M. Dickson & T. Q. Lian (2010a) Correlated single quantum dot blinking and interfacial electron transfer dynamics. *Chemical Science,* 1, 4, (Oct 2010a), 519-526, 2041-6520

Jin, S. Y. & T. Q. Lian (2009) Electron Transfer Dynamics from Single CdSe/ZnS Quantum Dots to TiO2 Nanoparticles. *Nano Letters,* 9, 6, (Jun 2009), 2448-2454, 1530-6984

Jin, S. Y., N. H. Song & T. Q. Lian (2010b) Suppressed Blinking Dynamics of Single QDs on ITO. *Acs Nano,* 4, 3, (Mar 2010b), 1545-1552, 1936-0851

Ju, T., R. L. Graham, G. M. Zhai, Y. W. Rodriguez, A. J. Breeze, L. L. Yang, G. B. Alers & S. A. Carter (2010) High efficiency mesoporous titanium oxide PbS quantum dot solar cells at low temperature. *Applied Physics Letters,* 97, 4, (Jul 2010), 0003-6951

Kamat, P. V. (2008) Quantum Dot Solar Cells. Semiconductor Nanocrystals as Light Harvesters. *Journal of Physical Chemistry C,* 112, 48, (Dec 2008), 18737-18753, 1932-7447

Kim, S. J., W. J. Kim, Y. Sahoo, A. N. Cartwright & P. N. Prasad (2008) Multiple exciton generation and electrical extraction from a PbSe quantum dot photoconductor. *Applied Physics Letters,* 92, 3, (Jan 2008), 0003-6951

Kohn, F., J. Hofkens, R. Gronheid, M. Van der Auweraer & F. C. De Schryver (2002) Parameters influencing the on- and off-times in the fluorescence intensity traces of single cyanine dye molecules. *Journal of Physical Chemistry A,* 106, 19, (May 2002), 4808-4814, 1089-5639

Krauss, T. D. & J. J. Peterson (2010) Bright Future for Fluorescence Blinking in Semiconductor Nanocrystals. *Journal of Physical Chemistry Letters,* 1, 9, (May 2010), 1377-1382, 1948-7185

Kulzer, F., S. Kummer, R. Matzke, C. Brauchle & T. Basche (1997) Single-molecule optical switching of terrylene in p-terphenyl. *Nature,* 387, 6634, (Jun 1997), 688-691, 0028-0836

Kuno, M., D. P. Fromm, H. F. Hamann, A. Gallagher & D. J. Nesbitt (2000) Nonexponential "blinking" kinetics of single CdSe quantum dots: A universal power law behavior. *Journal of Chemical Physics,* 112, 7, (Feb 2000), 3117-3120, 0021-9606

Kuno, M., D. P. Fromm, H. F. Hamann, A. Gallagher & D. J. Nesbitt (2001) "On"/"off" fluorescence intermittency of single semiconductor quantum dots. *Journal of Chemical Physics,* 115, 2, (Jul 2001), 1028-1040, 0021-9606

Lee, Y. L. & Y. S. Lo (2009) Highly Efficient Quantum-Dot-Sensitized Solar Cell Based on Co-Sensitization of CdS/CdSe. *Advanced Functional Materials,* 19, 4, (Feb 2009), 604-609, 1616-301X

Luther, J. M., M. C. Beard, Q. Song, M. Law, R. J. Ellingson & A. J. Nozik (2007) Multiple exciton generation in films of electronically coupled PbSe quantum dots. *Nano Letters,* 7, 6, (Jun 2007), 1779-1784, 1530-6984

Luther, J. M., M. Law, M. C. Beard, Q. Song, M. O. Reese, R. J. Ellingson & A. J. Nozik (2008) Schottky Solar Cells Based on Colloidal Nanocrystal Films. *Nano Letters,* 8, 10, (Oct 2008), 3488-3492, 1530-6984

Michalet, X., S. Weiss & M. Jager (2006) Single-molecule fluorescence studies of protein folding and conformational dynamics. *Chemical Reviews,* 106, 5, (May 2006), 1785-1813, 0009-2665

Moerner, W. E. & D. P. Fromm (2003) Methods of single-molecule fluorescence spectroscopy and microscopy. *Review of Scientific Instruments,* 74, 8, (Aug 2003), 3597-3619, 0034-6748

Nirmal, M., B. O. Dabbousi, M. G. Bawendi, J. J. Macklin, J. K. Trautman, T. D. Harris & L. E. Brus (1996) Fluorescence intermittency in single cadmium selenide nanocrystals. *Nature,* 383, 6603, (Oct 1996), 802-804, 0028-0836

Oregan, B. & M. Gratzel (1991) A Low-cost, High-efficiency Solar-cell Based on Dye-sensitized Colloidal TiO$_2$ Films. *Nature,* 353, 6346, (Oct 1991), 737-740, 0028-0836

Peterson, J. J. & D. J. Nesbitt (2009) Modified Power Law Behavior in Quantum Dot Blinking: A Novel Role for Biexcitons and Auger Ionization. *Nano Letters,* 9, 1, (Jan 2009), 338-345, 1530-6984

Plass, R., S. Pelet, J. Krueger, M. Gratzel & U. Bach (2002) Quantum dot sensitization of organic-inorganic hybrid solar cells. *Journal of Physical Chemistry B,* 106, 31, (Aug 2002), 7578-7580, 1520-6106

Ramakrishna, G., D. A. Jose, D. K. Kumar, A. Das, D. K. Palit & H. N. Ghosh (2005) Strongly coupled ruthenium-polypyridyl complexes for efficient electron injection in dye-

sensitized semiconductor nanoparticles. *Journal of Physical Chemistry B,* 109, 32, (Aug 2005), 15445-15453, 1520-6106

Robel, I., V. Subramanian, M. Kuno & P. V. Kamat (2006) Quantum dot solar cells. Harvesting light energy with CdSe nanocrystals molecularly linked to mesoscopic TiO2 films. *Journal of the American Chemical Society,* 128, 7, (Feb 2006), 2385-2393, 0002-7863

Sambur, J. B., T. Novet & B. A. Parkinson (2010) Multiple Exciton Collection in a Sensitized Photovoltaic System. *Science,* 330, 6000, (Oct 2010), 63-66, 0036-8075

Sens, R. & K. H. Drexhage (1981) Fluorescence Quantum Yield of Oxazine and Carbazine Laser-dyes. *Journal of Luminescence,* 24-5, NOV, 1981), 709-712, 0022-2313

She, C. X., N. A. Anderson, J. C. Guo, F. Liu, W. H. Goh, D. T. Chen, D. L. Mohler, Z. Q. Tian, J. T. Hupp & T. Q. Lian (2005) pH-dependent electron transfer from re-bipyridyl complexes to metal oxide nanocrystalline thin films. *Journal of Physical Chemistry B,* 109, 41, (Oct 2005), 19345-19355, 1520-6106

Tang, J. & R. A. Marcus (2005a) Diffusion-controlled electron transfer processes and power-law statistics of fluorescence intermittency of nanoparticles. *Physical Review Letters,* 95, 10, (Sep 2005a), 0031-9007

Tang, J. & R. A. Marcus (2005b) Mechanisms of fluorescence blinking in semiconductor nanocrystal quantum dots. *Journal of Chemical Physics,* 123, 5, (Aug 2005b), 0021-9606

Tvrdy, K., P. A. Frantsuzov & P. V. Kamat (2011) Photoinduced electron transfer from semiconductor quantum dots to metal oxide nanoparticles. *Proceedings of the National Academy of Sciences of the United States of America,* 108, 1, (Jan 2011), 29-34, 0027-8424

VandenBout, D. A., W. T. Yip, D. H. Hu, D. K. Fu, T. M. Swager & P. F. Barbara (1997) Discrete intensity jumps and intramolecular electronic energy transfer in the spectroscopy of single conjugated polymer molecules. *Science,* 277, 5329, (Aug 1997), 1074-1077, 0036-8075

Veerman, J. A., M. F. Garcia-Parajo, L. Kuipers & N. F. van Hulst (1999) Time-varying triplet state lifetimes of single molecules. *Physical Review Letters,* 83, 11, (Sep 1999), 2155-2158, 0031-9007

Wang, Y. M., X. F. Wang, S. K. Ghosh & H. P. Lu (2009) Probing Single-Molecule Interfacial Electron Transfer Dynamics of Porphyrin on TiO2 Nanoparticles. *Journal of the American Chemical Society,* 131, 4, (Feb 2009), 1479-1487, 0002-7863

Wilkinson, F., G. P. Kelly, L. F. V. Ferreira, V. Freire & M. I. Ferreira (1991) Benzophenone Sensitization of Triplet Oxazine and of Delayed Fluorescence by Oxazine in Acetonitrile Solution. *Journal of the Chemical Society-Faraday Transactions,* 87, 4, (Feb 1991), 547-552, 0956-5000

Xie, X. S. & R. C. Dunn (1994) Probing Single-molecule Dynamics. *Science,* 265, 5170, (Jul 1994), 361-364, 0036-8075

Yip, W. T., D. H. Hu, J. Yu, D. A. Vanden Bout & P. F. Barbara (1998) Classifying the photophysical dynamics of single- and multiple-chromophoric molecules by single molecule spectroscopy. *Journal of Physical Chemistry A,* 102, 39, (Sep 1998), 7564-7575, 1089-5639

Yu, P. R., K. Zhu, A. G. Norman, S. Ferrere, A. J. Frank & A. J. Nozik (2006) Nanocrystalline TiO2 solar cells sensitized with InAs quantum dots. *Journal of Physical Chemistry B,* 110, 50, (Dec 2006), 25451-25454, 1520-6106

Yu, W. W., L. H. Qu, W. Z. Guo & X. G. Peng (2003) Experimental determination of the extinction coefficient of CdTe, CdSe, and CdS nanocrystals. *Chemistry of Materials,* 15, 14, (Jul 2003), 2854-2860, 0897-4756

Porphyrin Based Dye Sensitized Solar Cells

Matthew J. Griffith and Attila J. Mozer
ARC Centre of Excellence for Electromaterials Science and Intelligent Polymer Research Institute, University of Wollongong, Squires Way, Fairy Meadow, NSW, Australia

1. Introduction

Dye-sensitized solar cells (DSSCs) have emerged as an innovative solar energy conversion technology which provides a pathway for the development of cheap, renewable and environmentally acceptable energy production (Gledhill, Scott et al., 2005; O'Regan & Grätzel, 1991; Shaheen, Ginley et al., 2005). A typical DSSC consists of a sensitizing dye chemically anchored to a nanocrystalline wide band gap semiconductor, such as TiO_2, ZnO or SnO_2. The oxide structure is mesoporous in order to produce a high surface area for dye coverage, allowing the adsorbed monolayer to capture the majority of the incident solar flux within the dye band gap. The porous photoanode is immersed in an electrolyte which contains a redox mediator to transport positive charge to the counter electrode and maintain net electrical neutrality (Figure 1). Efficient charge separation is achieved through photoinduced electron injection from the excited state of the sensitizing dye into the conduction band of the metal oxide semiconductor. The resulting dye cations are subsequently reduced by the redox electrolyte, which also conducts the holes to the platinum-coated cathode. The solar to electric power conversion efficiencies of DSSCs depend on a delicate balance of the kinetics for injection, dye regeneration and recombination reactions (Haque, Palomares et al., 2005), with the best devices, currently based on ruthenium polypyridyl sensitizers and an iodide/triiodide redox mediator, exhibiting certified power conversion efficiencies of over 11% (Chiba, Islam et al., 2006).
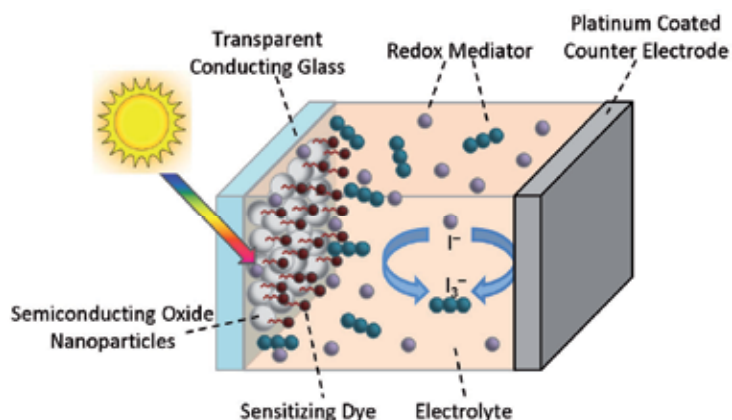
Fig. 1. Schematic illustration of a typical dye-sensitized solar cell (DSSC).

Porphyrin dyes have attracted significant interest as alternative sensitizers in DSSCs due to advantages with moderate material costs, ease of synthesis, large extinction coefficients and high stabilities. However, these dyes present a unique challenge since they have been found to possess very different operational photophysics to the majority of other sensitizing agents. Accordingly, porphyrin sensitizers create the opportunity to study some of the most fundamental limiting factors of DSSCs. In this chapter we will provide a detailed overview of the distinctive properties of porphyrin molecules and their behaviour as sensitizers in DSSCs. We focus on the major limitations affecting the performance of porphyrin DSSCs, including light harvesting, electron injection and charge recombination affects. We will also examine several strategies that have been employed to circumvent these limitations.

1.1 Operational principles of DSSCs

Unlike traditional silicon-based photovoltaic devices, charge separation and recombination in DSSCs are exclusively interfacial reactions. Furthermore, the initial photoexcited species in organic molecules are very different from those of silicon. Since organic molecules have lower dielectric constants and weaker Van der Waals interactions between molecules than their silicon counterparts, photoexitation of organic dyes produces a tightly bound neutral Frenkel exciton. This is in contrast to the loosely bound Werner excitons produced when silicon is photoexcited, which can essentially be considered free charges. Accordingly, DSSCs require an additional charge separation step to generate free charges. The viability of DSSCs for efficient photovoltaic energy conversion therefore relies almost entirely on achieving a delicate kinetic balance between the desired electron injection and dye cation regeneration reactions and the undesirable recombination reactions with either the dye cations or the acceptor species in electrolyte. The free energy driving forces for these various reactions are therefore crucial in determining the operational efficiency of DSSCs. These driving forces are often indicated by potential energy diagrams such as Figure 2, although such descriptions neglect entropy affects and thus do not strictly represent free energy.
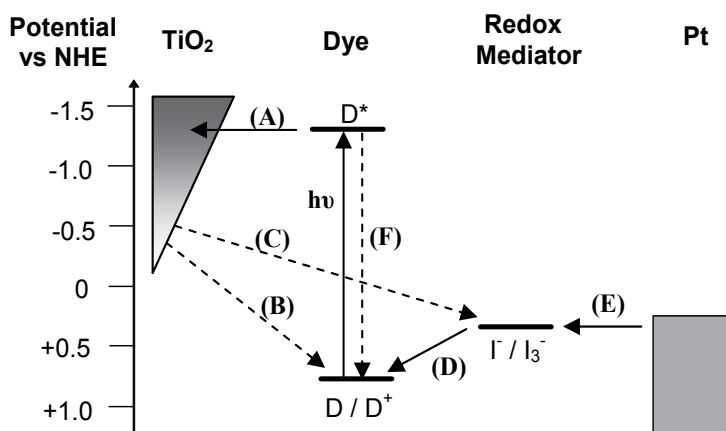
Fig. 2. Schematic representation of the energy levels of a DSSC indicating competing photophysical pathways, including (A) electron injection, (B) electron recombination with dye cations and (C) with the acceptor species in the electrolyte, (D) regeneration of dye cations by I⁻, and (E) recycling of I₃⁻ at the counter electrode. Figure taken from (Wagner, Griffith et al., 2011) and reproduced by permission of The American Chemical Society.

Current generation in the DSSC is dependent on three independent processes; the absorption of light by the photosensitizer, the injection of electrons from the excited photosensitizer, and the charge transport through the semiconductor film. The incident photon-to-current conversion efficiency (IPCE), also referred to as the external quantum efficiency (EQE), which corresponds to the electron flux measured as photocurrent compared to the photon flux that strikes the cell, is simply a combination of the quantum yields for these three processes as expressed in Equation 1.

$$IPCE(\lambda) = LHE(\lambda) \varphi_{inj} \eta_{coll} \tag{1}$$

Here $LHE(\lambda)$ is the light harvesting efficiency for photons of wavelength λ, φ_{inj} is the quantum yield for electron injection and η_{coll} is the electron collection efficiency. The short circuit current density (J_{sc}) achieved by the device is simply the integrated overlap between the IPCE spectrum and the solar irradiance spectrum ($I_0(\lambda)$) over all wavelengths:

$$J_{sc} = \int q \, I_0(\lambda) \, IPCE(\lambda) \, d\lambda \tag{2}$$

The photovoltage generated by a DSSC is given by the difference in the Fermi energy, E_F, of electrons at the two contacts. Under electrochemical equilibrium in the dark, E_F must be equal for all components of the DSSC. Since the density of states in the semiconductor is not large enough to appreciably affect $E_{F,redox}$, the redox mediator Fermi level, the dark Fermi level is extremely close to $E_{F,redox}$. At open circuit and under illumination, the concentration of electrons in the TiO_2 film increases to a steady state value, n_{light}, determined by the balance of electron injection and recombination. The photovoltage, V_{photo} which corresponds to the increase in the electron Fermi level, is therefore determined by the ratio of the free electron concentration in the TiO_2 under illumination and in the dark:

$$V_{photo} = \frac{1}{q} \left(E_F - E_{F,\mathrm{Re}\,dox} \right) = \frac{K_B T}{q} \ln \frac{n_{light}}{n_{dark}} \tag{3}$$

The overall power conversion efficiency of a DSSC, η_{global}, is then determined from the intensity of the incident light (I_0), the short circuit current density (J_{sc}), the open-circuit photovoltage (V_{oc}), and the fill factor of the cell (FF) (which is simply the ratio of the maximum power obtained from a device to the theoretical maximum $J_{sc}V_{oc}$):

$$\eta_{global} = \frac{J_{sc} V_{oc} FF}{I_0} \tag{4}$$

The maximum value of η_{global} which can be obtained from a single junction solar cell is established as 32% (Shockley & Quiesser, 1961), which accounts for photon absorption, thermalization, and thermodynamic losses encountered in converting the electrochemical energy of electrons into free energy to perform work. However, given the additional charge separation step required in a DSSC, a realistic efficiency limit is likely to fall well below this Shockley-Quiesser barrier due to restrictions on the allowable optical band gap (in order to maintain sufficient driving force for injection into TiO_2) and the significant loss of potential through the driving force required for regeneration of dye cations by the redox mediator.

If the semiconductor is chosen to be TiO_2, which to date is the only material to produce efficiencies over 10%, then the absorption onset limit at which the injection yield can still remain close to unity is currently observed to be around 900 nm for a ruthenium triscyanto terpyridyl complex ("black dye") (Nazeeruddin, Pechy et al., 2001). Beyond this limit a larger proportion of the solar flux can be harvested, but the reduction in the lowest unoccupied molecular orbital (LUMO) energy of the dye lowers the free energy driving force for electron injection, causing a subsequent reduction in the injection yield. Assuming a 10% loss of incident photons due to reflection from the top glass surface of the anode, an idealized IPCE spectrum with an absorption onset of 900 nm can be created by presuming a rise to maximum IPCE over ~50 nm and light harvesting, injection and collection efficiencies of unity for all wavelengths between 400 nm and 850 nm (a situation which can already be achieved with sensitizers where the absorption onset is 750 nm and which has almost been achieved with the black dye itself). The maximum possible photocurrent can then be calculated by integrating the overlap of this IPCE spectrum with the AM 1.5 solar irradiance spectrum (Figure 3a), and yields a value of 30 mAcm^{-2}.

(a)   (b)
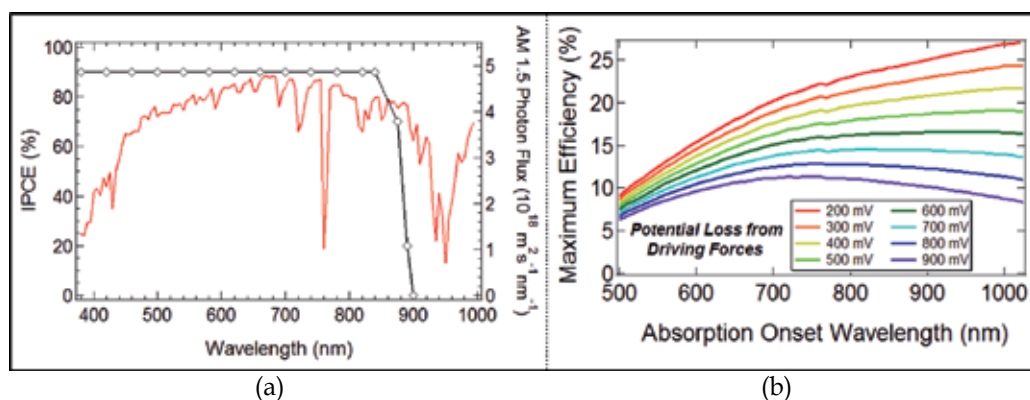
Fig. 3. (a) An idealized DSSC IPCE spectrum for a device with an absorption onset of 900 nm. The AM 1.5 solar irradiance spectrum (100 mWcm^{-2}) is also shown (red). (b) The maximum DSSC efficiency obtained from various absorption onsets with several possible potential energy losses from electron injection and dye regeneration driving forces.

To compute the maximum photovoltage, the free energy driving forces necessary to drive both electron injection and dye cation regeneration with yields of close to unity must be known. The sum of these driving forces is then removed from the optical band gap of the dye to calculate the maximum obtainable V_{oc}. There is a general lack of understanding regarding the minimum required driving forces, although previous studies indicate that the driving force required to achieve quantitative electron injection is ~200 mV (Hara, Sato et al., 2003; Katoh, Furube et al., 2002). The driving force required for dye regeneration will depend on the redox mediator, and is unusually high (~500 mV) for the commonly employed I^-/I_3^- system as this is a two electron process (Boschloo & Hagfeldt, 2009). If we assume that the regeneration driving force can be reduced to approximately 350 mV with an alternative redox mediator which involves only a single electron transfer, then the loss of potential from injection and regeneration driving force requirements would be 550 mV. Including the photon absorption, thermalization and energy conversion losses inside these driving force potentials, a 550 mV loss of potential would yield a maximum V_{oc} of 0.83 V.

Calculating the fill factor of a DSSC remains an ambiguous task. Bisquert et al. reported that the Shockley diode equation can be employed to calculate the fill factor as a function of the photovoltage. However, this approach requires knowledge of the diode ideality factor, which is still an unclear value for DSSCs (Bisquert & Mora-Sero, 2010). Since this is a matter of debate in the field, for the current calculations we have assumed a value of 0.70, which is either achieved or surpassed in many of the current benchmark devices. From equation (4), it is then possible to compute the maximum theoretical efficiency for such a DSSC. Since there will inevitably be debate about the acceptable assumptions for the maximum absorption onset and minimum driving forces for injection and regeneration, we have also computed the theoretical efficiency for several alternative values using a fill factor of 0.70 (Figure 3b). These values range from 14.5% (absorption onset 800 nm, loss of potential 700 mV) to 21.3% (absorption onset 950 nm, loss of potential 400 mV). Using realistic assumptions for absorption onset (900 nm) and loss of potential (550 mV), we calculate the maximum practical efficiency for a DSSC to be 17.6%. Considering the highest reported certified efficiency for a DSSC is 11.1%, there are clearly many limitations which still affect these devices and must be removed in order to approach this practical efficiency limit.

1.2 Porphyrin sensitizers in DSSCs

Emulation of the extraordinary chlorophyll-based photosynthetic light harvesting apparatus has inspired researchers to investigate synthetically prepared porphyrin dyes as sensitizers for dye-sensitized light harvesting applications (Kay & Grätzel, 1993), and they remain one of the most frequently studied dyes (Campbell, Burrell et al., 2004; Campbell, Jolley et al., 2007; Imahori, 2010). They are attractive for such purposes as their synthesis is relatively straightforward and their optical and electronic properties can be tuned via chemical modification of the porphyrin core (Dos Santos, Morandeira et al., 2010), the number of porphyrin units (Mozer, Griffith et al., 2009), and the linker between the core and the inorganic oxide (Lo, Hsu et al., 2010). It was originally assumed that porphyrin dyes would function identically to other analogous chromophores inside a DSSC, however, extensive studies of porphyrin dyes have shown that they are distinctive, and possess very different photophysics to the majority of other sensitizers (Bessho, Zakeeruddin et al., 2010; Campbell, Jolley et al., 2007; Imahori, Umeyama et al., 2009). The structure of some of these key porphyrin sensitizers are shown in Figure 4. Consequently, porphyrin dyes offer a unique opportunity to understand some fundamental limitations of DSSCs and trial innovative strategies which manipulate their unusual photophysical properties.

Porphyrin molecules typically display several strong visible light absorption bands due to the π–π^* electron transitions of the macrocycle. Optical transitions from the two closely spaced highest occupied molecular orbitals (HOMO and HOMO + 1) to degenerate lowest unoccupied molecular orbitals (LUMOs) interact strongly to produce a high energy S_2 excited state with a large oscillator strength around 420 nm (Soret band), and a lower energy S_1 excited state with diminished oscillator strength between 500 nm and 650 nm (Q-band). Several Q-band absorptions are normally observed due to the vibronic transitions of the S_1 excited state, with the exact number depending on the symmetry of the porphyrin core (Gouterman, 1978). The position of these absorption bands can be tuned by structural modifications to the porphyrin molecule, and thus provide an extremely promising method of maximizing absorption of incident photon flux.

Porphyrin photoluminescence spectra display very small Stokes shifts and appear as two peaks due to transitions from different vibronic levels of the S_1 state back to the S_0 ground

state. Interestingly, metalloporphyrins, and in particular many zinc porphyrins, can display dual fluorescence, that is, emission from both the S_2 and S_1 excited states, due to the large energy gap between S_2 and S_1 excited states causing slow internal conversion. The relaxation dynamics of excited porphyrin complexes are well established. Singlet excited state lifetimes are normally ~1 ps from the S_2 state and ~2 ns from the S_1 state for metalloporphyrins and ~10ns from S_1 for free base (metal free) molecules. Electrochemically porphyrin molecules are quite stable, with metalloporphyrins generally displaying two reversible oxidations of the porphyrin ring to form a radical cation or dication, while free base molecules generally show at least a single reversible oxidation. The assignment of the free base species is complicated by the stability of the mono and dications being strongly influenced by the identity of the solvent (Geng & Murray, 1986). The typical absorption, photoluminescence and electrochemical properties of porphyrin dyes are illustrated in Figure 5.
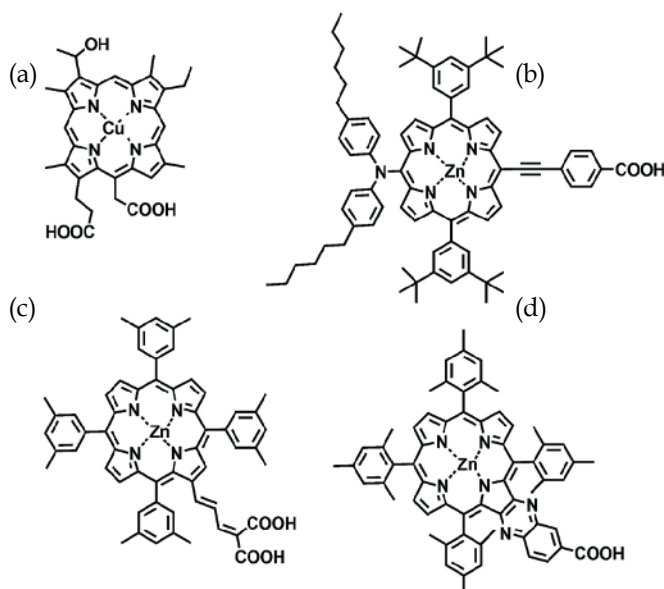
Fig. 4. The structure of (a) a pioneering synthetic porphyrin dye, and highly efficient porphyrin dyes (b) YD2, (c) GD2 and (d) Zn-4 published by various groups.

The development of new porphyrin dyes has been coupled with an increased understanding of the photophysics in operational DSSCs. For example, through various collaborations our group has previously shown that the luminescence lifetime, indicative of charge injection, depends on both the thermodynamic free energy driving force for injection and the conjugation through the linker moiety (Dos Santos, Morandeira et al., 2010). Furthermore, the electron lifetime in two of the most efficient porphyrin-sensitized solar cells was shown to be an order of magnitude lower than in identically prepared state of the art ruthenium bipyridyl (N719)–sensitized solar cells (Mozer, Wagner et al., 2008). This limitation can be somewhat circumvented by various post-treatments of the porphyrin-sensitized solar cells (Allegrucci, Lewcenko et al., 2009; Wagner, Griffith et al., 2011). However, despite this advanced understanding, the power conversion efficiencies of the best porphyrin-sensitized solar cells remains around 11%, well short of the theoretical maximum calculated earlier. The remainder of this chapter will focus on the fundamental limitations of these devices and explore some strategies which have been implemented to circumvent these limitations.
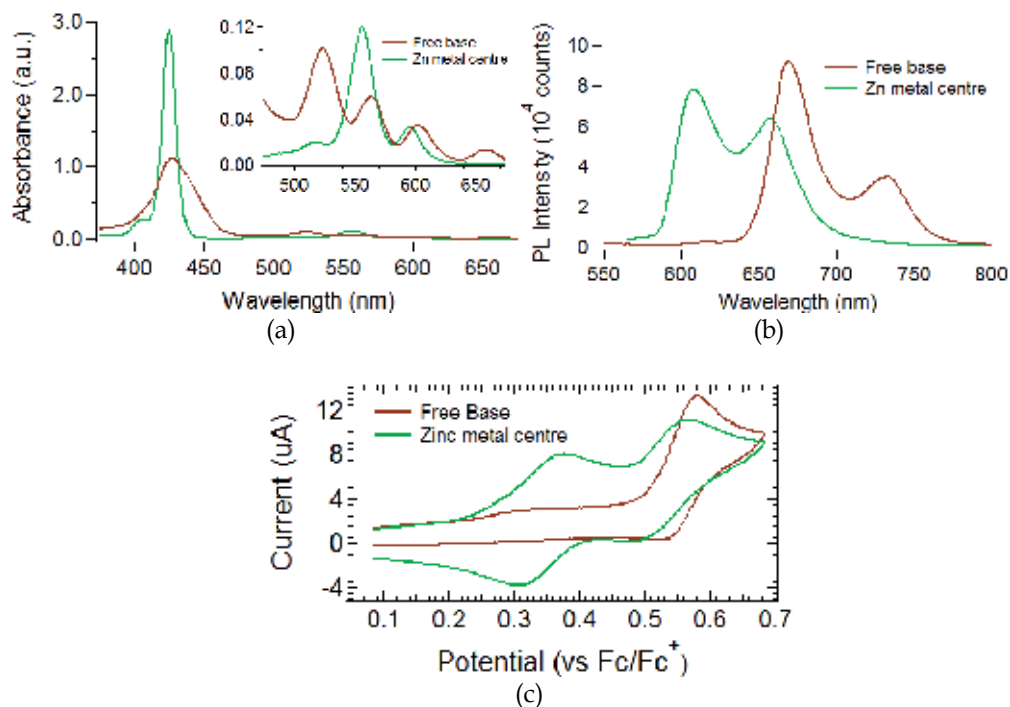
Fig. 5. The typical photophysical properties for 5 x 10⁻⁶ M solutions of zinc (green) and free base (brown) porphyrin molecules, showing (a) UV-vis absorption, (b) photoluminescence and (c) cyclic voltammograms (supporting electrolyte = 0.1 M TBAP).

2. Charge generation

The generation of free charges is the first critical step in achieving high efficiency in DSSCs. As indicated by equation (1), the charge generation processes consists of three steps; light absorption by the dye, injection of electrons from the photoexcited dye, and charge transport through the semiconductor film to prevent recombination. There are fundamental limitations with each of these three processes for porphyrin-sensitized solar cells. Some of these issues are intrinsic to the sensitizer and are difficult to remove. However, many of these basic problems can be circumvented using innovative approaches to device design. In this section we discuss some of the major limitations with charge generation in porphyrin-sensitized solar cells and summarize some of the important strategies that can be employed to reduce or indeed remove these limitations.

2.1 Light harvesting efficiency

Since the cross section for photon absorption of most photosensitizers is much smaller than the geometric area occupied on the semiconductor surface, light absorption by a pigment monolayer is small (Grätzel, 2005). To circumvent this, nanostructured semiconductor electrodes with a surface roughness factor (internal surface area normalized to the geometric area) on the order of a 1000 have been used, however these still require semiconductor films of at least 6 μm to produce a light harvesting efficiency close to unity. The requirement for this semiconductor thickness places significant constraints on the design of the DSSC. One

limitation is that dyes which are prone to recombination, such as porphyrin sensitizers, suffer increasing limitations with thicker semiconductor films due to the larger surface area for interfacial electron transfer reactions such as recombination. Furthermore, the viscosity of the electrolyte must be kept low to enable complete filling of the nanopores throughout the entire film thickness. Since such solvents are typically organic, their volatility leads to problems with hermetic sealing and long term stability of devices.

Incorporating multichromophore light harvesting arrays with increased absorption cross sections could potentially solve both of these issues, enabling efficient DSSCs with thinner films using ionic liquid (Kuang, Ito et al., 2006) or solid state electrolytes (Bach, Lupo et al., 1998). Multichromophore dyes could also allow novel electrode structures with smaller internal surface areas, such as nanotubes (Mor, Shankar et al., 2006), nanowires (Martinson, Elam et al., 2007), or large porosity mesoscopic structures to be employed. Our group investigated such an approach by joining two identical porphyrin chromophores together to create a dimer with twice the extinction coefficient but an unchanged molecular footprint on the semiconductor surface (Figure 6a). However, to ensure the enhanced light harvesting results in increased charge generation, efficient electron injection from both chromophores must be achieved. This condition is extremely difficult to demonstrate for dyes employing identical chromophores due to the matching spectroscopic features of each unit making them impossible to distinguish. In collaboration with Japanese co-workers we were able to produce the first spectroscopic evidence for electron injection from both chromophores of this porphyrin dimer by employing femtosecond time-resolved transient absorption (Mozer, Griffith et al., 2009). Since photons at the probe beam wavelength of 3440 nm are primarily absorbed by electrons in the TiO$_2$ in the absence of dye aggregates (Furube, Katoh et al., 2005), electron injection from the photoexcited dye is directly monitored by this technique. Furthermore, after normalization of the signal to correct for the absorbed pump beam intensity, a comparison of both the injection yield and kinetics can be performed. With reference to an N719 standard dye reference to determine the 100% injection yield value, the injection yield of the porphyrin dimer was determined to be ~70% (Figure 6b). The >50% quantum yield for the porphyrin dimer clearly demonstrates electron injection from *both* photoexcited porphyrin units within the dimer.

(a)   (b)
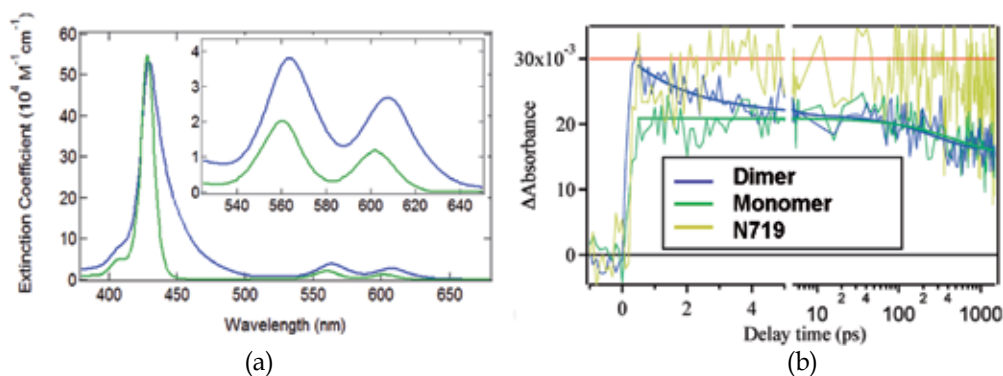
Fig. 6. Molar extinction coefficients of a porphyrin monomer (green) and dimer (blue) in solution. (b) Fs-TA signals (corrected for the absorbed pump intensity) of porphyrin-sensitized TiO$_2$ films in a redox containing electrolyte. An N719 signal obtained in air is also shown. Samples were excited by 150 fs pulses at 532 nm. Figure 6b taken from (Mozer, Griffith et al., 2009) and reproduced by permission of The American Chemical Society.

A second issue with light harvesting using porphyrin molecules is that the absorption bands of the sensitizers are quite discrete. Whilst the extinction coefficients in these absorption bands can be very high by employing for instance, a multichromophore dye, there are significant areas of the solar irradiance spectrum that are not covered by the absorption spectrum. Most notably, the vast majority of porphyrins do not absorb light beyond 700 nm. Additionally, the region between the Soret and Q-bands (450 nm-550 nm) also has a low absorption of incident photons. This lack of absorption significantly constrains the photocurrent which can be obtained from a porphyrin-based DSSC. Several strategies have been explored in an attempt to harvest an additional proportion of the incident solar flux using porphyrin dyes. One approach is to explore synthetic routes to extend the sensitizer absorption further towards the red end of the spectrum. Extension of the π conjugation and removal of symmetry in the porphyrin core can lead to splitting of the π and π^* levels and a decrease in the HOMO-LUMO gap, resulting in significant broadening and a red shift of the absorption bands. Imahori et al. were able to employ such an approach by using π-extended and fused porphyrin dyes to enhance the IPCE and overall device efficiency in a series of porphyrin molecules (Imahori, Umeyama et al., 2009).

A second approach used to extend the light harvesting efficiency of porphyrin-sensitized solar cells is to co-sensitize the semiconductor electrode with additional dyes which have complimentary absorption spectra to the porphyrin (Figure 7).
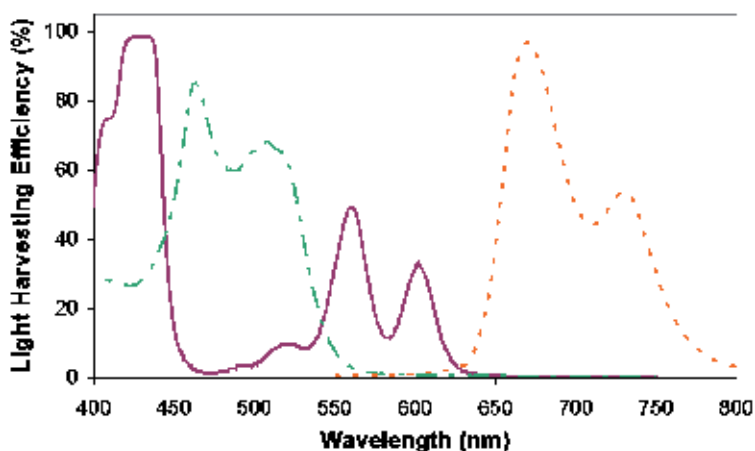
Fig. 7. An example of the extension in the porphyrin light harvesting efficiency (purple) that can be achieved by adding rhodium complex (green) and phthalocyanine (orange) dyes.

This approach has been utilized for many types of dyes, and was recently employed by Bessho et al. to enhance the photocurrent extracted from DSSCs prepared with a zinc porphyrin dye (Bessho, Zakeeruddin et al., 2010). The co-sensitization approach allows the absorption spectrum to be successfully extended; however, given the finite number of dye binding sites available on the semiconductor surface, there is still an intrinsic limitation on overall light harvesting potential. Our group explored methods to circumvent such limits by investigating a model system which combined free base and zinc porphyrin dyes. This study utilized not only the complimentary absorption spectra of the two dyes but also examined other possible synergistic interactions between the two dyes which are necessary in order to overcome the limit of a fixed amount of dye binding sites on the surface. We

were able to demonstrate an enhancement in both light harvesting *and* the injection yield when zinc and free base porphyrin dyes were combined on the same TiO_2 surface (Griffith, Mozer et al., 2011). Other groups have also pursued similar studies, focusing on extending the co-sensitization concept using energy relay systems. This approach involves dissolving the co-sensitizer in the electrolyte so that it no longer competes with the major sensitizer for binding sites on the semiconductor. Absorbed photon energy is transferred from the dissolved co-sensitizer to the chemically bound major sensitizer where it is then injected into the semiconductor. This approach achieved photocurrent enhancements of ~30% compared to direct co-sensitization on the same semiconductor surface (Hardin, Hoke et al., 2009).

2.2 Electron injection into semiconducting oxides

Electron injection from the photoexcited dye into the acceptor states of the semiconductor conduction band is perhaps the key mechanistic step in achieving efficient charge generation in DSSCs. According to the classical theory of electron transfer developed by Marcus, the rate of electron transfer, k_{ET}, between discrete donor and acceptor levels under non-adiabatic conditions is given by (Marcus, 1964):

$$k_{ET} = \frac{2\pi}{\hbar} \frac{H^2}{\sqrt{4\pi\lambda k_B T}} \exp\left(\frac{-\left(\lambda + \Delta G_0{}^2\right)}{4\pi\lambda k_B T}\right) \tag{5}$$

where H^2 is the electronic coupling between donor and acceptor states, ΔG_0 is the free energy driving force for electron transfer, λ is the total reorganization energy, T is the absolute temperature and h and k_B the Planck and Boltzmann constants respectively. The electronic coupling (H^2) decreases exponentially with increasing distance, d, between the donor and the acceptor as:

$$H^2 = H_0{}^2 \exp\left(-\beta d\right) \tag{6}$$

where β is related to the properties of the medium between donor and acceptor, and $H_0{}^2$ is the coupling at distance d = 0. To achieve high efficiencies for injection in DSSCs, electron injection must be at least an order of magnitude faster than the competing deactivation of the dye excited state. Extensive studies of this charge separation process have typically shown sub-ps injection dynamics, suggesting electron injection competes efficiently with excited state decay, which occurs on the 1-10 ns timescale for porphyrin dyes. However, despite such fast kinetics, many porphyrin dyes still show very poor injection efficiencies. One possible reason for this poor injection is the heterogeneous nature of the process. Koops and Durrant demonstrated a distribution of injection half-life time constants from 0.1 – 3 ns for devices sensitized with various ruthenium polypyridyl dyes. They attributed this result to variations in the local density of acceptor states in the semiconductor for electron injection and therefore in the integrated electronic coupling, H^2, for this reaction (Koops & Durrant, 2008). Since such behaviour is dependent on the density of states in the semiconductor and not on the dye itself, it would seem acceptable to assume that such heterogeneous injection kinetics also apply to porphyrin dyes, and thus there may be some slow injecting dyes which cannot compete with excited state deactivation.

The structure of the dye is clearly one crucial factor which will determine the injection efficiency. Campbell et al. investigated a wide range of porphyrin dyes and discovered that

the binding group which provides the electronic linkage between the chromophore and the semiconducting oxide plays an important role on the extracted photocurrent of devices. Given the similarity in the overall dye structures tested, this difference was attributed to variations in the injection efficiency achieved by varying the electronic coupling with different binding groups. Furthermore, the position of the binding group with respect to the porphyrin ring also affected the injection efficiency, with β-pyrollic linked groups showing better efficiency than meso linked groups. Our group extended such investigations in collaboration with co-workers in England. It was shown using luminescence quenching coupled with time correlated single photon counting detection to probe injection, that both the conjugation in the linker moiety and the metallation of the porphyrin can affect the injection yield in porphyrin systems (Figure 8). Peripheral substituents in the meso positions of the porphyrin core have also been shown to effect injection, with bulky groups (phenyl or tert-butyl) providing steric hindrance effects which reduces dye aggregation or electron donating groups affecting the HOMO–LUMO gap of the dye and thus the driving force for injection (Lee, Lu et al., 2009).

	FbNC[a]	FbC[a]	ZnNC[a]	ZnC[a]	ZnC[b]
τ_{Zr} / ns	7.5	4.2	1.5	1.5	0.8
τ_{Ti} / ns	4.8	2.5	0.8	<0.1	0.6
$(k_{inj})^{-1}$ / ns	14	6.2	1.9	<0.1	1.7
J_{SC} / mAcm^{-2}	0.11	0.6	1.2	4.3	4.3

[a] Kinetics for films covered with propylene carbonate. [b] Films covered with electrolyte.
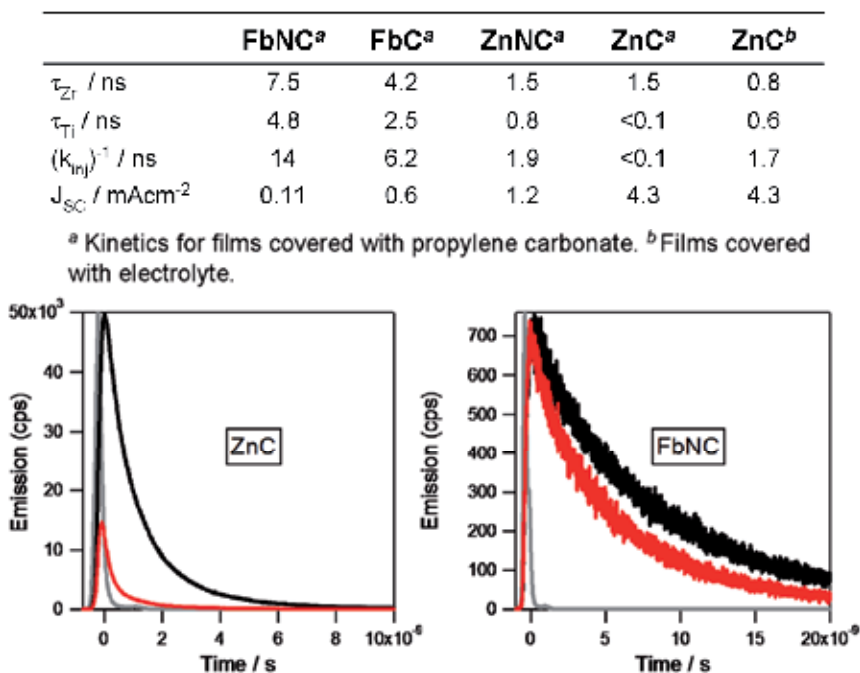
Fig. 8. (Top) Emission decay lifetimes, injection rate constants and device photocurrents for a series of porphyrin dyes with different metallation and linker conjugations. (Bottom) Transient emission decays of (a) a zinc porphyrin with a conjugated linker, and (b) a free base porphyrin with a saturated benzoic acid linker. Both dyes are adsorbed to TiO$_2$ (red), and ZrO$_2$, a high band gap semiconducting oxide which prevents electron injection (black). The instrument response function (IRF) is shown in grey. Figure taken from (Dos Santos, Morandeira et al., 2010) and reproduced by permission of The American Chemical Society.

Another concept which has been applied to improve injection in DSSCs is to synthesize dyes with an electron acceptor component close to the TiO$_2$ and an electron donor component

furthest from the TiO$_2$ linker. This ensures the electron density in the excited state is concentrated in the vicinity of the TiO$_2$, promoting injection and localizing the resultant positive charge away from the interface, thereby reducing recombination. Given the ease with which porphyrin compounds can be synthetically modified, this class of dyes offers an ideal system to explore this donor–acceptor concept. Clifford et al tested the theory by modifying a zinc porphyrin with a triphenylamine electron donor, and showed that recombination of the injected electron with the dye was an order of magnitude slower than for a comparable dye that lacked the electron-donor groups (Clifford, Yahioglu et al., 2002). Hsieh et al extended such investigations when they tested a comprehensive range of electron donors and acceptors attached to the same porphyrin core. They demonstrated that several different electron donors attached to the optimal position of the porphyrin core were able to increase both the J_{sc} and the V_{oc} of the DSSCs, attributing this result to improved electron injection and reduced recombination due to the localization of electron density in the dye upon photoexcitation (Hsieh, Lu et al., 2010).

From equation (6) it is clear that the electronic coupling, and thus the rate of electron transfer for injection, is strongly dependent on the distance over which electron transfer occurs. If transfer between the porphyrin core and semiconductor occurs through the connecting binding group, extending the length of this group should reduce the speed with which injection occurs. Imahori et al tested this concept in a range of zinc porphyrin dyes, and found that contrary to expectation, the electron transfer process for longer linking groups were accelerated. They rationalized this result by postulating that some fraction of the porphyrin molecules are bound at an angle to the semiconductor surface as the linker becomes longer, with electron transfer in these dyes occurring through space, without facilitation through the linker. According to classical tunnelling theory, without the enhanced electronic coupling provided by the linker group, through-space injection could only occur if the sensitizer is within ~1 nm of the semiconductor surface. A distribution of electronic couplings from different injection routes would help explain the observed heterogeneity of the injection rates in DSSCs, however, dye orientation information remains quite limited. This lack of knowledge is problematic since the surface orientation of dyes will strongly affect the functioning of DSSCs, altering the effective barrier width for through-space charge tunnelling (Hengerer, Kavan et al., 2000) or the alignment of the dipole moment of the dye (Liu, Tang et al., 1996), which in turn can influence injection and recombination (Figure 9a). Several measurement techniques have been trialled, such as near edge X-ray absorption fine structure measurements (Guo, Cocks et al., 1997), scanning electron microscopy (Imahori, 2010), and X-ray photoelectron spectroscopy (Westermark, Rensmo et al., 2002), however each of these techniques suffers from the requirement for high vacuum. Our group recently investigated employing X-ray reflectivity under ambient conditions to convert the measured interference spectra (Figure 9b) into a dye thickness and subsequently a molecular orientation for a dye/TiO$_2$ bilayer (Wagner, Griffith et al., 2011). However, this technique is still limited by the need for a flat surface rather than measuring nanoporous DSSC electrodes directly. Despite experimental difficulties with confirming orientation, the design of porphyrin dyes which can inject both directly through space or facilitated by the linker group presents a promising method for enhancing overall injection.

In addition to modifying the dye structure to enhance injection efficiency, there are a range of additives which can be introduced to the electrolyte or sensitizing dye bath solutions to achieve enhanced injection. For instance, one potential issue with injection in porphyrin-sensitized solar cells is the limited free energy driving forces available for some dyes. This

becomes a problem for dyes with a large red-shift in the standard porphyrin absorption spectrum, and in particular, the free base porphyrin dyes, which can often display LUMO energies approaching that of the semiconductor conduction band potential. The absence of significant free energy driving forces is intrinsic to the dye/semiconductor combination, and is difficult to alter with structural modifications of the dye. However, the conduction band edge potential (E_{CB}) is related to the surface potential of the oxide. Introducing charged species into the electrolyte which subsequently adsorb to the semiconductor surface can therefore shift the value of E_{CB} and change the relative driving force for injection. Placing alkali metal cations in the electrolyte is the most common way to achieve a positive shift of E_{CB}, thereby improving the injection driving force for dyes with low (more positive) LUMO energies (Liu, Hagfeldt et al., 1998). Another additive which has been shown to improve injection in porphyrin-sensitized solar cells is chenodeoxycholic acid (CDCA). This additive is generally dissolved in the sensitizing dye solution and acts to prevent aggregation of the dyes on the surface, a significant issue for porphyrin sensitizers, which interact strongly through π–π stacking forces (Planells, Forneli et al., 2008). Surface aggregation induces injection from excited dyes into neighbouring dye molecules, thus reducing the injection efficiency through a self-quenching mechanism. CDCA molecules co-adsorb to the oxide surface with the dye, preventing aggregate formation and elevating the injection efficiency.

(a)   (b)
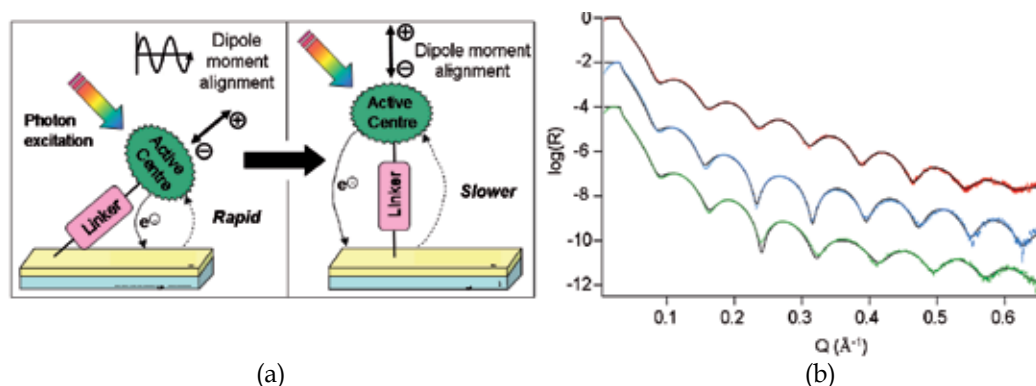
Fig. 9. (a) An illustration of the effect of dye adsorption orientation on the charge transfer and dipole alignment at a dye sensitised electrode. (b) Observed (data points) and calculated (solid lines) X-ray reflectivity spectra for a TiO_2 substrate (red), and porphyrin-sensitized TiO_2 before (blue) and after (green) 1 hour light exposure. Figure 9b taken from (Wagner, Griffith et al., 2011) and reproduced by permission of The American Chemical Society.

An alternative method to electrolyte additives which can be employed to modulate the semiconductor conduction band is to change the material employed as the semiconductor. The density of states (DOS) distribution for semiconductors is normally expressed as an exponential function with a characteristic broadening parameter, unique for each different metal oxide. As such, different materials will display various potentials at matched electron densities, leading to different E_{CB} values (Grätzel, 2001). In order to obtain a more positive E_{CB} to enhance the driving force for injection, the standard TiO_2 semiconductor can be replaced with materials such as SnO_2 (Fukai, Kondo et al., 2007), In_2O_3 (Mori & Asano, 2010) or WO_3 (Zheng, Tachibana et al., 2010), which all possess a narrower DOS distribution and thus lower E_{CB} values than TiO_2 at the same charge densities. Each of these materials

produce higher photocurrents than TiO$_2$-based systems due to enhanced injection, however the electron mobility in these oxides is much higher than in TiO$_2$ and thus they suffer from faster recombination reactions which minimize or can even reverse the overall efficiency gains achieved by enhancing injection.

The injection yield of porphyrin-sensitized devices can also be improved by innovative device design or the use of various post-treatments to improve the system. Our group recently explored such post-treatments, demonstrating improvements in the J_{sc} of a zinc porphyrin DSSC arsing from enhanced injection after the cell was exposed to AM 1.5 illumination for 1 hr (Wagner, Griffith et al., 2011). The injection yield was measured using absorbed photon-to-current conversion efficiency (APCE), which is calculated by normalizing the IPCE for light absorption:

$$APCE = \frac{IPCE}{LHE} = \phi_{inj}\, \eta_{coll} \tag{7}$$

By employing thin (~2 µm) film DSSCs, transport losses are assumed to be negligible and thus η_{coll} is close to 100% and the APCE measurements enable determination of ϕ_{inj} under short circuit conditions. The increased APCE (from 65% to approximately 90%) following light exposure (Figure 10a) therefore demonstrated an increased injection yield for the porphyrin dye. We have also employed APCE measurements to demonstrate an enhancement in the injection yield when zinc and free base porphyrin dyes were combined on the same TiO$_2$ surface. The APCE of the mixture was ~300% higher than either individual dye. It was proposed that this enhanced injection could arise from energy transfer from the zinc dye with an inefficient linker to the free base dye which possesses a conjugated linker, possible due to the spectral overlap between zinc porphyrin emissions and free base porphyrin absorption (Griffith, Mozer et al., 2011). This process could allow the zinc dye to inject through a more efficient conjugated pathway on the free base dye (Figure 10b).
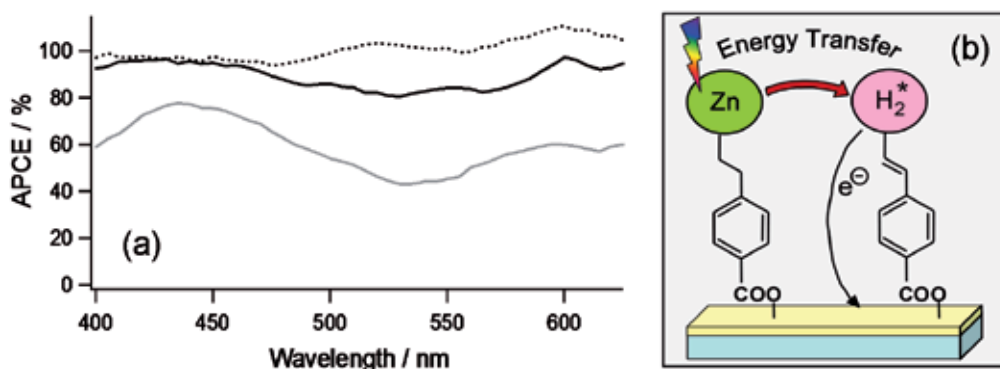
Fig. 10. (a) Absorbed photon to current conversion efficiencies (APCE) which estimate the injection yield for porphyrin-sensitized thin-film TiO$_2$ devices before (grey solid line) and after (black solid line) 1 hour light exposure. Data for the N719 dye is included for comparison (dashed line). (b) Energy transfer from a zinc to a free base porphyrin to utilize the conjugated injection pathway. Figure 10a taken from (Wagner, Griffith et al., 2011) and reproduced by permission of The American Chemical Society.

2.3 Charge transport

Since the nanoparticles of typical DSSC anodes are too small to sustain a space charge layer, electron transport in DSSCs is dominated by diffusion with negligible drift contributions. In this situation, the charge collection efficiency, η_{coll}, is related to the electron diffusion coefficient (D) and electron lifetime (τ) in the semiconductor electrode (where electron lifetime is the average time spent in the electrode). If the electron diffusion length, L, where:

$$L = \sqrt{D\tau} \tag{8}$$

is shorter than the thickness of the semiconductor electrode, then electrons will recombine with the dye cation or the acceptor species in the redox mediator during charge transport, limiting η_{coll}. Typical diffusion lengths for the benchmark ruthenium dyes are 30-60 μm, leading to high collection efficiencies on 20 μm semiconductor films. The diffusion coefficients for porphyrin DSSCs are comparable to most other dyes. However, many porphyrins, and in particular free base dyes, suffer from high levels of recombination which lower the electron lifetime and thus the diffusion length. The effective diffusion length of sensitizers can be estimated from the film thickness at which the measured IPCE or J_{sc} saturates. However, such measurements cannot deconvolute the competing affects of increasing light harvesting and decreasing collection efficiency. Since the film thickness required for unity absorption of incident photons is ~6 μm, J_{sc} saturation values below this limit suggest there will be charge transport losses, as has been measured for some porphyrin DSSCs (Figure 11a). To determine L, D and τ values more rigorously, small amplitude perturbation techniques such as intensity modulated photovoltage or photocurrent spectroscopy, impedance spectroscopy or stepped-light induced measurements of photocurrent and photovoltage are generally employed, producing plots such as the one displayed in Figure 11b. However, there is some debate regarding the accuracy of these transient techniques, with Barnes et al. arguing that IPCE measurements performed with front and backside illumination are more relevant than small perturbation relaxation techniques (Barnes, Liu et al., 2009). In order to remove or minimize the charge transport losses in some porphyrins, strategies which reduce the recombination must be explored.
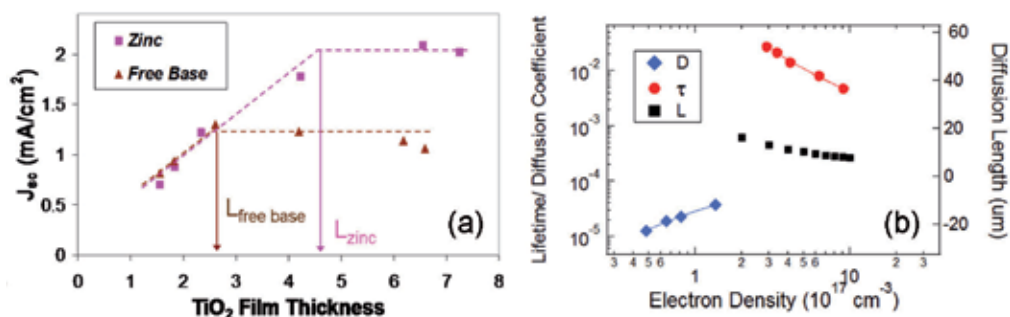
Fig. 11. (a) Diffusion length estimated from J_{sc} saturation values for inefficient zinc and free base porphyrins. (b) D (blue diamonds) and τ (red circles) values measured by stepped light-induced photovoltage and photocurrent techniques plotted against electron density for a porphyrin-sensitized DSSC. The calculated electron diffusion length, L, is also shown (black squares).

3. Charge recombination

As described earlier, the J_{sc} of porphyrin-sensitized solar cells is determined by their spectral response, injection efficiency and charge transport characteristics, all of which are quite well understood. Conversely, the open circuit voltage (V_{oc}) of porphyrin DSSCs is generally observed to be 100–200 mV lower than the commonly used ruthenium dyes, the origin of which is only partially elucidated. Since the photovoltage under illumination is dependent on the Fermi level in the semiconducting oxide, the lower V_{oc} for porphyrin DSSCs may be related to either a positive shift of the conduction band potential (E_{CB}) of the semiconducting oxide following dye sensitization or a lower electron density due to a reduced electron lifetime. Our group investigated each of these possibilities in collaboration with Japanese co-workers in order to determine the origin of the lower V_{oc} in porphyrin DSSCs. It was found that when the V_{oc} was plotted against the electron density (ED) in the TiO$_2$ film, neither the slope nor the y-intercept of the V_{oc} vs logED plot differed between ruthenium and porphyrin sensitized solar cells (Mozer, Wagner et al., 2008) (Figure 12d). Since the redox mediator Fermi level was constant in each case, the V_{oc} vs logED plot is indicative of the TiO$_2$ conduction band potential. Hence these results demonstrated that the lower V_{oc} of porphyrin-sensitized solar cells is not due to an E_{CB} shift following dye uptake. We found instead that the low photovoltages were a result of electron lifetimes in porphyrin dyes being reduced by a factor of ~200 at matched electron densities, independent of their chemical structure (Figure 12b). Furthermore, we showed that the shorter electron lifetimes were not related to electron transport differences, since the diffusion coefficients were identical for porphyrin and ruthenium dyes (Figure 12c).
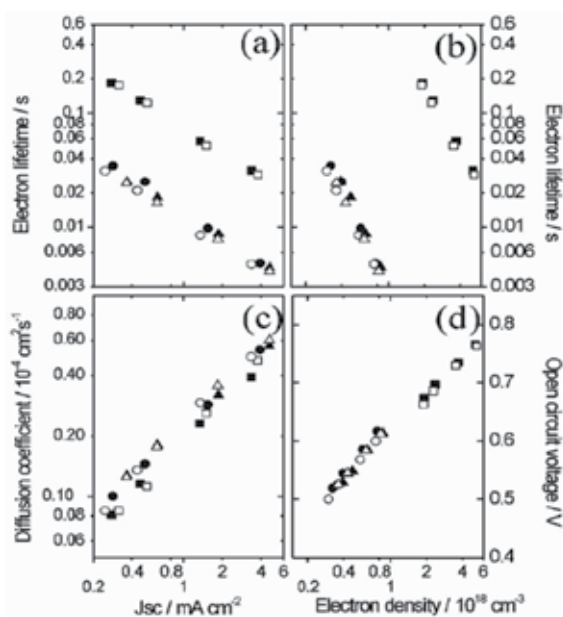
Fig. 12. (a) Electron lifetime and (c) diffusion coefficient versus short circuit current density. (b) Electron lifetime and (d) open circuit voltage versus electron density for ruthenium (squares) and porphyrin (circles, triangles) DSSCs. Figure taken from (Mozer, Wagner et al., 2008) and reproduced by permission of The Royal Society of Chemistry

Since charge is a conserved quantity in any system, a continuity equation for the charge density, n, can be derived for a DSSC. The time-dependent form of this equation is:

$$\frac{\partial n}{\partial t} = \phi_{inj}\,\alpha\,I_0\,\exp(-\alpha x) + D_0\frac{\partial^2 n}{\partial x^2} - \left(\frac{n}{\tau_{redox}} + \frac{n}{\tau_{dye}}\right) \qquad (9)$$

where the first term on the right-hand side of the equation describes the electron injection into the oxide from dyes at position x (α is the absorption coefficient, I_0 is the incident photon flux and $x = 0$ at the anodic contact). The second term accounts for the diffusion of electrons (D_0 is the diffusion coefficient of electrons), whilst the third term describes the two simultaneously occurring recombination reactions (where τ_{redox} and τ_{dye} are the lifetimes determined by the recombination reactions of conduction band electrons with the redox acceptor species and the oxidised dye, respectively). Since the lower V_{oc} of porphyrin DSSCs arises from a reduced electron lifetime which is not affected by electron transport, it must be related to an enhancement in one (or both) of the two recombination processes.

Dye cation recombination in DSSCs has been extensively studied using transient absorption spectroscopy to probe the rate of disappearance of the dye cation absorption following its creation. For the majority of dyes, the cations are regenerated with a time constant of 1-10 μs, even in viscous or semi-solid electrolytes which slow down the reaction due to diffusion limitations (Nogueira & Paoli, 2001; Wang, Zakeeruddin et al., 2003). These kinetics are generally much faster than the recombination reaction between dye cations and electrons in the semiconductor, which has a time constant of 100 μs – 1 ms (Willis, Olson et al., 2002). Our group has demonstrated this situation holds true for porphyrin dyes by measuring transient absorption kinetics for the dye cation (with an absorption peak at 700 nm) in the absence and the presence of a standard I⁻/I₃⁻ redox mediator (Figure 13). Without the redox mediator the half signal decay was 60 μs, whilst in the presence of the redox mediator, the half-signal decay was accelerated to 2 μs (Wagner, Griffith et al., 2011). This suggests efficient prevention of recombination through regeneration of the dye cations by the redox mediator. It is therefore very unlikely that the short electron lifetime for porphyrin DSSCs results from recombination with the dye cation.
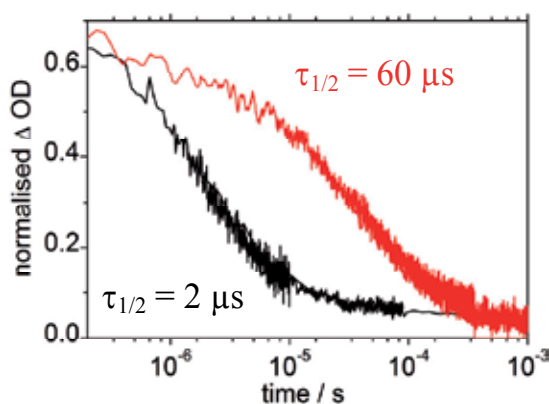
Fig. 13. Transient absorption kinetic traces recorded at 700 nm for porphyrin-sensitized TiO₂ films covered with acetonitrile electrolyte in the absence (red) and presence (black) of an I⁻/I₃⁻ redox mediator. The films were photoexcited by nanosecond pulses at 532 nm.

As dye cation recombination is a negligible problem for porphyrin DSSCs, the shorter electron lifetime must arise from increased recombination between conduction band electrons and the acceptor species in the redox mediator. Such a process can only occur from an increased proximity of the acceptor species to the semiconductor surface. For the standard I^-/I_3^- redox mediator, it has been proposed that most organic dyes (specifically including porphyrins) either attract I_3^- to the dye–semiconductor interface (Miyashita, Sunahara et al., 2008) or catalyse the recombination reaction with acceptor species in the electrolyte, such as I_3^- or the iodine radical I_2^- (O'Regan, López-Duarte et al., 2008). Several different strategies have been implemented in an attempt to improve the electron lifetime, and we now examine some of the major innovations which have lead to enhancements in the overall device V_{oc}.

3.1 Molecular structure

The molecular structure of dyes can have a large impact on the concentration of the redox mediator at the semiconductor surface. Nakade et al. reported that adsorption of ruthenium dye N719 will decrease the concentration of acceptor species I_3^- in the vicinity of the TiO_2 surface due to shielding from the negative SCN^- ligands on the dye molecule (Nakade, Kanzaki et al., 2005). A similar physical shielding effect can be achieved with organic dyes by introducing bulky substituent groups to sterically hinder the approach of the redox mediator to the semiconductor surface (Koumura, Wang et al., 2006) (Figure 14). This approach was shown to increase the electron lifetime and V_{oc} for DSSCs constructed with carbazole (Miyashita, Sunahara et al., 2008), phthalocyanine (Mori, Nagata et al., 2010) and osmium (Sauvé, Cass et al., 2000) complexes. Several of these authors reported minimal effects when the dye loading on the surface was reduced, confirming that the structure of the dye, and its steric crowding of the semiconductor surface, was the major factor driving the increase in electron lifetime. This strategy has been successfully implemented to porphyrin sensitizers, with the introduction of octyl chains to a high efficiency zinc porphyrin dye producing the highest efficiency ionic liquid-based porphyrin DSSC (Armel, Pringle et al., 2010). Imahori et al. have demonstrated the value of amending the porphyrin structure by adding bulky mesityl groups at the meso positions of the porphyrin core to both reduce the dye aggregation (which limits electron injection) and enhance the V_{oc} by blocking the surface from the approach of the redox mediator.
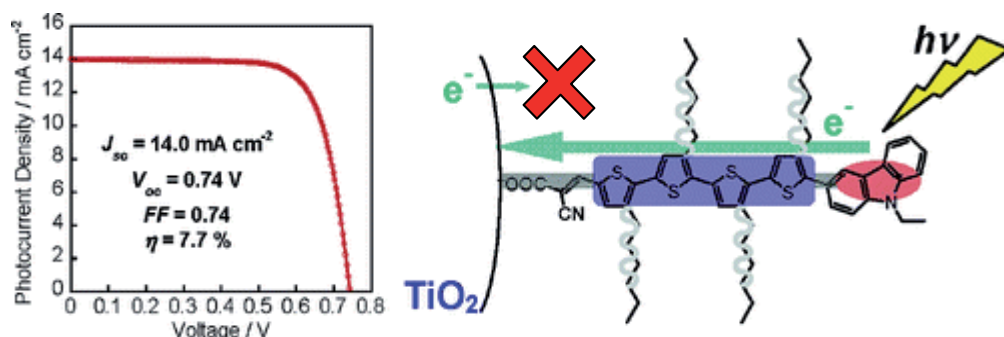
Fig. 14. PV parameters and an illustration of a carbazole dye with long alkyl chains to stop the redox mediator reaching the semiconductor surface. Figure taken from (Koumura, Wang et al., 2006) and reproduced by permission of The American Chemical Society.

3.2 Semiconductor blocking effects

As was earlier described for electron injection, strategies to inhibit recombination between conduction band electrons and the redox mediator can focus on either the dye or the semiconductor side of the major electronic interface. Accordingly, an alternative strategy to dye structure modification which can be employed to extend the electron lifetime in porphyrin DSSCs is to insulate exposed sites on the semiconductor surface. Rather than block the approach of the redox mediator to these active sites, this method attempts to deactivate the electron transfer process at these sites using an insulating surface covering. Deposition of a compact TiO_2 layer from a titanium tetrachloride ($TiCl_4$) precursor has been previously used to block electron transfer between the redox mediator and the back FTO-glass contact (Burke, Ito et al., 2008), and the same approach has also been successfully applied to insulating the semiconductor surface. O'Regan et al. utilized photocurrent and photovoltage transient measurements to show that deposition of a compact TiO_2 blocking layer on top of the mesoporous TiO_2 electrode produces an 80 mV downward shift in the TiO_2 conduction band edge potential and a 20-fold decrease in the electron/electrolyte recombination rate constant (O'Regan, Durrant et al., 2007). Following these findings, a range of organic acids have been trialled as surface insulating agents. Phosphinic acids are particularly useful in this regard since they form strong bonds with titania but, in contrast to commonly employed carboxylic or phosphonic acids, also have two organic substituents which can potentially provide more complete insulation of the semiconductor surface. Accordingly our group, in collaboration with Australian co-workers, employed a phosphinic acid surface treatment to a zinc porphyrin DSSC and demonstrated a successful suppression of the surface recombination and a simultaneous positive conduction band shift, resulting in 15% improvements in the photocurrent and 20% increases in the overall device efficiency. Measurements of time-resolved photovoltage transients demonstrated that these improvements resulted from an increased electron lifetime (Figure 15a), although the expected V_{oc} improvement was limited by a simultaneous positive shift in the semiconductor conduction band potential (Allegrucci, Lewcenko et al., 2009) (Figure 15b). Nonetheless, these results establish that the short electron lifetimes which limit porphyrin DSSCs can be improved with a semiconductor surface treatment.

(a) (b)
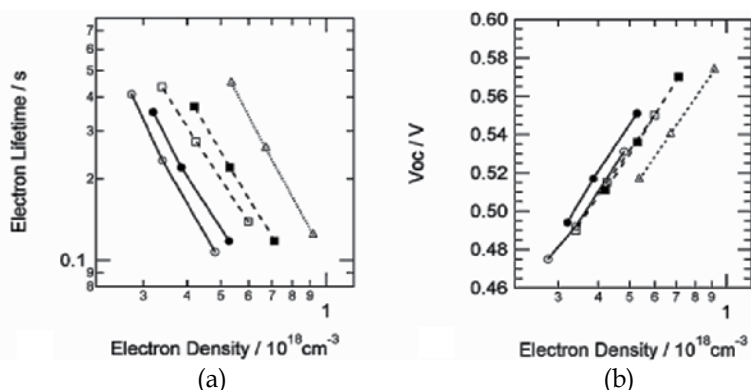
Fig. 15. (a) Electron lifetime, and (b) V_{oc}, as a function of electron density in the TiO_2 film for porphyrin DSSCs after 0 mins (circles), 5 mins (squares) and 30 mins (triangles) of a phosphinic acid surface treatment. Figure taken from (Allegrucci, Lewcenko et al., 2009) and reproduced by permission of The Royal Society of Chemistry.

3.3 Manipulating interfacial charges

The predominate recombination pathway in porphyrin DSSCs is between electrons and the acceptor species in the redox mediator. Consequently, the cations and additives which are typically dissolved in the electrolyte play an important role in mediating this reaction. The roles of the cations have been found to influence the electron injection yield, the open-circuit voltage, the electron diffusion coefficient, and the rate of dye-cation regeneration (Kambe, Nakade et al., 2002; Zaban, Ferrere et al., 1998). With careful design, the influence of these supporting cations can be manipulated to remove the acceptor species in the redox mediator from the vicinity of the semiconductor surface, thereby extending the electron lifetime and raising the V_{oc}. Nakade et al investigated such effects by varying the size of the cation additive for a ruthenium-sensitized solar cell with a standard I^-/I_3^- redox mediator. They found that the size of the cation has a large impact on the thickness of the electrical double layer (Helmholtz and diffuse layers), effectively altering the local (surface) concentration of I_3^-, which is the concentration of I_3^- within the distance from the TiO_2 surface at which electrons can be transferred (Nakade, Kanzaki et al., 2005). When electrons are injected into the TiO_2, the surface becomes negatively charged and an electrical double layer is formed at the surface. For cations which are small enough to penetrate between the adsorbed dye molecules this double layer is formed over ~1 nm, effectively screening the surface charge and allowing I_3^- to approach close to the TiO_2 surface. However, for bulky cations such as tetrabutylammonium (TBA^+) which cannot penetrate between the dye and TiO_2, a distance much longer than the size of the dye is needed for the screening. In this case, anions feel a repulsive force to penetrate between the dye and TiO_2 due to the negative surface charge. This reduces the local I_3^- concentration and results in a longer electron lifetime (Figure 16).

(a)   (b)
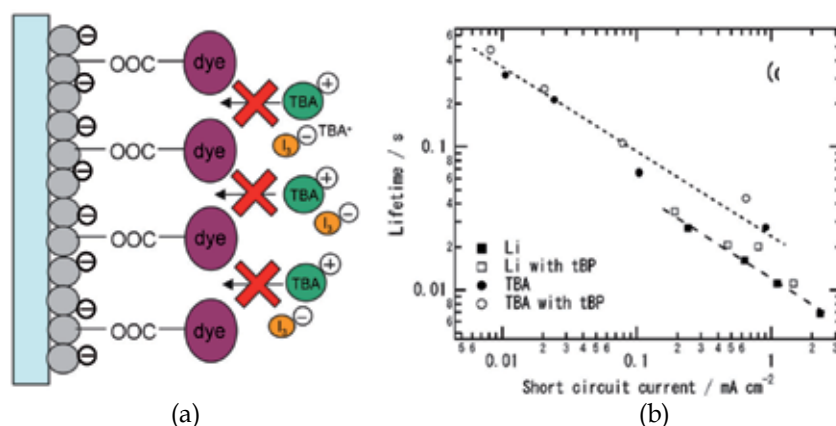
Fig. 16. (a) The extended electric double layer at the surface using a bulky supporting cation. (b) The electron lifetime for DSSCs employing TBA^+ and Li^+ in the electrolyte. Figure 16b taken from (Nakade, Kanzaki et al., 2005) and reproduced by permission of The American Chemical Society.

Nakade et al. showed that this increased electron lifetime led to a 300 mV increase in V_{oc}, although the increase was aided by a negative shift in E_{CB} which reduced the photocurrent. Since such an approach simply manipulates the position of intrinsically formed charged layers using a generic electrolyte, it should be generally applicable to all dye systems, including porphyrins.

Post-treatments or dye interactions could also lead to longer electron lifetimes and improved V_{oc} in porphyrin DSSCs. Our group have demonstrated using photovoltage decay measurements that exposure of a zinc porphyrin DSSC to AM 1.5 illumination conditions for a period of 1 hour produces an increase in the electron lifetime by a factor of 2 to 3. This result was also accompanied by a comparable decrease in the electron diffusion coefficient. The improved electron lifetime combined with the increased J_{sc} obtained from the same post-treamtment resulted in increased electron densities at open circuit conditions, leading to improved V_{oc} (Wagner, Griffith et al., 2011). It was postulated that the origin of this effect could be either the photo-generation of electronic states within the band gap of TiO_2 or a change in the behavior of electrolyte addtives when the solar cell is illmuinated, both of which could lead to improved injection, longer electron lifetimes and slower electron transport.

Charge transfer interactions could also act to decrease recombination in porphyrin DSSCs in certain circumstances. Our group recently reported an enhanced injection yield when zinc and free base porphyrin dyes were combined, however we also noted that this mixture resulted in a higher V_{oc} than that obtained from both individual dyes. Measured energy levels for the two dyes indicate that the zinc dye (ZnNC) had both a higher HOMO and a higher LUMO energy than the free base dye (FbC), which could lead to hole transfer from FbC^+ to neutral ZnNC (Figure 17a). It was noted that similar charge transfer processes between zinc and free base porphyrins have been previously observed to occur on very fast (picosecond) timescales (Koehorst, Boschloo et al., 2000). It was speculated that hole transfer (HT) could potentially improve the charge generation yield of FbC by preventing recombination. This would be feasible if $k_{HT} \gg k_{EDR,FbC} \gg k_{DR,FbC}$, where $k_{EDR,FbC}$ is the rate constant for charge recombination between TiO_2 electrons and FbC^+, and $k_{DR,FbC}$ is the rate constant for dye regeneration of FbC (Griffith, Mozer et al., 2011) (Figure 17b). Such charge transfer processes have been shown to reduce recombination and improve the V_{oc} for other co-sensitized DSSC systems (Clifford, Forneli et al., 2011; Clifford, Palomares et al., 2004), and offer an attractive pathway to simultaneously remove both injection and recombination limitiations in porphyrin DSSCs.

(a)   (b)
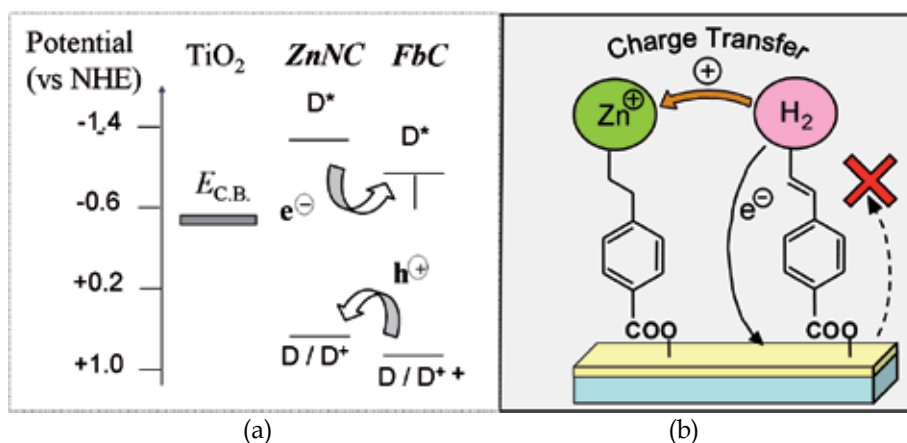
Fig. 17. (a) Calculated dye HOMO and LUMO energy levels and potential charge transfer processes for a zinc/free base mixed dye system. (b) Charge transfer from oxidized free base to neutral zinc molecules to prevent recombination.

4. Conclusion

The efficient light harvesting potential of porphyrin dyes, exemplified by their primary role in photosynthesis, makes them ideal candidates for use as photosensitizers within dye sensitized solar cells. Their synthesis is relatively straightforward, and their optical and electronic properties can be tuned via chemical modification of the coordinating metal centre, the porphyrin core, the number of porphyrin units, and the linker between the core and the inorganic oxide. Recent porphyrin DSSC developments have been accompanied by a simultaneous improvement in the understanding of the photophysics governing operational solar cells. In particular, many of the fundamental limitations which constrain the performance of these dyes have been elucidated.

The major limitations which continue to hinder the performance of porphyrin DSSCs are the light harvesting of incident photons, injection into the semiconducting oxide and the recombination with the acceptor species in the redox mediator. Light harvesting limitations, which mainly surround the limited absorption of low energy (red) photons, can be circumvented by combining several dyes with complimentary absorption spectra or by employing multichromophore dyes to boost the effective absorption coefficients and allow thinner semiconductor films to be employed. Electron injection yields for porphyrin dyes, studied by techniques including time resolved luminescence quenching, ultrafast transient absorption spectroscopy and absorbed photon-to-current conversion efficiency, have been shown to be much lower than the kinetics of injection compared to dye deactivation would predict. Such limitations can be caused by dye structural considerations, heterogeneous injection kinetics, or poor free energy driving forces. These limitations can be addressed by modifying the dye structure, addition of various chemicals to the electrolyte to modify the free energy driving force for injection, employing post-treatments to enhance injection efficiency after fabrication or by combining different dyes to achieve improved injection efficiencies through synergistic interactions. Recombination limitations, now understood to be the major impediment to achieving high efficiency in porphyrin DSSCs, have been shown to arise from the back reaction between electrons in the oxide conduction band and the acceptor species in the redox mediator. Characterization of the electron lifetime, studied by techniques such as intensity modulated voltage spectroscopy (IMVS), electrochemical impedance spectroscopy and stepped-light induced measurements of photocurrent and photovoltage (SLIM-PCV) reveals that this recombination reaction can be influenced by several factors, such as a physical blocking effect on either the dye structure or the semiconductor surface, electrostatic interactions which control the location of charges at the interface or combining dyes to harness various photoinduced charge transfer mechanisms.

Given the attractive features of porphyrin chromophores, the improved understanding of porphyrin DSSCs which has been compiled in recent years, and the many innovative strategies still emerging, there remains much promise in the development of these devices. Porphyrin based DSSCs continue to offer a fruitful topic for exploring the fundamental processes which limit the efficiency of dye-sensitized light harvesting applications, inspiring the development of innovative strategies to circumvent these basic limitations. The remaining challenge is to integrate each of these new strategies to produce a porphyrin DSSC with a power conversion efficiency which surpasses the current maximum of 11% and allows these devices to become a commercial reality.

5. Acknowledgments

6. References

Allegrucci, A., Lewcenko, N. A., et al. (2009). "Improved performance of porphyrin-based dye sensitised solar cells by phosphinic acid surface treatment." *Energy and Environmental Science*, Vol. 2, pp 1069.

Armel, V., Pringle, J. M., et al. (2010). "Ionic liquid electrolyte porphyrin dye sensitised solar cells." *Chemical Communications*, Vol. 46, pp 3146.

Bach, U., Lupo, D., et al. (1998). "Solid-state dye-sensitized mesoporous TiO_2 solar cells with high photon-to-electron conversion efficiencies." *Nature*, Vol. 395, pp 583.

Barnes, P. R., Liu, L., et al. (2009). "Re-evaluation of recombination losses in dye-sensitized cells: the failure of dynamic relaxation methods to correctly predict diffusion length in nanoporous photoelectrodes." *Nano Letters*, Vol. 9, pp 3532.

Bessho, T., Zakeeruddin, S. M., et al. (2010). "Highly efficient mesoscopic dye-sensitized solar cells based on donor–acceptor-substituted porphyrins." *Angewandte Chemie (International Edition)*, Vol. 49, pp 6646.

Bisquert, J. & Mora-Sero, I. (2010). "Simulation of steady-state characteristics of dye-sensitized solar cells and the interpretation of the diffusion length." *Journal of Physical Chemistry Letters*, Vol. 1, pp 450.

Boschloo, G. & Hagfeldt, A. (2009). "Characteristics of the iodide/triiodide redox mediator in dye-sensitized solar cells." *Accounts of Chemical Research*, Vol. 42,(11), pp 1819.

Burke, A., Ito, S., et al. (2008). "The function of a TiO_2 compact layer in dye-sensitized solar cells incorporating "planar" organic dyes." *Nano Letters*, Vol. 8, pp 977.

Campbell, W. M., Burrell, A. K., et al. (2004). "Porphyrins as light harvesters in the dye sensitized solar cell." *Coordination Chemistry Reviews*, Vol. 248, pp 1363.

Campbell, W. M., Jolley, K. W., et al. (2007). "Zn porphyryrins as highly efficient sensitizers in dye sensitized solar cells." *Journal of Physical Chemistry C*, Vol. 111, pp 11760.

Chiba, Y., Islam, A., et al. (2006). "Dye sensitized solar cells with conversion efficiency of 11.1%." *Japanese Journal of Applied Physics*, Vol. 48, pp L638.

Clifford, J. N., Forneli, A., et al. (2011). "Co-sensitized DSCs: dye selection criteria for optimized device V_{oc} and efficiency " *Journal of Materials Chemistry*, Vol. 21, pp 1693.

Clifford, J. N., Palomares, E., et al. (2004). "Multistep electron transfer processes on dye co-sensitized nanocrystallineTiO$_2$ films." *Journal of the American Chemical Society*, Vol. 126, pp 5670.

Clifford, J. N., Yahioglu, G., et al. (2002). "Molecular control of recombination dynamics in dye sensitised nanocrystalline TiO_2 films." *Chemical Communications*, Vol., pp 1260.

Dos Santos, T., Morandeira, A., et al. (2010). "Injection limitations in a series of porphyrin dye sensitized solar cells." *Journal of Physical Chemistry C*, Vol. 114, pp 3276.

Fukai, Y., Kondo, Y., et al. (2007). "Highly efficient dye-sensitized SnO_2 solar cells having sufficient electron diffusion length " *Electrochemistry Communications*, Vol. 9, pp 1439.

Furube, A., Katoh, R., et al. (2005). "Lithium ion effect on electron injection from a photoexcited coumarin derivative into a TiO_2 nanocrystalline film investigated by visible-to-IR ultrafast spectroscopy." *Journal of Physical Chemistry B*, Vol. 109, pp 16406.

Geng, L. & Murray, R. W. (1986). "Oxidative microelectrode voltammetry of tetraphenylporphyrin and copper tetraphenylporphyrin in toluene solvent." *Inorganic Chemistry*, Vol. 25, pp 3115.

Gledhill, S. E., Scott, B., et al. (2005). "Organic and nano-structured composite photovoltaics: An overview " *Journal Material Research*, Vol. 20, pp 3167.

Gouterman, M. (1978). "Electronic Spectra", In: *The Porphyrins (Vol. III)*. D. Dolphin (ed.), Academic Pess Inc., New York.

Grätzel, M. (2001). "Photoelectrochemical cells." *Nature*, Vol. 414, pp 338.

Grätzel, M. (2005). "Solar energy conversion by dye sensitized photovoltaic cells." *Inorganic Chemistry*, Vol. 44, pp 6841.

Griffith, M. J., Mozer, A. J., et al. (2011). "Remarkable synergistic effects in a mixed porphyrin dye-sensitized TiO_2 film." *Applied Physics Letters*, Vol. 98, pp 163502.

Guo, Q., Cocks, I., et al. (1997). "The orientation of acetate on a $TiO_2(110)$ surface." *Journal of Physical Chemistry*, Vol. 106,(7), pp 2924.

Haque, S. A., Palomares, E., et al. (2005). "Charge separation versus recombination in dye sensitized solar cells: The minimization of kinetic redundancy." *Journal of the American Chemical Society*, Vol. 127, pp 3456.

Hara, K., Sato, T., et al. (2003). "Molecular design of coumarin dyes for efficient dye sensitized solar cells." *Journal of Physical Chemistry B*, Vol. 107, pp 597.

Hardin, B. E., Hoke, E. T., et al. (2009). "Increased light harvesting in dye-sensitized solar cells with energy relay dyes." *Nature Photonics*, Vol. 3, pp 406.

Hengerer, R., Kavan, L., et al. (2000). "Orientation dependence of charge-transfer processes on TiO_2 (anatase) single crystals." *Journal of the Electrochemical Society*, Vol. 147,(4), pp 1467.

Hsieh, C.-P., Lu, H.-P., et al. (2010). "Synthesis and characterization of porphyrin sensitizers with various electron-donating substituents for highly efficient dye-sensitized solar cells." *Journal of Materials Chemistry*, Vol. 20, pp 1127.

Imahori, H. (2010). "Porphyrins as potential sensitizers for dye sensitized solar cells." *Key Engineering Materials*, Vol. 451, pp 29.

Imahori, H., Umeyama, T., et al. (2009). "Large π-aromatic molecules as potential sensitizers for highly efficient dye sensitized solar cells." *Accounts of Chemical Research*, Vol. 42, pp 1809.

Kambe, S., Nakade, S., et al. (2002). "Influence of the electrolytes on electron transport in mesoporous TiO_2 electrolyte systems." *Journal of Physical Chemistry B*, Vol. 106, pp 2967.

Katoh, R., Furube, A., et al. (2002). "Efficiencies of electron injection from excited sensitizer dyes to nanocrystalline ZnO films as studied by near-IR optical absorption of injected electrons." *Journal of Physical Chemistry B*, Vol. 106, pp 12957.

Kay, A. & Grätzel, M. (1993). "Artificial photosynthesis. 1. Photosensitization of TiO_2 solar cells with chlorophyll derivatives and related natural porphyrins." *Journal of Physical Chemistry*, Vol. 97, pp 6272.

Koehorst, R. B. M., Boschloo, G. K., et al. (2000). "Spectral sensitization of TiO_2 substrates by monolayers of porphyrin heterodimers." *Journal of Physical Chemistry B*, Vol. 104, pp 2371.

Koops, S. E. & Durrant, J. R. (2008). "Transient emission studies of electron injection in dye sensitised solar cells." *Inorganica Chimica Acta*, Vol. 361, pp 8.

Koumura, N., Wang, Z.-S., et al. (2006). "Alkyl-functionalized organic dyes for efficient molecular photovoltaics." *Journal of the American Chemical Society*, Vol. 128, pp 14256.

Kuang, D., Ito, S., et al. (2006). "Stable mesoscopic dye-sensitized solar cells based on tetracyanoborate ionic liquid electrolyte." *Journal of the American Chemical Society*, Vol. 128, pp 4146.

Lee, C.-W., Lu, H.-P., et al. (2009). "Novel zinc porphyrin sensitizers for dye sensitized solar cells: Synthesis and spectral, electrochemical, and photovoltaic properties." *Chemistry; A European Journal*, Vol. 15, pp 1403.

Liu, C.-Y., Tang, H., et al. (1996). "Effect of orientation of porphyrin single crystal slices on optoelectronic properties." *Journal of Physical Chemistry*, Vol. 100, pp 3587.

Liu, Y., Hagfeldt, A., et al. (1998). "Investigation of influence of redox species on the interfacial energetics of a dye-sensitized nanoporous TiO_2 solar cell " *Solar Energy Materials and Solar Cells*, Vol. 55, pp 267.

Lo, C.-F., Hsu, S.-J., et al. (2010). "Tuning spectral and electrochemical properties of porphyrin-sensitized solar cells." *Journal of Physical Chemistry C*, Vol. 114, pp 12018.

Marcus, R. A. (1964). "Chemical and electrochemical electron-transfer theory." *Annual Review of Physical Chemistry*, Vol. 15, pp 155.

Martinson, A. B. F., Elam, J. W., et al. (2007). "ZnO nanotube based dye sensitized solar cells." *Nano Letters*, Vol. 8, pp 2183.

Miyashita, M., Sunahara, K., et al. (2008). "Interfacial electron-transfer kinetics in metal-free organic dye sensitized solar cells: Combined effects of molecular structure of dyes and electrolytes." *Journal of the American Chemical Society*, Vol. 130, pp 17874.

Mor, G. K., Shankar, K., et al. (2006). "Use of highly-ordered TiO_2 nanotube arrays in dye-sensitized solar cells." *Nano Letters*, Vol. 2, pp 215.

Mori, S. & Asano, A. (2010). "Light intensity independent electron transport and slow charge recombination in dye-sensitized In_2O_3 solar cells: In contrast to the case of TiO_2." *Journal of Physical Chemistry C*, Vol. 114, pp 13113.

Mori, S., Nagata, M., et al. (2010). "Enhancement of incident photon-to-current conversion efficiency for phthalocyanine-sensitized solar cells by 3D molecular structuralization." *Journal of the American Chemical Society*, Vol. 132, pp 4054.

Mozer, A. J., Griffith, M. J., et al. (2009). "Zn-Zn porphyrin dimer-sensitised solar cells: Towards 3-D light harvesting." *Journal of the American Chemical Society*, Vol. 131,(43), pp 15621.

Mozer, A. J., Wagner, P., et al. (2008). "The origin of open circuit voltage of porphyrin-sensitised TiO$_2$ solar cells." *Chemical Communications*, Vol., pp 4741.

Nakade, S., Kanzaki, T., et al. (2005). "Role of electrolytes on charge recombination in dye-sensitized TiO$_2$ solar cell (1): The case of solar cells using the I$^-$/I$_3^-$ redox couple." *Journal of Physical Chemistry B*, Vol. 109, pp 3480.

Nazeeruddin, M. K., Pechy, P., et al. (2001). "Engineering of efficient panchromatic sensitizers for nanocrystalline TiO$_2$-based solar cells." *Journal of the American Chemical Society*, Vol. 123, pp 1613.

Nogueira, A. F. & Paoli, M.-A. D. (2001). "Electron transfer dynamics in dye sensitized nanoctystalline solar cells using a polymer electrolyte." *Journal of Physical Chemistry B*, Vol. 105, pp 7517.

O'Regan, B. & Grätzel, M. (1991). "A low-cost, high-efficiency solar cell based on dye-sensitized colloidal TiO$_2$ films." *Nature*, Vol. 353, pp 737.

O'Regan, B. C., Durrant, J. R., et al. (2007). "Influence of the TiCl$_4$ treatment on nanocrystalline TiO$_2$ films in dye-sensitized solar cells. 2. Charge density, band edge shifts, and quantification of recombination losses at short circuit." *Journal of Physical Chemistry C*, Vol. 111, pp 14001.

O'Regan, B. C., López-Duarte, I., et al. (2008). "Catalysis of recombination and its limitation on open circuit voltage for dye sensitized photovoltaic cells using phthalocyanine dyes." *Journal of the American Chemical Society*, Vol. 130, pp 2906.

Planells, M., Forneli, A., et al. (2008). "The effect of molecular aggregates over the interfacial charge transfer processes on dye sensitized solar cells." *Applied Physics Letters*, Vol. 92, pp 153506.

Sauvé, G., Cass, M. E., et al. (2000). "Dye sensitization of nanocrystalline titanium dioxide with osmium and ruthenium polypyridyl complexes." *Journal of Physical Chemistry B*, Vol. 104, pp 6821.

Shaheen, S. E., Ginley, D. S., et al. (2005). "Organic Based Photovoltaics: Towards Lower Cost Power Generation." *MRS Bulletin*, Vol. 20, pp 10.

Shockley, W. & Queisser, H. J. (1961). "Detailed balance limit of efficiency of p-n junction solar cells." *Journal of Applied Physics*, Vol. 32, pp 510.

Wagner, K., Griffith, M. J., et al. (2011). "Significant performance improvement of porphyrin-sensitised TiO$_2$ solar cells under white light illumination." *Journal of Physical Chemistry C*, Vol. 115, pp 317.

Wang, P., Zakeeruddin, S. M., et al. (2003). "A new ionic liquid electrolyte enhances the conversion efficiency of dye sensitized solar cells." *Journal of Physical Chemistry B*, Vol. 107, pp 13280.

Westermark, K., Rensmo, H., et al. (2002). "PES studies of Ru(dcbpyH2)2(NCS)2 adsorption on nanostructured ZnO for solar cell applications." *Journal of Physical Chemistry B*, Vol. 106, pp 10102.

Willis, R. L., Olson, C., et al. (2002). "Electron dynamics in nanocrystalline ZnO and TiO$_2$ films probed by potential step chronoamperometry and transient absorption spectroscopy." *Journal of Physical Chemistry B*, Vol. 106, pp 7605.

Zaban, A., Ferrere, S., et al. (1998). "Relative energetics at the semiconductor/sensitizing dye/electrolyte interface." *Journal of Physical Chemistry B*, Vol. 102, pp 452.

Zheng, H., Tachibana, Y., et al. (2010). "Dye sensitized solar cells based on WO$_3$." *Langmuir*, Vol. 26, pp 19148.

The Chemistry and Physics of Dye-Sensitized Solar Cells

William A. Vallejo L., Cesar A. Quiñones S. and Johann A. Hernandez S.
Universidad Nacional de Colombia,
Universidad de Cartagena
Universidad Distrital F.J.D.C, Bogotá,
Colombia

1. Introduction

Climate change is one of the major environmental problems that affect our society. At present annually more than 40 billons Tons of greenhouses gases are exhausted to atmosphere and the tendency is to the rise; the main reason for this situation is the high and uncontrolled use of fossil resource in energy generation. Development an environmental, friendly and reliable energy technology is a necessity. *Solar Energy* emerged as possible solution to confront this problem. This technology permits a direct conversion of sunlight into electrical power without exhaust of both greenhouse gases and another polluting agent. Actually silicon technology is market leader in photovoltaic technologies, however since a pioneering (Grätzel & O'Regan, 1991) dye-sensitized solar cells (DSSCs) have become in one important and promising technology in photovoltaic field. DSSCs given born to new solar cells generation replaced classical solid-state homo and hetero-junction device by a new concept with a nano-working electrode in photo-electrochemical cell. This technology offers a very low cost fabrication and easy industry introduction prospective; furthermore efficiencies near to 10% AM1.5 for DSSCs have been confirmed. DSSCs consists of three main components: A dye-covered nanoporous TiO_2 layer on a glass substrate coated with a transparent conductive oxide (TCO) layer, an redox electrolyte and a electrical contact deposited on conducting glass. Different parameters affect efficiency of the DSSCs: types of materials used as electrolyte, dye and electric contact, and synthesis method used to obtain these materials. In this chapter DSSCs components and different aspects related with photovoltaic principles and DSSCs performance will be studied. Special emphasis will put on to review physical, chemical and electrochemical principles of DSSCs operation.

2. Mechanism operation

All photovoltaic devices present two important steps to convert sunlight into electrical energy:
1. Radiation absorption with electrical excitation.
2. Charge carriers separation.
The way which radiation is absorbed and carriers are separated are two of the main differences between DSSCs and classical p-n junction. Conventional photovoltaic principle

relies on differences in work functions between the electrodes of the cell in which photo-generated carriers could be separated, an asymmetry through cell is necessary to obtain electrical power. In classical p-n junction of solid state device the separation of photo-generated carriers relies on separation through depletion region built at p-n interface materials (Neamen, 1997). A different process occurs in DSSCs. Figure 1 shows typical scheme for DSSCs. The working electrode of DSSCs is conventionally constituted by mesoporous network of TiO_2 nanocrystalline (5-15μm, thickness) covered with a dye monolayer (conventionally Ru complex); this working electrode is supported on conducting glass (transparent conducting oxide, TCO). Different materials as platinum, palladium and gold could be use as counter-electrode of the cell; finally the gap between the electrodes is typically filled with a molten salt which containing a redox couple (A/A-); this salt is a hole conductor. Most DSSCs studied so far employ redox couple as iodide/tri-iodide (I-/I_3-) couple as electrolyte because of its good stability and reversibility (Pooman & Mehra), however others hole conductors as solid and ionic electrolytes also can be used. In overall process, the DSSCs generate electric power from light without suffering any permanent chemical transformation (Kelly & Meyer, 2001)
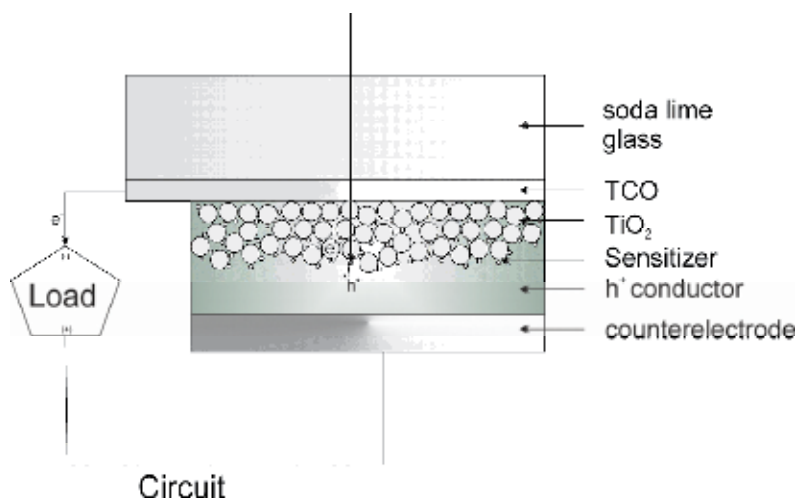
Fig. 1. General Structure of a dye-sensitized solar cell, the electron migration is showing.

In DSSCs, the basic photovoltaic principle relies on the visible photo-excitation of dye molecule; the esquematic reaction of overall process is follows:

$$TiO_2/D + h\nu \leftrightarrow TiO_2/D^*_{LUMO} \tag{1}$$

$$D^*_{LUMO} + CB_{TiO2} \rightarrow TiO_2/D^+ + e_{CB^-} \tag{2}$$

$$Pt + [I_3]^- \rightarrow 3I^- \tag{3}$$

$$TiO_2/D^+ + 3I^- \rightarrow [I_3]^- + D \tag{4}$$

$$e_{CB^-} + D_{HOMO} \rightarrow D + CB_{TiO2} \tag{5}$$

$$e_{CB^-} + [I_3]^- \rightarrow 3I^- + CB_{TiO2} \tag{6}$$
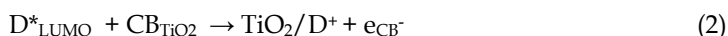
Where CB_{TiO2} is TiO_2 conduction band and D is dye molecule. First, an electron is photoexcited from highest occupied molecular orbital (HOMO) level to lowest unoccupied molecular orbital (LUMO) level into dye molecule (eq. 1). Then, electron injection from excited dye (D*) into TiO_2 conduction band occurs (eq. 2), excitation of dye usually is a transition-metal complex whose molecular properties are specifically for the task is able to transfer an electron to TiO_2 by the injection process. After that, electron migrates through TiO_2 network toward the TCO susbtrate (fig. 2(a)). The physics of charge transfer and transport in molecular and organic materials is dominated by charge localization resulting from polarization of the medium and relaxation of molecular ions. As a result of weak intermolecular interactions, the carriers in these materials are strongly localized on a molecule, and transport occurs via a sequence of charge-transfer steps from one molecule to other, similar to the hopping between defects states in inorganic semiconductors or band gap states in amorphous inorganic semiconductors. A main difference between organic and inorganic disordered semiconductors is the shape of the density of states (DOS). In the inorganic semiconductors, the band gap states usually follow an exponential distribution. The energies of localized states in organic conductors are widely distributed due to several causes: the fluctuation of the lattice polarization energies, dipole interactions, and molecular geometry fluctuations (Bisquert & Quiñones, 2006).
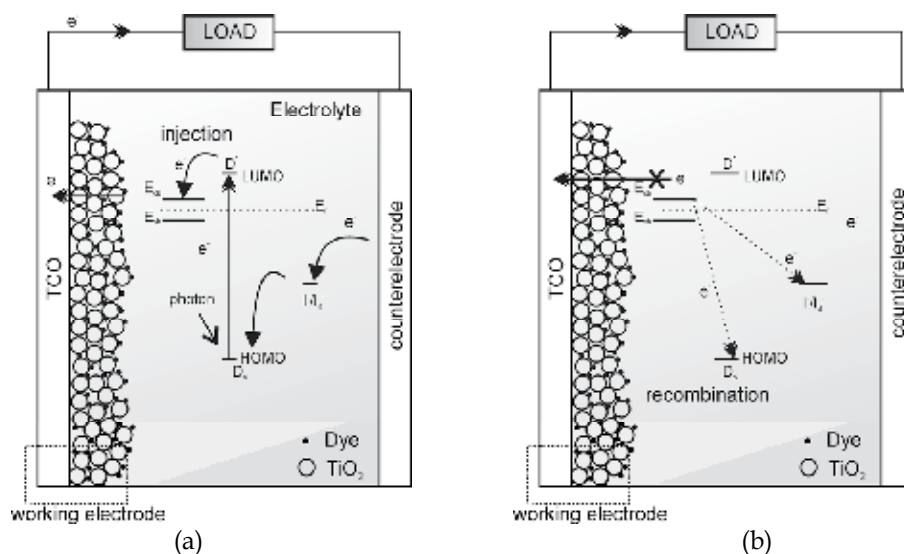
Fig. 2. (a) General schema for DSSCs, it is showed electron migration from dye molecule (D) through solar cell, (b) possible recombination process and, (c) Energy diagram for DSSCs.

Electron does a electric work at external load after go out from solar cell and then, come back through counterelectrode. Electrolyte transports the positive charges (holes) toward the counterelectrode and couple redox is reduced over its surface (eq. 3), on same time couple redox reduce the oxidized dye and regenerate the dye (eq. 4). Additionally In this process, some electrons can migrate from CB_{TiO2} to the HOMO level of the dye or electrolyte due to electron trapping effects; this process results in electron recombination (eq. 5, 6). These processes decrease the cell performance for affecting all its parameters (Fig. 2(b)); these process are presented because of differences on electron transfer rates between LUMO

level CB_{TiO2} and the electron transfer rate into CB_{TiO2} (Kay & Grätzel 2002, S.S. Kim et. al 2003, Grätzel 2004).To achieve a cell efficient operation, the electron injection rate must be faster than the decay of the dye excited state. Also, the rate of reduction of the oxidized sensitizer (D^+) by the electron donor in the electrolyte (eq. 4), must be higher than the rate of back reaction of the injected electrons with the dye cation (eq. 5), as well as the rate of reaction of injected electrons with the electron acceptor in the electrolyte (eq. 3). Finally, the kinetics of the reaction at the counter electrode must also guarantee the fast regeneration of redox couple (eq. 3) (Kalaignan & Kang, 2006). The oxidized dye must be regenerated by the redox couple at the speed of nanoseconds to kinetically compete with the metal oxide electrons for subsequent electron injection as well as to prevent the recombination, which depends on the energetic of metal oxide/dye/electrolyte interface (V. Thavasi et al, 2009).
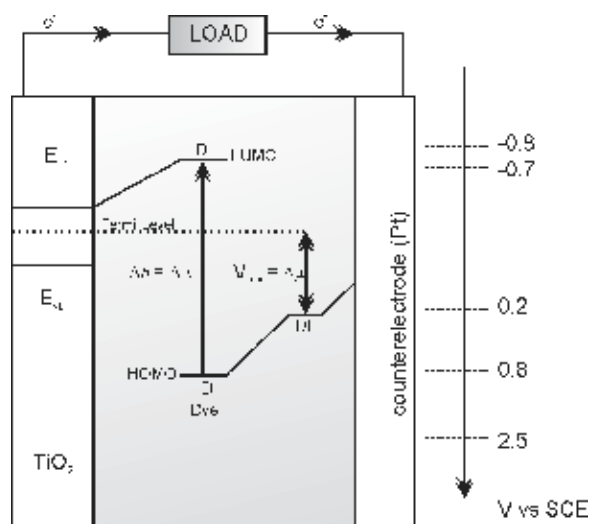
Fig. 3. General schema Energy diagram for DSSCs; and Voltage scale relative to SCE.

In terms of energetic levels shown in figure 3, electronic excitation in the dye (by light absorption) promotes the system into a high energy state, with associated electronic energy level, (LUMO level), simultaneously creating an electron deficient on low energy state (HOMO level). The electrons in these two states are separated by a difference in enthalpy *(h)*, as follows (Bisquert et al, 2004):

$$\Delta h = \Delta E = E_{LUMO} - E_{HOMO} \tag{7}$$

$$\Delta E = E_C - E_V \text{ (in semiconductors)} \tag{8}$$

The departure of the population of the states from their thermal equilibrium values implies a difference in their chemical potential ($\Delta\mu$) as follows:

$$\Delta\mu = \mu_{LUMO} - \mu_{HOMO} \tag{9}$$

$$\Delta\mu = \mu_C - \mu_V \text{ (in semiconductors)} \tag{10}$$

Efficient operation of DSSCs relies on both efficient electron injection and efficient dye regeneration. Additionally, the LUMO energy level should be sufficiently higher than the

TiO_2 conduction band (E_{CB}) for efficient electron injection. And the $\Delta\mu$ of the redox couple should be higher than the HOMO energy level for efficient dye regeneration and sustained photocurrent production (see fig. 3). The maximum voltage of a DSSCs under illumination corresponds to the difference of the TiO_2 Fermi level (E_f) and the $\Delta\mu$ of the electrolyte (relative to Standard Calomel Electrode, see figure 2(c)). In the DSSCs, the voltage is between 0.6-0.8V, and currents between 16-25mA/cm² can be achieved under standard operating conditions; the world record on efficiency is 10.4% (Wang 2010, Green 2010).

3. Constituents of DSSCs

3.1 Working electrode (TiO_2)

TiO_2 thin films are extensively studied because of their interesting chemical, electrical and optical properties; TiO_2 film in anatase phase could accomplish the photocatalytic degradation of organic compounds under the radiation of UV. Therefore, it has a variety of application prospects in the field of environmental protection (Quiñones & Vallejo, 2010). TiO_2 thin film in rutile phase is known as a good blood compatibility material and can be used as artificial heart valves. In addition, TiO_2 films are important optical films due to their high reflective index and transparency over a wide spectral range (Mechiakh et. al, 2010). Despite the existence of other types of oxide semiconductor with high band-gap and band gap positions as SnO_2 and ZnO, the TiO_2 thin films are the most investigated material as photo-electrode to be used in DSSCs; because of the efficiency DSSCs constructed with TiO_2 electrodes yield the highest values of Isc, Voc, η and the IPCE (Bandaranayake, 2004). In this section we will review the main characteristics of TiO_2 thin film used as photoelectrode.

3.1.1 Structural properties of TiO_2

Titanium dioxide presents three mainly different crystalline structures: *rutile, anatase,* and *brookite* structures; and other structures as *cotunnite* has been synthesized at high pressures; in table 1 are listed some physical and chemical properties for three major structures of TiO_2. Despite their three stable structures, only rutile and anatase play any role on DSSCs, the unit cell for anatase and rutile structures are shown in figure (4a,b); in both structures the building block consists of a titanium atom surrounded by six oxygen atoms in a more or less distorted octahedral configuration. In each structure, the two bonds between the titanium and the oxygen atoms at the aspices of the octahedron are slightly longer (U. Diebold , 2003). In figure 5 is shown a typical X-ray diffraction pattern (XRD) of TiO_2 thin film (about 14µm of thickness) deposited by Atomic Pressure Chemical Vapor Deposition (APCVD) method; the bigger peak observed at 2θ=25.16° corresponds to preferential crystalline plane (110) of the crystalline phase anatase. It is important take into account that crystalline structure depends on deposition method and synthesis conditions used to obtain TiO_2 thin films; and different methods have been used to deposit TiO_2 thin films. Among these are the Sol–gel method by hydrolysis of $Ti(OiPr)_4$ followed by annealing at 500–600 ∘C, chemical vapor deposition (CVD), physical vapor deposition, chemical bath deposition (CBD), reactive sputtering and atomic layer deposition (ALD) (Quiñones & Vallejo, 2010).

3.1.2 Electrochemical properties of TiO_2

It is broadly accepted that DSSCs efficiency is mainly governed by the kinetics of charge transfer at the interface between TiO_2, the dye, and the hole transport material.

a   b
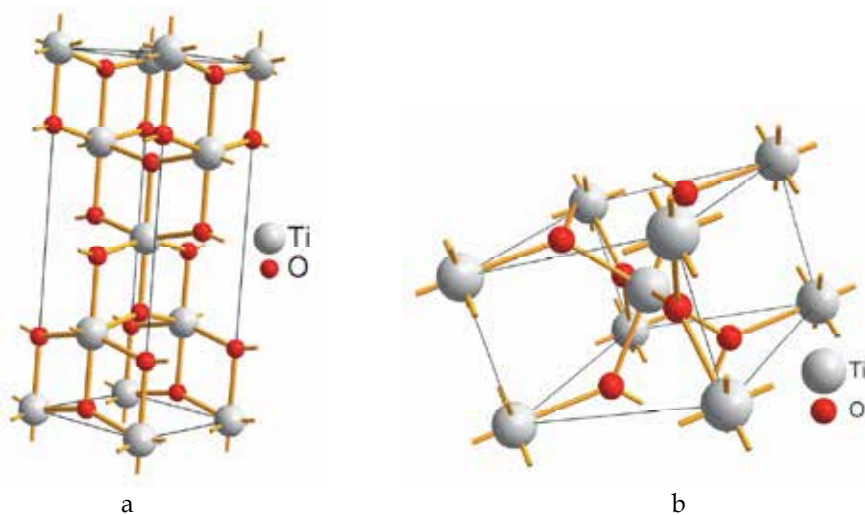
Fig. 4. Unit cell for: (a) anatase TiO_2 and (b) rutile TiO_2.
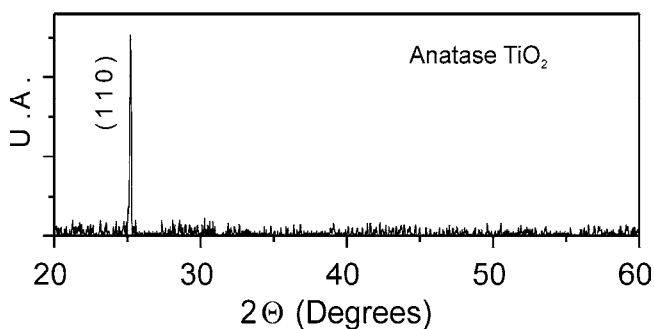
Fig. 5. XRD pattern of TiO_2 thin film, (take it on Shimadzu 6000 diffractometer with Cu-K$_\alpha$ radiation (λ = 0.15418 nm) source.

Crystal Structure	System	Space Group	Lattice constant (nm)			
			A	B	c	c/a
Rutile	Tetragonal	$D_{4h}^{14} - P4_2 / mnm$	0.4584	--	0.2953	0.644
Anatase	Tetragonal	$D_{4h}^{19} - I4_1 / amd$	0.3733	--	0.937	2.51
Brookite	Rhombohedral	$D_{2h}^{15} - Pbca$	0.5436	0.9166	0.5135	0.944

	Density (Kg/m³)	Band gap Energy (eV)	Standard heat capacity (J/mol °C)
Rutile	4240	3.0 Indirect	55.06
Anatase	3830	3.2 Indirect	55.52
Brookite	4170	----	298.15

Table 1. TiO_2 bulk properties

The initial steps of charge separation in a DSSCs are the injection of an electron from a photoexcited dye to the conduction band of the TiO_2 and subsequently, the transfer of an electron from the hole transport molecule to the dye (Figure 2). The first process is usually completed within 200 ps, and the latter, the regeneration of the oxidized dye, is completed within the nanosecond time scale for liquid electrolyte DSSCs containing an (I^-/I_3^-) redox couple (Bisquert & Quiñones, 2006). It is very important to study this phenomenon with an appropriate analytical technique. Electrochemical impedance spectroscopy (EIS) is an experimental method of analyzing electrochemical systems; this method can be used to measure the internal impedances for the electrochemical system over a range of frequencies between mHz-MHz (Wang et al, 2005); additionally EIS allows obtaining equivalent circuits for the different electrochemical systems studied. Figure 6(a) shows a typical equivalent circuit for DSSCs; this model has four internal impedances. The first impedance signal (Z_1) related to the charge transfer at the platinum counter electrode in the high-frequency peak (in kHz range) and the sheet resistance (R_h) of the TCO in the high frequency range (over 1 MHz); the second signal (Z_2) related to the electron transport in the TiO_2/dye/electrolyte interface in the middle-frequency peak (in the 1–100 Hz), and the third signal (Z_3) related to the Nernstian diffusion within the electrolyte in the low-frequency peak (in the mHz range); in figure 6(b) is shown Nyquist diagram of a DSSCs from the result of a typical EIS analysis. Finally, the total internal impedance of the DSSCs is expressed as the sum of the resistance components (R_1, R_2, R_3, and R_h). High performance of the DSSCs is achieved when this total internal resistance is small (Shing et al, 2010).
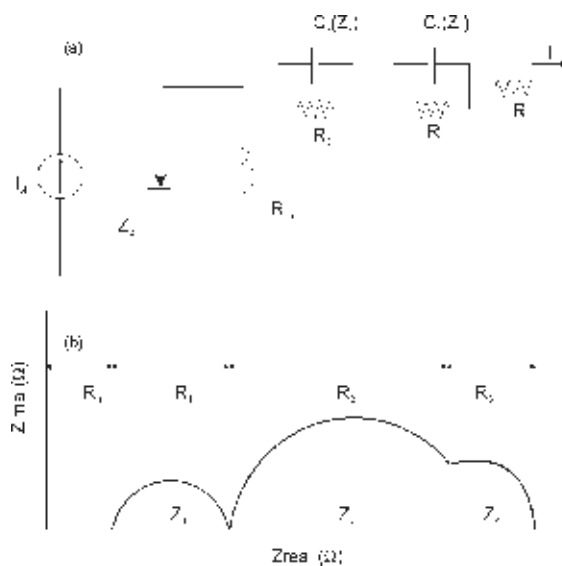
Fig. 6. Scheme of: (a) Equivalent circuit model for DSSCs and (b) Nyquist plot of the DSSCs from EIS analysis (adapted from Shin, 2010).

When you compared the equivalent circuit for DSSCs and conventional pn-junction solar cells, appears two large capacitance elements C_1 (in 10 µF/Cm^2 range) and C_3 (in 1F/Cm^2 range). Additionally R_{sh} can be described as (Islam & Han, 2006):

$$R_s = R_h + R_1 + R_3 \tag{11}$$

Under direct current conditions, the equivalent circuit for DSSCs is similar to conventional equivalent circuit for conventional solar cells, although the working mechanism is very different.

3.2 Sensitizer

One drawback with DSSCs is the high band gap of the core materials, e.g. TiO_2 particles <50–70nm in size (3.2 eV, wavelength <385nm in the ultraviolet range), compared to other semiconductors, which is illustrated by its absorption of UV light but not visible light. In the case of solar ultraviolet rays, only 2–3% of the sunlight (in the UV spectrum) can be utilized (Lee & Kang, 2010). To solve this, it appears the main characteristic of DSSCs: the dye, one of the most important constituents of the DSSCs. Some of the requirements that an efficient sensitizer has to fulfill include:

- A broad and strong absorption, preferably extending from the visible to the near-infrared.
- Minimal deactivation of its excited state through the emission of light or heat.
- Irreversible adsorption (chemisorption) to the surface of the semiconductor and a strong electronic coupling between its excited state and the semiconductor conduction band.
- Chemical stability in the ground as well as in the excited and oxidized states, so that the resulting DSSCs will be stable over many years of exposure to sun light.
- A reduction potential sufficiently higher (by 150–200mV) than the semiconductor conduction band edge in order to bring about an effective electroninjection.
- An oxidation potential sufficiently lower (by 200–300mV) than the redox potential of the electron mediator species, so that it can be regenerated rapidly.

A variety of transition-metal complexes and organic dyes has been successfully employed as sensitizers in DSSCs thus far, however the most efficient photosensitizers are ruthenium(II) polypyridyl complexes that yielded more than 11% sunlight to electrical power conversion efficiencies. The first two sensitizers used in DSSCs were N3 and N719. These are showed in figure 7. The molecular difference between these two compounds is the presence of tetrabutylammoniun ion to form two esters groups in N719. N3 and N719, affording DSSCs with overall power conversion efficiencies of 10.0% and 11.2 %respectively, harvest visible light very efficiently with their absorption threshold being at about 800 nm; figure 7 shows also the UV/VIS curve for N3 and N719 dyes, this profile is typical for al Rutenium complex used as dyes in DSSCs. Other important issue concerning dyes is their cost. Ruthenium, for instance, which is currently the most commonly utilized metal in metal-containing dyes for DSSCs, is a rare metal with a high price. Despite the fact that the contribution of the sensitizer to the total cell cost is limited, as efficient light harvesting requires a monolayer of sensitizer molecules, stable long-living ruthenium-based dyes are always highly desirable. Efficient, ruthenium-free sensitizers could also lead to such a cost decrease (Vougioukalakis et al, 2010).

Since the first Grätzel report, special attention has been paid to a number of details in the development of sensitizers in order to improve the photoelectric conversion efficiency and stability. A series of modifications of these early Ru(II) complexes have, among others, led to sensitizers with amphiphilic properties and/or extended conjugation. These amphiphilic new dyes try to achieve some of the following properties:

- A higher ground state pK_a of the binding moiety thus increasing electrostatic binding onto the TiO_2 surface at lower pH values.

- The decreased charge on the dye attenuating the electrostatic repulsion in between adsorbed dye units and thereby increasing the dye loading.
- Increasing the stability of solar cells towards water-induced dye desorption.
- The oxidation potential of these complexes is cathodically shifted compared to that of the N3 sensitizer, which increases the reversibility of the ruthenium III/II couple, leading to enhanced stability.
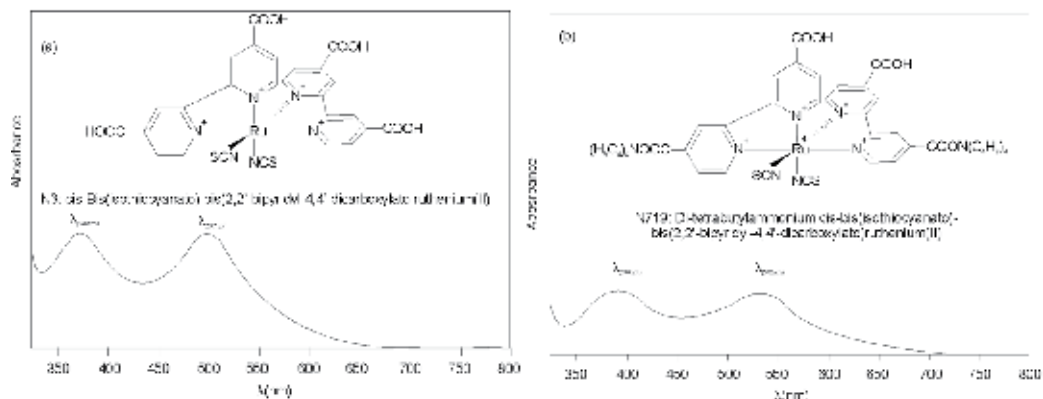
Fig. 7. Molecular structure of: (a) N3 and (b)N719.
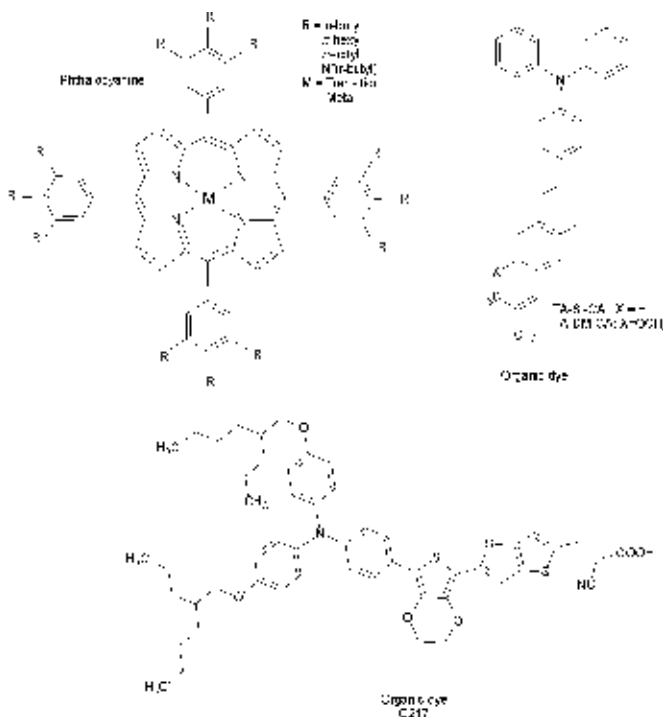
Fig. 8. The molecular structures of tetrakis(4-carboxyphenyl)porphyrin (Phthalocyanine) and two organic dyes (adapted from Vougioukalakis et al, 2010).

With respect to metal polypyridine complexes, organic dyes have been less investigated for sensitization of wide band gap semiconductors. Apart from the coumarin derivative, organic dyes such as porphyrins, phthalocyanines, perylene bis-amides, xanthenes and polyenes show low photon to electron conversion efficiencies. The understanding of the factors that determine these low performances could lead to the development of new efficient dyes, cheaper to manufacture than transition metal complexes (Argazzi et al, 2004). Figure 8 (a) shows some typical molecular structure of a basic phthalocyanine, (special polypyridine complexes); in this figure, R means a radical like: *t*-butl, *n*-hexil, *n*-octyl, in some cases R can be a substituted amine, and M means a metallic cation. Figure 8(b) shows some organic dye sensitizers used in DSSCs; TA-St-CA nad TA-TM-TA dyes contain a p-conjugated oligo-phenylenevinylene unit with an electron donor–acceptor moiety for intramolecular charge transfer, and a carboxyl group as an anchoring unit for the attachment of the dye onto TiO_2 nanoparticles; efficiences about 9% have been reported for DSSCs based in organic dyes. Additionally, C217 dye employing a lipophilic dihexyl oxy-substituted triphenylamine electrondonor, a cyanoacrylic electron acceptor, a distinguishable feature of this new amphiphilic D–π–A chromophore consists in a binary π-conjugated spacer. Here, an electron-rich 3,4-ethylenedioxythiophene unit is connected to electron-donor to lift the energy of the highest occupied molecular orbital (HOMO), while thienothiophene conjugated with A leads to a suitable lowest unoccupied molecular orbital (LUMO) energy; DSSCs based on C217 dye have reported efficiencies about 9.8%.

3.3 Electrolyte solution
3.3.1 Volatile Organic Solvents (VOS)
A typical DSSCs consists of a dye-coated mesoporous TiO_2 nano-particle film sandwiched between two conductive transparent electrodes, and a liquid electrolyte traditionally containing the (I^-/I_3^-) couple redox to fill the pores of the film and contact the nano-particle. The electrolyte, as one of the key components of the DCCS, provides internal electric ion conductivity by diffusing within the mesoporous TiO_2 layer and is an important factor for determining the cell performance (Wang, 2009). Volatile organic solvents (VOS) are commonly used as electrolyte (hole conductor), and nowadays, high efficiencies can be obtained for DSSCs using electrolytes based on VOS. When you compare the IPEC peak of a DSSCs construed with different types of electrolyte solutions, the biggest values are obtained with VOS; conventionally it IPEC peak value is about (74-78%) whilst others as ionic electrolytes present values about 53% and less solar efficiency. Typical VOS are acetonitrile, propionitrile, methoxyacetonitrile, and methoxypropionitrile, which present a high degree of ion conductivity, relatively high dielectric constant and ability to dissolve electrolytes; figure 9 shows the chemical strucuture of some typical VOS used in DSSCs.

Fig. 9. Chemical strucuture of some typical VOS used in DSSCs.

Despite the relative high efficiency values of VOS in DSSCs (about 10%), the usage of these VOS electrolytes seriously limits a large scale implementation of this technology due to the poor long-term stability of the cells and the necessity of a complex sealing process (Wachter

et al, 2010). Today this is one of the major drawbacks of DSSCs to implementation in a factory production line, and a new field research tries to replace the VOS in DSSCs by new type of electrolytes as: ionic liquid electrolytes, p-type inorganic semiconductors and polymer electrolytes. In principle, all materials with p-type semiconducting behavior, capable of accepting holes from the dye cation, are potential candidates to replace the liquid electrolyte in DSSCs. We will review main aspects of these possible substitutes.

3.3.2 Ionic liquid electrolytes

As an alternative to VOS, the use of room temperature ionic liquids (RTIL) and low molecular weight organic solvents with polar ligand have received considerable attention in recent decades. RTIL have several superior properties such as the non-volatility, chemical stability, not inflammability and high-ionic conductivity at room temperature. Nevertheless, the viscosity of the non-volatile solvents is usually higher than those of conventional volatile solvents, leading the energy conversion efficiency, which does not reach those of DSSCs employing conventional VOS electrolytes. The viscosity of typical ionic liquids is about 100 times larger than conventional VOS, and also 30 times larger than water at room temperature. Photocurrents in such systems are affected by the series resistances of the electrolytes, which are usually in proportion to the viscosity.

Fig. 10. Chemical strucuture of some typical ionic liquid electrolytes used in DSSCs (adapted from Zafer et al, 2009).

The low mass transport of redox couples is a limiting factor of applicability of these solvents in DSSCs. Therefore, high concentration of redox couples is required to obtain considerable conductivity in the electrolyte medium; however, in this case, the dark current may be increased owing to the high concentration of redox couples near to dye-attached to TiO_2 and the photocurrent generation is also interrupted by the absorption of visible light into the electrolyte medium (Kang et al, 2008). Currently, RTIL based on 1,3-dialkilimidazolium salts, have been studied as a electrolyte components for DSSCs. Relatively high viscosity of these type electrolytes appears to limit their applications. In order to improve charge transport properties, di-cationic bis-imidazolium based Ionic liquid electrolytes (ILs) with alkyl and polyether chains have been successfully investigated. Polyether groups improve the self organization of molecules in electrolyte which increase the charge transfer and the wetting capacity of the TiO_2 surface. Overall light-to-electric conversion efficiencies of 5.6%

have been achieved by dicationic bis-imidazolium iodide under simulated sunlight (Zafer et al 2009). It is of great interest that the fill factors of ionic liquid electrolytes-based DSSCs easily reach extremely high values of over 75% even in full sunlight. Dilution of the same ionic liquid with a low-viscosity organic solvent often decreases the fill factor. Figure 10 shows the chemical strucuture of some typical ionic liquids electrolytes used in DSSCs.

3.3.3 P-type semiconductors

The most common approach to fabricate solid-state DSSCs is by using p-type semiconductors. Several aspects are essential for any p-type semiconductor in a DSSCs:

- It must be able to transfer holes from the sensitizing dye after the dye has injected electrons into the TiO_2; that is, the upper edge of the valence band of p-type semiconductors must be located above the ground state level of the dye.
- It must be able to be deposited within the porous nanocrystalline layer.
- A method must be available for depositing the p-type semiconductors without dissolving or degrading the monolayer of dye on TiO_2 nanocrystallites.
- It must be transparent in the visible spectrum, or, if it absorbs light, it must be as efficient in electron injection as the dye.

Many inorganic p-type semiconductors satisfy several of the above requirements. However, the familiar large-band gap p-type semiconductors such as SiC and GaN are not suitable for use in DSSCs since the high-temperature deposition techniques for these materials will certainly degrade the dye. After extensive experimentation, a type of inorganic p-type semiconductor based on copper compounds such as CuI, CuBr, or CuSCN was found to meet all of these requirements (Li et al, 2006).

3.3.4 Polymer electrolytes

According to the physical state of the polymer, there are two types of polymer electrolytes used in DSSCs: (1) solid polymer electrolytes and (2) gel polymer electrolytes.

3.3.4.1 Solid polymer electrolytes

Compared with inorganic p-type semiconductors, organic p-type semiconductors (i.e. organic hole-transport materials) possess the advantages of having plentiful sources, easy film formation and low cost production. However, the conversion efficiencies of most of the solid-state DSSCs employing organic p-type semiconductors are relatively low particularly under high light irradiation. This is due to the low intrinsic conductivities of organic hole-transport material (HTMs), the high frequencies of charge recombination from TiO_2 to HTMs, and the poor electronic contact between dye molecules and HTMs, because of incomplete penetration of solid HTMs in the pores of the mesoporous TiO_2 electrodes. The ionic conductivity of solid polymer electrolytes is dependent on molar ratio of the polymer and the iodide salt due to the transfer efficiency of charge carriers and complex formation between metal cations and polymer atoms.

3.3.4.2 Gel polymer electrolytes (GPE)

Compared to other types of HTM, GPE are constructed by trapping liquid electrolytes, which usually contain organic solvents and inorganic salt ssuch as propylene (PC), Ehylene Carbonate (EC) or acetonitryle, lithium iodide (LiI), sodium iodide (NaI) and potassium iodide (KI). Compared to the corresponding parameters of the DSSCs based on liquid electrolytes, after gelation the decrease of J_{SC} (short-circuit density) due to the comparatively

lower conductivity and the increase of VOC (open-circuit voltage) because of the suppression of dark current by polymer chains covering the surface of TiO_2 electrode result in the almost same efficiency for the DSSCs with GPE and with liquid electrolytes. Achieved by ''trapping'' a liquid electrolyte in polymer cages formed in a host matrix, GPE have some advantages, such as low vapor pressure, excellent contact in filling properties between the nanostructured electrode and counter-electrode, higher ionic conductivity compared to the conventional polymer electrolytes. Furthermore GPE possess excellent thermal stability and the DSSCs based on them exhibit outstanding stability to heat treatments. There was negligible loss in weight at temperatures of 200°C for ionic liquid-based electrolytes of poly (1-oligo(ethyleneglycol) methacrylate-3-methyl-imidazoliumchloride) (P(MOEMImCl). Thus the DSSCs based on GPE have outstanding long-term stability. Therefore, GPE have been attracting intensive attentions and these advantages lead to broad applications in the DSSCs Nowadays, several types of GPEs based on different types of polymers have already been used in the DSSCs, such as poly(acrolynitrile), poly(ethyleneglycol), poly(oligoethylene glycol methacrylate), poly(butylacrylate), the copolymers such as poly(siloxane-co-ethyleneoxide) and PVDF-HFP (Wang, 2009).

3.4 Redox couple

It is well known that the iodide salts play a key role in the ionic conductivity in DSSCs. Moreover, the basis for energy conversion is the injection of electrons from a photoexcited state of the dye sensitizer into the conduction band of the TiO_2 semiconductor on absorption of light. However, despite of its qualities; (I^-/I_3^-) couple redox has some drawbakcs, such as the corrosion of metallic grids (e.g., silver or vapor-deposited platinum) and the partial absorption of visible light near 430 nm by the I_3^- species. Another drawback of the (I^-/I_3^-) couple is the mismatch between the redox potentials in common DSSCs systems with Ru-based dyes, which results in an excessive driving force of 0.5~0.6 eV for the dye regeneration process. Because the energy loss incurred during dye regeneration is one of the main factors limiting the performance of DSSCs, the search for alternative redox mediators with a more positive redox potential than (I^-/I_3^-) couple is a current research topic of high priority. In order to minimize voltage losses, due to the Nernst potential of the iodine-based redox couple, and impede photocurrent leakage due to light absorption by triiodide ions, other redox couples have been also used, such as $SCN^-/(SCN)^3$; $SeCN^-/(SeCN)^{3-}$, (Co^{2+}/Co^{3+}), (Co^+/Co^{2+}), coordination complexes, and organic mediators such as 2,2,6,6-tetramethyl-1-piperidyloxy (Min et al, 2010). Notwithstanding of different options and alternatives to replace (I^-/I_3^-) couple redox: this system presents highst solar cell efficiency. Additional, alternatives have been proposal to improve the efficiency of this type of DSSCs, as the adition of organic acid to electroylte solution or others aditives but until now best effiency has been reached with (I^-/I_3^-) couple redox.

3.5 Counter electrode

In DSSCs, counter-electrode is an important component, the open-circuit voltage is determined by the energetic difference between the Fermi-levels of the illuminated transparent conductor oxide (TCO) to the nano-crystalline TiO_2 film and the platinum counter-electrode where the couple redox is regenerated (McConnell, 2002). Platinum counter-electrode is usually TCO substrate coated with platinum thin film. The counter-electrode task is the reduction of the redox species used as a mediator in regenerating the sensitizer after electron injection, or collection of the holes from the hole conducting

materials in DSSCs (Argazzi et al, 2004). Electrochemical impregnation from salts and physical deposition such as sputtering are commonly employed to deposit platinum thin films. Chemical reduction of readily available platinum salts such as H_2PtCl_6 or $Pt(NH_3)_4Cl_2$ by $NaBH_4$ is a common method used to obtain platinum electrodes. Platinum has been deposited over or into the polymer using the impregnation–reduction method (Yu et al, 2005). It is known that the final physical properties of Pt thin films depend on deposition method. Figure 11 shows SEM images of platinum thin films deposited by sputtering and electrochemical method as function of substrate type. Figure 11(a) corresponds to TCO substrate without platinum thin film, and Figure 11(b) shows a platinum thin film on TCO substrates deposited by electrochemical method. It is clear that TCO substrate grain size is smaller than platinum thin film grain size; this figure shows different size grain and Pt particles distribute randomly through out the substrate surface; this image shows some cracks in some places of the substrate. Furthermore, figure 11(c) shows platinum thin films deposited on TCO by sputtering method, it shows that platinum thin films have better uniformity than platinum thin film deposited by electrochemical method and the size grain is greater than size grain of thin film deposited by electrochemical method. In fig. 11(c) the Pt particles are distributed randomly through out the substrate without any crack; this is different to the electrochemical method, and indicates that the surface is uniformly coated. This thin film is less rough and corrects imperfections of substrate. Finally platinum thin film grown on glass SLG shows both smaller size grain particles and lower uniformity than platinum thin film deposited on TCO (Quiñones & Vallejo, 2011).
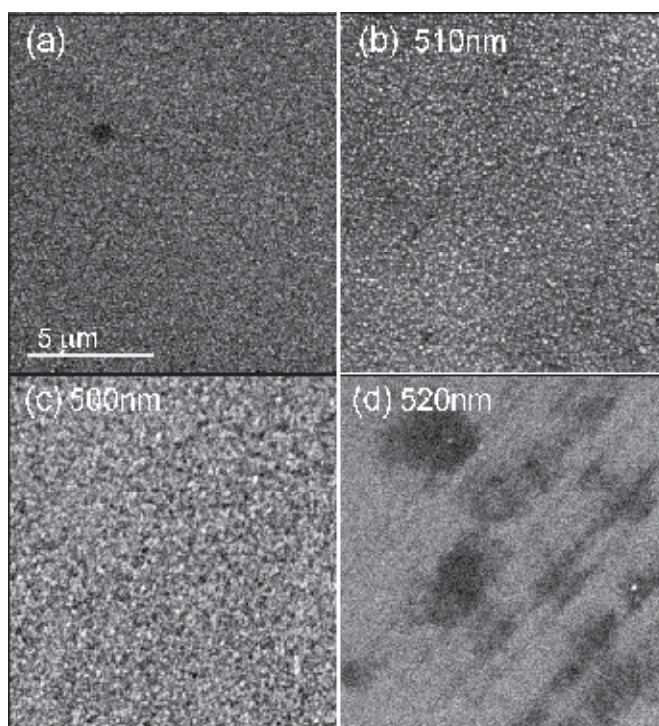
Fig. 11. SEM images (20000x) from: (a) TCO substrate; (b) Pt/TCO by electrochemical method; (c) Pt/TCO by sputtering; (d) Pt/SLG by sputtering (Quiñones & Vallejo et al, 2011).

Despite Pt has been usually used as counter electrode for the I_3^- reduction because of its high catalytic activity, high conductivity, and stability, Pt counter-electrode is one of the most expensive components in DSSCs. Therefore, development of inexpensive counter electrode materials to reduce production costs of DSSCs is much desirable. Several carbonaceous materials such as carbon nanotubes, activated carbon, graphite, carbon black and some metals have been successfully employed as catalysts for the counter electrodes. The results shows that carbonaceous materials not only gave ease in creating good physical contact with TiO_2 film but also functioned as efficient carrier collectors at the porous interface (Lei et al, 2010). Some possible substitutes to Pf thin films counter-electrode are:

3.5.1 Metal counter electrodes

Metal substrates such as steel and nickel are difficult to employ for liquid type DSSCs because the I^-/I_3^- redox species in the electrolyte are corrosive for these metals. However, if these surfaces are covered completely with anti-corrosion materials such as carbon or fluorine-doped SnO_2, it is possible to employ these materials as counter-electrodes. Metal could be beneficial to obtain a high fill factor for large scale DSSCs due to their low sheet resistance. Efficiencies around 5.2% have been reported for DSSCs using a Pt-covered stainless steel and nickel as counter-electrode (Murakami & Grätzel, 2008).

3.5.2 Carbon counter electrode

First report of carbon material as counter electrode in DSSCs was done by Kay and Grätzel. In this report they achieved conversion efficiency about 6.7% using a monolithic DSSCs embodiment based on a mixture of graphite and carbon black as counter electrode (Kay & Grätzel, 1997).
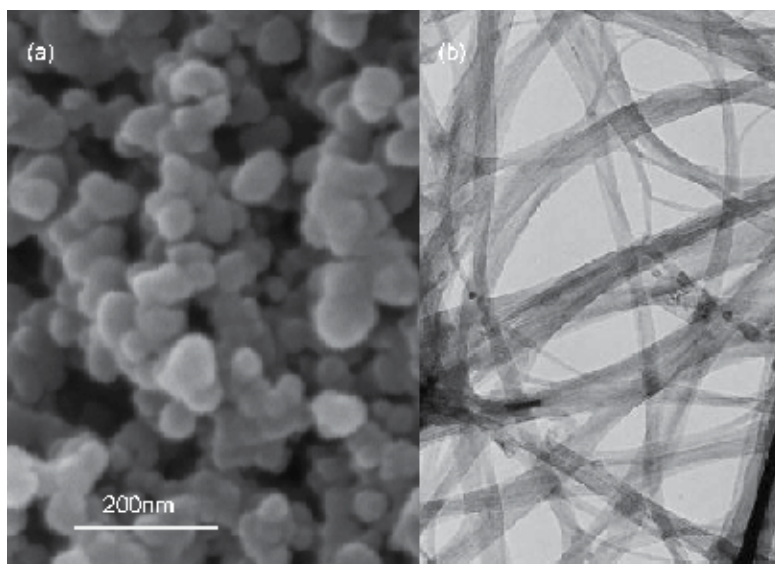
Fig. 12. SEM images (30000x) from: (a) Carbon nanoparticles and (b) Carbon nanotubes.

The graphite increases the lateral conductivity of the counter electrode and it is known that carbon acts like a catalyst for the reaction of couple redox (I_3^-/I^-) occurring at the counter

electrode. Recently, carbon nanotubes have been introduced as one new material for counter electrodes to improve the performance of DSSCs (Gagliardi et al, 2009). The possibility to obtain nanoparticles and nanotubes of carbon permits investigation of different configuration in synthesis of counter electrode fabrication, to improve the DSSCs efficiency. In figure 12 are showing the scanning electron microsocopy images of nanoparticles and nanotubes of carbon.

4. Efficiency and prospects

From first Grätzel report, the efficiency of DSSCs with nano-porous TiO_2 has not changed significantly. Currently, the world record efficiency conversion for DSSCs is around 10.4% to a solar cell of 1 cm² of area; in table 2 are shown the confirmed efficiencies for DSSCs.

The high efficiency (table 2) of DSSCs has promoted that many institutes and companies developed a commercial research on up-scaling technology of this technology. The Gifu University in Japan, developed colorful cells based on indoline dye and deposited with zinc oxide on large size of plastic substrate. The Toin University of Yokohama in Japan fabricated the full-plastic DSSCs modules based on low-temperature coating techniques of TiO_2 photoelectrode. Peccell Technologies in Japan, and Konarka in US, practiced the utility and commercialization study about flexible DSSCs module on polymer substrate. Léclanche S.A, in Switzerland, developed outer-door production of DSSCs. INAP in Germany gained an efficiency of 6.8% on a 400 cm² DSSCs module. However, despite prospective of DSSCs technology, the degradation and stability of the DSSCs are crucial topics to DSSCs up-scaling to an industrial production (Wang et al, 2010).

Device	Efficiency (%)	Area (cm²)	V_{oc} (V)	J_{sc} (mA)	FF	Test center
DSSCs$_{cell}$	11.2 +/-0.3	0.219	0.738	21	72.2	AIST*
DSSCs$_{cell}$	10.4+/-0.3	1.004	0.729	22.0	65.2	AIST
DSSCs$_{ubmodule}$	9.9+/-0.4	17.11	0.719	19.4	74.1	AIST

*Japanese National Institute of Advanced Industrial Science and technology.

Table 2. Confirmed terrestrial DSSCs efficiencies measured under the global AM1.5 spectrum (1000W/m²) at 25°C (Green et al 2010).

According to the operation principle, preparation technology and materials characteristics of DSSCs, they are susceptible to:

- Physical degradation: the system contains organic liquids which can leak out the cells or evaporate at elevated temperatures. This could be overcome using appropriate sealing materials and low volatiles solvents.
- Chemical degradation: The dye and electrolyte will photochemically react or thermal degrade under working conditions of high temperature, high humidity, and illumination. The performance DSSCs will irreversibly decrease during the process causing the life time lower than commercial requirements (>20 years)

Unfortunately, there are not international standards specific in DSSCs. Nowadays, most of the performance evaluation of DSSCs is done according to International electrotechnical commission (IEC), norms (IEC-61646 and IEC-61215), prepared for testing of thin film photovoltaic modules and crystalline silicon solar cells. Most of the on up-scaling technology was made with these IEC international standards (Wang et al, 2010).

5. Conclusion

In this Chapter, the physics and chemistry of the dye sensitizer solar cells were reviewed using own studies and some of the last reports in the area. Different aspects related with basic principle and developments of each component of the solar cell was presented. This type of technology presents different advantages with its homologues inorganic solar cells, and nowadays DSSCs are considered one economical and technological competitor to pn-junction solar cells. This technology offers the prospective of very low cost fabrication and easy industry introduction. However, the module efficiency of DSSCs needs to be improved to be used in practical applications. It is necessary to achieve the optimization of the production process to fabricate photoelectrodes with high surface area and low structural defects. It is necessary to solve problems asociated to encapsulation of (I^-/I_3^-) redox couple in an appropiate medium such Ionic liquid electrolytes, p-type semiconductors, Solid polymer electrolytes, Gel polymer electrolytes and the deposited stable and cheap counterelectrode. If this problems are solved is possible that in near future DSSCs technology will become in a common electrical energy source and widely used around the world.

6. References

O'Regan, M. Grätzel (1991). A low cost high efficiency solar cell based on dye sensitized colloidal TiO_2. *Nature,* Vol. 353, pp. 737–740.

Donald Neamen (1997). *Semiconductor Physics and Deivices*, Second Edition, Mc Graw Hill, pp. 130.

S. Pooman, R. M. Mehra (2007). Effect of electrolytes on the photovoltaic performance of a hybrid dye ZnO solar cell. *Solar Energy Materials & Solar Cells*, Vol. 91, pp. 518-524.

C.A. Kelly, G.J. Meyer (2001). Excited state processes at sensitized nanocrystalline thin film semiconductor interfaces. *Coordination Chemistry Reviews*. Vol. 211, pp. 295.

M. Grätzel (2004). Conversion of sunlight to electric power by nanocrystalline dye-sensitized solar cells. *Journal of Photochemistry and Photobiology A: Chemistry*. Vol. 164, pp. 3–14.

A. Kay, M. Grätzel (2002). Dye-Sensitized Core-Shell Nanocrystals: Improved Efficiency of mesoporous Tin Oxide Electrodes Coated with a thin layer of an Isulating Oxide. *Chemistry of Materials*, Vol. 14 pp. 2930.

S.S. Kim, J.H. Yum, Y.E. Sung (2003). Improved performance of a dye-sensitized solar cell using a $TiO_2/ZnO/Eosin$ Y electrode. *Solar Energy Materials & Solar Cells*. Vol. 79, pp. 495.

G. Kalaignan, Y. Kang (2006). *Journal of Photochemistry and Photobiology C: Photochemistry Reviews*, Vol. 7 pp. 17–22.

V. Thavasi, V. Renugopalakrishnan, R. Jose, S. Ramakrishna (2009). Controlled electron injection and transport at materials interfaces in dye sensitized solar cells. *Materials Science and Engineering: Reports,* Vol. 63 pp. 81–99.

J. Bisquert, D. Cahen, G. Hodes, S. Rühle, A. Zaban, (2004). Physical Chemical Principles of Photovoltaic Conversion with Nanoparticulate, Mesoporous Dye-Sensitized Solar Cells. *Journal of Physical Chemistry B,* Vol. 108 pp. 8106

J. Bisquert, E. Palomares, C. Quiñones, (2006). Effect of Energy Disorder in Interfacial Kinetics of Dye-Sensitized Solar Cells with Organic Hole Transport Material. *The Journal of Physical Chemistry B*, Vol. *110, pp.* 19406-19411.

M. Wang, J. Liu, N. Cevey-Ha, S. Moon, P. Liska, R. Humphry-Baker, J. Moser, C. Grätzel, P. Wang, S. Zakeeruddin, M Grätzel (2010). High Efficiency solid-state sensitized heterojunction photovoltaic device. *Nano Today,* Vol. 5, pp. 169-174.

M. A. Green, K. Emery, Y. Hishikawa, W. Warta (2011). Solar cell efficiency tables (version 37). *Progress in Photovoltaics: Research and Applications.* Vol. 19, pp. 84.

C. Quiñones, J. Ayala, W. Vallejo (2010). Methylene blue photoelectrodegradation under UV irradiation on Au/Pd-modified TiO$_2$ films. Applied Surface Science, Vol. 257, pp. 367–371

C. Quiñones, W. Vallejo, G. Gordillo (2010). Structural, optical and electrochemical properties of TiO2 thin films grown by APCVD method'. *Applied Surface Science* Vol. 256, pp. 4065–4071.

R. Mechiakh, N. Ben Sedrine, R. Chtourou, R. Bensaha (2010). Correlation between microstructure and optical properties of nano-crystalline TiO$_2$ thin films prepared by sol–gel dip coating. *Applied Surface Science,* Vol. 257 pp. 670–676.

K.M.P. Bandaranayake, M.K. I. Senevirathna, P. Weligamuwa, K. Tennakone (2004). Dye-sensitized solar cells made from nanocrystalline TiO$_2$ films coated with outer layers of different oxide materials. *Coordination Chemistry Reviews*, Vol 248, pp. 1277–1281.

U. Diebold (2003). The Surface Science of TiO$_2$. *Surface Science Reports*, Vol. 48, pp. 53.

Bin Li, Liduo Wang, Bonan Kang, Peng Wang, Yong Qiu (2006). 'Review of recent progress in solid-state dye-sensitized solar cells'. *Solar Energy Materials & Solar Cells,* Vol. 90 pp. 549–573.

Y. Lee, M. Kang (2010). Comparison of the photovoltaic efficiency on DSSCs for nanometer sized TiO2 using a conventional sol–gel and solvothermal methods. *Journal of Industrial and Engineering Chemistry*, Vol. 122, pp. 284–289.

P. Wachter, M. Zistler, C. Schreiner, M. Berginc, U. O. Krasovec, D. Gerhard, P. Wasserscheid, A. Hinsch, H. J. Gores (2008). *Journal of Photochemistry and Photobiology A: Chemistry,* Vol. 197, pp. 25–33.

B. Lei, W. Fang, Y. Hou, J. Liao, D. Kuang, C. Su (2010). Characterisation of DSSCs-electrolytes based on 1-ethyl-3-methylimidazolium dicyanamide: Measurement of triiodide diffusion coefficient, viscosity, and photovoltaic performance'. *Journal of Photochemistry and Photobiology A: Chemistry*, Vol. 216, pp. 8–14.

Y. Wang (2009). Recent research progress on polymer electrolytes for dye-sensitized solar cells. *Solar Energy Materials & Solar Cells*, Vol. 93, pp. 1167–1175.

A. Luque, S. Hegedus. *Handbook of Photovoltaic Science and Enginnering*. John Wiley & Sons. USA. 2005.

M. Kang, K. Ahn, J. Lee, Y. Kang. Dye-sensitized solar cells employing non-volatile electrolytes based on oligomer solvent. *Journal of Photochemistry and Photobiology A: Chemistry* 195 (2008) 198–204

C. Zafer, K. Ocakoglu, C. Ozsoy, S. Icli. Dicationic bis-imidazolium molten salts for efficient dye sensitized solar cells: Synthesis and photovoltaic properties. *Electrochimica Acta* 54 (2009) 5709–5714.

A. J. Frank, N. Kopidakis, J. V. Lagemaat (2004). Electrons in nanostructured TiO$_2$ solar cells: transport, recombination and photovoltaic properties. *Coordination Chemistry Reviews*, Vol. 248, pp. 1165–1179.

J. Min, J. Won, Y.S. Kang, S. Nagase (2010). Benzimidazole derivatives in the electrolyte of new-generation organic dyesensitized solar cells with an iodine-free redox mediator. *Journal of Photochemistry and Photobiology A: Chemistry* (2010). doi:10.1016/j.jphotochem.2011.02.004

R. Argazzi, N. Iha, H. Zabri,F. Odobel, C. Bignozzi (2004). Contributions to the development of ruthenium-based sensitizers for dye-sensitized solar cells. *Coordination Chemistry Reviews*, Vol. 248, pp. 1299–1316.

P. Yu, J. Yan, J. Zhang, L. Mao. Cost-effective electrodeposition of platinum nanoparticles with ionic liquid droplet confined onto electrode surface as micro-media. *Electrochemistry Communications*, Vol. 9, pp. 1139–1144.

R.D. McConnell (2002). Assessment of the dyesensitized solar cell. *Renewable & Sustainable Energy Reviews*, Vol. 6, pp. 273–295.

G. C. Vougioukalakis, A.Philippopoulos, T. Stergiopoulos, P. Falaras (2010). Contributions to the development of ruthenium-based sensitizers for dye-sensitized solar cells. *Coordination Chemistry Reviews* (2010),doi:10.1016/j.ccr.2010.11.006

T. N. Murakami, M. Grätzel (2008). Counter electrodes for DSC: Application of functional materials as catalysts. *Inorganica Chimica Acta*, Vol. 361 pp. 572–580

A. Kay, M. Grätzel. On the relevance of mass transport in thin layer nanocrystalline photoelectrochemical solar cells. *Solar Energy Materials & Solar Cells,* Vol. 44, pp. 99.

S. Gagliardi, L. Giorgi, R. Giorgi, N. Lisi, Th. D. Makris, E. Salernitano, A. Rufoloni (2009). Impedance analysis of nanocarbon DSSCs electrodes. *Superlattices and Microstructures*, Vol. 46, pp. 205-208.

R. Argazzi, N. Y. M. Iha, H. Zabri, F. Odobel, C. A. Bignozzi (2004). Design of molecular dyes for application in photoelectrochemical and electrochromic devices based on nanocrystalline metal oxide semiconductors. *Coordination Chemistry Reviews,* Vol. 248, pp. 1299–1316.

Q.Wang, J. Moser, M. Grätzel (2005). Electrochemical Impedance Spectroscopic Analysis of Dye-Sensitized Solar Cells. *Journal of Physical Chemistry B*, Vol. 109, pp. 14945–14953

I. Shin, H. Seo, M. Son, J. Kim, K. Prabakar, H. Kim (2010). Analysis of TiO$_2$ thickness effect on characteristic of a dye-sensitized solar cell by using electrochemical impedance spectroscopy'. *Current Applied Physics* Vol. 10, pp. 422–424

C. Zafer, K. Ocakoglu, C. Ozsoy, S. Icli (2009). Dicationic bis-imidazolium molten salts for efficient dye sensitized solar cells: Synthesis and photovoltaic properties. Electrochemica Acta, Vol. 54, pp. 5709-5714.

N. K. A. Islam, Y. C. L. Han (2006). Improvement of efficiency of dye-sensitized solar cells based on analysis of equivalent circuit. *Journal of Photochemical and Photobiology A Chemistry,* Vol. 182, pp. 296-305.

L. Wang, X. Fang, Z. Zhang (2010). Design methods for large scale dye-sensitized solar modules and the progress of stability research'. Renewable and Sustainable Energy Reviews, Vol. 14, pp. 3178-3184.

C. Quiñones, W. Vallejo, F. Mesa (2010). Physical and electrochemical study of platinum thin films deposited by sputtering and electrochemical methods, *Applied Surface Science* 257 (2011) 7545–7550

Preparation of Hollow Titanium Dioxide Shell Thin Films from Aqueous Solution of Ti-Lactate Complex for Dye-Sensitized Solar Cells

Masaya Chigane, Mitsuru Watanabe and Tsutomu Shinagawa
Osaka Municipal Technical Research Institute
Japan

1. Introduction

As photovoltaic devices possessing potential for low processing costs and flexible architectures, dye-sensitized solar cells (DSSCs) using nanocrystalline TiO_2 (nc-TiO_2) electrodes have been extensively studied.(Bisquert et al., 2004; O'Regan & Grätzel, 1991) Congruently with increasingly urgent dissemination of solar cells against crisis of a depletion of fossil fuel, DSSCs are as promising alternative to conventional silicon-type solar cells. The main trend of investigations of DSSCs originates from the epoch-making works by Grätzel and co-workers in the early 1990s. (O'Regan & Grätzel, 1991) A typical construction of the cells are composed of dye-molecules (usually Ru complexes) coated nc-TiO_2 electrodes on transparent-conductive (TC) backcontact (usually fluorine-doped tin oxide (FTO)) glass substrate and counter Pt electrodes sandwitching triiodine/iodine [I_3^-/I^-] redox liquid electrolyte layer maintaining electrical connection with the counter Pt electrode. The voids of the network of TiO_2 nanoparticles connection form nanopores which are efficiently filled with electrolyte solution. An operation mechanism of DSSC begins with harvesting incident light by dye-molecules via photoexcitation of electron from the highest occupied molecular orbital (HOMO) to the lowest unoccupied molecular orbital (LUMO). The photoexcited electrons are transferred to the conduction band of the nc-TiO_2 and diffuse in TiO_2 matrix to TC layer followed by ejection to outer electric load. The oxidized dye is reduced by the electrolyte (I^-) and the positive charge is transported to Pt counter electrode. As well as close fitting of photo-absorption spectra of dyes to the spectrum of sunlight mainly in visible light region (nearly panchromatic dyes) (Nazeeruddin et al., 2001) the strong dye-TiO_2 coupling leading to rapid electron transfer from excited dye to TiO_2 (Tachibana et al., 1996) realizes practically promising solar-to-electrical conversion efficiency: more than 10 %. The charge separation of DSSCs occurs at the interface TiO_2 nanoparticles / dye molecules / [I^-/I_3^-] electrolyte. Therefore the combination of Ru-complex and TiO_2 is currently almost ideal choice in DSSC. Some problems of the TiO_2 nanoparticles electrode, however, remain room to investigate. Connection points of TiO_2 nanoparticles decrease an effective area of interface, and play a role on electron scattering sites, leading to restrict the conversion efficiency.(Enright & Fizmaurice, 1996; Peng et al., 2003) Though denser films seemingly improve the electron migration, they result in decrease of surface area for dye adsorption. Additionally TiO_2 nanoparticles electrodes are

usually prepared by embrocation methods, e. g., a squeegee method, whereas via these methods great amount of Ti resource is consumed.

For the settlement several nanostructures of TiO_2 electrodes for DSSCs containing the array of nanorods,(Kang et al., 2008) nanotubes (Kang et al., 2009; Paulose et al., 2008) and assembly of spherical hollow (Kondo et al., 2006) or hemispherical (Yang et al., 2008) shells particles have been proposed owing to their ordered structures leading to ordered electron transport and large surface area for small amount of titanium as depicted in Fig. 1.
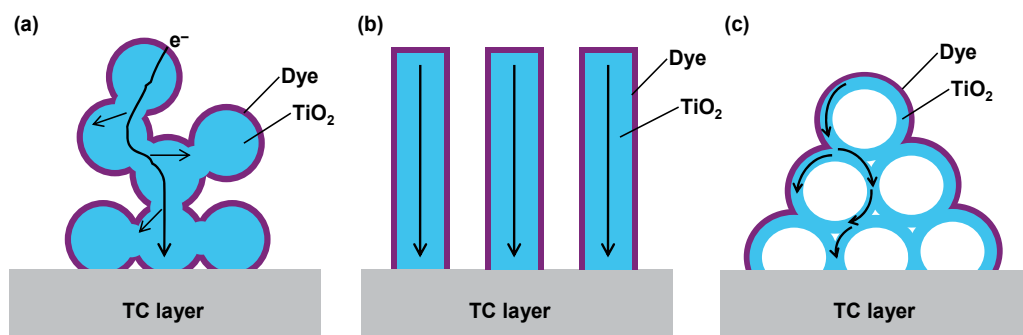

Fig. 1. Models of TiO_2 nano-structure electrode for DSSCs, (a) standard nanocrystalline particles, (b) nano tube or nano pillar arrays and (c) hollow shells.

Some works on ordered and multilayered hollow TiO_2 shells, which are inverse opal structure, have shown photonic crystalline effects leading to red shift in incident photon-to-current conversion efficiency (IPCE). (Nishimura et al., 2003; Yip et al., 2008) Recently energy conversion efficiencies of DSSCs using inverse TiO_2 opal, including 1.8 %, (Guldin et al., 2010) 3.47 % (Kwak et al., 2009) and 4.5 % (Qi et al., 2009) have been reported. In the previous work we prepared hollow TiO_2 shell monolayer films by the electrolysis of an aqueous $(NH_4)_2TiF_6$ solution on complicated polystyrene (PS) particles-preadsorbed substrate followed by calcination. (Chigane et al., 2009) Among few papers (Karuppuchamy et al., 2001; Yamaguchi et al., 2005) reporting the electrolytic preparation of TiO_2 for DSSC anode, the previous work first reported the DSSC conversion efficiency (0.63 %) using TiO_2 film prepared via electrolysis to our knowledge. From standpoint of methodology for a preparation of TiO_2 films electrolyses (electrodeposition) from aqueous solutions are a low cost and low resource consuming fabrication techniques since the deposition reaction occurs only nearby substrate. The $(NH_4)_2TiF_6$ solution is stable for long term, being able to undergo repeated electrolyses. However some industrial problems: liberation of highly toxic F- during electrochemical deposition reaction leading to bad working environment. Moreover insufficient conversion efficiency calls multilayered hollow structures. As a water-soluble and environment-benign titanium compound titanium bis(ammonium lactato)dihydroxide (TALH) increasingly attracts attention. (Caruso et al., 2001; Rouse & Ferguson, 2002) Especially Ruani and co-workers (Ruani et al., 2008) have developed single-step preparation of PS-TALH core-shell precursor from a suspension containing both PS and TALH, followed by fabrication inverse opal TiO_2 films by calcination. The process seems to be simple and time-saving compared with other conventional methods: PS template followed by infiltration of Ti oxides or Ti compounds sol. (Galusha et al., 2008; King et al., 2005; Liu et al., 2010; Nishimura et al., 2002) However DSSC electrode properties of the film have not been

evaluated. There assumably are two reasons that the films becomes noncontiguous by calcination owing to drastic volume change from Ti-lactate to oxide and that H-TiO$_2$ film are difficult to be prepared in wide area. The latter problem is mainly due to aninonic surface functional groups of PS in usual cases despite electrostatically repulsive Ti-lactate anion leading to difficult formation of homogeneous structure. Based upon these trend and problems we propose in the present article some preparation methods of three-dimensional assembly of H-TiO$_2$ shells being applied to DSSC. Figure 2 illustrates our preparation process of H-TiO$_2$ shell films.
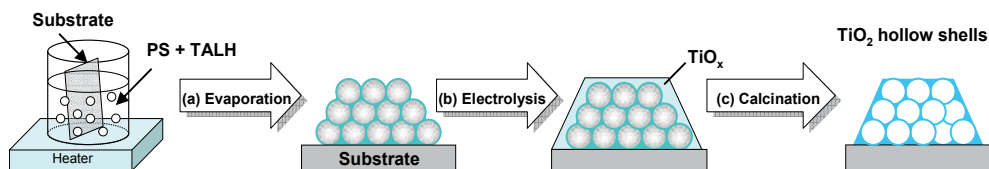

Fig. 2. Schematic representation of preparation process of hollow TiO$_2$ shell film.

The immersion of substrate in the initial suspension which contains both PS and TALH, followed by evaporation of water, forms a PS template coated with TALH (PS-TALH) precursor (Fig. 2 (a)). So as to avoid the volume change of films we supported the PS-TALH by electrodeposition of titanium oxide (TiO$_x$) thin film (Fig. 2(b)) thereon. The novelty of this method includes i) employing non-toxic TALH and PS with cationic surface groups which are supposedly good affinity with each other and ii) electrolysis of TALH solution for TiO$_x$ coverage. As a whole, this article highlights a low cost, facile and soft fabrication process of hollow TiO$_2$ (H-TiO$_2$) shell films and aggressive participation of them in DSSC as a trendy nano-architechtural electrode.

2. Experimentals

Two types of PS possessing anionic (A-PS) and cationic (C-PS) functional group on the surface, prepared by an emulsifier-free emulsion polymerization of styrene monomer with potassium persulfate (KPS) and 2,2′-azobis(2-methylpropionamidine) dihydrochloride (AIBA) as a radical initiator, respectively, were used.(Watanabe et al., 2007) From SEM observations a diameter of A-PS and C-PS beads was ca. 400 nm and ca. 300 nm, respectively. A TC glass plate coated with fluorine-doped tin oxide (FTO, 10 Ω/square, ASAHI GLASS Co., Ltd, A11DU80) and quartz glass plate (1 mm of thickness) were used as substrates. As pretreatments of substrates, FTO (15 mm × 20 mm) was degreased by anodic polarization (+5 mA cm^{-2}) against Pt counter electrode for 30 s in a 1 mol dm^{-3} NaOH and quartz glass plate (20 mm × 40 mm) was immersed in a 10 % NaOH solution for 10 min at 333 K. Both substrates were thoroughly rinsed with deionized water and immersed in the colloidal suspension of PS and TALH in a cylindrical glass bottle being bent backward at about 60° against bottom. (Hartsuiker & Vos, 2008; Ye et al., 2001) The glass bottle containing the suspension and substrate was placed on a hot plate the temperature of surface of which was set at 345 K. In this way the temperature of the suspension was maintained at 325 K for 5–24 h until complete evaporation of water. The initial concentrations of PS and TALH in the suspension were 0.28 % and 0.0025 or 0.005 mol dm^{-3}, respectively. Hollow shells TiO$_2$ (H-TiO$_2$) films were formed by the calcinations of the PS-TALH precursor at 723 K for 1 h. In the calcination, the temperature was raised in rate of 2 h

from room temperature to 723 K. In some cases TiO_x films were electrodposited on the PS-TALH precursor films before calcination by a cathodic electrolysis in the electrolyte solution containing a 0.05 mol dm^{-3} TALH (Aldrich; reagent grade) and a 0.1 mol dm^{-3} NH_4NO_3 at –2 mA cm^{-2} of current density for 6 C cm^{-2} of charge density.

X-ray diffraction (XRD) patterns of the films in 3 cm^2 of deposition area were recorded on a RIGAKU RINT 2500 diffractometer (Cu Kα; λ = 0.1541 nm; 40 kV; 100 mA), with the incident angle (θ) fixed at 1°, scanning the diffraction angle (2θ) stepwise by 0.05° with a counting time of 10 s.

Transmission spectra and relative diffuse reflection (DR) spectra in ultraviolet (UV)–visible range of hollow shells were measured by means of Shimadzu UV-3150 spectrometer. An integral spherical detector equipment (Shimadzu ISR-3100) was used for DR spectroscopy with $BaSO_4$ powder (Wako Pure Chemical Industries) as a reference reflector. For the powder sample the hollow shell film was detached from quartz glass substrate by scratching with spatula.

X-ray photoelectron (XP) spectra of the films were obtained by means of Kratos AXIS-ULTRA DLD. A monochromated Al Kα (1486.6 eV; 150 W) line was used as the X-ray source. The pressure in the analyzing chamber was lower than < 1×10^{-8} Torr during measurements. Binding energies of Ti 2p and O 1s photoelectron peaks were corrected from the charge effect by referencing the C 1s signal of adventitious contamination hydrocarbon to be 284.8 eV.

For DSSC measurements, a composite TiO_2 (C-TiO_2) film composed of flat bottom TiO_2 layer and hollow shell film was prepared. The deposition area, corresponding to an active area of the cell, was adjusted to be 0.25 cm^2 using a mask. Initially TiO_x film was galvanostatically electrodeposited on the FTO in the electrolyte solution containing a 0.05 mol dm^{-3} TALH (Aldrich; reagent grade) and a 0.1 mol dm^{-3} NH_4NO_3 at –3 mA cm^{-2} of current density for 10 C cm^{-2} of charge density as a blocking layer of DSSC electrode. On the FTO/TiO_x layer the PS-TALH precursor was coated from aqueous suspension of 0.28 % C-PS and 0.0025 mol dm^{-3} TALH and thereon $TiOx$ was coated by electrolysis. The TiO_2 hollow films on FTO substrates were immersed in an ethanolic solution of 0.3 mmol dm^{-3} ruthenium dye (bistetrabutylammonium cis-di(thiocyanato)-bis(2,2'-bipyridine-4-carboxylic acid, 4'-carboxylate ruthenium(II), Solaronix N719) for 14–16 h at room temperature. An electrolyte solution for DSSC was composed of 0.1 mol dm^{-3} LiI, 0.05 mol dm^{-3} I_2, 0.6 mol dm^{-3} 1,2-dimethyl-3-propylimidazolium iodine (DMPII, Solaronix) and 0.5 mol dm^{-3} 4-tert-butylpyridine in acetonitrile. A platinum-coated glass substrate was used for a counter electrode. The dye-coated TiO_2 electrode and the counter electrode were set sandwiching a separation polymer sheet (25 µm of thickness; Solaronix SX-1170) and the electrolyte. Photovoltaic current density (J)-voltage (V) curves were obtained using an instrument for the measurements of solar cell parameters (Bunkoh-Keiki Co., Ltd K0208, with a Keithley 2400) with photoirradiation by a 150 W xenon lamp under the condition that was simulated airmass 1.5 solar irradiance with the intensity of 100 mW cm^{-2}. Incident photon-to-electron conversion efficiency (IPCE) spectra ranging 400 to 800 nm of wavelength were measured by means of a spectral photosensitivity measurement system (Bunkoh-Keiki) with a 150 W xenon lamp light source. Calibration was performed using a standard silicon photodiode (Hamamatsu Photonics, S1337-1010BQ).

As a reference sample, TiO_2 nanocrystalline particles (nc-TiO_2) electrode prepared by a squeegee method from TiO_2 colloidal solution (Solaronix Ti-Nanoxide D) and calcination in the same way as the hollow films was subjected to DSSC measurements.

The area density: amount of deposited TiO_2 against area (mg cm^{-2}) was determined using an X-ray fluorescent spectrometer (Rigaku RIX3100).

3. Results and discussion

3.1 Characterization of H-TiO$_2$ films

Figure 3 shows SEM photographs of PS-TALH precursors. For both A-PS and C-PS, the sizes of spherical PS-TALH units appeared to be almost same as PS itself and core/shell structures of PS/TALH were not clearly observed as shown in expanded images (Fig. 3(b) and (d)). Some bulgy junctions between adjacent spheres, however, suggest accumulation of TALH. From appearance with eyes and SEM images, PS particles and TALH were uniformly mixed.
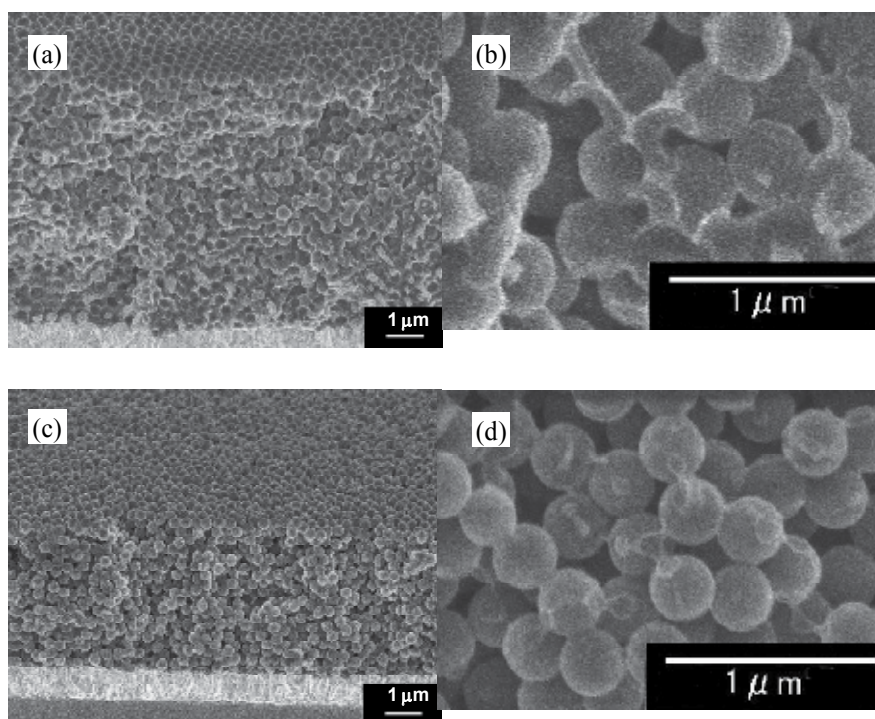
Fig. 3. Cross-sectional SEM photographs of PS-TALH films on FTO substrates from (a) or (b) A-PS and (c) or (d) C-PS, respectively.

Figure 4 shows SEM photographs of H-TiO$_2$ films. More than 20 layers of quasi-ordered spherical hollow shells were observed at some view points. The thickness of shell wall was *ca.* 10 nm. For the sample started from suspension containing A-PS and TALH 0.0025 mol dm^{-3}, the fcc configuration was observed especially on the surface in one to several millimeters range. However, the quasi-fcc ordered shells were discretely scattered on the substrate, and some parts of the substrate were not covered with films. On the other hand, although for the sample from C-PS the ordered structure was not observed (Fig. 4(d)) in micrometer view, the hollow shells smoothly coated almost all over the substrate. This more excellent dispersion by C-PS in appearance is due to uniform mixture of PS and

TALH in the precursor originating from their affinitive relationship. In both cases, there are observed many broken points of shells owing to PS-PS spheres contact at the initial precursor as shown in an inserted scheme in Fig. 4, leading to skeleton-like structure after calcinations.
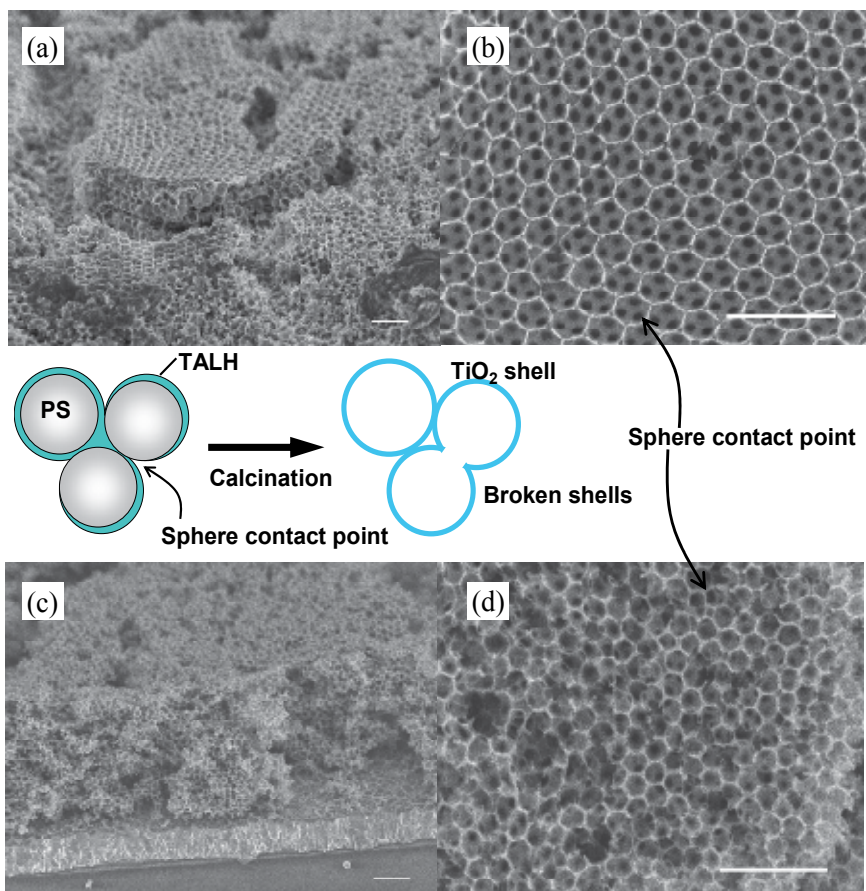
Fig. 4. Cross-sectional or suface SEM photographs of H-TiO$_2$ films on FTO substrates prepared from (a) or (b) A-PS and (c) or (d) C-PS, respectively. Scale bars correspond 1 µm.

Figure 5 shows XRD pattern of hollow shells film prepared on a quartz glass substrate by calcination of C-PS-TALH precursor. The pattern shows the TiO$_2$ shell film to be predominantly anatase type crystalline phase while the peaks were broad owing to nanocrystalline.(International Center for Diffraction Data, 1990)

The crystallite size (D) of the calcined film can be estimated from Scherrer's formula (Kim et al., 2008)

$$D = \frac{0.89\lambda}{\beta\cos\theta} \tag{1}$$

where λ is the wavelength of the X-ray, β is the peak width and θ is the Bragg angle of the peak.
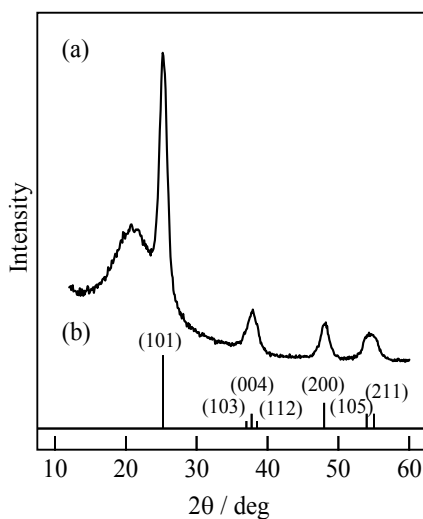
Fig. 5. XRD patterns of (a) H-TiO$_2$ film on quartz glass substrate and (b) an authentic pattern of anatase-type TiO$_2$.(International Center for Diffraction Data, 1990)
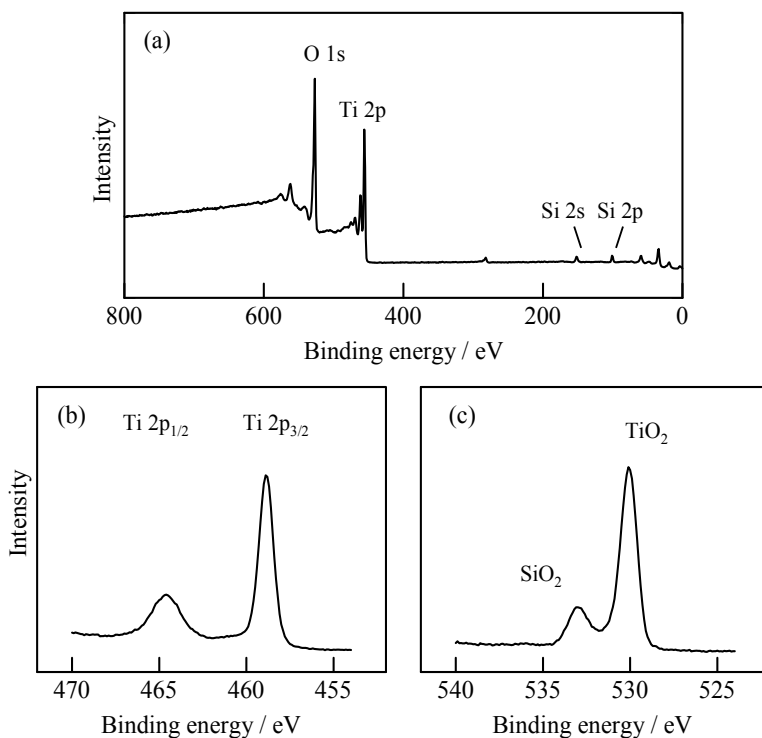
Fig. 6. XP spectra of hollow TiO$_2$ film on quartz glass substrate prepared from C-PS (0.28 %) and 0.005 mol dm^{-3} TALH; (a) wide scan spectrum, (b) Ti 2p and (c) O 1s photoelectron spectra.

On the hypothesis that the sample is constituted by isotropic and spherical crystallites, the width of the most intensive X-ray diffraction peak, corresponding to anatase (101) plane at 25.273°, is adopted for the calculation of the β value. With the β value: 0.0153 (radian) obtained after the exclusion of the effect of Kα2 line and optical system of the instrument, the D value is estimated to be 7.7 nm.

Figure 6 shows XP spectra of the surface of hollow shells film. In the wide energy range spectrum (Fig. 6 (a)) small peaks of Si 2p and Si 2s photoelectron originating from quartz glass substrate were observed as well as main titanium and oxygen peaks. Almost identical peak positions (within 1 eV) of Ti $2p_{3/2}$ region spectrum for the film and standard TiO_2 (Chigane et al., 2009) at 458.9 and 458.7 eV, respectively, suggest that the chemical state of the hollow shells film can be assigned to TiO_2. The main peak and secondary peak at 530 eV and at around 533 eV in O 1s photoelectron region spectrum can be attributed to titanium oxide (Ti–O–Ti) and silica of substrate, respectively, from references. (Moulder et al., 1992)

Figure 7 shows optical properties of H-TiO_2 films prepared from C-PS and TALH.
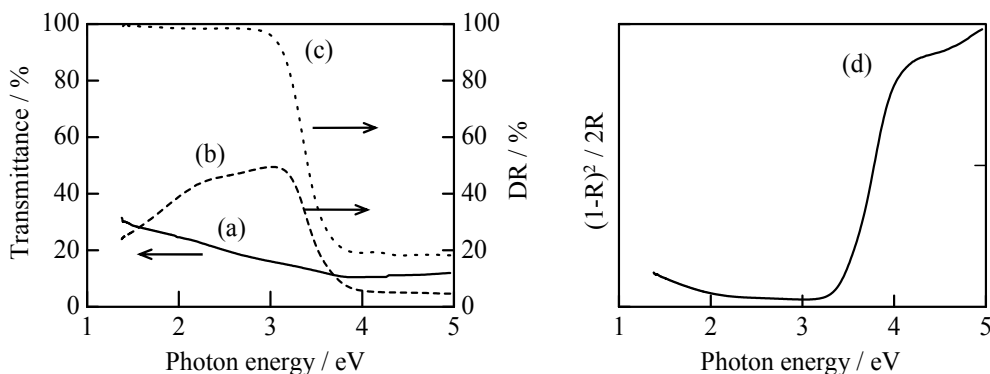
Fig. 7. Relationship between H-TiO_2 film on quartz glass substrate from C-PS-TALH and UV-visible photon energy: (a, solid line) transmission spectrum of the film and (b, dashed line) or (c, dotted line) diffuse reflection spectrum of film or powder sample, respectively and (d) Kubelka-Munk function plots for the powdered sample transformed from DR spectrum corresponding to (c).

Absence of clear attenuation dip in transmission spectrum indicates random configuration of hollow shells. Decrease and increase of transmittance and DR of film samples, respectively, according to photon energy up to ca. 3 eV are due to scattering of light by aggregation of TiO_2 hollows. Taking account of DR of powder sample the decrease of both transmittance and DR of film sample at higher than 3 eV are due to interband photo-absorption of TiO_2. Such change of DR of powder sample can be associated with absorption coefficient (α) using Kubelka-Munk function (Kortüm, 1969; Murphy, 2007)

$$F(R) = \frac{(1-R)^2}{2R} = \frac{\alpha}{S} \tag{2}$$

as shown in Fig. 7(d), where R and S indicate diffuse reflectance and scattering coefficient, respectively. Although all terms depend on energy (wavelength) of incident light, the sizes

of hollow shells collectives (more than 1 μm) are enough larger than wavelength and in the wavelength range between 310 nm (ca. 4 eV) and 410 nm (ca. 3 eV) concerning photoabsorption (Fig. 7(c)) the change of S value might be little. Therefore in relation to absorption S can be assumed to be constant and then we investigated band edge using α/S values. The relationship of α and photon energy (hv) of semiconductors near the absorption edge region for direct or indirect transition is given by

$$(\alpha h v)^2 = A(h v - E_g) \tag{3}$$

or

$$(\alpha h v)^{1/2} = A(h v - E_g) \tag{4}$$

respectively, where A and E_g are proportion constant and band gap energy.(Pankove, 1971) The linear relationship of Eq. (3) and (4) indicate that in the plots of $(\alpha h v)^2$ or $(\alpha h v)^{1/2}$ versus hv the optical band gap can be determined by intersection of extrapolated straight line with hv axis. (Barton et al., 1999; Han et al., 2007; Nowak et al., 2009) Based on above mentioned assumption we derived the optical band gaps as 3.5 eV and 3.2 eV from intersection points of linear fitting line with $(\alpha h v/S)^2$ and $(\alpha h v/S)^{1/2}$ versus hv for direct and indirect process, respectively, as shown in Fig. 8. At present we propose the latter value because 3.2 eV of E_g for anatase TiO_2 is commonly accepted.(O'Regan & Grätzel, 1991; Tang et al., 1994) However more investigation is necessary since it has not been clarified whether interband transition of anatase TiO_2 is direct or indirect. (Asahi et al., 2000; Mo & Ching, 1995)
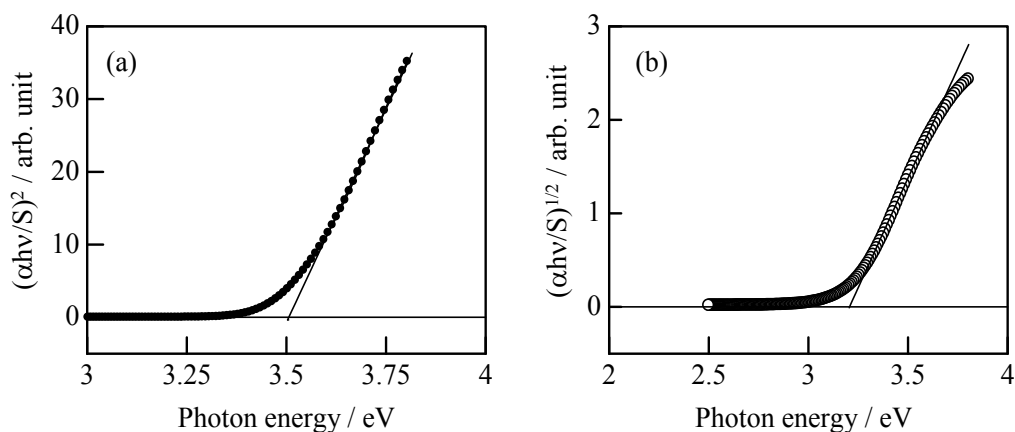
Fig. 8. Plots of (a) $(\alpha h v/S)^2$ and (b) $(\alpha h v/S)^{1/2}$ against UV-visible photon energy of powdered H-TiO_2 transferred from α/S spectrum corresponding to Fig. 7(d). Linear lines are drawn to determine band gap energies.

3.2 Enhanced film quality by electrodeposition

Figure 9(a) shows low magnification SEM image of the films indicating considerable volume change by calcination. After calcination the film was constricted and broken apart as expected in introduction section. Moreover maybe owing to the stress by crystallization and plastic strain the film easily detached from substrate. Such poor quality of the films and

large crack made us expect low utility for DSSC electrode. Figure 9(b) and (c) show SEM images of TiO_2-coated H-TiO_2 film by electrodeposition before calcination. Although on the top surface view some narrow cracks were observed within 1 µm width, recognition of only hollow spheres in the back of the cracks indicates that the FTO substrate are not exposed. Cross-sectional view shows hollow shells suggesting successful maintenance of PS-TALH structure during electrodeposition.
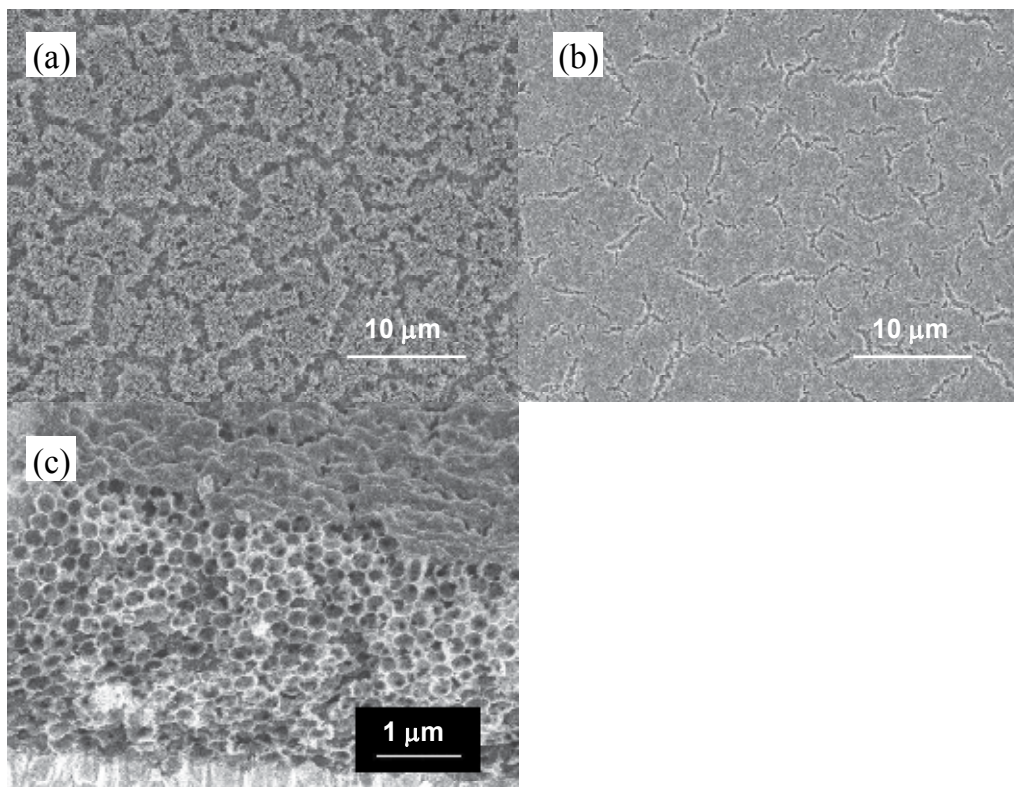
Fig. 9. SEM photographs of H-TiO_2 films on FTO substrates; (a) or (b) surface view of the film without or with electrodeposition TiO_x coating, respectively, and (c) cross-sectional view of the film with electrodeposition TiO_x coating. In both cases the precursors are C-PS-TALH.

3.3 DSSC properties

Figure 10 and Table 1 show typical results of DSSC assessment for three type TiO_2 electrodes. The conversion efficiency value of the cell using only H-TiO_2 electrode: 0.91 % (Fig. 10(a)) was about 4 times lower than that for the cell: 3.98 % using standard nc-TiO_2 electrode (Fig. 10(b)).

The conversion efficiency value of the cell using only H-TiO_2 electrode: 0.91 % (Fig. 10(a)) was about 4 times lower than that for the cell: 3.98 % using standard nc-TiO_2 electrode (Fig. 10(b)), despite 3.2 times smaller amount of TiO_2. There can be thought to be two reasons for such insufficient efficiency. One is lower short circuit current density (J_{SC}). The compli-cated morphology of hollow TiO_2 film might contribute to the increase of specific contact area

with dye molecules and to harvesting light by scattering in the hollow shells. However a large number of broken points in the skeleton structure and few contact points with substrate supposedly leaded poor conduction of photo-induced electrons. The other is lower open circuit voltage (V_{OC}) due to direct contact between electrolyte solution and FTO substrate through wider film crack points. So as to improve the two problems we inserted initial flat TiO_2 layer on the substrate by electrolysis of TALH solution. Remarkably improved DSSC performance: 2.90 % for the composite (C-TiO_2) film composed of electrodeposited TiO_2 bottom layer and hollow TiO_2 top layer has been shown (Fig. 10(c) and Table 1) compared with single hollow layer (0.91 %), including enhancement of V_{OC} and FF values. The area density of TiO_2 of nanoparticles electrode was as more than 2.4 times as the composite hollow shell film, whereas the change of the conversion efficiency was 1.4 times. This indicates the conversion efficiency per-TiO_2-weight for the composite hollow shell film is higher than nc-TiO_2 film owing to homogeneity effect of blocking layer making complicated structure of H-TiO_2 available
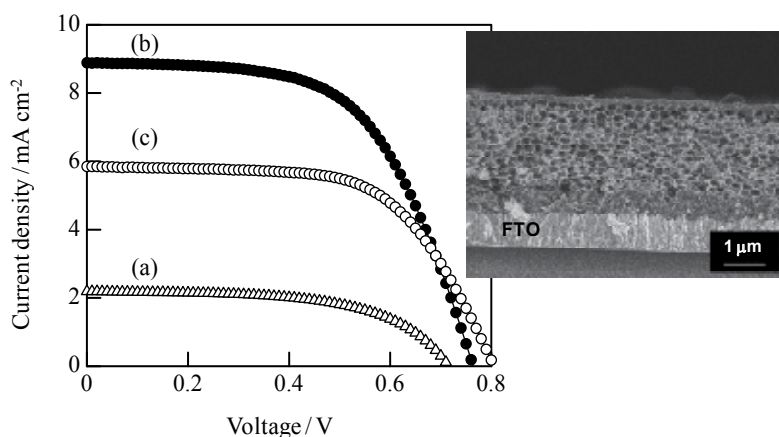
Fig. 10. Photocurrent density voltage curves of DSSCs using (a) H-TiO_2, (b) nc-TiO_2 and (b) C-TiO_2 film. The cross-sectional SEM photograph indicates the C-TiO_2 sample corresponding to curve (c).

TiO_2 films	Area density of TiO_2 / mg cm^{-2} (by XRF)	J_{SC} / mA cm^{-2} [a]	V_{OC} / V [b]	FF[c]	Eff / % [d]
Hollow shell	0.179	2.19	0.716	0.580	0.911
Composite	0.244	5.85	0.805	0.615	2.90
Nano-particles	0.587	8.89	0.763	0.585	3.98

[a]Short circuit current density. [b]Open circuit voltage. [c]Fill factor. [d]Conversion efficiency.

Table 1. DSSC properties of two TiO_2 film electrodes.

Figure 11 shows IPCE assessments of cells using three type TiO_2 electrodes: nc-TiO_2, simply electrodeposited TiO_2 (E-TiO_2) and C-TiO_2 film. In this comparison we electrodeposited thicker first film than that in above J-V characterization. By this effect the conversion efficiency of C-TiO_2 film was somewhat enhanced to 3.44 %. The normalized IPCE curves for the films (Fig. 11(e), (f), (g)) have shown good spectral accordance of photocurrent with

photoabsorption of dye (Fig. 10(d)). Moreover heightening of composite TiO_2 film (Fig. 11(f)) by 14 % and 11 % at 450 nm and 600 nm of wavelength, respectively, against simple electrodeposited film (Fig. 11(e)), proves wavelength-independent increase of photocurrent by the addition of hollow shells as top layer. This seems to arise simply from increase of amount of TiO_2 and to imply low optical effect of our hollow shells, remaining what should be improved.
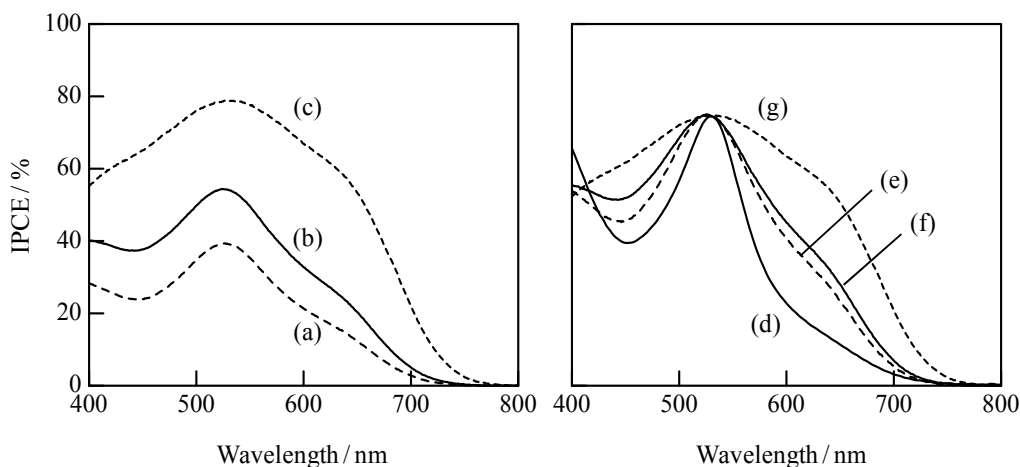
Fig. 11. IPCE spectra of DSSC using (a, dashed line) or (e, dashed line) E-TiO_2 film, (b, solid line) or (f, solid line) C-TiO_2 film and (c, dotted line) or (g, dotted line) nc-TiO_2 film.

4. Conclusions

Hollow TiO_2 (H-TiO_2) shell films have been prepared using environmentally benign Ti-lactate complex (TALH) as a titanium source. A precursor has been prepared from an aqueous colloidal suspension containing both polystyrene (PS) and TALH. Successive calcination of the PS-TALH precursor at 723 K led to the decomposition of PS and formation of hollow spherical shells. Employing PS with cationic surface functional group (C-PS) gave rise to smoothly spreading of hollow shells films in wider area compared with conventional PS possessing anionic groups (A-PS). The characterizations by X-ray diffraction and X-ray photoelectron spectroscopy have proved that the hollow shell films can be assigned to anatase TiO_2. Optical characteristics of H-TiO_2 films from C-PS-TALH have shown they are not in an inverse opal structure. Diffuse reflection spectroscopy combined with Kubelka-Munk treatment has revealed wide optical band gap as equal or more than 3.2 eV, indicating transparency of the films for visible light. It has been found that combination with electrodeposition of TiO_x films strongly supports quality and DSSC properties of H-TiO_2 films in two aspects. First the electrodeposition onto the PS-TALH precursor film effectively prevented widely cracking in the calcination process. Moreover the electrodeposition onto FTO substrate before H-TiO_2 layer, namely fabrication of composite film (C-TiO_2 film), substantially enhanced DSSC energy conversion efficiency: 2.9 % which was comparable to an electrode using commercially available TiO_2 nanocrystalline particle (nc-TiO_2). The IPCE curve of C-TiO_2 film has revealed the increase of photocurrent due to light-harvesting effect.

On the other hand its independence of wavelength has indicated that H-TiO$_2$ lacks photonic crystal effect and then a future investigation on improvement of arraying of H-TiO$_2$ is needed.

5. References

Asahi, R.; Taga, Y.; Mannstadt, W. & Freeman, A. J. (2000). Electronic and optical properties of anatase TiO$_2$, *Physical Review B*, Vol.61, No.11, pp 7459–7465, ISSN 1098-0121

Barton, D. G.; Shtein, M.; Wilson, R. D.; Soled, S. L. & Iglesia, E. (1999). Structure and Electronic Properties of Solid Acids Based on Tungsten Oxide Nanostructures, *Journal of Physical Chemistry B*, Vol.103, No.4, pp 630-640, ISSN 1520-6106

Bisquert, J.; Cahen, D.; Hodes, G.; Rühle, S. & Zaban, A. (2004). Physical Chemical Principles of Photovoltaic Conversion with Nanoparticulate, Mesoporous Dye-Sensitized Solar Cells, *Journal of Physical Chemistry B*, Vol.108, No.24, pp 8106–8118, ISSN 1520-6106

Caruso, F.; Shi, X.; Caruso, R. A. & Susha, A. (2001). Hollow Titania Spheres from Layered Precursor Deposition on Sacrificial Colloidal Core Particles, *Advanced Materials*, Vol.13, No.10, pp 740–744, ISSN 0935-9648

Chigane, M.; Watanabe, M.; Izaki, M.; Yamaguchi, I. & Shinagawa, T. (2009). Preparation of Hollow Titanium Dioxide Shell Thin Films by Electrophoresis and Electrolysis for Dye-Sensitized Solar Cells, *Electrochemical and Solid-State Letters*, Vol.12, No.5, pp E5–E8, ISSN 1099-0062

Enright, B. & Fizmaurice, D. (1996). Spectroscopic Determination of Electron and Hole Effective Masses in a Nanocrystalline Semiconductor Film, *Journal of Physical Chemistry*, Vol.100, No.3, pp 1027–1035, ISSN 0022-3654

Galusha, J. W.; Tsung, C-K.; Stucky, G. D. & Bartl, M. H. (2008). Optimizing Sol-Gel Infiltration and Processing Methods for the Fabrication of High-Quality Planar Titania Inverse Opals, *Chemistry of Materials*, Vol.20, No.15 pp 4925–4930, ISSN 0897-4756

Guldin, S.; Httner, S.; Kolle, M.; Welland, M. E.; Müller-Buschbaum, P.; Friend, R. H.; Steiner, U. & Ttreault, N. (2010). Dye-Sensitized Solar Cell Based on a Three-Dimensional Photonic Crystal, *Nono Letters*, Vol.10, No.7, pp 2303–2309, ISSN 1530-6984

Han, T. -Y.; Wu, C. -F. & Hsieh, C. -T. (2007). Hydrothermal synthesis and visible light photocatalysis of metal-doped titania nanoparticles, *Journal of Vacuum Science & Technology, B: Microelectronics and Nanometer Structures--Processing, Measurement, and Phenomena*, Vol.25, No.2, pp 430-435, ISSN 1071-1023

Hartsuiker, A. & Vos, W. L. (2008). Structural Properties of Opals Grown with Vertical Controlled Drying, *Langmuir*, Vol.24, No.9, pp 4670–4675, ISSN 0743-7463

International Center for Diffraction Data, Joint Committee on Powder Diffraction Standards, (1990). *Powder Diffraction File*, set 21, No.1272, Swarthmore, Pennsylvania, USA

Kang, S. H.; Choi, S-H.; Kang, M-S.; Kim, J-Y.; Kim, H-S.; Hyeon, T. & Sung, Y. -E. (2008). Nanorod-Based Dye-Sensitized Solar Cells with Improved Charge Collection Efficiency, *Advanced Materials*, Vol.20, No.1, pp 54–58, ISSN 0935-9648

Kang, T-S.; Smith, A. P.; Taylor, B. E. and Durstock, M. F. (2009). Fabrication of Highly-Ordered TiO₂ Nanotube Arrays and Their Use in Dye-Sensitized Solar Cells, *Nono Letters*, Vol.9, No.2, pp 601–606, ISSN 1530-6984

Karuppuchamy, S.; Amalnerkar, D. P.; Yoshida, T.; Sugiura, T. & Minoura, H. (2001). Cathodic electrodeposition of TiO₂ thin films for dye-sensitized photoelectrochemical applications, *Chemistry Letters*, Vol.30, No.1, pp 78-79, ISSN 0366-7022

Kim, G. -M.; Lee, S. -M.; Michler, G. H.; Roggendorf, H.; Gösele, U. & Knez, M. (2008). Nanostructured pure anatase titania tubes replicated from electrospun polymer fiber templates by atomic layer deposition, *Chemistry of Materials*, Vol.20, No.9, pp 3085-3091, ISSN 0897-4756

King, J. S.; Grangnard, E. & Summers, C. J. (2005). TiO₂ Inverse Opals Fabricated Using Low-Temperature Atomic Layer Deposition, *Advanced Materials*, Vol.17, No.8, pp 1010–1013, ISSN 0935-9648

Kondo, Y.; Yoshikawa, H.; Awaga, K.; Murayama, M.; Mori, T.; Sunada, K.; Bandow, S. & Iijima S. (2008). Preparation, Photocatalytic Activities, and Dye-Sensitized Solar-Cell Performance of Submicron-Scale TiO₂ Hollow Spheres, *Langmuir*, Vol.24, No.2, pp 547–550, ISSN 0743-7463

Kortüm, G. (1969). *Reflectance Spectroscopy*, pp 103-127, Springer-Verlag, ISBN 978-3540045872, New York, USA

Kwak, E. S.; Lee, W.; Park, N-G.; Kim, J. & Lee, H. (2009). Compact inverse-opal electrode using non-aggregated TiO₂ nanoparticles for dye-sensitized solar cells, *Advanced Functional Materials*, Vol.19, No.7, pp 1093–1099, ISSN 1616-301X

Liu, W.; Zou, B.; Zhao, J. & Cui, H. (2010). Optimizing sol-gel infiltration for the fabrication of high-quality titania inverse opal and its photocatalytic activity, *Thin Solid Films*, Vol.518, No.17, pp 4923–4927, ISSN 0040-6090

Mo, S. –D. & Ching, W. Y. (1995). Electronic and optical properties three phases of titanium dioxide: Rutile, anatase, and brookite, *Physical Review B*, Vol.51, No.19, pp 13023–13032, ISSN 1098-0121

Moulder, J. F.; Stickle, W. F.; Sobol P. E. & Bomben, K. D. (1992). *Handbook of X-ray Photoelectron Spectroscopy*, Perkin-Elmer, p. 45, ISBN 0-9627026-2-5, Minnesota, USA

Murphy, A. B. (2007). Band-gap determination from diffuse reflectance measurements of semiconductor films, and application to photoelectrochemical water-splitting, *Solar Energy Materials and Solar Cells*, Vol.91, No.14, pp 1326-1337, ISSN 0927-0248

Nazeeruddin, M. K.; Péchy, P.; Renouard, T.; Zakeeruddin, S. M.; Humphry-Baker, R.; Comte, P.; Liska, P.; Cevey, L.; Costa, E.; Shklover, V.; Spiccia, L.; Deacon, G. B.; Bignozzi, C. A. & Grätzel, M. (2001). Engineering of Efficient Panchromatic Sensitizers for Nanocrystalline TiO₂-Based Solar Cells, *Journal of the American Chemical Society*, Vol.123, No.8, pp 1613–1624, ISSN 0002-7863

Nishimura, S.; Shishido, A.; Abrams, N. & Mallouk, T. E. (2002). Fabrication technique for filling-factor tunable titanium dioxide colloidal crystal replicas, *Applied Physics Letters*, Vol.81, No.24, pp 4532–4534, , ISSN 0003-6951

Nishimura, S.; Abrams, N.; Lewis, B. A.; Halaoui, L. I.; Mallouk, T. E.; Benkstein, K. D.; van de Lagemaat, J. & Frank, A. J. (2003). Standing Wave Enhancement of Red

Absorbance and Photocurrent in Dye-Sensitized Titanium Dioxide Photoelectrodes Coupled to Photonic Crystals, *Journal of the American Chemical Society*, Vol.125, No.20, pp 6306–6310, ISSN 0002-7863

Nowak, M.; Kauch, B. & Szperlich, P. (2009). Determination of energy band gap of nanocrystalline SbSI using diffuse reflectance spectroscopy, *Review of Scientific Instruments*, Vol.80, No.4, pp 046107-1-046107-3, ISSN 0034-6748

O'Regan, B. & Grätzel, M. (1991). A low-cost, high-efficiency solar cell based on dye-sensitized colloidal TiO_2 films, *Nature*, Vol.353, No.6346, pp. 737–740, ISSN 0028-0826

Pankove, J. I. (1971). *Optical processes in semiconductors*, pp 34-42, Dover Publications, ISBN 0-486-60275-3, New York, USA

Paulose, M.; Shankar, K.; Varghese, O. K.; Mor, G. K. & Grimes, C. A. (2006). Application of highly-ordered TiO_2 nanotube-arrays in heterojunction dye-sensitized solar cells, *Journal of Physics D: Applied Physics*, Vol.39, No.12, pp 2498–2503, ISSN 0022-3727

Peng, T. Y.; Hasegawa, A.; Qui, J. R. & Hirao, K. (2003). Fabrication of Titania Tubules with High Surface Area and Well-Developed Mesostructural Walls by Surfactant-Mediated Templating Method, *Chemistry of Materials*, Vol.15, No.10, pp 2011–2016, ISSN 0897-4756

Qi, L.; Sorge, J. D.; & Birnie III, D. P. (2009). Dye-sensitized solar cells based on TiO_2 coatings with dual size-scale porosity, *Journal of the American Ceramic Society*, Vol.92, No.9, pp 1921–1925, ISSN 0002-7820

Rouse, J. H. & Ferguson, G. S. (2002). Stepwise Formation of Ultrathin Films of a Titanium (Hydr) Oxide by Polyelectrolyte-Assisted Adsorption, *Advanced Materials*, Vol.14, No.2, pp 151–154, ISSN 0935-9648

Ruani, G.; Ancora, C.; Corticelli, F.; Dionigi, C. & Rossi, C. (2008). Single-step preparation of inverse opal titania films by the doctor blade technique, *Solar Energy Materials and Solar Cells*, Vol.92, No.5, pp 537–542, ISSN 0927-0248.

Tachibana, Y.; Moser, J. E.; Grätzel, M.; Klug, D. R. & Durrant, J. R. (1996). Subpicosecond Interfacial Charge Separation in Dye-Sensitized Nanocrystalline Titanium Dioxide Films, *Journal of Physical Chemistry*, Vol.100, No.51, pp 20056–20062, ISSN 0022-3654

Tang, H.; Prasad, K.; Sanjinès, R.; Schmid, P. E. & Lévy, F. (1994). Electrical and optical properties of TiO_2 anatase thin films, *Journal of Applied Physics*, Vol.75, No.4, pp 2042-2047, ISSN 0021-8979

Watanabe, M.; Aritomo, H.; Yamaguchi, I.; Shinagawa, T.; Tamai, T.; Tasaka, A. & Izaki, M. (2007). Selective Preparation of Zinc Oxide Nanostructures by Electrodeposition on the Templates of Surface-functionalized Polymer Particles, *Chemistry Letters*, Vol.36, No.5, pp 680–681, ISSN 0366-7022

Yamaguchi, K.; Sawatani, S.; Yoshida, T.; Ohya, T.; Ban, T.; Takahashi Y. & Minoura, H. (2005). Electrodeposition of TiO_2 thin films by anodic formation of titanate/benzoquinone hybrid, *Electrochemical and Solid-State Letters*, Vol.8, No.5, pp C69-C71, ISSN 1099-0062

Yang, S-C.; Yang, D-J.; Kim, J.; Hong, J-M.; Kim, H-G.; Kim, I-D. & Lee, H. (2008). Hollow TiO_2 Hemispheres Obtained by Colloidal Templating for Application in Dye-

Sensitized Solar Cells, *Advanced Materials*, Vol.20, No.5, pp 1059–1064, ISSN 0935-9648

Ye, Y. -H.; LeBlanc, F.; Hache, A.; Truong, V. -V. (2001). Self-assembling three-dimensional colloidal photonic crystal structure with high crystalline quality, *Applied Physics Letters*, Vol.78, No.1, pp 52-54, ISSN 0003-6951

Yip, C. -H.; Chiang, Y. -M. & Wong, C. -C. (2008). Dielectric Band Edge Enhancement of Energy Conversion Efficiency in Photonic Crystal Dye-Sensitized Solar Cell, *Journal of Physical Chemistry C*, Vol.112, No.23, pp 8735–8740, ISSN 1932-7447

Fabrication of ZnO Based Dye Sensitized Solar Cells

A.P. Uthirakumar

Nanoscience Centre for Optoelectronics and Energy Devices,
Sona College of Technology, Salem, Tamilnadu,
India

1. Introduction

Why solar power is considered as one of the ultimate future energy resources? To answer this, drastic depletion of fossil fuels and the challenges ahead on needs for the specific requirements are the major causes for the need alternative power. At the beginning of February, 2007, the Intergovernmental Panel on Climate Change (*IPCC*) presented a report concluding that global concentrations of carbon dioxide, methane and nitrous oxide have increased markedly as a result of human activities since 1750. The report states that the increase in carbon dioxide, the most important greenhouse gas, is primarily due to fossil fuel use. The report further indicates that the increased concentrations of carbon dioxide, methane, and nitrous oxide have increased the average global temperature, a phenomenon known as "global warming". Eventually, if the temperature continues to increase, this will influence our everyday lives, since it changes the conditions of, for example, agriculture and fishing. In order to preserve the surplus energy coming out from the Sun, an alternative technique is necessary for our future energy needs. The potential of using the sun as a primary energy source is enormous. For example, sunlight strikes the Earth in one hour (4.3×10^{20} J) is sufficient to satisfy the more than the globel energy consumed on the planet in a year (4.1×10^{20} J). In other words, it has been calculated that covering 0.1% of the earth's surface area with solar cells of 10% efficiency, corresponding to 1% of desert areas or 20% of the area of buildings and roads, would provide for global electricity consumption. As for as to convert the solar power into the basic electricity, there may be the new technology to be implimented to harvest the solar energy in an effective manner. In this regard, one way to consume solar power, the photovoltaic cell will be suitable one to convert sunlight into electrical energy. The challenge in converting sunlight into electricity via photovoltaic solar cells is dramatically reducing the cost/watt of delivered solar electricity, by approximately a factor of 5–10 times to compete with fossil and nuclear electricity and by a factor of 25–50 to compete with primary fossil energy.

Recently, many of research groups are actively involving to harvest maximum conversion of solar power into electricity. Hence, varieties of new materials that are capable to absorb solar spectrum are successfully prepared in different methods. These new materials should satisfy the following important points to be act as the effective light harvesting materials. It should be efficiently absorb sunlight, should cover the full spectrum of wavelengths in solar radiation, and new approaches based on nanostructured architectures can revolutionize the technology used to produce energy from the solar radiation. The technological development in novel approaches exploiting thin films, organic semiconductors, dye sensitization, and

quantum dots offer fascinating new opportunities for cheaper, more efficient, longer-lasting systems. The conversion from solar energy to electricity is fulfilled by solar-cell devices based on the photovoltaic effect. Many photovoltaic devices have already been developed over the past five decades (Liu et al., 2008). However, wide-spread use is still limited by two significant challenges, namely conversion efficiency and cost (Bagnall et al., 2008). One of the traditional photovoltaic devices is the single-crystalline silicon solar cell, which was invented more than 50 years ago and currently makes up 94% of the market (Chapin et al., 1954). In addition to this other compound semiconductors, such as gallium arsenide (GaAs), cadmium telluride (CdTe), and copper indium gallium selenide, receive much attention because they present direct energy gaps, can be doped to either p-type or n-type, have band gaps matching the solar spectrum, and have high optical absorbance (Afzaal & O'Brien, 2006). These devices have demonstrated single-junction conversion efficiencies of 16–32% (Birkmire, 2001). Although those photovoltaic devices built on silicon or compound semiconductors have been achieving high efficiency for practical use, they still require major breakthroughs to meet the long-term goal of very-low cost.

In case of lowering the cost of production, dye-sensitized solar cells (DSSCs) based on oxide semiconductors and organic dyes or metallorganic-complex dyes have recently emerged as promising approach to efficient solar-energy conversion. The DSSCs are a photoelectrochemical system, which incorporate a porous-structured oxide film with adsorbed dye molecules as the photosensitized anode. A typical DSSC system composed of a mesoporous titanium dioxide (TiO_2) film on a transparent conductor. Dye molecules are absorbed on the entire porous TiO_2 that is perfused with an electrolyte containing iodide and tri-iodide. A layer of additional electrolyte separates the porous TiO_2 from a counter electrode. When a photon is absorbed by a dye, the excited dye transfers an electron to the TiO_2 (termed injection). The then oxidized dye can be reduced by iodide (regeneration) or can recapture an electron from the TiO_2. The electron in the TiO_2 can diffuse to a collection electrode (transport) or can be captured by a triiodide molecule in the electrolyte. Electrons that reach the collection electrode flow through the external circuit and reduce tri-iodide to iodide at the counter electrode.

Compared with the conventional single-crystal silicon-based or compound-semiconductor thin-film solar cells, DSSCs are thought to be advantageous as a photovoltaic device possessing both practicable high efficiency and cost effectiveness. To date, the most successful DSSC was obtained on TiO_2 nanocrystalline film combined with a ruthenium–polypyridine complex dye (Gra¨tzel et al., 2000, 2001, 2003 & 2007). Following this idea, a certified overall conversion efficiency of 10.4% was achieved on a TiO_2–RuL′(NCS)3 ("black dye") system, in which the spectral response of the complex dye was extended into the near-infrared region so as to absorb far more of the incident light. The porous nature of nanocrystalline TiO_2 films drives their use in DSSCs due to the large surface area available for dye-molecule adsorption. Meanwhile, the suitable relative energy levels at the semiconductor–sensitizer interface (i.e., the position of the conduction-band edge of TiO2 being lower than the excited-state energy level of the dye) allow for the effective injection of electrons from the dye molecules to the semiconductor (Nelson & Chandler, 2004).

2. The dye-sensitized solar cell

A promising alternative energy source of DSSC will be expected to increase the significant contribution to overall energy production over the coming years. This is mainly due to the offering a low-cost fabrication and attractive features such as transparency, flexibility, etc.

that might facilitate the market entry. Among all of them, DSSCs are devices that have shown to reach moderate efficiencies, thus being feasible competitors to conventional cells. DSSC combine the optical absorption and charge-separation processes by the association of a sensitizer as light-absorbing material with a wide band-gap semiconductor (usually titanium dioxide). A schematic representation of energy flow in DSSC is illustrated in Figure 1. As early as the 1970s, it was found that TiO_2 from photoelectrochemical cells could split water with a small bias voltage when exposed to light (Fujishima & Honda, 1972). However, due to the large band-gap for TiO_2, which makes it transparent for visible light, the conversion efficiency was low when using the sun as illumination source. This pioneering research involved an absorption range extension of the system into the visible region, as well as the verification of the operating mechanism by injection of electrons from photoexcited dye molecules into the conduction band of the n-type semiconductor. Since only a monolayer of adsorbed dye molecules was photoactive, light absorption was low and limited when flat surfaces of the semiconductor electrode were employed. This inconvenience was solved by introducing polycrystalline TiO_2 (anatase) films with a surface roughness factor of several hundreds Desilvestro et al., 1985). The amount of adsorbed dye was increased even further by using mesoporous electrodes, providing a huge active surface area thereby, and cells combining such electrodes and a redox electrolyte based on iodide/triiodide couple yielded 7% conversion efficiencies in 1991 (Nazeerudin et al., 1993). The next highest energy conversion efficiency is over 11% (Chiba et al., 2006), and further increase of the efficiency is possible by designing proper electrodes and sensitization dyes. Michael Grätzel is a professor at the École Polytechnique Fédérale de Lausanne where he directs the Laboratory of Photonics and Interfaces. He pioneered research on energy and electron transfer reactions in mesoscopic-materials and their optoelectronic applications and discovered a new type of solar cell based on dye sensitized mesoscopic oxide particles and pioneered the use of nanomaterials in lithium ion batteries. Today, record efficiencies above 13% have been presented at an illumination intensity of 1000 Wm-2, and the device displays promising stability data (Gra¨tzel et al., 2000, 2001, 2003 & 2007).
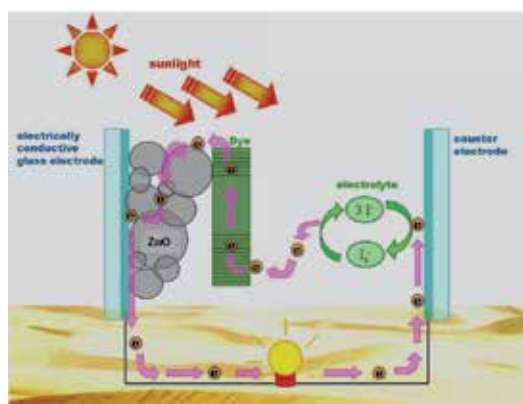
Fig. 1. Schematic diagram of the energy flow in the dye-sensitized solar cell.

The possible mechanism of electron hole interaction during DSSC operation is illustrated in Figure 2. After the successful excitation of dye molecules with the sun light, the ground state electrons at the highest occupied molecular orbital will be photoexcited and residing at unoccupied molecular orbital. Then, the photoexcited electrons are passing through the

nanomaterials to reach electrodes for completion. The detailed mechanism for the electron transports within DSSC device is described as shown in Figure 2. Here, photoexcited electrons are injected from the dye to the conduction band (denoted as ''c.b.'') of the nanocrystallite (1), the dye is regeneratedby electron transfer from a redox couple in the electrolyte (3), and a recombination may take place between the injected electrons and the dye cation (2) or redox couple (4). The latter (4) is normally believed to be the predominant loss mechanism. Electron trapping in the nanocrystallites (5) is also a mechanism that causes energy loss.
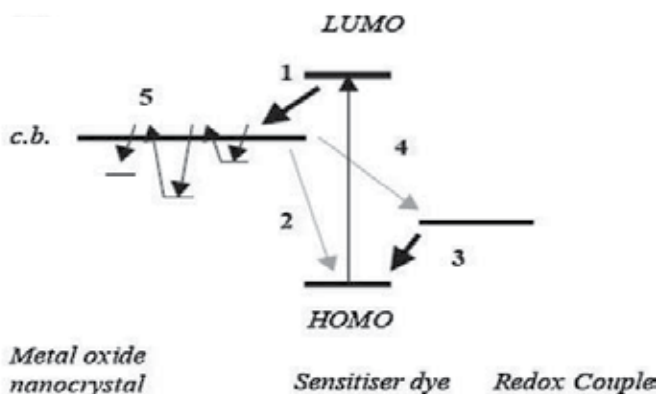

Fig. 2. A schematic illustrates the electron-hole interactions after the excitation of dye molecules with the sun light.

In the recent years, the DSSCs offer to achieve moderate conversion efficiency to the maximum of ~14%. In this case, a wide band gap, mesoporous nanocrystalline TiO_2 was used as photoanodic material, on which dye molecules are adsorbed for the photo harvesting. Major achievers in the DSSC developments are mainly from the recent technology development and optimization. Now in the place of TiO_2, an another alternative, a direct wide band gap metal oxide material is zinc oxide (ZnO), a wurtzite type semiconductor with an energy gap of 3.37 eV at room temperature, as summerziaed in Table 1. Due to its large bandgap, ZnO is an excellent semiconductor material like other wide bandgap materials of GaN and SiC. The crystal strcture, energy band gap, electron mobility and electron diffusion coefficient of both ZnO and TiO_2 nanomaterials were summerized in Table 1, for comparison. The band gap energy of ZnO nanomaterials is almost same as that of TiO_2 and the electron mobility and electron diffusion coefficient of ZnO showed much highier values than the TiO_2, which faciliates the important for the DSSC application.

To understand this issue, DSSC technology based on ZnO has been explored extensively. ZnO is a wide-band-gap semiconductor that possesses an energy-band structure and physical properties similar to those of TiO_2 (Table 1), but has higher electronic mobility that would be favorable for electron transport, with reduced recombination loss when used in DSSCs. Hence, many studies have already been started and reported on the useage of ZnO nanomaterial for application in DSSCs. Although the conversion efficiencies of 0.4–5.8% obtained for ZnO are much lower than that of 11% for TiO_2, ZnO is still thought of as a distinguished alternative to TiO_2 due to its ease of crystallization and anisotropic growth. These properties allow ZnO to be produced in a wide variety of nanostructures, thus

presenting unique properties for electronics, optics, or photocatalysis (Tornow et al., 2007 & 2008 and Djurisic et al 2006). Parallely, numerous works have been published to explore in-depth analysis of their shape controllable synthesis that includes needles, rods, tubes, towers, hollow prisms, tetra-legs, flowers, stars, helices, belts and springs via simple method. For example, the major reason for useage of nanostructures with a large specific surface area help in many particular behaviors in electron transport or light propagation in view of the surface effect, quantum-confinement effect or photon localization (Bittkau et al., 2007). Those nanostructural forms of ZnO developed during the past several decades mainly include nanoparticles, nanorod, nanotubes, nanobelts, nanosheets and nanotips. The production of these structures can be achieved through sol–gel synthesis, hydrothermal /solvothermal growth, physical or chemical vapor deposition, low-temperature aqueous growth, chemical bath deposition, or electrochemical deposition.

	ZnO	TiO$_2$
Crystal structure	rocksalt, zinc blende, and wurtzite	rutile, anatase, and brookite
Energy band gap [eV]	3.2–3.3	3.0–3.2
Electron mobility [cm^2 Vs^1]	205–300 (bulk ZnO), 1000 (single nanowire)	0.1–4
Refractive index	2.0	2.5
Electron effective mass[me]	0.26	9
Relative dielectric constant	8.5	170
Electron diffusion coefficient [cm^2 s^1]	5.2 (bulk ZnO), 1.7 $_x$ 10^4 (nano-particulate film)	0.5 (bulk TiO$_2$), 10^8–10^4 (nano- particulate film)

Table 1. A comparison of physical properties of ZnO and TiO$_2$.

In particular, recent studies on ZnO-nanostructure-based DSSCs have delivered many new concepts, leading to a better understanding of photoelectrochemically based energy conversion. This, in turn, would speed up the development of DSSCs that are associated with TiO$_2$. Moreover, these ZnO nanomaterials can be synthesized through simple chemical methods with the wide range of structural evolution, fabricating DSSCs with ZnO nano-structured materials will be advisable and reliable in place of TiO$_2$, whose structural controllability is not easy in a conversional chemical synthetic route. In this chapter, recent developments in ZnO nanostructures, particularly for application in DSSCs, are reported. It will show that photoelectrode films with nanostructured ZnO can significantly enhance solar-cell performance by offering a large surface area for dye adsorption, direct transport pathways for photoexcited electrons, and efficient scattering centers for enhanced light-harvesting efficiency. The limitations of ZnO-based DSSCs are also discussed. In the final section, several attempts to expand ZnO concepts to TiO$_2$ are presented to motivate further improvement in the conversion efficiency of DSSCs.

3. Crystal and surface structure of ZnO

At ambient pressure and temperature, ZnO crystallizes in the wurtzite (B4 type) structure, as shown in Figure 3 (Jagadish et al., 2006). This is a hexagonal lattice, belonging to the space group P$_{63}$*mc* with lattice parameters a = 0.3296 and c = 0.52065 nm. Usually, we can treat it

as a number of two type planes, i.e. tetrahedrally coordinated O^{2-} and Zn^{2+} ions, and stacked alternately along the c-axis. Or in another way, it also can be characterized by two interconnecting sublattices of Zn^{2+} and O^{2-}, such that each Zn ion is surrounded by tetrahedra of O ions, and vice-versa. No doubt, this kind of tetrahedral coordination in ZnO will form a noncentral symmetric structure with polar symmetry along the hexagonal axis, which not only directly induces the characteristic piezoelectricity and spontaneous polarization, but also plays a key factor in crystal growth, etching and defect generation of ZnO.
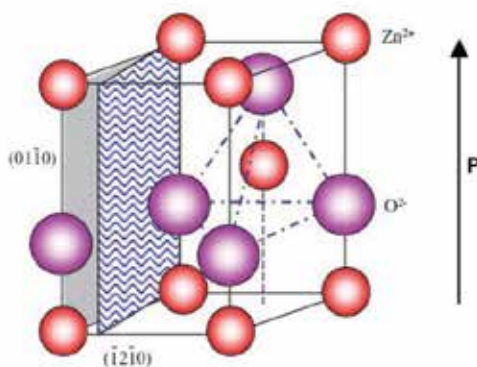

Fig. 3. The wurtzite structure model of ZnO. The tetrahedral coordination of Zn–O is shown.

The polar surface is another important characteristic of ZnO structure. As well as we known, wurtzite ZnO crystallizes do not have a center of inversion. If the ZnO crystals such as nanorods and nanotubes grow along the c axis, two different polar surfaces will be formed on the opposite sides of the crystal due to the suddenly termination of the structure, i.e. the terminated Zn-(0001) surface with Zn cation outermost and the terminated O-(000) surface with O anion outermost. Naturally, these positively charged Zn-(0001) and negatively charged O-(000) surfaces are the most common polar surfaces in ZnO, which subsequently results in a normal dipole-moment and spontaneous polarization along the c-axis as well as a divergence in surface energy. Generally, the polar surfaces have facets or exhibit massive surface reconstructions in order to maintain a stable structure. However, ZnO-± (0001) are exceptions: they are atomically flat, stable and without reconstruction (Dulub et al., 2002 & Wander et al. 2001). Efforts to understand the superior stability of the ZnO ± (0001) polar surfaces are at the forefront of research in today's surface physics (Staemmler et al, 2003 & Singh et al., 2007).

4. Basic physical parameters for ZnO

The basic physical parameters of ZnO were compiled and placed as in Table 2 (Pearton et al., 2005 & Florescu et al., 2002). The physical parameters include energy band gap, excitons binding energy, electron effective mass, hole effective mass, hole hall mobility and lattice paramerter for easy understanding. It should also be noted that there still exists uncertainty in some of these values. For example, there have few reports of p-type ZnO and therefore the hole mobility and effective mass are still in debate. Similarly, the values for thermal conductivity show some spread in values and this may be a result of the influence of defects such as dislocations (Hosokawa et al., 2007), as was the case for GaN. The values for carrier

mobility will undoubtedly increase as more control is gained over compensation and defects in the material.

Physical parameters	Values
Stable phase at 300 K	Wurtzite
Energy band gap	3.37 eV, direct
Density	5.606 g/cm^3
Refractive index	2.008, 2.029
Melting point	1975°C
Thermal conductivity	0.6, 1–1.2
Exciton binding energy	60 meV
Electron effective mass	0.24
Electron Hall mobility at 300 K for low n-type conductivity	200 cm^2/V s
Linear expansion coefficient(/^{o}C)	a_0: 6.5 ×10^{-6} and c_0: 3.0 × 10^{-6}
Static dielectric constant	8.656
Hole effective mass	0.59
Hole Hall mobility at 300 K for low p-type conductivity	5–50 cm^2/V s
Intrinsic carrier concentration	<106 cm^{-3} (max n-type doping >1020 cm^{-3} electrons; max p-type doping <1017 cm^{-3} holes)
Lattice parameters at 300 K	
a_0	0.32495 nm
c_0	0.52069 nm
a_0/c_0	1.602 (ideal hexagonal structure shows 1.633)
U	0.345

Table 2. Physical parameters of ZnO.

5. Synthesis of ZnO nanomaterials for DSSC

The major objective of selecting a photoanodic nanomaterials film for DSSC, it should offer large internal surface area whereby to adsorb sufficient dye molecules for the effect capture of incident photons from the solar power. This objective will be solved by the formation of a porous interconnected network in which the specific surface area may be increased by more than 1000 times when compared with bulk materials (Lee et al., 2003). In this respect, ZnO is a key technological material and it has a wide band-gap compound semiconductor that is suitable for optoelectronic applications. In addition to this, the abundant forms of ZnO nanostructures provide a great deal of opportunities to obtain high surface-area-to-volume ratios, which helps to contribute the successful dye adsorption leading to a better light harvesting, in DSSCs. Therefore, many research groups are actively intriguing to dealings with this task of preparing various structurally different types of ZnO nanostructures to fabricate the DSSC for future energy crisis. Hence, variety of different synthetic methods, such as vapor-phase transport (Zhao et al., 2007, Huang et al., (2001) & Sun et al., (2004), pulsed laser deposition (Wu et al., 2002), chemical vapor deposition (Park et al., 2002, Yu et al., 2005) and electrochemical deposition (Zeng et al., 2006).

Structure	Ru based dyes	Efficiency
Nanoparticles	N719	0.44%, 2.1% (0.06 sun), 2.22%
	N719	5% (0.1 sun)
	N3	0.4%, 0.75%, 2% (0.56 sun), 3.4%
Nanorods	N719	0.73%
	N719	0.22%
	N719	1.69%
Nanotips	N719	0.55%, 0.77%
Nanotubes	N719	1.6%, 2.3%
Nanobelts	N719	2.6%
Nanosheets	N719	2.61%, 3.3%
	N3	1.55%
Nanotetrapods	N719	1.20%, 3.27%
Nanoflowers	N719	1.9%
Nanoporous films	N3	5.08% (0.53 sun)
	N719	3.9%, 4.1%
	N719	0.23%
Nanowires	N3	0.73%, 2.1%, 2.4%, 4.7%
	N719	0.3%, 0.6%, 0.9%,1.5%, 1.54%
Aggregates	N3	3.51%, 4.4%, 5.4%

Table 3. Summary of DSSCs based on ZnO nanostructures.

ZnO nanostructured materials with diverse range of structureally distinct morphologies were synthesized from different methods as listed in Table 3. The detailed behind the morphologically distinct ZnO nanomaterials utilization in the DSSC application with the help of Ru dye complex and their impact of solar power geneuration also displayed in Table 3. The followings are the few examples of diverse group of ZnO growth morphologies, such as nanoparticles (Keis et al., 2000, Suliman et al., 2007 & Gonzalez-Valls et al., 2010), nanorod (Lai et al., 2010, Hsu et al., 2008 & Charoensirithavorn et al., 2006), nanotips (Martinson et al., 2007), nanotubes (Lin et al., 2008), nanobelts (Kakiuchi et al., 2008), nanosheets (Chen et al., 2006) , nanotetrapods (Jiang et al, 2007), nanoflowers (Chen et al., 2006), nanoporous films (Hosono et al., 2005, Kakiuchi et al., 2006 & Guo et al., 2005), nanowires (Guo et al., 2005, Rao et al., 2008, Wu et al., 2007 & Law et al., 2005) and aggregates (Chou et al., 2007 & Zhang et al., 2008). These ZnO nanostructures are easily prepared even on cheap substrates such as glass and utilized for the DSSC application as photoanodic materials. Hence, they have a promising potential in the nanotechnology future. The specific impact of individually distinct ZnO nanomaterials will be discussed in the subsequent section in details.

5.1 Useage of ZnO nanoparticles as photoanodic material
The first and foremost interest on ZnO structural morphology is of spherical shaped nanoparticles (NPs) that suit in both synthetic methodoly as well as process simplicity. In particular, ZnO NPs can easily be prepared in simple methods by proper judification of their reaction conditions and parameters. Uthirakumar et al. reported simple solution method for the preparation of verity of ZnO nanostructured materials out of which is ZnO NP, one of the significant nanomaterials. The diverse morphology of ZnO nanostructures synthesized from solution method is displayed in Figure 4. They continued to utilize these nanoparticles for

DSSC device fabrication (Uthirakumar et al., 2006, 2007, 2008 & 2009). ZnO NPs with N3 dye sensitizer produced the higher solar power conversion efficiency ranges from 0.44 to 3.4% (Keis et al., 2000, Uthirakumar et al., 2009). However, further improvement of maximum of 5% conversion efficiency with N719 dye. Hosono et al systematically studied the DSSC performance of nanoporous structured ZnO films fabricated by the CBD technique (Hosono et al., 2004, 2005 & 2008). They achieved an overall conversion efficiency of 3.9% when as-prepared 10-mm-thick ZnO films were sensitized by N719 dye with an immersion time of 2 h (Hosono et al., 2005). Further improvement to 4.27% in the conversion efficiency was reported recently by Hosono et al. when the dye of N719 was replaced with a metal-free organic dye named D149 and the immersion time was reduced to 1h (Hosono et al., 2008). The enhancement in solar-cell performance was attributed to the use of D149 dye and a nanoporous structure that contained perpendicular pores. This allowed for a rapid adsorption of the dye with a shorter immersion time and thus prevented the formation of a $Zn^2þ$/dye complex. This complex is believed to be inactive and may hinder electron injection from the dye molecules to the semiconductor [66]. In another study, a high photovoltaic efficiency of up to 4.1% was also obtained for nanoporous ZnO films produced by the CBD (Kakiuchi et al., 2006). However, the excellence of the solar-cell performance was ascribed to the remarkably improved stability of as-fabricated ZnO films in acidic dye.
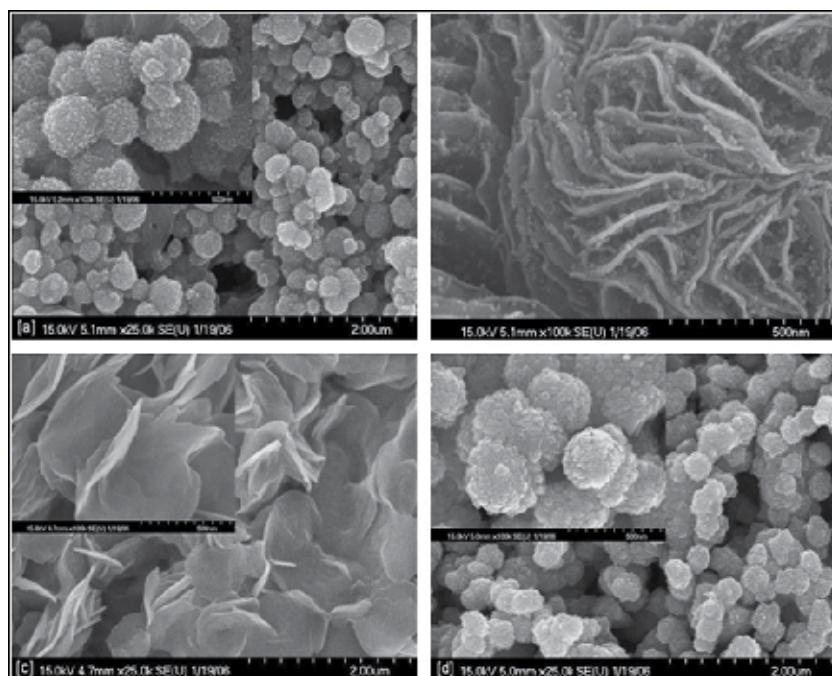
Fig. 4. Diverse morphology of ZnO nanomaterials from solution method.

5.2 Useage of ZnO nanorods as photoanodic material

Controllable length of ZnO nanorods can be grown in solution. The ZnO nanorods are formed at a relatively high temperature (~90 °C), where the reaction solution is enriched with colloidal $Zn(OH)_2$ and therefore allows a fast growth of ZnO nanocrystals along the [001] orientation to form nanorods. ZnO nanorods were grown on the seeded substrates in a

sealed chemical bath containing 10 mM each of zinc nitrate (Zn[NO$_3$]$_2$·6H2O) and hexamine ([CH2]$_6$N$_4$) for 15 h at 90 °C. Photoanodic ZnO nanorod electrodes can be made with vertically-aligned ZnO nanorods and analyzed the usage of DSSC. The highest solar cell efficiency obtained was 0.69% after UV light irradiation (at 72 °C, 0.63 V, 2.85 mA cm^{-2}, 0.39 FF) (Gonzalez-Valls et al., 2010). Typical nanorod-based DSSCs are fabricated by growing nanorods on top of a transparent conducting oxide, as shown in Figure 5. The heterogeneous interface between the nanorod and TCO forms a source for carrier scattering. The new DSSCs yield a power conversion efficiency of 0.73% under 85 mW/cm2 of simulated solar illumination (Lai et al., 2010). Hydrothermally grown and vapor deposited nanorods also exhibit different dependence of photovoltaic performance on the annealing conditions of the rods, indicating significant effect of the native defects on the achievable photocurrent and power conversion efficiency. Efficiency of 0.22% is obtained for both as grown hydrothermally grown nanorods and vapor deposited nanorods annealed in oxygen at 200°C (Hsu et al., 2008). P. Charoensirithavorn et al., proposed a new possibility in designing a cell structure produced an open circuit voltage (Voc) of 0.64 mV, a short circuit current density (Jsc) of 5.37 mA/cm2, a fill factor (FF) of 0.49, and conversion efficiency (η) of 1.69 %, primarily limited by the surface area of the nanorod array (sirithavorn et al., 2006).
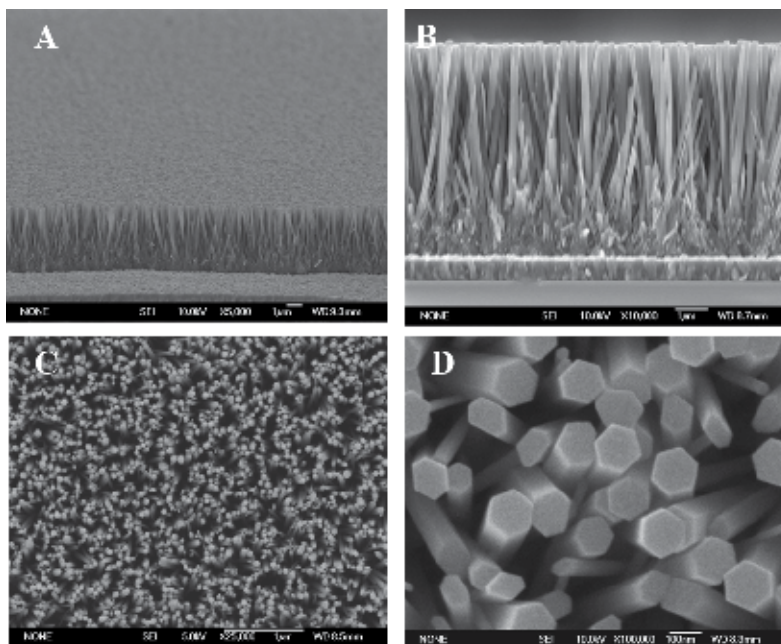
Fig. 4. SEM images of ZnO nanorods grown on FTO substrate (A) tilt, (B) side and (C) top and (D) bottom view at low and high magnification.

5.3 Usage of ZnO nanotubes as photoanodic material

Among one-dimensional ZnO nanostructures, the tubular structures of ZnO become particularly important in DSSC are required their high porosity and large surface area to fulfill the demand for high efficiency and activity. A subsequent decrease in the temperature yields a supersaturated reaction solution, resulting in an increase in the concentration of OH$^-$ ions as well as the pH value of the solution. Colloidal Zn(OH)$_2$ in the supersaturated solution tends to

precipitate continually. However, because of a slow diffusion process in view of the low temperature and low concentration of the colloidal $Zn(OH)_2$, the growth of nanorods is limited but may still occur at the edge of the nanorods due to the attraction of accumulated positive charges to those negative species in the solution, ultimately leading to the formation of ZnO nanotubes, as clearly represented in Figure 5(a). The role of changing the pH value observed in the growth of ZnO crystals is shown also to have a relationship to the change of the surface energy. In the course of growing ZnO nanorods, changing the growth temperature, from a high (90 °C) to a low temperature (60 °C), leads to some change in the pH value. At the low pH value, the polar face has such a high surface energy that it permits the growth of nanorods. However, the grain growth can be inhibited by a high pH value at a low growth temperature. The competition between the change of surface energy due to pH value and growth rate dictated by the temperature can be assumed to lead to the ZnO tube structure, as shown in Figure 5(b). This investigation provides more options and flexibility in controlling methods to obtain various morphologies of ZnO crystals in terms of the change of growth temperature and pH value. Other synthetic methods for the preparation of nanotubes are realized by electrochemical method, low temperature solution method, vapor phase growth and the simple chemical etching process to convert the nanorods into nanotubes. The chemical etching process was carried out by suspending the nanorods sample upside down in 100 ml aqueous solution of potassium chloride (KCl) with 5M concentration for 10 h at 95 °C.

(a)

(b)
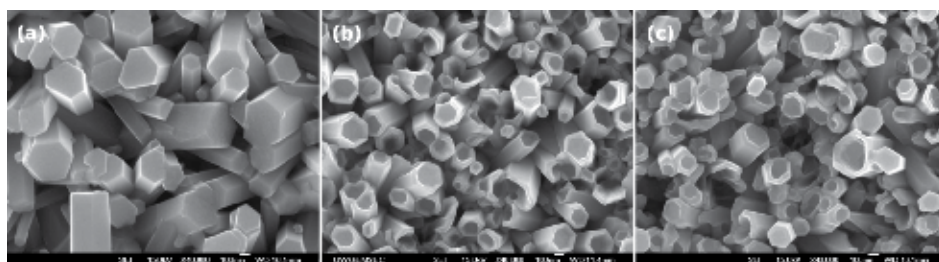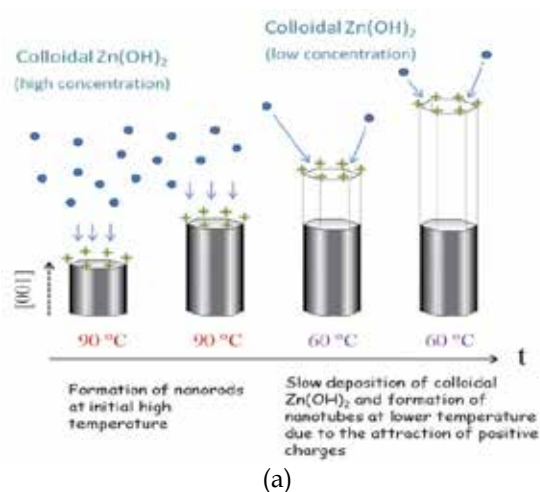
Fig. 5. A schematic representation and B) SEM images on evolution of ZnO nanorods to tubes while the solution was kept at 90 °C for 3 h and then cooled down to (a) 80 °C (20 h), (b) 60 °C (20 h) and (c) 50 °C (20 h).

High-density vertically aligned ZnO nanotube arrays were fabricated on FTO substrates by a simple and facile chemical etching process from electrodeposited ZnO nanorods. The nanotube formation was rationalized in terms of selective dissolution of the (001) polar face. The morphology of the nanotubes can be readily controlled by electrodeposition parameters for the nanorod precursor. By employing the 5.1 µm-length nanotubes as the photoanode for a DSSC, a full-sun conversion efficiency of 1.18% was achieved (Han *et al.*, 2010). Alex et al introduce high surface area ZnO nanotube photoanodes templated by anodic aluminum oxide for use in dye-sensitized solar cells (DSSCs). Compared to similar ZnO-based devices, ZnO nanotube cells show exceptional photovoltage and fill factors, in addition to power efficiencies up to 1.6%. The novel fabrication technique provides a facile, metal-oxide general route to well-defined DSSC photoanodes (Martinson et al., 2010). Nanotubes differ from nanowires in that they typically have a hollow cavity structure. An array of nanotubes possesses high porosity and may offer a larger surface area than that of nanowires. An overall conversion efficiency of 2.3% has been reported for DSSCs with ZnO nanotube arrays possessing a nanotube diameter of 500 nm and a density of 5.4×10^6 per square centimeter. ZnO nanotube arrays can be also prepared by coating anodic aluminum oxide (AAO) membranes via atomic layer deposition. However, it yields a relatively low conversion efficiency of 1.6%, primarily due to the modest roughness factor of commercial membranes (Chae et al., 2010).

5.4 Usage of ZnO nanowires as photoanodic material

In 2005, Law et al. first reported the usage of ZnO nanowire arrays in DSSCs by with the intention of replacing the traditional nanoparticle film with a consideration of increasing the electron diffusion length (Law et al., 2007). Nanowires were grown by immersing the seeded substrates in aqueous solutions containing 25 mM zinc nitrate hydrate, 25 mM hexamethylenetetramine, and 5–7 mM polyethylenimine (PEI) at 92 8C for 2.5 h. After this period, the substrates were repeatedly introduced to fresh solution baths in order to obtain continued growth until the desired film thickness was reached. The use of PEI, a cationic polyelectrolyte, is particularly important in this fabrication, as it serves to enhance the anisotropic growth of nanowires. As a result, nanowires synthesized by this method possessed aspect ratios in excess of 125 and densities up to 35 billion wires per square centimeter. The longest arrays reached 20–25 mm with a nanowire diameter that varied from 130 to 200 nm. These arrays featured a surface area up to one-fifth as large as a nanoparticle film.
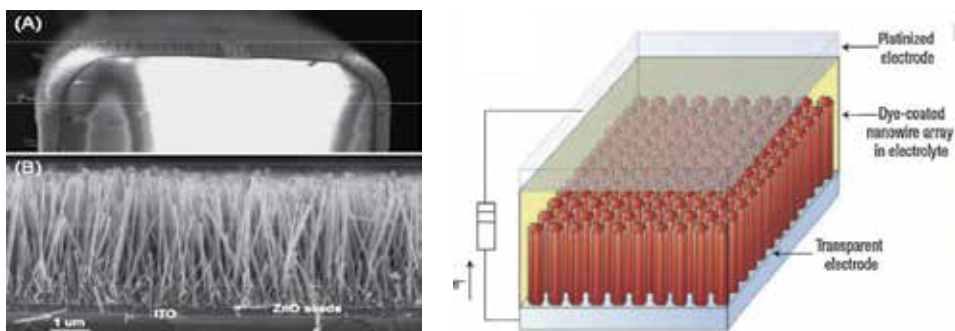

Fig. 6. a) Cross-sectional SEM image of the ZnO-nanowire array and b) Schematic diagram of the ZnO-nanowire dye-sensitized solar cells.

Figure 6a shows a typical SEM cross-section image of an array of ZnO nanowires. It was found that the resistivity values of individual nanowires ranged from 0.3 to 2.0 V cm, with an electron concentration of $1–5 \times 10^{18}$ cm^3 and a mobility of $1–5$ cm^2 V^{1}s^1. Consequently, the electron diffusivity could be calculated as $0.05–0.5$ cm^2 s^1 for a single nanowire. This value is several hundred times larger than the highest reported electron diffusion coefficients for nanoparticle films in a DSSC configuration under operating conditions, that is, 10^7–10^4 cm^2 s^1 for TiO$_2$ and 10^5–10^3 cm^2 s^1 for ZnO. A schematic of the construction of DSSC with nanowire array is shown in Figure 6b. Arrays of ZnO nanowires were synthesized in an aqueous solution using a seeded-growth process. This method employed fluorine-doped tin oxide (FTO) substrates that were thoroughly cleaned by acetone/ethanol sonication. A thin film of ZnO quantum dots (dot diameter ~3–4 nm, film thickness ~10–15 nm) was deposited on the substrates via dip coating in a concentrated ethanol solution. For example, at a full sun intensity of 100×3mW cm^2, the highest-surface-area devices with ZnO nanowire arrays were characterized by short-circuit current densities of $5.3–5.85$ mA cm^2, open-circuit voltages of 610–710 mV, fill factors of 0.36–0.38, and overall conversion efficiencies of 1.2–1.5% (Kopidakis et al., 2003).

5.5 Usage of ZnO nanoflowers as photoanodic material

Another interesting morphology is of using ZnO nanoflowers as photoanodic materials for DSSC device fabrication. The shape of nanoflower consists of upstanding stem with irregular branches in all sides of base stem and overall it looks like a flower like morphology. Importance of Nanoflower structure is coverage of ZnO-adsorped dye molecules for effective light harvesting than in in nanorod itself. Because of the fact that nanoflower can be stretch to fill intervals between the nanorods and, therefore, provide both a larger surface area and a direct pathway for electron transport along the channels from the branched ''petals'' to the nanowire backbone (Fig. 7). ZnO film consisits of nanoflowers can be grown by a hydrothermal method at low temperatures. The typical procedure is as follows: 5 mM zinc chloride aqueous solution with a small amount of ammonia. These as-synthesized nanoflowers, as shown in Figure 7b, have dimensions of about 200 nm in diameter. Then, the ZnO films with ''nanoflowers'' have been also reported for application in DSSCs. The solar-cell performance of ZnO nanoflower films was characterized by an overall conversion efficiency of 1.9%, a current density of 5.5mA cm^2, and a fill factor of 0.53. These values are higher than the 1.0%, 4.5 mA cm^2, and 0.36 for films of nanorod arrays with comparable diameters and array densities that were also fabricated by the hydrothermal method (Jiang et al., 2007).
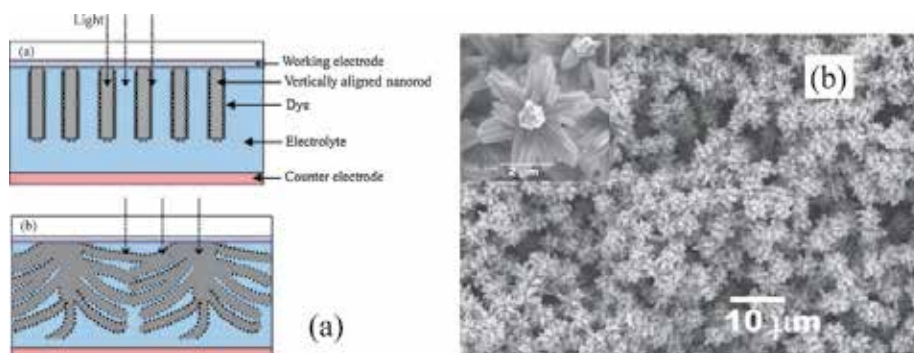

Fig. 7. a) Schematic diagram of the ZnO nanoflower-based dye-sensitized solar cells and b) Top view SEM image of the ZnO-nanoflowers.

5.6 Usage of ZnO nanosheets as photoanodic material

Rehydrothermal growth process of previously hydrothermally grown ZnO nanoparticles can be used to prepare ZnO nanosheets, which are quasi-two-dimensional structures (Suliman et al., 2007, Kakiuchi et al., 2008). Figure 8 shows the SEM images of ZnO nanosheets of low and high magnignified images. ZnO nanosheets are used in a DSSC application, which possess a relatively low conversion efficiency, 1.55%, possibly due to an insufficient internal surface area. It seems that ZnO nanosheetspheres prepared by hydrothermal treatment using oxalic acid as the capping agent may have a significant enhancement in internal surface area, resulting in a conversion efficiency of up to 2.61% (Suliman et al., 2007, Kakiuchi et al., 2008). As for nanosheet-spheres, the performance of the solar cell is also believed to benefit from a high degree of crystallinity and, therefore, low resistance with regards to electron transport.
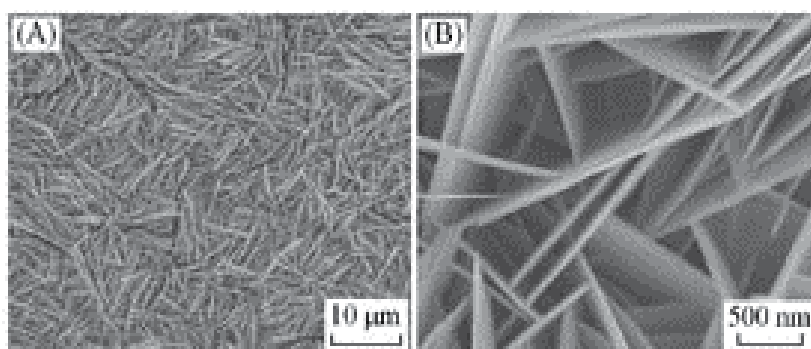

Fig. 8. a) Low and b) High magnified SEM images of the ZnO-nanosheets.

5.7 Usage of ZnO nanobelts as photoanodic material

ZnO nanobelts as photoanodic material can be prepared via an electrodeposition technique. Typically, 1 g of zinc dust mixed with 8 g of NaCl and 4 mL of ethoxylated nonylphenol $[C_9H_{19}C_6H_4(OCH_2CH_2)_nOH]$ and polyethylene glycol $[H(OCH_2CH_2)_nOH]$, and subsequently ground for one hour. The ground paste-like mixture was loaded into an alumina crucible and covered with a platinum sheet leaving an opening for vapor release. The crucible was then loaded into a box furnace and heated at 800°C. Here, ZnO films consists of nanobelt arrays as shown in Figure 9a and it also proposed to use for DSSC applications. In fabricating these nanobelts, polyoxyethylene cetylether was added in the electrolyte as a surfactant. The ZnO nanobelt array obtained shows a highly porous stripe structure with a nanobelt thickness of 5 nm, a typical surface area of 70 $m^2 g^1$, and a photovoltaic efficiency as high as 2.6%.

5.8 Usage of ZnO nanotetrapods as photoanodic material

A three-dimensional structure of ZnO tetrapod that consisting of four arms extending from a common core, as showin in Figure 9b (Jiang et al., 2007 & Chen et al., 2009). The length of the arms can be adjusted within the range of 1–20 mm, while the diameter can be tuned from 100 nm to 2 mm by changing the substrate temperature and oxygen partial pressure during vapor deposition. Multiple-layer deposition can result in tetrapods connected to each other so as to form a porous network with a large specific surface area. The films with ZnO tetrapods used in DSSCs have achieved overall conversion efficiencies of 1.20– 3.27%. It was
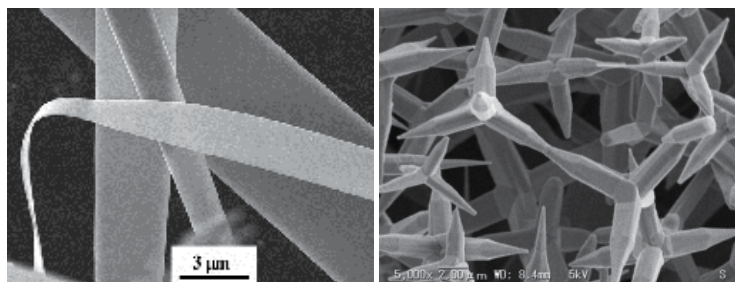
Fig. 9. SEM images of a) ZnO-nanobelt and b) ZnO nanotetrapods.

reported that the internal surface area of tetrapod films could be further increased by incorporating ZnO nanoparticles with these films, leading to significant improvement in the solar-cell performance. Another type of nanomaterials such as nanoporous film also leads to have the maximum coversion efficiency of 4.1% with N719 dye (Hosono et al., 2005).

5.9 Usage of ZnO aggregates as photoanodic material

So far, the maximum overall energy conversion efficiency was reported up to 5.4% from the ZnO film consisits of polydisperse ZnO aggregates, when compared to other nanostructures conversion efficiency of 1.5–2.4% for ZnO nanocrystalline films, 0.5–1.5% for ZnO Nanowire films, and 2.7–3.5% for uniform ZnO aggregate films (Desilvestro et al., 1985, Chou et al., 2007 & Zhang et al., 2008). The overall conversion efficiency of 5.4% with a maximum short-circuit current density of 19mA cm^2 are observed. In other words, the aggregation of ZnO nanocrystallites is favorable for achieving a DSSC with high performance, as shown in Figure 10. This result definitely shock us, since, many gourps were seriously working in synthesizing nanostructured material for DSSC. Here, though the ZnO aggregates are falls in submicron range, individual ZnO nanoparticles are in less than 20 nm. In Figure 10, the film is well packed by ZnO aggregates with a highly disordered stacking, while the spherical aggregates are formed by numerous interconnected nanocrystallites that have sizes ranging from several tens to several hundreds of nanometers. The preparation of these ZnO aggregates can be achieved by hydrolysis of zinc salt in a polyol medium at 160 °C (Chou et al., 2007). By adjusting the heating rate during synthesis and using a stock solution containing ZnO nanoparticles of 5 nm in diameter, ZnO aggregates with either a monodisperse or polydisperse size distribution can be prepared (Zhang et al., 2008).
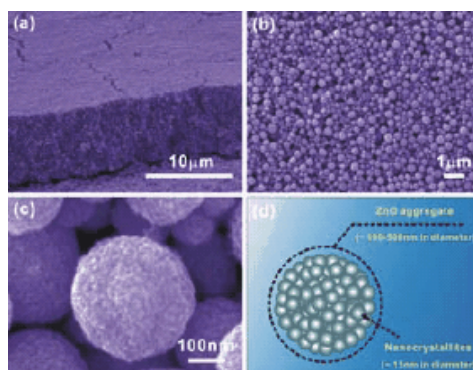

Fig. 10. SEM images of ZnO film with aggregates synthesized at 160 °C and a schematic showing the structure of individual aggregates.

6. Limitation on ZnO-based DSSCs

Although ZnO possesses high electron mobility, low combination rate, good crystallization into an abundance of nanostructures and almost an equal band gap and band position as TiO$_2$, the photoconversion efficiency of ZnO based DSSC still limited. The major reason for the lower performance in ZnO-based DSSCs may be explained by the a) formation of Zn^{2}þ/dye complex in acidic dye and b) the slow electron-injection flow from dye to ZnO. Zn^{2}þ/dye complex formation mainly occurs while ZnO is dipped inside the acidic dye solution for the dye adsorption for a long time. Ru based dye molecules consisits of carboxylic functional group for coordination, dye solution mostly existing in acidic medium. Therefore, the Zn^{2}þ/dye complex is inevitable. The formation of Zn^{2}þ/dye complex has been attributed to the dissolution of surface Zn atoms by the protons released from the dye molecules in an ethanolic solution. For lower electron-injection efficiency is reported of using ZnO material with Ru-based dyes when compared to TiO$_2$. In ZnO, the electron injection is dominated by slow components, whereas for TiO$_2$ it is dominated by fast components, leading to a difference of more than 100 times in the injection rate constant. For example, either ZnO or TiO$_2$, the injection of electrons from Ru-based dyes to a semiconductor shows similar kinetics that include a fast component of less than 100 fs and slower components on a picosecond time scale (Anderson et al., 2003). That is, the ZnO conduction bands are largely derived from the empty s and p orbitals of Zn^{2}þ, while the TiO2 conduction band is comprised primarily of empty 3d orbitals from Ti^{4}þ (Anderson et al., 2004). The difference in band structure results in a different density of states and, possibly, different electronic coupling strengths with the adsorbate.

7. Alternative dyes for ZnO

According to the limitations of ZnO based DSSC, the lower electron injection and the instability of ZnO in acidic dyes, the alternative type dyes will provide a new pathway for useage of ZnO nanomaterials as photoanodic materials for effective solar power conversion. The list of other alternative dyes were compiled and given in Table 4. The new types of dyes should overcome above mentioned two different limitations and it should be chemically bonded to the ZnO semiconductor for effective for light absorption in a broad wavelength range. Already few research groups were already developed with the aim of fulfilling these criteria. The various new types of dyes include heptamethine-cyanine dyes adsorbed on ZnO for absorption in the red/near-infrared (IR) region (Matsui et al., 2005 & Otsuka et al., 2006), and unsymmetrical squaraine dyes with deoxycholic acid, which increases photovoltage and photocurrent by suppressing electron back transport (Hara et al., 2008). Mercurochrome (C$_{20}$H$_8$Br$_2$HgNa$_2$O) is one of the newly developed photosensitizers that, to date, is most suitable for ZnO, offering an IPCE as high as 69% at 510 nm and an overall conversion efficiency of 2.5% (Hara et al., 2008 & Hosono et al., 2004). It was also reported that mercurochrome photosensitizer could provide ZnO DSSCs with a fill factor significantly larger than that obtained with N3 dye, where the latter device was believed to possess a higher degree of interfacial electron recombination due to the higher surface-trap density in the N3-dye-adsorbed ZnO. Eosin Y is also a very efficient dye for ZnO-based DSSCs, with 1.11% conversion efficiency for nanocrystalline films (Rani et al., 2008). When eosin Y is combined with a nanoporous film, overall conversion efficiencies of 2.0–2.4% have been obtained (Hosono et al., 2004 & Lee et al., 2004). Recently, Senevirathne et al. reported that the use of acriflavine (1,6diamino-10-methylacridinium chloride) as a photosensitizer

for ZnO could generate photocurrents that are an order of magnitude higher than in the case of TiO$_2$ (Senevirathne et al., 2008). Three triphenylamine dyes based on low-cost methylthiophene as the p-conjugated spacer were designed and synthesized as the dye sensitizers for DSSCs applications. The high photovoltaic performances of the DSSCs based on these as-synthesized dyes were obtained. Though the introduction of vinyl unit in the p-conjugated spacer can obtainred-shifted absorption spectra, it does not give a positive effect on the photovoltaic performance of the DSSCs due to unfavorable back-electron transfer and decrease of the open-circuit voltage. On the basis of optimized conditions, the DSSCs based on these three as-synthesized dyes exhibited the efficiencies ranging from 7.83% to 8.27%, which reached 80 to 85% with respect to that of an N719-based device. The high conversion efficiency and easy availability of rawmaterials reveal thatthese metal-free organic dyes are promising in the development of DSSCs (Tian et al., 2010).

Structure	Photosensitizer	Efficiency
Nanoparticles	heptamethine cyanine	0.16%, 0.67
	unsymmetrical squaraine	1.5%
	eosin-Y	1.11%
	acriflavine	0.588%
	mercurochrome	2.5%
Nanoporous films	D149	4.27%
	eosin-Y	2.0%, 2.4%
	eosin-Y	3.31%(0.1 sun)
Nanowires	QDs (CdSe)	0.4%

Table 4. The list of other alternative dyes for ZnO based DSSC.

8. Conclusions

ZnO is believed to be a superior alternative material to replace the existing TiO$_2$ photoanodic materials used in DSSC and has been intensively explored in the past decade due to its wide band gap and similar energy levels to TiO$_2$. More important, its much higher carrier mobility is favorable for the collection of photoinduced electrons and thus reduces the recombination of electrons with tri-iodide. Although the formation of Zn²þ/dye complex is inevitable due to the dissolution of surface Zn atoms by the protons released from the dye molecules in an ethanolic solution, selection of other alternative dye molecules will definitely helps to boost the conversion efficiency to much higher level. Therefore, the recent development on the synthesis of metal-free dye molecules will lead the DSSC device fabrication to the new height as for the cost effectiveness and simple technique are concern.

9. References

Liu, J. (2008). Oriented Nanostructures for Energy Conversion and Storage. Chem. *Sus. Chem.,* 1, pp. 676.

Bagnall, D. M. (2008). *Photovoltaic technologies*. Energ. Pol., 36, pp. 4390.

Chapin D. M. (1954). A new silicon p-n junction photocell for converting solar radiation into electrical power. *J. Appl. Phys.* 25, pp. 676.

Afzaal, M. (2006). Recent developments in II–VI and III–VI semiconductors and their applications in solar cells. *J. Mater. Chem.* 16, pp. 1597.

Birkmire, R. W. (2001). Compound polycrystalline solar cells: Recent progress and Y2 K perspective. *Sol. Energ. Mat. Sol.* 65, pp. 17.

Gratzel, M. (2001). Review article Photoelectrochemical cells. *Nature,* 414, pp. 338.

Gratzel, M. (2000). Perspectives for dye-sensitized nanocrystalline solar cells. *Prog. Photovoltaics*, 8, pp. 171.

Gratzel, M. (2003). Dye-sensitized solar cells. *J. Photochem. Photobiol. C.* 4, pp. 145.

Gratzel, M. (2007). Photovoltaic and photoelectrochemical conversion of solar energy. *Phil. Trans. Math. Phys. Eng. Sci.* 365, pp. 993.

Nelson, J. (2004). Random walk models of charge transfer and transport in dye sensitized systems. *Coord. Chem. Rev.* 248, pp. 1181.

Fujishima, A. (1972). Electrochemical photolysis of water at a semiconductor electrode. *Nature*, 38, pp. 5358.

Desilvestro, J.; Gratzel, M.; Kavan, L.; Moser, J. & Augustynski, J. (1985). Highly Efficient Sensitization of Titanium Dioxide. *Journal of the American Chemical Society,* 107, 10, pp. 2988-2990.

Nazeerudin, M. K. (2003). Conversion of light to electricity by cis-X2bis(2,2'-bipyridyl-4,4'-dicarboxylate)ruthenium(II) charge-transfer sensitizers (X = Cl-, Br-, I-, CN-, and SCN-) on nanocrystalline titanium dioxide electrodes *Journal.of the American Chemical Society* 115, 14, pp. 6382.

Chiba, Y. (2006). Conversion efficiency of 10.8% by a dye-sensitized solar cell using a TiO2 electrode with high haze. *Applied Physics Letters*, 88, 22 pp. 223505.

Tornow, J. Transient Electrical Response of Dye-Sensitized ZnO Nanorod Solar Cells. *J. Phys. Chem. C.* 111, pp. 8692.

Djurisic, A.B. (2006). Optical Properties of ZnO Nanostructures. *Small.* 2, pp. 944.

Tornow, J. (2008). Voltage bias dependency of the space charge capacitance of wet chemically grown ZnO nanorods employed in a dye sensitized photovoltaic cell. *Thin Solid Films.* 516, pp. 7139.

Bittkau, K. (2007). Near-field study of optical modes in randomly textured ZnO thin films. *Superlatt. Microstuct.* 42, pp. 47.

Xi, Y.Y. (2008). Electrochemical Synthesis of ZnO Nanoporous Films at Low Temperature and Their Application in Dye-Sensitized Solar Cells . *J. Electrochem. Soc.* 155, pp. D595.

Jagadish, C. (2006). Zinc oxide bulk, thin films and nanostructures: processing, properties and applications, Publisher: Elsevier Science, 1 edition, pp 3.

Dulub, O. (2002). STM study of the geometric and electronic structure of ZnO(0001)-Zn, (0001)-O, (1010), and (1120) surfaces, *Surf. Sci.* 519, pp. 201-217.

Wander, A. (2001). Stability of polar oxide surfaces, *Phys.Rev. Lett.* 86, pp. 3811-3814.

Staemmler, V. (2003). Stabilization of polar ZnO surfaces: validating microscopic models by using CO as a probe molecule, *Phys. Rev. Lett.* 90, pp. 106102-1-4.

Singh, S. (2007). Structure, microstructure and physical properties of ZnO based materials in various forms: bulk, thin film and nano, *J. Phys. D: Appl. Phys.* 40, pp. 6312-6327.

Pearton, S.J. (2005). Recent progress in processing and properties of ZnO, *Progress in Materials Science*. 50, pp. 293- 340.

Florescu, D. (2002). High spatial resolution thermal conductivity of bulk ZnO (0001), *J Appl Phys*. 91, pp. 890-892.

Hosokawa, M. (2007). Nanoparticle Technology Handbook Elsevier, Amsterdam.

Lee, J. S. (2003). ZnO nanomaterials synthesized from thermal evaporation of ballmilled ZnO powders, *J. Cryst. Growth*. 254, pp. 423-431.

Zhao, Q. X. (2007). Growth of ZnO nanostructures by vapor–liquid–solid method, *Appl. Phys. A*, 88, pp. 27-30.

Huang, M. H. (2001). Catalytic growth of zinc oxide nanowires by vapor transport, *Adv. Mater*. 13, pp. 113- 116.

Sun, Y. (2004). Growth of aligned ZnO nanorod arrays by catalyst-free pulsed laser deposition methods, *Chem. Phys. Lett*. 39, pp. 621-26.

Wu, J . (2002). Low-temperature growth of well-aligned ZnO nanorods by chemical vapor deposition, *Adv .Mater*. 14, pp. 215-218.

Park, W. I. (2002). Metalorganic vapor-phase epitaxial growth of vertically well-aligned ZnO nanorods, *Appl. Phys. Lett*. 80, pp. 4232-4234.

Yu, H. D. (2005). A general lowtemperature route for large-scale fabrication of highly oriented ZnO nanorod/nanotube arrays. *J. Am. Chem. Soc*. 127, pp. 2378-2379.

Zeng, L.Y. (2006). Dye-Sensitized Solar Cells Based on ZnO Films. *Plasma Sci. Tech*. 2006, 8, pp. 172.

Keis, K. (2000). Studies of the Adsorption Process of Ru Complexes in Nanoporous ZnO Electrodes. *Langmuir*. 16, pp. 4688.

Suliman, A.E.(2007). Preparation of ZnO nanoparticles and nanosheets and their application to dye-sensitized solar cells Sol. *Energ. Mat. Sol. Cells*. 91, pp. 1658.

Gonzalez-Valls, I. (2010). Dye sensitized solar cells based on vertically-aligned ZnO nanorods: effect of UV light on power conversion efficiency and lifetime. *Energy Environ. Sci.*, 3, pp. 789-795.

Lai, M. H. (2010). ZnO-Nanorod Dye-Sensitized Solar Cells: New Structure without a Transparent Conducting Oxide Layer. *International Journal of Photoenergy,* pp. Article ID 497095, 5 pages

Hsu, Y.F. (2008). ZnO nanorods for solar cells: Hydrothermal growth versus vapor deposition, *Appl. Phys. Lett*. 92, pp. 133507.

Chen, H.H. (2008). Dye-sensitized solar cells using ZnO nanotips and Ga-doped ZnO films. *Semicond. Sci. Technol*. 23, pp. 045004.

Martinson, A.B.F. (2007). ZnO Nanotube Based Dye-Sensitized Solar Cells. *Nano Lett*. 7, pp. 2183.

Lin, C. F. (2008). Electrodeposition preparation of ZnO nanobelt array films and application to dye-sensitized solar cells. J. *Alloys Compd*. 462, pp. 175.

Kakiuchi, K. (2008). Fabrication of ZnO films consisting of densely accumulated mesoporous nanosheets and their dye-sensitized solar cell performance. *Thin Solid Films*. 516, pp. 2026.

Chen, W. (2009). A new photoanode architecture of dye sensitized solar cell based on ZnO nanotetrapods with no need for calcination. *Electrochem. Commun.* 11, pp. 1057.

Jiang, C. Y. (2007). Improved dye-sensitized solar cells with a ZnO-nanoflower photoanode. *Appl. Phy. Lett.* 90, pp. 263501.

Chen, Z.G. (2006). Electrodeposited nanoporous ZnO films exhibiting enhanced performance in dye-sensitized solar cells. *Electrochim. Acta.* 51, pp. 5870.

Hosono, E. (2005). The Fabrication of an Upright-Standing Zinc Oxide Nanosheet for Use in Dye-Sensitized Solar Cells. *Adv. Mater.* 17, pp. 2091.

Kakiuchi, K. (2006). Enhanced photoelectrochemical performance of ZnO electrodes sensitized with N-719. *J. Photochem. Photobiol. A* 179, pp. 81.

Guo, M. (2005). Hydrothermal growth of perpendicularly oriented ZnO nanorod array film and its photoelectrochemical properties. *Appl. Surf. Sci.* 249, pp. 71.

Guo, M. (2005). The effect of hydrothermal growth temperature on preparation and photoelectrochemical performance of ZnO nanorod array films. J. Solid State Chem. 178, pp. 3210.

Rao, A. R. (2008). Achievement of 4.7% conversion efficiency in ZnO dye-sensitized solar cells fabricated by spray deposition using hydrothermally synthesized nanoparticles. *Nanotechnology.* 19, pp. 445712.

Wu, J. J. (2007). Effect of dye adsorption on the electron transport properties in ZnO-nanowire dye-senstized solar cells. *Appl. Phy. Lett*. 2007, 90, pp. 213109.

Law, M. (2005). Nanowire dye-sensitized solar cells. *Nat. Mater.* 4, pp. 455.

Zhang, R. (2008). High-Density Vertically Aligned ZnO Rods with a Multistage Terrace Structure and Their Improved Solar Cell Efficiency. *Cryst. Growth Des.* 8, pp. 381.

Chou, T.P. (2007). Hierarchically Structured ZnO Film for Dye-Sensitized Solar Cells with Enhanced Energy Conversion Efficienc. *Adv. Mater.* 19, pp. 2588.

Zhang, Q.F. (2008). Polydisperse aggregates of ZnO nanocrystallites: a method for energy-conversion-efficiency enhancement in dye-sensitized solar cells, *Adv. Funct. Mater.* 18, pp. 1654.

Chou, T.P. (2007). Effects of Dye Loading Conditions on the Energy Conversion Efficiency of ZnO and TiO_2 Dye-Sensitized Solar Cells. *Phys. Chem. C.* 111, pp.18804.

Uthirakumar, p. (2006). ZnO nanoballs synthesized from a single molecular precursor via non-hydrolytic solution route without assistance of base, surfactant, and template etc . *Phys. Lett. A*, 359, pp. 223.

Uthirakumar, p. (2007). Nanocrystalline ZnO particles: Low-temperature solution approach from a single molecular precursor. *J. Cryst. Growth*. 304, pp. 150.

Uthirakumar, p. (2009). Zinc Oxide Nanostructures Derived from a Simple Solution Method for Solar Cells and LEDs. *Chemical Engineering Journal*, 155, pp. 910-915.

Uthirakumar, p. (2009). Effect of Annealing Temperature and pH on the Morphology and Optical Properties of Highly Dispersible ZnO nanoparticles. *Material Characterization*, 60(11), pp. 1305-1310.

Eom, S. H. (2008). Preparation and characterization of nano-scale ZnO as a buffer layer for inkjet printing of silver cathode in polymer solar cells. *Sol. Energy Mater. Sol. Cells,* 92, pp. 564.

Hosono, E. (2004). Growth of layered basic zinc acetate in methanolic solutions and its pyrolytic transformation into porous zinc oxide films. *J. Colloid Interface Sci.* 272, 391.

Hosono, E. (2008). Metal-free organic dye sensitized solar cell based on perpendicular zinc oxide nanosheet thick films with high conversion efficiency. *Dalton Trans.* pp. 5439.

Charoensirithavorn, P. (2006). Dye-sensitized Solar Cell Based on ZnO Nanorod Arrays. *The 2nd Joint International Conference on Sustainable Energy and Environment.* 21-23 November 2006, Bangkok, Thailand.

Han, J. (2010). ZnO nanotube-based dye-sensitized solar cell and its application in self-powered devices, *Nanotechnology* 21, pp. 405203.

Martinson, A.B.F. (2007). ZnO Nanotube Based Dye- ensitized Solar Cells. *Nano letters.* 7, pp. 2183.

Chae, K. W. (2010). Low-temperature solution growth of ZnO nanotube arrays, *Beilstein J. Nanotechnol.* 1,pp. 128–134.

Kopidakis, N. (2003). Transport-Limited Recombination of Photocarriers in Dye-Sensitized Nanocrystalline TiO$_2$ Solar Cells. *J. Phys. Chem. B*. 107, pp. 11307.

Zhang, Q. (2010). Synthesis of ZnO Aggregates and Their Application in Dye-sensitized Solar Cells. *Material Matters. 5.2*, pp. 32.

Anderson, N.A. (2003). X. Ai,T.Q. Lian, Electron Injection Dynamics from Ru Polypyridyl Complexes to ZnO Nanocrystalline Thin Films. *J. Phys. Chem. B* 107, pp. 14414.

Anderson, N.A. (2004). Ultrafast electron injection from metal polypyridyl complexes to metal-oxide nanocrystalline thin films. *Coord. Chem. Rev.* 248, pp. 1231.

Matsui, M. (2005). Application of near-infrared absorbing heptamethine cyanine dyes as sensitizers for zinc oxide solar cell . *Synth. Met.* 148, pp. 147.

Otsuka, A. (2008). Simple Oligothiophene-Based Dyes for Dye-Sensitized Solar Cells (DSSCs): Anchoring Group Effects on Molecular Properties and Solar Cell Performance. *Chem. Lett.* 37, pp. 176.

Otsuka, A. (2006). Dye Sensitization of ZnO by Unsymmetrical Squaraine Dyes Suppressing Aggregation. *Chem. Lett.* 35, pp. 666.

Hara, K. (2003). Molecular Design of Coumarin Dyes for Efficient Dye-Sensitized Solar Cells. *Phys. Chem. B*, 107 (2), pp 597–606.

Hara, K. (2000). Highly efficient photon-to-electron conversion with mercurochrome-sensitized nanoporous oxide semiconductor solar cells. *Sol. Energ. Mat. Sol. Cells.* 64, pp. 115.

Hosono, (2004). Synthesis, structure and photoelectrochemical performance of micro/nano-textured ZnO/eosin Y electrodes. *Electrochim. Acta.* 49 (14), pp. 2287.

Rani, S. (2008). Synthesis of nanocrystalline ZnO powder via sol–gel route for dye-sensitized solar cells. *Sol. Energ. Mat. Sol. Cells.* 92, pp. 1639.

Lee, W. J. (2004). Fabrication and Characterization of Eosin-Y-Sensitized ZnO Solar Cell, *Jpn. J. Appl. Phys.* 43, pp. 152.

Senevirathne, M.K.I. (2008). Sensitization of TiO$_2$ and ZnO nanocrystalline films with acriflavine. *Photochem. Photobiol. A.* 195, pp. 364.

Tian, Z. (2010). Low- cost dyes based on methylthiophene for high-performance dye-sensitized solarcells. *Dyes and Pigments* 87, pp. 181-187.

Carbon Nanostructures as Low Cost Counter Electrode for Dye-Sensitized Solar Cells

Qiquan Qiao
South Dakota State University
United States

1. Introduction

In the last two decades, dye sensitized solar cells (DSSCs) have gained extensive attention as a low cost alternative to conventional Si solar cells (Oregan & Gratzel 1991; Fan et al. 2008; Xie et al. 2009; Alibabaei et al. 2010; Gajjela et al. 2010; Xie et al. 2010; Yum et al. 2010). A typical DSSC is made of a TiO_2 photoanode and a Pt counter electrode separated by an electrolyte comprising an iodide/triiodide ($I^-/I3^-$) redox couple. The photoanode is usually prepared from TiO_2 nanoparticles on a transparent conducting oxide (TCO), while the counter electrode is a thin layer of Pt deposited on another TCO substrate. The dye molecules are adsorbed onto TiO_2 surface. When exposed to sunlight, photoelectrons are generated and injected into the photoanode. Afterward, the electrons travel to counter electrode through an outside load. The oxidized dye molecules then retake electrons from I^- ions and oxidize I^- into $I3^-$. Meanwhile, the $I3^-$ is reduced into I^- by taking electrons from counter electrode. Pt counter electrode has been extensively used as an efficient electrocatalyst for reduction of I^{3-} ions in DSSCs (Gratzel 2003; Sun et al. 2010). However, Pt is an expensive metal and can also be corroded by I^-/I^{3-} redox couple (Kay & Gratzel 1996). Recently, various carbonaceous materials including graphite, carbon black, and carbon nanotubes have been studied as a low cost replacement for Pt as an electrocatalyst for reduction of I^{3-} ions (Kay & Gratzel 1996; Burnside et al. 2000; Imoto et al. 2003; Imoto et al. 2003; Suzuki et al. 2003; Murakami et al. 2006; Ramasamy et al. 2007; Fan et al. 2008; Hinsch et al. 2008; Joshi et al. 2009; Lee et al. 2009; Skupien et al. 2009; Calandra et al. 2010). The carbonaceous materials are plentiful, inexpensive, and also exhibit high resistivity to corrosion (Ramasamy et al. 2007). Replacement of Pt with carbon-based materials can also speed up DSSC commercialization (Burnside et al. 2000; Hinsch et al. 2008; Han et al. 2009; Skupien et al. 2009; Joshi et al. 2010).

In this chapter, we review some carbon nanostructures including carbon nanoparticles and electrospun carbon nanofibers that have been successfully used as a low cost alternative to Pt in DSSCs. The carbon nanoparticle- and carbon nanofiber-based DSSCs showed comparable performance as that of Pt-based devices in terms of short circuit current density (Jsc) and open circuit voltage (Voc). Electrochemical impedance spectroscopy (EIS) measurements indicated that the carbon nanoparticle and carbon nanofiber counter electrodes showed lower charge transfer resistance (Rct), suggesting that carbon nanoparticle and carbon nanofiber counter electrodes are an efficient electrocatalyst for DSSCs. In addition, the series resistance of carbon-based counter electrodes was found to be a little

higher than that of Pt cells, leading to a slightly lower FF. Herein, we will first introduce the preparation and characterization of carbon nanoparticle and carbon nanofiber counter electrodes. Then, the fabrication of DSSC devices with these carbon-based counter electrodes will be described and compared with Pt-based cells. The use of carbon nanoparticle and carbon nanofiber counter electrodes has a great potential to make low cost DSSC technology one step closer to commercialization.

2. Carbon/TiO$_2$ composite as counter electrode

Low cost carbon/TiO$_2$ composite was used as an alternative to platinum as a counter-electrode catalyst for tri-iodide reduction. In the carbon/TiO$_2$ composite, carbon is nanoparticles and acts as an electrocatalyst for triiodide reduction, while the TiO$_2$ functions as a binder. The carbon/TiO$_2$ composite can be deposited by spin coating or doctor blading onto a fluorine-doped Tin Dioxide (FTO).

2.1 Preparation of carbon/TiO$_2$

Carbon nanoparticles (Sigma-Aldrich) have a particle size < 50 nm and a surface area > 100 m^2/g. The TiO$_2$ paste was prepared by dispersing TiO$_2$ nanoparticles (P25 Degussa, average size of 25 nm) into water. The carbon/TiO$_2$ composite was made by mixing 650 mg carbon nanoparticles with 1 ml TiO$_2$ colloid paste at a concentration of 20 wt%. Then 2 ml deionized (DI) water was added, followed by grinding and sonication. 1 ml Triton X-100 was added during grinding. The final paste was then spin coated onto a FTO glasses to form the counter electrode, followed by sintering at 250^0 C for an hour.

The scanning electron microscopy (SEM) images of carbon/TiO$_2$ composite and pure TiO$_2$ nanoparticle films are shown in Figure 1a and b, respectively. It can be seen that the carbon/TiO$_2$ composite counter-electrode film is highly porous with a large surface area, which can function effectively for tri-iodide reduction. The pore size ranges from 20 nm to 200 nm throughout the film, which is large enough for I$^-$/I$_3^-$ ions that are only a few angstroms to diffuse into the pores and get reduced at the carbon nanoparticle surface(Ramasamy et al. 2007). The particle size in carbon/TiO$_2$ composite film (Figure 1a) is apparently larger than those in pure TiO$_2$ nanoparticle film (Figure 1b). This suggests that the carbon nanoparticle dominates in carbon/TiO$_2$ mixture and effectively serves as a catalyst for tri-iodide reduction. A cross-section SEM image (Figure 1c) shows that the carbon/TiO$_2$ composite counter electrode has a thickness of about 11.2 um.
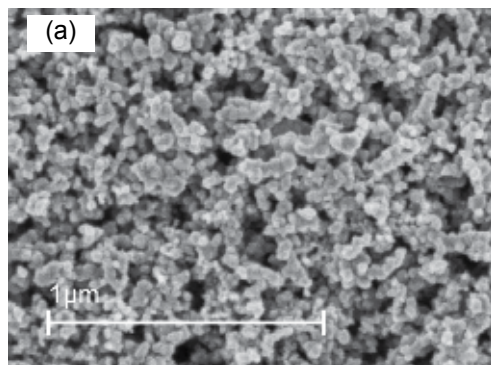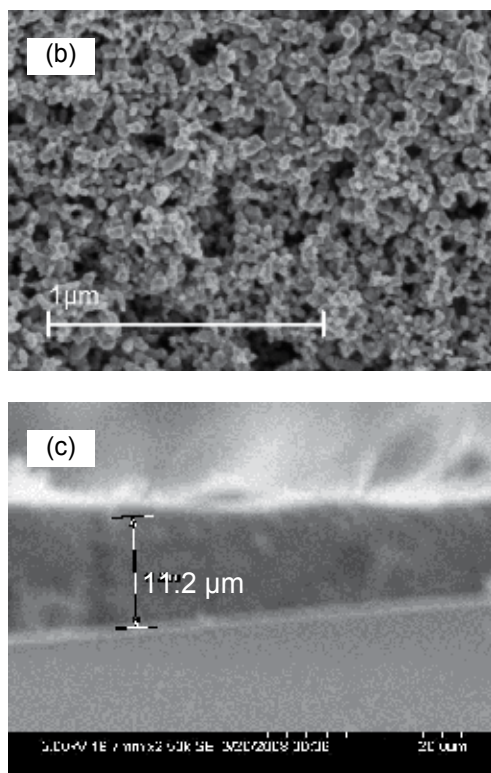
Fig. 1. SEM images of (a) 11.2 um thick carbon/TiO$_2$ composite layer and (b) pure TiO$_2$ nanoparticle layer on a FTO substrate. Cross section SEM image of (c) the carbon/TiO$_2$ composite layer. Reproduced with permission from Ref (Joshi et al. 2009).

2.2 Calculation of series resistance, left justified

Ramasamy et al. measured the charge transfer resistance (R$_{ct}$) of carbon electrode via electrochemical impedance spectroscopy (EIS) and found that R$_{ct}$ was 0.74 Ω cm^{-2}, two times less than that of the screen printed Pt (Ramasamy et al. 2007). Since the thickness of carbon-based counter electrode is tens of micrometers that are much higher than Pt at a thickness of about tens of nanometers, the internal series resistance (R$_{se}$) of carbon-based DSSCs are found to be higher (Ramasamy et al. 2007; Joshi et al. 2009). The lower R$_{ct}$ counterbalances the higher R$_{se}$ of carbon-based device. The series resistance of carbon/TiO$_2$ composite based DSSCs was also studied and compared with that of platinum-based devices under multiple light intensities.

Current density (J$_{sc}$) through the series resistance is as below (Matsubara et al. 2005):

$$J = J_{PH} - \frac{V - IR_s}{AR_{sh}} - J_0 \left(\exp[q(V - JA \ R_s)/nkT] - 1 \right) \tag{1}$$

This equation can be modified as:

$$J_{PH} - J = \frac{V - JAR_s}{AR_{sh}} + J_0 \left(\exp[q(V - JA \ R_s)/nkT] - 1 \right) \tag{2}$$
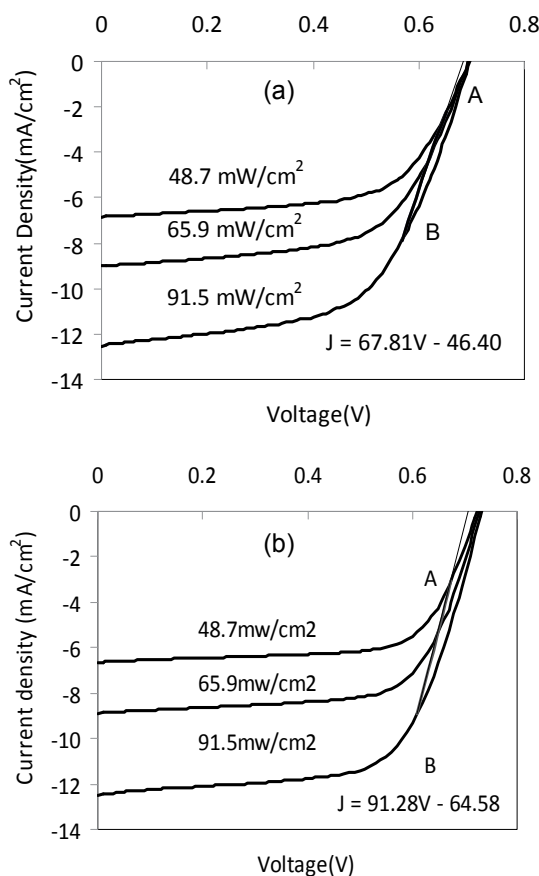
Fig. 2. J-V curves of DSSC devices at different light intensity from (a) carbon/TiO$_2$ composite and (b) Pt counter electrode. Reproduced with permission from Ref (Joshi et al. 2009).

When we plot current density-voltage (J-V) curves at multiple light intensities and select the points of (J,V) which satisfy the following condition:

$$J_{PH} - J = \Delta J = \ constant \tag{3}$$

The points should lie in the straight line and follow:

$$J = V \ / \ RsA + constant \tag{4}$$

Thus, the series resistance can be determined from the slope of a straight line. The current density-voltage (J-V) curves at different light intensities of the carbon/TiO$_2$-based and Pt-based DSSC devices are shown in Figure 2a and b, respectively.

2.3 Device performance of carbon/TiO$_2$ composite counter electrode
The active area of carbon/TiO$_2$ composite is 0.20 cm². while that of Pt devices is 0.24 cm². The slope of the straight line AB in carbon/TiO$_2$ composite devices is 67.81 mA/(cm²V),

with a reciprocal of 14.75 Ωcm^2. The slope of the straight line AB in Pt-based devices is 91.28 mA/(cm²V) and its reciprocal is 11.37 Ωcm^2. Apparently the series resistance of carbon/TiO₂ devices is larger than that of Pt devices. This can be possibly attributed to the much thicker layer and larger resistivity of carbon/TiO₂ counter electrode than those of Pt (Imoto et al. 2003). However, the carbon/TiO₂ counter electrode has its own advantage that is the large surface area. This results in a lower R_{ct}, which was found to be less than half of that in the Pt counter electrode (Ramasamy et al. 2007). The lower R_{ct} can compensate the effects of higher series resistance.
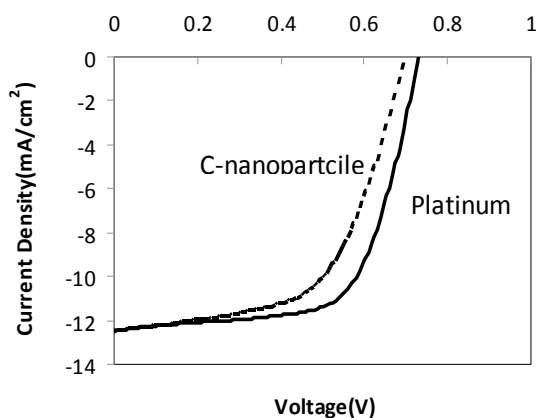

Fig. 3. J-*V* curves of DSSC devices with carbon/TiO₂ composite (dash line) and Pt (solid line) counter electrode under AM 1.5 illumination (light intensity: 91.5 mW/cm²). Reproduced with permission from Ref (Joshi et al. 2009).

Figure 3 shows a comparison of J-V curves from carbon/TiO₂ and Pt devices under an AM 1.5 solar simulator at an intensity of ~ 91.5 mW/cm². DSSCs with carbon/TiO₂ counter electrode achieve an efficiency of 5.5 %, which is comparable to 6.4 % of Pt counter electrode devices. The photovoltaic parameters in terms of short circuit current density (Jsc), open circuit voltage (Voc), fill factor (FF) and efficiency (η) are listed in Table 1. The FF of carbon/TiO₂ devices was found to be slightly lower than Pt devices. This may be attributed to higher series resistance (14.75 Ωcm^2) in the former compared to that (11.37 Ωcm^2) in the latter. Ramasamy et al. studied the robustness of carbon-based DSSCs and their results showed that carbon-based cells have a comparable stability as Pt-based devices (Ramasamy et al. 2007).

Counter electrodes	Jsc (mA/cm²)	Voc (V)	FF	η	Rs (Ω)
carbon/TiO₂ composite	12.53	0.70	0.57	5.5 %	14.75 Ωcm^2
Platinum	12.48	0.73	0.65	6.4 %	11.37 Ωcm^2

Table 1. DSSC device parameters from carbon/TiO₂ composite and Pt counter electrode. Reproduced with permission from Ref (Joshi et al. 2009).

3. Carbon nanofibers as counter electrode

Carbon nanofibers prepared by electrospinning were also explored as low cost alternative to Pt for triiodide reduction catalyst in DSSCs. The carbon nanofiber counter electrode was characterized by EIS and cyclic voltammetry measurements. The carbon nanofiber counter electrode exhibited low charge transfer resistance (R_{ct}), small constant phase element (CPE) exponent (β), large capacitance (C), and fast reaction rates for triiodide reduction.

3.1 Preparation of carbon nanofiber counter electrode

The carbon nanofiber paste was made by mixing 0.1 g ECNs with 19.6 g polyoxyethylene(12) tridecyl ether (POETE) in a similar method reported by others (Mei & Ouyang 2009). The mixture was then grinded, sonicated, and centrifuged at a spin speed of 10,000 rpm to uniformly disperse the ECNs in POETE. Any extra POETE that floated on top of the mixture after the centrifuge was removed via a pipette. Afterwards, the counter electrode was made by doctor-blading the mixture onto FTO (~8 Ω/□ and ~400 nm), followed by sintering at 200 °C for 15 min and then at 475 °C for 10 min. Figure 4 shows SEM and transmission electron microscope (TEM) images of the original carbon nanofibers prepared by electrospinning and the carbon nanofiber counter electrode on FTO deposited by doctor blading. In the original electrospun carbon nanofiber samples, the ECNs were relatively uniform in diameter with an average value of ~ 250 nm (Figure 4a). The TEM image in Figure 4b shows that the structure of ECNs was primarily turbostratic instead of graphitic; *i.e.,* tiny graphite crystallites with sizes of a few nanometers were embedded in amorphous carbonaceous matrix. The nanofiber sheet did not show evidence of microscopically identifiable beads or beaded-nanofibers. The BET surface area of the carbon nanofiber sheet was measured to be ~100 m²/g via a Micromeritics ASAP 2010 surface area analyzer using N_2 adsorption at 77 K.
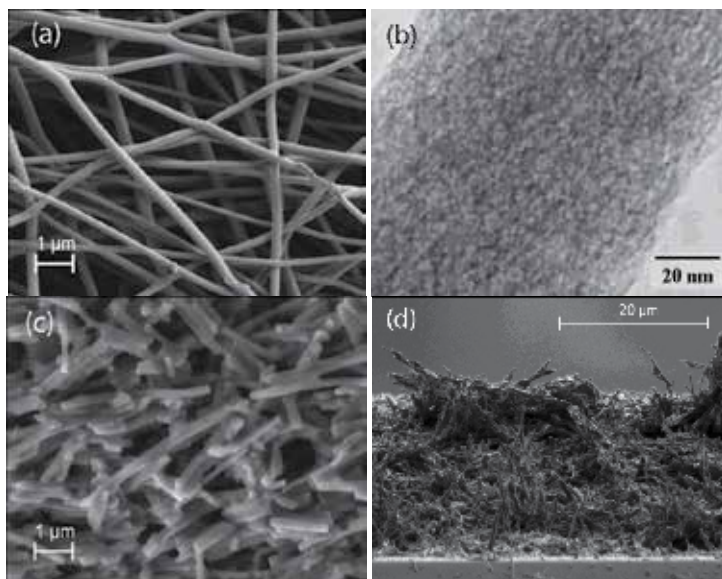

Fig. 4. (a) SEM image of electrospun carbon nanofiber film; (b) TEM image of a typical single carbon nanofiber; SEM image of (c) top-view and (d) cross-section of carbon nanofiber counter electrode. Reprinted with permission from {Joshi et al. 2010}. Copyright {2010} American Chemical Society.

Because it was difficult to attach the original carbon nanofiber sheet onto FTO, we added POETE into the carbon nanofiber, followed by grinding and sonication. As shown in Figure 4c, the nanofibers that were originally tens of microns long were broken into submicrons to microns after grinding and sonication. The conductivity of original electrospun carbon nanofibers (Figure 4a) is ~ 1538 Sm-1, but decreased to ~ 164 Sm-1 after converted to the counter electrode as shown in Figure 4c. This can possibly be attributed to the much smaller lengths of the carbon nanofibers that reduced conduction network. Also, the POETE was burned away at high temperature, causing additional voids between carbon nanofibers. However the smaller length of carbon nanofibers may increase the surface area of the counter electrode, which can be seen by comparing Figure 4a with Figure 4c. The thickness of counter electrode was about of 24 µm (Figure 4d), which is much higher than that of carbon nanoparticle counter electrodes. The effects of carbon nanoparticle counter electrode thickness on DSSC parameters including Jsc, Voc, FF and cell efficiency (η) was studied by others (Murakami et al. 2006). They found that the thickness mainly affects FF and the optimal thickness was ~ 14.5 µm for carbon nanoparticle counter electrode. A thickness of ~11.2 µm was used in a carbon nanoparticle counter electrode DSSC device (Joshi et al. 2009). However, Ramasamy et al. prepared a carbon nanoparticle counter electrode with a larger thickness of ~ 20 µm (Ramasamy et al. 2007). Here, the thickness of carbon nanofiber counter electrode was higher than that of typical carbon nanoparticle counter electrode. As shown in Figure 4c, the shorter nanofibers are loosely packed with large voids and this can lead to smaller surface area than that of carbon nanoparticle counter electrode. A higher thickness was used to make the carbon nanofiber counter electrode to ensure a significant surface area.
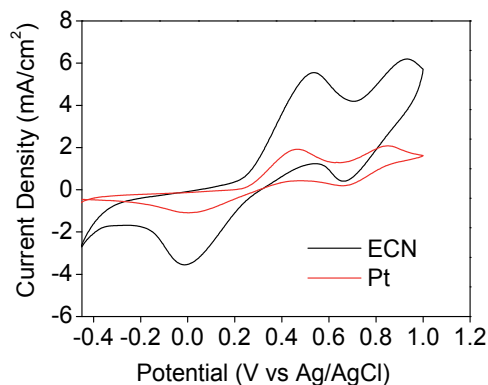
Fig. 5. Cyclic voltammograms of carbon nanofiber (black) and Pt (red) counter electrode. The measurement was performed in an acetonitrile solution comprising 10 mM LiI and 0.5 mM I_2. 0.1M tetra-*n*-butylammonium tetrafluoroborate was used as supporting electrolyte. Ag/AgCl was used as reference electrode. The thickness of carbon nanofiber and Pt counter electrode is ~24 µm and ~40 nm, respectively. Reprinted with permission from {Joshi et al. 2010}. Copyright {2010} American Chemical Society.

3.2 Characterization of carbon nanofiber counter electrode

Cyclic voltammograms (Figure 5) of the carbon nanofiber and Pt counter electrode were performed in an acetonitrile solution that comprises 10 mM LiI and 0.5 mM I_2 using 0.1 M

tetra-*n*-butylammonium tetrafluoroborate as the supporting electrolyte. In the cyclic voltammetry (CV) measurements, Pt wire was used as counter electrode, Ag/AgCl as reference electrode, and a carbon nanofiber or Pt coated FTO as working electrode. Two pairs of oxidation and reduction peaks were found that are similar to those in the Pt electrodes. The oxidation and reduction pair on the left was from the redox reaction of $I_3^- + 2e^- = 3I^-$, while that on the right was attributed to the redox reaction of $3I_2 + 2e^- = 2I_3^-$ (Sun et al. ; Huang et al. 2007). The right pair from the carbon nanofiber sample exhibited a larger oxidation current density, but a smaller reduction current density than those of Pt electrode. This pair that was assigned to $3I_2 + 2e^- = 2I_3^-$ had little effect on DSSC performance (Mei et al. 2010). The left pair of carbon nanofiber counter electrode showed both a larger oxidation and reduction current density than those of the Pt electrodes. This pair that was assigned to $I_3^- + 2e^- = 3I^-$ directly affected DSC performance, indicating a fast rate of triiodide reduction.

The catalytic properties of counter electrode are usually characterized by EIS (Papageorgiou et al. 1997; Hauch & Georg 2001). In order to eliminate the effects of TiO$_2$ photoanode, a symmetrical carbon nanofiber – carbon nanofiber and Pt-Pt cells were fabricated for EIS study. These cells were prepared by assembling two identical carbon nanofiber (or Pt) electrodes face to face that were separated with an electrolyte of I^-/I_3^- redox couple. The EIS characterization was performed using an Ametek VERSASTAT3-200 Potentiostat equipped with frequency analysis module (FDA). The amplitude of AC signal was 10 mV with a frequency range of 0.1 - 10^5 Hz. The Nyquist plots of the symmetrical carbon nanofiber – carbon nanofiber and Pt-Pt cells are shown in Figure 6. Figure 6b shows the equivalent circuit that was used to fit impedance spectra. The equivalent circuit included charge transfer resistance (R$_{ct}$) at the carbon nanofiber or Pt electrode/electrolyte interface, constant phase element (CPE), series resistance (R$_s$) and Warburg impedance (Z$_W$) (Murakami et al. 2006). The R$_{ct}$ at the electrode/electrolyte interface can be obtained from the high frequency semicircle, while the Z$_W$ of the I^-/I_3^- redox couple in the electrolyte can be fitted from the low frequency arc (Wang et al. 2009; Jiang et al. 2010; Li et al. 2010; Mei et al. 2010). The fitted results from the Nyquist plots were summarized in Table 2. The R$_{ct}$ of carbon nanofiber counter electrode was 0.7 Ωcm^2, less than half of that (1.9 Ωcm^2) of the Pt electrode, suggesting a sufficient electro-catalytic capability. The CPE represents the capacitance at the interface between the carbon nanofiber or Pt and electrolyte, which can be described as:

$$Z_{CPE} = \frac{1}{Y_0}(j\omega)^{-\beta} \qquad (5)$$

in which Y$_0$ is the CPE parameter, ω the angular frequency, and β the CPE exponent (0 < β < 1), and. The Y$_0$ and β are constant that is independent of frequency.

An ideal capacitance has a perfect semicircle where β is equal to 1. However, the porous films, leaky capacitor, surface roughness and non-uniform current distribution frequently cause a non-ideal capacitance that deviates β value away from 1 (Hauch & Georg 2001; Murakami et al. 2006). The fitted β value of the carbon nanofiber counter electrode was 0.82, smaller than that (0.95) of the Pt electrode. A lower β value suggested a higher porosity in carbon nanofiber electrode than that of Pt electrode (Murakami et al. 2006). In previous study, a β value of 0.81 was found in a highly porous carbon nanoparticle counter electrode (Murakami et al. 2006). Also, the capacitance (C) in carbon nanofiber counter electrode was larger than that of Pt electrode, suggesting a higher surface area in carbon nanofiber counter

electrode. A larger capacitance (C) was also found in other nanostructured counter electrodes with high porosity (Murakami et al. 2006; Jiang et al. 2010). Unfortunately, the fitted series resistance (R_s) of carbon nanofiber counter electrode was 5.12 Ωcm^2, more than twice of that of 2 Ωcm^2 for Pt electrode. This can be attributed to the higher thickness (~24 µm) of carbon nanofiber counter electrode. It was previously reported that thicker films increase R_s in carbon nanoparticle counter electrodes (Murakami et al. 2006).
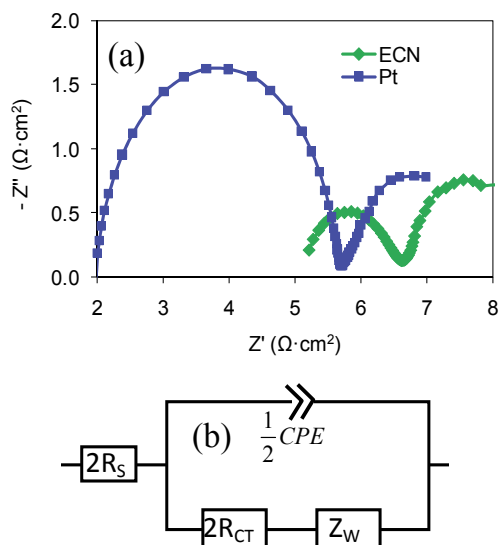

Fig. 6. (a) Nyquist plots of symmetrical carbon nanofiber-carbon nanofiber or Pt-Pt electrode cell; (b) equivalent circuit that was used to fitted the EIS results. Rs is series resistance at the counter electrode, R_{ct} charge transfer resistance, Z_w Nernst diffusion impedance and CPE constant phase element. Reprinted with permission from {Joshi et al. 2010}. Copyright {2010} American Chemical Society.

Counter Electrode	R_s (Ωcm^2)	R_{ct} (Ωcm^2)	C (Fcm^{-2})	β
ECN	5.12	0.70	5.6×10^5	0.82
Pt	2.00	1.89	2.0×10^5	0.95

Table 2. Fitted results extracted from Nyquist plots of the respective symmetrical cells using carbon nanofiber or Pt as electrode. Reprinted with permission from {Joshi et al. 2010}. Copyright {2010} American Chemical Society.

3.3 DSSC performance using carbon nanofiber counter electrode

The TiO_2 photoanode contained a blocking layer, a $TiCl_4$-treated nanocrystalline TiO_2 layer (Solaronix Ti-Nanoxide HT/SP) and a light scattering layer (Dyesol WER4-0). After sintering, the photoanode was soaked in a dye solution made of 0.5 mM Ruthenizer 535-bisTBA dye (Solaronix N-719) in acetonitrile/valeronitrile (1:1). The photoanode was then assembled with carbon nanofiber counter electrode using a thermoplastic sealant. The I^-/I_3^- electrolyte was finally injected into the cells. The reference DSSC devices with sputtered Pt layer (40 nm) as counter electrode were also fabricated for comparison in the same method.
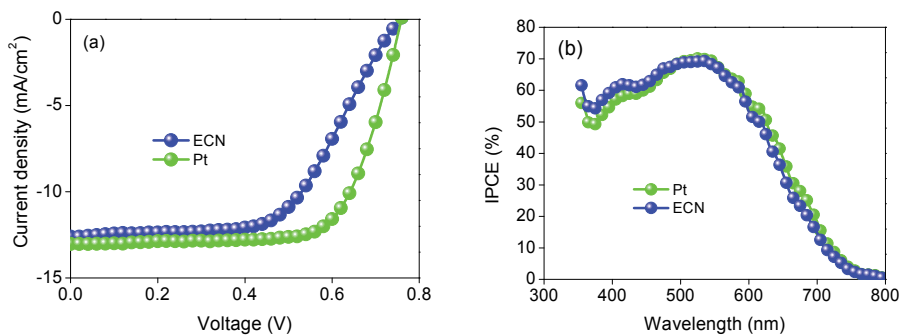
Fig. 7. (a) The J-V curves and (b) IPCE spectral action responses of carbon nanofiber (blue) and Pt (green) counter electrode DSSCs. Reprinted with permission from {Joshi et al. 2010}. Copyright {2010} American Chemical Society.

The J-V curves of carbon nanofiber and Pt DSSCs are shown in Figure 7a, tested under AM 1.5 solar simulator illumination at 100 mWcm^{-2}. Table 3 summaries the device parameters from these two different types of cells. The carbon nanofiber counter electrode DSSCs achieved a J_{sc} of 12.6 mAcm^{-2}, a V_{oc} of 0.76 V, a FF of 0.57, and efficiency (η) of 5.5 %. The corresponding parameters (J_{sc}, V_{oc}, FF, and η) of Pt counter electrode DSSCs were 13.02 mAcm^{-2}, 0.75 V, 0.71, and 6.97 %, respectively. The V_{oc}s of carbon nanofiber and Pt counter electrode DSSCs were very close. The reverse saturation current (J_0) of carbon nanofiber counter electrode DSSCs was 4.47×10^{-9} mAcm^{-2}, comparable to that of 3.58×10^{-9} mAcm^{-2} for Pt counter electrode devices. J_0 is usually regarded as a measure of recombination in solar cells. The comparable value to J_0 suggested that carbon nanofiber counter electrode DSSCs had a comparable recombination as that of Pt counter electrode devices. It was previously reported that charge recombination at FTO/TiO$_2$ and TiO$_2$/electrolyte interfaces in DSSCs led to a V_{oc} loss (Huang et al. 1997; Gratzel 2000; Xia et al. 2007). The comparable Voc in carbon nanofiber and Pt counter electrode DSSCs further conformed that the former did not affect the charge recombination in the DSSCs. However, the J_{sc} is lower in carbon nanofiber counter electrode DSSCs than that of Pt counter electrode DSSCs. Figure 7b shows incident photon-to-current conversion efficiency (IPCE) spectral action responses of the two devices. It was found that IPCE of carbon nanofiber cells was slightly smaller than that of Pt devices in the 550–750 nm spectral range, consistent with the relatively lower J_{sc}. This was probably caused by that the Pt counter electrode can reflect unabsorbed light back to TiO$_2$ photoanode for re-absorption by the dye (Fang et al. 2004; Lee et al. 2009; Wang et al. 2009). However, carbon nanofiber counter electrode cannot reflect such unabsorbed light. However, the reduction of J_{sc} was insignificant and the real reason for lower η in carbon nanofiber cells was the lower FF.

Counter Electrode	J_{sc} (mAcm^{-2})	V_{oc} (V)	FF	η (%)	J_0 (mAcm^{-2})	R_{Stot} (Ωcm^2)
Carbon Nanofiber	12.60	0.76	0.57	5.5	4.47×10^{-9}	15.5
Pt	13.02	0.75	0.71	6.97	3.58×10^{-9}	4.8

Table 3. The comparison of device parameters of carbon nanofiber and Pt counter electrode (R_{Stot}: total series resistance, and J_0: reverse saturation current). Reprinted with permission from {Joshi et al. 2010}. Copyright {2010} American Chemical Society.

The reduced FF may be caused by the increase of overall series resistance (R_{Stot}) of the cells. The R_{Stot} of carbon nanofiber counter electrode was 15.5 Ωcm^2, much larger than that (4.8 Ωcm^2) of Pt devices. Two possible reasons can explain the larger R_{Stot} in carbon nanofiber counter electrode DSSCs. First, the thickness of carbon nanofiber counter electrode (~24 µm) was much thicker than that (40 nm) of Pt electrode. Although the larger thickness provided a larger surface area for triiodide reduction with a reduced R_{ct}, it may increase electron transport length before reaching triiodide reduction sites and lead to higher internal series resistance (Murakami et al. 2006).
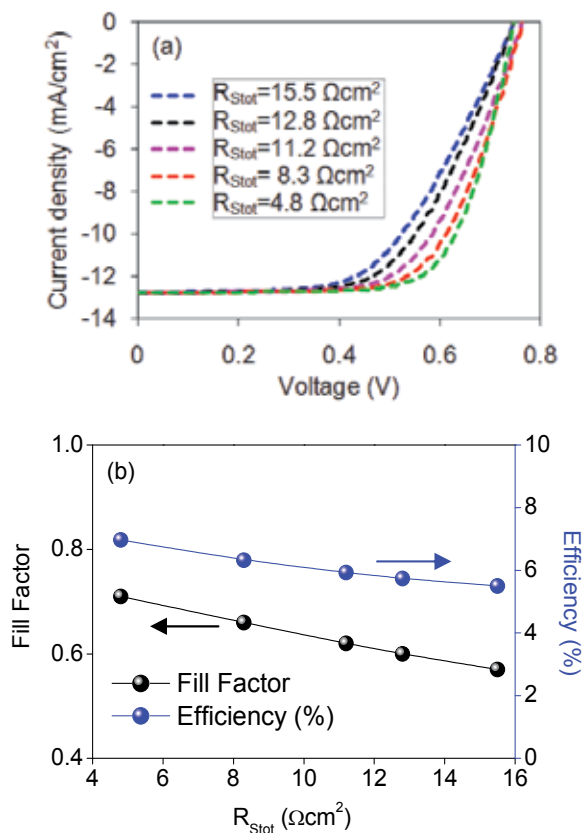
Fig. 8. (a) Simulated J-V curves of carbon nanofiber DSSCs with R_{Stot} at 15.5 Ωcm^2 (blue), 12.8 Ωcm^2 (dark), 11.2 Ωcm^2 (purple), 8.3 Ωcm^2 (red), 4.8 Ωcm^2 (green); (b) Relationship between FF (black), η (blue) and R_{Stot}. Reprinted with permission from {Joshi et al. 2010}. Copyright {2010} American Chemical Society.

The larger internal series resistance was consistent with the higher R_s in carbon nanofiber counter electrode, which was more than twice of that of Pt electrode obtained in symmetrical cells via EIS measurements. Second, carbon nanofiber counter electrode may have a higher Z_W of triiodide ions than Pt electrode because the thicker porous carbon nanofiber film increased the diffusion length of triiodide ions. This can also lead to a larger internal series resistance (Lee et al. 2009). A higher Z_W was also reported previously in other nanostructured counter electrodes including surface-nitrided nickel (Jiang et al. 2010),

carbon nanotubes (Lee et al. 2009; Li et al. 2010), and carbon nanoparticles (Murakami et al. 2006). A series of J-V curves at different R_{Stot} were simulated in order to quantitatively study the R_{Stot} effects on carbon nanofiber counter electrode DSSC performance. The dependence of FF and η on R_{Stot} in carbon nanofiber counter electrode is plotted in Figure 8b. When decreasing R_{Stot} from 15.5 to 4.8 Ωcm^2, FF and η can be significantly improved and approach that of Pt DSSCs. A promising approach to decreasing R_{Stot} is to reduce the thickness of carbon nanofiber counter electrode via a thinner and more porous carbon nanofiber sheet.

4. Conclusion

The carbon/TiO$_2$ composite and carbon nanofiber were used as low cost alternative to Pt counter electrode for DSSCs. Although the efficiencies of carbon/TiO$_2$ composite and carbon nanofiber DSSC devices were lower than that of Pt devices, some of the parameters including J_{sc}, V_{oc} or FF are comparable. The carbon/TiO$_2$ composite and carbon nanofiber counter electrodes have shown potential as an efficient electrocatalyst with low charge transfer resistance (R_{ct}) and large surface area for reduction of I_3^- ions.

5. Acknowledgment

6. References

Alibabaei, L., M. K. Wang, et al. (2010). "Application of Cu(II) and Zn(II) Coproporphyrins as Sensitizers for Thin Film Dye Sensitized Solar Cells." *Energy & Environmental Science* 3(7): 956-961.

Burnside, S., S. Winkel, et al. (2000). "Deposition and Characterization of Screen-Printed Porous Multi-layer Thick Film Structures from Semiconducting and Conducting Nanomaterials for Use in Photovoltaic Devices." *Journal of Materials Science - Materials in Electronics* 11(4): 355-362.

Calandra, P., G. Calogero, et al. (2010). "Metal Nanoparticles and Carbon-Based Nanostructures as Advanced Materials for Cathode Application in Dye-Sensitized Solar Cells." *International Journal of Photoenergy* 2010: 109495.

Fan, B. H., X. G. Mei, et al. (2008). "Conducting Polymer/Carbon Nanotube Composite as Counter Electrode of Dye-Sensitized Solar Cells." *Applied Physics Letters* 93(14).

Fang, X. M., T. L. Ma, et al. (2004). "Effect of the Thickness of the Pt Film Coated on a Counter Electrode on the Performance of a Dye-Sensitized Solar Cell." *Journal of Electroanalytical Chemistry* 570(2): 257-263.

Gajjela, S. R., K. Ananthanarayanan, et al. (2010). "Synthesis of Mesoporous Titanium Dioxide by Soft Template Based Approach: Characterization and Application in Dye-Sensitized Solar Cells." *Energy & Environmental Science* 3(6): 838-845.

Gratzel, M. (2000). "Perspectives for Dye-Sensitized Nanocrystalline Solar Cells." *Progress in Photovoltaics: Research and Applications* 8(1): 171-185.

Gratzel, M. (2003). "Dye-sensitized solar cells." *Journal of Photochemistry and Photobiology C-Photochemistry Reviews* 4(2): 145-153.

Han, H. W., U. Bach, et al. (2009). "A Design for Monolithic All-Solid-State Dye-Sensitized Solar Cells with a Platinized Carbon Counterelectrode." *Applied Physics Letters* 94(10).

Hauch, A. and A. Georg (2001). "Diffusion in the electrolyte and charge-transfer reaction at the platinum electrode in dye-sensitized solar cells." *Electrochimica Acta* 46(22): 3457-3466.

Hinsch, A., S. Behrens, et al. (2008). "Material Development for Dye Solar Modules: Results from an Integrated Approach." *Progress in Photovoltaics: Research and Applications* 16(6): 489-501.

Huang, S. Y., G. Schlichthorl, et al. (1997). "Charge Recombination in Dye-Sensitized Nanocrystalline TiO2 Solar Cells." *Journal of Physical Chemistry B* 101(14): 2576-2582.

Huang, Z., X. Liu, et al. (2007). "Application of Carbon Materials as Counter Electrodes of Dye-Sensitized Solar Cells." *Electrochemistry Communications* 9(4): 596-598.

Imoto, K., M. Suzuki, et al. (2003). "Activated carbon counter electrode for dye-sensitized solar cell." *Electrochemistry* 71(11): 944-946.

Imoto, K., K. Takahashi, et al. (2003). "High-performance carbon counter electrode for dye-sensitized solar cells." *Solar Energy Materials and Solar Cells* 79(4): 459-469.

Jiang, Q. W., G. R. Li, et al. (2010). "Surface-Nitrided Nickel with Bifunctional Structure As Low-Cost Counter Electrode for Dye-Sensitized Solar Cells." *The Journal of Physical Chemistry C* 114(31): 13397-13401.

Joshi, P., Y. Xie, et al. (2009). "Dye-Sensitized Solar Cells based on Low Cost Nanoscale Carbon/TiO2 Composite Counter Electrode." *Energy & Environmental Science* 2(4): 426-429.

Joshi, P., L. Zhang, et al. (2010). "Electrospun Carbon Nanofibers as Low-Cost Counter Electrode for Dye-Sensitized Solar Cells." *ACS Applied Materials & Interfaces* 2(12): 3572-3577.

Kay, A. and M. Gratzel (1996). "Low Cost Photovoltaic Modules Based on Dye Sensitized Nanocrystalline Titanium Dioxide and Carbon Powder." *Solar Energy Materials and Solar Cells* 44(1): 99-117.

Lee, W. J., E. Ramasamy, et al. (2009). "Efficient Dye-Sensitized Solar Cells with Catalytic Multiwall Carbon Nanotube Counter Electrodes." *ACS Applied Materials & Interfaces* 1(6): 1145-1149.

Li, G.-R., F. Wang, et al. (2010). "Carbon Nanotubes with Titanium Nitride as a Low-Cost Counter-Electrode Material for Dye-Sensitized Solar Cells13." *Angewandte Chemie International Edition* 49(21): 3653-3656.

Matsubara, T., R. Sakaguchi, et al. (2005). "Measurement and Analysis of the Series Resistance in a Dye Sensitized Solar Cells " *Electrochemistry* 73(1): 60 - 66.

Mei, X. and J. Ouyang (2009). "Gels of carbon nanotubes and a nonionic surfactant prepared by mechanical grinding." *Carbon* 48: 293-299.

Murakami, T. N., S. Ito, et al. (2006). "Highly Efficient Dye-Sensitized Solar Cells based on Carbon Black Counter Electrodes." *Journal of the Electrochemical Society* 153(12): A2255-A2261.

Oregan, B. and M. Gratzel (1991). "A Low-Cost, High-Efficiency Solar-Cell Based on Dye-Sensitized Colloidal Tio2 Films." *Nature* 353(6346): 737-740.

Papageorgiou, N., W. F. Maier, et al. (1997). "An Iodine/Triiodide Reduction Electrocatalyst for Aqueous and Organic Media." *Journal of The Electrochemical Society* 144(3): 876-884.

Ramasamy, E., W. J. Lee, et al. (2007). "Nanocarbon counterelectrode for dye sensitized solar cells." *Applied Physics Letters* 90(17): 173103.

Skupien, K., P. Putyra, et al. (2009). "Catalytic Materials Manufactured by the Polyol Process for Monolithic Dye-sensitized Solar Cells." *Progress in Photovoltaics: Research and Applications* 17(1): 67-73.

Sun, H., Y. Luo, et al. "In Situ Preparation of a Flexible Polyaniline/Carbon Composite Counter Electrode and Its Application in Dye-Sensitized Solar Cells." *The Journal of Physical Chemistry C* 114(26): 11673-11679.

Sun, K., B. H. Fan, et al. (2010). "Nanostructured Platinum Films Deposited by Polyol Reduction of a Platinum Precursor and Their Application as Counter Electrode of Dye-Sensitized Solar Cells." *Journal of Physical Chemistry C* 114(9): 4237-4244.

Suzuki, K., M. Yamaguchi, et al. (2003). "Application of carbon nanotubes to counter electrodes of dye-sensitized solar cells." *Chemistry Letters* 32(1): 28-29.

Wang, M., A. M. Anghel, et al. (2009). "CoS Supersedes Pt as Efficient Electrocatalyst for Triiodide Reduction in Dye-Sensitized Solar Cells." *Journal of the American Chemical Society* 131(44): 15976-15977.

Xia, J., N. Masaki, et al. (2007). "Sputtered Nb2O5 as a Novel Blocking Layer at Conducting Glass/TiO2 Interfaces in Dye-Sensitized Ionic Liquid Solar Cells." *The Journal of Physical Chemistry C* 111(22): 8092-8097.

Mei, X., S. J. Cho, et al. (2010). "High-performance dye-sensitized solar cells with gel-coated binder-free carbon nanotube films as counter electrode." *Nanotechnology* 21(39): 395202.

Xie, Y., P. Joshi, et al. (2010). "Electrolyte Effects on Electron Transport and Recombination at ZnO Nanorods for Dye-Sensitized Solar Cells." *The Journal of Physical Chemistry C* 114(41): 17880-17888.

Xie, Y., P. Joshi, et al. (2009). "Structural effects of core-modified porphyrins in dye-sensitized solar cells." *Journal of Porphyrins and Phthalocyanines* 13(8-9): 903-909.

Yum, J. H., E. Baranoff, et al. (2010). "Phosphorescent Energy Relay Dye for Improved Light Harvesting Response in Liquid Dye-Sensitized Solar Cells." *Energy & Environmental Science* 3(4): 434-437.

Dye Sensitized Solar Cells as an Alternative Approach to the Conventional Photovoltaic Technology Based on Silicon - Recent Developments in the Field and Large Scale Applications

Elias Stathatos
Technological-Educational Institute of Patras,
Electrical Engineering Department, Patras,
Greece

1. Introduction

Utilization of renewable energies is of major importance because of the increase in fossil energy costs in combination with carbon dioxide reduction preventing global warming. The importance of the solar energy can be considered as the sustainable energy which may successfully satisfy a part of the energy demand of future generations. The 3×10^{24} joule/year energy supply from sun to the earth is ten thousand times more than the global need. It means that the use of 10% efficiency photovoltaic cells could cover the present needs in electricity covering only the 0.1% of earth's surface (Wu, et al. 2008). Handling this opportunity of solar energy utilization is a big bet for the future. Besides the development of new clean techniques to the electrical power generation is urgently important in order to protect global environment and assure economic growth of sustainable resources. Taking into account the present status in photovoltaic technology, some improvements have to be made which are summarized in three basic fields: (a) in costs, (b) in their applicability and (c) sustainability. Although the cost per peak watt of crystalline silicon solar cells has significantly dropped, it is still expensive compared to the conventional grid electricity resources. Silicon wafers made of pure semiconducting material to avoid limitations in energy conversion, are still expensive. For this reason developments on potentially cheaper solar cells based on thin-film technology have been made. According to this technology, thin films made of purely inorganic materials such as amorphous silicon, cadmium telluride, and copper indium diselenide successfully prepared on glass substrates.

Almost two decades ago, dye sensitized solar cells (DSSCs) were proposed as low cost alternatives to the conventional amorphous silicon solar cells, owing to the simplicity of their fabrication procedures, practically under ambient conditions with mild chemical processes. DSSCs are placed in the category of third generation photovoltaics where new trends in the photovoltaic technology are applied. In the 1st generation PV cells, the electric interface is made between doped n-type and p-type bulk silicon. 1st generation PV cells provide the highest so far conversion efficiency. The 2nd generation PV cells are based on

thin film technology. These cells utilize less material and they thus drop the production cost, however, they are less efficient than the bulk cells. Both 1st and 2nd generation cells are based on opaque materials and necessitate front-face illumination and moving supports to follow sun's position. Thus they may be either set up in PV parks or on building roofs. 3rd generation solar cells, are based on nanostructured (mesoscopic) materials and they are made of purely organic or a mixture of organic and inorganic components, thus allowing for a vast and inexhaustible choice of materials. Because of their mesoscopic character, it is possible to make transparent cells, which can be used as photovoltaic windows. Photovoltaic windows can be functioned by front-face light incidence but also by diffuse light and even by back face light incidence. Also because of their mesoscopic nature, 3rd generation solar cells are easy to make at ambient conditions, not necessitating severe measures of purity, thus dropping production cost. Among the different possibilities of 3rd generation solar cells, DSSC have the most promising prospect. The overall efficiency of ~12% (in laboratory and small size cells) placed DSSCs as potential inexpensive alternatives to solid state devices. Since the pioneer work of M. Grätzel and co-workers an intense interest to the development of such kind of solar cells has been recorded because of their low cost, simple preparation procedures and benign methods of construction compared with conventional methods applied in first and second generation photovoltaic technology (O'Regan & Grätzel, 1991). Although the solar to electrical energy conversion efficiencies recorded for DSSCs are lower than those measured for silicon based solar cells, a high potential for improvement in their efficiency, stability and commercialization has been announced till nowadays (Grätzel, 2006; Goldstein et al., 2010; Hinsch et al., 2009).

2. Principles of operation and cell structure

The working principle of a DSSC substantially differs from that of a conventional solar cell based on silicon. In silicon solar cell a *p-n* junction by joining semiconductors of different
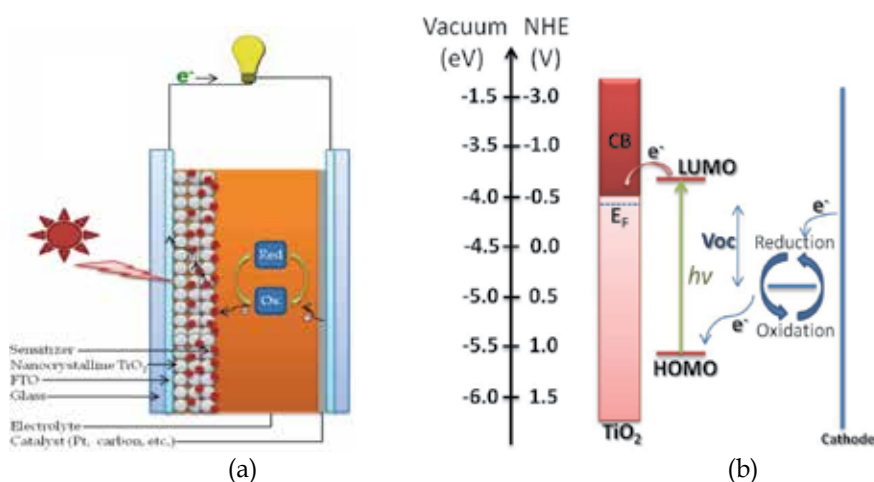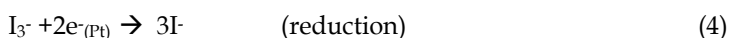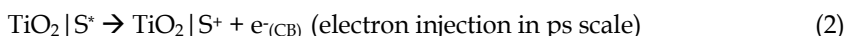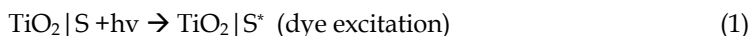

Fig. 1. (a) Principle of operation for a DSSC and (b) an energy diagram of DSSC's operation.

charge carriers' concentration in a very close contact is necessary. In this case the processes of light absorption and charge transport are caused in the same material. In DSSCs, these

fundamental processes are occurred in different materials which avoid the premature recombination of electrons and holes. As these processes do not happen at the same material ultrapure materials are not required for a high performance DSSC. DSSCs are composed of four major components: a nanostructured n-type semiconductor, typically TiO_2, a dye-sensitizer to absorb visible light, an electrolyte, which creates the interface with the semiconductor and a counter electrode carrying an electrocatalyst, which facilitates transfer of electrons to the electrolyte. Figure 1a illustrates the basic principle of cell operation while Figure 1b the energy diagram of basic components of the DSSC.

Charge separation is occurred by the different electrochemical potentials between different species such as negative electrode (TiO_2/sensitizer) and electrolyte. Any electrostatic potential like in the case of silicon based solar cells is then ignored when a minimum concentration of 0.4M of mobile ions exist in the electrolyte (Grätzel & Durrant, 2008). The semiconductor must provide large active interface both for the attachment of the sensitizer and the contact with the electrolyte. Therefore, the semiconductor can be only conceived in nanostructured form. The sensitizer must have a large extinction coefficient and its energy states must match with those of the semiconductor so as to allow extensive light absorption and efficient excited–electron injection into the conduction band of the semiconductor. The electrolyte must have appropriate electrochemical potential so as to combine with the semiconductor and to efficiently provide charge mobility in a cyclic manner. The dye is regenerated by electrons donated from the electrolyte. The iodide is then regenerated by the reduction of triiodide at the positive electrode, and the circuit is completed by the electron migration through the external circuit. Finally, the counter electrode must efficiently catalyze the transfer of electrons from the external circuit to the liquid phase, i.e. the electrolyte. The open circuit voltage of the cell generated under illumination is attributed to the difference between the Fermi level of the nanostructured semiconductor and the electrochemical potential of the electrolyte. The photoelectrochemical processes occur in a DSSC can be expressed in equations 1-6 (Wu et al., 2008).

$$TiO_2|S + h\nu \rightarrow TiO_2|S^* \quad \text{(dye excitation)} \tag{1}$$

$$TiO_2|S^* \rightarrow TiO_2|S^+ + e^-_{(CB)} \quad \text{(electron injection in ps scale)} \tag{2}$$

$$TiO_2|S^* + 3I^- \rightarrow TiO_2|S + I_3^- \quad \text{(dye regeneration in μs scale)} \tag{3}$$

$$I_3^- + 2e^-_{(Pt)} \rightarrow 3I^- \quad \text{(reduction)} \tag{4}$$

While the dark reactions which may also happen are:

$$I_3^- + 2e^-_{(CB)} \rightarrow 3I^- \quad \text{(recombination to electrolyte from ms to s scale)} \tag{5}$$

$$TiO_2|S^+ + e^-_{(CB)} \rightarrow TiO_2|S \quad \text{(recombination from μs to ms scale)} \tag{6}$$

From equations described above it is obvious that several issues have to be simultaneously satisfied in order to achieve an efficient solar cell based on nanostructured dye sensitized semiconductors. As a first issue we may refer that the dye has to be rapidly reduced to its ground state after it is oxidized while the electrons are injected into the conduction band of the TiO_2 otherwise the solar cell performance will be low. This means that the chemical potential of the iodide/triiodide redox electrolyte should be positioned in more negative values than the oxidised form of the dye. Furthermore the nanocrystalline TiO_2 film must be

able to permit fast diffusion of charge carriers to the conductive substrate and then to external circuit avoiding recombination losses, while good interfacial contact between electrolyte and semiconductor has to be ensured (Bisquert et al., 2004). Electrolyte long term stability (chemical, thermal, optical) which will guarantee solar cell high performance is under continuous consideration as in common DSSC structures the electrolyte is in the form of a volatile liquid bringing out the obvious problem of sealing (Zhang et al., 2011). Finally, the optimized concentration of redox couple for the cell efficiency has to satisfy one more parameter of the optical transparency in the visible region otherwise the absorbed light from the dye will be minimized and also triiodide can react with injected electrons increasing the dark current of the cell.

Although, the charge transport rate in DSSCs is relatively slow compared with conventional photovoltaics and the interface where the charge carrier could recombine is wide. Because of the mesoporous structure the charge collection quantum efficiency is surprisingly close to unity (Grätzel & Durrant, 2008). This is caused because of the slow rate constant for the interfacial charge recombination of injected electrons with the oxidised redox couple. The presence of a suitable catalyst (e.g. Pt) raises an activation barrier in one of the intermediate steps of redox reactions resulting in a slow overall rate constant for this reaction. This low rate constant for this recombination reaction on TiO_2, affect to an increased efficiency for DSSCs.

The kinetic competition between charge transport and recombination in DSSCs can be analysed in terms of an effective carrier diffusion length L_n, given by $L_n = [D_{eff} \tau]^{1/2}$ where D_{eff} is the effective electron diffusion length, and τ the electron lifetime due to the charge-recombination reaction given by eq. 5 (Peter & Wijayantha, 2000). D_{eff} strongly depends on the position of the quasi Fermi level in the semiconductor and therefore on the light intensity. Typical values at 1 sun are $1.5 \ 10^{-5} \ cm^2 s^{-1}$. Since diffusion is the only driving force for electron transport, the diffusion length DL must be at least as long a the thickness of the TiO_2 electrode. D_{eff} generally increases with light intensity while τ proportionally decreases. As a consequence the diffusion length is independent of the light intensity. Typical values for diffusion length are 5–20 µm. These limitations set the rules according to which the researchers are challenged to make a choice of materials that will lead to efficient cell functioning.

3. DSSCs' basic components

The basic structure of a DSSC, as it is referred in previous section, is consisted of two glass electrodes in a sandwich configuration. For the first electrode (negative) a nanocrystalline n-type semiconductor, typically titanium dioxide film is deposited on a transparent conductive glass (TCO) (Fig.2) and then a dye-sensitizer is adsorbed and chemically anchored in order to sensitize the semiconductor in the visible. For this purpose, the dye sensitizer bears carboxylate or phosphonate groups, which interact with surface –OH groups on the titanium dioxide. Several efforts have been made to apply dyes of various structures; however, Ru-bipyridine complexes have established themselves as choice sensitizers (Xia & Yanagida, 2009). This is the negative electrode of the solar cell. A similar transparent conductive glass (positive electrode) covered with a thin layer of platinum is faced to the previous electrode. The space between the two electrodes is filled with an electrolyte. The most efficient electrolytes applied with DSSCs are liquid electrolytes with dissolved I^-/I_3^- redox couple, which are obtained by co-dissolving an iodide salt with iodine (Hagfeldt & Grätzel, 2000). Since some crystallization problems have been encountered

with simple salts, like LiI or KI, recent research is concentrated on the employment of ionic liquids, principally, alkylimidazolium iodides (Papageorgiou et al., 1996).
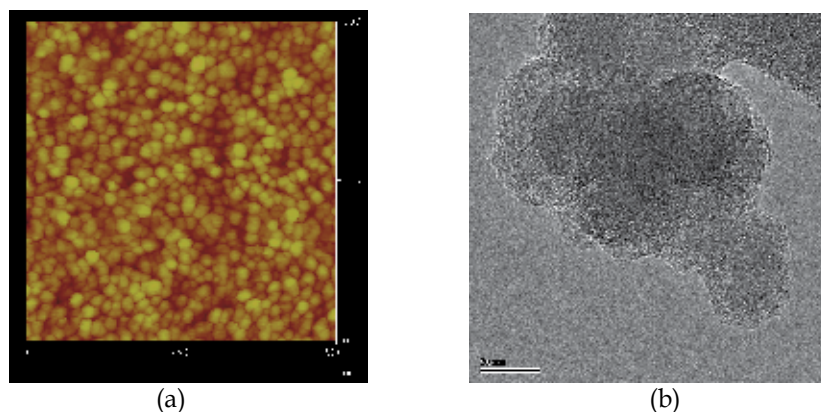

| (a) | (b) |

Fig. 2. AFM (a) and HR-TEM (b) images of a nanocrystalline TiO_2 film.

3.1 Nanocrystalline semiconductor

In DSSC technology a variety of nanocrystalline mesoporous metal oxides have been used such as TiO_2, ZnO, SnO_2 and Nb_2O_5 (Sayama, et al., 1998, Jose, et al., 2009). Despite the fact that some of them exhibited promising results in cells' performance only titanium dioxide has extensively used because of some advantages which are only present in this oxide. TiO_2 performs excellent thermal stability; it is impervious to chemicals and non-toxic and finally a cheap material. The common crystalline form in application to solar cells is the anatase although a mixture of anatase/rutile form is often used mainly by the formation of very active commercial Degussa-P25 powder. Rutile has proved to be less active as it is less chemical stable than anatase form. Combinations of metal oxides as negative electrodes have also been examined such as WO_3/TiO_2, TiO_2/ZrO_2 and SnO_2/ZnO or SnO_2/TiO_2 with moderate results (Tennakone, et al., 1999). In the case of mixed oxides, the core-shell nanostructure formation is mentioned as a new class of combinational system which is typically comprised of a core made of nanomaterials and a shell of coating layer covering on the surface of core nanomaterials (Zhang & Cao, 2011). The use of core-shell nanostructures is usually refereed to lower the charge recombination in the TiO_2 nanoparticles and it is based on the hypothesis that a coating layer may build up an energy barrier at the semiconductor/electrolyte interface retarding the reaction between the photogenerated electrons and the redox species in electrolyte. Different systems that consisted of mesoporous TiO_2 films coated with oxides such as Nb_2O_5, ZnO, $SrTiO_3$, ZrO_2, Al_2O_3 and SnO_2 are also referred. The results revealed that, compared to photoelectrode made of bare TiO_2 nanoparticles, the use of e.g. Nb_2O_5 shell might increase both the open circuit voltage and the short circuit current of the cells.

The basic goal in films preparation is the high surface area of the inorganic semiconductor particles in order to achieve high amounts of dye adsorbed on it. Therefore, a much interest has been drawn to the preparation of highly crystalline mesoporous materials in the form of homogeneous films with an average thickness of 6-12 μm. Usually TiO_2 nanoparticles are fabricated by the aqueous hydrolysis of a titanium alkoxide precursor. It is then followed by autoclaving at temperatures up to 240^0C to achieve the desired nanoparticle size and

crystallinity (anatase) (Barbe et al., 1997). The nanoparticles are deposited as a colloidal suspension by screen printing or by spreading with a doctor blade technique, followed by sintering at ~450^{0}C to achieve good interparticle connections. The film porosity is maintained by the addition of surfactants or organic fillers; the organic content is removed after sintering of the films in order to obtain pure titanium dioxide (Stathatos et al., 2004). Figure 3 shows a SEM cross sectional image of a mesoporous TiO$_2$ film prepared by titanium dioxide powder formed with screen printing method. The average pore size is 15 nm and particle diameter 20-25 nm. Film morphology is a crucial parameter in DSSCs' performance mainly to the influence in electron recombination rate. As referred in literature this phenomenon usually happens in the contact between TiO$_2$ film and conductive substrate (Zhu, et al., 2002). Therefore, a condensed non-porous thin film of TiO$_2$ is formed between nanocrystalline thick film and TCO substrate and referred as "blocking layer". The thickness of the compact film is around a few hundreds of nanometres. An alternative method to prepare highly porous nanocrystalline TiO$_2$ with even more smaller particles is the sol-gel. The sol-gel method for the synthesis of inorganic or nanocomposite organic/inorganic gels has become one of the most popular chemical procedures (Stathatos et al., 1997). This popularity stems from the fact that sol-gel synthesis is easy and it is carried out at ambient or slightly elevated temperatures so that it allows non-destructive organic doping (Brinker & Scherer, 1990).
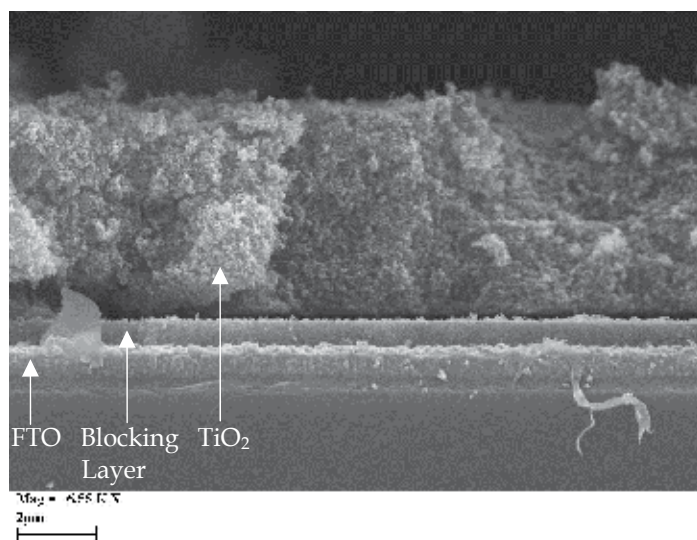
Fig. 3. Nanocrystalline TiO$_2$ film made of Degussa-P25 powder. A TiO$_2$ blocking layer is also present.

Indeed, the sol-gel method has led to the synthesis of a great variety of materials, the range of which is continuously expanding. Thus the simple incorporation of organic dopants as well as the formation of organic/inorganic nanocomposites offers the possibility of efficient dispersion of functional compounds in gels, it allows modification of the mechanical properties of the gels and provides materials with very interesting optical properties. A typical sol-gel route for making oxide matrices and thin films is followed by hydrolysis of alkoxides, for example, alkoxysilanes, alkoxytitanates, etc (Brinker & Scherer, 1990).

However, a review of the recent literature reveals an increasing interest in another sol-gel route based on organic acid solvolysis of alkoxides (Birnie & Bendzko, 1999; Wang et al., 2001). This second method seems to offer substantial advantages in several cases and it is becoming the method of choice in the synthesis of organic/inorganic nanocomposite gels. As it has been earlier found by Pope and Mackenzie (Pope & Mackenzie, 1986) and later verified by others, organic (for example, acetic or formic) acid solvolysis proceeds by a two step mechanism which involves intermediate ester formation (Ivanda et al., 1999). Simplified reaction schemes showing gel formation either by hydrolysis or organic acid solvolysis are presented by the following reactions. (Note that in these reactions only one metal-bound ligand is taken into account, while acetic acid (AcOH) is chosen to represent organic acids in organic acid solvolysis):

Hydrolysis	$\equiv M\text{-}OR + H_2O \rightarrow \equiv M\text{-}OH + ROH$	(7a)
Polycondensation	$\equiv M\text{-}(OH) \rightarrow \text{-}M\text{-}O\text{-}M\text{-} + H_2O$	(7b)
Acetic acid solvolysis	$\equiv M\text{-}OR + AcOH \rightarrow \equiv M\text{-}OAc + ROH$	(8a)
	$ROH + AcOH \rightarrow ROAc + H_2O$	(8b)
	$\equiv M\text{-}OAc + ROH \rightarrow ROAc + \equiv M\text{-}OH$	(8c)
	$\equiv M\text{-}OR + \equiv M\text{-}OAc \rightarrow ROAc + M\text{-}O\text{-}M$	(8d)
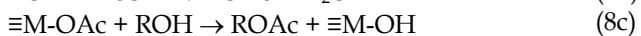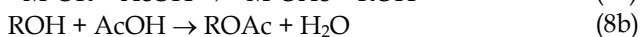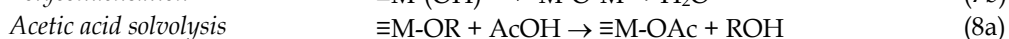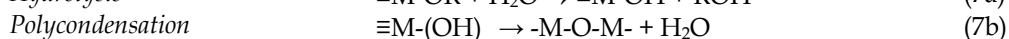
where M is a metal (for example, Si or Ti) and R is a short alkyl chain (for example, ethyl, butyl, or isopropyl). Hydrolysis (7a) produces highly reactive hydroxide species M-OH, which, by inorganic polymerization, produce oxide, i.e. M-O-M, which is the end product of the sol-gel process. More complicated is acetic acid solvolysis (8) where several different possibilities may define different intermediate routes to obtain oxide. Reaction (8a) is a prerequisite of the remaining three reactions. Occurrence of reaction (8b) would mean that water may be formed which may lead to hydrolysis. Reaction (8c) would create reactive M-OH which would form oxide, while reaction (8d) directly leads to oxide formation. The above possibilities have been demonstrated by various researchers by spectroscopic techniques. However, there still exists a lot of uncertainly and there is no concrete model to describe a well established procedure leading to oxide formation by organic acid solvolysis. For this reason, more work needs to be carried out on these systems. Reactions (8) reveal one certain fact. The quantity of acetic acid in solution will be crucial in affecting intermediate routes.   Thus reaction (8b) is possible only if an excess of acetic acid is present. Also the quantity of acetic acid will define whether the solvolysis steps will simultaneously affect all available alkoxide ligands or will leave some of them intact and subject to hydrolysis reactions. Figure 4 shows a SEM cross sectional image of a mesoporous TiO_2 film prepared by sol-gel method with dip-coating. The average pore size is lower than 10 nm and particle diameter 10-12 nm. In this case, it is proved that no compact TiO_2 layer acting as "blocking layer" is needed for high performance DSSCs.

From previous paragraphs is obvious that nanoparticulate films are the common choice in photoelectrode preparation for use in DSSCs. However, the nanoparticulate films are not thought to be ideal in structure with regard to electron transport. For this reason, recent developments in nanostructured electrodes are proposed such as nanowires, nanotubes, nanorods which belong to 1-Dimensional structures in contrast to 3-D structures referred to films consisted of nanoparticles.
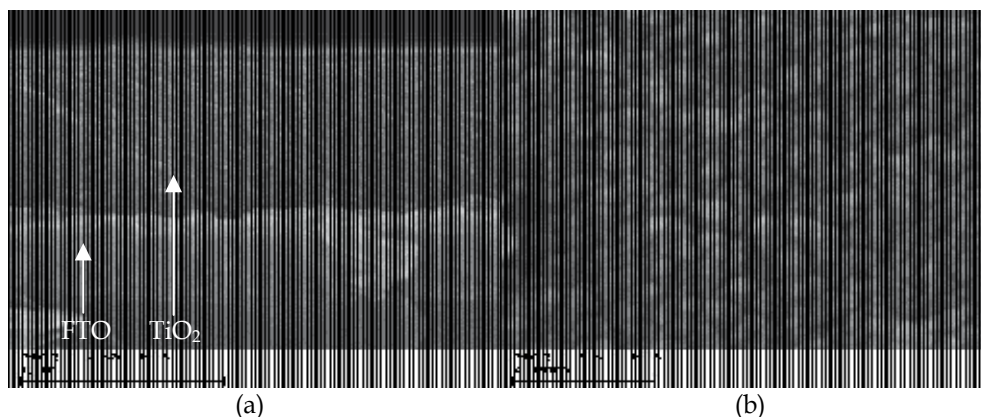
Fig. 4. TiO$_2$ nanocrystalline film made of sol-gel procedure (a) cross sectional image and (b) higher magnification of the film.

One-dimensional nanostructures might provide direct pathways for electron transport in DSSCs and ~25 µm thick film consisting of ZnO nanowires in diameter of ~130nm was mentioned to be able to achieve a surface area up to one-fifth as large as a nanoparticle film used in the conventional DSSCs (Law et al., 2005).
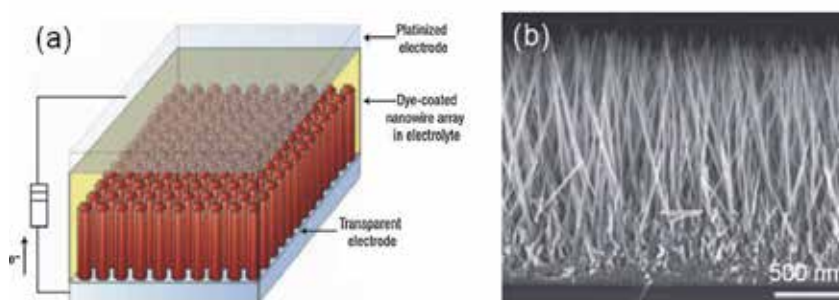

Fig. 5. (a) Schematic diagram of a DSSC with titania nanotubes, (b) a SEM image of titania nanotubes taken from reference (Zhang & Cao, 2011).

Moreover, the low manufacturing cost by using roll-to roll coating process creates the need of replacing the glass substrate with light weighted flexible plastic electrodes, expanding this way the area of DSSCs' applications. Flexible plastic electrodes like polyethylene terephthalate sheet coated with tin-doped indium oxide (PET-ITO) appear to possess many technological advantages (no size/shape limitations, low weight, high transmittance) as they present very low production cost in relation to F:SnO$_2$ (FTO) conductive glasses. The use of such plastic substrates requires that all processes needed for the fabrication of DSSC, including the formation of TiO$_2$ nanocrystalline films, to be designed at temperatures lower than 150^{0}C. In the direction of replacing the glass substrates with flexible plastics, mesoporous TiO$_2$ films have to be prepared at low temperature and also with nanocrystalline dimensions for better efficiency to energy conversion. So far, the methods that obtain the most-efficient TiO$_2$ films for DSSCs have been based on high-temperature calcination. High-temperature annealing, usually at 450-500^{0}C, is necessary to remove

organic material needed to suppress agglomeration of TiO_2 particles and reduce stress during calcination for making crack-free films with good adhesion on substrates. Besides, high-temperature treatment of films promotes crystallinity of TiO_2 particles and their chemical interconnection for better electrical connection. Low sintering temperature yields titania nanocrystalline films with high active surface area but relatively small nanocrystals with many defects and poor interconnection, thus lower conductivity. High sintering temperature for TiO_2 films is then the most efficient method for the preparation of high performance DSSCs but it is also a cost intensive process. In addition, high temperature treatment of TiO_2 films cannot be applied to flexible plastic electrodes which in recent years emerge as an important technological quest. Different approaches appear in the literature to avoid high temperature annealing of thick and porous TiO_2 films. Among a variety of methods used for the low-temperature treatment of TiO_2 films like hydrothermal crystallization (Huang et al., 2006), chemical vapor deposition of titanium alkoxides (Murakami et al., 2004), microwave irradiation (Uchida et al., 2004), ultraviolet light irradiation treatment (Lewis et al., 2006), and sol-gel method (Stathatos et al., 2007), the efficiency of DSSCs employing ITO-PET substrates was in the range of 2-3% at standard conditions of 100 mW/cm² light intensities at AM 1.5. A very simple and also benign method for the formation of pure TiO_2 nanoparticles surfactant-free films of nanocrystalline TiO_2 at room temperature with excellent mechanical stability is the mixture of a small amount of titanium isopropoxide with commercially available P25-TiO_2 (surface area of 55 m²/g, mean average particle size of 25 nm and 30/70% rutile/anatase crystallinity) powder. The hydrolysis of the alkoxide after its addition helps to the chemical connection between titania particles and their stable adhesion on plastic or glass substrate without sacrificing the desired electrical and mechanical properties of the film. Promising results have obtained by the use of this method.

3.2 Sensitizers

The dye plays the important role of sensitizing the semiconductor in the visible and infrared region of solar light. For this reason several requirements have to be succoured at the same time such as, broad absorption spectrum, good stability, no toxicity, good matching of the HOMO, LUMO levels of the dye with semiconductor's bottom edge of conduction band and chemical potential of redox system of the electrolyte. Besides, the chemical bonding between the dye and semiconductor's surface is absolutely necessary for effective electron transfer. The ideal sensitizer for nanocrystalline TiO_2 particles has to absorb all the light below a threshold wavelength of about 900nm. Moreover it has to carry out carbolxylate or phosphonate groups which are permanently grafted on oxide surface by chemical bonds so as after excitation to inject electrons into the semiconductor with a quantum yield close to unity. The stability of the sensitizer is ensured by 100 million turnover cycles which refer to approximate twenty years of light soaking (Grätzel & Durrant, 2008). The common sensitizers for DSSCs are ruthenium complexes with bipyridine ligands and they follow the structure $ML_2(X)_2$ where L is the organic ligand and M the metal ion (either Ru or Os) and X can be cyanide, thiocarbamate or thiocyanate groups. Electron transfer from sensitizer to semiconductor after optical excitation is based on metal to ligand charge transfer and then the transfer to the semiconductor via the chemical bond between them. The N3 dye (*cis*-bis(isothiocyanato)bis(2,2'-bipyridyl-4,4'-dicarboxylato)-ruthenium(II)) was first reported as the most efficient sensitizer for DSSCs (Nazeeruddin et al., 1999). Then Black Dye [*cis*-

diisothiocyanato-bis(2,2'-bipyridyl-4,4'-dicarboxylato)   ruthenium(II)   bis(tetrabutyl ammonium) was also introduced by Grätzel and co-workers as a most efficient sensitizer because it covers solar light in longer wavelengths than N3 (Nazeeruddin et al., 2001). Modified N3 with tetrabutyl ammonium groups (N719) triisothiocyanato-(2,2':6',6"-terpyridyl-4,4',4"-tricarboxylato) ruthenium(II) tris(tetra-butyl ammonium) was finally found to be the most applicable dye in DSSCs' technology as it enhances the open circuit voltage of the cells of at least 15%. Next generation of dyes is based on the formula of N3 while it contains different size groups on the ligands covering two basic demands: (a) chemical stability and good penetration of electrolyte because of suitable organic groups (b) absorbance in longer wavelengths. Recent years the combination of dye properties with organic p-type semiconducting side groups seems to attract much attention. Another case of sensitizers is pure organic dyes in replacement of costly ruthenium complexes. Metal free sensitizers for DSSCs are referred: hemicyanines, indoline dyes, phthalocyanines, coumarins, perylene derivatives etc. Promising results have been obtained where in the case of D149 indoline dye an efficiency of 9.5% was recorded while SQ2 (5-carboxy-2-[[3-[(2,3-
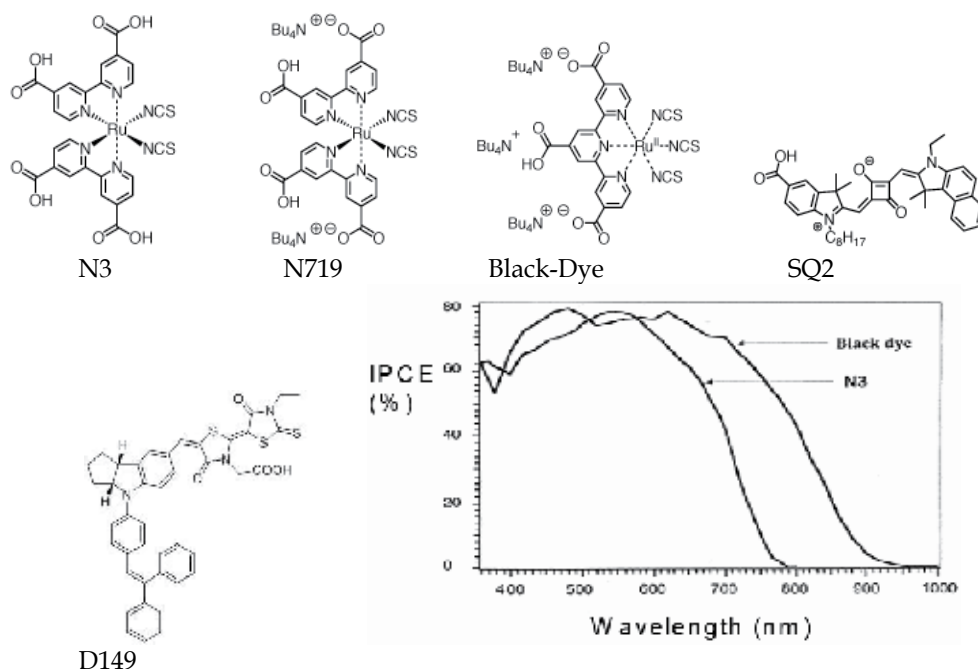
Fig. 6. Incident Photon to current efficiency for N3 and Black dye (Grätzel, 2006).

dihydro-1,1-dimethyl-3-ethyl-1H-benzo[e]indol-2-ylidene)   methyl   ]-2-hydroxy-4-oxo-2-cyclobuten-1-ylidene]methyl]-3,3-dimethyl-1-octyl-3H-indolium) an efficiency of 8% was also recorded (Goncalves et al., 2008).   Finally the strengths and weaknesses of organic dyes in DSSCs are the followings:
The strengths are:
• They exhibit high absorption coefficient (abundant π→π* within molecules)
• it is easy to design dyes with various structures and adjust absorption wavelength range

- uses no metal and they have no limitation to resources
- lower cost than organic metal dye and enables synthesis.

While the weaknesses of organic dyes are:

- still lower efficiency than organic metal dye
- short post-absorption excited state (π*) lifetime
- narrow absorption spectrum wavelength in visible ray field that it is difficult to absorb light from all visible range.

3.3 Electrolytes

The key composition elements for DSSC include fluorinated tin oxide (FTO) which is used for either electrode substrate, nanoparticulated oxide semiconductor layer like TiO_2 and ZnO, sensitizer, metallic catalysts like platinum which plays the role of the opposite electrode and the electrolyte which includes redox couple and it is positioned between the two electrodes. The composition and the form of the electrolyte have great affect on the total energy conversion efficiency. The majority of the proposed DSSCs is based on liquid electrolytes with a variety of solvents where an overall maximum efficiency of ~12% was finally achieved. Nevertheless, there are still questions which own an answer about the stability and sealing in order to prevent the leakage of the solvent. Solid or quasi solid electrolytes could be an answer to the questions. In the case of solid electrolytes we may refer polymeric materials which incorporate the iodide/triiodide redox, organic hole transporting materials or inorganic p-type semiconductors. As quasi-solid electrolytes we can refer composite organic/inorganic materials which appear as a gel or highly viscous ionic liquids.

3.3.1 Liquid electrolytes

The electrolyte is generally composed with oxidation-reduction of I^-/I_3^- where LiI, NaI, alkyl ammonium iodine or imidazolium iodine is used for materials of I^- ion. For instance, 0.1M LiI, 0.05M I_2, and 0.5M *tert*-butyl pyridine (TBP) are mixed in acetonitrile solution or 3-methoxypropionitrile, propylenecarbonate, γ-butyrolaqctone, *N*-methylpyrrolidone as alternative solvents. I^- ion is responsible for offering electrons for holes generated in dye molecule's HOMO level, whereas the oxidized I_3^- ion accepts electrons that reach counter electrode to be reduced (Snaith & Schmidt-Mende, 2007).

3.3.2 Solid electrolytes

When it is referred the use of solid electrolytes it is generally accepted that people mean the use of p-type semiconducting materials either organic or inorganic. In the case of organic materials the most popular is spiro-MeOTAD which initially proposed by Grätzel and co-workers (Kruger et al., 2002). The recorded efficiency was about 4% while new organic semiconductors were appeared in the meanwhile. Polymer based solid electrolytes are usually referred as efficient alternatives to liquid based electrolytes but the efficiency is still poor. Polymer usually containing polyether units can be used as solid electrolytes in DSSCs. These types of electrolytes are solid ionic conductors prepared by the dissolution of salts in a suitable high molar mass polymer containing polyether units (de Freitas et al., 2009).

In the case of inorganic materials, CuSCN (O'Regan & Schwartz, 1998) and CuI (Tennakone et al. 1995) are the most popular, but the efficiency of the solar cells is lower than 2% because of the poor contact between TiO_2 and p-type inorganic semiconductor. Optimized interface

between the two different types of semiconductors and instability problems of copper based p-type semiconductors have to be improved before the p-n junction between them to be more efficient.

3.3.3 Quasi-solid electrolytes

In some cases the very viscous ionic liquids but in most cases the composite organic/inorganic materials are referred as quasi-solid electrolytes. Nanocomposite organic/inorganic materials are constituted of two interpenetrating subphases which are mixed in nanoscale. The organic subphase is usually consisted of few surfactants or polyether chains and the inorganic subphase is made of an inorganic network which typically is silicon dioxide or titanium dioxide. Such nanocomposite gels can accommodate appropriate solvents within the organic subphase (that is within the pores left by the inorganic network) so that ionic conductivity can be raised to a satisfactory degree. The design and synthesis of such materials makes for fascinating research with numerous scientific and technological implications in iono-electronics, mechanics and optics. There are two prospects of making organic/inorganic blends which are depended on the specific interactions between the two subphases (scheme 1). Such blends which were obtained by simply mixing of the two components together, characterized as materials of *Class I* corresponding no covalent or iono-covalent bonds. In these materials the various components only exchange weak interactions such as hydrogen bonding Van Der Waals interactions or electrostatic forces. On the other hand, materials which are formed by chemically bonding between the two subphases are characterized as *Class II* (hybrid materials). *Class II* materials organic/inorganic components are linked through strong chemical bonds e.g. covalent, iono-covalent or Lewis acid-base bonds. Usually materials of *Class II* have better mechanical properties than *Class I* as they present rubbery behavior (Stathatos, 2005).

Sol-Gel chemistry allows the combination at the nanosize level of inorganic and organic since solubility of most organic substances, especially, hydrophobic ones, is limited in pure oxides (e.g. SiO_2) causing migration and aggregation with subsequent decrease of their functionality. Nanocomposite gels made of the two different subphases the oxide network, as the inorganic subphase and the polymer or surfactant as the organic subphase mixed in nanoscale providing in this way an access to an immense new area of materials science. In principal, in sol-gel chemistry a metal alkoxide (including silicon alkoxides) is hydrolyzed and the subsequent inorganic polymerization leads to the formation of the corresponding oxide with an oncoming condensation of the material. The whole process is carried out at ambient conditions. The process can be summarized to reactions 7 mentioned before.

An alternative route to the oxide synthesis is the slow water release in the solution with no initial water addition into the solution. In this case the existence of an organic acid in the sol is indispensable, typically acetic or formic acid as initially referred in reactions 8.

(In reactions 7a and b, as well as in the above reaction 8, only one of usually four reacting alkoxy groups is taken into account, for reasons of simplicity). Reactions 8 show that the end product of the sol-gel process is -M-O-M-, which can be obtained by successive chemical reactions. Metal ester (M-OAc) as a result of (2) can react with the metal alkoxide forming -M-O-M-, additionally; water released through esterification reaction 3 can yield oxide by the hydrolysis route. When ethanol is introduced in the sol, which is a common recipe in many works, even more water can be released by direct esterification reaction between the ethanol (EtOH) and the acetic acid (AcOH). Furthermore, intermediate M-OAc ester or -M-O-M-

oligomers may create entities which offer polymorphism to the sol-gel evolution. Thus the presence of a self-organizing agent, e.g. a surfactant, plays a crucial role in organizing the structure of the material and in creating well defined and reproducible nanophases. Slow
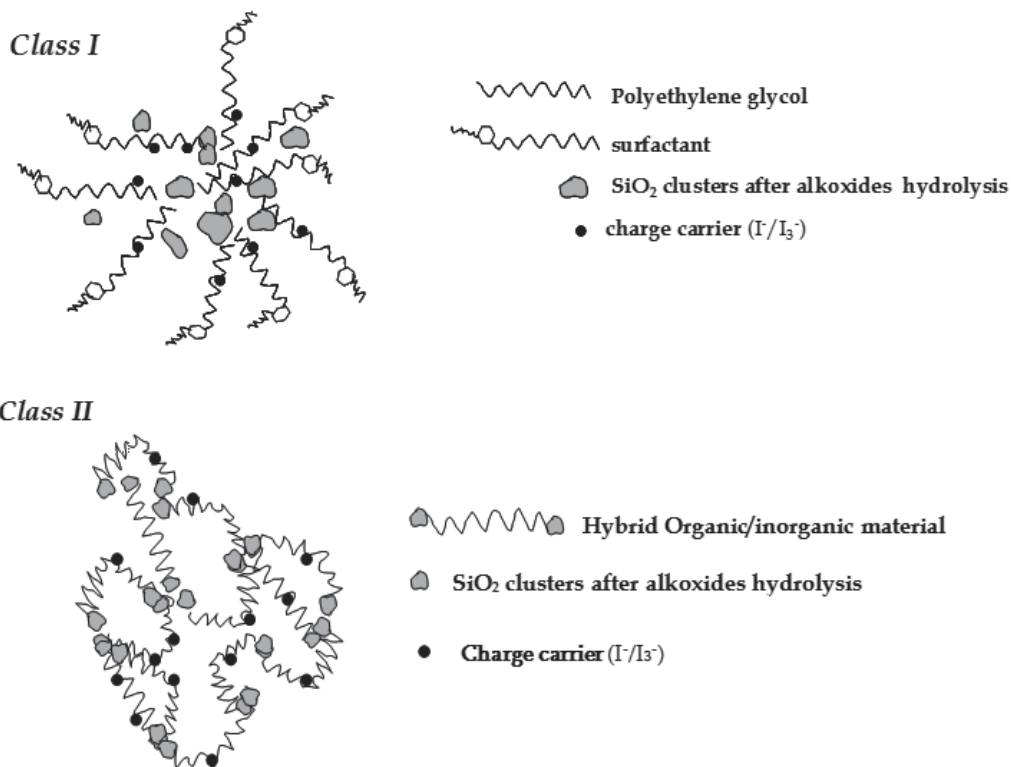

Scheme 1. (a) Class I of composite organic-inorganic electrolyte (b) Class II of hybrid organic-inorganic electrolyte

water release, organic acid solvolysis and surfactant organization are then the key factors that dictate the structure and the quality of the nanocomposite organic/inorganic gel. A different approach to the gel process of quasi-solid electrolytes is the use of modified materials (Jovanovski et al., 2006) with silicon alkoxy-groups which may easily hydrolyzed and finally lead to a gel formation (e.g. scheme 2). The modified materials could be a series of additives usually employed in liquid electrolytes e.g. benzyl-imidazoles for open circuit voltage enhancement which are now bearing alkoxy-groups for jellifying process.

As a consequence, gel electrolytes are roughly distinguished into three categories: (1) One way to make a gel electrolyte is to add organic or inorganic (or both) thickeners. Such materials may be long-chain polymers like poly (ethylene oxide) or inorganic nanoparticles like titania or silica; (2) A second way is to introduce a polymerizable precursor into the electrolyte solution and polymerize the mixture in situ; (3) a third route is to produce a gel incorporating the I^-/I_3^- redox couple through the sol-gel process by using a sol-gel precursor, like a titanium or silicium alkoxide. This precursor may be a functionalized derivative of one of the components of the electrolyte. This last method has been very successful since the sol-gel process leads to the formation of nanocomposite organic-

inorganic materials. Such materials are composed of an inorganic subphase, which binds and holds the two electrodes together and seals cell and an organic subphase, which assures dispersion of ionic species and supports ionic conductivity. The whole composition is compatible with titania nanocrystalline electrode and provides good electrical conduct and finally satisfactory ionic conductivity. Such cells are easy to make. After dye-adsorption on titania electrode, it suffices to place a small drop of the sol on the surface of the electrode and then press the counter electrode on the top by hand under ambient conditions. The two electrodes bind together while the fluid sol enters into titania nanoporous structure and achieves extensive electrical conduct.
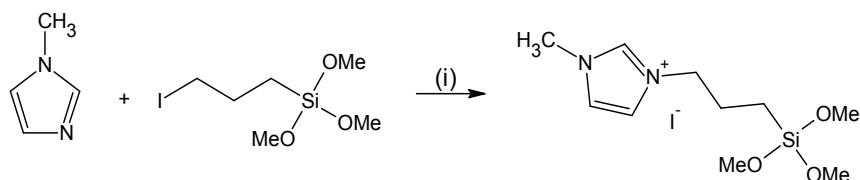
Scheme 2. Example of a hybrid organic/inorganic material used as quasi-solid electrolyte. (Jovanovski et al., 2006)

3.4 Positive electrode (catalysts)

The counter electrode is one of the most important components in the dye-sensitized solar cell. The major role of the counter electrode in addition to the cell finalization is the reduction of the redox species used as a mediator in regenerating the sensitizer after electron injection, or collection of the holes from the hole conducting material in a solid-state DSSC. Counter electrodes of dye-sensitized solar cells can be prepared with different materials and methods. Platinum, graphite, activated carbon, carbon black, single-wall carbon nanotubes, poly(3,4-ethylenedioxythiophene) (PEDOT), polypyrrole, and polyaniline can be used as catalysts for the reduction of triiodide. Moreover, for the ultimate in low-cost counter electrodes, it is also referred in literature a carbon-black-loaded stainless steel electrode for use as a novel counter electrode (Murakami & Grätzel, 2008).

4. Manufacturing of Dye sensitized solar cells

While many research groups investigate the working principles of DSSCs and new developments have been achieved concerning their efficiency and large scale applications, new companies founded in the meanwhile try to carry DSSC technology in market place evaluating all process steps are needed for industrial production. Experimental results for small size solar cells cannot directly applied in large scale DSSCs as the efficiencies measured for small size solar cells cannot be repeated in large scale (Späth et al., 2003). This is caused by the high internal resistance of FTO substrates which eliminates their efficiency and it is found to be drastically decreased. Below are referred some of the main issues which have to be taken into account before DSSCs go to a production line:

- Large area deposition of TiO_2 layers. The layers have to be homogeneous and uniform
- New methods for dye staining and electrolyte filling
- Electrical interconnection of individual cells. A major factor for limited efficiency of the DSSC is the ineffective contacts on FTO glass. The external connections of the individual cells are also a problem.

- Sealing process for modules in case of liquid electrolytes
- Long-term stability of at least 10 years for outdoor use.
- Evaluation costs, which is believed to be approximately 10% of that needed for silicon solar cells

Moreover, for the durability of the cells, it was considered necessary to replace the liquid electrolyte with quasi-solid state, solid, polymer electrolytes or p-type inorganic semiconductors as the manufacturing cost and convenience of preparation is highly simplified. However, the low manufacturing cost by using the recently developed roll-to-roll coating process especially for DSSCs creates the need of replacing the glass substrate with light weighted flexible plastic electrodes, expanding this way the area of DSSCs' applications. Three basic structures for large scale DSSCs are proposed either for high current (cells in parallel) or for high voltage (cells in series) collection:

4.1 Monolith module

The monolith modules have similar structure to amorphous silicon modules that are currently used in the market. Monolith modules use a single sheet of conductive glass (FTO) where successive layers of TiO_2 are formed on the substrate. Prior films deposition the glass is scribed by a laser in order to isolate one cell from the other. Direct wiring is not needed in this type of modules. It records relatively broad available area and high conversion efficiency, and enables simultaneous production of multiple cells (Wang et al., 2010). Usually, the TiO_2 stripes are formed according to screen printing method. It also entails shortcomings that it must secure even efficiency of each cell since it is in serial connection mode, it may by damaged due to relatively weak surface, and it rather has low transmittance. The figure 7 appears below, illustrates the manufacturing method of a monolith module:
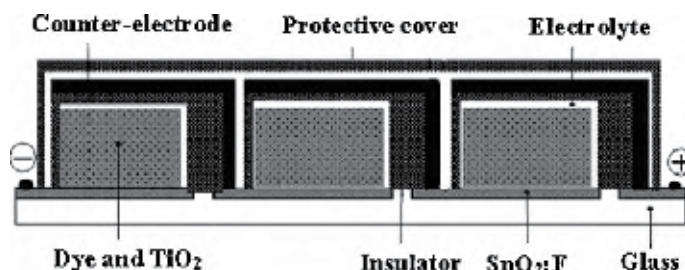

Fig. 7. Monolithic DSSC module, taken from reference (Dai et al., 2008)

4.2 Z-module

It concerns series connections of individual cells and consists of two opposing electrodes with inner-connections between neighbouring cells by a metal conductor. A sealing material is needed to protect the metal conductor from corrosion by iodide ions. It has wide available area to realize relatively high photoelectric conversion efficiency and enables transparent and double sided cell production. The Z-module entails shortcomings that it is difficult to match the junction for large-area cell production, it needs to reduce each cell efficiency deviation due to the series connection, and it is greatly affected by inner-connector reliability and conduction property (Sastrawan et al., 2006). The advantage of Z-type module fabrication is the high voltage output. On the other hand, the disadvantage of this

connection is the low active area and overall efficiency because of the complicated structure and the resulting high series resistance. Figure 8b illustrates a possible Z-module manufacturing process.

4.3 W-module

It also concerns a series connection of the cells while inner-connections are avoided. Unlike the z-module and monolith module that are manufactured in the same direction to the adjacent cell, the W-module secures a structure that are in an opposite direction of the adjacent cell. Hence, it does not require direct wiring or bus electrode and realizes high reliability since the inner-cell contact occurs directly on the substrate. It also secures a structure to maximize the available area to record relatively high conversion efficiency. It is able to simultaneously manufacture multiple cells and can also manufacture cell and module at the same time. It entails shortcomings as well that it needs to adjust the output since the amount of light absorption is different in each serially connected cell and the colorants of adjacent cells are different. The main disadvantage of this structure is the differences referred for currents of single cells which are illuminated from back side and front size resulting different values of current because of the different light transmittance of the two cells.

4.4 Parallel-module

A simple fabrication procedure of making DSSC modules is parallel connection. According to this structure small cells in the form of long stripes are connected in parallel.
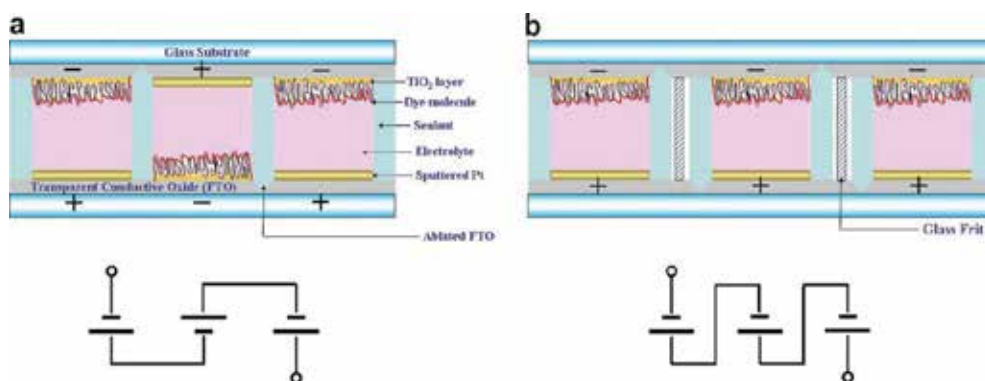

Fig. 8. (a) W-Module (b) Z-Module DSSC (Seo et al., 2009)

In this structure parallel grids utilizing conductive fingers to collect current are printed on the two electrodes of the cells. The printing method of current collectors is quite similar to that applied in conventional photovoltaics based on silicon. Common metals used as current collectors reducing the distance of electron transfer and internal resistance of FTO glass are: Ag, Cu, Ni, Ti. The solar cell efficiency is considerably reduced when it is converted to module despite the high unit cell efficiency. This is because of the increased possibility to lose electrons, which are created by light absorption, through either internal defect or recombination with hole at interface with other materials during the delivery when the electrode area to absorb light enlarges. Therefore, the efficiency radically decreases when DSSC active electrode width becomes greater than 1 cm (Wang et al., 2010).
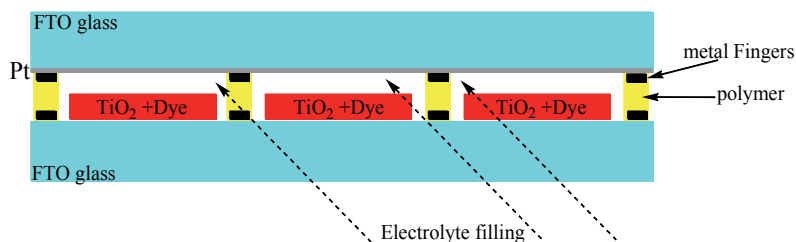
Fig. 9. Parallel connection of DSSC in a module

It is essential to design and manufacture effective packaging system along with designing photovoltaic absorption-use electrode and charge collection-use grid in order to allow the electron flow to collect without losses in large-areas like module. Mainly opposed cell module has been manufactured and researched since 1995 until now. The opposed cell module used ceramic fragment paste (glaze) or polymer in order to protect the conductive internal pattern from electrolytes. Such opposed cell R&D activities slowed down until 2001 and newly begun afterwards (Displaybank, 2010). The parallel type module records broad active area and high conversion efficiency. Large-area photoelectric chemical solar cell must use transparent electrode which has weaker electric conductivity than the metal wiring that it requires a grid to play a role of charge collection to realize smooth electron delivery. Therefore, the large-area solar cell exhibits different carrier generation and delivery from the unit cell.
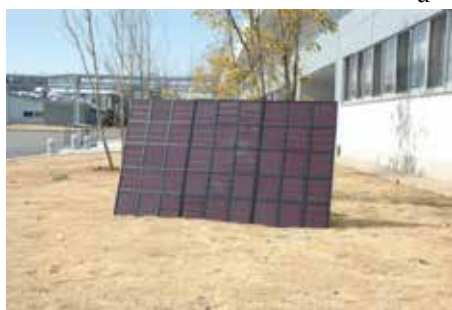
Fig. 10. (a) artistic DSSC module by Sony (http://www.sony.net/SonyInfo/technology/technology/theme/solar_01.html) and (b - c)DSSC panels made of Fujikura (http://www.fujikura.co.jp/eng/rd/field/mt.html)

A general grid in DSSCs mainly uses metal material. This is connected to active area decrease and becomes the factor to increase the generation unit cost of cell. Therefore, it is essential to secure effective module design and manufacturing technology for commercialization.

The DSSC is manufactured by a process that is relatively simpler than the conventional solar cells made of silicon and compound semiconductor solar cells, but it entails a shortcoming to generate metal corrosion when using the metal with outstanding electric conductivity as grid due to iodine based electrolyte. Therefore, the DSSC is in need for electrolyte development with outstanding activity without corrosive property or metal development with outstanding electric conductivity without being separated or corroded from the electrolyte. The inverter development must progress to be appropriate for DSSC which secures electric property that is different from the conventional silicon based solar cell.

In order to accomplish this, a circuit must be composed to match arrangement and response properties of DSSC module. The inverter technology development maximizes the DSSC power generation efficiency. The system is matched to the solar cell's generation property in order to effectively supply the power of electric condenser, which stores electricity generated during daytime, at desirable time. The commercialization of DSSC requires power system development together with unit cell efficiency enhancement technology development. The DSSC commercialization is delayed due to unprepared peripheral technologies despite the fact that its current power generation unit cost can realize commercialization (Displaybank, 2010). Right now, the ultra small high efficiency inverter technology is insufficient for module/system efficiency enhancement and manufacturing technology of module which can be installed in targets such as buildings.

5. Outlook

The quest and demand for clean and economical energy sources have increased interest in the development of solar applications. DSSCs have proved to be an alternative approach to the conventional silicon based solar cells. Research on DSSCs has grown rapidly in the recent years due to the several attractive figures of this interesting field: The international awareness of the necessity to develop new technologies in Renewable Energy Resources; The need of easy and inexpensive procedures for fabricating Solar cells; The fact that DSSCs can be transparent so that they can be integrated into mobile or immobile constructions as Photovoltaic Windows. All these features are carried by DSSCs and for this reason they are popular and they are expected to be even more popular in the near future. Till then some issues have to be overcome in order this technology considerably has commercial interest. The overall efficiency of ~12% for small size cells (~0.2cm^2) which substantially gets lower (~5%) when modules of DSSCs are prepared is a reason for further improvement is many stages of cells preparation. Improvement of the cells is focused on (a) the enhancement of electron transport and electron lifetime in the mesoporous metal oxide (b) design of new high-extinction coefficient dyes which will effectively cover the whole range of visible light and near infra red and finally (c) new stable solid electrolytes which will have effective penetration into semiconductors pores and enhanced. Moreover, in large scale applications the effective collection of the current is also an issue as the internal resistance from conductive glass substrates and metal grids which are necessary for current collection and need to be covered from corrosive electrolyte, drastically eliminate the DSSCs efficiency if they are not seriously taken into account.

6. References

Barbé, C.J.; Arendse, F.; Comte, P.; Jirousek, M.; Lenzmann, F.; Shklover, V.; Grätzel, M. (1997). Nanocrystalline titanium oxide electrodes for photovoltaic applications. *Journal of the American Ceramic Society* vol. 80, pp. 3157-3171

Birnie. DP.; Bendzko, NJ. (1999). H-1 and C-13 NMR observation of the reaction of acetic acid with titanium isopropoxide. *MATERIALS CHEMISTRY AND PHYSICS* Vol. 59, pp. 26-35

Bisquert, J.; Cahen, D.; Hodes, G.; Ruhle, S.; Zaban, A. (2004). Physical Chemical Principles of photovoltaic conversion with nanoparticulate, mesoporous dye-sensitized solar cells. *J. Phys. Chem.* vol. 108, pp. 8106-8118

Brinker, C.J.; Scherer, G.W. (1990). Sol-Gel Science, The physics and Chemistry of Sol-Gel Processing. *Academic Press, Inc*

Dai, S.; Weng, J.; Sui, Y.; Chen, S.; Xiao, S.; Huang, Y.; Kong, F.; Pan, X.; Hu, L.; Zhang, C.; Wang K. (2008). The design and outdoor application of dye-sensitized solar cells. *Inorganica Chimica Acta*. Vol. 361, pp. 786-791

de Freitas, J.N.; Nogueira, A.F.; De Paoli, M.A. (2009). New insights into dye-sensitized solar cells with polymer electrolytes. *Journal of Materials Chemistry*. Vol. 19, pp. 5279-5294

Displaybank (2010). DSSC Technology Trend and Market Forecast 2009-2013 (*www.displaybank.com)*

Hagfeldt, A.; Grätzel, M. (2000). Molecular photovoltaics. *Acc. Chem. Res.* Vol. 33, pp. 269–277

Jose, R.; Thavasi, V.; Ramakrishna S. (2009). Metal Oxides for Dye-Sensitized Solar Cells. *J. Am. Ceram. Soc.* vol. 92, pp. 289–301

Goncalves, L.M.; de Zea Bermudez, V.; Ribeiro, H.A.; Mendes, A.M. (2008). Dye-sensitized solar cells: A safe bet for the future. *Energy Environ. Sci.* vol. 1, pp. 655-667

Goldstein, J.; Yakupov, I.; Breen, B. (2010). Development of large area photovoltaic dye cells at 3GSolar. *Solar Energy Materials and Solar Cells.* Vol. 94, pp. 638-641

Grätzel, M. (2006). Photovoltaic performance and long-term stability of dye-sensitized mesoscopic solar cells. *C.R. Chimie*, vol.9, pp.578-583

Grätzel, M.; Durrant, J.R. (2008). Dye sensitized mesoscopic solar cells. *Series on Photoconversion of Solar Energy Vol.3 Nanostructured and Photoelectrochemical systems for solar photon conversion*. Imperial College Press.

Hinsch, A.; Brandt, H.; Veurman, W.; Hemming, S.; Nittel, M.; Wurfel, U.; Putyra, P.; Lang-Koetz, C.; Stabe, M.; Beucker, S.; Fichter, K. (2009). Dye solar modules for façade applications: Recent results from project ColorSol. *Solar Energy Materials and Solar Cells.* Vol. 93, pp. 820-824

Huang, C.-Y.; Hsu, Y.-C.; Chen, J.-G.; Suryanarayanan, V.; Lee, K.-M.; Ho, K.-C. (2006). The effects of hydrothermal temperature and thickness of TiO_2 film on the performance of a dye-sensitized solar cell. *Solar Energy Materials and Solar Cells*. Vol. 90, p. 2391

Ivanda, M.; Musić, S.; Popović, S.; Gotić, M. (1999). XRD, Raman and FT-IR spectroscopic observations of nanosized TiO_2 synthesized by the sol–gel method based on an esterification reaction. *Journal of Molecular Structure*. Vol. 480-481, pp. 645-649

Jovanovski, V.; Stathatos, E.; Orel, B.; Lianos, P. (2006). Dye-sensitized solar cells with electrolyte based on a trimethoxysilane-derivatized ionic liquid. *Thin Solid Films*. Vol. 511, pp. 634-637

Kruger, J.; Plass, R.; Gratzel, M.; Matthieu, H. (2002). Improvement of the photovoltaic performance of solid-state dye-sensitized device by silver complexation of the sensitizer cis-bis(4,4 '-dicarboxy-2,2 ' bipyridine)-bis(isothiocyanato) ruthenium(II). *Applied Physics Letters.* Vol. 81, pp. 367-369

Law, M.; Greene, LE.; Johnson, JC.; Saykally, R.; Yang, PD. (2005). Nanowire dye-sensitized solar cells. *Nature Materials.* Vol. 4   pp. 455-459

Murakami, TN.; Gratzel, M. (2008). Counter electrodes for DSC: Application of functional materials as catalysts. Inorganica Chimica Acta. Vol. 361, pp. 572-580

Murakami, T.N.; Kijitori, Y.; Kawashima N.; Miyasaka, T. (2004). Low temperature preparation of mesoporous TiO_2 films for efficient dye-sensitized photoelectrode by chemical vapor deposition combined with UV light irradiation. *J. Photochem. Photobiol. A: Chem.* Vol. 164, p. 187

Nazeeruddin, M. K.; Kay, A.; Rodicio, I.; Humphry-baker, R.; Muller, E.; Liska, P. (1993). Conversion of light to electricity by cis-X2-bis(2,2'-bipyridyl-4,4'-dicarboxylate)ruthenium(II) charge-transfer sensitizers (X = Cl⁻, Br⁻, I⁻, CN⁻ and SCN⁻) on nanocrystalline TiO_2 electrodes. *J. Am. Chem. Soc.* Vol. 115, pp.6382–6390

Nazeeruddin, M. K.; Pechy, P.; Renouard, T.; Zakeeruddin, S. M.; Humphry-Baker ,R.; Comte, P. (2001). Engineering of efficient panchromatic sensitizers for nanocrystalline TiO_2-based solar cells. *J. Am. Chem. Soc*. Vol. 123, pp. 1613–1624.

Papageorgiou, N.; Athanassov, Y.; Armand, M.; Banhote, P.; Lewis, L.N.; Spivack, J.L.; Gasaway, S.; Williams, E.D.; Gui, J.Y.; Manivannan, V.; Siclovan, O.P. (2006). A novel UV-mediated low-temperature sintering of TiO2 for dye-sensitized solar cells. *Solar Energy Materials and Solar Cells*. Vol. 90 p. 1041

O'Regan, B.; Grätzel, M. (1991). A low-cost, high-efficiency solar-cell based on dye-sensitized colloidal TiO_2 films. *Nature,* vol. 353, pp.737–740

O'Regan, B.; Schwartz, DT. (1998). Large enhancement in photocurrent efficiency caused by UV illumination of the dye-sensitized heterojunction TiO2/RuLL ' NCS/CuSCN: Initiation and potential mechanisms. *Chemistry of Materials.* Vol. 10, pp. 1501-1509

Peter, L.M.; Wijayantha, K.G.U. (2000). Electron transport and back reaction in dye sensitised nanocrystalline photovoltaic cells. *Electrochim. Acta.* vol. 45, pp. 4543–4551

Petterson, H.; Azam, A.; Grätzel, M. (1996). The Performance and Stability of Ambient Temperature Molten Salts for Solar Cell Applications.   *Electrochem. Soc.* Vol. 143, pp. 3099-3108

Pope, E.J.A.; Mackenzie, J.D. (1986). Sol-gel processing of silica: II. The role of the catalyst. *Journal of Non-Crystalline Solids*. Vol. 87, pp. 185-198

Sastrawan, R.; Beier, J.; Belledin, U.; Hemming, S.; Hinsch, A.; Kern, R.; Vetter, C.; Petrat, F.M.; Prodi-Schwab, A.; Lechner, P.; Hoffmann, W. (2006). A glass frit-sealed dye solar cell module with integrated series connections. *Solar Energy Materials and Solar Cells*. Vol. 90 pp. 1680-1691

Sayama, K.; Sugihara, H.; Arakawa, H. (1998). Photoelectrochemical properties of a porous Nb$_2$O$_5$ electrode sensitized by a ruthenium dye. *Chem. of Materials* vol. 10, pp. 3825–3832.

Seo, H.; Son, M.; Hong, J.; Lee, D.-Y.; An, T.-P.; Kim, H.; Kim, H.-J. (2009). The fabrication of efficiency-improved W-series interconnect type of module by balancing the performance of single cells. *Solar Energy.* Vol. 83, pp. 2217-2222.

Snaith, H.J.; Schmidt-Mende, L. (2007). Advances in Liquid-Electrolyte and solid-state dye-sensitized solar cells. *Advanced Materials*. Vol. 19, pp. 3187-3200

Späth, M.; Sommeling, P.M.; van Roosmalen, J.A.M.; Smit, H.J.P.; van der Burg, N.P.G.; Mahieu, D.R.; Bakker, N.J.; Kroon, J.M. (2003). Reproducible manufacturing of Dye-sensitized solar cells on a semi-automated baseline. *Progress in Photovoltaics: Research and applications.* Vol. 11 pp. 207-220

Stathatos, E.; Lianos, P.; Tsakiroglou, C. (2004). Highly efficient nanocrystalline titania films made from organic/inorganic nanocomposite gels. *Microporous and Mesoporous Materials*. vol. 75, pp. 255-260

Stathatos, E.; Choi, H.; Dionysiou, D.D. (2007). Simple procedure of making room temperature mesoporous TiO$_2$ films with high purity and enhanced photocatalytic activity. *Environmental Engineering Science.* vol. 24, p. 13

Stathatos, E.; Lianos, P.; Del Monte, F.; Levy, D.; Tsiourvas, D. (1997). Formation of TiO$_2$ nanoparticles in reverse micelles and their deposition as thin films on glass substrates. *Langmuir*. Vol. 13, pp. 4295-4300

Stathatos, E. (2005). Organic-inorganic nanocomposite materials prepared by the sol-gel route as new ionic conductors in quasi solid state electrolytes.   Ionics. Vol. 11 pp. 140-145

Tennakone, K.; Kumara, GRRA.; Kottegoda, IRM.; Perera, V. P. S. (1999). An efficient dye-sensitized photoelectrochemical solar cell made from oxides of tin and zinc. Chemical Communications pp. 15-16

Tennakone, K.; Kumara, GRRA.; Kumarasinghe, AR.; Wijayantha, KGU.; Sirimanne, PM. (1995). A dye sensitized nano-porous solid state photovoltaic cell. *Semiconductor science and Technology.* Vol. 10 pp. 1689-1693

Uchida, S.; Tomiha, M.; Takizawa, H.; Kawaraya, M. (2004). Flexible dye-sensitized solar cells by 28 GHz microwave irradiation. *J. Photochem. Photobiol. A: Chem.* Vol. 164, p. 93

Wang, C.; Deng, ZX.; Li, YD. (2001). The synthesis of nanocrystalline anatase and rutile titania in mixed organic media. *Inorganic Chemistry*. Vol. 40,   pp. 5210-5214

Wang, L.; Fang, X.; Zhang, Z. (2010). Design methods for large scale dye-sensitized solar modules and the progress of stability research. *Renewable and Sustainable energy reviews.* Vol. 14, pp. 3178-3184

Wu, J.; Lan, Z.; Hao, S.; Li, P.; Lin, J.; Huang, M.; Fang, L.; Huang, Y. (2008). Progress on the electrolytes for dye-sensitized solar cells. *Pure Applied Chemistry*, vol.80, No.11, pp.2241-2258

Zhang, Q.; Cao, G. (2011). Nanostructured photoelectrodes for dye-sensitized solar cells. *Nano Today* vol. 6, pp. 91−109

Zhang, W.; Cheng, Y.; Yin, X.; Liu, B. (2011). Solid-state dye-sensitized solar cells with conjugated polymers as hole-transporting materials. *Macromolecular Chemistry and Physics.* Vol. 212, pp. 15-23

Zhu, K.; Schiff, E.A.; Park, N.-G.; van de Lagemaat, J.; J. Frank, A. (2002). Determining the locus for photocarrier recombination in dye-sensitized solar cells. *Applied Physics Letters.* Vol.80, pp. 685-687

Xia, J.; Yanagida, S. (2011) Strategy to improve the performance of dye-sensitized solar cells: Interface engineering principle. *Solar Energy* in press available in www.sciencedirect.com

Edited by Leonid A. Kosyachenko

The second book of the four-volume edition of "Solar cells" is devoted to dye-sensitized solar cells (DSSCs), which are considered to be extremely promising because they are made of low-cost materials with simple inexpensive manufacturing procedures and can be engineered into flexible sheets. DSSCs are emerged as a truly new class of energy conversion devices, which are representatives of the third generation solar technology. Mechanism of conversion of solar energy into electricity in these devices is quite peculiar. The achieved energy conversion efficiency in DSSCs is low, however, it has improved quickly in the last years. It is believed that DSSCs are still at the start of their development stage and will take a worthy place in the large-scale production for the future.

IntechOpen